Numerical Investigation for Slope Stability of Expansive soils and Large Strain Consolidation of Soft Soils

By

SHUNCHAO QI

B.Sc., Sichuan University, China

M.Sc., Zhejiang University, China

Thesis submitted in partial fulfillment of the requirements of

Doctor of Philosophy in Civil Engineering Degree

Department of Civil Engineering, Faculty of Engineering

University of Ottawa

December, 2017

The Doctor of Philosophy in Civil Engineering is a Joint Program between Carleton University and University of Ottawa, which is administered by the Ottawa-Carleton Institute for Civil Engineering

ABSTRACT

Several geotechnical processes can only be reliably interpreted by taking account of the soil-atmosphere interactions. This thesis investigates two geotechnical problems involving soil-atmosphere interactions that drive water flow through the soil skeleton in two opposite directions; Problem 1: slope failure in expansive soils induced by water infiltration, Problem 2: large strain consolidation of soft soils induced by water evaporation. Both problems are of practical interest for safe and economical design of various geotechnical infrastructures. Two major geotechnical activities in the world; namely, the construction of water transfer canal in expansive soil area in China and the deposition of oil sands and hard rock tailings in Canada can be cited as classic examples of Problems 1 and 2, respectively. In such problems, substantial zones of the domain may switch between an unsaturated and saturated condition. Therefore, rational analysis requires simultaneous modelling of both unsaturated and saturated soil behaviour.

The first goal of this thesis is to investigate the influence of swelling (the most characteristic behaviour of expansive soils) on slope stability using numerical methods. Swelling of expansive soils contributes to slope instability during rainfall because of two key reasons (*i*) soil swelling affects the flow process that actually induces swelling, (i.e. a typical coupling phenomenon), and (*ii*) swelling-induced stress redistribution and displacement development. In this thesis, the first effect is studied by a coupled (mechanical-hydraulic) numerical analysis of the response of a slope to rainfall using commercial software (GeoSlope). The second effect, the swelling-induced stress redistribution and displacement development after wetting, is tracked using a newly developed numerical program. In the program strain softening behaviour is introduced into the elasto-plastic Mohr-Coulomb Model for modelling unsaturated soil. A novel stress (net stress and suction)-dependent model for moduli of elasticity, combined with the predictive model for shear strength based on Soil Water Retention Behaviour are incorporated into the numerical program to achieve a smooth transition between saturated and unsaturated states. The results show that soil swelling can decrease the factor of safety by accelerating the wetting front depth due to hydro-mechanical coupling, while changes of sliding mass geometry has a

negligible influence. The change of stress regime associated with soil swelling is significant to induce plastic strain softening (swelling-induced softening) and contribute to the slope failures.

The second goal of thesis is to develop a novel computer program for simulation of large strain consolidation of soft soil under both self-weight and evaporation conditions. This program is both theoretically sound and practically applicable. Several basic/advanced constitutive models for unsaturated soils, including State Surface Model (SSM), Barcelona Basic model (BBM), Glasgow Coupled model (GCM) and bounding surface water retention model, are innovatively implemented into a piece-wise linear framework solved using finite difference technique. The developed program is referred to as UNSATCON-(ML), which has been tested using (a) existing analytical/numerical solutions and (b) various laboratory and field studies for single-layer and multiple-layer deposition of hard rock and oil sands tailings. Features of UNSATCON-(ML) that are improvements over existing models typically used to analyze consolidation-desiccation in soft soils include: (i) coupling of soil large deformation with true unsaturated water flow; (ii) correct reproduction of the shrinkage behaviour of soil under evaporation-induced desiccation; (iii) smooth transition between saturated and unsaturated states despite that some selected models are established using two independent stress variables, (iv) ensuring strictly mass conservation of water, and (v) simulation of irrecoverable volume change and hydraulic hysteresis to properly analyze multilayer tailings deposition. A number of hypothetical field case analyses are carried out using UNSATCON-ML, illustrating its applicability to industry.

ACKNOWLEDGEMENTS

The opportunity to pursue my PhD studies would not have been possible without the guidance of my supervisors, Professor Sai K. Vanapalli, and Professor Paul H. Simms. I would like to express the deepest appreciation to my supervisor Professor Sai K. Vanapalli for his continuous motivation, patience, and encouragement throughout my doctoral study. His ability in explaining unsaturated soil behaviour (which is complicated), in a simple way and in an environment that is relaxing (at SITE cafe), has been undoubtedly helpful during this work, particularly, during the hardest time of my study. I owe my deepest gratitude to my co-supervisor, Professor Paul H. Simms, for providing great insights and timely encouragements. I have been continuously encountering countless obstacles and challenges in developing the computer program UNSATCON-ML from ground up, which can never be overcome without his constructive and enlightening suggestions during those important weekly discussions. Thank you very much for the countless hours of revision (including holidays) and advice on shaping this thesis on a tight schedule.

Thank you for both their high standard of supervision. Without their generous help this dissertation would have not been completed. The benefits I gain from you are not just regarding the way I do research, but also the way I present and deliver my work through multiple routes, which is one important aspect that I need to improve further. Their inputs will definitely and continuously have profound influence on me in the future. I feel so lucky to have enjoyed the significant research freedom and benefits in the *Joint Program between Carleton University and University of Ottawa*.

The financial supports received from the *China Scholarship Council (CSC) - University of Ottawa Joint Scholarship*, are gratefully acknowledged. I am also grateful again to both of my supervisors for generous financial support allowing for great mobility, attendance of various conferences, LARAM high-level doctoral school, COSIA/NSERC workshop, the Annual Michael Bozozuk Student Forum, and having these excellent opportunities to learn form leading researchers from North-America and others.

I am also grateful to Professors D. V. Griffiths (Colorado School of Mines, USA), Sivathayalan, Magdi Mohareb, Julio Angel Infante Sedano for serving as committee members and providing insightful criticism and guidance. Your comments were valuable for improving this thesis.

Thank you to all my fellow graduate students. I am very lucky to have had the opportunity to work with them and to be inspired by all of them. Our discussions and debates regarding theories, results and construction practices provided an excellent dimension to my learning experience. A special mention goes to Dr. Weilie Zou, Dr. Won, Fathi, Hana, Javad, Singyu, Zhong, Xueming, Mohammed, Yunlong, Ping, Hongyu, Junping, Penghai, Xiaokun, Xiuhan, Shabnam, Yagmur, Muhammad Salam, Oswaldo, Hissan.

The author is indebted to his family for their encouragement, support and understanding throughout his education. Thank you to my family for being so accommodating all these years.

Contents

ABSTRACT ..... **II**

ACKNOWLEDGEMENTS ..... **IV**

List of Figures ..... **XI**

List of Tables ..... **XIX**

Chapter 1 Introduction **1**

1.1 Background 1
1.1.1 Slope stability of expansive soil 1
1.1.2 Significance of evaporation on consolidation and strengthening of soft soil - using tailings management as an example 6
1.2 Objectives of the study and Intended Novel Contributions 17
1.3 Outlines of the thesis 19
1.4 References 21

Chapter 2 Literature Review **24**

2.1 Constitutive modelling of unsaturated soil 24
2.1.1 State surface model 30
2.1.2 Elasto-plastic model 32
2.1.3 Models for unsaturated expansive soils 38
2.1.4 Water retention model 39
2.1.5 Shear strength of unsaturated soil 42
2.2 Slope stability analysis 44
2.2.1 Definitions of FS and calculation method 45
2.2.2 Infinite (1D) slope stability analysis 50
2.2.3 Two and three-dimensional (2D and 3D) slope stability analysis 52
2.3 Existing models for large strain consolidation 54
2.3.1 Large strain consolidation theory 54
2.3.2 Existing models that consider evaporation 61
2.3.3 Development history of UNSATCON-ML prior to writing of the thesis 63
2.4 Conclusion 66
2.5 References 70

Chapter 3 Hydro-mechanical Coupling Effect on Slope Stability of Expansive Soils **79**

3.1 Introduction 79
3.2 Slope stability analysis of unsaturated soils 83

3.2.1 Coupled and uncoupled analyses 83
3.2.1.1 Governing equations 83
3.2.1.2 Constitutive relationships 84
3.2.1.3 Numerical uncoupled and coupled solutions 86
3.2.2 Infinite slope formulation 87
3.2.3 Procedures followed for evaluating the expansive soil slope stability 91
3.3 Numerical studies 92
3.3.1 Model slope establishment 92
3.3.2 Initial conditions 93
3.3.3 Boundary conditions 94
3.3.4 Soil properties 95
3.4 Results presentation 102
3.4.1 Variation of PWP profile 102
3.4.1.1 Effect of elasticity parameters value on predicted PWP 103
3.4.1.2 PWP profile variation 107
3.4.2 Evolution of FS profile 112
3.5 Discussions 116
3.5.1 Strength and failure mechanism 116
3.5.2 Influence of change of slope geometry due to swelling on the stability 120
3.5.3 Selection of appropriate hydraulic properties for modeling expansive soils 121
3.6 Conclusions 124
3.7 References 128

Chapter 4 Effect of Swelling on the Stability of Slopes in Expansive Soils 132

4.1 Introduction 133
4.2 Elasto-plastic constitutive matrix for unsaturated soils 137
4.3 Infinite slope formulation for expansive soils 142
4.3.1 Stress field within an infinite slope profile 142
4.3.2 Yield function for infinite slope formulation 144
4.3.3 Analyses of infiltration-induced stress evolution in the infinite slope formulation 145
4.3.4 Collapse of expansive soil infinite slope 152
4.3.5 Evaluation of infinite slope stability in expansive soil 153
4.4 Description of the illustrative example 154
4.5 Numerical results 160
4.5.1 Comparison between softening and non-softening analyses 161
4.5.2 Evolution of stress at the failure depth 165
4.5.3 Results of parametric analysis 171
4.5.3.1 Effect of initial stress ratio 172
4.5.3.2 Effect of softening rate 176
4.5.3.3 Effect of slope angle 179
4.6 Discussion 181
4.7 Conclusions 183
4.8 References 187

Chapter 5 Simulating the hydraulic and mechanical responses of an unsaturated expansive soil slope to rainfall: a case history 192

5.1 Introduction 193
5.2 General information of the field test 196
5.3 Methodology 199
5.3.1 Hydraulic analysis 199
5.3.2 Mechanical analysis 202
5.4 Simulating hydraulic response 207
5.4.1 Model description 207
5.4.2 Soil hydraulic properties 209
5.4.3 Pore water pressure 213
5.5 Simulating mechanical response 217
5.5.1 Model description 217
5.5.2 Soil mechanical properties 220
5.5.3 Horizontal/vertical stress ratio 224
5.5.4 Swelling and displacement 230
5.6 Discussion on applicability of infinite slope formulation to analysis of wetting-induced expansive soil slope failure 233
5.7 Concluding remarks 234
5.8 References 239

Chapter 6 Piecewise-Linear Formulation of Coupled Large Strain Consolidation and Unsaturated Flow. I: Model Development and Implementation 248

6.1 Introduction 249
6.2 The model 251
6.2.1 Constitutive relationships 251
6.2.2 Configuration and initialization 255
6.2.3 Flow in saturated and unsaturated zones and top boundary condition 256
6.2.4 Deformation in unsaturated zone 260
6.2.5 Deformation in saturated zone and quasi-unsaturated formulation 263
6.2.6 Time increment 265
6.3 Code development 266
6.4 Verification against Saturated Large Strain Consolidation 271
6.5 Verification against an analytical solution to unsaturated flow 273
6.6 Conclusion 277
6.7 References 281

Chapter 7 Piecewise-Linear Formulation of Coupled Large Strain Consolidation and Unsaturated Flow. II: Testing and Performance 284

7.1 Introduction 285
7.2 Verification of Quasi-Unsaturated Analysis 286
7.3 Column Test 290
7.3.1 Column test and material properties 290
7.3.2 Calibration of hydraulic properties 294
7.3.3 Comparison between predictions and measurements 297
7.4 Case Study of Field Trial of Deposition of Polymer-amended MFT 302
7.4.1 General information on the field trial 302
7.4.2 Comparison between the SA, the QUA, and the UA 304

7.4.3 Comparison between UA predictions and field measurements 308
7.5 Model Limitations 311
7.6 Conclusion 312
7.7 References 315

Chapter 8 Piecewise-linear formulation of large strain consolidation with irrecoverable volume change and hydraulic hysteresis 317

8.1 Introduction 318
8.2 The model 319
8.2.1 Constitutive relationships 319
8.2.2. The piece-wise linear formulation 325
8.3 Numerical implementation 327
8.4 Modelling of multi-layer deposition of gold tailings 334
8.4.1 Mesoscale Drying box test 334
8.4.2 Initial and boundary conditions 334
8.4.3 Material properties 335
8.4.4 Results 338
8.5 Discussion and limitations 347
8.6 Conclusions 348
8.7 References 353

Chapter 9 Enhanced piece-wise linear formulation of large strain consolidation using other soils models 365

9.1 Introduction 365
9.2 BBM implementation 366
9.2.1 Analytical form of BBM 366
9.2.2 Implementing BBM into UNSATCON-ML 371
9.2.3 Reanalysing the mesoscale drying box test 375
9.3 Bounding surface SWRM implementation 379
9.3.1 Expressions of the SWRM by Gallipoli (2015) 379
9.3.2 Testing the correctness of implementation 382
9.3.3 Reanalysing the mesoscale drying box test 388
9.4 GCM implementation 392
9.4.1 Analytical form of GCM 392
9.4.2 Implementing GCM into UNSATCON-ML 403
9.4.3 Reanalysing the mesoscale drying box test 407
9.5 Conclusion 420
9.7 References 426

Chapter 10 Hypothetical field case analysis of tailings deposition 428

10.1 Introduction 428
10.2 Hypothetical case analyses of oil sands tailings deposits 429
10.2.1 Material properties and boundary condition 429
10.2.2 The influence of deposition season 431
10.2.3 The influence of multi-layer deposition 437
10.2.4 Analyses with different soil models (SSM and GCM) 451

10.3. Hypothetical case analyses of hard rock tailings deposits 469
10.3.1 Material properties..... 469
10.3.2 Simulating the column test on hard rock tailings 471
10.3.3 Hard rock tailings field case analysis 477
10.4. Conclusion..... 491
10.5. References 494

Chapter 11 Conclusions and Recommendations for Future Work 503

11.1 Conslusions 503
11.1.1 Stability of expansive soil 504
11.1.2 Large strain consolidation of soft soil 505
11.2 Recommendations for future work..... 510

***References*..... 513**

***Publications*..... 535**

List of Figures

Fig. 1.1 Extremely arid, arid, and semi-arid areas of the world (Fredlund and Rahardjo 1993).

Fig. 1.2. An illustration of several different tailings ponds (from http://www.gardguide.com/index.php?title=Chapter_6)

Fig. 1.3. An illustration of tailings seepage recapturing and monitoring systems (Ministry of Environment and Sustainable Resource Development, Government of Alberta, http://www.nrcan.gc.ca/energy/publications/18752).

Fig. 1.4. Tailings ponds are repositories for the toxic sludge that is produced when bitumen oil is separated from sand and gravel. Wildlife often mistake them for freshwater lakes. (https://www.thestar.com/news/atkinsonseries/2015/09/04/tailings-ponds-a-toxic-legacy-of-albertas-oilsands.html).

Fig. 1.5. Subaerial deposition of mine tailings

Fig. 2.1. The marvelous contribution of water in (a) sandcastle and (b) a natural wonder at a beach

Fig. 2.2. Soils partially saturated with water (a) at higher degree of saturation and (b) at lower degree of saturation.

Fig. 2.3. Differential settlement of foundation due to non-uniform distribution of water content, particularly due to wetting-induced collapse of unsaturated soil.

Fig. 3.1. The forces acting on the infinite slope

Fig. 3.2. Stability analysis procedure based on coupled and uncoupled analyses

Fig. 3.3. Established model slope

Fig. 3.4. Hydraulic and mechanical boundary conditions

Fig. 3.5. SWCCs of Regina clay

Fig. 3.6. Hydraulic conductivities of Regina clay

Fig. 3.7. Variation of modulus of elasticity with respect to suction for Regina clay predicted using semi-empirical model (Oh et al. 2009, Vanapalli and Oh 2010)

Fig. 3.8. Monthly precipitation in Regina, Canada in 2013

Fig. 3.9. Illustration of *E* profile at some time steps for middle slope

Fig. 3.10. Investigation locations and points within surface layer

Fig. 3.11. Effect of elasticity parameters value on predicted PWP for (a) At depth of 0.75; (b) At depth of 1.50 m; (c) At depth of 2.25 m

Fig. 3.12. Variation of PWP profile for (a) Coupled analysis at L1; (b) Coupled analysis at L2; (c) Coupled analysis at L3; (d) Uncoupled analysis at L1; (e) Uncoupled analysis at L2; (f)

Uncoupled analysis at L3

Fig. 3.13. Volumetric water content profile at L2 after 150 days of rainfall

Fig. 3.14. The depth of wetting front with respect to time at location L1

Fig. 3.15. Suction at wetting front with time and depth for (a) L1; (b) L2; (c) L3

Fig. 3.16. Evolution of FS profile for (a) Coupled analysis at L1; (b) Coupled analysis at L2; (c) Coupled analysis at L3; (d) Uncoupled analysis at L1; (e) Uncoupled analysis at L2; (f) Uncoupled analysis at L3

Fig. 3.17. Variation of critical FS with respect to time and depth for (a) L1; (b) L2; (c) L3

Fig. 3.18. The critical FS after 150 days at location L2

Fig. 3.19. Bimodal SWCC and Predicted shear strength for surficial layer for (a) Bimodal SWCC for the surficial layer in the suction range of interest in the present study; (b) Variation of shear strength with suction predicted using Vanapalli et al. model (1996) based on the bimodal SWCC

Fig. 3.20. Potential failure mechanism triggered by rainfall

Fig. 3.21. Vertical displacement with time along the ground surface

Fig. 3.22. The swell-shrink path of Regina clay (modified after Azam and Ito (2011))

Fig. 3.23. The corrected and uncorrected SWCC for Regina clay

Fig. 3.24. PWP after 90 days at L2 using corrected SWCC

Fig. 3.25. FS after 90 days at L2 using corrected SWCC

Fig. 4.1. Geometrical scheme of the infinite slope.

Fig. 4.2. Evolution of stress state within the infinite slope upon wetting: (a) FIRST PHASE; (b) SECOND PHASE; (c) THIRD PHASE.

Fig. 4.3. Variation of mobilized material parameters with plastic deviatoric shear strain.

Fig. 4.4. The SWCC used in the seepage analysis.

Fig. 4.5. The permeability functions used in the seepage analysis.

Fig. 4.6. The nonlinear elasticity parameters: (a) variation of E with respect two stress state variables; (b) variation of H with respect to two stress state variables (after Vu and Fredlund 2006).

Fig. 4.7. The variation of pore water pressure profile within the infinite slope from seepage analysis.

Fig. 4.8. Variation of FS profile from non-softening analysis.

Fig. 4.9. Variation of FS profile from softening analyses.

Fig. 4.10. Evolutions of stress profile, σ_η, at several elapsed times from non-softening and softening analyses.

Fig. 4.11. The evolution of suction at the several depths with time.

Fig. 4.12. The evolution of net stress in the sloping direction, σ_η, at the several depths with time.

Fig. 4.13. The evolution of angle of internal friction at the several depths with time

Fig. 4.14. The evolution of FS at the several depths with time

Fig. 4.15. The evolution of stress in three dimensional space at the several depths with time

Fig. 4.16. The stress state at the failure depth at several typical elapsed times in two dimensional space plots: (a) elastic phase; (b) perfectly plastic phase; (c) softening phase

Fig. 4.17. Effect of initial stress ratio on the "critical suction" profile

Fig. 4.18. The relationship between the stress, σ_η, and suction, s, for three initial stress ratios at shallower (0.5 m) and deeper (2.5 m) depths

Fig. 4.19. Graphical determination of the failure time and depth for different initial stress ratios

Fig. 4.20. Effect of softening rate on the "critical suction" profile

Fig. 4.21. Degradation of shear strength parameter, ϕ', with suction unloading for several softening rates, at shallower (0.5 m) and deeper (2.0 m) depths

Fig. 4.22. Graphical determination of the failure time and depth for different softening rates

Fig. 4.23. Effect of slope angle on the "critical suction" profile

Fig. 4.24. Graphical determination of the failure time and depth for different slope angle

Fig. 5.1. Plane layout of the measurements simulated in the present study (modified after Ng et al. 2003)

Fig. 5.2. Seepage model established for hydraulic analysis.

Fig. 5.3. SWCCs for Zaoyang Clay in terms of volumetric water content and degree of saturation.

Fig. 5.4. Hydraulic conductivity functions for Zaoyang Clay used in seepage analysis.

Fig. 5.5. Comparison of pore water pressure between prediction and measurement at several depths at middle slope.

Fig. 5.6. Comparison of pore water pressure profile between prediction and measurement at several dates at middle slope.

Fig. 5.7. Comparison of pore water pressure profile between prediction and measurement at several dates at R1 near the slope top.

Fig. 5.8. Comparison of pore water pressure profile between prediction and measurement at several dates at R1.

Fig. 5.9. Stress field within an infinite slope (modified after Qi and Vanapalli (2016)).

Fig. 5.10. Nonlinear variation of E with respect to two stress state variables.

Fig. 5.11. Nonlinear variation of H with respect to two stress state variables.

Fig. 5.12. Predicted horizontal vs. vertical stress ratios at several depths at L2 and comparison with available measurements.

Fig. 5.13. Predicted horizontal vs. vertical stress ratios at several depths near L1 and comparison with available measurements.

Fig. 5.14. Predicted development of plastic straining profile near the ground surface at L2.

Fig. 5.15. Predicted stress paths followed at several depths near the ground surface at L2.

Fig. 5.16. Predicted stress paths followed at depth of 1.0 m near the ground surface.

Fig. 5.17. Variation of plastic straining over suction at several depths near the ground surface.

Fig. 5.18. Comparison of predicted and measured vertical swelling at R2.

Fig. 5.19. Comparison of predicted and measured vertical swelling at R1.

Fig. 5.20. Comparison of predicted and measured vertical swelling at R3.

Fig. 5.21. Comparison of predicted and measured down-slope displacement near R2 at several dates.

Fig. 6.1. Conceptual sketch of model formulation, using 3D consitutive surfaces for unsaturated zone and 2D constutive relationships for saturated zone

Fig. 6.2. Flow chart of computational procedure

Fig. 6.3. Transition between saturation and unsaturation: (a) determination of suction for unsaturated elements; (b) determination of void ratio for unsaturated elements; (c) determination of the state of elements, and finding the effective stress for saturated elements as well as quasi-unsaturated analysis

Fig. 6.4. Analysis results with decantation: (a) Height *vs.* Time curve; (b) void ratio profile after 400 days

Fig. 6.5. Pore water pressure profiles predicted by UNSAT-CON

Fig. 6.6. Comparison of state steady pressure head profiles above the water table predicted by UNSAT-CON and analytical solution by Sadeghi et al. (2012)

Fig. 7.1. Analysis results of Example from Seneviratne et al. (1996) for (a) with decantation; (b) without decantation

Fig. 7.2. The surface flux and the water mass balance at the top: (a) potential evaporation rate (PER) = 0.3 m/yr with decantation; (b) PER = 0.3 m/yr without decantation; (c) PER = 3.0 m/yr with decantation; (d) PER = 3.0 m/yr without decantation

Fig. 7.3. Profiles one year after the tailings filled at 3.0 m/yr evaporation: (a) void ratio, (b) pore water pressure

Fig. 7.4. Two 3D constitutive surfaces (a) void ratio surface; (b) gravimetric water content surface

Fig. 7.5. Hydraulic conductivity of polymer-amended MFT (a) saturated hydraulic conductivity; (b) hydraulic conductivity surface

Fig. 7.6. Comparison in tailings heights over time between measurements and calculations using three sets of hydraulic conductivity

Fig. 7.7. Comparison in PWP (suction) and VWC over time between measurements and calculation using hydraulic conductivity of Set (iii): (a) PWPs at fixed elevations of 25 and 140 mm; (b) VWCs at fixed elevations of 80 and 180 mm

Fig. 7.8. Comparison of void ratio between predictions from three sets of parameters and measurements

Fig. 7.9. Variation of profiles with time calculated using UNSAT-CON: (a) void ratio profile, (b) pore water pressure, (c) total stress, (d) degree of saturation

Fig. 7.10. Comparison in the final profiles between three analyses: (a) void ratio profile, (b) pore water pressure, (c) solid content, (d) degree of saturation

Fig. 7.11. Comparison in the time history at three initial elevations between three analyses: (a) pore water pressure, (b) void ratio, (c) degree of saturation, (d) solid content, (e) total stress

Fig. 7.12. The paths of state variables predicted by UA at the initial elevations of 3.75 m and 4.05 m: (a) along with void ratio surface, (b) along with gravimetric water content surface

Fig. 7.13. Results of UA at different times in 2013: (a) solid content compared with field data, (b) pore water pressure, (c) void ratio profile, (d) degree of saturation profile

Fig. 7.14. Comparison of height *vs.* time between UA and measurement.

Fig. 7.15. Comparisons of pore water pressure between UA and measurement at three fixed elevations

Fig. 8.1. Conceptual sketch of consitutive relationships

Fig. 8.2. Constitutive relationship for saturated zone

Fig. 8.3. Bisection method for unsaturated analysis

Fig. 8.4. Stress paths followed in constitutive analysis

Fig. 8.5. Constitutive relationships: (a) volume change behaviour; (b) water retention behaviour; (c) hydraulic conductivity

Fig. 8.6. Comparison between modelled and measured results: (a) pore water pressure or suction; (b) gravimetric water content; (c) void ratio

Fig. 8.7. Profiles of pore water pressure and degree of saturation after depositing each of the first four layers

Fig. 8.8. State variable path fallowed by soil element at the top of layer one along the water retention and volume change constitutive relationship in three dimensional space

Fig. 8.9. Stress path at top of first layer along the void ratio dependent water retention constitutive relationship

Fig. 8.10. Modelled and measured results during the two wetting events and after depositing the 5^{th} layer: (a) pore water pressure or suction; (b) gravimetric water content

Fig. 8.11. “S” shape curve defined by Eq. (1): (a) on the e vs. net stress plane (b) on the e vs. suction plane.

Fig. 8.12. Water flow across inter-layer face

Fig. 9.1. An example of virgin drying surface and normal consolidation surface from BBM

Fig. 9.2. An example of plastic and elastic surfaces from BBM

Fig. 9.3. Another visualization of the yielding curves LC and SI in BBM and evoluation of their

intersection during plastic compression (a) the positions of two yield curves when a soil sample is ever dried/loaded to situation where any wetting path could only induce elastic volume swelling, (b) the positions of two yield curves when a soil sample is ever dried/loaded to situation where a wetting path could probably induce plastic volume collapse, (c) the path of corner of SI and LC with yielding (hardening)

Fig. 9.4. Algorithm for implementation of BBM in conjunction with a SWRC

Fig. 9.5. Predicted results for depositions of layer 1 and 2 in drying box test (Daliri et al. 2016) using BBM: (a) void ratio (b) gravimetric water content and (c) pore water pressure for λ_s = 0.057; (b) void ratio (d) gravimetric water content and (f) pore water pressure for λ_s = 0.1.

Fig. 9.6. UNSATCON-ML algorithm and analytical solution using BBM and Gallipoli et al. (2003) retention model during first wetting–drying cycle of test EDO-200 in D'Onza et al. (2011): variation of degree of saturation plotted against suction

Fig. 9.7. UNSATCON-ML algorithm and analytical solution using BBM and Gallipoli et al. (2003) retention model during loading– unloading–reloading cycle of test EDO-200 in D'Onza et al. (2011): (a) variation of void ratio and degree of saturation plotted against vertical net stress

Fig. 9.8. UNSATCON-ML algorithm and analytical solution using BBM and Gallipoli et al. (2003) retention model during second wetting path of test EDO-200 in D'Onza et al. (2011): variation of void ratio and degree of saturation plotted against vertical net stress

Fig. 9.9. Results from reanalysis of Daliri et al. (2016)'s case using Gallipoli et al. (2015) model

Fig. 9.10. Curved SWRC used here and simpler SWRC used in previous chapter

Fig. 9.11. Path of water retention point followed by the top element of first layer using the curved SWRC

Fig. 9.12. Derivation of NCLs and PRLs of GCM

Fig. 9.13. Example of determining the interval bounding the root

Fig. 9.14. Results from reanalysis of Daliri et al. (2016)'s case using GCM

Fig. 9.15. Stress path followed by the top element of 1st layer using GCM, during first wetting and drying cycle.

Fig. 9.16. Stress path followed by the bottom element of 1st layer using GCM and corresponding coupled movement of SI, SD, LC, NLC and PRL, during first drying.

Fig. 9.17. The paths of state followed by soil element in the middle of bottom layer during first four layer deposition

Fig. 9.18. Variation of specific volume plotted against the suction for the soil element in the middle of bottom layer

Fig.9.19. The paths of state followed by one soil element in the middle of bottom layer during first four layer deposition

Fig. 9.20. The variation of predicted profiles of S_r and s over time after each deposition

Fig.10.1. Replotting Fig. 7.13 in chapter 7: Results of UA at different times in 2013: (a) solid content compared with field data, (b) pore water pressure, (c) void ratio profile, (d) degree of saturation profile

Fig.10.2. the variation of overall GWC over one year from winter deposition to summer deposition for each subcase

Fig.10.3. The void ratio profiles calculated by UNSATCON-ML for multiple layer deposition

Fig.10.4. The void ratio profiles calculated by UNSATCON-ML for single layer deposition

Fig.10.5. Comparison in void ratio between multilayer and single deposition for each thickness

Fig.10.6. Variation of profile over time during the deposition process for the case of 1.2 m per year over 10 years

Fig.10.7. Variation of profile over time during the deposition process for the case of 1.0 m per year over 10 years

Fig.10.8. Comparisons in void ratio profiles after 10 years from multiple layer deposition (including one deposition per year and more than one deposition within each year) and single layer deposition.

Fig.10.9. A summary of void ratio profiles calculated by UNSATCON-ML with GCM and SSM

Fig.10.10. Comparison of void ratio profiles calculated by UNSATCON-ML: (a) different deposition thicknesses with SSM; (b) different deposition thicknesses with GCM; (c) 1.5 m thick deposit per year with SSM and GCM; (d) 1.2 m thick deposit per year with SSM and GCM; (e) (d) 0.8 m thick deposit per year with SSM and GCM

Fig.10.11. Calculated constitutive paths followed by the top element of the 1st layer for the case of 1.2 per year during the first 2 years using SSM and GCM.

Fig. 10.12 Calculated constitutive paths followed by the top and bottom elements of the 1st layer for the case of 1.2 m per year during 10 years using SSM: (a) both elements in three dimensional space, (b) top element in net stress vs. suction plane, (c) top element in void ratio vs. net stress plane, (d) top element in void ratio vs. suction plane, (e) bottom element in net stress vs. suction plane, (f) bottom element in void ratio vs. net stress plane, (g) bottom element in void ratio vs. suction plane.

Fig. 10.13 Calculated change of several state parameters (pore water pressure, void ratio, total stress and degree of saturation) over 10 years at top and bottom elements of the 1st layer using SSM

Fig. 10.14 The calculated stress, compression and retention paths followed by the top and bottom elements of the 1st layer during 10 years using GCM in four planes: Bishop's stress - modified suction, specific volume - Bishop stress, Degree of saturation - modified suction and specific volume – suction.

Fig. 10.15 Calculated change of several state parameters (pore water pressure, void ratio, total stress and degree of saturation) over 10 years at top and bottom elements of the 1st layer using GCM

Fig. 10.16 Calculated variations of profiles of several parameters (pore water pressure, void ratio, total stress and degree of saturation) over time using SSM: (a) during the 1st year (1st layer deposition), (b) during the 2nd year (2nd layer deposition), and (c) during the 3rd year (3rd layer deposition).

Fig. 10.17 Calculated variations of profiles of several parameters (pore water pressure, void

ratio, total stress and degree of saturation) over time using GCM: (a) during the 1st year (1st layer deposition), (b) during the 2nd year (2nd layer deposition), and (c) during the 3rd year (3rd layer deposition)

Fig. 10.18. Two comparable state surface with different maximum void ratios

Fig. 10.19. The instrument for column test at Carleton University

Fig. 10.20 Variation of profiles with time calculated using UNSAT-CON: (a) for initial void ratio of 1.4014 (b) for initial void ratio of 1.7608

Fig. 10.21. Comparison between predicted and measured variations of heights (the heights of both tailings and water) over time for this column test.

Fig. 10.22. Comparison between predicted and measured average void ratio over time for this column test.

Fig. 10.23. Comparison between predicted pore water pressure profile with measurements at two elapsed times.

Fig. 10.24. Predicted tailings height *vs.* time for different deposition schemes: (a) absolution height and (b) normalised height.

Fig. 10.25. Predicted void ratio *vs.* time for different deposition schemes: (a) overall average void ratio, (b) average void ratio of 1st layer (c) average void ratio of 2nd layer (d) average void ratio of 3rd layer

Fig. 10.26. Predicted GWC *vs.* time for different deposition schemes: (a) overall average GWC, (b) average GWC of 1st layer (c) average GWC of 2nd layer (d) average GWC of 3rd layer

Fig. 10.27. Predicted profiles after 1 year for all deposition schemes for (a) void ratio, (b) solid content, (c) PWP, (d) total stress, (e) Degree of saturation and (f) GWC

Fig. 10.28. Predicted profiles after 3 years for all deposition schemes for (a) void ratio, (b) solid content, (c) PWP, (d) total stress, (e) Degree of saturation and (f) GWC

Fig. 10.29. Comparison between 1 layer deposition per year and 2 layers deposition per year (3m per year in total): (a) tailings height (b) GWC and (c) void ratio

Fig. 10.30. Comparison between 1 layer deposition per year and 2 layers deposition per year (2m per year in total): (a) Tailings height (b) GWC and (c) void ratio

Fig. 10.31.Calculated variations of profiles of several parameters (pore water pressure, void ratio, total stress and degree of saturation) over time using SSM: (a) during the 4th year (4th layer deposition), (b) during the 5th year (5th layer deposition), (c) during the 6th year (6th layer deposition), (d) during the 7th year (7th layer deposition), (e) during the 8th year (8th layer deposition), (f) during the 9th year (9th layer deposition), and (g) during the 10th year (10th layer deposition).

Fig. 10.32.Calculated variations of profiles of several parameters (pore water pressure, void ratio, total stress and degree of saturation) over time using SSM: (a) during the 4th year (4th layer deposition), (b) during the 5th year (5th layer deposition), (c) during the 6th year (6th layer deposition), (d) during the 7th year (7th layer deposition), (e) during the 8th year (8th layer deposition), (f) during the 9th year (9th layer deposition), and (g) during the 10th year (10th layer deposition).

List of Tables

Table 1.1. Tailings by the numbers (from Flanagan and Grant 2013)

Table 1.2. Chronology of major tailings dam failures during the author's PhD program (from http://www.wise-uranium.org/mdaf.html)

Table 2.1. Several well-known models for shear strength of unsaturated soil

Table 3.1 Summary of Regina clay soil properties used in the present study

Table 4.1. Hydraulic parameters of Regina clay used in the present study

Table 4.2. Regina clay mechanical properties used in the present study

Table 5.1. Hydraulic parameters used in the present study

Table 5.2. Mechanical properties used in the present study

Table 6.1 Basic properties for the example from McVay et al. (1986)

Table 7.1. Basic properties for the example from Seneviratne et al. (1996)

Table 7.2. Basic properties for column test

Table 7.3. Constitutive surfaces

Table 7.4. The parameters of hydraulic conductivity function used for calibration

Table 7.5. Basic properties of the field trial

Table 7.6. Three different analyses of the field trial

Table 8.1. Parameters for constitutive relationships

Table 9.1. Parameters of BBM

Table 9.2. Parameters of BBM and Gallipoli et al. (2003) retention model used by D'Onza et al. (2011)

Table 9.3. Analytical solution analytical solution to BBM and Gallipoli et al. (2003) retention model for stress path of test EDO-200 in D'Onza et al. (2011)

Table 9.4. UNSATCON-ML algorithm solution to BBM and Gallipoli et al. (2003) retention model for stress path of test EDO-200 in D'Onza et al. (2011)

Table 9.5. Parameter values for Gallipoli et al. (2015) model

Table 9.6. Parameters of GCM

Table 10.1. Oil sands tailing parameters based on study in chapter 7

Table 10.2. Short-term (1 years) deposition scheme (starting from summer)

Table 10.3. Long-term (10 years) deposition scheme

Table 10.4. Parameters of SSM

Table 10.5. Parameters of GCM

Table 10.6. Long-term (10 years) deposition scheme

Table 10.7. Parameters for constitutive relationships

Table 10.8. Simulated deposition schemes for Musselwhite tailings (one layer deposition per year)

Chapter 1 Introduction

1.1 Background

1.1.1 Slope stability of expansive soil

Expansive soil, referred also to as swelling soil, is a kind of problematic soil with high plasticity. Expansive soils contain clay minerals such as montmorillonite, illite or kaolinite that abstract and absorb water. The composition of minerals, particularly montmorillonite, with high water retention capacity, makes expansive soil exhibit dramatic swell characteristics. The volume increase of an expansive soil element can reach 30% or even more. This process is partially reversible when water content decreases due to evaporation or desiccation, in the meantime, expansive soil contracts contributing to the development of cracks and fissures. Numerous wetting and drying cycles in nature can substantially alter the micro-structure and degrade the macro properties of expansive soil as an engineering material.

The civil engineering-related problems associated with expansive soil were first recognized in 1938 by the United States Bureau of Reclamation, which was in connection with a foundation of a steel siphon in Oregon (Chen, 1975). Since then, the damage caused by expansive soils to a variety of civil engineering projects, ranging from cracks of lightly loaded residual buildings to instability of slope of canals or dams, has received increasing attention from geotechnical engineers and researchers.

Expansive soils are typically distributed in semi-arid and arid regions around the world (see Fig. 1.1). According to Donaldson (1969), the expansive soils primarily originates from two

group of parent materials : (*i*) igneous rock containing feldspar and pyroxene minerals that can decompose to form montmorillonite, and (*ii*) sedimentary rocks that contain montmorillonite. A typical example is the Regina clay (Saskatchewan, Canada) that evolved due to geologic weathering of glacio-lacustrine sediments under restrained leaching in a semi-arid climate (Christiansen and Saure 2002). The countries in which expansive soils have been reported are: Argentina, Australia, Burma, Canada, China, Cuba, Ethiopia, Ghana, Great Britain and Northern Ireland, India, Iran, Kenya, Mexico, Morocco, Rhodesia, South Africa, Spain, Turkey, USA, and Venezuela (Chen 1975, Fredlund and Rahardjo 1993).

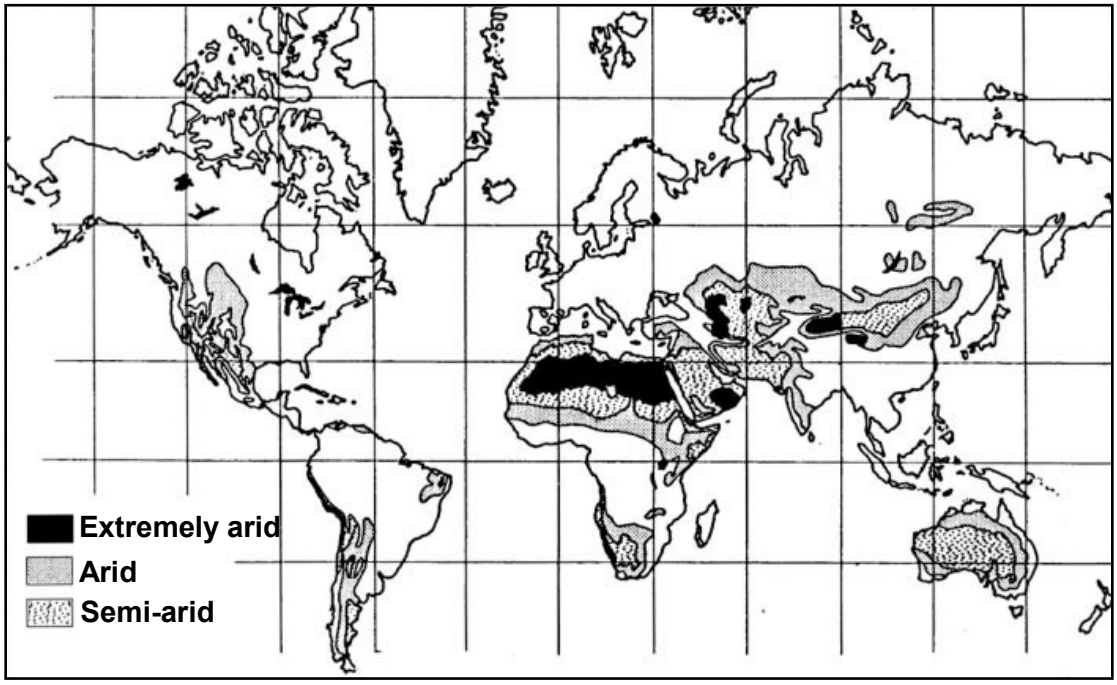

Fig. 1.1 Extremely arid, arid, and semi-arid areas of the world (Fredlund and Rahardjo 1993)

One of the most common problems caused by expansive soils in North America is distress and cracks of lightly loaded buildings (usually one-two stories constructed of wood) due to differential swell and shrinkage of soil foundation. Research studies of this region focused on interpretation, prediction and mitigation of one-dimensional swelling and swelling pressure

exhibited by expansive soil foundation at K_0 condition (e.g. Fredlund and Rahardjo 1993, Nelson 2015). In China, expansive soils have been found in more than 20 out of the 27 provinces, occupying approximately 600,000 km^2 (Shi et al. 2002). One of the key geotechnical problems related to expansive soil is slope failure triggered by rainfall. Several giant civil engineering projects, including the well-known Three Gorges Dam and South-to-North Water Transfer Project (SNWTP), go through or are built in expansive soil areas. Niu et al. (2005) reported that in the Three Gorges Reservoir Region, the water level fluctuations (due to environmental changes and regular operations for hydro-power generation) lead frequently to change in the water content of expansive soils in these areas. The repeated shrinkage and swelling of expansive soils upon drying and wetting can alter their structure, promoting the development of fissures and cracks, lowering the strength, and contributing eventually to numerous slope failures. The SNWTP is used to carry potable water from the Yangtze River in the south to the arid areas in north China, which includes three main routes. About 386 km of canal in the middle route of the SNWTP passes through the unsaturated expansive soil areas (Ng et al. 2003), many landslides of expansive soil deposits similar to those in Three Gorges Reservoir Region have also been reported in these areas (Bao 2000), which significantly slowed down the project progress and caused sizable economic loss. Thus, designing safe slopes and maintaining their stability taking account of economic constraints during post-construction (or regular operation) stages are among the largest challenges associated with these engineering projects of unprecedented scale. The extensive attention paid to expansive soil slope stability may be due to the considerable importance and grandiosity of these projects in China (Ng et al. 2003). However, landslides in expansive soil have also been often reported in some other countries, such as, Canada (Widger and Fredlund 1979), Spain (Alonso et al. 2003; Azañón et al. 2010) and United States (Day 1994).

It is well established that water infiltration (whether in the form of rainfall, snow melting, rise of water level in reservoir, or other types) constitutes the most primary factor that triggers landslides in both swelling and non-swelling soils. However, the response of expansive soils to infiltration is more complex than that of soil without swelling potential. Various types of experimental tests have been conducted on expansive soils to better understand the engineering properties of unsaturated expansive soil and their influence on the slope failures.

These experiments ranged from micro-scale to various levels of macro-scales, such as, (i) the Mercury Intrusion Porosimetry (MIP) for measuring change in pore size distribution (Gens and Alonso et al. 1992; Simms and Yanful 2002; Simms and Yanful 2005), (ii) oedometer (Huang and Fredlund 1998), direct shear (Zhan et al. 2007) and triaxial shear (Zhan 2003) tests on elemental soil sample for measuring volume change, stress-strain and shear strength behaviour, (iii) model (Cheng et al. 2013) and centrifugal (Zhang et al. 2011) tests for simulating real scenarios using a slope constructed in laboratory under controllable environmental conditions, and (iv) in situ measurements (Ng et al. 2003) on real slopes in field.

Traditional, modified and newly designed apparatus or instruments for unsaturated soil are adopted in these tests, for example, (i) meteorological stations to record the climate data in the field (Chen et al. 2007) ; (ii) specifically designed sprinkles to simulate rainfall (Chen et al. 2009); (3) earth pressure cells to measure the change of stress regime within slope profile in addition to hydraulic response measurements (Ng et al. 2003), considering the difference between swelling and non-swelling soils, etc. These tests have provided valuable information with respect to the fundamental mechanisms of slope failure in expansive soils, some of them are summarized below:

(1) The influence of infiltration on the hydraulic flow regime (substantial change of water content/suction) in the slope is generally limited to a certain depth, resulting in sliding

of failure mass over a shallow slip surface, where soil's shear strength due to suction contribution is significantly lost.

(2) The response of an expansive slope to wetting, which contributes to an increase in the soil's volume, is a highly coupled hydro-mechanical process that should be taken into consideration in slope stability analysis.

(3) Accompanying swelling deformation activated by infiltration, the stress regime changes significantly in this shallow layer. The stress redistribution might be responsible for the observed irrecoverable displacements (plastic straining upon yielding).

(4) Expansive soil is usually over-consolidated and exhibits softening behaviour for a variety of stress paths (e.g., the stress paths in the constant suction test or in the shear infiltration test).

Although there is an increasing interest and effort in evaluation of slope stability on the basis of unsaturated soil mechanics, comparative and quantitative studies on the influence of the above-listed phenomena on slope stability has rarely been conducted, particularly in *expansive* soils**.** Numerical analyses that explicitly quantifies these influences is much needed for understanding how these specific phenomena contribute to the global failure. Such research will therefore aid the design and maintenance of expansive soil slopes for various geotechnical engineering applications.

1.1.2 Significance of evaporation on consolidation and strengthening of soft soil - using tailings management as an example

Another problem where hydromechanical coupling in an unsaturated material is important is the management of subaerially deposited mine tailings. A vast amount of tailings are produced all over the world every year from mining. In Canada, tailings are produced by both hard rock mining and oil sands mining for bitumen extraction (Simms 2017, Daliri 2013, Bussiere 2007). Tailings, a byproduct of mining operations comprise either the ground up rock or residual overburden material mixed with relatively high amount of water, are usually deposited as a slurry to a selected area bounded by dams or dykes, see Fig. 1.2, for example.

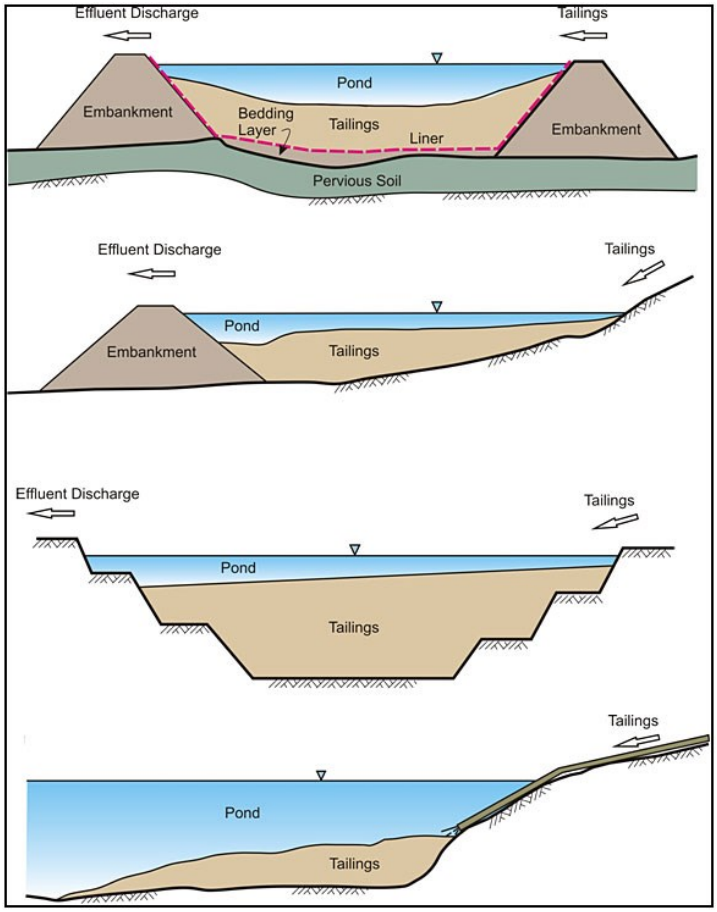

Fig. 1.2. An illustration of several different tailings ponds (from http://www.gardguide.com/index.php?title=Chapter_6)

Tailing generated from grinding of rock typically contain sand to silt size particles, as the ideal target to optimize mineral extractions is to grind particles to between 10 to 100 microns in size. Tailings from overburden mining (oil sands, bauxite deposits) also may contain substantial amounts of clay minerals. For the latter, the hydraulic conductivity may be quite low and impedes dewatering and therefore reclamation of tailings deposits. For some tailings generated from oil sands mining, Wells (2011) reported that quite deep deposits show very low strength (< 1 kPa) and very high water content (180%) even after 30 years. Further, the human production of tailings has increased by several orders of magnitude in the modern age and led to widespread environmental contamination in mining areas, (http://www.groundtruthtrekking.org/Issues/MetalsMining/MineTailings.html#ixzz4mRRwoDwe), see, for example, Table 1.1, which reports some ***numbers*** associated with tailings in Northern Alberta, Canada (Flanagan and Grant 2013).

Table 1.1. Tailings by the numbers (modified from Flanagan and Grant 2013)

176 km^2 **Area of Northern Alberta now covered by tailings lakes**	***25,000 m^3*** **Volume of tailings waste produced per day at current mining production rates**	***2060*** **Year when tailings growth is predicted to stabilize, barring significant advancements in technology**
1.5 times bigger **Surface area of tailings lakes compared to the City of Vancouver**	***2 times as much*** **Amount of water operators are licensed to divert from the Athabasca River per year compared to the amount of water used annually by the City of Calgary**	***1.3 billion m^3*** **Predicted volume of liquid tailings waste produced by 2060**
0.2 % **Amount of the land disturbed by oilsands development that has been certi"ed as reclaimed**	***2–4*** **Number of barrels of freshwater used per barrel of bitumen produced through mining**	***11,000 m^3*** **Estimated volume of contaminated water seeping from tailings lakes into adjacent surfaces and groundwater each day**

Accelerating the consolidation/dewatering process of these tailings is important in mining operations, due to several reasons:

(i) The water that rises to the top of fluid tailings ponds (from the consolidation process) can be recycled back into the plant and used for processing ore, and reducing fresh water needs for mining operation, see Fig. 1.3;

(ii) The land footprint the tailings occupy can be largely reduced, since the volume of water constitutes a large portion of total volume of fluid tailings;

(iii) The consequence of failures of tailings dams is devastating (numerous cases over the last century (Daliri 2013; ICOLD 2001), see Table 1.2, for the incomplete list of major tailings dam failures around the world reported during the author's PhD program), which are due to improper design of dams, overestimation of tailings' resistance to shearing in various deposition stages. Sufficient dewatering of tailings in a time efficient manner would be beneficial for both short term and long term stability of tailings dykes/dams; and probably reduce their construction cost;

(iv) Reduction of potential threat to surrounding wildlife (e.g. the residual bitumen found at the surface in most ponds, see Fig. 1.4) can pose a threat to birds and waterfowl if they try to land on ponds. Leaks of the tailings ponds with heavy metals, acids, and other contaminants are probably inevitable, which end up polluting underlying soils, groundwater, lakes and rivers, e.g. the Athabasca River;

(v) The ultimate step is to transform tailings areas into reclaimed land, this requires a sufficient tailings' stiffness/strength gain through dewatering/consolidation after deposition.

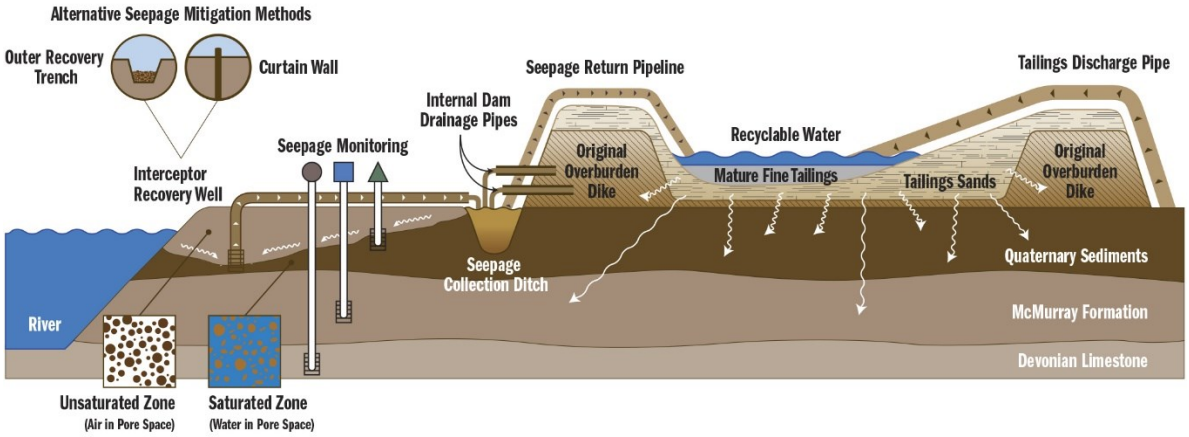

Fig. 1.3 An illustration of tailings seepage recapturing and monitoring systems (Ministry of Environment and Sustainable Resource Development, Government of Alberta, http://www.nrcan.gc.ca/energy/publications/18752).

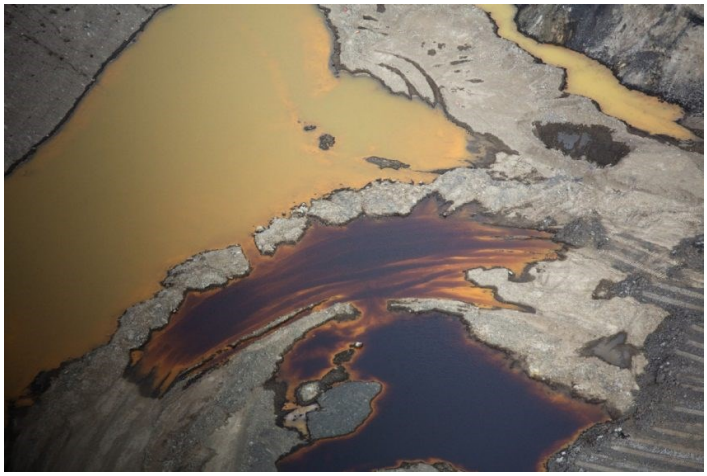

Fig. 1.4 Tailings ponds are repositories for the toxic sludge that is produced when bitumen oil is separated from sand and gravel. Wildlife often mistake them for freshwater lakes. (https://www.thestar.com/news/atkinsonseries/2015/09/04/tailings-ponds-a-toxic-legacy-of-albertas-oilsands.html).

Table 1.2. Chronology of major tailings dam failures during the author's PhD program (from http://www.wise-uranium.org/mdaf.html)

Date	Location	Parent company	Ore type	Type of Incident	Release	Impacts
2017, June 30	Mishor Rotem, Israel	Rotem Amfert Negev Ltd. , Israel Chemicals (ICL)	Phosphate	phosphogypsum dam failure	100,000 cubic metres of acidic waste water	The toxic wastewater surged through the dry Ashalim riverbed and left a wake of ecological destruction more than 20 km long
2017, Mar. 12	Tonglvshan Mine, Hubei province, China	China Daye Non-Ferrous Metals Mining Limited	copper, gold, silver, iron	a partial dam failure occurred at the northwestern corner of the tailings pond, opening a crevasse (gap) of approx. 200 metres	approx. 200,000 cubic metres of tailings	The tailings flooded the fish pond downstream of approx. 27 hectares. Two persons were reported dead and one was reported missing.
2016, Aug. 27	New Wales plant, Mulberry, Polk County, Florida, USA	Mosaic Co	phosphate	a 14 metre-wide sinkhole appeared in a phosphogypsum stack, opening a pathway for contamined liquid into the underground; the liquid reached the Floridan Aquifer, a	840,000 cubic metres of contaminated liquid released (as of Sep. 17, 2016)	

				major drinking water resource		
2016, Aug. 8	Dahegou Village, Luoyang, Henan province, China	Luoyang Xiangjiang Wanji Aluminium Co., Ltd.	bauxite	failure of a tailings dam holding about 2 million cubic metres of red mud	/	village totally submerged in red mud, around 300 villagers evacuated, many farm and domestic animals killed
2015, Nov. 21	Hpakant, Kachin state, Myanmar		jade	waste heap failure	/	at least 113 people killed
2015, Nov. 5	Germano mine, Bento Rodrigues, distrito de Mariana, Região Central, Minas Gerais, Brazil	Samarco Mineração S.A. (50%) BHP Billiton , 50% Vale)	iron	Failure of the Fundão tailings dam due to insufficient drainage, leading to liquefaction of the tailings sands shortly after a small earthquake. For details, see: The Fundão Tailings Dam Investigation	32 million m^3	slurry wave flooded town of Bento Rodrigues, destroying 158 homes, at least 17 persons killed and 2 reported missing; slurry pollutes North Gualaxo River, Carmel River and Rio Doce over 663 km, destroying 15 square kilometers of land along the rivers and cutting residents off from potable water supply

2014, Sep. 10	Herculano mine, Itabirito, Região Central, Minas Gerais, Brazil	Herculano Mineração Ltda	iron	tailings dam failure	/	two workers killed and one missing
2014, Aug. 7	Buenavista del Cobre mine, Cananea, Sonora, Mexico	Southern Copper Corp. (Grupo México)	copper	tailings dam failure	40,000 m^3 of copper sulphate	flow into the 420km-long Bacanuchi river waterway, a tributary of the Sonora River, directly affecting 800,000 people
2014, Aug. 4	Mount Polley mine, near Likely, British Columbia, Canada	Imperial Metals Corp.	copper, gold	Tailings dam failure due to foundation failure	7.3 million m^3 of tailings, 10.6 million m^3 of water, and 6.5 million m^3 of interstitial water	tailings flowing into adjacent Polley Lake and, through Hazeltine Creek, into Quesnel Lake (Mitchell Bay)
2014, Feb. 2	Dan River Steam Station, Eden, North Carolina, USA	Duke Energy	coal ash	collapse of an old drainage pipe under a 27-acre ash waste pond	about 82,000 short tons [74,400 t] of toxic coal ash and 27 million gallons [100,000 m^3] of contaminated water	ash flowing through drainage pipe into Dan River

2013, Nov. 15-19	Zangezur Copper Molybdenum Combine , Kajaran, Syunik province, Armenia	Cronimet Mining AG	copper, molybdenum	damage of tailings pipeline	/	tailings flowing into Norashenik River for several days
2013, Oct. 31	Obed Mountain Coal Mine, northeast of Hinton, Alberta, Canada	Sherritt International	coal	breach of wall in containment pond	spill of 670,000 m^3 of coal wastewater and 90,000 tonnes of muddy sediment	plume of slurry containing fine coal particles, clay and heavy metals into the Apetowun und Plate creeks and eventually the Athabasca River
2012, Dec. 17	former Gullbridge mine site, Newfoundland, Canada		copper	embankment dam failure, width 50 m		non-consumption water advisory has been issued for the Town of South Brook-Newfoundland and Labrador Department of Environment and Conservation)

The significant repercussion of existing vast tailings ponds has promoted new regulations and polices to reduce the tailings inventory. For example, the *Directive 074: Tailings Performance Criteria and Requirements for Oil Sands Mining Schemes*, released in 2009 by Energy Resource Conservation Board (ERCB), Alberta's governing body that oversees the oil sands industry. In order to obtain a trafficable surface on the tailings deposit, *Directive 074* contains this criteria: "*the minimum undrained shear strength of the tailings was required to be 10 kPa; and the minimum undrained shear strength of any tailings deposited in the previous year must achieve 5 kPa. In five years, after active deposition had ended, the deposit must have achieved trafficability or an undrained shear strength of 10 kPa* (Energy Resources Conservation Board, 2009)". A new version, *Directive 085: Fluid Tailings Management for Oil Sands Mining Projects,* was released in July 14, 2016, this new version is being completed and enhanced in this year, 2017. *Directive 085* enabled the implementation of the *Tailings Management Framework (TMF) for the Mineable Athabasca Oil Sands* (available on the Government of Alberta's website). The TMF specifies "new fluid tailings from the project must be *ready to reclaim* (*RTR*) ten years after the end of mine life, while all legacy tailings must be *RTR* by the end of mine life". An example is given regarding the Derivation of *RTR* Performance Criteria in *Directive 085.* Ready to reclaim is interpreted by some geotechnical practitioners to mean the tailings must possess undrained shear strength of at least 30 kPa, in order to avoid slope stability failures when the tailings are positioned in a final landform.

The effectiveness of different existing and new techniques used to accelerate dewatering and consolidation of the tailings are being investigated in both industry and academia, for example: (i) beaching; (ii) atmospheric fines drying (AFD); (iii) thickened tailings; (iv) filtered tailings; (v) composite Tailings; (vi) In-line flocculation; and many others see https://www.youtube.com/watch

?v=zcVvwat4MM8 and the report published by BGC Engineering (2010). Different mechanisms are involved in these techniques to accelerate the tailings dewatering/consolidation, including those depending on physical/mechanical processes (such as filtered tailings), natural processes (e.g. AFD), chemical/biological amendments (e.g. composite tailings), mixtures/co-disposal and permanent storage. Rozina et al. (2015) provided a brief summary of several technologies. It is still safe to say that none of these techniques has been proven to be quite effective and particularly applicable in commercial scale.

For atmospheric fines drying (AFD) technique (concerned in this thesis), the polymer solution is injected into the tailings transferred by pipelines, which is discharged in thin-lift deposition. Significant instantaneous dewatering can be achieved as fines aggregate into flocs, improving the permeability and water release of the tailings. Settlement, seepage, desiccation and freeze-thaw contribute to further dewatering (Beier et al. 2013). Suncor and Shell have commercially implemented this technology. Performance of this technique has recently been extensively and exhaustively studied using the Mesoscale Drying Box (1·0 m by 0·7 m in plan) at Carleton University (Simms, 2017; Daliri et al, 2014, 2016; Daliri 2013; Simms et al. 2017; Soleimani (2014); Mizani, 2016, 2017; Dunmola 2012; Rozina et al. 2015; Innocent-Bernard (2014); Simms et al. 2013, etc.).

For atmospheric fines drying (AFD) technique, evaporation constitutes a natural contributor without a direct investment to the dewatering process. From the geotechnical point of view, several possible benefits are expected from this natural process, e.g. (a) Evaporation is used during the time period between two successive depositions to accelerate the dewatering, see Fig. 1.5, Fig. 1.5 shows a typical process of Subaerial deposition of mine tailings; (b) Tailings initially oversaturated with water/other liquid will become gradually partially saturated. The way the water

plays a role in the overall mechanical behaviour of tailings skeleton switches from negative (bulk water provides resistance to the particle-particle contact and development of effective stress) to positive (interstitial liquid/water provides adhesive forces between particles, such as sandcastles discussed in the next chapter); (c) The measurable suction in meniscus water can help to densify (consolidate) the tailings, and can also increase the resistance of the overall tailings skeleton to the external mechanical loading (compression/shearing); (d) the gained strength/stiffness can be partially maintained at the time of reclamation; (e) The water adsorption capacity of the underlying dried tailings can help to accelerate the dewatering of newly deposited tailings, see Fig. 1.5.

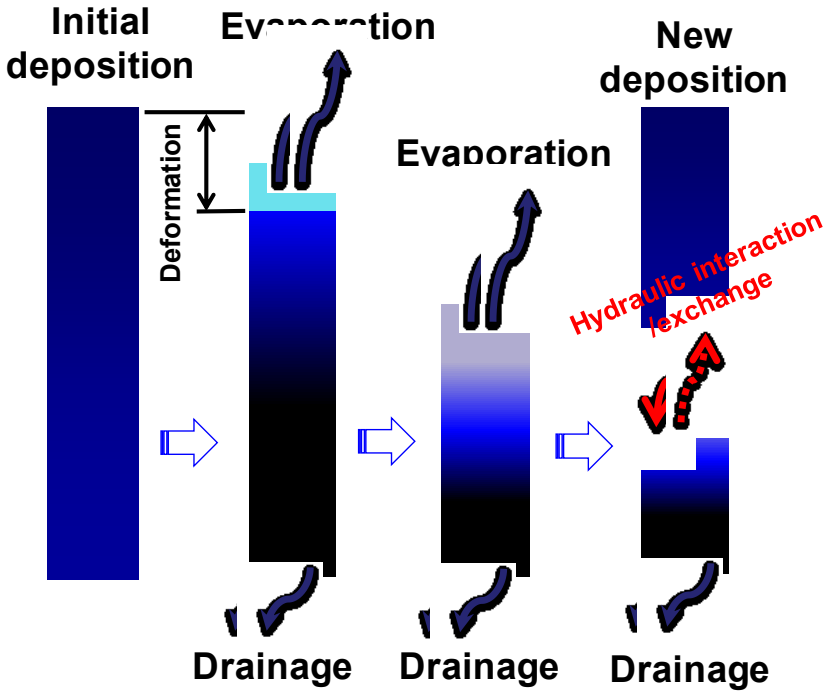

Fig. 1.5. Subaerial deposition of tailings

Quantifying these benefits would be quite necessary for guiding the final reclamation design. An optimal deposition scheme that can maximize these possible benefits for a quicker reclamation would always be pursued in the industry. To reach an optimal deposition scheme (including selecting optimal thickness and rate of rise, at a certain evaporation rate), two important

time-dependent geotechnical processes, namely, (*i*) saturated-unsaturated water flow driven by evaporation, (*ii*) large deformation of tailing skeleton, and the two-way coupling between deformation of tailings skeleton and flow of interstitial water: the deformation drives flow and vice versa, have to be understood to quantify the contribution of evaporation on dewatering and consolidation. Note the evaporation rate according to the local meteorological conditions, and can be estimated or predicted numerically.

A numerical model that can simulate the deposition process (quantifying the overall performance of the subaerially deposited tailings) with an adequate treatment of this unsaturated poromechanical coupling could be a useful tool to optimize the deposition scheme Existing numerical models can just partially account for the evaporation effect with a saturation assumption for tailings volume change behaviour (Terzaghi's effective stress principle is assumed to control the volume change behaviour of unsaturated tailings). The unsaturated poroelastic and poroplastic behaviour (models at the constitutive level are also actively under development in the geotechnical academia) need to be properly simulated in such a numerical model. Such a numerical program (if efficient and cost-effective) would be promising not only for tailings managements but other practices involving deposition of soft soils, which make use of evaporation to accelerate dewatering and consolidation.

1.2 Objectives of the study and Intended Novel Contributions

The objective of the study is twofold:

- *to investigate and quantify the effect of swelling on slope failure in expansive soils using numerical analysis on the basis of unsaturated soil mechanics. Specific goals includes:*

(1) Quantifying the hydro-mechanical coupling effect on the slope stability of expansive soils by comparing a hydro-mechanical and a pure seepage analyses, followed by calculation of the Factor of Safety;

(2) Developing a numerical program using the infinite slope framework, to track the change of stress regime, plastic straining, and strain softening within the wetted shallow layer, and evaluate effects of these changes on Factor of Safety;

(3) Refining existing elastic moduli model for unsaturated soils, and incorporating it along with nonlinear shear strength criterion for yielding into the numerical program, to realize a smooth state (saturated and unsaturated) transition modelling during both elastic and plastic stages.

(4) Verifying the numerical program by simulating a well-documented field case.

- *To develop a computer program for analysis of large strain consolidation of soft soil coupled with unsaturated flow, which can be used, with a low computational cost, in tailings management. Specifically,*

(5) Implementing the unsaturated constitutive relationship (involving monotonically mechanical/hydraulic loading conditions) established using state surface approach with two stress state variables into the piece-wise linear finite difference scheme, to analyze single layer deposition of initially slurry soils. Particular emphasis is put on developing a novel algorithm, from a local to global level, to the model the transition between unsaturated and saturated zone (in saturated zone soil deformation is described using Terzaghi's effective stress principle)

(6) Upgrading the program to analyze multilayer deposition of slurry soil or tailings, by incorporating elasto-plastic constitutive models for volume change and void ratio-dependent hysteretic model for water retention behaviour of unsaturated soils. Several challenges will be overcome in the algorithm: (a) mass imbalance issues related to the nonlinearity; (b) numerical errors associated with some selected incremental constitutive formulations; (c) coupled solution to plastic volumetric behaviour in conjunction with hysteretic water retention behaviour.

(7) Testing the program, extensively, against analytical solution, numerical solutions, small-scale model tests, large-scale model tests, and field trials.

(8) Application of this novel program to field cases.

1.3 Outlines of the thesis

The thesis consists of 11 chapters. This first chapter presents a background and the objectives of the research.

Chapter 2 presents the literature review, including: (i) constitutive models of unsaturated (expansive) soils, including volume change, water retention and shear strength behaviour; (ii) methodologies for slope stability analysis in unsaturated soils, i.e. calculation of Factor of Safety (FS); (iii) existing models for large-strain consolidation incorporating some degree of unsaturated water flow.

Chapter 3 presents the numerical investigation on coupling effect related to soil swelling on the Factor of Safety of unsaturated expansive soil slope upon wetting. (A technical paper published in *Computers and Geotechnics*, DOI: 10.1016/j.compgeo.2015.07.006)

Chapter 4 presents the development of numerical model for assessing expansive soil slope stability considering the effect of swelling-induced stress and associated softening behaviour. The numerical results have some important implications for engineering practice. (A technical paper published in *Computers and Geotechnics*. DOI: 10.1016/j.compgeo.2016.02.018)

Chapter 5 summarizes simulations of a field study using the method presented in chapter 4, and a novel model has been proposed to predict the moduli of unsaturated soils. (A case study paper accepted for publication in *International Journal of Geomechanics,* in production).

Chapter 6 presents the theoretical development of the program (named 'UNSAT-CON') for modeling unsaturated flow coupled with large strain consolidation of soft soils. (A technical paper published in *Journal Geotechnical and Geoenvironmental engineering*)

Chapter 7 presents testing of UNSAT-CON against the numerical solution and various experimental results (including those from laboratory and field trial) for modeling single layer deposition of tailings (A technical paper published in *Journal Geotechnical and Geoenvironmental engineering*).

Chapter 8 presents development of UNSATCON-ML (upgraded from UNSAT-CON) for modeling multilayer deposition, and testing of the program against experimental results.

Chapter 9 presents further development of UNSATCON-ML by implementing several advanced unsaturated soil constitutive models (including BBM and GCM etc.) and testing of the program against experimental results.

Chapter 10 presents several hypothetical field cases analyses using UNSATCON-ML to (1) show its potential application in the industry, and (2) provide some practical implications for the industry.

Chapter 11 presents the summary and recommendations for future research.

1.4 References

Alonso, E. E., Gens, A., & Delahaye, C. H. (2003). Influence of rainfall on the deformation and stability of a slope in overconsolidated clays: a case study. Hydrogeology Journal, 11(1), 174-192.

Azañón, J. M., Azor, A., Yesares, J., Tsige, M., Mateos, R. M., Nieto, F., & Rodríguez-Fernández, J. (2010). Regional-scale high-plasticity clay-bearing formation as controlling factor on landslides in Southeast Spain. Geomorphology, 120(1), 26-37.

Bao, C. G., & Ng, C. W. W. (2000). Some thoughts and studies on the prediction of slope stability in expansive soils. In Unsaturated soils for Asia. Proceedings of the Asian Conference on Unsaturated Soils, UNSAT-ASIA 2000, Singapore, 18-19 May, 2000 (pp. 15-31). AA Balkema.

BGC Engineering Inc. (2010). Oil Sands Tailings Technology Review. Oil Sands Research and Information Network (Vol. OSRIN Repo, p. OSRIN Report No. TR–1. 136 pp.). Edmonton, Alberta.

Bussiere, B. (2007). Colloquium 2004: Hydrogeotechnical properties of hard rock tailings from metal mines and emerging geoenvironmental disposal approaches. Canadian Geotechnical Journal, 44(9), 1019-1052.

Chen, C. F., Liu, H. X., & Li, Y. P. (2007). Study on grassroots-reinforced soil by laboratory triaxial test. Yantu Lixue(Rock and Soil Mechanics), 28(10), 2041-2045.

Chen, F. H. (1975). Foundation on Expansive Soil, Development in Geotechnical Engineering 12.

Cheng, Y. H., Cheng, Z. L., & Zhang, Y. B. (2011). Centrifugal model tests on expansive soil slope under rainfall. Chinese Journal of Geotechnical Engineering, 33(1), 409-414.

Cheng, Z., Ding, J., Rao, X., Cheng, Y., & Xu, H. (2013). Physical model tests of expansive soil slope. In Geo-Congress 2013: Stability and Performance of Slopes and Embankments III (pp. 731-740).

Daliri, F. (2013). The influence of desiccation and stress history on monotonic and cyclic shear response of thickened gold tailings (Doctoral dissertation, Carleton University Ottawa).

Daliri, F., Kim, H., Simms, P., & Sivathayalan, S. (2014). Impact of desiccation on monotonic and cyclic shear strength of thickened gold tailings. *Journal of Geotechnical and Geoenvironmental Engineering*, *140*(9), 04014048.

Day, R. W. (1994). Surficial stability of compacted clay: case study. Journal of geotechnical engineering, 120(11), 1980-1990.

Dunmola (2012). Predicting Evaporative Fluxes in Saline Soil and Surface-deposited Thickened Mine Tailings. Ph.D. thesis.

Elizaveta Rozina (2015) Bearing Capacity of Multilayer-deposited In-line Flocculated Oil Sands Tailings, Master thesis, Carleton University, Canada.

Flanagan, Erin, and Jennifer Grant. "Losing Ground–Why the problem of oil sands tailings waste keeps growing." Pembina Institute (2013): 1-6.

Gens, A., & Alonso, E. E. (1992). A framework for the behaviour of unsaturated expansive clays. Canadian Geotechnical Journal, 29(6), 1013-1032.

Government of Alberta, "Fact Sheet Tailings" (PDF), Government of Alberta, September 2013, archived from the original (PDF) on 25 March 2014, retrieved 12 April 2014.

Gui, M. W., & Wu, Y. M. (2014). Failure of soil under water infiltration condition. Engineering Geology, 181, 124-141.

Huang, S., Fredlund, D. G., & Barbour, S. L. (1998). Measurement of the coefficient of permeability for a deformable unsaturated soil using a triaxial permeameter. Canadian Geotechnical Journal, 35(3), 426-432.

ICOLD (2001) Tailings Dams, Risk of dangerous occurrences, Bulletin 121. Paris, 45 pp.

Innocent-Bernard, T., Simms, P., Xiaoli, Y., & Sedgwick, A. (2014, December). Multilayer deposition of two batches of thickened oil sands tailings: experiments and modeling. In *Proceedings of the International Oil Sands Tailings Conference, Lake Louise, Alta* (pp. 7-10).

Meilani, I., Rahardjo, H., & Leong, E. C. (2005). Pore-water pressure and water volume change of an unsaturated soil under infiltration conditions. Canadian geotechnical journal, 42(6), 1509-1531.

Mizani, S., & Simms, P. (2016). Method-dependent variation of yield stress in a thickened gold tailings explained using a structure based viscosity model. *Minerals Engineering*, *98*, 40-48.

Mizani, S., Simms, P., & Wilson, W. (2017). Rheology for deposition control of polymer-amended oil sands tailings. *Rheologica Acta*, 1-12.

Nelson, J. D., Chao, K. C., Overton, D. D., & Nelson, E. J. (2015). Foundation engineering for expansive soils. John Wiley & Sons.

Ng, C. W. W., Zhan, L. T., Bao, C. G., Fredlund, D. G., & Gong, B. W. (2003). Performance of an unsaturated expansive soil slope subjected to artificial rainfall infiltration. Geotechnique, 53(2), 143-157.

Rozina, E., Mizani, S., Malek, M., Sanchez, M., & Simms, P. (2015). Desiccation and consolidation in a laboratory simulation of multilayer deposition of oil sands fine tailings. In *Proceedings of Paste*.

Rozina, E., Mizani, S., Malek, M., Sanchez, M., & Simms, P. (2015). Desiccation and consolidation in a laboratory simulation of multilayer deposition of oil sands fine tailings. In *Proceedings of Paste*.

Shi, B., Jiang, H., Liu, Z., & Fang, H. Y. (2002). Engineering geological characteristics of expansive soils in China. Engineering Geology, 67(1), 63-71.

Simms, P. (2017). 2013 Colloquium of the Canadian Geotechnical Society: Geotechnical and geoenvironmental behaviour of high-density tailings. Canadian Geotechnical Journal, 54(4), 455-468.

Simms, P. H., & Yanful, E. K. (2002). Predicting soil—water characteristic curves of compacted plastic soils from measured pore-size distributions. Géotechnique, 52(4), 269-278.

Simms, P. H., & Yanful, E. K. (2005). A pore-network model for hydromechanical coupling in unsaturated compacted clayey soils. Canadian Geotechnical Journal, 42(2), 499-514.

Simms, P., Sivathayalan, S., & Daliri, F. (2013). Desiccation in dewatering and strength development of high-density hard rock tailings. In *Proc., 16th Int. Seminar on Paste and Thickened Tailings* (pp. 75-86). Australian Centre for Geomechanics, Crawley, Australia.

Simms, P., Soleimani, S., Mizani, S., Daliri, F., Dunmola, A., Rozina, E., & Innocent-Bernard, T. (2017). Cracking, salinity and evaporation in mesoscale experiments on three types of tailings. Environmental Geotechnics, 1-15.

Soleimani, S., Simms, P., Dunmola, A., Freeman, G., & Wilson, G. W. (2014) Desiccation and consolidation in thin-lift deposition of polymer-amended mature fine tailings. Proceedings of the 17th International Seminar on Paste and Thickened Tailings, R. Jewell, A. Fourie, P. S. Wells and D. van Zyl, eds., Australian Centre for Geomechanics, Crawley, Australia, 307-322.

Wells, P. S. (2011). Long term in-situ behaviour of oil sands fine tailings in Suncor's Pond 1A. Proceeding of the Conference on Tailings and Mine Waste 2011. Vancouver, BC

Wells, P.S., Revington, A., and Omotoso, O. (2011). Mature fine tailings drying –technology update. In Proceedings of Paste 2011. Edited by R.J. Jewel and A.B. Fourie, 5–7 April 2011. Australia Centre for Geomechanics, Perth, Australia. pp. 155–166.

Widger RA, Fredlund DG. Stability of swelling clay embankments. Canadian Geotechnical Journal, 1978;16: 140 -151.

Zhan, L. (2003). Field and laboratory study of an unsaturated expansive soil associated with rain-induced slope instability (Doctoral dissertation).

Zhan, T. L. T., Chen, R., & Ng, C. W. (2014). Wetting-induced softening behavior of an unsaturated expansive clay. Landslides, 11(6), 1051-1061.

Zhan, T. L., & Ng, C. W. (2006). Shear strength characteristics of an unsaturated expansive clay. Canadian Geotechnical Journal, 43(7), 751-763.

Zhan, T. L., Ng, C. W., & Fredlund, D. G. (2007). Field study of rainfall infiltration into a grassed unsaturated expansive soil slope. Canadian Geotechnical Journal, 44(4), 392-408.

Zhang, F. Z., & X.P., Chen. (2010). Influence of repeated drying and wetting cycles on mechanical behaviors of unsaturated soil. Chinese Journal of Geotechnical Engineering, 32(1), 41-46.

Chapter 2 Literature Review

2.1 Constitutive modelling of unsaturated soil

Fig. 2.1(a) and (b) show the marvelous role played by water to keep the sandcastle standing without any materials, like steel, used in modern civil engineering. A scientific interpretation behind this would be that the nanometre-scale layers of liquid on millimetre-scale grains in the sandcastle can dramatically increase the repose angle (the steepest stable slope that the substance can form) and allow the development of long-range correlations, or clumps (Hornbaker et al. 1997). Small quantities of water in the granular materials provides adhesive forces through an interstitial liquid bridges (See Fig. 2.2 (a)) between grains. The performance of such forces, provided by water at a relative small (micro-scopic) scale, in altering the macroscopic mechanical behaviours of soils are generally reflected by introduction of suction (and other physical quantities relative to water phase) into those continuum mechanics models (commonly used in geotechnical engineering).


(a)

(b)

Fig. 2.1 the marvelous contribution of water in (a) sandcastle and (b) Sandcastle Revere Beach, dubbed “Islands in the Sky by Matt Kaliner (http://www.wbur.org/artery/2015/07/27/sandcastle-matt)

Bishop (1959) first introduced the "suction" into the stress variable (basic variables of a continuum constitutive model), named Bishop's effective stress, to interpret the shear strength behaviour of soil at unsaturated state, which is expressed as

$$(\sigma_n - u_a) + \chi(u_a - u_w) \tag{2.1}$$

where the total normal stress, σ_n, in excess to the pore air pressure, u_a, is defined as net normal stress, and suction is defined as the excess of the pore air pressure over pore water pressure u_w. χ is the Bishop's parameter varying from 0 to 1(depending on the degree of saturation). Bishop's effective stress is defined by simply adding the suction term (due to moisture-induced correlation between grains or particles, scaled by the χ) to the net stress term (due to mainly contribution from mechanical loading). The use of χ, to scale down and average the interstitial adhesive force over a representative elementary volume, seems to be a reasonable approximation considering the fact that this force is only transmitted through the water fraction (see Fig. 2.2, the χ usually increases with increasing degree of saturation, S_r, as the saturated state varies in a soil) and has a reduced effect on the overall behaviour of the element, compared to the mechanical loading. However, the following efforts (e.g. Jennings and Burland 1962) suggested that use of Bishop's effective stress faces difficulties in representing some experimental features of unsaturated soils, for example, the wetting-induced collapse. As can be visualized in Fig. 2.3, wetting under relatively high net stress would like to cause soils' volume collapse (volume decrease). Meanwhile, the decrease of Bishop's effective stress would be provoked by suction decrease as the soil is saturated with more water. The release of effective stress should induce an increment in void ratio by definition. But the void ratio is observed to decrease upon wetting, which may be due to disappearance of interstitial liquid bridges (see Fig. 2.2(b)) that can provide adhesive forces and increase the soil

stiffness. This effect is hard to be accounted for by use of a single stress variable, such as Bishop's effective stress. This has prompted researchers to seek alternative continuum approaches for interpretation of unsaturated soil behaviour, such as, use of two stress state variables.

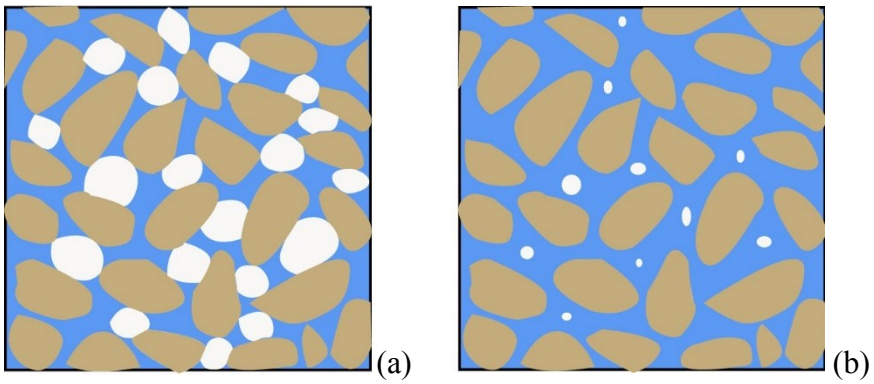

Fig. 2.2 Soils partially saturated with water (a) at higher degree of saturation and (b) at lower degree of saturation.

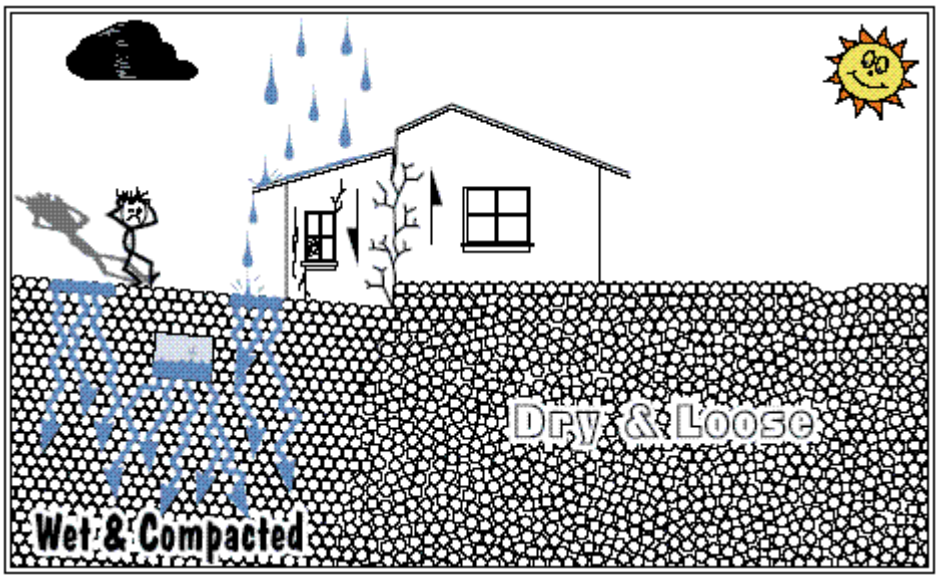

Fig. 2.3 Differential settlement of foundation due to non-uniform distribution of water content, particularly due to wetting-induced collapse of unsaturated soil (http://www.aegweb.org/)

Fredlund and Morgenstern (1977), from a theoretical equilibrium analysis for an unsaturated soil element based on concepts of multiphase continuum mechanics, suggested that

any two of the following three stress state variables can be combined to describe the stress state of an unsaturated soil

$$\boldsymbol{\sigma} - \mathbf{m}u_w \tag{2.2}$$

$$\boldsymbol{\sigma} - \mathbf{m}u_a \tag{2.3}$$

$$u_a - u_w \tag{2.4}$$

in which, $\boldsymbol{\sigma}$ is the (symmetric) total stress tensor consisting of six independent components, expressed in vector form as $\{\sigma_x, \sigma_y, \sigma_z, \tau_{xy}, \tau_{yz}, \tau_{xz}\}$ if Cartesian coordinate system is used with *x, y* and *z* denoting the base axes. u_w and u_a are pore air and pore water pressures, respectively, **m** is the column vector with 1 at normal stress entries and 0 at shear stress entries, i.e. **m** = {1, 1, 1, 0, 0, 0}, since neither air or water can sustain any shear stress (forces). Eq. (2.2) is in the same form of effective stress for saturated soils, but u_w is negative in unsaturated soils. Out of the three stress variables listed above, the pair constituted by second (Eq. (2.3)) and third (Eq. (2.4)) one received the widest acceptance as two independent stress state variables (Fredlund and Rahardjo 1993), terminated as net stress and suction.

Houlsby (1997), from a thermodynamics analysis, showed that, under the approximation that both the soil grains and the pore ¯uid are incompressible, the rate of work input per unit volume of unsaturated granular material, *L*, can be expressed as

$$\begin{aligned} L = & -u'^{(\mathrm{w})}_{,j} w^{(\mathrm{w})}_j - u'^{(\mathrm{a})}_{,j} w^{(\mathrm{a})}_j \\ & + n(1-S_{\mathrm{r}})u^{(\mathrm{a})}\dot{\mathrm{v}}^{(\mathrm{a})} \\ & + \left\{\sigma_{ij} - \left(S_{\mathrm{r}}u^{(\mathrm{w})} + (1-S_{\mathrm{r}})u^{(\mathrm{a})}\right)\delta_{ij}\right\}\dot{\varepsilon}_{ij} \\ & - (u^{(\mathrm{a})} - u^{(\mathrm{w})})n\dot{S}_{\mathrm{r}} \end{aligned} \tag{2.5}$$

The first two terms represent the power dissipated by water and air flow (where the $u'_{,j}{}^{(w)}$ and $u'_{,j}{}^{(a)}$ are excess pore pressure gradients in water and air phases, and $w_j^{(w)}$ and $w_j^{(a)}$ are artificial seepage velocities of water and air phases, respectively. The superscripts within brackets represent each of the flow phases ((w) for water and (a) for air), as in Houlsby (1997)), the third term represents the power input to compress the air phase ($\dot{v}^{(a)}$ is the volumetric strain of air phase). The fourth and fifth terms indicate that the quantities that are work-conjugate to two strain rates ($\dot{\varepsilon}_{ij}$ for soil skeleton and $\dot{S}_r$ for water phase) are

$$\boldsymbol{\sigma} - S_r u_w - (1 - S_r) u_a \tag{2.6}$$

$$n(u_a - u_w) \tag{2.7}$$

in which, S_r is the degree of saturation and n soil porosity (The superscripts are removed and replaced with a more common (subscript) style). Eq. (2.6) is termed as average soil skeleton stress (Wheeler et al. 2003) or constitutive stress (Sheng et al. 2004), which is similar to Bishop's effective stress for unsaturated soils. Eq. (2.7) is termed as modified suction (Wheeler et al. 2003). Several constitutive models have adopted this pair of stress variables to work with, e.g., the Glasgow Coupled Model proposed by Wheeler et al. (2003). Sheng et al. (2008) suggested this pair of stress variables are dependent on each other (e.g. change of suction will induce change in both), but their work-conjugate strains ($\boldsymbol{\varepsilon}$ and S_r) are independent of each other. Some researchers (e.g. Sheng et al. 2004; Sun and Sun 2012) prefer to use suction instead of modified suction in Eq. (2.6) along with the average soil skeleton stress. Sheng et al. (2004) suggested that, the porosity n plays a role similar to a scaling parameter and there is no essential difference in these two stress quantities. Eq. (2.5) can also be rearranged to give (Houlsby 1997)

$$
\begin{aligned}
L = & -u'^{(\mathrm{w})}_{,j} w_j^{(\mathrm{w})} - u'^{(\mathrm{a})}_{,j} w_j^{(\mathrm{a})} \\
& + n(1-S_\mathrm{r}) u^{(\mathrm{a})} \dot{\mathrm{v}}^{(\mathrm{a})} \\
& \left(\sigma_{ij} - u^{(\mathrm{a})}\delta_{ij}\right)\dot{\varepsilon}_{ij} \\
& + (u^{(\mathrm{a})} - u^{(\mathrm{w})})\left(S_\mathrm{r}\dot{\varepsilon}_{jj} - n\dot{S}_\mathrm{r}\right)
\end{aligned}
\tag{2.8}
$$

Now, the last two terms indicate that the strain rates which are work-conjugate to two stress variables (net stress and suction as represented by Eq. (2.3)) and Eq. (2.4)) are soil skeleton strain rate $\dot{\varepsilon}_{ij}$ and specific water volume change (strain-like quantity) rate $-\dot{\mathrm{v}}_\mathrm{w}/\mathrm{v} = \left(S_\mathrm{r}\dot{\varepsilon}_{jj} - n\dot{S}_\mathrm{r}\right)$, where v is the specific volume 1+*e*, and $\dot{\mathrm{v}}_\mathrm{w}$ is the specific water volume $1+S_\mathrm{r}e$, and *e* is the void ratio. These two strain rates are not independent variables, since the specific water volume change will change with changing soil skeleton strain, but the net stress and suction are independent of each other.

The pair of stress state variables preferred by different researchers are not limited to the aforementioned two. For example, Alonso et al. (2013) used a different pair of stress variables:

$$\boldsymbol{\sigma} - u_a + \overline{S_r}(u_a - u_w) \tag{2.9}$$

$$\overline{S_r}(u_a - u_w) \tag{2.10}$$

They formulated an elasto-plastic framework to interpret compacted soils behavior incorporating microstructural information. The constitutive stress (Eq. (2.9)) and effective suction (Eq. (2.10)) are dependent on void ratio, microstructural void ratio and degree of saturation through the effective degree of saturation (Alonso et al. 2013). Classification of existing pairs of stress variables used in the literature can be found in Gens (1996) and D'onza et al. (2011). On the eve

of completion of this thesis, the author has found another definition of stress proposed by Gallipoli and Bruno (2017), which is called "scaled stress":

$$[p - S_r u_w - (1 - S_r) u_a] S_r^{\lambda_r / \lambda_p} \tag{2.11}$$

Eq. (2.11) is the production of Bishop's effective stress and power function of degree of saturation (where p is the total mean stress, the model is only formulated for isotropic state), λ_r is the slope of the linear relation between log$e$/e_s and logS_r, e_s is the value of void ratio at saturated condition, λ_p is the slope of the saturated normal compression line. This single stress is adopted to formulate a bounding surface compression model which can also predict the collapse behaviour without using a second stress variable.

2.1.1 State surface model

Matyas and Radhakrishna (1986) were probably earliest researchers who suggested the concept of constitutive state surface for modeling the unsaturated soil behaviour, in which void ratio and water content were plotted as functions of the net normal stress and matric suction in three dimensional space. The two surfaces can be regarded as extensions of compressibility curve of saturated soils to the dimension of suction, and soil water characteristic curve from soil science to the dimension of net normal stress, respectively. Since then, this concept that uses net stress and suction as two independent stress variables has been followed by numerous researchers (e.g. Fredlund and Morgenstern 1977, Alonso et al. 1985). Fredlund and Rahardjo (1993) verified the uniqueness of the state surfaces under monotonic loading condition (i.e. the water content and void ratio varies monotonically) and established a complete framework of unsaturated soil mechanics. Alonso (1985) examined the applicability and flexibility of eight mathematical expressions to

describe the variation of void ratio with a large range of stress variables. These equations have been modified for better representing a certain type of soil behaviour (e.g. Fredlund 2000; Vu and Fredlund, 2006), or refined to avoid numerical issues at low net stress and zero suction levels (Vu and Fredlund 2006).

The state surface model can be used as a nonlinear elastic model for cases where both deformation and water content change are monotonic (involving both elastic and plastic changes but distinguishing the plastic strain from total strain is not necessary). The tangential elastic moduli at any stress (net stress and suction) level can be obtained by differentiating these two surfaces with an assumed Poisson's ratio (Cho and Lee 2001; Vu and Fredlund 2006; Alonso et al. 2003, Zhang and Briaud 2015) for application to problems involving general stress state.

It is known from the early works that some of the important features of unsaturated soils (e.g. stress-path dependent volume change behaviour and non-recoverable volumetric and shear straining, etc.) are difficult to predict using the state surface approach. More recently, Zhang and Lytton (2009 a, b) proposed a modified state-surface approach based on the systematic framework established by Fredlund and his co-workers, in which two conceptual type of surfaces are combined and utilized to describe the irrecoverable volume change behaviour of unsaturated soils: one is referred to as plastic hardening surface that can be represented using the traditional void ratio surface and the other elastic rebounding surface. The plastic hardening surface for a soil is stationary while the location of elastic rebounding surface depends on the stress history. Using the modified state surface formulation, Zhang and Lytton (2009a,b) reanalyzed the volumetric (isotropic) part of the Barcelona Basic Model (BBM) proposed by Alonso (1990) (this model belongs to the category of classic elasto-plastic incremental model and will be reviewed in details in the following section). The volumetric component of BBM essentially comprises two plastic

hardening surfaces (one collapsible surface associated primarily with mechanical loading and one expansive surface associated primarily with suction increase) and one elastic rebound surface. These surfaces constitute the analytical solution to BBM under isotropic stress conditions. The modified state surface model for volume change (Zhang and Lytton 2009a,b) was later extended to be coupled with the hydraulic behaviour of unsaturated soils by Zhang and Lytton (2011), in which similar concepts were adopted to construct the plastic and elastic gravimetric water content surfaces.

2.1.2 Elasto-plastic model

Alonso et al. (1990) proposed the first elasto-plastic model for unsaturated soils, which is referred to as the Barcelona Basic Model (BBM) in the literature. This model can be regarded as an extension of the well-known Modified Cam Clay (MCC) to unsaturated state, or mathematically extension to the dimension of suction. Since then, a large number of elasto-plastic models have been formulated (e.g. Wheeler and Sivakumar 1995; Cui and Delage 1996; Bolzon et al. 1996, Gens and Alonso 1992; Alonso et al. 1999; Delage and Graham 1996; Wheeler 1996; Dangla et al.1997; Vaunat et al. 2000; Wheeler et al. 2003; Gallipoli et al. 2003; Sheng et al. 2004; Vassallo et al. 2007, Sheng et al. 2008). Most of these models, through the use of either first pair of stress variables (i.e. net stress and suction) or second pair of stress variable (i.e. soil average skeleton stress and (modified) suction) (reviewed in the previous section), have been developed based largely on the BBM, and can be regarded, as stated by Sheng (2004), as variants of the BBM. Detailed reviews of these models can be found in several studies (Wheeler and Karube 1996; Gens et al. 1996; Sheng et al. 2008; Sheng et al. 2011). Only three of them as representatives are reviewed herein with only their important and distinguishing features , namely, Barcelona Basic

Model (BBM) (Alonso et al. 1990); Glasgow Coupled Model (GCM) (Wheeler et al. 2003) and Sheng, Fredlund and Gens Model (SFG) (Sheng et al. 2008).

BBM (Alonso et al. 1990). The BBM was originally formulated in classic incremental form. The model uses net stress and suction as the independent stress variables, and the formulation was first carried out in the net normal stress and suction (*p, s*) space (i.e. isotropic stress states) and then extended to triaxial states following the MCC for saturated soils. First, the virgin compression behaviour of unsaturated soil is described by the straight line in the *v*-log*p* plane, where *v* is the specific volume (equal to 1+*e*), as MCC. But the straight lines at unsaturated condition have different slopes and intercepts at reference net stress value, both of which are functions of suction. While in elastic domain, the slopes of isotropic unloading-reloading line (at constant suction) and suction unloading lines (wetting lines at constant net stress) are assumed to be two constants, and independent of any stress variables. The relationship between yielding stresses (or hardening parameters) at saturated and unsaturated conditions can be derived by following first a unloading and then a wetting path at an equal volumetric plastic strain level (i.e. relating the specific volumes along this stress path). This resulted relationship is the curve called Loading Collapse (LC) curve in the (*p*, *s*) space. In deriving LC curve, another assumption adopted is that the swelling at the reference net stress state from unsaturated to saturated virgin compression lines is also elastic. Another yielding curve exists in the (*p*, *s*) space to consider the plastic straining induced by the virgin drying (suction increase), which is the straight line parallel the *p*-axis, called SI yield curve. The virgin suction increase relation (*v*-log*s*) is also assumed to be a straight line. The two curves in the *p*-*s* plane jointly constitutes the yield surface for isotropic stress states. Both their locations are controlled by the total plastic strain, in other words, they are coupled with each other.

The model is completed by extending the above formulation into three dimensional stress state at different suction levels. The yield surfaces at different suction levels in the (q, p) stress space follows the MCC ellipse whose size is controlled by the suction-related hardening parameter and suction-related tensile stress. The tensile stress or the shear strength is linked to suction using the simplest linearity. A non-associated flow rule is modified following Ohmaki (1982) to define the direction of plastic strain.

GCM (Wheeler et al. 2003). The Glasgow Coupled Model (GCM) proposed by Wheeler et al. (2003) is quite appealing as its ability to model both the mechanical and water retention behaviour of unsaturated soil in a highly coupled fashion. Solowski (2008) stated that this fashion, not included in some traditional constitutive model for unsaturated soils (such as the BBM), would become one of the most important features of next generations of constitutive models for unsaturated soils.

The model due to Wheeler et al. (2003) uses the second pair of stress variables (i.e. the average soil skeleton stress and modified suction). The physical meaning of these two stress variables has been interpreted by Wheeler et al. (2003), from a microscopic point of view, as (*i*) the average soil skeleton stress reflecting combined contributions of total stress, pore air pressure, and pore-water pressure within bulk water on the stresses transmitted through the soil skeleton, with two pore pressures being weighted by degree of saturation, and (*ii*) modified suction representing the effect of meniscus water. Correspondingly, soil skeleton strain and degree of saturation are used as the strain variables as per thermodynamics principle.

The model is formulated in isotropic stress state in terms of the total stress (or in terms of the average soil skeleton stress since the two pore pressures are isotropic in nature). Three yield

curves are given in the plane of average soil skeleton stress and modified suction, based on the microscopic analysis:

(1) **LC** (load collapse) yield curve: a straight line parallel to modified suction axis. Plastic straining of soil skeleton (process of slippage at inter-particle or inter-packet contacts) is associated with this curve. The straight line assumption for the LC is based on a microscopic analysis: the effect of suction value in the meniscus water on overall skeleton stability is much less important than number of contacts where meniscus water lens is present. The amount of meniscus of water within a soil corresponds plastic change of degree of saturation. Thus effect of meniscus water on plastic straining of soil skeleton is considered by a coupled movement of **LC** yielding curve (**LC** moves when there is plastic change of degree of saturation), which will be discussed in the following.

(2) **SI** (suction increase) yield curve: a straight line parallel to average soil skeleton stress axis. Plastic decrease of degree of saturation is associated with this curve, which is different from the SI in BBM. The SI in BBM indicates the maximum suction that a soil has ever been subjected, past which, plastic straining of soil skeleton occurs. Thus, SI in BBM is in fact for mechanical behaviour, while SI in GCM model is in terms of hydraulic behaviour.

(3) **SD** (suction decrease) yield curve: another straight line also parallel to average soil skeleton stress axis. Plastic increase of degree of saturation is associated with this curve.

The elastic and plastic volumetric strain are calculated using the similar philosophy as in MCC, but with effective stress replaced by average soil skeleton stress (Bishop's stress). The water retention behaviour is modeled as an elasto-plastic process similar to mechanical plasticity. Specifically, two primary (wetting and drying) curves in the degree of saturation vs. modified

suction plane represent the elasto-plastic process while elastic process (recoverable change of degree of saturation with changing modified suction) is represented by the scanning curves in between. This technique of analogy was suggested by Dangla et al. (1997) and then followed by other researchers (e.g. Sheng et al. 2004). Thus, the locations of SI and SD are related to the current states (modified suction and degree of saturation) in the hysteretic SWCC, which will move at the same time. However, plastic degree of saturation change and plastic volumetric straining may not occur simultaneously.

The plastic volumetric strain occurs only on LC yielding curve, the plastic degree of saturation change occurs only on SI or SD yielding curves. But the one plastic process may not be accompanied by the other, which implied an associated flow rule. Only these two curves (LC and SI (or SD)) are activated simultaneously, both plastic processes occur. However, movement of any one of the three yielding curves will induce coupled movements of the other two for any stress path. These synchronized movements reflect the interaction between the mechanical and hydraulic behaviours of unsaturated soils: the movement of LC accompanying those of SI or SD accounts for the influence of plastic change of degree of saturation (or the amount of meniscus water lens) on the overall stability of soil skeleton; the movements of SI and SD accompanying that of LC reflect the influence of plastic volumetric strains on the location of the primary drying and primary wetting curves. This hydro-mechanical coupled movement is mathematically described using two constants. The hardening of any yield surface comprises two parts (plastic volumetric strain and degree of saturation change) in this coupling model. The hydro-mechanical coupling behaviour of unsaturated soils is also reflected in the two stress variables adopted. Use of average soil skeleton stress indicates a degree of saturation-dependent stress-strain relationship, and use of modified suction implies a porosity-dependent saturation-suction relationship.

The model by Wheeler et al. (2003) can reproduce some important behavioural features of unsaturated soils, such as collapse during wetting as BBM. In fact, the path traced by the cross point of SD and LC during yielding on SD upon wetting is analogous to the shape of LC in BBM. And the model can also simulate some feathers that cannot be modelled using more traditional model, such as the cumulative plastic volume compression during wetting and drying cycles even over fixed range of suction. Further developments of GCM can be found in Raveendiraraj (2009) and Lloret-Cabot et al. (2013).

SFG (Sheng et al. 2008). Most components of the SFG model formulated by Sheng et al. (2008) are originated from Cam Clay Model, including plastic volume change behaviour, elastic volume change behaviour, yield function on the *p-s* plane, hardening law etc. The incremental stress-strain relationship are derived from the log linear relationship between "specific volume" and "effective stress" by dividing effective stress to net stress and suction into two separate parts. The same technique is used for yielding function. The consequence is that these equations can smoothly recover to those for saturated soil established using effective stress principle, provided that the functional compressibility (the one associated with stress is different from the one associated suction, both are functions of net stress and suction) are properly defined. The yield function are defined in the space of suction and net stress, thus it can be regarded that this model are working with the stress variable pair: net stress and suction. Mostly, the selected functional compressibility makes the stress-strain relation non-integrable. Thus, the resulted virgin drying/compression surface in the space of void ratio-net stress-suction are not unique, but stress path dependent, so do the elastic rebound plane and yield curve in the net stress-suction plane. The evolution of yield function should be carefully evaluated for use of SFG model based on the

applied stress path. Use of SFG need a numerical integration procedure even for very simple stress path.

The SFG is able to predict the large irreversible compression induced by initial drying for initially slurry soil under relatively low stress level. This is simulated as an elasto-plastic process (different from most of the models, including BBM and GCM). It can also predict the wetting-induced collapse behaviour of compacted soil, in a similar way to the BBM. Soil water retention model can be coupled with the SFG, which can also be used independently for modeling the mechanical behaviour of unsaturated soils.

2.1.3 Models for unsaturated expansive soils

The models discussed in the earlier sections and most of existing models in the literature can simulate most of the important features of unsaturated soil under various stress path conditions (including hydraulic/mechanical loading/unloading). For example, wetting-induced elastic swelling under low net stress or plastic collapse under high net stress condition (BBM, GCM and SFG), shrinkage behaviour of initially slurry soils during drying (GCM and SFG), cumulative plastic volume compression under cyclic suction and the effect of cyclic suctions on soil response to subsequent mechanical loading(GCM). However, one behavioural feature of unsaturated expansive soil, that is irrecoverable/plastic swelling (volume increase) during cyclic hydraulic loading, is not covered. This behaviour is significant at low stress conditions and may have an important influence on the performance of geotechnical infrastructure.

There are a couple of models that are formulated for modeling this behaviour of expansive soils (Gens and Alonso, 1992; Alonso at al. 1999; Sánchez et al. 2005; Sun and Sun 2012; Wang and Wei 2014). Some of these models are proposed based on a consideration of the double-level

structure of soil, which includes a coupling mechanism (function) between these two structures (Gens and Alonso, 1992; Alonso at al. 1999; Sánchez et al. 2005). Some other models are proposed from a phenomenological perspective (Sun and Sun 2012), similar to conventional models. Besides these models, some researchers suggested that this behaviour of expansive soils (i.e. irrecoverable/plastic swelling (volume increase) during cyclic hydraulic loading) can be modelled by introducing a non-associated flow laws in some coupled hydro-mechanical models (Wheeler et al. 2003, Sheng 2004), in which plastic change of degree of saturation is modeled by introducing the hydraulic yield surfaces. Yielding on hydraulic yield surface can induce both plastic change of degree of saturation and plastic volumetric strain if a non-associated flow law is adopted. However, to the best of the author's knowledge, this has not been explicitly achieved with a defined non-associated flow law in the literature.

In this study, the slope stability of expansive soil slope is affected by its swelling behaviour, through a swelling-induced softening (decrease strength parameters) behaviour. Softening may be induced by two mechanism (plastic straining): (i) swelling will induce stress redistribution, which, if exceeding the soil resistance, will induce plastic shear strain, (ii) plastic (volumetric) swelling itself. The second one is more important for cyclic hydraulic loading (cyclic suction changes). This thesis is focused on investigating slope stability under a monotonic suction decrease condition, so the former is more significant. Thus, the shear strength behaviour of unsaturated soil and its evolution trends with plastic straining is of more importance, and will reviewed in section 2.1.5.

2.1.4 Water retention model

The water retention capacity of unsaturated soils is traditionally defined using the relationship between water content (which can be gravimetric water content, degree of saturation

or volumetric water content) with soil suction (Fredlund and Rahardjo 1993 and Fredlund et al. 2012). In earlier works, a single curve is used to quantify the water retention capacity of unsaturated soils, named as the Soil Water Characteristic Curve (SWCC) or Soil Water Retention Curve (SWRC), such as, the well-known Brooks and Corey (1964), van Genuchten (1980) and Fredlund and Xing (1994) models, etc. Note the terminologies, SWCC SWRC, and SWRM (Soil Water Retention Model) are used to represent the the same behaviour of unsaturated soils, i.e., the soil water rentetion behaviour, in this thesis. These traditional models are used to fit the experimental data from the elemental samples which do or do not undergo significant volume change when subjected to the suction changes during testing.

Research in the past decade has shown that the soil-water retention curve (SWRC), is not unique or in other words, water content is not in one-to-one correspondence with suction. This arises from not only hydraulic hysteresis but changes in the pore-size distribution (PSD) dependent on stress path (Klausner 1991). Such observed macroscopic behaviours can be explained by soil particle-water interaction and changes of soil structure at microscale (Simms and Yanful 2002, 2005). The conventional single curve models are therefore not sufficient to fully describe the water retention behaviour of unsaturated soils in a real boundary value problem where the soil elements can be subjected to complicated stress paths (hydraulic/mechanic loading/unloading/ reloading). Recent efforts have been used to advance/enhance the traditional water retention models to include the effects of hydraulic hysteresis (e.g. Li 2005; Pham et al., 2003), changing PSD (e.g. Gallipoli et al. 2003, Mašín 2010) or both (e.g. Nuth & Laloui 2008; Hu et al. 2013; Tsiampousi et al. 2013; Gallipoli et al. 2015) for being implemented into the numerical analysis. The Brooks and Corey (1964) and van Genuchten (1980) models have been the most popular two used as basis into which advanced features are inserted: hydraulic hysteresis is described using two main (drying/wetting)

degree of saturation vs. suction relationships with numerous scanning paths in between, while effect of changing pore-size distribution have been accounted for by relating these relations to a mechanical variable, e.g. mechanical stress, (plastic) volumetric strain (e.g. Wheeler et al. 2003) or void ratio (e.g. Gallipoli et al. 2015). It seems that void ratio-dependent SWRC are easier to be used to explain the experimental data without the necessity of converting the measured void ratio to strain.

In terms of the shape of the water retention behaviour, the void ratio-dependent retention model being advanced most recently can be categorized into and also studied within four main groups according to the shape of main isochoric (iso-volumetric) curve: (i) continuous curve in logS_r-log$s$ plane, e.g. Gallipoli (2012); Gallipoli et al. (2015); (ii) continuous curve in S_r-log$s$ plane, e.g. Pedroso and Williams (2010); Tsiampousi et al. (2013); (iii) straight line in S_r -log$s$ plane, e.g. Nuth and Laloui (2008), Sun et al. (2012); (iv) straight line in logS_r -log$s$ plane, e.g. Mašín (2010), Khalili (2008). Many of these models (for example Gallipoli et al. 2015 and Nuth and Laloui 2008), although represented as curves or straight lines defined in either spaces, put more emphasis on the effect of void ratio on air entry value, resulting only in change of position of isochoric curve with void ratio, and do not change the shape or slope of the SWRC. Physically (experimentally), the shape of water retention curve can change with void ratio (Vanapalli et al. 1999), or with pore size distribution (Simms and Yanful 2002, 2005). Models that account for the effect of void ratio on shape/slope of isochoric curve includes Mašín (2010), Salager et al. (2013), D'Onza et al. (2011), Pasha et al. (2016). Some other modellers have applied the framework analogous to mechanical elasto-plasticity to incrementally describe the water retention behaviour by several constants, which may be easier to be thoroughly coupled with a mechanical behaviour, resulting

in an integrated hydro-mechanical model (Wheeler et al. 2003). Bounding surface plasticity is also used to formulate the SWRM (e.g. Gallipoli et al. 2015).

All these mechanical variable-dependent models can be used in conjunction with a mechanical model (reviewed in the previous sections, sections 2.1.1-2.1.3) to describe the hydro-mechanical behaviour of unsaturated soil for numerical analysis of boundary value problems. The nature of mechanical variable dependence is of more importance in modeling large deformation problem. In this thesis, some of these models (e.g. the one proposed by Gallipoli (2015) are adopted in conjunction with a mechanical model (e.g. BBM)) are used in developing the UNSATCON-ML. The highly integrated hydro-mechanical model, i.e. GCM (Wheeler et al. 2003), is also implemented into UNSATCON-ML.

2.1.5 Shear strength of unsaturated soil

The shear strength behaviour of saturated soils has been often described by the Mohr-Coulomb Criteria, following which, the shear strength of unsaturated soils is described by including a term accounting for the suction contribution. In the past several decades, various different equations have been proposed based on the experimental observations for interpreting, predicting or estimating the (peak) shear strength of unsaturated soils since measurements at different degree of saturations (different suction) condition are very time-consuming. Review on different shear strength equations can be found in Sheng (2011), Vanapalli (2009), etc. Vanapalli (2009) suggested that there are 46 equations in the literature with different number of fitting parameters until then. The author believes that more equations may have already been and will likely be proposed in the future. The performance of several commonly-used equations has been compared in Sheng (2011). Several commonly-used equations, which have been implemented in

some commercial software, e.g. SoilVision (Fredlund et al. 2012; Zhang et al. 2015), for facilitating use in practice, are summarized in Table 2.1 .

The underlying philosophies for proposing these six equations (in Table 2.1), physical meanings or typical values of fitting parameters (if any) embedded in theses equations, and their performance for 1D/2D slope stability by limit equilibrium method are discussed in Zhang et al. (2015). Among these, two equations have received significant attention for computing factor of safety in slope stability analysis due to their simplicity: (1) Fredlund and Morgenstern (1978) model assumes a linear increase of shear strength with suction; and (2) Vanapalli et al. (1996) model needs no fitting parameter, providing a nonlinear increase of shear strength with suction. These two equations will be adopted in our study as either failure criteria for calculating the FS or yield criteria in an extended Mohr-Coulomb elasto-plastic model for evaluating the stress-deformation in slope stability analysis, with incorporation of strain-softening behaviour.

Table 2.1. Several well-known models for shear strength of unsaturated soil (after Zhang et al. 2015)

References	**Equations**
Fredlund and Morgenstern (1978)	$\tau_f = c' + (\sigma - u_a)\tan\phi' + (u_a - u_w)\tan\phi^b$
Fredlund et al. (1996) Vanapalli et al. (1996)	$\tau_f = c' + (\sigma - u_a)\tan\phi' + (u_a - u_w)(\frac{\theta_w}{\theta_s})^\kappa \tan\phi'$
Vanapalli et al. (1996)	$\tau_f = c' + (\sigma - u_a)\tan\phi' + (u_a - u_w)\left(\frac{\theta_w - \theta_r}{\theta_s - \theta_r}\right)\tan\phi'$ $\tau_f = c' + (\sigma - u_a)\tan\phi' + (u_a - u_w)\left(\frac{S - S_r}{1 - S_r}\right)\tan\phi'$
Vilar (2006)	$c_{tot} = c' + \frac{(u_a - u_w)}{a_f + b_f(u_a - u_w)}$
Khalili and Khabbaz (1998)	$\tau_f = c' + (\sigma - u_a)\tan\phi' + (u_a - u_w)(\lambda')\tan\phi'$ where, $\lambda' = 1.0 \qquad u_a - u_w \le AEV$

	$\lambda' = \{(u_a - u_w)/AEV)\}^{-0.55}$ $u_a - u_w > AEV$
Bao et al. (1998)	$\tau_f = c' + (\sigma - u_a)\tan\phi' + (u_a - u_w)(\zeta)\tan\phi'$ where, $\zeta = 1.0$ $(u_a - u_w) \le AEV$ $\zeta = \frac{\log(u_a - u_w)_r - \log(u_a - u_w)}{\log(u_a - u_w)_r - \log AEV}$ $AEV < (u_a - u_w) < (u_a - u_w)_r$ $\zeta = 0$ $(u_a - u_w) \ge (u_a - u_w)_r$

where

- τ_f is the shear strength; c' is effective cohesion for a saturated soil; ϕ' is effective angle of internal friction; $(\sigma - u_a)$ is the net stress on the failure plane where σ is total normal stress and u_a is pore air pressure. The angle ϕ^b represents the rate of increase in shear strength relative to the matric suction.
- θ_w is volumetric water content and θ_s is the saturated volumetric water content, and κ is a fitting parameter.
- θ_r is the residual volumetric water content, S is the degree of saturation, and S_r is the residual degree of saturation.
- c_{tot} is the total cohesion and a and b are fitting parameters.
- AEV is the air-entry value of the soil.
- $(u_a - u_w)_r$ is the residual suction.

2.2 Slope stability analysis

Approaches for assessment of slope stability can be categorized into two groups: (i) deterministic assessment and (ii) probabilistic assessment. The deterministic assessment of slope stability is essentially the calculation of the Factor of Safety (FS) for a given slope (i.e. known soil shear strength properties, geological stratum and slope geometry) at a given condition (i.e. pore water pressure contour within the slope profile and external loading if any). Slope stability assessment relies solely on this single scalar of FS, and many existing design codes provide the minimal requirement (criteria) in terms of FS for various types of slope at different condition. The probabilistic assessment provides the probability of slope failure at any possible conditions, which

takes into consideration uncertainties in either soil properties or environmental conditions or both by using the probability theory. Several researchers have made significant progress in probabilistic assessment of geotechnical infrastructure (e.g. Griffiths and Fenton 2000, Griffiths and Fenton 2004, Fenton and Griffiths; 2008). The number and uncertainties of unsaturated soil properties are greater than those of saturated soils, hence uncertainties associated with unsaturated slope are considerable, Research in this direction started to receive attention quite recently (e.g. Le et al. 2013; Ali et al. 2014 etc.). However, the probabilistic approach serves as a good supplement to deterministic approaches in slope stability analysis but has not replaced it in practice (Duncan 1996). A successful probabilistic assessment depends on an accurate deterministic method, in other words, the deterministic method is the basis for probabilistic analysis which involves calculation of numerous FSs (when Monte Carlo technique is used) for any possible parameters and/or conditions. This thesis only focuses on deterministic approaches for slope stability assessment, which are briefly reviewed herein.

2.2.1 Definitions of FS and calculation method

The limit equilibrium method, finite element method and limit analysis method are the three most commonly used deterministic methods for slope stability analysis. The physical definitions of FS are similar but not exactly the same amongst these methods, the differences arise from the specific calculation procedures in each method. Several definitions that are in frequent use are reviewed here.

In the limit equilibrium method, the FS is defined as the ratio of available shear strength to the equilibrium shear stress at any point within slope soils

$$FS = \frac{\tau_f}{\tau} \tag{2.12}$$

If the well-known Mohr-Coulomb model is adopted to characterize available shear strength of soil, the above equation can be written as

$$\tau = \frac{c' + \sigma \tan\phi'}{FS} = \frac{c'}{FS} + \sigma \frac{\tan\phi'}{FS} \tag{2.13}$$

Thus, another statement for this definition is "when the soil shear strength parameters are reduced to c'/FS and $\tan\phi'/FS$, all points along a given slip surface will reach a state of limit equilibrium conditions." Although some inherent limitations exist in this definition, this definition based on strength storage has been widely accepted by researchers around the world, abundant practical experience has been accumulated by its extensive use since the early 20th century.

Although this FS and the associated Limit Equilibrium Methods has many advantages, the inherent limitations have to be kept in mind when using them.

(i) An assumption is implied in almost all the Limit Equilibrium Methods for two-dimensional and three-dimensional analyses but generally overlooked by practitioners, i.e. the FS remains a constant along the slip surface, which has been criticized by many researchers. For example, Wright et al. (1973) and Tavenas et al. (1980) pointed out that the value of FS varies from one location to another along the slip surface, particularly for those through multiple soil layers.

(ii) An iterative procedure is required for computing *FS* for LEMs that are relatively rigorous in terms of the static equilibrium condition satisfied (e.g. the Morgenstern-Price Method), this is because the normal stress on the slip surface is expressed as a function of FS when

establishing the governing equations. i.e. $\sigma = f(FS)$. Thus, the stress acting on the slip surface computed from limit equilibrium method cannot be representative of the actual stress state; in addition, the effect of definition of *FS* based on strength storage is beyond reducing the strength parameters.

(iii) A same magnitude of reduction factor (i.e. *FS*) applied to both c' and $\tan\phi'$ seems to be not appropriate, because of different physical meaning between c' and $\tan\phi'$, which also play different roles in the governing equations.

(iv) The reduced strength parameters (i.e. c'/FS and $\tan\phi'/FS$) used in the LEMs are not the true strength parameters of soils, thus, the failure modes are just fictitious collapse mechanisms (Michalowski, 2002). In other words, the critical slip surface obtained using limit equilibrium method is not the real one corresponding to slope failure.

The above four limitations apply to slopes in either saturated or partially saturated conditions. For slopes in unsaturated conditions, Limitations (3) and (4) can be extended for the component of shear strength due to suction contribution, i.e. non-appropriateness of reducing this component by the same magnitude of *FS*, which, nevertheless, is assumed in almost all current analyses of slope in partially unsaturated condition.

In finite element methods, different computational procedures have been used to obtain a *FS*, which either make use of the stress field from a stress-strain analysis or is incorporated into stress-strain analysis. Thus, the finite element-based method to calculate the *FS* are further subdivided into two categories: (*i*) Stress-Based Finite Element Methods (SBFEM); (*ii*) Shear Strength Reduction Finite Element Methods (SSRFEM). Correspondingly, there exist two groups of *FS* definition:

Group 1 (SBFEM):

$$FS = \frac{\int_0^l \tau_f dl}{\int_0^l \tau dl} = \frac{\int_0^l (c' + \sigma' \tan\phi') dl}{\int_0^l \tau dl} \tag{2.14}$$

$$FS = \frac{\int_0^l dl}{\int_0^l \frac{(\sigma'_1 - \sigma'_3)}{(\sigma'_1 + \sigma'_3)} dl} \tag{2.15}$$

$$FS = \frac{\int_0^l (c' + \sigma' \tan\phi') dl}{\int_0^l \frac{(\sigma'_1 - \sigma'_3)}{(\sigma'_1 + \sigma'_3)} (c' + \sigma' \tan\phi') dl} \tag{2.16}$$

where, *dl* is infinitesimal length along the potential slip surface, σ', effective normal stress; σ'_1 and σ'_3, major and minor effective principal stresses, respectively; τ, mobilized shear stress along the potential slip surface. In the SBFEM, the stress field within the slope are calculated by the Finite Element Analysis. The the FS along the potential slip surface can be calculated by substituting the stresses into Eqs. (2.14), (2.15) or (2.16). An optimization technique is used to search for the slip surface with the lowest factor of safety. Eq. (2.14) is first proposed by Kulhawy (1969), which has the same form as that of method of slices. However, the stress field obtained using finite element analysis is different from that using method of slices. Scoular (1997) used Eq. (2.14) to solve a series of slope stability problems and then identified this method as having the most appropriate factor of safety definition. However, the result from Zheng et al. (2006) suggested that the FS obtained from Eq. (2.14) were different from those using either LEM or SSRFEM, and use of Eq. (2.14) may lead to some unreasonable results for certain scenarios. Li (2010) pointed out that the FS obtained using Eq. (2.14) has rational mechanical definition only if the slip surfaces are either circular arcs or straight lines. Pham et al. (2003) suggested the definition of FS for Eq. (2.14) is not appropriate when computed shear stress from finite element analysis has negative sign. Eqs

(2.15) and (2.16) were proposed by Zienkiewicz et al. (1975) and Adikari and Cummins (1985), respectively. The effect of principal stress on FS is considered in both Eqs. (2.15) and (2.16), which, however, are shown to lead to a higher FS than those defined by Eq. (2.14) (Fredlund et al. 1997) and therefore are seldom accepted.

Group 2 (SSRFEM):

$$c_f = \frac{c}{FS} \qquad \tan\phi_f = \frac{\tan\phi}{FS} \tag{2.17}$$

The technique incorporating Eq. (2.17) in Finite Element Analysis is first suggested by Zienkiewicz et al. (1975), who found that reducing the coefficient that brought the slope into a state of critical state condition was essentially the same as that from traditional Limit Equilibrium Method. Since then, many researchers have been made great contribution on the application of the SSRFEM to practical engineering problems, e.g. Griffiths 1980, Griffiths and Lane 1999. This definition in SSRFEM (Eq. (2.17)) is similar to that of traditional LEM discussed in the preceding chapter. It should be noted that there exists some differences; e. g., the stress field from SSRFEM is more accurate than those from LEM which required a number of assumptions in order to make the equations determinate. The stress state and potential failure mode computed using the reduced strength parameters are not the real stress state and failure mode for a slope, and is just a possible fabricate state of a slope. This is similar to limitation (ii) of LEM. mentioned above.

However, it cannot be denied that the SSRFEM has many advantages compared with the LEM, as summarized by Griffiths and Lane (1999)*:*

(a) No assumption needs to be made in advance about the shape or location of the failure surface;

(b) No need for assumptions about side forces;

(c) If realistic soil compressibility data are available, the FE solutions will give information about deformations at working stress levels;

(d) The FE method is able to monitor progressive failure up to and including overall shear failure in, for example, an analysis involving sequential construction of an excavation or embankment.

The last one also applies for condition where the slope is gradually brought to failure by rainfall, if the hydro-mechanical response of the slope to rainfall is well analysed using FEM.

Both the SBFEM and SSRFEM are first used/tested for analysis of a dry slope with simple geometric characteristics. They were then adopted to analyse complex saturated soil slope stability and slopes with a *stable* ground water table using the effective stress principle. In recent years, attempts have been made to apply these methods in computing the FS of slope in which part of the soils are in a state of unsaturated condition (Griffiths and Lu 2005; Zhang et al. 2014). No matter what conditions these methods are being used in, their principles and procedures generally remain the same.

2.2.2 Infinite (1D) slope stability analysis

In terms of geometry characteristics, any slope stability analysis cannot be idealised as a 1D problem. Nevertheless, infinite (1D) slope simplification are tremendously widely used by both researchers and practitioners. There may be two reasons for this: (*i*) some natural and engineered slope failures exhibit a shallow sliding surface which encompasses a failure mass with a high length/depth ratio (Milledge et al. (2012) from a comprehensive numerical study suggested critical length/depth ratio above which the errors induced by 1D simplification are acceptable (within 5%));

(*ii*) the simplified 1D problem is an idealised starting point for understanding the complicated hydro-mechanical response of each soil element to changes of various external factors, that lead eventually to global collapse. These two are both especially true for rainfall-induced failure of initially unsaturated soil slopes, considering that the constitutive relationships (including the stress-strain relationship and water retention behaviour) are much more complicated than those for saturated soils.

The early simplistic use of infinite slope formulation is to calculate the factor of safety through application of overall force equilibrium condition for a thin and dry shallow layer in the vertical direction (e.g. Duncan and Wright 2014). The infinite slope formulation has later been extended to include saturated (Lade 2010; Conte and Troncone 2012) or unsaturated (Rahardjo 1995; Huang et al. 2016) water flow regimes. These types of studies firstly conduct more advanced numerical analysis to obtain the flow regime. Then the force equilibrium condition is used to calculate the factor of safety using the definition of Eq. (2.13). For partially saturated conditions, the effective cohesion is replaced with apparent cohesion considering the contribution of suction. As can be seen, for use of some shear strength equation, in addition to suction, the water content (degree of saturation) on any potential failure surface should be determined or extracted from a advanced numerical analysis.

Within the framework of infinite slope formulation, stress and displacement developments that result in failure have been investigated either analytically or numerically (e.g. Teunissen and Spierenburg 1996; Di Prisco and Pisanò 2011; Griffiths et al. 2011). Elasto-plastic models are often utilised to simulate the mechanical behaviour of soil element at point level, the elasto-perfectly plastic model (a linear elastic component combined with a Mohr-Coulomb yield criteria) is most preferred by researchers in the context of fully saturated problem, for which the strain-

softening behaviour is also incorporated in some studies (e.g. Di Prisco and Pisanò 2011). Recently, some investigators also started to use the infinite slope model to study meticulously the sliding mechanism of failure mass under unsaturated condition (e.g. Buscarnera and Di Prisco 2011). This technique seems to be very useful since the rainfall induced failure mostly exhibits a shallow slip surface. But incorporating those complex constitutive models (e.g. the suction-dependent yield criteria, which is sometime also dependent on degree of saturation, moreover, the elastic behaviour of unsaturated soils is highly nonlinear) into a hydro-mechanical coupled framework to fully capture all the behavioural features of soils leading to failure is not as simple as the "early simplistic use of infinite slope formulation". One of the contribution of the thesis is to obtain some promising results for explaining the surficial failure mechanism of unsaturated soil slopes induced by rainfall, within the framework of infinite slope formulation.

2.2.3 Two and three-dimensional (2D and 3D) slope stability analysis

The first method to calculate the FS under 2D condition was probably proposed by Petterson in 1916 (documented later in Petterson 1955). Since then, very fruitful achievements have been made in development of methodologies to analyse the slope stability (primarily to calculate the FS) under both 2D and 3D conditions. The development of methodologies is closely linked to the developments of computer technology. During the period when modern computer facilities were not available, most of the methods were established using the 2D limit equilibrium (slice-method) concept, which may or may not use a simple iterative procedure (e.g. Fellenius 1936; Bishop 1955; Janbu 1954), that can be accomplished by hand calculations. A little more rigorous LEMs has been made possible with the slow but gradual popularization of modern computers (e.g. Spencer 1967; Morgenstern and Price 1965; Sarma 1973; Fredlund and Krahn 1977), the same is true for more advanced methods based on finite element technique (Griffiths

and Lane 1999; Kulhawy 1969; Scoular 1997). The various 2D methods and their limitations and strengths can be found in a number of the review papers, books and software manuals (e.g. Duncan 1996). During the past several decades, analysis of slope stability under 3D conditions have been receiving an increasing research attention. Most of these 3D methods can be regarded as extension of those existing 2D methods, which use limit equilibrium (Qi 2013) or finite element techniques (Griffiths and Marquez 2007), to the third dimension in space. This extension provides more possibilities regarding the assumptions embedded into those LEMs. Due to this reason, it seems that there are more different types of 3D LEMs in the literature. A comprehensive review of various 3D LEMs has been made in the author's Master's thesis (Qi 2013). Even though the capacity of high-speed modern computer will not be the main obstacle to 3D slope stability analysis that is much more computationally expensive, 3D methods are still not routinely used in practice, unlike 2D methods. Research on limitations, accuracy, numerical robustness and applicability of various 3D methods is still warranted.

In terms of constitutive models, soils in these 2D/3D slope stability analyses are commonly modeled as a simple Mohr-Coulomb material in the content of saturated soil mechanics using the effective stress principle. Only recently, incorporation of the unsaturated soil models into slope stability analysis has been investigated for cases where a significant portion of unsaturated zone exists. Considering the complexities of both unsaturated soil models (formulated using two stress state variables as outlined in section 2.1) and 2D/3D geometrical failure characteristics, slope stability analyses are conducted in the framework of infinite slope formulation in this thesis, which focuses on the responses/features of unsaturated expansive soils upon wetting and their effects on the slope failure. As discussed in Section 2.2.2 and many other geotechnical problems, e.g., consolidation (also investigated in this thesis), 1D formulation would be a more suitable

framework within which the most important features of geotechnical problem (stress, strain and water flow, etc.) can be explained/investigated in a more explicit manner, as stated by Wood (2009), prior to extending general 2D/3D formulations.

2.3 Existing models for large strain consolidation

2.3.1 Large strain consolidation theory

Terzaghi's one-dimensional consolidation theory is only applicable for small strain and fully saturated condition. The finite strain consolidation theory for saturated soils was established by Gibson et al. (1967, 1981), which is also based on the classical effective stress principle. Different coordinate systems, including Lagrangian coordinate (a), convective coordinate (ξ), material coordinate (z); have been used to derive and establish the governing equations from equilibrium and water phase continuity conditions. The three coordinates are related to each other as

$$\frac{d\xi}{da} = \frac{1+e}{1+e_0} \tag{2.18}$$

$$\frac{dz}{da} = \frac{1}{1+e_0} \tag{2.19}$$

$$\frac{d\xi}{dz} = 1+e \tag{2.20}$$

in which, e_0 and e are the initial void ratio and the void ratio at the respective elevation at the deformed configuration, respectively. The governing equations expressed using the three coordinate systems are written as follows

$$(G_s-1)\frac{d}{de}\left[\frac{k}{1+e}\right]\frac{\partial e}{\partial a}-\frac{\partial}{da}\left[\frac{k(1+e_0)}{\gamma_w(1+e)}\frac{d\sigma'}{de}\frac{\partial e}{\partial a}\right]=\frac{1}{(1+e_0)}\frac{\partial e}{\partial t} \tag{2.21}$$

$$\frac{d}{d\xi}\left[\frac{k}{\gamma_w}\frac{du}{d\xi}\right]=\frac{1}{1+e}\frac{\partial e}{\partial t} \tag{2.22}$$

$$(G_s-1)\frac{d}{de}\left[\frac{k}{1+e}\right]\frac{\partial e}{\partial z}-\frac{\partial}{dz}\left[\frac{k}{\gamma_w(1+e)}\frac{d\sigma'}{de}\frac{\partial e}{\partial z}\right]=\frac{\partial e}{\partial t} \tag{2.23}$$

where, G_s is the specific gravity, k the vertical permeability of the soil, γ_w the unit weight of water, t the time, and σ' is the vertical effective stress. Two constitutive relationships (relating void ratio with permeability and effective stress, respectively) need to be specified to make the governing equation determinate. These sets of the governing equations use void ratio as the independent variables, which also directly represents the large strain state at the constitutive (local) level. The definition of "strain" is not explicitly made here as in "*Continuum Mechanics*" where strain state in large deformation is represented by "Lagrange strain" or "Eulerian strain" (Bower 2009; Lai et al. 2009). In fact, use of "void ratio" under 1D condition in soil mechanics is consistent with the large strain concept in "Continuum Mechanics, where, the Lagrange strain is defined as

$$E=\frac{1}{2}(F^TF-I) \tag{2.24}$$

where, F is deformation gradient, I is identity matrix. The physical significance of Lagrange strain is

$$\varepsilon_L=\frac{l^2-l_0^{\,2}}{2l_0^{\,2}} \tag{2.25}$$

where, l and l_0 are the lengths of a very short tensile specimen within original and deformed configuration, respectively. As can be seen, the Lagrange strain measures the deformation characteristics with reference to the initial state. The deformation gradient in 1D condition is

$$F = \frac{d\xi}{da} \tag{2.26}$$

Using Eq. (2.18) gives

$$F = \frac{1+e}{1+e_0} \tag{2.27}$$

Substituting Eq. (2.27) into Eq. (2.25) (noting under 1D condition, the only non-zero component of the strain tensor is ε_L), gives

$$\varepsilon_L = \frac{1}{2}\left[\left(\frac{1+e}{1+e_0}\right)^2 - 1\right] \tag{2.28}$$

Substituting this equality

$$\frac{1+e}{1+e_0} = \frac{l}{l_0} \tag{2.29}$$

to Eq. (2.28), gives

$$\varepsilon_L = \frac{1}{2}\left[\left(\frac{l}{l_0}\right)^2 - 1\right] = \frac{l^2 - {l_0}^2}{2{l_0}^2} \tag{2.30}$$

which is identical to physical significance of Lagrange strain. In this thesis, change of void ratio is also used to measure the large strain deformation characteristics (in both global equations and

local constitutive equations). The ambiguity in selecting the initial state to evaluating strain (also occurs when using the strain concept in the mechanics of continuous media) can be avoided by taking e_0 in the above equation as that in the most initial condition (Monte and Krizek 1976).

To further show the consistency between Gibson's theory and continuum mechanics, a *Derivation of Gibson's theory from continuums mechanics* is provided here. The mass conservation laws from continuum mechanics gives

$$\frac{\partial}{\partial t}\left(\rho^w n\right)+div\left(\rho^w n v^w\right)=0 \quad \text{and} \quad \frac{\partial}{\partial t}\left(\rho^s (1-n)\right)+div\left(\rho^s (1-n) v^s\right)=0 \tag{2.31}$$

for water and solid phases, respectively. n is porosity, v^w and v^s are velocities of water and solid phases, respectively. ρ^w and ρ^s are the true densities of water and solid phases, respectively, and t is time. Assuming that the water and solids are incompressible, both density terms drop from both the equations:

$$\frac{\partial}{\partial t}(n)+div\left(n v^w\right)=0 \quad \text{and} \quad -\frac{\partial}{\partial t}(n)+div(v^s)-div(n v^s)=0 \tag{2.32}$$

Summation of the above two gives

$$div(v^s)+div\left(n v^w-n v^s\right)=0 \tag{2.33}$$

In 1D dimensional condition:

$$\frac{\partial v^s}{\partial \xi}+\frac{\partial}{\partial \xi}\left(n v^w-n v^s\right)=0 \tag{2.34}$$

Since

$$v^s = \frac{\partial \xi}{\partial t} \tag{2.35}$$

thus

$$\frac{\partial}{\partial a}\left(\frac{\partial \xi}{\partial t}\right)\frac{\partial a}{\partial \xi} + \frac{\partial}{\partial \xi}\left(nv^w - nv^s\right) = 0 \tag{2.36}$$

or

$$\frac{\partial}{\partial t}\left(\frac{\partial \xi}{\partial a}\right)\frac{\partial a}{\partial \xi} + \frac{\partial}{\partial \xi}\left(nv^w - nv^s\right) = 0 \tag{2.37}$$

Substituting Eq. (2.18) into Eq. (2.37), yields

$$\frac{1}{1+e}\frac{\partial}{\partial t}(1+e) + \frac{\partial}{\partial \xi}\left(nv^w - nv^s\right) = 0 \tag{2.38}$$

which is the same as Eq. (2.22) from Gibson's theory by substituting Darcy's law.

Analytical solutions for Gibson's equation has been derived only for certain conditions, e.g. specific forms of constitutive relationships (for reducing the governing equation to a linear form), simple time-dependent boundary condition (Gibson et al. 1967, 1981; Lee and Sills 1979; Morris 2002, 2005). Analytical solutions can be used to (i) simulate well-controlled experimental observations, (ii) test newly proposed numerical solutions, and (iii) conduct preliminary engineering design. However, most of the field conditions are much more complex than the situations where analytical solutions are available. Thus, numerical solutions, based on either finite element or finite difference scheme, seems to be more popular in the literature by many researchers (Cargill 1984; McVay et al. 1986; Bartolomeeusen et al. 2002; Fox and Berles 1997; Hawlader et al. 2008). Among these numerical solutions, the piece-wise linear solution formulated

by Fox and Berles (1997) appears to be more versatile and accurate. The fundamental concept of the piece-wise linear solution is that all the information (or the parameters), including the geometric information, will be updated after each time step. Thus, the piece-wise linear solution actually uses a Lagrangian approach that follows the motion of the solid phase to deal with the large deformation problem. The argument made by some researchers (e.g. Townsend and McVay (1990) several decades ago, concerning the expensive computational resources required by piece-wise linear solution, becomes increasingly less important with the subsequent increase in the speed of computers. Another advantage of piece-wise linear formulation is that no-decantation boundary condition (a layer of water will be accumulated on the deposition surface in the case where evaporation is not high enough to remove all the water due to self-weight consolidation) can be more easily applied on the top boundary, which moves with consolidation.

The unsaturated version of does not exist in the literature. Following the same procedure, the governing equation of large strain consolidation of unsaturated soils is derived by the author and presented in this part as fundamentals. The continuity equation for unsaturated condition turns out to be

$$\frac{\partial}{\partial \xi}\left(k\frac{\partial h}{\partial \xi}\right)=\frac{1}{1+e}\frac{\partial\left(wG_s\right)}{\partial t} \tag{2.39}$$

Eq. (2.18) still holds for unsaturated condition, which can be substituted into the above equation, gives

$$\frac{\partial\left(k\dfrac{\partial h}{\partial a}\dfrac{\partial a}{\partial \xi}\right)}{\partial a}\frac{\partial a}{\partial \xi}=\frac{1}{1+e}\frac{\partial\left(wG_s\right)}{\partial t} \tag{2.40}$$

$$\frac{\partial\left(\frac{k(1+e_0)}{1+e}\frac{\partial h}{\partial a}\right)}{\partial a}=\frac{1}{1+e_0}\frac{\partial\left(wG_s\right)}{\partial t} \tag{2.41}$$

Since

$$\frac{\partial h}{\partial \xi}=\frac{1}{\gamma_w}\frac{\partial u}{\partial \xi}+1=\frac{1}{\gamma_w}\frac{1+e_0}{1+e}\frac{\partial u}{\partial a}+1 \tag{2.42}$$

then,

$$\frac{\partial\left(\frac{k}{\gamma_w}\frac{1+e_0}{1+e}\frac{\partial u}{\partial a}+k\right)}{\partial a}=\frac{1}{1+e_0}\frac{\partial\left(wG_s\right)}{\partial t} \tag{2.43}$$

The force equilibrium condition is given by

$$\frac{\partial \sigma_v}{\partial a}+\left(\frac{G_s+wG_s}{1+e_0}\right)\gamma_w=0 \tag{2.44}$$

If the volume change behaviour for unsaturated soils is given using net stress and suction as independent stress variables:

$$e=\mathrm{f}(\text{-}u,\sigma_v) \text{ or } de=\alpha du+\beta d\sigma_v \text{ where } \alpha=-\frac{\partial \mathrm{f}}{\partial(\text{-}u)},\ \beta=\frac{\partial \mathrm{f}}{\partial \sigma_v} \tag{2.45}$$

thus, we have

$$\frac{\partial u}{\partial a}=\alpha^{-1}\frac{\partial e}{\partial a}-\alpha^{-1}\beta\frac{\partial \sigma_v}{\partial a}=\alpha^{-1}\frac{\partial e}{\partial a}-\alpha^{-1}\beta G_s\left(\frac{1+w}{1+e_0}\right)\gamma_w \tag{2.46}$$

The governing equation for large strain consolidation of unsaturated soils is formulated as

$$\frac{\partial}{\partial a}\left(\frac{k}{\gamma_w}\frac{1+e_0}{1+e}\alpha^{-1}\frac{\partial e}{\partial a}\right)-\frac{\partial}{\partial e}\left(\alpha^{-1}\beta G_s k\frac{1+w}{1+e}+k\right)\frac{\partial e}{\partial a}=\frac{1}{1+e_0}\frac{\partial\left(wG_s\right)}{\partial t} \qquad (2.47)$$

in which, the gravimetric water content, w, is related to S_r, e, and therefore u, which means another constitutive relationship, i.e. the soil water retention behaviour (that is e-dependent as reviewed in the section entitled as "2.1.4 Water retention model") is needed to make this equation determinate. The hydraulic conductivity, k, with not only varies void ratio but also with the degree of saturation. The governing equation is, therefore, highly (both geometric and material) nonlinear and it is impossible to obtain an analytical solution to its original formulation for unsaturated case. It is by no means implying that there is no possibility of obtaining an analytical solution to a *simplified/linearised version* of this equation. However, , The author is not aware of any attempts that have been made to simplify/linearize this equation (or other similar type for large strain consolidation of unsaturated soils) until now. Generality/applicability of this equation (i.e., the nonlinear nature of unsaturated soil properties) may be lost if simplification/linearization was improperly made, resulting in a solution with very limited applicablility. To account for various complexities (e.g. deposition of soft materials (tailings) in layers) in practice, this thesis will focus on developing a numerical solution for large strain consolidation extended to unsaturated soils.

2.3.2 Existing models that consider evaporation

The two software, MINTACO (Seneviratne et al. 1996) and CONDES (Yao et al. 2002) are most widely used to account for the effect of evaporation on large strain consolidation behaviour of soft soils. Both models solve numerically the Gibson's equation in Lagrangian coordinate or material coordinate systems, by finite element (Seneviratne et al. 1996) or finite difference (Yao et al. 2002) techniques. The power-law constitutive relationships (between void

ratio and effective stress, and hydraulic conductivity and void ratio) have been used to characterise the mechanical and hydraulic behaviours of soil element in both models. In other words, the effective stress principle, which is found ineffective for unsaturated soils, is still followed in MINTACO and CONDES models, even though the concept of "suction" is introduced for negative pore water pressure condition. Thus, in this thesis, this type of formulation is referred to as quasi-unsaturated formulation. The effect of evaporation induced flow or volume change has been modeled with different considerations or assumptions: (i) CONDES models desiccation by considering 3D volume change in elements that are reduced below a critical void ratio due to drying. Deformation in these cracking elements is linked to evaporation, which is assumed to proceed at the potential rate from the surface, or at an empirically corrected reduced rate from crack surfaces. Crack depth increases as the soil shrinks below the critical void ratio, which is defined as a four parameter empirical function of vertical effective stress. Deformation terminates in any element near the surface when the shrinkage limit is reached, and full soil saturation is assumed: (ii) The MinTaCo model handles evaporation by specifying a maximum value of suction at the soil surface, usually corresponding to the shrinkage limit of the soil, such that the top boundary condition switches from a constant flux boundary to a constant head boundary, after which point evaporation reduces below the potential rate. The MinTaCo model does not explicitly consider cracks nor does it model desaturation. Although the formulation of CONDES introduced a concept of "virtual' cracks in soil induced by evaporation and took into consideration its influence on evaporation, and while the formulation of MinTaCo considers the influence of unsaturated condition on evaporation rate using an assumption of maximum suction allowed at the top surface (Similar to some popular unsaturated flow codes, such as HYDRUS (Šimunek et al. 2012)), the truly unsaturated flow in deformable soil is not modeled in either software from the

above discussion. The theoretical limitations, in view of recent advancements in unsaturated soil mechanics, include: (i) the adopted effective stress principle is not able to model the volume change behaviour; (ii) soil is still assumed fully saturated (voids are filled with water). Thus the volume change is restrictedly linked to the net water outflow (inflow) of the soil element (this is physically incorrect), the water retention behaviour cannot, therefore, be incorporated. (iii) Hydraulic conductivity of soil is not linked to degree of saturation, which is known to have a significant influence on water flow in unsaturated soils. Several practical problems would benefit from a more theoretically sound model for coupled unsaturated flow and large strain consolidation. In the mining industry, for example, evaporation is used to accelerate the dewatering of sub-aerially deposited tailings, where the hydraulic interaction between layers deposited in sequence, is important and must be modelled using software that can simulate a truly unsaturated scenario. However, saturated assumption does not allowed this to be simulated. In hard rock mining, the degree of saturation regulates oxygen transport into the tailings and therefore the amount of acid rock drainage generation. These practical needs constitute the motivation for development of UNSATCON-ML.

2.3.3 Development history of UNSATCON-ML prior to writing of the thesis

The development of UNSATCON_ML took place entirely during the PhD program of the author. The development is documented in proceeding chapters, some of which are published papers. To assist the reader, the development history is given here.

At the commencement of the research program, several challenges were envisaged, for example, (1) geometric nonlinearity; (2) material (unsaturated poromedia) models' nonlinearity, complexity and sophistication (They are under development and validation) (3) mass imbalance

(globally or locally) issues. With these in mind, the author decided to select the piece-wise linear framework (Fox and Berles 1997) (ituses Lagrangian approach that follows the motion of the solid phase to deal with the geometric nonlinearity, as reviewed in "section 2.3.1") as a basis for development.

(1) After testing the new code using numerical solution to saturated large-strain self-weight consolidation problem (checking the correctness of coding), and analytical solution to an idealised evaporation-induced steady-state unsaturated flow problem, the author modified the code using piece-wise linear solution to accommodate the quasi-unsaturated condition (assuming volume change is controlled by Terzaghi's effective stress variable but suction is allowed to develop under evaporation). This allowed for validation using the solution of MINTACO (a finite element code solving the quasi-unsaturated problem using a different numerical procedure, as reviewed in "section 2.3.2").

(2) To accommodate the real unsaturated flow coupled with the large deformation process, the unsaturated soil constitutive model using the state surface approach was implemented into the code. The state surface models are reviewed in section 2.2.1, a specific model proposed by Vu and Fredlund 2006 is used. During the implementation, discretization is performed on the mixed form of the governing equation (pore pressure at the left-hand side, and void ratio e and gravimetric water content w on the right-hand side for saturated zone and unsaturated zone). It is found, in this way, the mass conversation can be strictly ensured in solving the governing equation. Since w and total stress can be easily obtained, by using gravimetric water content surface for the water retention behaviour, the other constitutive parameters can be easily and analytically solved, which not only satisfies the mass-conservation, but also results in high-accuracy solutions. The procedure was found to be very effective for modeling single layer deposition, as shown in the results from

testing the codes using laboratory column and in-situ field tests. We named the program "UNSAT-CON".

(3) To simulate the real field scenarios of multilayer deposition, we upgraded "UNSAT-CON" to UNSATCON-ML by adding the features of simulating irrecoverable volume change behaviour and hydraulic hysteresis. A movable elastic rebound surface is added and combined with the original void ratio surface for volume change behaviour (a modified state surface model) , the gravimetric water content surface is replaced with a void ratio-dependent soil water retention model (described initially using log-linear planes in the $S_r - e - s$ space) (SWRM is reviewed in "Section 2.1.4"). Although degree of saturation is used as the constitutive variable, the upgraded algorithm (using a binary method, the solution is found to physically and/or numerically located within a known interval) can still solve all the unknown constitutive variables analytically from gravimetric water content and total stress (different from a standard finite element procedure). In other words, the accuracy and mass-conservation are not lost in the new algorithm. In views of these advantages, a number of other unsaturated constitutive models, including BBM (a mechanical model by Alonso et al. 1990, reviewed in "section 2.1.2"), bounding surface water retention model (a hydraulic model proposed by Gallipoli et al. 2015), and GCM (a highly coupled model proposed by Wheeler et al. 2003, reviewed in "section 2.1.2") are also implemented into UNSATCON-ML using a similar numerical procedure. For all these models (whether in terms of independent stress variables or effective stress variable), state transition can be simulated smoothly. The algorithm seems to be able to provide a general and accurate solution to most of the integrable unsaturated constitutive models (a mechanical model coupled with a hysteretic), UNSATCON-ML with these different models has been tested using a drying box experimental results (Introduction of these drying box tests can be found in Daliri et al. 2016 and in Simms et al. (2017)).

(4) UNSAT-CON is still being actively developed for applications in the industry, for example, adding the capacity to simulate the thixotropic behaviour of tailings (beyond the scope of this thesis)

2.4 Conclusion

This chapter first reviewed the constitutive modelling approaches of unsaturated soils that has been developed recently, including several elasto-plastic models, SWRMs, and shear strength equations. Then a general review on the slope stability analysis is made, including FS definition and computation methods. Lastly, the studies on large strain consolidation of soft soils are reviewed, including the basic theory for saturated soils, and a few existing numerical models with their drawbacks on the material models. The fundamental framework for large strain consolidation of unsaturated soils is developed by the author and presented in this chapter. The necessity for developing a new numerical program is evidenced considering the practical problem introduced in Chapter 1. The development history of UNSATCON-ML is summarized with connections with the material (unsaturated soils) models reviewed at the beginning of this chapter. Merits of the new code are only briefly mentioned here, but will be detailed in the main body of thesis.

Glossary

Symbols

σ_n	Total normal stress
u_a	Pore air pressure
u_w	Pore water pressure.
χ	Bishop's parameter
$\boldsymbol{\sigma}$	Total stress tensor
x, y, z	Base axes
$\mathbf{m}$	Column vector
L	Power input per unit volume of soil
S_{r}	Degree of saturation
N	Porosity
$u'_{,j}{}^{(\mathrm{w})}$	Excess pore water pressure gradient
$u'_{,j}{}^{(\mathrm{a})}$	Excess pore air pressure gradient
$w_j^{(\mathrm{w})}$	Artificial seepage velocity of water phase
$w_j^{(\mathrm{a})}$	Artificial seepage velocity of air phase
$\dot{\mathrm{v}}^{(\mathrm{a})}$	Volumetric strain of air phase
$\dot{\varepsilon}_{ij}$	Soil skeleton strain rate
$\dot{S}_{\mathrm{r}}$	Water phase strain rate
$u^{(\mathrm{a})}$	Pore air pressure in
$u^{(\mathrm{w})}$	Pore water pressure
δ_{ij}	kronecker's delta
$\overline{S}_{\mathrm{r}}$	Effective degree of saturation
p	Total mean stress
λ_r	Slope of the linear relation between $\log(e/e_s)$ and $\log S_{\mathrm{r}}$
e_s	Value of void ratio at saturated condition
λ_p	Slope of the saturated normal compression line in Gallipoli and Bruno (2017)
s	Suction
e	Void ratio
v	Specific volume
q	Deviator stress
τ_f	Shear strength
c'	Effective cohesion for a saturated soil
ϕ'	Effective internal friction angle

ϕ^b	Rate of increase in shear strength relative to the matric suction
θ_w	Volumetric water content
θ_s	Saturated volumetric water content
κ	Fitting parameter in Vanapalli et al (1996)'s model
θ_r	Residual volumetric water content
c_{tot}	Total cohesion
a_f, b_f	Fitting parameters in Vilar (2006) Model
AEV	Air-entry value
$(u_a - u_w)_r$	Residual suction
τ	Equilibrium shear stress at any point within slope soils
c_f	Factored cohesion
ϕ_f	Factored internal friction angle
dl	Incremental length on the slip surface
σ'_1	Major effective principal stresses along the slip surface
σ'_2	Medium effective principal stresses along the slip surface
σ'_3	Minor effective principal stresses along the slip surface
a	Lagrangian coordinate
ξ	Convective coordinate
z	Material coordinate
e_0	Initial void ratio for large strain consolidation analysis
G_s	Specific gravity
k	Permeability of the soil
γ_w	Unit weight of water
t	Time
E	Lagrangian strain
F	Deformation gradient,
I	Identity matrix
l	Length of a very short tensile specimen within deformed configuration
l_0	Length of a very short tensile specimen within original configuration
ε_L	The only non-zero component of the strain tensor in 1D condition
v^w	Velocity of water phase
v^s	Velocity of solid phase
ρ^w	True density of water phase
ρ^s	True density of solid phase
w	Gravimetric water content

Abbreviations

MCC	Modified Cam Clay
SWCC	Soil Water Characteristic Curve
BBM	Barcelona Basic Model
GCM	Glasgow Coupled Model
SFG	Sheng, Fredlund, Gens Model
LC	Loading Collapse yield curve
SI	Suction Increase yield curve
SD	Suction Decrease yield curve
SWRC	Soil Water Retention Curve
SWRM	Soil Water Retention Model
PSD	Pore Size Distribution
LEM	Limit Equilibrium Method
FEM	Finite Element Method
FE	Finite Element
SBFEM	Stress-Based Finite Element Method
SSRFEM	Shear Strength Reduction Finite Element Method
FS	Factor of Safety
1D	One-dimensional
2D	Two-dimensional
3D	Three-dimensional

2.5 References

Adikari G S N, Cummins P J. An effective stress slope stability analysis method for dams[C]. In Proceedings of the Eleventh International Conference on Soil Mechanics and Foundation Engineering, San Francisco Calif, A A Balkema, Rotterdam, the Netherlands, 1985: 713-718.

Ali J, Huang S, Lyamin AV, Sloan SW, Cassidy MJ. Boundary effects of rainfall-induced landslides. Computers and Geotechnics. 2014;61: 341-354.

Alonso, E. E., Gens, A., & Delahaye, C. H. (2003). Influence of rainfall on the deformation and stability of a slope in overconsolidated clays: a case study. Hydrogeology Journal, 11(1), 174-192.

Alonso, E. E., Gens, A., & Josa, A. (1990). A constitutive model for partially saturated soils. Géotechnique, 40(3), 405-430.

Alonso, E. E., Pinyol, N. M., & Gens, A. (2013). Compacted soil behaviour: initial state, structure and constitutive modelling. Géotechnique, 63(6), 463.

Alonso, E. E., Vaunat, J., & Gens, A. (1999). Modelling the mechanical behaviour of expansive clays. Engineering Geology, 54(1), 173-183.

Bao, C., Gong, B., and Zhan, L. 1998. Properties of unsaturated soils and slope stability of expansive soils. In Proceedings of the Second International Conference on Unsaturated Soils (UNSAT 98), Beijing. Vol. 1, pp. 71–98.

Bartholomeeusen, G., Sills, G. C., Znidarcic, D., Van Kesteren, W., Merckelbach, L. M., Pyke, R., ... & Masala, S. (2002). Sidere: numerical prediction of large-strain consolidation.

Bishop, A. W. (1959). The principle of effective stress. Teknisk ukeblad, 39, 859-863.

Bishop, A. W. 1955. The use of the slip circle in the stability analysis of slopes. Géotechnique, (5): 7-17.

Blatz, J. A., & Graham, J. (2003). Elastic-plastic modelling of unsaturated soil using results from a new triaxial test with controlled suction. Géotechnique, 53(1), 113-122.

Bower, A. F. (2009). Applied mechanics of solids. CRC press.

Brooks, R. H., & Corey, A. T. (1964). Hydraulic properties of porous media and their relation to drainage design. Transactions of the ASAE, 7(1), 26-0028.

Buscarnera, G., & Prisco, C. D. (2012). Discussing the definition of the second‐order work for unsaturated soils. International Journal for Numerical and Analytical Methods in Geomechanics, 36(1), 36-49.

Bussiere, B. (2007). Colloquium 2004: Hydrogeotechnical properties of hard rock tailings from metal mines and emerging geoenvironmental disposal approaches. Canadian Geotechnical Journal, 44(9), 1019-1052.

Cardoso, R., Alonso, E. E., & Neves, E. M. D. (2013). A constitutive model for compacted expansive and bonded marls. Géotechnique, 63(13), 1116.

Cargill, K. W. (1984). Prediction of consolidation of very soft soil. Journal of Geotechnical Engineering, 110(6), 775-795.

Cho SE, Lee SR. Instability of unsaturated soil slopes due to infiltration. Computers and Geotechnics, 2001;28(3): 185–208.

Christiansen, E. A., & Sauer, E. K. (2002). Stratigraphy and structure of Pleistocene collapse in the Regina Low, Saskatchewan, Canada. Canadian Journal of Earth Sciences, 39(9), 1411-1423.

Conte, E., & Troncone, A. (2012). Stability analysis of infinite clayey slopes subjected to pore pressure changes. Géotechnique, 62(1), 87-91.

Cui, Y. J., & Delage, P. (1996). Yielding and plastic behaviour of an unsaturated compacted silt. Géotechnique, 46(2), 291-311.

D'Onza, F., Gallipoli, D., Wheeler, S., Casini, F., Vaunat, J., Khalili, N., ... & Pereira, J. M. (2011). Benchmark of constitutive models for unsaturated soils. Géotechnique, 61(4), 283-302.

D'Onza, Francesca, et al. "Benchmark of constitutive models for unsaturated soils." Géotechnique 61.4 (2011): 283-302.

Daliri, F., Simms, P., & Sivathayalan, S. (2016). Shear and dewatering behaviour of high density gold tailings in a laboratory simulation of multi-layer deposition. Canadian Geotechnical Journal, 2016, 53(8): 1246-1257.

Dangla, P., Malinsky, L., & Coussy, O. (1997, July). Plasticity and imbibition-drainage curves for unsaturated soils: a unified approach. In Proc. 6th Int. Symp. Numer. Models Geomech.(NUMOG VI) (pp. 141-146).

Delage, P., & Graham, J. (1996). Mechanical behaviour of unsaturated soils: understanding the behaviour of unsaturated soils requires reliable conceptual models. In PROCEEDINGS OF THE FIRST INTERNATIONAL CONFERENCE ON UNSATURATED SOILS/UNSAT'95/PARIS/FRANCE/6-8 SEPTEMBER 1995. VOLUME 3.

Di Prisco, C., & Pisanò, F. (2011). An exercise on slope stability and perfect elastoplasticity. Géotechnique, 61(11), 923.

Donaldson, G. W. (1969). The Occurrence of Problems of Heave and the Factors Affeting its Nature. In Second International Research and Engineering Conference on Expansive Clay Soils (pp. 25-36). Texas A & M Press.

Duncan, J. M. (1996). Soil slope stability analysis. Landslides: Investigation and Mitigation, Transportation Research Board Special Report 247, 337-371.

Duncan, J. M., Wright, S. G., & Brandon, T. L. (2014). Soil strength and slope stability. John Wiley & Sons.

Fellenius, W. 1936. Calculation of the stability of earth dams. In Transactions of the 2nd congress on large dams, Washington, D.C. Vol. 4, pp. 445-463.

Fenton, G. A., & Griffiths, D. V. (2008). Risk assessment in geotechnical engineering (Vol. 461). Hoboken, NJ: John Wiley & Sons.

Fisseha, B., Bryan, R., & Simms, P. (2010). Evaporation, unsaturated flow, and salt accumulation in multilayer deposits of "paste" gold tailings. Journal of Geotechnical and Geoenvironmental Engineering, 136(12), 1703-1712.

Fox, P. J., & Berles, J. D. (1997). CS2: A piecewise-linear model for large strain consolidation. International Journal for Numerical and Analytical Methods in Geomechanics, 21(7), 453-475.

Fredlund, D. G., & Krahn, J. (1977). Comparison of slope stability methods of analysis. Canadian Geotechnical Journal, 14(3), 429-439.

Fredlund, D. G., & Morgenstern, N. R. (1977). Stress state variables for unsaturated soils. Journal of Geotechnical and Geoenvironmental Engineering, 103(ASCE 12919).

Fredlund, D. G., & Rahardjo, H. (1993). Soil mechanics for unsaturated soils. John Wiley & Sons.

Fredlund, D. G., & Xing, A. (1994). Equations for the soil-water characteristic curve. Canadian geotechnical journal, 31(4), 521-532.

Fujiyasu, Y., & Fahey, M. (2000). Experimental study of evaporation from saline tailings. Journal of Geotechnical and Geoenvironmental Engineering, 126(1), 18-27.

Fredlund, D. G., and Krahn, J. 1977. Comparison of slope stability methods of analysis. Canadian Geotechnical Journal, 14(3): 429-439.

Fredlund, D. G., Morgenstern, N. R., & Widger, R. A. (1978). The shear strength of unsaturated soils. Canadian geotechnical journal, 15(3), 313-321.

Fredlund, D. G., Rahardjo, H., & Fredlund, M. D. (2012). Unsaturated soil mechanics in engineering practice. John Wiley & Sons.

Fredlund, D. G., Xing, A., Fredlund, M. D., & Barbour, S. L. (1996). The relationship of the unsaturated soil shear to the soil-water characteristic curve. Canadian Geotechnical Journal, 33(3), 440-448.

Fredlund, M. D., Fredlund, D. G., & Wilson, G. W. (2000). An equation to represent grain-size distribution. Canadian Geotechnical Journal, 37(4), 817-827.

Gallipoli, D., Bruno, A. W., D'Onza, F., & Mancuso, C. (2015). A bounding surface hysteretic water retention model for deformable soils. Géotechnique, 65(10), 793-804.

Gallipoli, D., Gens, A., Sharma, R., & Vaunat, J. (2003). An elasto-plastic model for unsaturated soil incorporating the effects of suction and degree of saturation on mechanical behaviour. Géotechnique., 53(1), 123-136.

Gallipoli, D., Wheeler, S. J., & Karstunen, M. (2003). Modelling the variation of degree of saturation in a deformable unsaturated soil. Géotechnique, 53(1), 105-112.

Gens, A. (1996). Constitutive modelling: Application to compacted soils. In proceedings of the first international conference on unsaturated soils/unsat'95/paris/france/6-8 september 1995. Volume 3.

Gens, A. (2010). Soil–environment interactions in geotechnical engineering. Géotechnique, 60(1), 3-74.

Gens, A., & Alonso, E. E. (1992). A framework for the behaviour of unsaturated expansive clays. Canadian Geotechnical Journal, 29(6), 1013-1032.

Gibson, R. E., England, G. L., & Hussey, M. J. L. (1967). The Theory of One-Dimensional Consolidation of Saturated Clays: 1. Finite Non-Linear Consildation of Thin Homogeneous Layers. Geotechnique, 17(3), 261-273.

Gibson, R. E., Schiffman, R. L., & Cargill, K. W. (1981). The theory of one-dimensional consolidation of saturated clays. II. Finite nonlinear consolidation of thick homogeneous layers. Canadian geotechnical journal, 18(2), 280-293.

Griffiths, D. V. (1980).Finite element analyses of walls, footings and slopes.PhD thesis, University of Manchester.

Griffiths, D. V., & Lane, P. A. (1999). Slope stability analysis by finite elements. Geotechnique, 49(3), 387-403.

Griffiths, D. V., & Fenton, G. A. (2004). Probabilistic slope stability analysis by finite elements. Journal of Geotechnical and Geoenvironmental Engineering, 130(5), 507-518.

Griffiths, D. V., & Fenton, G. A. (2000). Influence of soil strength spatial variability on the stability of an undrained clay slope by finite elements. In Slope stability 2000 (pp. 184-193).

Griffiths, D. V., & Lu, N. (2005). Unsaturated slope stability analysis with steady infiltration or evaporation using elasto - plastic finite elements. International journal for numerical and analytical methods in geomechanics, 29(3), 249-267.

Griffiths, D. V., Huang, J., & Fenton, G. A. (2011). Probabilistic infinite slope analysis. Computers and Geotechnics, 38(4), 577-584.

Hawlader, B. C., Muhunthan, B., & Imai, G. (2008). State-dependent constitutive model and numerical solution of self-weight consolidation. Géotechnique, 58(2), 133-141.

Heidarian, P. (2012). Effect of Initial Water Content and Stress History on Water-Retention Behaviour of Mine Tailings (Doctoral dissertation, Carleton University Ottawa).

Hornbaker, D. J., Albert, R., Albert, I., Barabási, A. L., & Schiffer, P. (1997). What keeps sandcastles standing?. Nature, 387(6635), 765.

Hornbaker, D. J., Albert, R., Albert, I., Barabási, A. L., & Schiffer, P. (1997). What keeps sandcastles standing?. Nature, 387(6635), 765.

Houlsby, G. T. (1997). The work input to an unsaturated granular material. Géotechnique, 47(1), 193-6.

http://www.wbur.org/artery/2015/07/27/sandcastle-matt.

Hu, R., Chen, Y. F., Liu, H. H., & Zhou, C. B. (2013). A water retention curve and unsaturated hydraulic conductivity model for deformable soils: consideration of the change in pore-size distribution. Géotechnique, 63(16), 1389.

Huang, W., Leong, E.C., & Rahardjo, H. 2016. Translational slip failures on slope incorporating unsaturated soil mechanics. In Proceedings of the 6th Asia-pacific Conference on unsaturated soils, Guilin, China. 23–26 Octerber 2015. pp. 771-775.

Janbu, N. 1954. Application of composite slip surfaces for stability analysis. InProc. European Conf. on Stability of Earth Slopes, Stockholm, 1954. Vol. 3, pp. 43-49.

Janbu, N. 1975, April. Slope stability computations: In Embankment-dam Engineering. Textbook. Eds. RC Hirschfeld and SJ Poulos. JOHN WILEY AND SONS INC., PUB., NY, 1973, 40P. In International Journal of Rock Mechanics and Mining Sciences and Geomechanics Abstracts Vol. 12, No. 4, p. 67. Pergamon.

Jennings, J. E. B., & Burland, J. B. (1962). Limitations to the use of effective stresses in partly saturated soils. Géotechnique, 12(2), 125-144.

Khalili, N., & Khabbaz, M. H. (1998). A unique relationship of chi for the determination of the shear strength of unsaturated soils. Geotechnique, 48(5).

Khalili, N., Habte, M. A., & Zargarbashi, S. (2008). A fully coupled flow deformation model for cyclic analysis of unsaturated soils including hydraulic and mechanical hystereses. Computers and Geotechnics, 35(6), 872-889.

Klausner, Y. (1991). Fundamentals of continuum mechanics of soils. Springer-Verlag, New York.

Kulhawy, F. H. (1969). Finite element analysis of the behavior of embankments (Doctoral dissertation, Library Photographic Service, University of California).

Lade, P. V. (2010). The mechanics of surficial failure in soil slopes.Engineering Geology, 114(1), 57-64.

Lai, W. M., Rubin, D. H., Rubin, D., & Krempl, E. (2009). Introduction to continuum mechanics. Butterworth-Heinemann.

Le, T. M. H., Gallipoli, D., Sanchez, M., & Wheeler, S. (2013). Rainfall-induced differential settlements of foundations on heterogeneous unsaturated soils. Géotechnique, 63(15), 1346.

Lee, K. U. A. N. T. S. A. I., & Sills, G. C. (1979). A moving boundary approach to large strain consolidation of a thin soil layer. In Proc., 3rd Int. Conf. on Numerical Methods in Geomechanics (Vol. 1, pp. 163-173). AA Balkema, Leiden, Netherlands.

Leong, E. C., & Rahardjo, H. (1997). Permeability functions for unsaturated soils. Journal of Geotechnical and Geoenvironmental Engineering, 123(12), 1118-1126.

Li, X. S. (2005). Modelling of hysteresis response for arbitrary wetting/drying paths. Computers and Geotechnics, 32(2), 133-137.

Li, Y. C., Chen, Y. M., Zhan, T. L., Ling, D. S., & Cleall, P. J. (2010). An efficient approach for locating the critical slip surface in slope stability analyses using a real-coded genetic algorithm. Canadian Geotechnical Journal, 47(7), 806-820.

Lloret‐Cabot, M., Sánchez, M., & Wheeler, S. J. (2013). Formulation of a three‐dimensional constitutive model for unsaturated soils incorporating mechanical–water retention couplings. International Journal for Numerical and Analytical Methods in Geomechanics, 37(17), 3008-3035.

Mašín, D. (2010). Predicting the dependency of a degree of saturation on void ratio and suction using effective stress principle for unsaturated soils. International Journal for Numerical and Analytical Methods in Geomechanics, 34(1), 73-90.

Mašín, D. (2010). Predicting the dependency of a degree of saturation on void ratio and suction using effective stress principle for unsaturated soils. International Journal for Numerical and Analytical Methods in Geomechanics, 34(1), 73-90.

Matsui T, San K C. Finite element slope stability analysis by shear strength reduction technique[J]. Soils and foundations, 1992, 32(1): 59-70.

Matyas, E. L., & Radhakrishna, H. S. (1968). Volume change characteristics of partially saturated soils. Géotechnique, 18(4), 432-448.

McVay, M., Townsend, F., & Bloomquist, D. (1986). Quiescent consolidation of phosphatic waste clays. Journal of Geotechnical Engineering, 112(11), 1033-1049.

Michalowski, R. L. (2002). Stability charts for uniform slopes. Journal of Geotechnical and Geoenvironmental Engineering, 128(4), 351-355.

Milledge, D. G., Griffiths, D. V., Lane, S. N., & Warburton, J. (2012). Limits on the validity of infinite length assumptions for modelling shallow landslides. Earth Surface Processes and Landforms, 37(11), 1158-1166.

Monte, J. L., & Krizek, R. J. (1976). One-dimensional mathematical model for large-strain consolidation. Geotechnique, 26(3), 495-510.

Morgenstern, N. R., and Price, V. E. 1965. The analysis of the stability of general slip surfaces. Géotechnique, 15(1): 79-93.

Morris, P. H. (2002). Analytical solutions of linear finite-strain one-dimensional consolidation. Journal of geotechnical and geoenvironmental engineering, 128(4), 319-326.

Morris, P. H. (2005). Analytical solutions of linear finite‐and small‐strain one‐dimensional consolidation. International journal for numerical and analytical methods in geomechanics, 29(2), 127-140.

Nuth, M., & Laloui, L. (2008). Advances in modelling hysteretic water retention curve in deformable soils. Computers and Geotechnics, 35(6), 835-844.

Pasha, A. Y., Khoshghalb, A., & Khalili, N. (2017). Hysteretic Model for the Evolution of Water Retention Curve with Void Ratio. Journal of Engineering Mechanics, 143(7), 04017030.

Pedroso, D. M., & Williams, D. J. (2010). A novel approach for modelling soil–water characteristic curves with hysteresis. Computers and Geotechnics, 37(3), 374-380.

Petterson, K. E. (1955). The early history of circular sliding surfaces. Geotechnique, 5(4), 275-296.

Pham H T V, Fredlund D G. The application of dynamic programming to slope stability analysis. Canadian Geotechnical Journal, 2003, 40: 830-847.

Pham, H. Q., Fredlund, D. G., & Barbour, S. L. (2003). A practical hysteresis model for the soil-water characteristic curve for soils with negligible volume change. Géotechnique, 53(2), 293-298.

Rahardjo, H., & Fredlund, D. G. (1995). Procedures for slope stability analyses involving unsaturated soils. Developments in deep foundations and ground improvement schemes. Balkema, Rotterdam, 33-56.

Raveendiraraj A (2009) Coupling of mechanical behaviour and water retention behaviour in unsaturated soils. Ph.D. Thesis, University of Glasgow

Rozina, E., Mizani, S., Malek, M., Sanchez-Sardon, M., & Simms, P. (2015). Dewatering in a laboratory simulation of a multilayer deposit of inline flocculated mature fine tailings. Proceedings of the 18th International Seminar on Paste and Thickened Tailings, R. Jewell and A. Fourie. Australian Centre for Geomechanics, Crawley, Australia, 81-94.

Salager, S., Nuth, M., Ferrari, A., & Laloui, L. (2013). Investigation into water retention behaviour of deformable soils. Canadian Geotechnical Journal, 50(2), 200-208.

Salfate, E. R. (2011). Predicting void ratio for surface paste tailings deposited in thin layers (Doctoral dissertation, University of British Columbia).

Sánchez, M., Gens, A., Guimarães, L., & Olivella, S. Implementation algorithm of a generalised plasticity model for swelling clays. Computers and Geotechnics, 2008;35(6): 860-871.

Sarma, S. K. 1973. Stability analysis of embankments and slopes. Géotechnique, 23(3), 423-433.

Scoular, R. E. G. (1997). Limit equilibrium slope stability analysis using a stress analysis. M. Sc, University of Saskatchewan, Saskatoon, Canada.

Seneviratne, N. H., Fahey, M., Newson, T. A., & Fujiyasu, Y. (1996). Numerical modelling of consolidation and evaporation of slurried mine tailings. International Journal for Numerical and Analytical Methods in Geomechanics, 20(9), 647-671.

Seneviratne, N. H., Fahey, M., Newson, T. A., & Fujiyasu, Y. (1996). Numerical modelling of consolidation and evaporation of slurried mine tailings. International Journal for Numerical and Analytical Methods in Geomechanics, 20(9), 647-671.

Sheng, D. (2011). Review of fundamental principles in modelling unsaturated soil behaviour. Computers and Geotechnics, 38(6), 757-776.

Sheng, D., Fredlund, D. G., & Gens, A. (2008). A new modelling approach for unsaturated soils using independent stress variables. Canadian Geotechnical Journal, 45(4), 511-534.

Sheng, D., Sloan, S. W., & Gens, A. (2004). A constitutive model for unsaturated soils: thermomechanical and computational aspects. Computational Mechanics, 33(6), 453-465.

Shunchao Qi. (2013). Slope Stability Analysis Based on Critical Stable State (Master's thesis, Zhejiang University).

Simms, P. H., & Yanful, E. K. (2002). Predicting soil-water characteristic curves of compacted plastic soils from measured pore-size distributions. Géotechnique, 52(4), 269-278.

Simms, P. H., & Yanful, E. K. (2005). A pore-network model for hydromechanical coupling in unsaturated compacted clayey soils. Canadian Geotechnical Journal, 42(2), 499-514.

Simms, P., Dunmola, A., Fisseha, B., & Bryan, R. (2010). Generic modeling of desiccation for cyclic deposition of thickened tailings to maximize density and to minimize oxidation. Proceedings of the 13th International Seminar on Paste and Thickened Tailings, R. Jewell and A. Fourie. Australian Centre for Geomechanics, Crawley, Australia, 293-303.

Simms, P., Grabinsky, M., & Zhan, G. (2007). Modelling evaporation of paste tailings from the Bulyanhulu mine. Canadian Geotechnical Journal, 44(12), 1417-1432.

Šimunek, J., Van Genuchten, M. T., & Šejna, M. (2012). HYDRUS: Model use, calibration, and validation. Transactions of the ASABE, 55(4), 1263-1274.

Soleimani, S., Simms, P., Dunmola, A., Freeman, G., & Wilson, G. W. (2014) Desiccation and consolidation in thin-lift deposition of polymer-amended mature fine tailings. Proceedings of the 17th International Seminar on Paste and Thickened Tailings, R. Jewell, A. Fourie, P. S. Wells and D. van Zyl. eds., Australian Centre for Geomechanics, Crawley, Australia, 307-322.

Spencer, E. 1967. A method of analysis of the stability of embankments assuming parallel inter-slice forces. Géotechnique, 17(1): 11-26.

Sun, W., & Sun, D. A. (2012). Coupled modelling of hydro‐mechanical behaviour of unsaturated compacted expansive soils. International Journal for Numerical and Analytical Methods in Geomechanics, 36(8), 1002-1022.

Sun, W., & Sun, D. A. (2012). Coupled modelling of hydro‐mechanical behaviour of unsaturated compacted expansive soils. International Journal for Numerical and Analytical Methods in Geomechanics, 36(8), 1002-1022.

Tarantino, A. (2009). A water retention model for deformable soils. Géotechnique, 59(9), 751-762.

Tavenas, F., Trak, B., & Leroueil, S. (1980). Remarks on the validity of stability analyses. Canadian Geotechnical Journal, 17(1), 61-73.

Teunissen, J. A. M., & Spierenburg, S. E. J. (1996). Stability of infinite slopes. In International Journal of Rock Mechanics and Mining Sciences and Geomechanics Abstracts (Vol. 3, No. 33, p. 137A).

Townsend, F. C., & McVay, M. C. (1990). SOA: Large strain consolidation predictions. Journal of geotechnical engineering, 116(2), 222-243.

Townsend, F. C., & McVay, M. C. (1990). SOA: Large strain consolidation predictions. Journal of Geotechnical Engineering.

Tsiampousi, A., Zdravkovic, L., & Potts, D. M. (2013). A three-dimensional hysteretic soil-water retention curve. Geotechnique, 63(2), 155.

Van Genuchten, M. T. (1980). A closed-form equation for predicting the hydraulic conductivity of unsaturated soils. Soil science society of America journal, 44(5), 892-898.

van Genuchten, M. T. (1980). A closed-form equation for predicting the hydraulic conductivity of unsaturated soils. Soil science society of America journal, 44(5), 892-898.

Vanapalli, S. K. (2009, November). Shear strength of unsaturated soils and its applications in geotechnical engineering practice. In Keynote Address. Proc. 4th Asia-Pacific Conf. on Unsaturated Soils. New Castle, Australia (pp. 579-598).

Vanapalli, S. K., Fredlund, D. G., & Pufahl, D. E. (1999). The influence of soil structure and stress history on the soil–water characteristics of a compacted till. Géotechnique, 49(2), 143-159.

Vanapalli, S. K., Fredlund, D. G., Pufahl, D. E., & Clifton, A. W. (1996). Model for the prediction of shear strength with respect to soil suction. Canadian Geotechnical Journal, 33(3), 379-392.

Vaunat, J., Romero, E., & Jommi, C. (2000). An elastoplastic hydromechanical model for unsaturated soils. Experimental evidence and theoretical approaches in unsaturated soils, 121-138.

Vilar, O. M. (2006). A simplified procedure to estimate the shear strength envelope of unsaturated soils. Canadian Geotechnical Journal, 43(10), 1088-1095.

Vu, H. Q., & Fredlund, D. G. (2006). Challenges to modelling heave in expansive soils. Canadian Geotechnical Journal, 43(12), 1249-1272.

Vu, H. Q., & Fredlund, D. G. (2006). Challenges to modelling heave in expansive soils. Canadian Geotechnical Journal, 43(12), 1249-1272.

Wang, G., & Wei, X. (2014). Modeling swelling–shrinkage behaviour of compacted expansive soils during wetting–drying cycles. Canadian Geotechnical Journal, 52(999), 1-12.

Wheeler, S. J., & Karube, D. (1996). Constitutive modelling. In proceedings of the first international conference on unsaturated soils/unsat'95/paris/france/6-8 september 1995. volume 3.

Wheeler, S. J., & Karube, D. (1996). Constitutive modelling. In proceedings of the first international conference on unsaturated soils/unsat'95/paris/france/6-8 september 1995. volume 3.

Wheeler, S. J., & Sivakumar, V. (1995). An elasto-plastic critical state framework for unsaturated soil. Géotechnique, 45(1), 35-53.

Wheeler, S. J., Sharma, R. S., & Buisson, M. S. R. (2003). Coupling of hydraulic hysteresis and stress–strain behaviour in unsaturated soils. Géotechnique, 53(1), 41-54.

Wilson, G. W., Fredlund, D. G., & Barbour, S. L. (1997). The effect of soil suction on evaporative fluxes from soil surfaces. Canadian Geotechnical Journal, 34(1), 145-155.

Wright, S. G., Kulhawy, F. G., & Duncan, J. M. (1973). Accuracy of equilibrium slope stability analysis. Journal of Soil Mechanics & Foundations Div, 99(Proc Paper 10097).

Yao, D. T., de Oliveira‐Filho, W. L., Cai, X. C., & Znidarcic, D. (2002). Numerical solution for consolidation and desiccation of soft soils. International journal for numerical and analytical methods in geomechanics, 26(2), 139-161.

Yao, D. T., de Oliveira‐Filho, W. L., Cai, X. C., & Znidarcic, D. (2002). Numerical solution for consolidation and desiccation of soft soils. International Journal for Numerical and Analytical Methods in Geomechanics, 26(2), 139-161.

Zhang, L. L., Fredlund, D. G., Zhang, L. M., & Tang, W. H. (2004). Numerical study of soil conditions under which matric suction can be maintained. Canadian Geotechnical Journal, 41(4), 569-582.

Zhang, L. L., Fredlund, M. D., Fredlund, D. G., Lu, H., & Wilson, G. W. (2015). The influence of the unsaturated soil zone on 2-D and 3-D slope stability analyses. Engineering Geology, 193, 374-383.

Zhang, X., & Briaud, J. L. (2015). Three dimensional numerical simulation of residential building on shrink–swell soils in response to climatic conditions. International Journal for Numerical and Analytical Methods in Geomechanics, 39(13), 1369-1409.

Zhang, X., & Lytton, R. L. (2009a). Modified state-surface approach to the study of unsaturated soil behavior. Part I: Basic concept. Canadian Geotechnical Journal, 46(5), 536-552.

Zhang, X., & Lytton, R. L. (2009b). Modified state-surface approach to the study of unsaturated soil behavior. Part II: General formulation. Canadian Geotechnical Journal, 46(5), 553-570.

Zheng, Hong, L. G. Tham, and Defu Liu. "On two definitions of the factor of safety commonly used in the finite element slope stability analysis." Computers and Geotechnics 33.3 (2006): 188-195.

Zienkiewicz O C, Humpheson C, Lewis R W. Associated and non-associated visco-plasticity and plasticity in soil mechanics. Geotechnique, 1975, 25(4): 671-689.

Znidarčić, D., Schiffman, R. L., Pane, V., Croce, P., Ko, H. Y., & Olsen, H. W. (1986). The theory of one-dimensional consolidation of saturated clays: part V, constant rate of deformation testing and analysis. Géotechnique, 36(2), 227-237.

Chapter 3 Hydro-mechanical Coupling Effect on Slope Stability of Expansive Soils[1]

This chapter investigates the coupling effect (induced by soil swelling) on the hydraulic response as well as the stability of surficial layer of expansive soil slope. Both hydro-mechanical (coupled) and hydraulic (uncoupled) responses of the slope to rainfall are modeled using the commercial software SIGMA/W and SEEP/W, respectively. Subsequently, the infinite slope formulation is used to compute the FS profiles extending both coupled (SIGMA/W) and uncoupled (SEEP/W) analysis. The results show that coupled analysis (considering swelling) leads to different suction (negative pore water pressure (PWP)) and FS profiles within the surficial layer from those resulting from uncoupled analysis at the same elapsed time. The wetting fronts in the PWP profile from coupled analysis advance at a relatively faster rate in comparison to uncoupled analysis contributing to more critical FS values or failure conditions. The study highlights that the hydro-mechanical coupling behaviour of expansive soil has an adverse effect on the slope stability.

3.1 Introduction

Highly plastic soils that are expansive in nature are widely distributed in many semi-arid and arid areas including some tropical regions of the world. These soils predominantly contain clay mineral montmorillonite that is sensitive to natural moisture content changes and exhibits dramatic swell and shrinkage characteristics. Some expansive soils volume increases up to thirty

[1] A version of this chapter has been published as Qi and Vanapalli (2015) in *Computers and Geotechnic*s. DOI: 10.1016/j.compgeo.2015.07.006

percent or even more due to an increase in the natural water content (http://www.foundation-repair-guide.com/expansive-soil.html). Water content losses and shrinkage in expansive soils are typically associated with evaporation or desiccation. In addition, several cracks and fissures develop during the drying period. The dramatic volume change behaviour of expansive soils associated with environmental or manmade changes contribute to damages to the civil infrastructure. The economic losses associated with expansive soils have been reported to be increasing at an alarming rate annually; for example in recent years, losses were estimated to be approximately several hundreds of millions of dollars to several billions of dollars in many countries (Adem and Vanapalli 2013). The focus of this chapter is directed towards suggesting a rational numerical procedure for assessing expansive soil slope surficial layer failures. The proposed methodology is presented using a typical slope in expansive soil from Regina of Saskatchewan province in Canada.

There has been a long history of observations of the rain-induced slope instabilities in cuts and fills near the city of Regina. This city is situated on glacial Lake Regina consisting of over-consolidated expansive clays (Widger and Fredlund 1978). Most of the rain-induced failures in this region occur 4-6 years after their construction and exhibit typical shallow and regressive characteristics initiating from the toe of the slope. Similar failure patterns in expansive soil slopes were also reported in many other regions of the world (Bao and Ng 2000).

The suction present within the surficial layer significantly contributes towards the shear strength which in turn enhances the stability of an unsaturated soil layer. Several researchers (Cho and Lee, 2002; Collins and Znidarcic, 2004; Ng et al. 2001; Rahardjo et al. 2007) suggested that the failure mechanisms of this surficial layer during wetting seasons mainly involve rainfall-induced wetting front propagation causing suction losses. In some scenarios it is also likely that

the formation and rise of the perched ground water table (GWT) will contribute to significant reduction in the shear strength of soils. Many numerical studies have been reported in the literature to investigate the hydraulic response of unsaturated slopes to rainfall infiltration and associated stability. For example, Zhang et al. (2004) illustrated the development of various suction profiles within slope soils having different hydraulic properties (i.e. soil-water characteristic curve (SWCC) and hydraulic conductivity) under different rainfall intensities for both steady state and transient conditions. Cai and Ugai (2004) first utilized the finite element saturated-unsatuated flow analysis for predicting the pore-water pressure (PWP) and used this information in the finite element strength reduction technique for computing the Factor of Safety (FS). This study highlighted the significant influence of initial relative degree of saturation, boundary conditions, and rainfall duration on the predicted PWP and the calculated FS. Based on a numerical analysis on the effect of combined role of saturated hydraulic conductivity and rainfall characteristics and analytically interpretation using infinite slope stability model, Li et al. (2013) concluded that propagation of wetting front depth will never result in slope failures when internal frictional angle of soils is greater than the slope angle; unless there is rise of the perched water table which initiate slope failures. More recently, Ali et al. (2014) investigated the boundary effects on rain-induced slope failures; the results showed that the hydraulic conductivity of boundary has different effects on the location and the timing of slip surface for slope under different intensity rainfalls. The study also highlights the boundary effects are also dependent of the slope angle, soil effective cohesion and the failure mechanisms (i.e. failures induced by reduction in negative PWP (suction) or generation of water table or positive PWP).

In addition to numerical investigation on hydraulic response of slopes to rainfall outlined above, some research has also been conducted using the coupled hydro-mechanical methods,

where the deformation of unsaturated soils is included (e.g. Alonso et al. 2003; Chen et al. 2009; Cho and Lee 2001, Ehlers et al. 2004, Zhang et al. 2005). These coupled hydro-mechanical studies are based on different constitutive models for describing the swelling behaviour that use different definitions of stress state variables within the framework of unsaturated soil mechanics. For example, the nonlinear elastic stress-strain relationship based on two stress state variables are utilized by some researchers, while, the elasto-viscoplastic and elasto-plastic model considering the plastic strains based on effective stress principle has been used by other researchers. Similar to the uncoupled hydraulic analyses above, the coupled analysis was usually followed by a calculation of FS based on the obtained PWP and/or the stress state within the slope profile. Again, different techniques were extended for calculation of FS, such as the finite element method based on the obtained stress field within the slope, and the traditional limit equilibrium methods. It is worth mentioning that Ehlers et al. (2004) obtained the localization of strains using the elasto-viscoplastic analysis directly instead of providing the slope FS.

In spite of the uncoupled and coupled analyses that were carried out within the framework of unsaturated soil mechanics, the effect of soil deformation or coupling behaviour on the slope stability has not been clearly interpreted or quantified in the literature. The coupled behaviour may be particularly significant in the slope stability analysis of expansive soils. This is because the surficial soils essentially experience substantial swelling during the rainfall period (Ng et al. 2003). Cheng et al. (2011) from the centrifugal modelling results suggested the instability of expansive soils can be attributed to the influence of swelling or heave within the slope surficial layer.

The key objective of the present study is to investigate the effect of coupling behaviour on slope stability of expansive soils. The hydro-mechanical and hydraulic responses of a typical representative slope in Regina are modeled using commercial software SIGMA/W and SEEP/W

(GeoSlope International Ltd., 2007). The hydraulic and mechanical properties measured on Regina clay are used as the input parameters in the Finite Element Analyses (FEA). The infinite (one-dimensional) slope stability analysis formulation that has been regarded as a justifiable method for shallow failure is utilized here for evaluating the stability of surficial layer of unsaturated expansive soil slope. The FS values at three sections (representing the slope top, mid slope and slope toe, respectively) along the slope surface are computed extending both coupled and uncoupled analyses to investigate the effect of coupling behaviour of expansive soils. The suction variation, associated heave amount and FS evolution during the rainfall period from coupled and uncoupled analyses are presented, compared and discussed. The studies show that the FS is significantly lower for coupled analysis in comparison to uncoupled analysis.

3.2 Slope stability analysis of unsaturated soils

3.2.1 Coupled and uncoupled analyses

3.2.1.1 Governing equations

Two sets of basic equations; namely, the partial differential force equilibrium and water continuity equations, form the fundamental equations governing the mechanical behaviour for soil structure and flow behaviour for water phase of an unsaturated soil element. The two finite element software; namely, SIGMA/W and SEEP/W are programmed based on these two sets of governing equations. Since the third phase (pore air) in the unsaturated soil elements within the slope surficial layer is essentially connected to the atmosphere, the problem was solved assuming constant air pressure.

The partial differential equations of overall static equilibrium with regard to an unsaturated soil element are written as follows:

$$\frac{\partial \sigma_{ij}}{\partial x_j} + b_i = 0 \tag{3.1}$$

where σ_{ij} are components of the total stress tensor, and b_i are components of the body force vector.

Water flow in unsaturated soil is analyzed extending continuity equation assuming water is incompressible and deformations in soils are incrementally infinitesimal. The water continuity equation for an unsaturated soil element can be written as follows:

$$\frac{\partial q_x}{\partial x} + \frac{\partial q_y}{\partial y} + \frac{\partial q_z}{\partial z} + \frac{\partial \theta_w}{\partial t} = 0 \tag{3.2}$$

where, q_x, q_y and q_z are the flow velocities in *x*- *y*- and *z*-directions, respectively, θ_w is volumetric water content, and *t* is time.

3.2.1.2 Constitutive relationships

The mechanical behaviour of saturated soil can be generally described by an effective stress-strain relationship for soil structure if both the soil particles and water phase are assumed to be incompressible. However, additional relationship between water content and stress variables is required to fully describe the mechanical behaviour of an unsaturated soil. Biot (1941) was the first investigator who suggested the use of two constitutive equations for both soil structure and water phase of an unsaturated soil containing occluded air bubbles in water phase. These equations

are similar in form to the constitutive equations established by Fredlund and Morgenstern (1976) based on two stress state variables. The two stress state variables, namely net stress and suction, are also used in the present study to describe the unsaturated soil constitutive relationships. The net stress, $\sigma_{ij} - u_a$, is the total stress, σ_{ij}, in excess of the pore air pressure, u_a, and the suction, $u_a - u_w$, is the pore air pressure, u_a, in excess of the pore water pressure, u_w. Since the pore air pressure is assumed to be constant and atmospheric, with $\sigma_{ij} - u_a$ and $u_a - u_w$ replaced by σ_{ij} and $-u_w$, these two incremental constitutive equations take the following simplified form:

$$d\varepsilon_{ij} = \frac{1+\mu}{E} d\sigma_{ij} - \frac{\mu}{E} d\sigma_{mean}\delta_{ij} - \frac{1}{H} du_w \delta_{ij} \tag{3.3}$$

$$d\theta_w = \frac{3}{H} d\sigma_{mean} - \frac{1}{H_w} du_w \tag{3.4}$$

where, ε_{ij} are the components of the strain tensor, $\sigma_{mean} = (\sigma_x + \sigma_y + \sigma_z)/3$, δ_{ij} is the Kronecker delta, E is the elastic modulus for the soil structure with respect to a change in the net stress, H is the elastic modulus for the soil structure with respect to a change in suction, μ is Poisson's ratio, and H_w is additional parameter relating the volumetric water content (VWC) to a change in PWP. Substituting Eq. (3.3) into Eq. (3.4) yields the following equation relating the change in VWC to change in volume of soil structure:

$$d\theta_w = \beta d\varepsilon_v - \omega du_w \tag{3.5}$$

where, $\beta = \dfrac{E}{H(1-2\mu)}$ and $\omega = \dfrac{1}{H_w} - \dfrac{3\beta}{H}$.

For water flow in unsaturated soil, the relationship between flow velocities and hydraulic heads (i.e. pressure head plus elevation head) are described by Darcy's Law as follows:

$$q_i = -k_{ij} \frac{\partial}{\partial x_j} \left(\frac{u_w}{\gamma_w} + y \right) \tag{3.6}$$

where, q_i is the flow velocity in *i* direction, k_i is the hydraulic conductivity in the *i* direction, which is a function of suction or water content for unsaturated soils, u_w is the value of PWP, γ_w is the density of water, and y is the elevation.

3.2.1.3 Numerical uncoupled and coupled solutions

If the volume change in unsaturated soils is negligible, only Eq. (3.2) with application of Darcy's law (Eq. (3.6)) is required to be solved in order to estimate unknowns (i.e. PWP) with a reasonable degree of accuracy. Substituting Eq. (3.6) into Eq. (3.2) results in the following form for analyzing two dimensional problems:

$$\frac{\partial}{\partial x}\left[k_x \frac{\partial}{\partial x}\left(\frac{u_w}{\gamma_w g} + y \right) \right] + \frac{\partial}{\partial y}\left[k_y \frac{\partial}{\partial y}\left(\frac{u_w}{\gamma_w g} + y \right) \right] = \frac{\partial \theta_w}{\partial t} \tag{3.7}$$

The uncoupled numerical analysis can be implemented by using the software SEEP/W, in which only hydraulic parameters of soil (i.e. SWCC and hydraulic conductivity function) are required to be specified. The SWCC can be used as a tool relating the VWC with the soil suction.

Substituting Eq. (3.3) and Eq. (3.5) into Eq. (3.1) and Eq. (3.2) yields the equations describing coupled hydro-mechanical behaviour of an unsaturated soil with two sets of unknowns in terms of PWP within soil and displacements of the soil structure. These two sets of unknowns

for a plane strain problem can be solved simultaneously by utilizing the software SIGMA/W that incorporates the hydraulic analysis code in SEEP/W into static force equilibrium analysis, resulting a coupled solution. The capability of SIGMA/W to conduct coupled saturated and unsaturated hydro-mechanical analysis has been verified by Wong et al. (1998), where the Mandel-Cryer and a coupled multidimensional consolidation problem for unsaturated soils are analysed. Additional mechanical parameters of soils (including E, μ and H) are required for a coupled hydro-mechanical analysis.

3.2.2 Infinite slope formulation

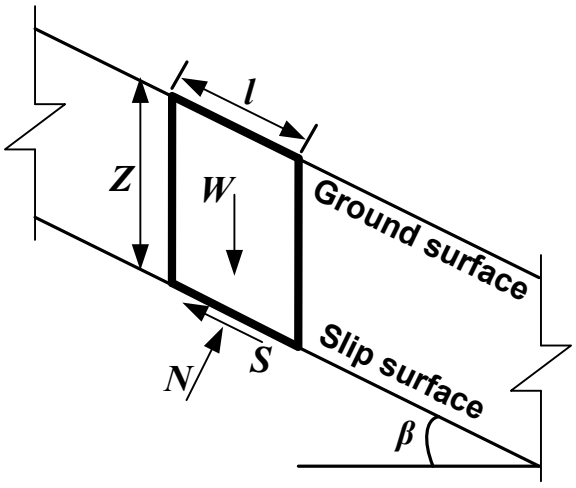

Fig. 3.1. The forces acting on the infinite slope

Shallow failures are those where only the surficial layer forms the sliding mass along a slip surface typically parallel to the face of the slope. For such a scenario, the failure mass can be assumed to extend infinitely along the sliding direction due to its considerably large length-to-depth ratio (Milledge et al. 2012). The FS of slope in such a scenario can be determined using only one force equilibrium equation in the vertical direction (as shown in Fig. 3.1). In infinite slope

model, the side forces on the two planes perpendicular to the slope surface are collinear, equal in magnitude and opposite in direction, since the sliding block is infinitely long. Therefore the side forces on two sides exactly balance each other and can be ignored (Milledge et al. 2012). The assumption of infinite slope further contributes to simplification of the slope stability analysis procedure. Such an approach has been extensively used in the literature for more than half-a-century to evaluate the slope stability of saturated soils (e.g. Griffiths et al. 2011; Skempton and Deloy 1957; Taylor 1948).

Many researchers (e.g. Ali et al. 2014; Collins and Znidarcic 2004; Iverson 2000; Jeldes et al. 2014; Lu and Godt 2008; Rahardjo et al. 1995) have extended the unsaturated soil mechanics into infinite slope formulation to investigate the effect of rainfall on the stability of slope surficial layer. Among these studies, the one-dimensional (1D) saturated-unsaturated seepage models are frequently used to obtain the changes in the near-surface PWP caused by rainfall. The 1D saturated-unsaturated seepage model can be solved either numerically or analytically. The validity of 1D seepage simplified model has been verified against results based on two-dimensional (2D) numerical analyses (Li et al. 2013; Zhan et al. 2013)) for rain-induced slope stability problems. In addition to the 1D seepage simplified model, the PWPs predicted using 2D numerical analyses were also used along with the infinite slope model to evaluate the stability of slope surficial layer (e.g. Alonso et al. 2003, Borja et al. 2012). Furthermore, the measured in-situ PWP changes was input to the infinite slope formulation by Jeldes et al. (2014) to calculate the seasonal variation of FS of steep reclaimed slopes in Appalachian region in United States.

The infinite slope formulation is also extended in the present study to calculate the FS of unsaturated expansive soil slope under rainfall conditions. Fig. 3.1 demonstrates an infinite slope with a potential slip surface at a depth of Z below the ground surface inclined at β degree from the

horizontal. The FS is defined as the ratio of magnitude of shear strength to magnitude of mobilized shear stress on the slip surface as many other 2D and 3D traditional limit equilibrium methods:

$$FS = \frac{\tau_f}{\tau} \tag{3.8}$$

where, τ is the mobilized stress on the slip surface, τ_f is the shear strength of unsaturated soils. Experimental determination of value of shear strength of unsaturated soils is costly and time-consuming; some empirical models for predicting the shear strength of unsaturated soils available in the literature can provide a satisfactory accuracy for slope stability analysis. In this study, the semi-empirical model proposed by Vanapalli et al. (1996) is used:

$$\tau_f = c' + (\sigma - u_a)\tan\phi' + (u_a - u_w)\left[\left(\frac{\theta_w - \theta_r}{\theta_s - \theta_r}\right)\tan\phi'\right] \tag{3.9}$$

where, c' and ϕ'= effective cohesion and internal friction angle at saturated condition, $(\sigma - u_a)$= net normal stress, $(u_a - u_w)$= suction, θ_w= volumetric water content, θ_s = saturated volumetric water content, θ_r = residual volumetric water content. This model appears to be of particular interest in practice among others (Jeldes et al. 2014). This is mainly because of the following reasons: (i) it allows the relationship between strength with suction via the SWCC instead of using time-consuming and expensive experimental procedures; (ii) the nonlinear relationship between strength and suction can be well explained and predicted by the model; (iii) no fitting parameters are required in this semi-empirical model.

It can be seen from Eq. (3.8) and Eq. (3.9) that the normal and shear stresses on the slip surface are required to be solved prior to obtaining the FS. Let us consider one soil slice with a

length of *l* along the sloping direction (Fig. 3.1), the thickness in the direction perpendicular to the plane in Fig. 3.1 is unity, the unit weight of this soil slice is calculated as:

$$W = \gamma l Z \cos\beta \tag{3.10}$$

where γ = the unsaturated soil unit weight. Applying the force equilibrium condition in the vertical direction, the normal and shear forces acting on the slip surface are obtained as follows:

$$N = \gamma l Z \cos^2\beta \tag{3.11}$$

$$S = \gamma l Z \cos\beta \sin\beta \tag{3.12}$$

Therefore, the normal and shear stresses on the slip surface for an infinite slope can be readily obtained by dividing N and S by the area of the plane (i.e. "l"), gives:

$$\sigma = \gamma Z \cos^2\beta \tag{3.13}$$

$$\tau = \gamma Z \cos\beta \sin\beta \tag{3.14}$$

Substituting Eqs. (3.9), (3.13) and (3.14) into Eq. (3.8) yield the expression for FS:

$$FS = \frac{c'}{\gamma Z \cos\beta \sin\beta} + \frac{\tan\phi'}{\tan\beta} + \frac{(u_a - u_w)[(\theta_w - \theta_r)/(\theta_s - \theta_r)]\tan\phi'}{\gamma Z \cos\beta \sin\beta} \tag{3.15}$$

The three terms on the right hand side of Eq. (3.15) represent the shear strength contribution due to effective cohesion, effective internal friction angle and suction for unsaturated conditions of the soil, respectively. When soil is saturated, the PWP would be equal to or greater than zero and $(\theta_w - \theta_r)/(\theta_s - \theta_r)$ is equal to unity. Eq. (3.15) reverts to the form at saturated conditions embracing effective stress principle. In other words, there is a smooth transition between

unsaturated and saturated soil shear strength when the PWP tends to zero or even greater than unity. Therefore, Eq. (3.15) is also applicable for conditions where slip surface is below GWT. The required parameters for computing the FS using Eq. (3.15) include the suction or negative PWP and VWC at the slip surface, the SWCC with well-defined saturated and residual water contents, in addition to the other basic soil properties (i.e. soil unit weight, effective cohesion, effective internal friction angle) and slope angle.

3.2.3 Procedures followed for evaluating the expansive soil slope stability

The required input parameters (e.g. PWP and VWC) must be determined or estimated prior to evaluating the stability of expansive soil slopes under rainfall infiltration using infinite slope formulation (i.e. Eq. (3.15)). Expansive soils swell upon wetting have a significant influence on the water flow within the soils. Only seepage analysis does not adequately capture the coupled hydro-mechanical behaviour of expansive soil slope under rainfall conditions. In this study, the response of a typical slope constructed of Regina clay in Canada that is subjected to a low intensity prolonged rainfall is modeled by conducting a coupled analysis using the commercial software SIGMA/W. For the purpose of comparison, a parallel uncoupled analysis is also carried out on the same slope using software SEEP/W. The PWPs and VWCs from both coupled and uncoupled analyses are then input into Eq. (3.15) to calculate the FS profile (variation with depth) change with respect to time. The procedure for evaluating the expansive soil slope surficial layer stability followed in this study is summarized succinctly using Fig. 3.2.

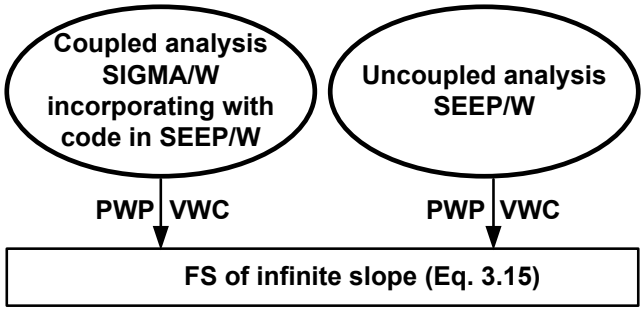

Fig. 3.2. Stability analysis procedure based on coupled and uncoupled analyses

3.3 Numerical studies

3.3.1 Model slope establishment

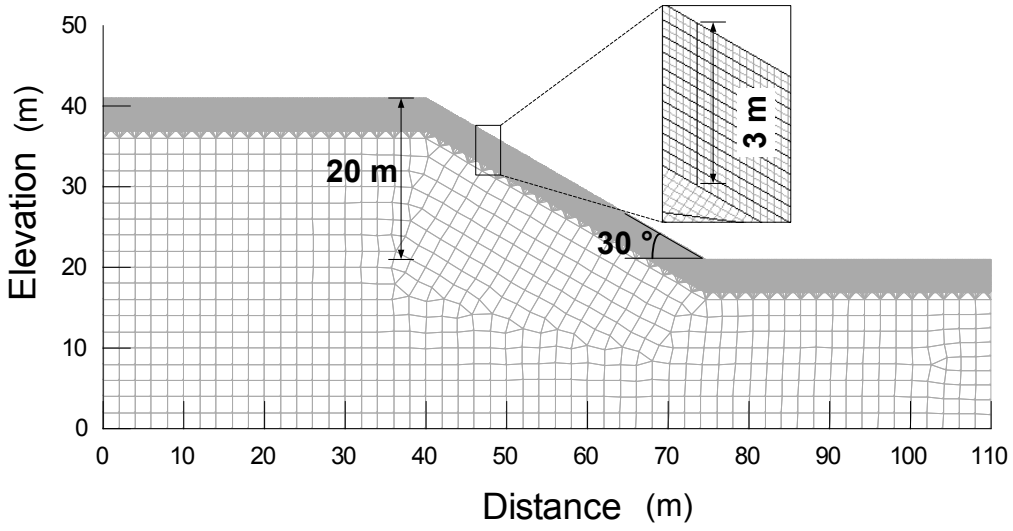

Fig. 3.3. Established model slope

A 20 m high model slope with an inclination of 30° is used in this study as a representative slope in Regina in Saskatchewan province of Canada, as shown in Fig. 3.3. Some recent field studies have shown that the expansive soil near the slope surface is significantly affected by rainfall and other parameters that are influenced by the climate (Ng et al. 2003). Such a behaviour can be attributed to the influence of cracks and fissures that are predominant in the surficial layer. The soil properties are significantly different in this layer; especially the hydraulic conductivity and the

SWCC. In the present study, the top 3 m thickness of soil layer is assumed to be cracked (i.e. active zone depth), substantially affected by climatic variations, and the soil below is assumed to be intact. The depth of active zone may vary with soil properties and environmental factors (McKeen and Johnson 1990). Yoshida et al. (1983) predicted the total heave of a slab-on-grade floor on Regina clay considering the active zone depth as 2.8 m. For this reason, the active zone depth is assumed as 3 m in the present study. Once the intact soil regions are properly discretized, the special surface layer command provided by SEEP/W is used to build up the cracked surficial layer along the surface of intact region. The surficial layer can be divided into single or multiple layers. The thickness of this layer can be set arbitrarily (a total of 3 m is used for this study). A quadrilateral element mesh with nodes along the vertical lines can be automatically assigned to the surface layer (see Fig. 3.3). Since the primary unknown hydraulic gradients causing water flow are essentially steeper in a direction perpendicular to the surface during the infiltration process, quadrilateral elements are a better choice to model the dramatic response of slope surface layer to rainfall in comparison to triangular elements (GeoSlope International Ltd., 2007). Using triangular elements may cause fluctuation in the computed results in such a thin layer due to its orientation unless the mesh size is small enough. Furthermore, use of elements with nodes along the vertical lines provides a convenience for picking up the PWP and VWC along a vertical section that can be used to calculate the FS in this present study. The much finer mesh in surface cracked layer ensures more accurate results, while the large portion of intact soil zone is discretized by larger size of meshes (see Fig. 3.3) for saving computational efforts.

3.3.2 Initial conditions

Since the climate of the Regina area is classified as a semi-arid to arid type according to the Köppen Climate Classification System (Ito and Azam 2009), the natural GWT is at a greater

depth with relatively high values of suction present near the ground surface (Fredlund and Rahardjo 1993). The initial GWT is assumed to be at depth ranging from about 8 to 23 m within the slope profile as shown Fig. 3.4. The hydrostatic variation of PWP with vertical distance above and below the GWT is formed as the initial hydraulic condition. By this method, the initial suction at the slope surface ranges from around 80 kPa (i.e. the GWT is at 8 m below the toe of slope) to approximately 230 kPa at the top of slope. The initial mechanical stress field within this model slope are constructed by using SIGMA/W with specified unit weights and Poisson's ratio values as explained in the user's manual (GeoSlope International Ltd., 2007).

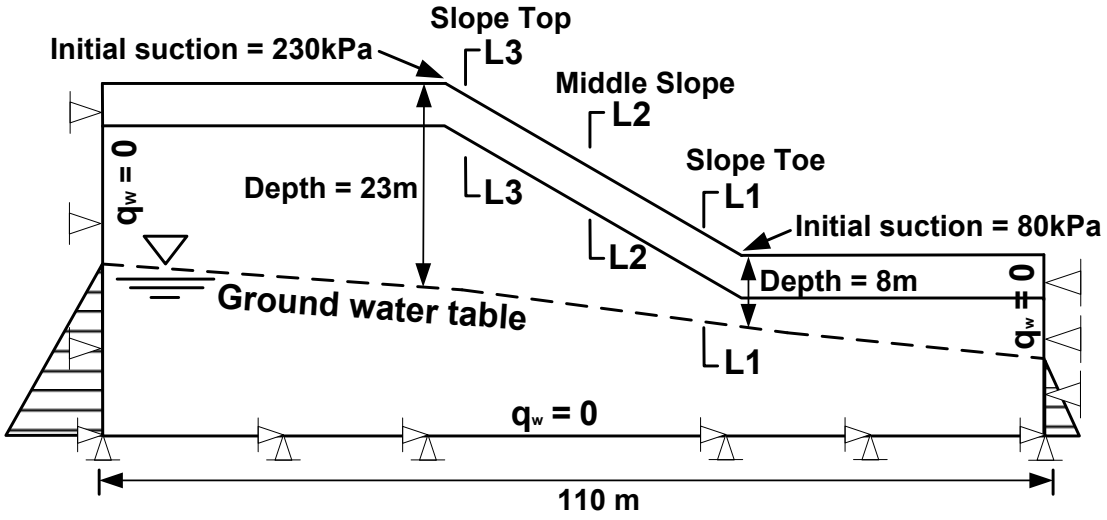

Fig. 3.4. Hydraulic and mechanical boundary conditions

3.3.3 Boundary conditions

Boundary conditions for this model slope under consideration are established as demonstrated in Fig. 3.4 for assessing the hydraulic and mechanical behaviour. It should be noted that only hydraulic boundary conditions need to be specified for uncoupled analysis, while coupled analysis requires both hydraulic and mechanical conditions to be defined. Both the PWPs at the

right and left lateral boundaries increase linearly with depth below the GWT. The lateral boundaries above the GWT as well as the bottom boundary of the computational domain for water flow have a zero flux. These conditions are reasonable, since: (i) only the flow within the surficial layer can be substantially influenced by rainfall as the GWT is typically at a greater depth and the hydraulic conductivity of intact soil is typically low; (ii) the lateral flow across the lateral boundaries above the GWT has little effect on the water flow within the sloping surficial layer due to a large distance between them. An influx is applied on the horizontal and slope sections of top ground surface with no ponding allowed to simulate low intensity prolonged rainfall. Both the displacements in the horizontal and vertical directions are fixed at the bottom boundary, while the two lateral boundaries are allowed to move only in the vertical directions for the purpose of modeling the swelling or heave that will occur particularly within slope surface layer. This is the commonly-used boundary condition for slope stability analysis.

3.3.4 Soil properties

The soil properties of Regina clay used in the present analysis are summarized in Table 3.1. The input parameters for uncoupled analysis include the SWCCs, hydraulic conductivity functions. The SWCC used here for the surficial cracked soil layer was measured by Azam and Ito (2011). As shown in Fig. 3.5, a bimodal trend with a first (fissure) air entry value (AEV) of 10 kPa and second AEV of 300 kPa was followed by the SWCC of the fissured Regina clay. It is well known that the shape of SWCC is strongly related to the pore size distribution of the soils (Fredlund and Xing 1994; Fredlund and Rahardjo 1993). The bimodal nature of SWCC is possible for soils with a dual porosity structure such as the compacted coarse colluvial soils and the gap-graded soils (Miguel and Bonder, 2012; Satyanaga et al. 2013; Li and Zhang, 2009; Li et al. 2011; Li et al. 2014). The presence of cracks in expansive soils can lead to a dual porosity structure, including

the macro-pores (i.e. the cracks) and micro-pores (i.e. the intra-aggregate pores) resulting in a bimodal SWCC. For the purpose of numerical simulation of unsaturated hydraulic properties of cracked soils, some attempts were recently made to predict the bimodal SWCC equations (Zhang and Fredlund, 2003) as well as corresponding bimodal hydraulic conductivity functions (Li et al. 2011). Alternative way to generate the continuous SWCC is to fit the measured data using polynomial spline function. This method is flexible and also efficient for numerical modeling if sufficient data is available. In this study, the spline functions built in the software are adopted to describe the bimodal SWCCs and other hydraulic properties of Regina Clay (Fig. 3.5 and 3.6). Since the bimodal SWCC can be regarded as a superposition of a unimodal SWCC for cracked (macropores) potion and that for intact (micro-pores) series (Li et al. 2014); the characteristic parameters of bimodal SWCC can be determined for two unimodal SWCCs using the construction procedure, separately. The associated characteristic parameters of bimodal SWCC of Regina clay are summarized in Table 3.1. The saturated water content is the water content at zero soil suction. The first air entry value and first residual suction correspond to the drainage through the cracked portion. The second air entry value, residual suction and residual water content are associated with the drainage of water stored in the intact soil portion. The unimodal SWCC for intact Regina Clay used herein (see Fig. 3.5) is obtained from the bimodal SWCC for cracked surficial soil layer according to the superposition technique suggested by some researchers (Fredlund et al. 2000; Li et al. 2011) for establishment of the bimodal SWCC. The AEV of unimodal SWCC of intact Regina Clay is equal to the second AEV of bimodal SWCC of fissured Regina clay (i.e. 300 kPa). The residual suction and water content of unimodal SWCC of intact Regina Clay are consistent with those of bimodal SWCC.

The hydraulic conductivity function of Regina clay measured by Shuai (1996) is utilized as shown in Fig. 3.6 for the intact soil layer, which has a low saturated hydraulic conductivity of 3.456×10^{-6} m/day. There is limited information about the measured hydraulic conductivity function of cracked Regina clay; however, some research (e.g. Li et al. 2011, Fredlund et al. 2012;) suggested that the hydraulic conductivity function of the cracked soil also exhibited a bimodal trend. The saturated hydraulic conductivity of such soil is reported to increase by one or more orders of magnitude compared to that of corresponding intact soils. The saturated hydraulic conductivity for the cracked Regina clay is assumed to be two orders of magnitude greater than that of intact condition in this study (see Fig. 3.6).

Table 3.1 Summary Regina clay soil properties used in the present study

Properties		Surface layer	Intact soil	Figure	Reference
SWCC	First air entry value (kPa)	10	300	Fig. 3.5	Azam and Ito (2011)
	Second air entry value (kPa)	300	----		
	First residual suction (kPa)	55	----		
	Residual suction (kPa)	70,000	70,000		
	Saturated water content (m^3/m^3)	0.52	0.41		
	Residual water content (m^3/m^3)	0.1	0.1		
k	k at saturated condition (m/day)	3.53×10^{-4}	3.53×10^{-6}	Fig. 3.6	Shuai (1996)
	k at turning point (m/day)	3.29×10^{-6}	----		
Modulus of elasticity, E (kPa)		Semi-empirical model	4000	Fig. 3.7	Adem and Vanapalli (2013)
Poisson's ratio, μ		0.4	0.4	----	Assumed
Unit weight, γ (kN/m³)		18.04	18.04	----	Widger and Fredlund (1978)
Effective internal friction angle, ϕ' (°)		17.5	----	----	
Effective cohesion, c' (kPa)		5	----	----	

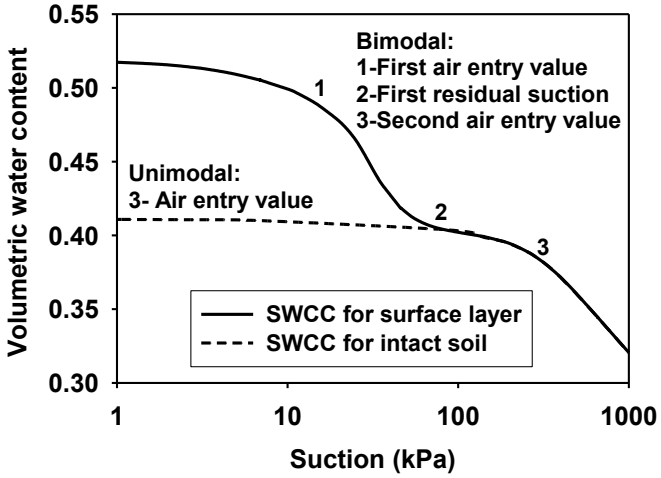

Fig. 3.5. SWCCs of Regina clay

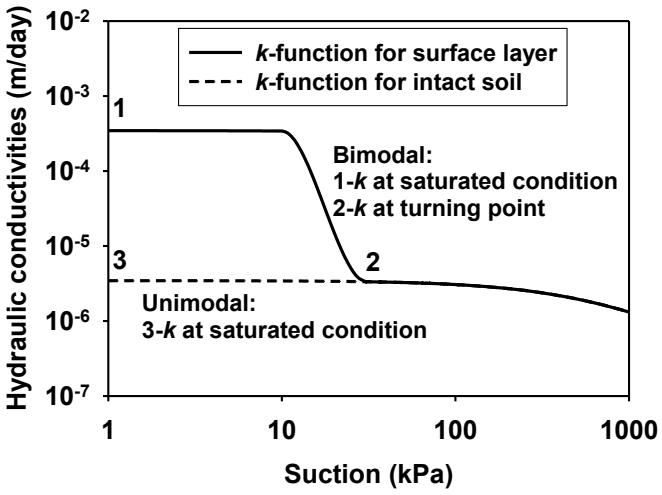

Fig. 3.6. Hydraulic conductivities of Regina clay

In addition to the hydraulic properties (i.e. saturated hydraulic conductivity and the SWCC), mechanical properties, including elasticity parameters E and H (E = elastic modulus for the soil structure with respect to a change in the net stress, H = elastic modulus for the soil structure with respect to a change in suction), and Poisson's ratio μ, are required to be determined for conducting the coupled hydro-mechanical analysis. The elasticity parameters E and H are functions of both

the net stress and suction for soils that are in a state of unsaturated condition. Determination of the elasticity parameters from laboratory tests requires construction of a constitutive surface in the form a relationship between void ratio and two stress state variables (Vu and Fredlund 2006). However, establishing such a surface is cumbersome and time consuming, especially for low permeable expansive soils. In the present study, a semi-empirical model (Oh et al. 2009; Vanapalli and Oh 2010) given below is used for prediction of the nonlinear variation of modulus of elasticity with matric suction using the SWCC as a tool.

$$E_{unsat} = E_{sat}\left[1+\alpha\frac{(u_a-u_w)}{P_a/101.3}S^{\beta}\right] \tag{3.16}$$

where, E_{unsat} represents the value of E under unsaturated condition, E_{sat} represents the value of E under saturated condition, (u_a-u_w) is the suction, P_a is the atmospheric pressure (101.3 kPa) used for maintaining consistency with respect to the dimensions and units on both sides of the equation, and S is the degree of saturation, α and β are two fitting parameters. As can be seen, use of this model requires two fitting parameters (α and β) in addition to E_{sat} and the SWCC. This semi-empirical model was originally proposed by Oh et al. (2009) for unsaturated coarse-grained soils, and then extended for both coarse-and fine-grained soils by Vanapalli and Oh (2010). The model was found to be valid for various fine-grained soils using a fixed value of β=2. In other words, only one parameter α needs to be fitted taking account of different conditions (e.g. soil properties and stress conditions). The applicability of this semi-empirical model for expansive soils was further examined by Adem and Vanapalli (2014) using three sets of experimental data on expansive soils. The fitting parameter α that provides a reasonable estimation of E_{unsat} under low net confining stress was found to fall within the range from 0.05-0.15. These results were

consistent with those from the comprehensive modelling studies on heave of expansive soils for several in-situ cases (Adem and Vanapalli, 2013, 2014). The semi-empirical model, with an average E_{sat} value of 1,000 kPa and fitting parameters α and β values of 0.1 and 2 provided a good estimate of elasticity of modulus for unsaturated Regina clay. For this reason, the semi-empirical model (Eq. (3.16)) (Oh et al. 2009; Vanapalli and Oh 2010) with the fitting parameter values of α =0.1 and β=2 are used in the present study for the surficial soil layer of the model slope. The variation of E_{unsat} with respect to suction achieved using this methodology is shown in Fig. 3.7. The H is related to E using the relation $H = E/(1-2\mu)$ programmed in SIGMA/W for modeling. The Poisson's ratio μ is assumed to be 0.4 for the Regina clay that has been often used in other numerical modelling studies (e.g. Vu and Fredlund, 2006; Adem and Vanapalli, 2014). For the intact soil layer, since it is not significantly affected by infiltration in this study, an average elasticity parameter, E=4000 kPa is assigned to this layer. Some advanced elasto-plastic models for expansive soils already exist in the literature, for example, the one proposed by Gens and Alonso (1992) and Alonso et al. (1999), can predict both the stress-strain and strength behaviour based on the double-structure framework. The other model proposed by Sun and Sun (2012) is able to couple the effects of degree of saturation on the mechanical behaviour and void ratio on the water retention behaviour. There are several numerical codes, such as the CODE_BRIGTH (Olivella et al. 1996; Sánchez et al. 2008) and SNAC (Sheng et al. 2003), in which some advanced elasto-plastic models for unsaturated (expansive) soils have been incorporated. Careful application of these models in analyzing the stability of unsaturated expansive soil slopes is expected to provide more information on failure mechanism, e.g. plastic straining and deformation. This will also, to some extent, increase the complexities, and require more efforts on accurately quantifying a number of constitutive model parameters. The relatively simple model used in present analysis

is able to highlight several interesting implications regarding the shallow failures when combined with the infinite slope stability formulation, which will be discussed later.

Once the coupled and uncoupled analysis are completed, the resulting PWP and VWC along with the unit weight and shear strength parameters can be input into the infinite slope stability analysis formulation to determine the FS. The basic mechanical parameters (including unit weight, effective cohesion and internal friction angle) for saturated conditions recommended by Widger and Fredlund (1978) through performing a back analysis on a failed embankment constructed of Regina clay at Belle Plaine, Saskatchewan are used in this study. The shear strength parameters are not required in intact soil layer, because the focus of the present study is related to the stability of surface layer.

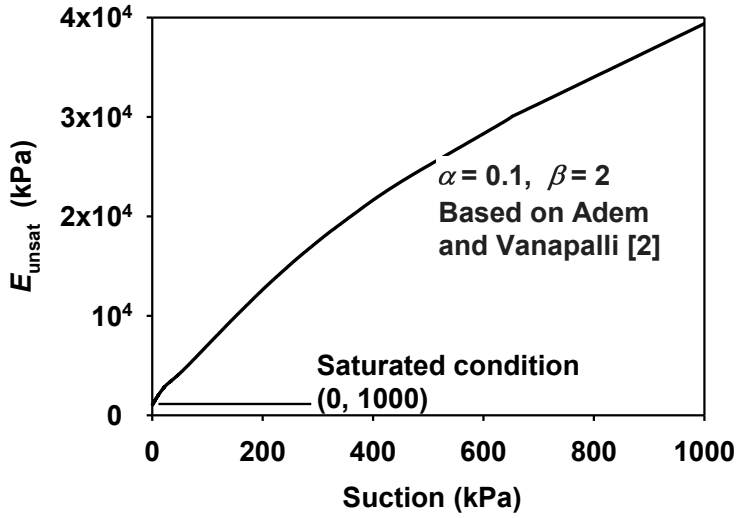

Fig. 3.7. Variation of modulus of elasticity with respect to suction for Regina clay predicted using the semi-empirical model (Oh et al. 2009)

3.4 Results presentation

3.4.1 Variation of PWP profile

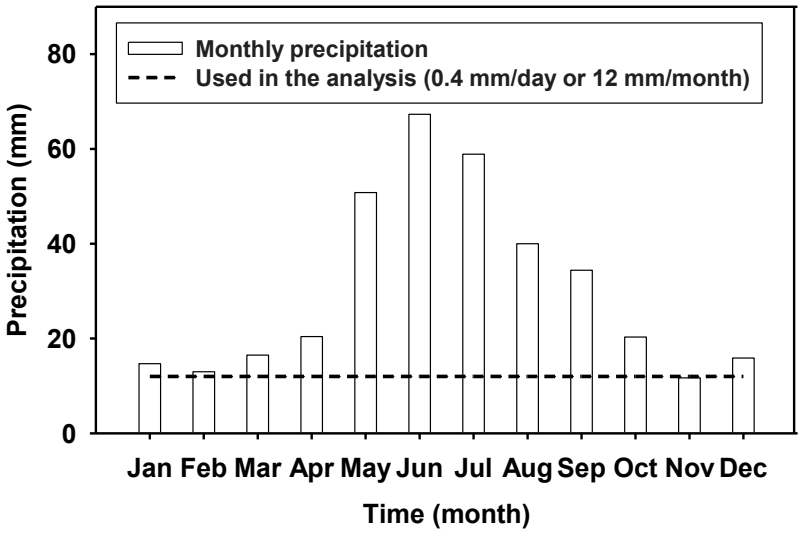

Fig. 3.8. Monthly precipitation in Regina, Canada in 2013

The precipitation in Regina primarily occurs during the period from April to September (about half year) with a certain amount resulting from melting of snow in spring when the temperature rises and remains above 0°C. Fig. 3.8 illustrates the monthly precipitation recorded in Regina in 2013. During the wetting season, the daily rainfall could be quite high, such as 34.8 mm recorded recently on June 18, 2014, which is greater than the saturated hydraulic conductivity of the surface layer of the slope. The precipitation can be simulated using a flux boundary condition applied on the top sloping surface of the slope in both SEEP/W and SIGMA/W. It should be noted that the maximum amount of rainwater that can infiltrate into the soils is limited to the saturated hydraulic conductivity of the surface soils. When the rainfall rate is greater than the saturated hydraulic conductivity of the surface soils, a runoff occurs along the slope surface. This condition

can be considered by changing the flux boundary into a hydraulic head boundary with PWP of 0 kPa specified at each element node on the slope surface in the numerical modeling, which is automatically accounted for by the software. In the present study, a daily flux boundary (4.00×10^{-4} m/day) (see Fig. 3.8) that is slightly greater than the saturated hydraulic conductivity of the surface layer is applied to the top surface of the model slope, for a period of 6 successive months, to simulate the recorded rainfall during the wetting season in one typical year. This rainfall pattern can be classified as a low intensity prolonged rainfall.

3.4.1.1 Effect of elasticity parameters value on predicted PWP

In the coupled analysis, the moduli of elasticity at different locations of the slope will change constantly with time due to the rainfall infiltration, according to nonlinear elastic model (i.e. semi-empirical model: Eq. (3.16)) used in this study. This nonlinear elastic model involving the variation of E_{unsat} with suction is currently not available in the commercial software SIGMA/W. An accurate solution essentially requires a numerical integration technique (e.g. Forward Euler Integration Scheme) considering nonlinearity of E_{unsat}. In the present study, an approximation technique which is similar to the tangent stiffness method for nonlinear material in FEA is used for the surficial layer. The 3 m thickness of surficial soil layer in the SIGMA/W slope model is divided into several small soil layers, and the moduli of elasticity of each layer is updated according to the suctions from the results of the previous time interval and the semi-empirical relationship (i.e. Fig. 3.7) during the whole coupled analysis. The modulus of elasticity parameters estimated at the mid slope (i.e. L2 in Fig. 3.10) at some time steps is illustrated in Fig. 3.9**.** The approximate incremental solution to the coupled nonlinear equations is considered to be reasonable to illustrate the effect of variation of E_{unsat} with respect to suction. For comparison purposes, a

constant modulus of elasticity value at saturated condition, E=1,000 kPa both spatially and temporally is also used in the analysis.

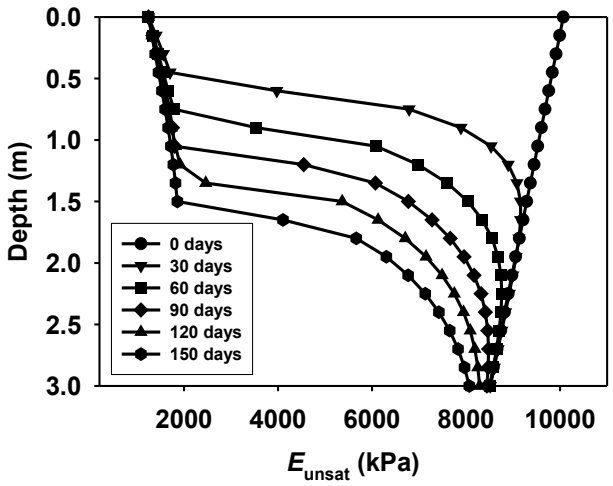

Fig. 3.9. Illustration of E profile at some time steps for middle slope

Three locations, L1, L2 and L3 as shown in Fig. 3.10, are selected to illustrate the variation of PWP profiles at the slope toe, mid slope, and slope top, respectively. Fig. 3.11 presents the time history of PWP at different depths (i.e. 0.75 m, 1.50 m, 2.25 m) (see Fig. 3.10) under slope ground surface at the three locations using E=1,000 kPa and semi-empirical model (i.e. Fig. 3.7), respectively. It can be seen that the suction predicted using a constant value E=1,000 kPa, which is the value under saturated condition, decreases at a much slower rate than those predicted using the semi-empirical model for unsaturated soils (Fig. 3.7) for all cases. The FS of the slope generally decreases at a rate proportional to the reduction in suction. These results suggest that using a constant value of modulus of elasticity may result in a higher FS, which is not conservative in practice. For this reason, in coupled analysis cases, the variation of modulus of elasticity with respect suction is considered by using the semi-empirical model (i.e. Fig. 3.7). It also should be

noted that the suctions at shallower depths reduce at a faster rate than those at greater depths; such a behaviour indirectly suggests gradual advancement of infiltrated water into greater depth of soil from the rainfall.

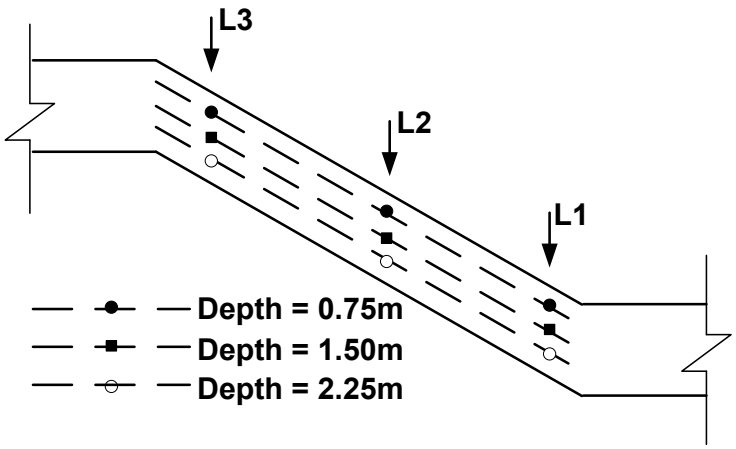

Fig. 3.10. Investigation locations and points within surface layer

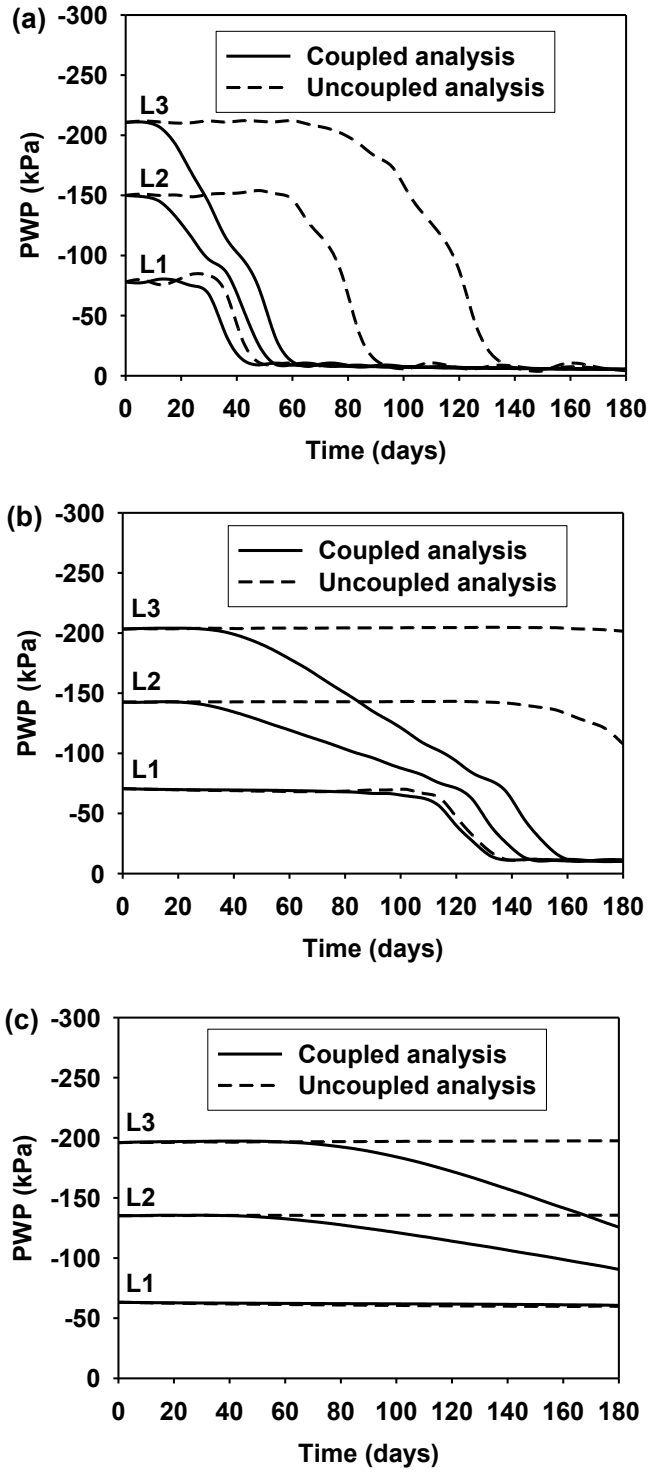

Fig. 3.11. Effect of elastic parameter on predicted PWP: (a) at depth of 0.75; (b) at depth of 1.50 m; (c) at depth of 2.25 m

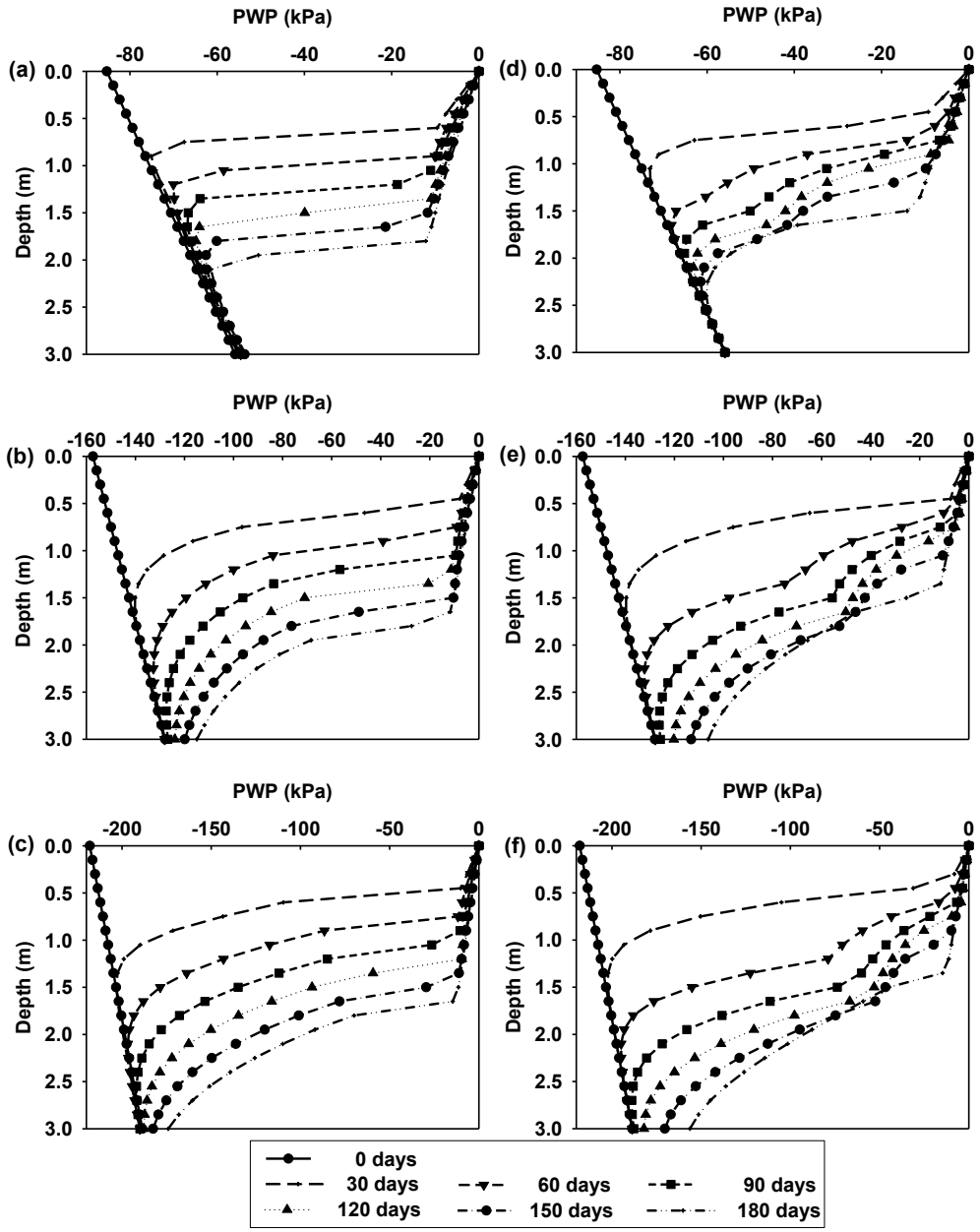

Fig. 3.12. Variation of PWP profile: (a) Coupled analysis at L1; (b) Coupled analysis at L2; (c) Coupled analysis at L3; (d) Uncoupled analysis at L1; (e) Uncoupled analysis at L2; (f) Uncoupled analysis at L3

3.4.1.2 PWP profile variation

Fig. 3.12 presents the PWP profile variations predicted using both coupled and uncoupled analyses at 30 day intervals since the commencement of the simulated rainfall. The PWP shown

in Fig. 3.12 is computed at each element node spaced at 150 mm along the vertical direction. The PWPs within the top 3 m thickness of soil layer are graphically illustrated because only this soil layer is significantly affected by rainfall infiltration and is prone to failure. More discussion on the PWP variations are provided in later sections along with the computed values of FS.

The initial PWP distributions are at the hydrostatic conditions but with different magnitudes at the three locations (PWP at L3> PWP at L2> PWP at L1) due to the different distances from the GWT. The PWPs at the slope surface immediately increase to zero once the rainfall commences. Such a behaviour can be expected due to the rainfall intensity which is slightly greater than the saturated hydraulic conductivity of the surface soil. Subsequently, there is a dramatic decrease in the suction (i.e. negative PWP) within the upper surficial layer while the value of the suction in the lower region remains essentially the same with the initial conditions for both coupled and uncoupled analyses. The wetting front, defined by Lumb (1962) as the sharp separation between the wetted zone and the initial condition, gradually advances to greater depths with the infiltrated rain water from the surface moving downward into the soil for both coupled and uncoupled analyses.

From Fig. 3.12, it can be seen that the shape of PWP profiles for the coupled analyses are quite different from those obtained by uncoupled analysis at the same elapsed time. The coupled analysis produces a sharper transition between PWP in the upper wetted zone and those at the initial condition than the uncoupled analysis. For uncoupled analysis, it takes more time for the upper zone of surficial layer to be wetted. This can be further seen in Fig. 3.13, which shows the VWC profiles at L2 after 150 days of rainfall.

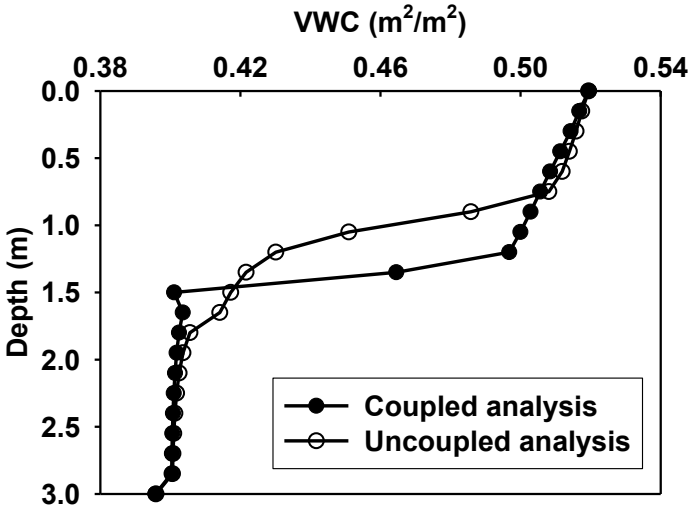

Fig. 3.13. Volumetric water content profile at L2 after 150 days of rainfall

The differences in the PWP profile from coupled and uncoupled analyses may be associated to the inclusion of the mechanical properties variation with suction (i.e. the soil softening during wetting) in the coupled analysis, which leads to larger volume changes, this, in turn, results in bigger changes in suctions. As a result, the wetted zones from the coupled analysis advances faster and therefore reaches greater depths for the same time period compared to the uncoupled analysis. For example, after 150 days of rainfall, the coupled analysis results in a wetting front at the depth of 1.5 m with a suction of 11.72 kPa at location L1, while the wetting front just advances to 1.05 m depth with a suction of 9.84 kPa for uncoupled analysis, as shown in Fig. 3.14. It can be expected that the increase in FS due to slightly higher suction (less than 2 kPa for this case) from coupled analysis can be neglected when compared with the reduction in FS resulted from the deeper wetting front depth. Fig. 3.14 also shows the suction computed using the uncoupled analysis at the same depth with wetting front depth from the coupled analysis (e.g. 37.85 kPa at 1.5 m depth) is much higher than that computed using the coupled analysis (i.e. 11.72

kPa). Thus, the FS around the wetting depth based on coupled analysis should be lower than that from uncoupled analysis.

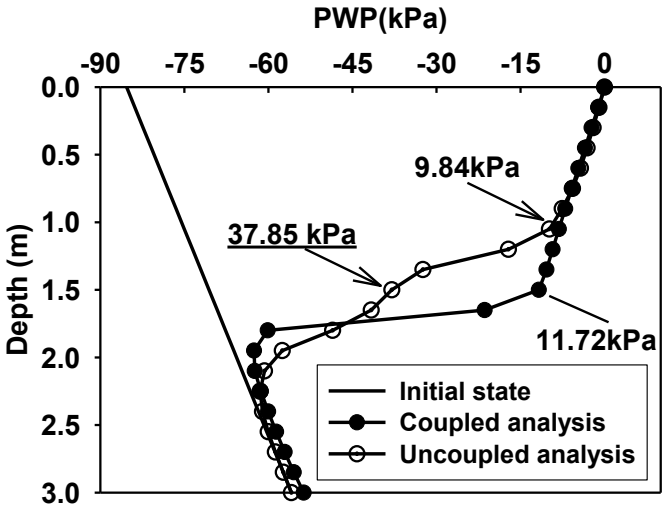

Fig. 3.14. The depth of wetting front with respect to time at location L1

Fig. 3.15 provides comparisons with the other wetting front depths at some time steps and corresponding suctions for both coupled and uncoupled analyses. Line 1 and Line 2 represent the suctions at their individual wetting front depths for each elapsed time from coupled and uncoupled analyses, respectively. Line 3 shows the suction from uncoupled analysis but at the depth that is the same as the wetting front depth from the coupled analysis. It is of interest to note that the suctions from the coupled and uncoupled analyses at their individual wetting front depths are comparable at the same time steps. But the difference in the wetting front depths between coupled and uncoupled analyses can be as high as 42.86% (i.e. 0.60 m for uncoupled analysis and 1.05 m for coupled analysis at L2 after 90 days of rainfall) among all the cases considered in this study. Thus, the FS computed around the wetting depth from coupled analysis might be expected to be lower than that from uncoupled analysis. This is because that the wetting front is deeper in coupled

analysis and the driving shear stress (τ in Eq. (3.8)) mobilized at greater depth is higher due to the effect of soil overburden pressure. This is illustrated and explained providing more details in the next section.

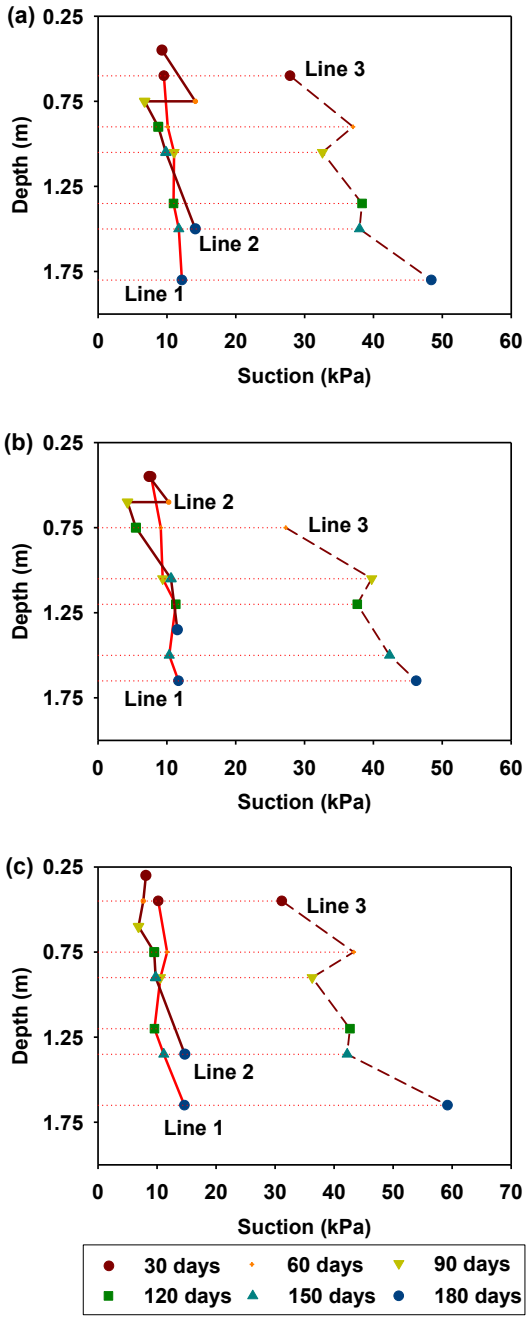

Fig. 3.15. Variation of suction at wetting front with respect to depth and time at (a) L1; (b) L2; (c) L3

3.4.2 Evolution of FS profile

In addition to PWP, another parameter required for computing the FS using Vanapalli et al (1996) model (i.e. Eq. (3.9)) is the VWC. This value can either be obtained directly by the FEA or derived from the computed suction profile and the SWCC. In the present study, the VWC profiles from both the coupled and uncoupled FEA are used in computing the evolution of FS profile with respect to time. The other mechanical properties of the soil are summarized in Table 3.1. The FS profile comprises the value of FS at different depths calculated using infinite slope model.

Fig. 3.16 presents the evolution of FS profile based on both the coupled and uncoupled analyses. The FS values within the top 3 m thickness of surface layer are examined in the present study, as this depth zone will be substantially affected by the rainfall. This figure shows that the FS values are relatively high when the slip surface is close to the face of slope. This is because the driving shear forces mobilized at these shallow positions due to the overburden pressure are low. However, once the rainfall commences, the local FS values decrease dramatically with depth with a lowest value occurring near the wetting front at each elapsed time. The positions of local lowest FS are essentially consistent with depths of nearly saturated zone shown Fig. 3.12 and Fig. 3.15. The decrease in FS values evolves to deeper depths as the rainfall continues. The evolution of FS value with respect to depth is consistent with the advancement of wetting front because the reduction in the soil strength and slope stability is primarily due to the loss of suction.

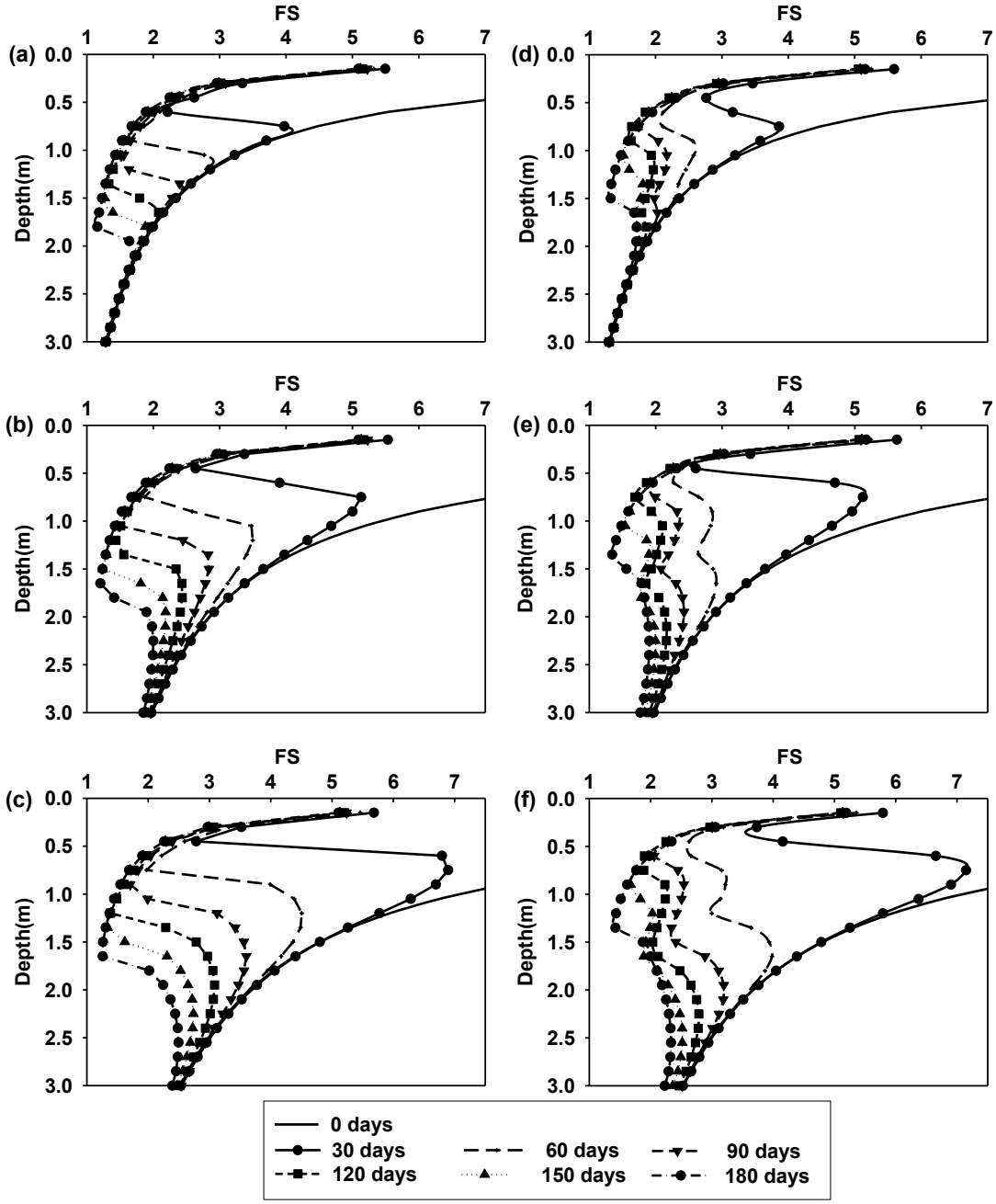

Fig. 3.16. Evolution of FS profile: (a) Coupled analysis at L1; (b) Coupled analysis at L2; (c) Coupled analysis at L3; (d) Uncoupled analysis at L1; (e) Uncoupled analysis at L2; (f) Uncoupled analysis at L3

The FS at the wetting front is the local lowest value within the transition zone, and therefore, the most critical FS which controls the slope stability. Fig. 3.17 shows the variation of critical FS with respect to time and depth. Line 1 and Line 2 represent the critical FS for each elapsed time from coupled and uncoupled analyses, respectively. Line 3 shows FS from uncoupled analysis, but at the depth that is the same with depth of critical FS from the coupled analysis (for example, the FS in Line 3 is calculated according to the condition 37.85 kPa at 1.5 m depth for uncoupled analysis in Fig. 3.14). The critical FS values from coupled analysis are lower than those determined from uncoupled analysis. For instance, the critical FS at the slope toe (i.e. L2) after 150 days of rainfall is 1.23 at depth of 1.5 m from coupled analysis while from uncoupled analysis is 1.53 at a depth of 1.05 m (see Fig. 3.18). This difference can be primarily attributed to the different suction profiles with different wetting front depths predicted using coupled and uncoupled analyses. The lower values of critical FS at deeper depths resulting from coupled analysis indicates that expansive soil coupling behaviour within surface layer has an adverse effect on the slope stability of expansive soils and should be taken into account in the slope stability analysis. For all the cases considered in this study, the uncoupled analysis can overestimate the critical FS for the surficial layer by 36.23% (critical FS=1.88 for uncoupled analysis and critical FS=1.38 for coupled analysis at L3 after 120 days of rainfall). Fig. 3.17 also illustrates that the values of critical FS at slope toe at every elapsed time are lower than those at both middle slope and slope top, because of a lower initial suction profile present at the slope toe. This may be a reasonable explanation why rain-induced expansive soil slope failures usually initialize from slope toe.

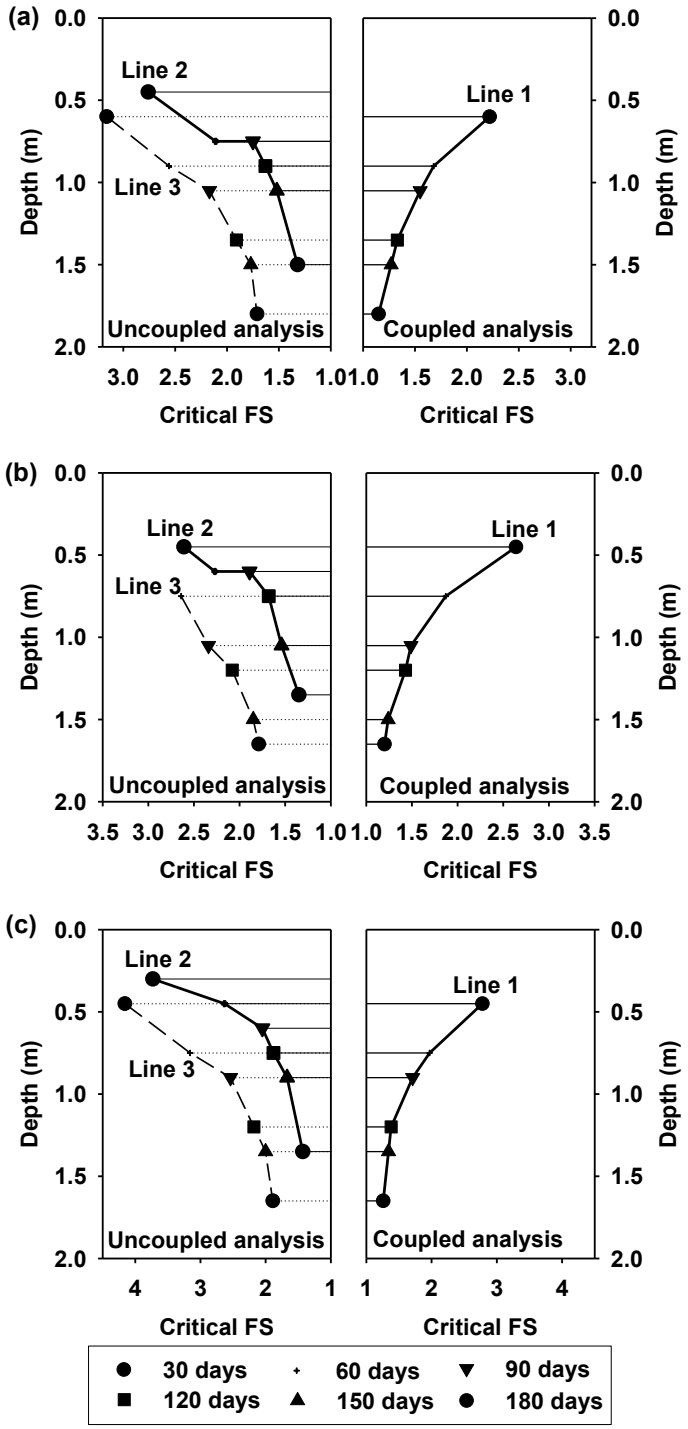

Fig. 3.17. Variation of critical FS with respect to time and depth: at (a) L1; (b) L2; (c) L3

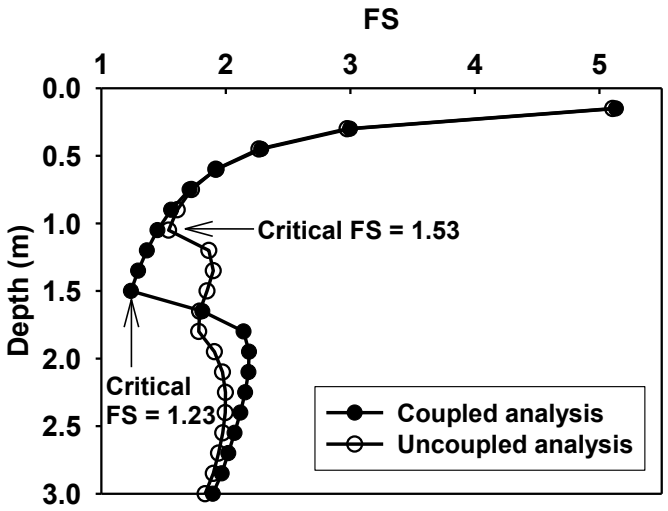

Fig. 3.18 The critical FS after 150 days at location L2

3.5 Discussions

3.5.1 Strength and failure mechanism

The FS in the infinite slope formulation consists of three components (i.e. the three terms on the right hand side of Eq. (3.15)), namely; shear strength contribution due to effective cohesion, effective internal friction angle and suction, respectively. The first two components will remain constant for a particular depth under the slope surface during the rainfall infiltration if the changes in unit weight of soils are not considered. In other words, the rainfall infiltration will lead to a reduction in the FS only by decreasing the third term on the right hand side of Eq. (3.15). This scenario can be induced by either a decrease in the suction for unsaturated condition or an increase in PWP for saturated conditions. These two conditions occur, respectively, during the two stages (the first stage involves propagation of the wetting front and second stage involves the rise of water table) divided by Li et al. (2013) for the response of infinite slope to rainfall infiltration. From

discussions summarized earlier (Section 4.1.2), all the hydraulic response scenarios of the considered slope in this study can be classified as the first stage, which means the shear strength only varies in the negative PWP range in the surficial zone (within 3 m depth).

Fig. 3.19(b) shows the variation of shear strength with suction predicted using Vanapalli et al. (1996) model based on the bimodal SWCC for the surficial layer (Fig. 3.19(a)) within the suction range of interest in this study. The relationship between strength and suction also exhibits a weak bimodal trend due to the bimodal SWCC. This is because the shear strength is related to the suction by the relative water contents within the soils (see Eq. (3.9)). The slope of the relationship between shear strength and suction in each suction range ((i) up to the first air entry value (AEV); (ii) first AEV to the first residual suction; (iii) the first residual suction to the second AEV) is consistent with variation of water content with suction in the SWCC (slope of SWCC). However, the shear strength still experiences a substantial decrease with decreasing suction in this range. Such a behaviour can be attributed to that the increase in relative water content is not so significant from the second AEV to the saturated state.

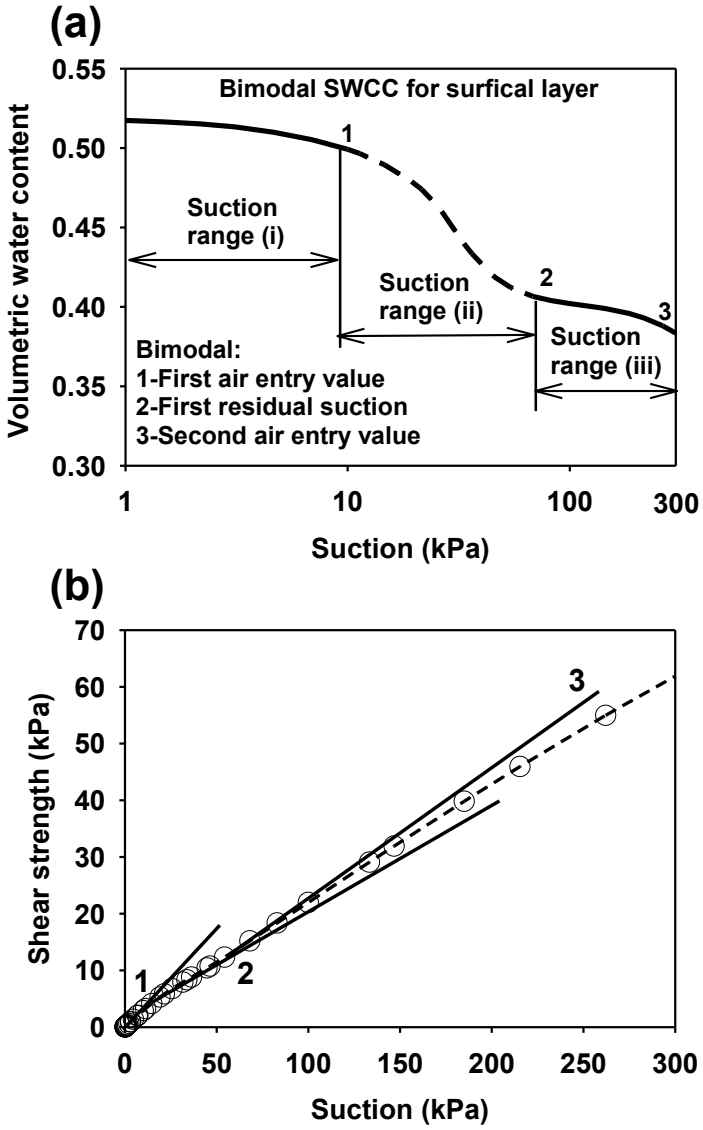

Fig. 3.19. (a) Bimodal SWCC for the surficial layer in the suction range of interest in the present study; (b) Variation of shear strength with respect to suction predicted using Vanapalli et al. (1996) model based on the bimodal SWCC

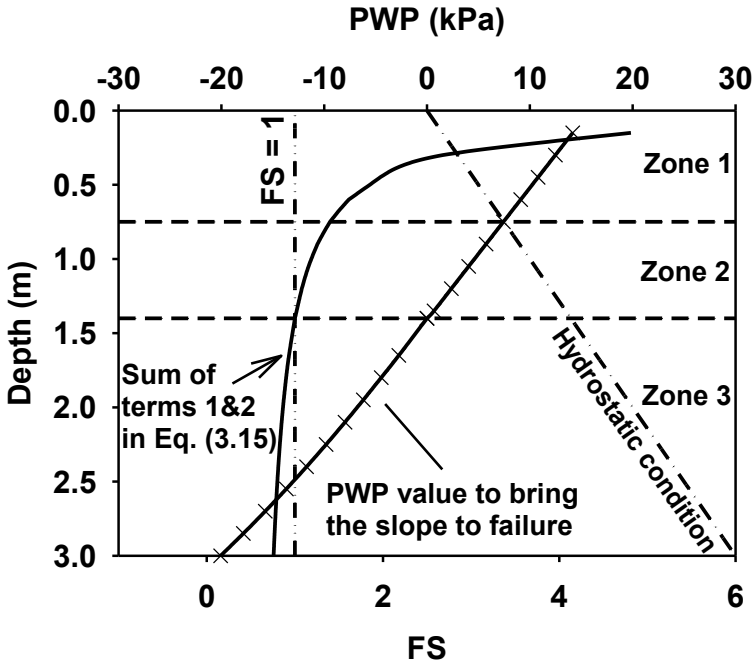

Fig. 3.20. Potential failure mechanism triggered by rainfall

According to the results of Li et al. (2013), the shallow failures can be possibly triggered by the propagation of wetting front, only when the slope angle is greater than the effective friction angle. Ali et al. (2014) showed that the time to failure decreases as the slope angle increases, which means a steeper slope will increase the possibilities of shallow failure. More precisely, the shallow failure will only occur when the summation of the first two terms in the right hand side of Eq. (3.15) is lower than unity. This is because the third term will never have a negative value during the propagation of wetting front. Fig. 3.20 shows the variation of the summation of the first two terms in the right hand side of Eq. (3.15) with depths, which is calculated using the soil properties and slope geometry characteristics. The value of PWP that brings the slope to failure (FS=1) at a particular depth are also determined using Eq. (3.15) and illustrated in Fig. 3.20. It can be seen that the propagation of wetting front can only trigger failures with a slip surface under the depth of 1.4

m (i.e. zone 3 in Fig. 3.20). Furthermore, in zone 3, the greater the depth, the higher will be the suction corresponding to failure conditions. In zone 2 (i.e. under 0.75 m and above 1.45 m depth), a positive PWP (i.e. rise of GWT) is required to cause failure. Theoretically, these conditions are only possible when it is underlain by an impermeable soil layer. However, these discussions are not provided in this paper as the focus is directed to understand the failure mechanism in the surficial layer only. Failures will never occur in zone 1 (above the 0.75m depth), because the required positive PWP for slope failure exceeds the hydrostatic conditions.

Based on the above discussions, failures can only occur within the zone 3 during the propagation of wetting front for the Regina clay considered in the present study. Furthermore, the deeper the slip surface locates, the more negative the PWP corresponding to failure is (see Fig. 3.20). Thus, the rate of wetting front propagation plays a critical role in controlling the stability of the surficial layer. The earlier the wetting front advances into zone 3, the shorter is the time required for the slope failure to occur. This further explains that coupling behaviour has an adverse effect on the slope stability due to faster wetting front propagation obtained from the coupled analysis. From the analysis present in this study, the uncoupled analysis typically overestimates the stability of surficial layer.

3.5.2 Influence of change of slope geometry due to swelling on the stability

The influence of geometry changes of expansive soils slopes on the FS also deserves critical discussion. Fig. 3.21 shows the predicted vertical displacements with time along the slope surface. The maximum vertical displacement is only 47.2 mm, which is 1.5% of the thickness of the surficial layer. This value is small in comparison to the difference in the wetting front depth between coupled and uncoupled analyses. Thus, it can be concluded that the changes in FS induced

by change of geometry is not significant when compared to the effect of different wetting depths on FS due to soil swelling.

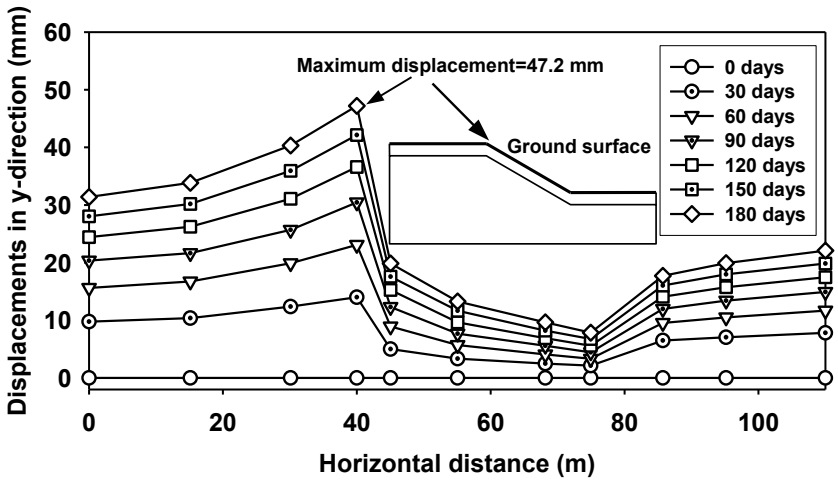

Fig. 3.21. Vertical displacement with time along the ground surface

3.5.3 Selection of appropriate hydraulic properties for modeling expansive soils

Since the expansive soil swells during an infiltration process, a volume change correction to the measured wetting SWCC appears to be important if the SWCC is represented in terms of degree of saturation or VWC (Fredlund and Houston 2013; Chao 2014; Bani Hashem 2013)). Since there is a limited data of wetting SWCC for cracked Regina clay, the bimodal SWCC used in the present study is a drying curve measured by Azam and Ito (2011) on a cracked Regina clay specimen which has undergone numerous drying and wetting cycles in the field. Thus an equilibrium condition is considered to have been attained, the hysteresis effect is considered to be alleviated to some extent for such a scenario. For the present study, based on the swell-shrinkage path (Fig. 3.22) measured on the same sample of Regina clay, a corrected SWCC is obtained and

shown in Fig. 3.23. The VWC along the uncorrected SWCC was calculated based on the measured gravimetric water content with reference to sample volume at the intersection point between the two SWCCs in Fig. 3.23, which also represents the field condition shown in Fig. 3.22. The corrected SWCC exhibits a similar bimodal trend to the uncorrected SWCC. When the corrected SWCC is input into the SEEP/W and SIGMA/W for comparison, the same conclusion can be drawn: the coupled analysis contributes to a faster wetting front depth with a lower critical FS. As an example, Fig. 3.24 and Fig. 3.25 illustrated the difference in the PWP and FS profile predicted after 90 days at L2 using corrected SWCC. Nevertheless, a measured wetting SWCC corrected regarding volume change is still recommended for practical use.

It should also be noted that the effect of volume change on hydraulic conductivities is not considered in the present study. The increase in void ratio during wetting (Fig. 3.22) increases the hydraulic conductivity of expansive soils. For such a scenario, wetting front depth advances at a faster rate in the coupled analysis. Furthermore, the effect of the stress condition on the hydraulic properties of cracked expansive soils might have an influence on the slope stability.

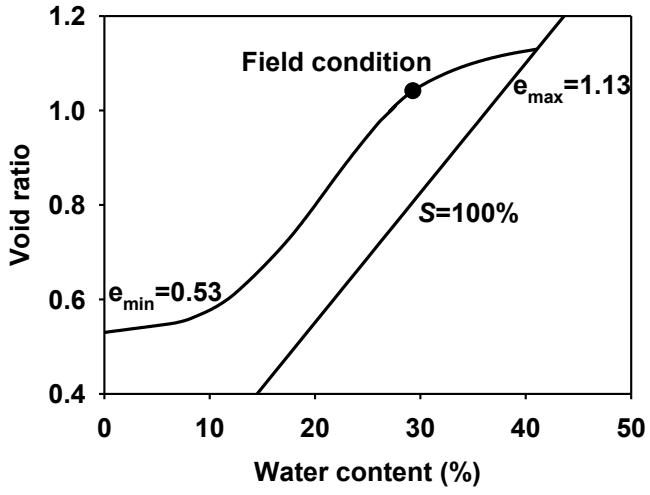

Fig. 3.22. The swell-shrink path of Regina clay (modified after Azam and Ito (2011))

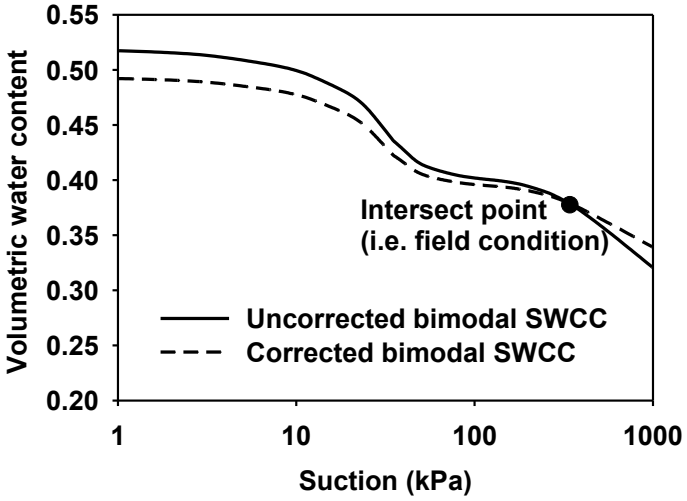

Fig. 3.23. The corrected and uncorrected SWCC for Regina clay

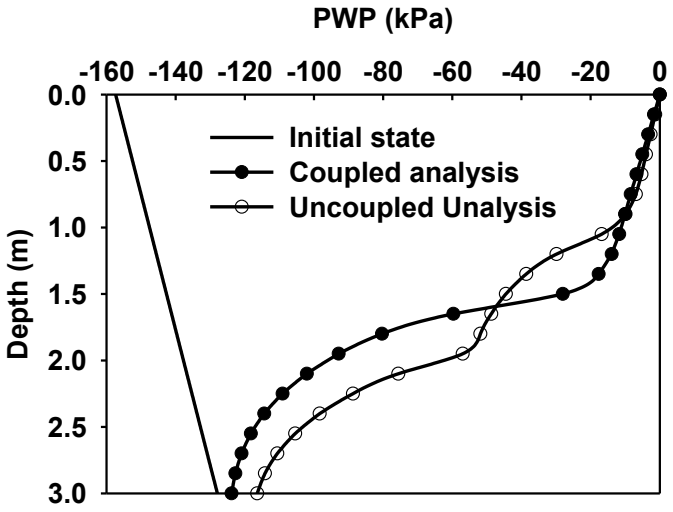

Fig. 3.24. PWP after 90 days at L2 using corrected SWCC

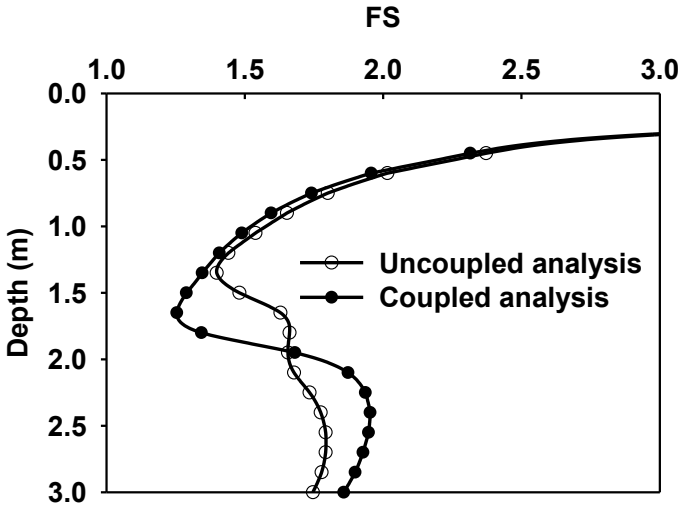

Fig. 3.25. FS after 90 days at L2 using corrected SWCC

3.6 Conclusions

The effect of coupled hydro-mechanical behaviour on slope stability for a typical expansive soil slope in Regina, Canada subjected to a prolonged rainfall (4.00×10^{-4} m/day for a period of six months) is numerically investigated using finite element analysis commercial software SIGMA/W, SEEP/W extending hydro-mechanical (coupled), and hydraulic (uncoupled) conditions. The nonlinear relationship between the modulus of elasticity parameters and suction is considered using the semi-empirical model in the coupled analysis. The numerically predicted variation of PWP and VWC within the surface layer during the considered time period is input into the infinite slope stability analysis formulation to calculate the FS profile evolution. This chapter is mainly focused on studying how the coupling behaviour influences the PWP and the FS values in the typical active zone depth.

The following conclusions can be drawn from the analysis of the results presented in this study:

(i) The shape of PWP profile from coupled analysis is different from that predicted from uncoupled analysis at the same elapsed time using both the corrected and uncorrected SWCC. The coupled analysis produces a reasonably well-defined wetting front than the uncoupled analysis. The advancement rate of wetting front in coupled analysis is faster in comparison to uncoupled analysis. In other words, suction loss occurs at a faster rate near the slope surface in coupled analysis.

(ii) The FS decreases with depth and is consistent with the PWP profile variation predicted from the numerical analysis. The critical FS appears to be at the same depth of wetting front. At the same elapsed time, the coupled analysis results in a lower critical FS at a greater depth than uncoupled analysis.

(iii) The values of critical FS at lower part of the slope at different time intervals is found to be lower than those at both middle slope and slope top, this is mainly because a lower initial suction profile presents at the slope toe. This may be one of the reasons why rain-induced expansive soil slope failures usually initiate at slope toe.

(iv) Based on the results presented in the chapter, coupling behaviour of soils has a negative effect on the stability of expansive slope as it contributes towards a faster wetting front depth that leads to an increase in the PWP.

Glossary

Symbols

σ_{ij}	Total stress tensor
b_i	Body force vector
q_x	Flow velocity in *x*- direction
q_y	Flow velocity in *y*- direction
q_z	Flow velocity in *z*-direction
t	Time
u_a	Pore air pressure
u_w	Pore water pressure
ε_{ij}	Strain tensor
σ_{mean}	Mean net stress
δ_{ij}	Kronecker delta
E	Elastic modulus for the soil structure with respect to a change in the net stress
H	Elastic modulus for the soil structure with respect to a change in suction
μ	Poisson's ratio
H_w	Parameter relating the volumetric water content to a change in PWP
k_i	Hydraulic conductivity in the *i* direction
γ_w	Density of water
y	Elevation
Z	Depth below the ground surface in infinite slope model
β	Inclination angle of the infinite slope
τ_f	Shear strength
τ	Mobilized stress on the slip surface
c'	Effective cohesion at saturated condition
ϕ'	Effective internal friction angle at saturated condition
θ_w	Volumetric water content
θ_s	Saturated volumetric water content
θ_r	Residual volumetric water content
γ	Unsaturated soil unit weight
l	Length along the sloping direction in the infinite slope model
W	Unit weight of the soil slice in the infinite slope model
N	Normal force acting on the slip surface in the infinite slope model
S	Shear force acting on the slip surface in the infinite slope model
P_a	Atmospheric pressure
E_{sat}	Value of E at saturated condition
E_{unsat}	Value of E at unsaturated condition

S_r	Degree of saturation
α, β	Fitting parameters in Vanapalli and Oh (2010) model

Abbreviations

VWC	Volumetric Water Content
AEV	Air Entry Value
PWP	Pore Water Pressure
FEA	Finite Element Analyses
GWT	Ground Water Table
SWCC	Soil Water Characteristic Curve
FS	Factor of safety

3.7 References

Adem HH, Vanapalli SK. A simple method for prediction of the modulus of elasticity of unsaturated expansive soils. In Proceedings of the 6th International Conference on Unsaturated Soils, Sydney, Australia, Unsaturated Soils: Research & Applications, Edited by N. Khalili, A. Russell, and A. Khoshghalb, CRC Press, 2014; 343-349.

Adem HH, Vanapalli SK. Constitutive modeling approach for estimating the 1-D heave with respect to time for expansive soils. International Journal of Geotechnical Engineering, 2013;7 (2): 199-204.

Adem HH, Vanapalli SK. Prediction of the modulus of elasticity of compacted unsaturated expansive soils. International Journal of Geotechnical Engineering, 2014;0(0): 1-13.

Ali J, Huang S, Lyamin AV, Sloan SW, Cassidy MJ. Boundary effects of rainfall-induced landslides. Computers and Geotechnics. 2014;61: 341-354.

Alonso EE, Gens A, Delahaye CH. Influence of rainfall on the deformation and stability of a slope in overconsolidated clays: a case study. Hydrogeology Journal 2003;11(1): 174–192.

Alonso EE, Vaunat J, Gens A. Modelling the mechanical behaviour of expansive clays. Engineering Geology, 1999; 54(12):173-183.

Azam S, Ito M. Unsaturated soil properties of a fissured expansive clay. Proceedings, 64th Canadian Geotechnical Conference, Toronto, Canada. 2011.313:1-5.

Bani Hashem E. Volume Change Consideration in Determining Appropriate Unsaturated Soil Properties for Geotechnical Applications. PhD Thesis. 2013. Arizona State University, USA.

Bao CG, Ng CWW. Keynote lecture: some thoughts and studies on the prediction of slope stability in expansive soils. Proc. 1st Asian Conf. on Unsaturated Soils, Singapore, 2000;15-31.

Biot MA. General theory of three-dimensional consolidation. Journal of Applied Physics, 1941;12(2): 155–164.

Borja RI, White JA, Liu XY, Wu W. Factor of safety in a partially saturated slope inferred from hydro-mechanical continuum modeling. International journal for numerical and analytical methods in geomechanics. 2012;36(10):23-248.

Cai F, Ugai K. Numerical analysis of rainfall effects on slope stability. International Journal of Geomechanics, 2004;4(2): 69-78.

Chao KC, Kang JB, Nelson JD. Challenges in Water Migration Modeling for Expansive Soils. Soil Behaviour and Geomechanics, GSP236 ASCE, 2014 204-213.

Chen RH, Chen HP, Chen KS, Zhung HB. Simulation of a slope failure induced by rainfall infiltration. Environmental Geology 2009;58(5): 943–952.

Cheng YH, Cheng ZL, Zhang YB. Centrifugal model tests on expansive soil slope under rainfall. Chinese Journal of Geotechnical Engineering, 2011;33(1):409-414. (in Chinese)

Cho SE, Lee SR. Evaluation of surficial stability for homogeneous slopes considering rainfall characteristics. Journal of Geotechnical and Geoenvironmental Engineering 2002;128, 756–763.

Cho SE, Lee SR. Instability of unsaturated soil slopes due to infiltration. Computers and Geotechnics, 2001;28(3): 185–208.

Collins BD, Znidarcic D. Stability analyses of rainfall induced landslides. Journal of Geotechnical and Geoenvironmental Engineering, ASCE, 2004;130(4): 362–372.

Duncan JM, Wright SG. 1995. Soil Strength and Slope Stability. Wiley, Hoboken, N J, USA.

Ehlers W, Graf T, Ammann M. Deformation and localization analysis of partially saturated soil. Computer methods in applied mechanics and engineering, 2004; 193(27): 2885-2910.

Foundation-repair-guide, http://www.foundation-repair-guide.com/expansive-soil.html.

Fredlund DG, Houston SL. Interpretation of soil water characteristic curves when volume change occurs as soil suction is changed. Proceedings, 1st Pan-American Conference on Unsaturated Soils, Cartagena de Indias, Colombia, 2013; vol. 1, pp. 15–31.

Fredlund DG, Morgenstern NR. Constitutive relations for volume change in unsaturated soils. Canadian Geotechnical Journal, 1976;13: 261–276.

Fredlund DG, Rahardjo H. 1993. Soil Mechanics for Unsaturated Soils. John Wiley & Sons, New York.

Fredlund DG, Rahardjo H. Fredlund MD. 2012. Unsaturated Soil Mechanics in Engineering Practice. John Wiley & Sons, New York.

Fredlund DG, Xing A. Equations for the soil-water characteristic curve. Canadian Geotechnical Journal, 1994;31(4): 521-532.

Fredlund MD, Fredlund DG, Wilson GW. An equation to represent grain-size distribution. Canadian Geotechnical Journal, 2000;37(4): 817-27. Gens A, Alonso EE. A framework for the behaviour of unsaturated expansive clays. Canadian Geotechnical Journal, 1992; 29(6):1013-1032.

GeoSlope International Ltd., 2007a. Seep/W User's Guide for Finite Element Seepage Analysis. GEO-SLOPE International Ltd, Calgary, Alta.

GeoSlope International Ltd., 2007b. Sigma/W User's Guide for Stress-Deformation Analysis. GEO-SLOPE International Ltd, Calgary, Alta.

Griffiths DV, Huang J, Dewolfe GF. Numerical and analytical observations on long and infinite slopes. International Journal for Numerical and Analytical Methods in Geomechanics, 2011;35(5): 569–585.

Ito M, Azam S. Engineering characteristics of a glacio-lacustrine clay deposit in a semi-arid climate. Bulletin of Engineering Geology and the Environment, 2009;68:551-557.

Iverson RM. Landslide triggering by rain infiltration. Water Resources Research, 2000;36(7): 1897-1910.

Jeldes IA, Drumm EC, Schwartz JS. Partial saturation and seismicity on steep reclaimed slopes. Geotechnical Geological Engineering, 2014;32:1065–1079.

Li JH, Zhang LM, Li X. Soil-water characteristic curve and hydraulic conductivity function for unsaturated cracked soil. Canadian Geotechnical Journal, 2011;48: 1010-1031.

Li WC, Lee LM, Cai H, Li HJ, Dai FC, Wang ML. Combined roles of saturated hydraulic conductivity and rainfall characteristics on surficial failure of homogeneous soil slope. Engineering Geology 2013;153: 105-113.

Li X, Li JH, Zhang LM. Predicting bimodal soil-water characteristic curves and hydraulic conductivity functions using physically based parameters. Computers and Geotechnics, 2014;57: 85-96.

Li X, Zhang LM. Characterization of dual-structure pore-size distribution of soil. Canadian Geotechnical Journal, 2009;46(2):129–41.

Lu N, Godt J. Infinite slope stability under steady unsaturated seepage conditions. Water Resources Research, 2008;44 (11):1-13.

Lumb P. 1962. Effect of rain storms on slope stability. In Symposium on Hong Kong Soils, Hong Kong, May 1962. Edited by P. Lumb. pp. 73–87.

McKeen R, Johnson L. Climate‐Controlled Soil Design Parameters for Mat Foundations. J. Geotech. Engrg., 1990; 116(7), 1073-1094.

Milledge, D. G., Griffiths, D. V., Lane, S. N., & Warburton, J. (2012). Limits on the validity of infinite length assumptions for modelling shallow landslides. Earth Surface Processes and Landforms, 37(11), 1158-1166.

Miguel MG, Bonder BH. Soil-water characteristic curves obtained for a colluvial and lateritic soil profile considering the macro and micro porosity. Geotechnical Geological Engineering, 2012;30:1405-20.

Muntohar AS, Liao HJ. Analysis of rainfall-induced infinite slope failure during typhoon using a hydrological geotechnical model. Environmental Geology, 2009;56(6): 1145-1159.

Ng CWW, Wang B, Tung YK. Three-dimensional numerical investigations of groundwater responses in an unsaturated slope subjected to various rainfall patterns. Canadian Geotechnical Journal 2001;38, 1049–1062.

Ng CWW, Zhan LT, Bao CG, Fredlund DG, Gong BW. Performance of an unsaturated expansive soil slope subjected to artificial rainfall infiltration. Geotechnique, 2003;53(2): 143-157.

Oh WT, Vanapalli SK, Puppala A. Semi-empirical model for the prediction of modulus of elasticity for unsaturated soils. Canadian Geotechnical Journal, 2009;46(8): 903-914.

Olivella, S., Gens, A., Carrera, J., & Alonso, E. E. Numerical formulation for a simulator (CODE BRIGHT) for the coupled analysis of saline media. Engineering computations, 1996;13(7): 87-112.

Rahardjo H, Lim TT, Chang MF, Fredlund DG. Shear strength characteristics of a residual soil. Canadian Geotechnical Journal, 1995;32(1): 60–77.

Rahardjo H, Ong TH, Rezaur RB, Leong EC. Factors controlling instability of homogeneous soil slopes under rainfall. Journal of Geotechnical and Geoenvironmental Engineering, 2007;133 (12), 1532–1543.

Sánchez, M., Gens, A., Guimarães, L., & Olivella, S. Implementation algorithm of a generalised plasticity model for swelling clays. Computers and Geotechnics, 2008;35(6): 860-871.

Santoso AM, Phoon KK, Quek ST. Effect of 1D infiltration assumption on stability of spatially variable slope. GeoRisk ASCE, 2011;704-711.

Satyanaga A, Rahardjo H, Leong EC, Wang JY. Water characteristic curve of soil with bimodal grain-size distribution. Computers and Geotechnics, 2013;48:51-61.

Sheng, D., Smith, D. W., W Sloan, S., & Gens, A. Finite element formulation and algorithms for unsaturated soils. Part II: Verification and application. International Journal for Numerical and Analytical Methods in Geomechanics, 2003;27(9): 767-790.

Shuai F. 1996. Simulation of Swelling Pressure Measurements on Expansive Soils. Ph.D. Thesis, University of Saskatchewan, Saskatoon, SK, Canada.

Skempton AW, Delory FA. 1957. Stability of natural slopes in London Clay. Proceedings of the 4th International Conference on Soil Mechanics and Foundation Engineering, vol. 2, pp. 378–381.

Sun W, Sun DA. Coupled modelling of hydro - mechanical behaviour of unsaturated compacted expansive soils. International Journal for Numerical and Analytical Methods in Geomechanics, 2012; 36(8): 1002-1022.

Taylor DW. 1948. Fundamentals of Soil Mechanics. John Wiley & Sons, Inc., New York, N. Y.

Vanapalli SK, Fredlund DG, Pufahl DE, Clifton AW. Model for the prediction of shear strength with respect to soil suction. Canadian Geotechnical Journal, 1996;33(3):379–392.

Vanapalli SK, Oh WT. A model for predicting the modulus of elasticity of unsaturated soils using the soil-water characteristic curve. International Journal of Geotechnical Engineering, 2010;4: 425-433.

Vu HQ, Fredlund DG. Challenges to modelling heave in expansive soils. Canadian Geotechnical Journal, 2006;43(12): 1249-1272.

Widger RA, Fredlund DG. Stability of swelling clay embankments. Canadian Geotechnical Journal, 1978;16: 140 -151.

Wong TT, Fredlund DG, Krahn J. A numerical study of coupled consolidation in unsaturated soils. Canadian Geotechnical Journal, 1998;35: 926–937.

Yoshida RT, Fredlund DG, Hamilton JJ. The prediction of total heave of a slab-on-grade floor on Regina clay. Canadian Geotechnical Journal, 1983; 20(1): 69-81.

Zhan TLT, Jia GW, Chen YM, Fredlund DG, Li H. An analytical solution for rainfall infiltration into an unsaturated infinite slope and its application to slope stability analysis, Int. J. Numer. Anal. Meth. Geomech. 2013;37:1737–1760.

Zhang LL, Fredlund DG, Zhang LM, Tang WH. Numerical study of soil conditions under which matric suction can be maintained. Canadian Geotechnical Journal, 2004;41: 569–582.

Zhang LL, Zhang J, Zhang LM, Tang WH. Stability analysis of rainfall-induced slope failure: a review. Geotechnical Engineering, 2010;164(GE5): 299–316.

Zhang LL, Zhang LM, Tang WH. Rainfall-induced slope failure considering variability of soil properties. Geotechnique, 2005;55(2): 183–188.

Zhang LM, Fredlund DG. Characteristics of water retention curves for an unsaturated fractured rock mass. In Proceedings of the Second Asian Conference on Unsaturated Soils, Osaka, Japan, 9–13 November 2003. Edited by D. Karrube, A. Iizuka, S. Kato, and K. Kawai. 2003;pp. 425–429.

Chapter 4 Effect of Swelling on the Stability of Slopes in Expansive Soils[2]

This chapter focuses on effect of the mechanical response (induced by swelling, including stress regime change and possible softening) on the slope stability of expansive soil. To isolate the effect (coupling effect (induced by swelling)) studied in chapter 3, a novel program is developed in this chapter for numerical analysis. The unsaturated soil elasto-plastic constitutive relationship is utilized for interpretation of stress regime evolution induced by expansive soil swelling during infiltration. The extended Mohr-Coulomb criterion for unsaturated soils is used as the failure surface, under which the nonlinear elastic behaviour is considered by quantifying the effect of two stress state variables (net stress and suction) on elasticity parameters. The strain softening behaviour in unsaturated soils is accounted for via reducing the material parameters of the yield surface with respect to plastic deviatoric strain. A numerical exercise is performed on a relatively gentle slope in Regina, Canada with highly expansive soil properties, using the developed computer program that implements the constitutive model into the infinite slope formulation. The results suggest that neglecting the swelling-induced stress change and associated softening behaviour can significantly overestimate the stability of expansive soil shallow layer under infiltration, in terms of both failure occurrence and failure time. Additional parametric study shows that all the considered parameters (including initial stress condition, softening rate and slope

[2] A version of this chapter has been published as Qi and Vanapalli (2016) in *Computers and Geotechnic*s. DOI: 10.1016/j.compgeo.2016.02.018

angle) have a considerable effect on the failure time and failure depth of the shallow deposit, which have important implications for the engineering design of expansive soil slopes.

4.1 Introduction

Infiltration (rainfall, ground snow melting or other types) induced shallow failures of expansive (swelling) soil slopes are frequently reported in many countries around the world, including Canada (e.g. Widger and Fredlund 1979), China (e.g. Bao et al. 2000; Hou et al. 2013; Zhan et al. 2014; Xu et al. 2014), Spain (e.g. Alonso et al. 2003; Azañón et al. 2010), and United States (e.g. Day 1994). The wetting-induced slope failure in expansive soil advances in a progressive pattern. Progressive failure of slopes was observed a long time ago (e.g. Terzaghi and Peck 1948), and were usually interpreted using strain softening behaviour of soils (e.g. Skempton 1964; Bjerrum 1967). Many investigators have used numerical techniques, such as the Finite Element Method (Griffiths and Li 1993; Lechman and Griffiths, 2000; Griffiths et al. 2006; Potts et al. 1990, 1997; Chen et al. 1992; Troncone 2005; Chai and Carter 2009) and the Material Point Method (Zabala and Alonso 2011; Bandara and Soga 2015), to reproduce and(or) quantify the progressive failures, based on strain softening Mohr-Coulomb elasto-plastic model (Chen et al. 1992; Potts et al. 1990, 1997; Zabala and Alonso 2011; Bandara and Soga 2015), elasto-viscoplastic model (Troncone, 2005) or pragmatic Modified Cam Clay model (Chai and Carter 2009).

Most of the previous numerical analyses were mainly conducted within the framework of saturated soil mechanics. The surficial layer of expansive soil slopes addressed in the present study occurs in a state of unsaturated condition, and are likely to fail before attaining fully saturated condition. There is significant evidence of the strain softening behaviour of unsaturated soil

specimens in the literature from laboratory test results (e.g. Hoyos et al. 2014; Miao et al. 2002; Zhan and Ng 2006; Zhan et al. 2014; Gui and Wu 2014). Hoyos et al. (2014) suggested that the residual shear strength contribution due to suction may be described using models similar to that postulated for peak shear strength of unsaturated soils (e.g. Fredlund et al. 1978; Vanapalli et al. 1996). The experimental results of triaxial tests conducted by Miao et al. (2002) on expansive soils at several constant suction values showed that the deviator stress gradually decreased with increasing axial strain after reaching peak values. Similar trends of results were also observed from the direct shear tests carried out by Zhan and Ng (2006) on expansive soils. In order to simulate stress path within the slope soil subjected to rainfall infiltration, a different loading sequence (i.e. in the so-called shearing infiltration test: reducing the suction after shearing by increasing the net deviator stress to a prescribed level) was applied to unsaturated expansive soil specimens by Zhan et al. (2014) and Gui and Wu (2014) in a series of triaxial tests. The results from both the shearing infiltration tests also indicated a softening behaviour as those observed in constant-suction shear tests (e.g. Miao et al. 2002).

The significant swelling of expansive soils upon wetting would be another important factor contributing to infiltration-induced shallow slope failures. This is because the swelling deformation can induce a constant and substantial change in the net stress regime of slope, especially within the surficial layer where the suction in soil element is reduced by water infiltration. The swelling-induced stress exerting on a soil element has the same effect as the external net stress. When the amount of non-uniform stress (in-situ stress plus the swelling-induced stress) state reaches the strength of soil element, local failure starts to occur at that particular point within the slope profile. Expansive soil exhibits swelling potential in any direction, however, the amount of swelling-induced pressure in one direction might be different from another, depending

on the deformation allowed in the corresponding direction. The vertical swelling pressure can be high and result in severe distress on lightly loaded buildings constructed on expansive soil ground. Vanapalli and Lu (2012) provided a comprehensive summary of these research studies. However, for the shallow layer of expansive soil, the swelling induced stress can be essentially released in the direction perpendicular to the sloping surface since soil is allowed to swell freely. While, a large amount of stress along the sloping direction will be formed due to constraints exerted on the soil deformation. Many previous laboratory measurements on expansive soils suggested that the lateral swelling stress can be several times higher than the vertical stress (e.g. 2 times from Fourie (1989), up to 10 times from Windal and Shahrour (2002), up to 3 times from Boyd and Sivakumar (2011)) under laterally confined condition. In-situ records also showed that the horizontal earth pressures due to soil expansion can be much higher than the vertical stress (e.g. 1.3-5.0 times from Richards and Kurzeme (1973) and 2-4 times from Brackley and Sanders (1992)). For sloping ground, the maximum ratio of stress parallel to the sloping direction to the total vertical stress was observed to be 3 by Ng et al. (2003) in an expansive slope in Zaoyang, China during an artificial rainfall period. Under such condition, the passive failures within an unsaturated soil element are likely to occur (Fredlund and Rahardjo 1993) and initiate the failure of expansive soil slopes.

There is a strong link between the above two phenomena (i.e. swelling-induced stress and softening behaviour) observed from experimental results. These phenomena can likely contribute to the shallow sliding in in-situ expansive soils. The effect of these phenomena on stability has not been explicitly considered or well discussed in the most existing numerical seepage analyses and coupled hydro-mechanics analyses (e.g. Qi and Vanapalli, 2015) extending the principles of unsaturated soils. The main objective of the present study is to investigate the evolution of stress

regime, softening behaviour, and their effect on expansive soil slope stability upon infiltration in the framework of infinite slope formulation.

The infinite slope formulation has been extensively used in assessing slope stability of shallow layer in the past (e.g. Duncan et al. 2014). One of the main advantages of this infinite slope model is that it provides a numerically cheap and rapid estimation of the factor of safety. The basic assumption of this simplified model is that the sliding mass extends infinitely in the sliding direction (i.e. generally in a downslope direction), which is considered rational for shallow landslides. Milledge et al. (2012) tested this assumption by comparing the results from infinite slope formulation against those obtained on 5000 synthetic two dimensional slopes using the finite element strength reduction approach presented by Griffiths and Lane (1999). This study provided quantitatively the errors that the infinite slope formulation may induce, as well as the critical length/depth ratio above which the errors are acceptable (within 5%) for different slope scenarios. In addition to calculation of FS, the infinite slope formulation has also been used to analyze stress and strain (displacement) evolution before slope collapse or interpret the shear mechanism responsible for the shallow slides (e.g. Teunissen and Spierenburg 1996; Urciuoli 2002; Urciuoli et al. 2007; Di Prisco and Pisanò 2011). More recently, this simplified model has been combined with probabilistic analysis to estimate failure probability of the shallow soil layer under both saturated (e.g. Griffiths et al. 2011) and unsaturated (e.g. Ali et al. 2014; Cho 2014) conditions. It is interesting to note that both the deterministic (Griffiths et al. 2011; Ali et al. 2014) and probabilistic Griffiths et al. (2011) analyses revealed that the failure surface does not necessarily occur at the base of shallow layer in either saturated or unsaturated conditions as opposite to the assumption adopted in conventional infinite slope stability analysis.

In this chapter, the infinite unsaturated expansive soil slope is addressed through a general elasto-plastic constitutive relationship based on two stress state variables for unsaturated soils. There are some sophisticated constitutive models proposed in the literature, which can describe the double-structure (e.g. Alonso et al. (2003) and coupled hydro-mechanical (e.g. Sun and Sun 2012) characteristics of expansive soil, but require a number of parameters to be defined for proper application. In this chapter, in order to maintain the simplicity as of the nature of infinite slope formulation, the Mohr-Coulomb plasticity model that only needs some common soil parameters is adopted. Specifically, the extended Mohr-Coulomb failure criterion is used as the yielding surface, under which the nonlinear variation of elasticity parameters with respect to both net stress and suction is considered. The possible evolution of stress regime within the infinite slope profile upon infiltration is critically discussed. The numerical exercise conducted on an illustrative example using the developed computer program also illustrates that the critical slip surface may not necessarily be at the base of shallow layer (e.g. Griffiths et al. 2011). The results from the parametric analyses highlight some engineering practice implications.

4.2 Elasto-plastic constitutive matrix for unsaturated soils

For saturated soils, the yield function in stress space, which separates purely elastic from elasto-plastic behaviour, can be expressed as

$$F\left(\{\sigma\},\{k\}\right)=0 \tag{4.1}$$

where $\{\sigma\}$ represents the stress state in stress space, $\{k\}$ are the state parameters. The state parameters define the size of yielding surface, which can be related to hardening (softening)

parameters (e.g. plastic strain or plastic work) to describe the hardening and softening behaviour of material.

For unsaturated soils, Fredlund et al. (1977) suggested using two independent stress state variables to describe the mechanical behaviour and establish the constitutive relationships. The best combination of stress state variables for geotechnical applications is net stress and suction, which, respectively, refer to total stress in excess of pore air pressure, (σ - u_a), and pore air pressure in excess of pore water pressure (u_a - u_w), where σ is the total stress, u_w and u_a are pore water pressure and pore air pressure, respectively. The net stress and suction should be treated separately to describe the stress state of unsaturated soils in the yield function. For most geotechnical problems, u_a can be assumed to remain constant (usually atmospheric), the net stress is equivalent to the total stress, and suction, s, is equivalent to negative pore water pressure. Thus, the general simplified form of yield function for unsaturated soils, defined in terms of net stress, suction, and state parameters, can be expressed as

$$F\left(\{\sigma\}, s, \{k\}\right) = 0 \tag{4.2}$$

Correspondingly, the plastic potential function for unsaturated soils, which is used to specify the plastic straining direction in the flow rule, is of the form

$$G\left(\{\sigma\}, s, \{g\}\right) = 0 \tag{4.3}$$

where $\{g\}$ is a vector of the state parameters.

The total incremental strains $\{d\varepsilon\}$ for unsaturated soil, based on the concept of two stress state variables, include two components: (i) the strains induced by net stress change, and (ii) the

strains induced by suction change. Considering the elasto-plastic behaviour, the total incremental strains can be further split into four parts:

$$\{d\varepsilon\} = \{d\varepsilon^e\} + \{d\varepsilon^p\} + \{d\varepsilon_s^e\} + \{d\varepsilon_s^p\} \tag{4.4}$$

where $\{d\varepsilon^e\}$ and $\{d\varepsilon^p\}$ are the elastic and plastic incremental strains due to changes in net stress, and $\{d\varepsilon_s^e\}$ and $\{d\varepsilon_s^p\}$ denote the incremental elastic and plastic strains due to changes in suction, respectively.

The change in net stress is considered to be only caused by corresponding incremental elastic strain $\{d\varepsilon^e\}$, as a result, the incremental net stress, $\{d\sigma\}$, can be calculated as

$$\{d\sigma\} = [D]\{d\varepsilon^e\} \tag{4.5}$$

where $[D]$ is the elastic constitutive matrix.

Similarly, the incremental elastic strain in response to suction change, $\{d\varepsilon_s^e\}$, can be calculated as

$$\{d\varepsilon_s^e\} = H^{-1}\{m\}ds \tag{4.6}$$

where H is the elastic modulus (a scalar) defined by Fredlund and Rahardjo (1993) for the soil structure with respect to incremental suction change, $\{m\}$ is the vector $\{1, 1, 1, 0, 0, 0\}^T$.

The incremental plastic strains are computed, via the flow rule, from the plastic potential function, as:

$$\{d\varepsilon^p\} = \Lambda\left\{\frac{\partial G}{\partial \sigma}\right\} \tag{4.7}$$

where Λ is the scalar plastic multiplier.

The plastic strain induced by change in suction, $\{d\varepsilon_s^p\}$, is assumed to be equal to zero. The plastic strain still develops during wetting, since that the suction decrease influences yield surface through net stress tensor (i.e. yield surface is suction-dependent). Substituting Eq. (4.4) into Eq. (4.5) yields:

$$\{d\sigma\} = [D](\{d\varepsilon\} - \{d\varepsilon^p\} - \{d\varepsilon_s^e\}) \tag{4.8}$$

Substituting Eqs. (4.6) and (4.7) into Eq. (4.8) gives:

$$\{d\sigma\} = [D](\{d\varepsilon\} - \Lambda\left\{\frac{\partial G}{\partial \sigma}\right\} - H^{-1}\{m\}ds) \tag{4.9}$$

The consistency equation for unsaturated soil is written as:

$$dF = \left\{\frac{\partial F}{\partial \sigma}\right\}^{\mathrm{T}}\{d\sigma\} + \frac{\partial F}{\partial s}ds + \left\{\frac{\partial F}{\partial k}\right\}^{\mathrm{T}}\{dk\} = 0 \tag{4.10}$$

Combining Eq. (4.9) and Eq. (4.10) gives:

$$\begin{aligned} &-\left\{\frac{\partial F}{\partial \sigma}\right\}^{\mathrm{T}}[D]\{d\varepsilon\} + \left\{\frac{\partial F}{\partial \sigma}\right\}^{\mathrm{T}}[D]\Lambda\left\{\frac{\partial G}{\partial \sigma}\right\} + \left\{\frac{\partial F}{\partial \sigma}\right\}^{\mathrm{T}}[D]H^{-1}\{m\}ds \\ &= \frac{\partial F}{\partial s}ds + \left\{\frac{\partial F}{\partial k}\right\}^{\mathrm{T}}\{dk\} \end{aligned} \tag{4.11}$$

Solving for Λ using Eq. (4.11) gives:

$$\Lambda = \frac{\left\{\frac{\partial F}{\partial \sigma}\right\}^{\mathrm{T}}[D]\{d\varepsilon\} + \left(\frac{\partial F}{\partial s} - \left\{\frac{\partial F}{\partial \sigma}\right\}^{\mathrm{T}}[D]H^{-1}\{m\}\right)ds}{\left\{\frac{\partial F}{\partial \sigma}\right\}^{\mathrm{T}}[D]\left\{\frac{\partial G}{\partial \sigma}\right\} + A} \tag{4.12}$$

where

$$A = -\frac{1}{\Lambda}\left\{\frac{\partial F}{\partial k}\right\}^{\mathrm{T}}\{dk\} \tag{4.13}$$

Substituting Eq. (4.12) into Eq. (4.9) gives:

$$\{d\sigma\} = [D^{p\varepsilon}]\{d\varepsilon\} + \{D^{ps}\}ds \tag{4.14}$$

where

$$[D^{p\varepsilon}] = \left([D] - \frac{[D]\left\{\frac{\partial G}{\partial \sigma}\right\}\left\{\frac{\partial F}{\partial \sigma}\right\}^{\mathrm{T}}[D]}{\left\{\frac{\partial F}{\partial \sigma}\right\}^{\mathrm{T}}[D]\left\{\frac{\partial G}{\partial \sigma}\right\} + A}\right) \tag{4.15}$$

$$\{D^{ps}\} = -[D^{p\varepsilon}]H^{-1}\{m\} - \{W^{ps}\} \tag{4.16}$$

$$\{W^{ps}\} = \frac{[D]\left\{\frac{\partial G}{\partial \sigma}\right\}\frac{\partial F}{\partial s}}{\left\{\frac{\partial F}{\partial \sigma}\right\}^{\mathrm{T}}[D]\left\{\frac{\partial G}{\partial \sigma}\right\} + A} \tag{4.17}$$

Eq. (4.14) describes the general increment elasto-plastic stress-strain relationship for unsaturated soils. There is an additional term associated with suction on the right hand side of Eq (4.14), compared to that of saturated soils. Eq. (4.14), mathematically, treats the suction as an additional strain component instead of its physical meaning, i.e. stress variable. This approach has the advantage of being incorporated into conventional displacement finite-element method, as suggested by Sheng et al. (2003) and Sánchez et al. (2008). In the present analysis, Eq. (4.14) will be used to track the change in stress-strain field within an infinite expansive soil slope after onset of yielding upon infiltration (i.e. decreasing suction).

4.3 Infinite slope formulation for expansive soils

4.3.1 Stress field within an infinite slope profile

Infiltration-induced slope failures in unsaturated expansive soils usually have shallow slip surfaces, as suggested in the introduction part of this chapter. For this reason, the infinite slope model is considered to be a practical model for analyzing the stability of the unsaturated expansive soil slope under infiltration condition. The problem in this study is idealized in Fig. 4.1, where η and ξ are the axes rotated by a slope angle, β, from the x and y axes in Cartesian coordinate system, respectively. When using two stress state variables theory, the stresses acting on a soil element include two independent parts: net stress, $\sigma = (\sigma - u_a)$, and suction, $s = (u_a - u_w)$.

The net normal stress, σ_ξ, and shear stress, $\tau_{\xi\eta}$, at a certain depth can be determined by applying the static force equilibrium condition in the vertical direction for a unit width soil slice:

$$\sigma_\xi = \gamma Z \cos^2 \beta \tag{4.18}$$

$$\tau_{\xi\eta} = \gamma Z \cos\beta \sin\beta \tag{4.19}$$

where γ stands for the unit weight of the soil, Z for the element depth under the ground surface measured along the y axis. The net normal stress, σ_η, in the η direction can be related to net normal stress, σ_ξ, by equation below:

$$\sigma_\eta = \mathrm{K}\sigma_\xi = \mathrm{K}\gamma Z \cos^2 \beta \tag{4.20}$$

where K is the stress ratio of the net normal stresses σ_η to σ_ξ. Similar relation between these two net normal stresses was adopted in Teunissen and Spierenburg (1996) and Urciuoli (2002)

for sloping ground. The stress ratio, K, is similar to the coefficient of earth pressure at rest, but it is with respect to the parallel and normal axes of the slope (see Fig. 4.1). The stress ratio, K, could also be calculated as $K = \mu/(1-\mu)$, where μ is the Poisson ratio, based on elastic theory. However, quantifying K value more accurately should take stress history of deposit of interest and other actual ground information into consideration. Lytton (2004) reported that the coefficient of earth pressure at rest in expansive soils can vary from 0 to 3 for different ground conditions from drying to wetting conditions. The initial stress field in the infinite slope model can be formulated using Eqs. (4.18)- (4.20) with an initial stress ratio, K_0, as detailed later.

The variation of suction, *s*, over time at any depth under infiltration condition can be obtained by either analytical (e.g. Srivastava and Yeh 1991; Iverson 2000, Wu and Zhang 2009; Wu et al. 2012), or numerical (e.g. SEEP/W software (Geo-Slope International Ltd. 2012) Hydrus-1D software (Šimůnek et al. 2013) solutions to a seepage model. It is worth mentioning that some analytical (e.g. Zhan et al. 2013) and numerical (e.g. Ali et al. 2014) solutions specifically for infinite slope case can be found in the literature.

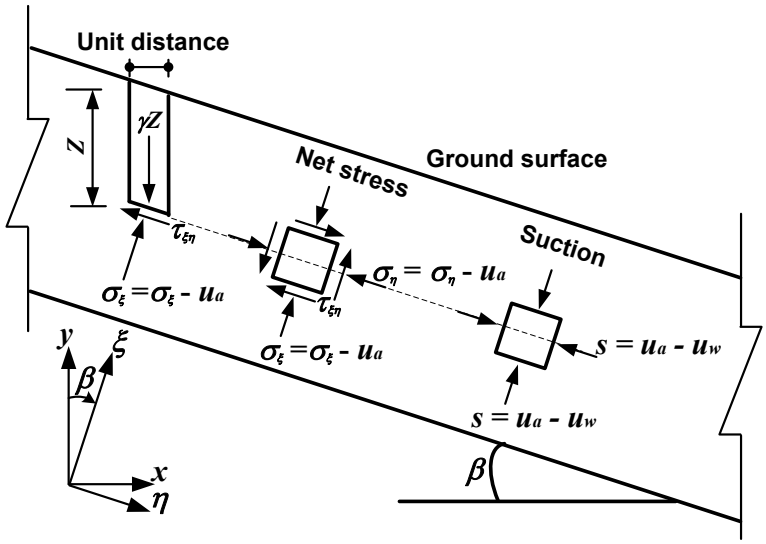

Fig. 4.1. Geometrical scheme of the infinite slope.

4.3.2 Yield function for infinite slope formulation

The well-known Mohr-Coulomb elastic perfectly plastic model is often used to describe the failure behaviour of saturated soils in interpreting the sliding mechanism of infinite slope (Urciuoli 2002; Urciuoli et al. 2007; Di Prisco and Pisanò 2011). For saturated soils, the Mohr-Coulomb yield function is expressed in terms of major and minor effective principal stresses as:

$$F\left(\{\sigma'\},\{k\}\right)=\sigma_1'-\sigma_3'-2c'\cos\phi'-\left(\sigma_1'+\sigma_3'\right)\sin\phi' \tag{4.21}$$

where σ_1' and σ_3' are major and minor principal effective stress acting on a soil element, respectively; c' and ϕ' are the effective cohesion and effective angle of internal friction, which constitute the state parameters of vector $\{k\}$.

The classic Mohr-Coulomb failure criterion was extended into unsaturated soils in Fredlund *et al.* (1978) using the concept of two stress state variables, in which the rate of increase in shear strength relative to suction is quantified using a constant parameter, ϕ^b. Although, the nonlinear variation of shear strength with respect to suction is reported in the literature (e.g. Escario and Saez 1986; Fredlund et al. 1987; Vanapalli et al. 1996), the extended Mohr-Coulomb shear strength envelope Fredlund et al. (1978) is still able to provide reasonable estimation of unsaturated shear strength for slope stability analysis in most cases using limit equilibrium analysis (Zhang et al. 2014). Most recently, this linear strength model has also been used as the yield function in elasto-plastic analysis by Sołowski et al. (2014), who simulated the shear bands developed in the unsaturated triaxial shear test specimen using Material Point Method. In the present study, the extended Mohr-Coulomb shear strength envelope (Fredlund et al. 1978) is utilized as failure

criterion for unsaturated expansive soils, and is expressed, in terms of suction, major and minor principal net stresses, as:

$$F\left(\{\sigma\},s,\{k\}\right)=\left(\sigma_1-\sigma_3\right)-2(c'+s\tan\phi^b)\cos\phi'-\left(\sigma_1+\sigma_3\right)\sin\phi' \tag{4.22}$$

where ϕ^b is the friction angle relative to suction. As can be seen, the net stress and suction constitute of the complete stress state in the function, and the vector of state parameters of unsaturated soil includes three components, namely, effective cohesion, effective angle of internal friction and friction angle relative to suction. When considering the stress condition within the infinite slope (Fig. 4.1), Eq. (4.22) can be rewritten as:

$$\begin{aligned}&F\left(\{\sigma\},s,\{k\}\right)\\&\quad=2\sqrt{0.25(\sigma_\eta-\sigma_\xi)^2+\tau_{\xi\eta}{}^2}-2\cos\phi'[c'+s\tan\phi^b]-(\sigma_\eta+\sigma_\xi)\sin\phi'\end{aligned} \tag{4.23}$$

The potential plastic function is assumed to have a similar form to the yield surface, but with the effective internal friction angle, ϕ', replaced by dilatancy angle, φ.

$$\begin{aligned}&G\left(\{\sigma\},s,\{g\}\right)\\&\quad=2\sqrt{0.25(\sigma_\eta-\sigma_\xi)^2+\tau_{\xi\eta}{}^2}-2\cos\varphi[c'+s\tan\phi^b]-(\sigma_\eta+\sigma_\xi)\sin\varphi\end{aligned} \tag{4.24}$$

4.3.3 Analyses of infiltration-induced stress evolution in the infinite slope formulation

As was suggested before, expansive soils exhibit significant swelling behaviour upon wetting. Therefore, the infiltrated water from the ground surface will not only decrease the suction, but lead to a considerable redistribution of the net stress field within the slope profile.

For the infinite slope case, the soil element in Fig. 4.1 will have a swelling trend in all directions with a decreasing suction. In the η direction, the normal strain induced by swelling is restrained due to the unlimited extension of the slope, so that the net normal stress σ_η will be increased such that there is no normal strain in this direction during a wetting process. This condition is similar to that of constant volume test conducted for measuring the swelling pressure of expansive soil (Shuai and Fredlund 1998).

In the ξ direction, the soil close to the ground surface can swell freely; however, at a deeper depth, it can only swell partially because of the influence of the overburden pressure. This scenario is similar to that of loaded-swell oedometer test for measuring the swelling pressure of expansive soil (Shuai and Fredlund 1998). Certain magnitude of normal strain in this direction can be induced by soil swelling. During the wetting process, the whole infinite slope layer within the depth of Z is always under a static force equilibrium condition even though soil swelling occurs within it. This argument can be extended for using Eqs. (4.18) and (4.19) for determining the net normal stress, σ_ξ, and shear stress, $\tau_{\xi\eta}$. This implies that these two stresses will keep constant if the effect of increase in soil unit weight during the wetting process is ignored. In addition, this also suggests that the induced swelling pressure in the ξ direction can be released by the swelling straining allowed.

However, the soil is not able to sustain unlimited increase in the net normal stress in the η direction with decreasing suction, since yielding and subsequent strain softening are likely to occur once a certain amount of irreversible plastic strain is accumulated. The evolution of stresses acting on a soil element within the infinite slope during wetting process can be generally divided into

three phases as shown in Fig. 4.2, and is interpreted as follows using extended Mohr-Coulomb elasto-plastic model.

FIRST PHASE (pure elastic phase): A relatively high initial suction (s_1) is assumed to be present within the infinite slope profile prior to the commencement of any types (e.g. rainfall or snow melting) of wetting process. The initial two stress components (σ_ξ, $\tau_{\xi\eta}$) are calculated from Eq. (4.18) and (4.19), and the other stress σ_η, can be determined using Eq. (4.20) by assuming a reasonable initial value of K_0. The initial stress Mohr's circle in the three-dimensional stress space can be plotted as shown in Fig. 4.2(a) in accordance to the known stress state (σ_ξ, σ_η, $\tau_{\xi\eta}$, s_1), which is far below the extended Mohr-Coulomb yield envelope.

When the soil element is wetting, the location of Mohr's circle is moving towards the frontal plane (i.e. plane $s = 0$) with decreasing suction, s. In the meantime, the size of the Mohr's circle increases due to increasing net normal stress, σ_η, although the two other stress components (σ_ξ, $\tau_{\xi\eta}$) are maintained constant as suggested in the preceding paragraphs. Further, the intersection line between the extended Mohr-Coulomb yield envelope and the vertical plane s = corresponding suction, gradually lowers with reference to the σ_n vs s plane (i.e. horizontal plane $\tau = 0$), as the apparent cohesion, $c_a = c' + s\ tan\phi^b$, is decreasing with decreasing suction. As a consequence, the stress Mohr's circle is gradually approaching and eventually tangential to the Mohr Coulomb yield envelope at suction $s = s_2$.

During this phase, the stress Mohr's circle is always under the extended Mohr-Coulomb yield envelope, the soil element behaves purely elastically, in other words, all strains occurring during FIRST PHASE are reversible. The stress strain relationship can be obtained by combining Eq, (4.6) and Eq. (4.8), as:

$$\{d\sigma\} = [D](\{d\varepsilon\} - \{d\varepsilon_s^e\}) = [D](\{d\varepsilon\} - H^{-1}\{m\}ds) \tag{4.25}$$

where the elastic constitutive matrix, $[D]$, associated with change in net stress can be determined using Young's modulus, E, and Poisson's ratio, μ.

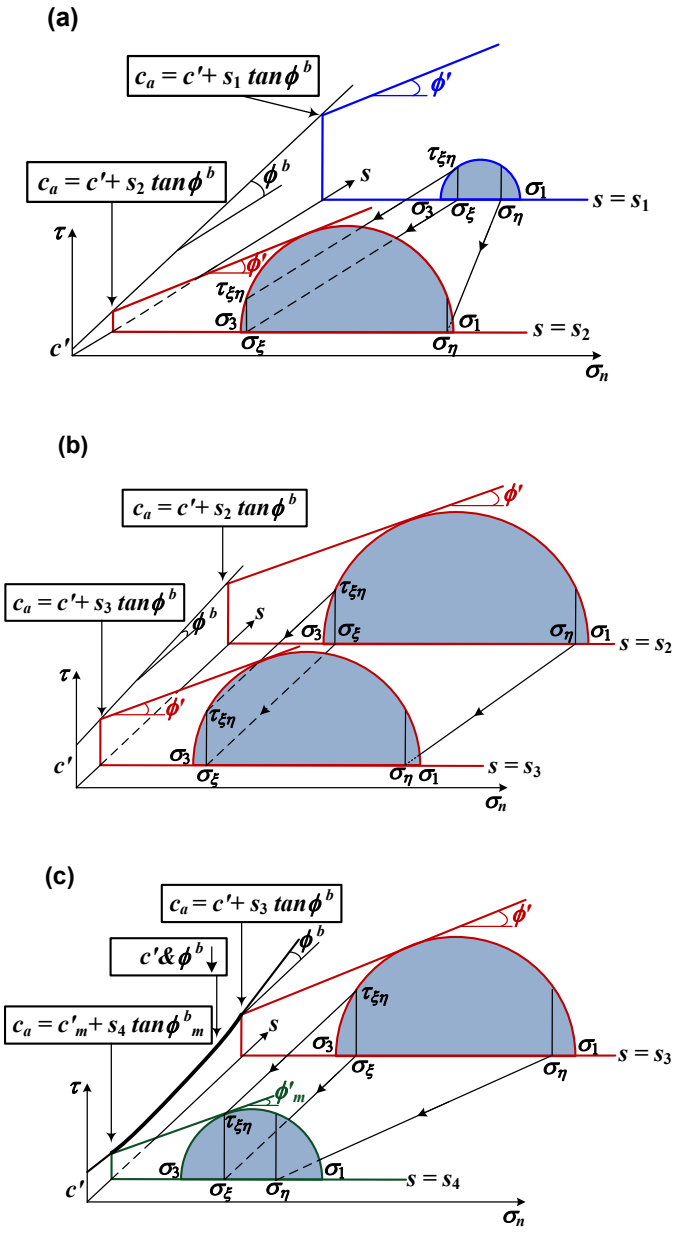

Fig. 4.2. Evolution of stress state within the infinite slope upon wetting: (a) FIRST PHASE; (b) SECOND PHASE; (c) THIRD PHASE.

SECOND PHASE (perfectly plastic phase): The soil element is assumed to behave perfectly plastically after yielding at suction $s = s_2$ until a certain amount of plastic strain is accumulated (Fig. 4.2(b)). For perfectly plastic material, any type of loading can only lead to a stress state moving within (along) rather than out of the yield surface; while, the plastic strain occurs and keeps increasing indefinitely in an element (e.g. Griffiths and lane 1999). For the infinite slope case, only when a collapse condition (slope failure) is developed, can the plastic strains within some soil elements increase indefinitely. Otherwise, the strains are restricted because it is not kinematically admissible. Failure condition will be discussed in greater detail in later sections.

As the suction within the unsaturated expansive soil element continues decreasing from s_2 during wetting, first, the location of Mohr's circle will move further towards the frontal plane (plane $s = 0$); second, the size of the Mohr's circle will reduce to keep tangential to the yield surface. This behaviour is somewhat different with those of saturated soil, for which the size of the Mohr's circle may not change for perfectly plastic behaviour. The ostensible discrepancy is due to the inclusion of suction, s, in the yield function for unsaturated soils (see Eq. (4.2), (4.22), and (4.24)). Suction decrease leads to lowering position of the intersection line between the extended Mohr-Coulomb yield envelope and the vertical plane s = corresponding suction, which will force the Mohr-circle to become smaller. As a result, the net normal stress, σ_η, will gradually reduce. The other two stress components (σ_ξ, $\tau_{\xi\eta}$), however, are unchanged as before. The position of three dimensional Mohr-Coulomb yield envelope is also unchanged, similar to the two dimensional Mohr-Coulomb yield envelope for perfectly plastic behaviour of saturated soil. In the SECOND PHASE, plastic straining (irreversible deformation) develops in the soil element, thus stress-strain

relationship needs to be described using the elasto-plastic constitutive matrix (i.e. Eq. (4.14)) given in section 4.2.

THIRD PHASE (strain softening phase): strain softening occurs within the soil elements once the plastic strain is beyond a certain amount at $s = s_3$. The change of Mohr's circle during the wetting process is generally same as that during the SECOND PHASE: (i) Further movement of the Mohr's circle towards the frontal plane; (ii) Further reduction in the Mohr's circle size; (iii) Further decrease in the net normal stress, σ_η. The important difference is that the state parameters ($\{k\}=\{c', \phi', \phi^p\}$) defining the position of yield surface will decrease with the development of plastic strain, which leads to a gradual shrinkage of the yield surface in the stress space (see Fig. 4.2(c)). Specifically, the angle of the intersection line between the extended Mohr-Coulomb yield envelope and the vertical plane s = corresponding suction will become gentler (i.e. decrease in ϕ'), its position will be significantly lowered by decrease not only in s but also in c', ϕ^p. Moreover, the intersection line between the extended Mohr-Coulomb yield envelope and τ versus s plane will be curved, as its angle (ϕ^p) with respect to s axes is gradually becoming gentler as well. It is obvious that the Mohr-Circle size will shrink faster when strain softening is taking place. However, the Mohr-Circle will be always tangential to the extended Mohr-Coulomb yield envelope.

In the THIRD PHASE, the elasto-plastic constitutive matrix (i.e. Eq. (4.14)) should be used as in the SECOND PHASE. A softening rule quantifying how the size of yielding surface reduces is also required. For saturated soils, a practical softening model was suggested and used to investigate the progressive failure (e.g. Griffiths 1981) and the delayed collapse of London clay slope (Potts et al. 1997). This softening model assumes that the state parameters (i.e. c', ϕ' and φ for saturated soils, φ is the dilatancy angle) reduce from peak to residual value in a linear manner

with accumulation of deviatoric plastic strain. This model was recently implemented into the Material Point Method (MPM) to analyze coupled soil deformation and pore fluid flow behaviour by Bandara and Soga (2015).

In the present study, this model has been extended for unsaturated soils as shown in Fig. 4.3, in which ϕ^b is assumed to vary in the same manner with respect to accumulated deviatoric plastic strain as those of c', ϕ' and φ. The deviatoric plastic strain is calculated as:

$$d\varepsilon_{d,p} = \frac{2}{\sqrt{3}}\sqrt{d\varepsilon_{\xi}^{\ 2} + 3d\gamma_{\xi\eta}^{2}} \tag{4.26}$$

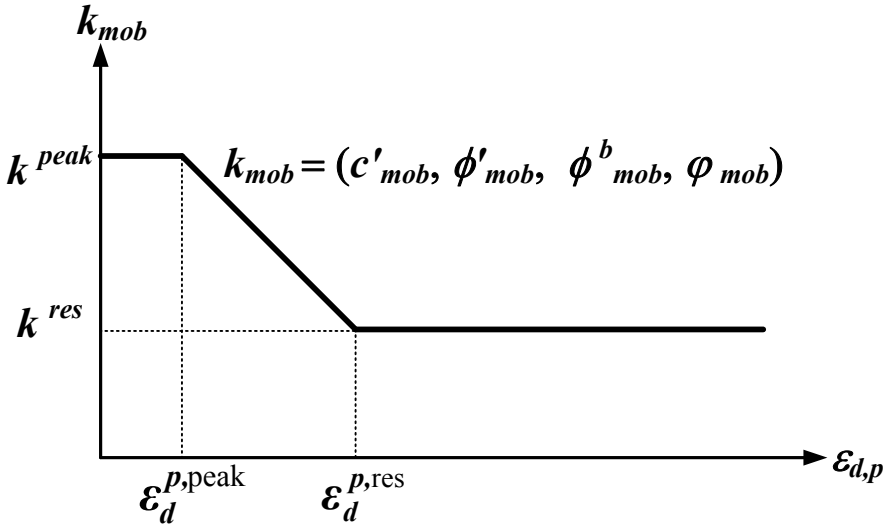

Fig. 4.3. Variation of mobilised material parameters with plastic deviatoric shear strain.

In Fig. 4.3, $\boldsymbol{k}^{peak}$ and $\boldsymbol{k}^{res}$ represent the peak and residual values of state parameters. $\varepsilon_d^{p,\text{peak}}$ represents the deviatoric plastic strain at which softening starts, and $\varepsilon_d^{p,\text{res}}$ represents the deviatoric plastic strain when softening is completed.

It should be noted that some constitutive models are available in the literature (Alonso et al. 1999 Sun and Sun 2012; Wang and Wei 2014) for interpreting expansive soil behaviour, which include components to quantify the plastic volumetric strain accumulated during cyclic suction changes at relatively low net stress level, from either double-level structure or macroscopic and phenomenological perspective. However, a softening law concerning this plastic strain has not been explicitly included yet into these existing models. This plastic volumetric strain accumulates gradually with wetting and drying cycles (Wang and Wei 2014), and has an influence on the mobilized shear strength. This influence is not considered in the adopted softening law, which assumes that the strength parameters varies with deviatoric plastic strain. This first approximation is made considering that current analysis involves mainly a monotonic decrease in suction. Incorporating the effect of plastic volumetric strain is a worthy effort in the future, particular for cases that involves a number of suction cycles leading to a certain amount of accumulated plastic volumetric strain.

4.3.4 Collapse of expansive soil infinite slope

Fig. 4.2 illustrates the possible three PHASEs of stress path followed within a soil element under the ground surface before the collapse (failure) of the infinite slope. When the stress Mohr's circle at a particular depth is tangential to the extended Mohr-Coulomb yield envelope at the point (σ_ξ, $\tau_{\xi\eta}$, s_4) as shown in Fig. 4.2(c), the infinite slope is about to collapse or fail along the straight line at that depth. This can be interpreted by recalling the traditional Factor of Safety (*FS*). The traditional FS for infinite slope case is defined as:

$$FS = \frac{c' + \sigma_\xi \tan\phi' + s \tan\phi^b}{\tau_{\xi\eta}} \tag{4.27}$$

For the condition when suction $s=s_4$ in Fig. 4.2(c), $\tau_{\xi\eta}= c'_m+\sigma_\xi \tan \phi'_m+s_4 \tan \phi^b_m$, which leads to a $FS = 1$. $FS = 1$ corresponds to a limiting condition for equilibrium. Any infinitesimal decrease in suction can result in an indefinite plastic straining along the straight line at this depth that forms the slip surface, since it is kinematically admissible now.

4.3.5 Evaluation of infinite slope stability in expansive soil

From the interpretation discussed earlier, a complete stability analysis, for an infinite expansive soil slope during wetting, requires solutions to Eq. (4.25) and Eq. (4.14), given suction (unloading) increments and an initial stress condition (including the initial suction and net stress components) within the infinite slope profile. Eq. (4.25) is used for stress state under the yield surface where soil element behaves purely elastically (FIRST PHASE), while Eq. (4.14) is adopted when the stress state is on the yield surface which involves elasto-plastic behaviour (SECOND and THIRD PHASEs). For unsaturated soils, the elastic constitutive matrix, [D], elastic parameter, H, and elasto-plastic matrices, [$D^{p\varepsilon}$] and [D^{ps}], are all not constants, but highly dependent of both net stress and suction (Fredlund and Rahardjo 1993; Oh and Vanapalli 2009). Thus, a stress integration algorithm based on two stress variables is required to obtain a solution to the highly nonlinear problem, as those based on single stress variable used in conventional Finite Element Method. Recently, several explicit stress integration schemes have been developed in the literature, such as the modified Euler algorithm Sheng et al. (2003), Sanchez et al. (2008) and Solowski and Gallipoli (2010) and Runge-Kutta algorithms Solowski and Gallipoli (2010) for different unsaturated soil constitutive models. In the present study, the modified Euler's scheme with error control is coded using FORTRAN language to perform stress integration over the strain and suction increment, which can be regarded as the extension of that described in Potts and Zdravkovic (1999) for

saturated soil elasto-plastic model. It is worth repeating that the stress integration scheme needs to be performed both for elastic and elasto-plastic phases. For the purpose of completeness, Eq. (4.27) is also coded in this program to calculate the variation of FS with time during wetting until failure (FS = 1), and then investigate the effect of swelling-induced strain softening on the stability of an expansive infinite slope.

4.4 Description of the illustrative example

The city of Regina is situated on a glacial deposit basin consisting of over-consolidated expansive clays, which is commonly referred to as Regina clay in the literature. Infiltration (from snow melting or rainfall)-induced shallow failures in cuts and fills constructed of Regina clay are widely reported (e.g. Chowdhury 2013). The basic soil properties of Regina clay have been investigated by several researchers (e.g. Shuai 1996, Ito and Azam 2010). The numerical analysis using the developed code is performed with reference to slopes using Regina clay soil properties.

The infinite slope analyzed in this study is assumed to have a thickness of 3 m, based on a comprehensive investigation presented in Aubeny and Lytton (2004), which suggested that the depths of shallow slip surfaces in several dozen of compacted high plasticity clay slopes ranged from 0.6 m to 3.0 m. Prior to the stress evolution analysis within the infinite slope profile, the suction profile variation with time upon wetting is required as the input parameters. This is obtained by conducting a finite element saturated and unsaturated seepage analysis on a one dimensional soil column using SEEP/W (Geo-Slope International Ltd. 2012.). The soil water characteristic curve (SWCC) used in the seepage analysis is shown in Fig. 4.4, the test data was measured by Shuai (1996) on a Regina clay along the wetting path under K_0 condition with an initial suction of 575 kPa, which is similar to the condition considered in the present study. Some

researchers suggested that the volume change has a significant influence on the measured SWCC expressed in terms of volumetric water content or degree of saturation for expansive soils (e.g. Chao et al. 2014), which, in turn, affects the hydraulic response in seepage analysis (Hashem, 2014). Thus, caution is exerted in selecting the measured data with a volume change correction. It is also interesting to note the relative steeper portion along the SWCC at low suction values, which is due to the wetting path followed and probably swelling allowed in the measurement. The van Genuchten SWCC equation van Genuchten (1980) is used to best fit the measured data and get a continuous relation between the water content and suction. The parameters used to fit the SWCC are summarized in Table 4.1. Two sets of data for permeability function were provided in Shuai (1996) on compacted Regina clay sample, one was for free swell and the other for constant volume test conditions. Since the soil element swelling is partially constrained within the infinite slope profile, thus an average permeability function between those two curves provided in Shuai (1996) is used to account for the effect of wetting induced swelling (void ratio increase) on permeability. One should note that both the SWCC and permeability function are affected by the net stress applied on the specimen, which can be considered through using three-dimensional water content and permeability surfaces as suggested in Vu and Fredlund (2006) in a fully coupled analysis. Every point within the infinite slope has a different stress state from other points at the same elapsed time, this is not explicitly accounted for by the average hydraulic properties in the uncoupled (seepage followed by mechanical analysis) analysis in the present study, which focuses on the effect of the swelling behaviour on the shallow layer stability only. It should also be noted that the coefficient of permeability measured on the laboratory clay specimen was quite low, which is not representative of the actual value of weathered in-situ surficial layer. Thus, in numerical analyses, the coefficients of permeability increased by 2-3 orders of magnitude in comparison to

the measured value from laboratory tests were usually used to obtain a better match between predictions and measurements in the literature (e.g. Alonso et al 2003; Rouainia et al 2009; Qi and Vanapalli 2015). In the present study, the saturated coefficient of permeability is increased to 5×10^{-7} m/s (see Table 4.1), while keeping the shape of the permeability function the same as that provided in Shuai (1996). Fig. 4.5 illustrates the permeability functions in the seepage analysis. The lower boundary for the one dimensional seepage analysis is assumed to be partially drained. The partially drained boundary condition is built using the technique suggested by Ali et al. (2014): i.e. another thickness of 3m soil layer with a lower coefficient of permeability is constructed beneath the upper 3m thickness layer of interest. This can be regarded to better represent the actual ground condition, because the soil at deeper depth is usually less weathered and has a lower coefficient of permeability. The permeability function used for the lower soil layer is also shown in Fig. 4.5, which is 2 orders of magnitude lower than that of the upper soil layer for the whole suction range. An infiltration with an intensity of $0.8k_s$) is applied on the upper boundary of soil profile for 7 days to simulate a wetting process. The initial suction value for the whole slope profile is set to be 450 kPa, which is commonly encountered in arid and semi-arid regions.

Table 4.1. Hydraulic parameters of Regina clay used in the present study

Parameters	**Symbol**	**Units**	**Value**
Saturated volumetric water content	θ_s	%	50.1
Residual volumetric water content	θ_r	%	10
* Fitting parameter	a	kPa^{-1}	1
* Fitting parameter	n		1.062
Saturated degree of saturation	S_s	%	95.4
Residual degree of saturation	S_r	%	30
† Fitting parameter	a	kPa^{-1}	1
† Fitting parameter	n		1.059
Saturated permeability	k_s	m/s	5×10^{-7}

Note: * van Genuchten fitting parameters for SWCC in terms of volumetric water content; † in terms of degree of saturation.

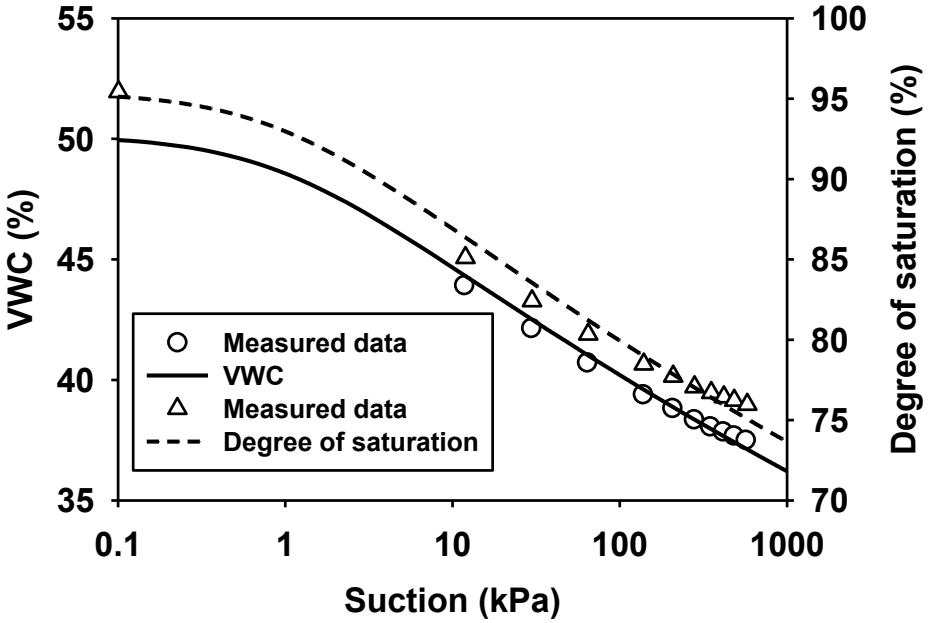

Fig. 4.4. The SWCC used in the seepage analysis.

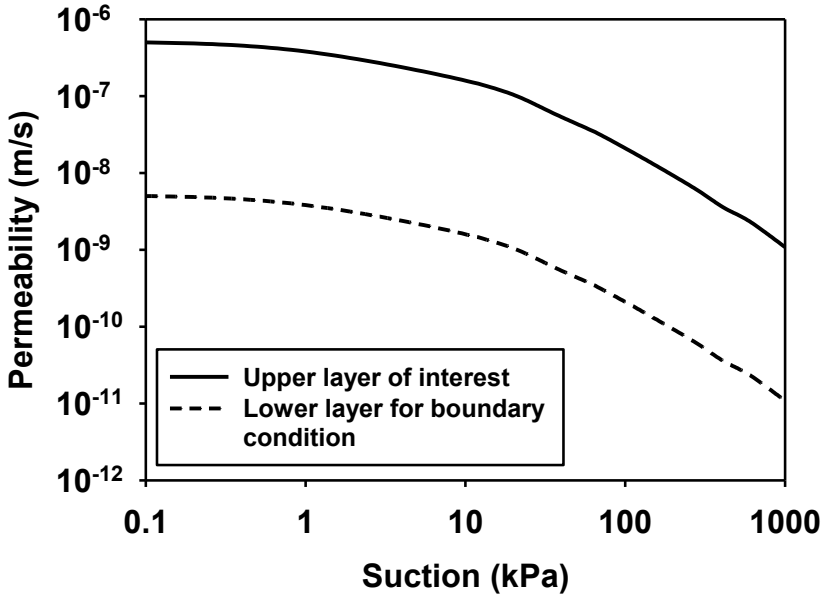

Fig. 4.5. The permeability functions used in the seepage analysis.

The suction profile variation obtained from the seepage analysis is then input into the developed code for stress evolution analysis and slope stability analysis. The soil mechanical property parameters required for the stress and stability analysis are summarized in Table 4.2. We first conducted a base analysis, followed by a parametric study to show the effect of several varying parameters (see Table 4.2), including slope angle, plastic deviatorical strain at residual state, and initial stress ratio. In the base analysis, the infinite slope is assumed to be relatively gentle with a slope angle, $\beta = 18°$, and have an initial stress ratio, $K = 1.5$. One set of strength data (i.e. the peak and residual shear strength parameters with corresponding strain values) measured by Widger and Fredlund (1979) using direct shear tests on the saturated samples from a failed embankment in Regina is selected to define the yielding surface. The angle indicating the rate of increase in shear strength relative to matric suction, ϕ^b, is assumed to equal 2/3 of effective internal friction angle, ϕ', at both peak and residual conditions. The soil unit weight was reported by Widger and Fredlund (1979) to be 18.04 kN/m³. Some early works used simplified assumptions for elasticity parameters, E and H; however, nonlinearity of the elasticity parameters with both net stress and suction has been recently implied for unsaturated soil modeling (e.g. Oh et al. 2009; Vu and Fredlund 2006; Sheng et al. 2008; Rahardjo 2011). Some explicit equations expressing the E as a function of two stress state variables have also been developed, such as: (*i*) the power function by Rahardjo (2011), and (*ii*) the semi-empirical model using SWCC as tool (63). An alternative and effective way to determine the two elasticity parameters (E and H) is to differentiate the void ratio constitutive surface function by assuming a value of Poisson's ratio, μ, as follows:

$$E = 3(1-2\mu)(1+e_0)/\frac{de}{d\sigma} \tag{4.28}$$

$$H = 3(1+e_0)/\frac{de}{ds} \tag{4.29}$$

where e_0 and e is the initial void ratio and the void ratio, respectively. Mathematical equations are usually used to describe the variation in void ratio, e, with respect to changes in two stress variables. Vu and Fredlund (2006) proposed a function to fit the void ratio data measured by Shuai (1996) for numerical modelling of swelling of Regina clay. The nonlinear moduli E and H generated by Vu and Fredlund (2006) are used in the present study. Consistency with the hydraulic properties discussed above is assured since the data used are from the same source Shuai (1996). The nonlinear elasticity parameters used for Regina clay is graphically illustrated in Fig. 4.6(a,b). The parametric analysis is performed in such a fashion: for each case, only the parameter under consideration is allowed to vary, all other parameters were kept as those used for the "base case".

Table 4.2. Regina clay mechanical properties used in the present study

Parameters	**Symbol**	**Units**	**Value**	
Slope angle	β	deg.	18	†(14, 16, 18, 20, 22)
Initial stress ratio	K_0		1.5	†(0.5, 1.0, 1.5, 2.0, 2.5)
Soil unit weight	γ	kN/m³	18.04	
Peak effective cohesion	c'^{peak}	kPa	0	
Residual effective cohesion	c'^{res}	kPa	0	
Peak effective frictional angle	ϕ'^{peak}	deg.	20	
Residual effective frictional angle	ϕ'^{res}	deg.	13	
Peak angle with suction	$\phi^{b\ \text{peak}}$	deg.	13.33	
Peak angle with suction	$\phi^{b\ \text{res}}$	deg.	8.67	
Plastic deviatorical strain at peak	$\varepsilon_d^{p,\text{peak}}$	%	3.2	
Plastic deviatorical strain at residual	$\varepsilon_d^{p,\text{res}}$	%	12	† (6, 9, 12, 18, 24, 32)
Elasticity modulus with stress	E	kPa	Eq. (4.28)	
Elasticity modulus with suction	H	kPa	Eq. (4.29)	
Poisson's ratio	μ		0.4	

Note: † value of parameters for parametric analysis;

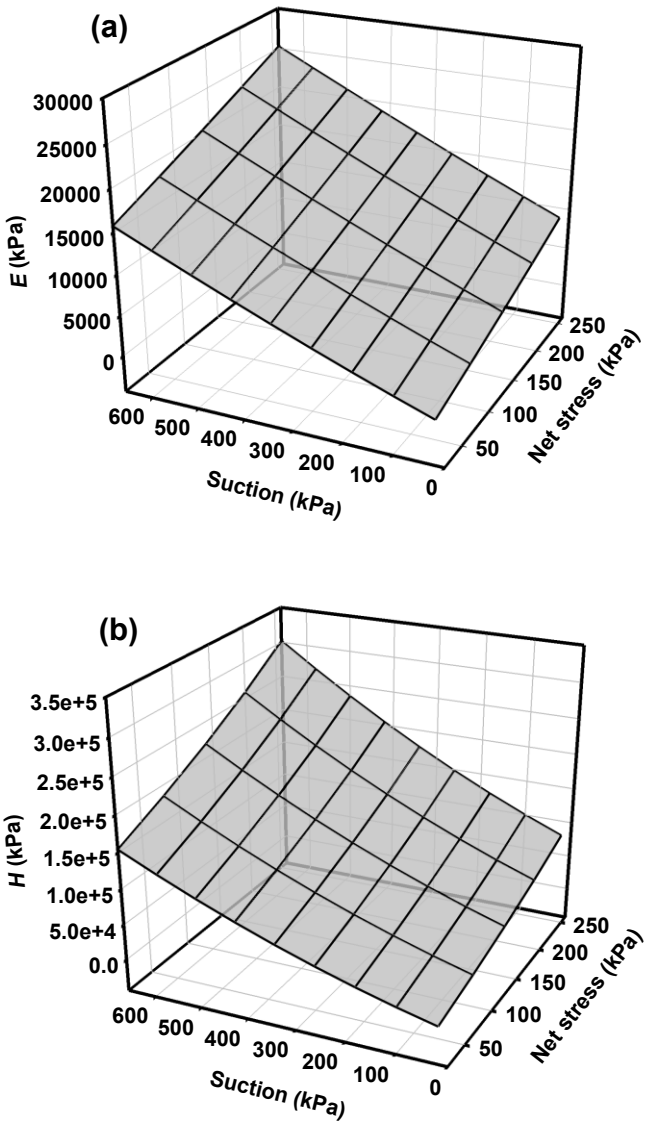

Fig. 4.6. The nonlinear elasticity parameters: (a) variation of E with respect to two stress state variables; (b) variation of H with respect to two stress state variables (after Vu and Fredlund (2006).

4.5 Numerical results

This section is organized as follows. The results between softening and non-softening analyses are compared in terms of the evolution of stress, σ_ξ, and Factor of Safety, *FS,* within the slope profile. The non-softening analysis herein means the expansive soils are assumed to be an

elastic perfectly plastic material, and there are no reductions in the material parameters (c', ϕ', ϕ^b and φ) with increasing deviatoric plastic strain. Then, the stress evolution with time at the failure depth from the base case analysis is detailed, followed by the results of parametric analysis.

4.5.1 Comparison between softening and non-softening analyses

Fig. 4.7 illustrates the variation of pore water pressure profile within the infinite slope from the saturated-unsaturated seepage analysis. The suction unloading that were converted from Fig. 4.7 are used for all the following analyses.

The variation of FS profile from non-softening and softening analyses are shown in Fig. 4.8 and Fig. 4.9, respectively. The initial FS at the shallower depth (for example, above the depth of 1 m) are significantly higher than those at deeper location, which is because the driving shear stresses mobilized at these positions due to the overburden pressure are quite low. The FS values reduce with decreasing suctions for both non-softening and softening analyses. For the softening analysis, the FS at depth of 0.9 m first decreased to 1 at the end of 6.16 days (147.8 hrs) (see Fig. 4.9), while, the FSs within the entire slope profile at the end of 7th day are still greater than 1 when softening is not considered (see Fig. 4.8). In other words, no failure is observed in the non-softening analysis for the suction unloading scenario considered in the present study. This can be explained using the alternative FS expression given below:

$$FS = \frac{c'}{\gamma Z \cos^2 \beta} + \frac{\tan \phi'}{\tan \beta} + \frac{s \tan \phi^b}{\gamma Z \cos^2 \beta} \tag{4.30}$$

Eq. (4.30) is obtained by substituting the Eqs. (4.18) and (4.19) into Eq. (4.27). The three terms on the right hand side of Eq. (4.30) represent the shear strength contribution due to effective cohesion, effective angle of internal friction and suction for unsaturated conditions, respectively. The first

term on the right hand side of Eq. (4.30) vanishes for this case, as $c' = 0$ kPa in the present study. The third term is always positive as long as $s > 0$ kPa (see Fig. 4.7). Therefore, the value of FS can be equal to or less than 1, only if the value of second term is less than 1. For non-softening analysis, the peak value of ϕ' selected in the present study is always greater than the slope angle, β (see Table 4.2). This leads to the second term being always larger than 1. In other words, failure ($FS \leq 1$) will never occur provided the slope is in a state of unsaturated condition. For softening analysis, the internal friction angle, ϕ', may be reduced to a value lower than the slope angle, leading to the second term to a value less than 1. For this scenario, the possibilities of failure ($FS \leq 1$) emerge even for unsaturated condition, as indicated in the results for the present case illustrated in Fig. 4.9. Therefore, it can be concluded that the methods neglecting softening behaviour may result in an unsafe design for the unsaturated expansive soil slopes.

Fig. 4.10 compares the evolutions of stress profile, σ_η, at several elapsed times from non-softening and softening analyses. It can be seen that, the stress, σ_η, at the whole profile first increase, and then decrease after reaching its maximum value for both non-softening and softening analyses. Change in the stress, σ_η, first occurs at shallow depth and gradually extends towards deeper depth over time. Correspondingly, the maximum value of σ_η also propagates from shallower to deeper depths over time. These changes in the stress, σ_η, are consistent with the variation of pore water pressure profile shown in Fig. 4.7. After first day, there is no difference in the stress profile, σ_η, between non-softening and softening analyses. At the end of 2 days, the stress, σ_η, from softening analysis is observed to be smaller than that from non-softening analysis at shallow depth (within the depth of around 0.5m in Fig. 4.10). This difference between non-softening and softening analyses becomes more evident, and gradually develops towards greater

depths over time. At the end of 6 days, the stress, σ_η, from softening analysis is smaller than that from non-softening analysis for the entire slope profile. Owing to the complex nature of spatial and temporal stress variation, the following sections provide details on the change of stress regime at the failure depth over time, tracing the three phases (pure elastic, perfectly plastic and softening) that the soil element undergoes until failure.

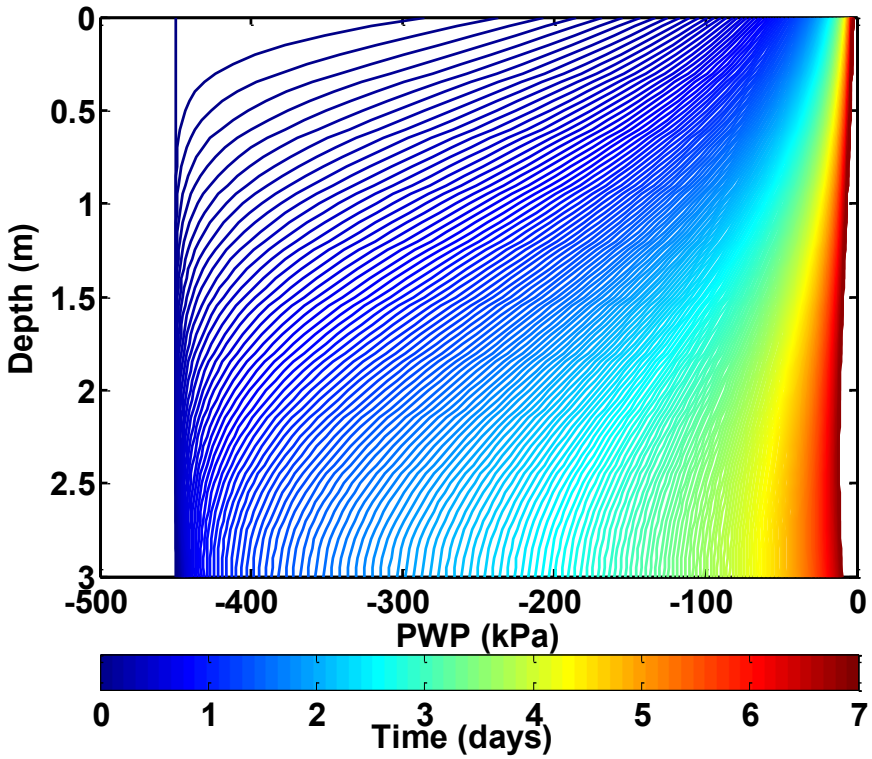

Fig. 4.7. The variation of pore water pressure profile within the infinite slope from seepage analysis.

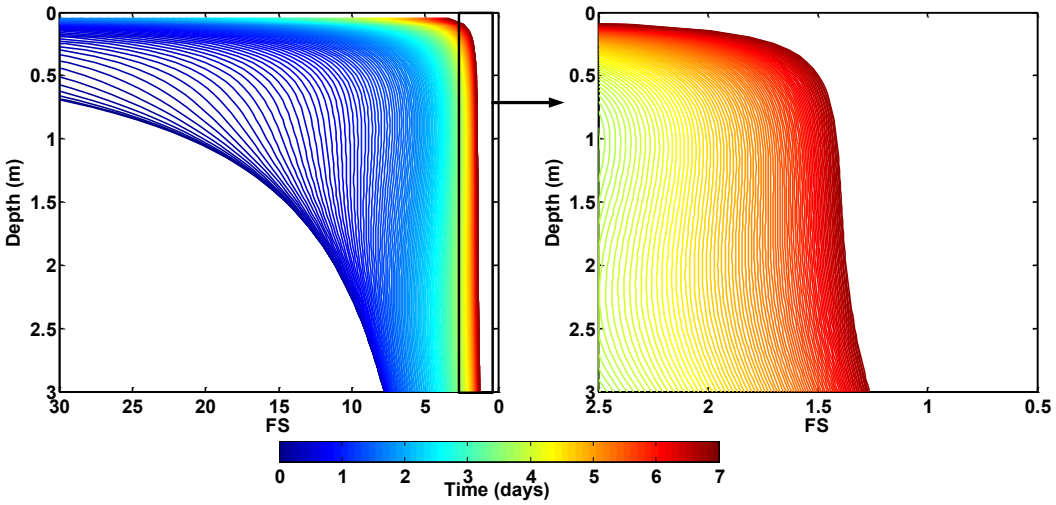

Fig. 4.8. Variation of FS profile from non-softening analysis.

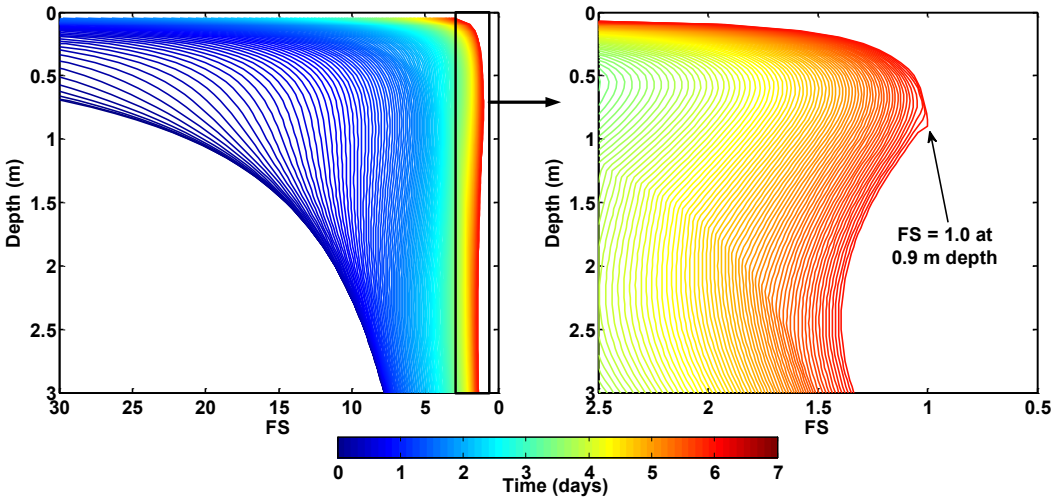

Fig. 4.9. Variation of FS profile from softening analyses.

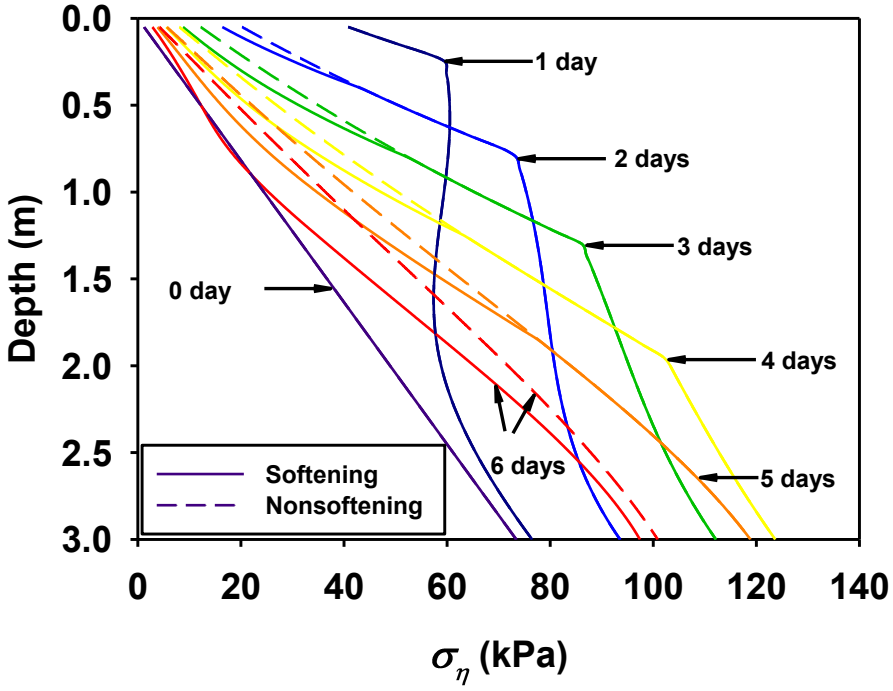

Fig. 4.10. Evolution of stress profile, σ_η, at several elapsed times from non-softening and softening analyses

4.5.2 Evolution of stress at the failure depth

The evolution of suction and net stress in the sloping direction, σ_η, at the failure depth with time (i.e. 0.9 m identified in the previous section) are shown in Fig. 4.11 and Fig. 4.12. Also, illustrated along with these are the timely evolution of two other parameters, namely, angle of internal friction and FS (see Fig. 4.13 and Fig. 4.14). In addition, the corresponding parameters at the depths of 2.0 m and 3.0 m are included in these figures, for comparison.

It can be seen from Fig. 4.11 and Fig. 4.12 that, there is a significant initial increase in the value of net stress, σ_η, at depth of 0.9 m, when suction is decreasing with time. The net stress

reaches its maximum value when soil yields at 2.24 days, which is more than 3 times its initial value. After yielding, the net stress decreases with further decease in suction until failure at 6.16 days. In the meantime, plastic straining develops within the soil at this depth. Once the accumulated plastic strain reaches a certain amount ($\varepsilon_{d,p}$ = 3.2% for this case), soil softening occurs with reductions in the material parameters, for example, the effective internal friction angle starts to decrease from its peak value at 3.19 days, as shown in Fig. 4.13. It should be noted that the net stress decreases at a slightly faster rate after softening than before. The is because, it is only the suction reduction that contributes to reduction in net stress before softening, in order to keep the stress state on the yield surface (i.e. the extended Mohr-Coulomb failure criterion), while after softening, stress is decreasing not only due to suction reduction but the change in the position of yield surface (reduction in the material parameters). It can also be observed that suction decrease has a dominant effect on the decreasing rate of net stress.

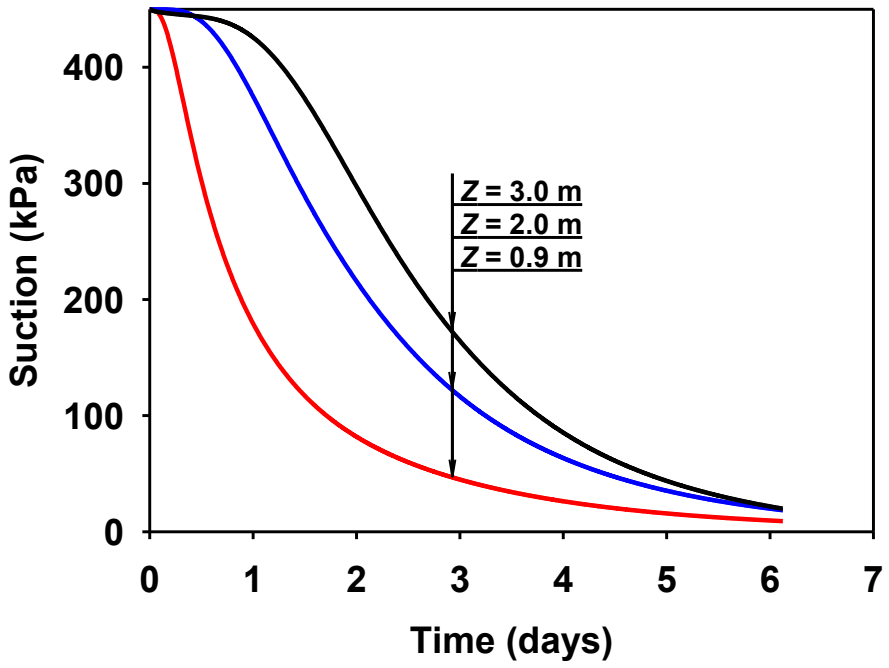

Fig. 4.11. The evolution of suction at the several depths with time.

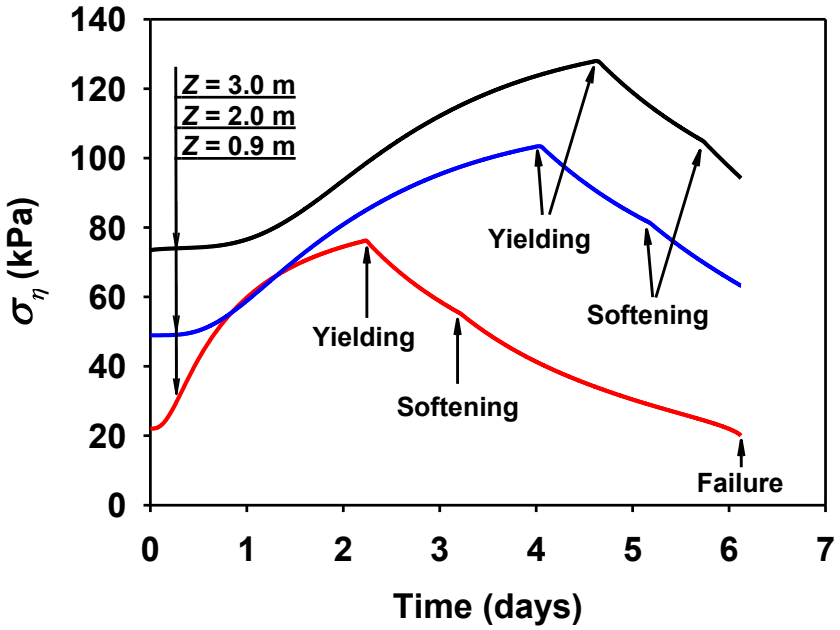

Fig. 4.12. The evolution of net stress in the sloping direction, σ_η, at several depths with time

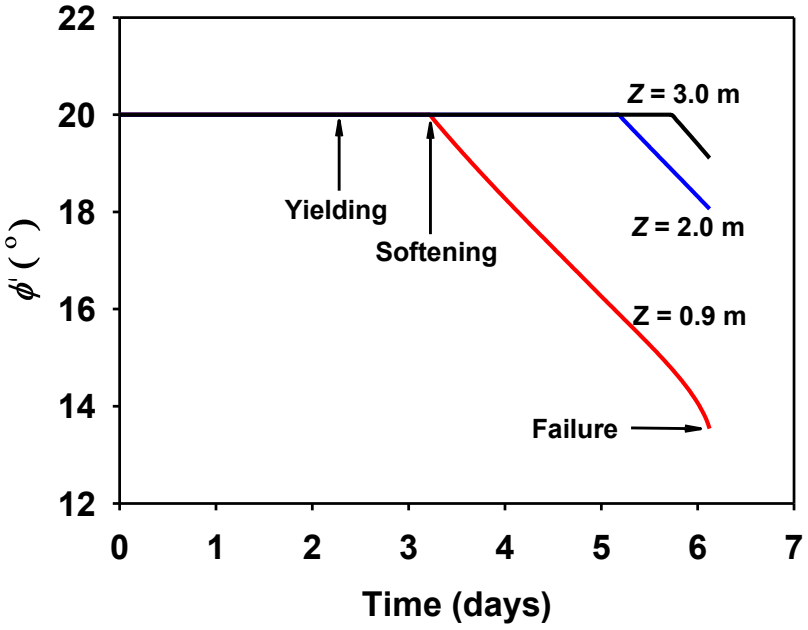

Fig. 4.13. The evolution of angle of internal friction at several depths with time

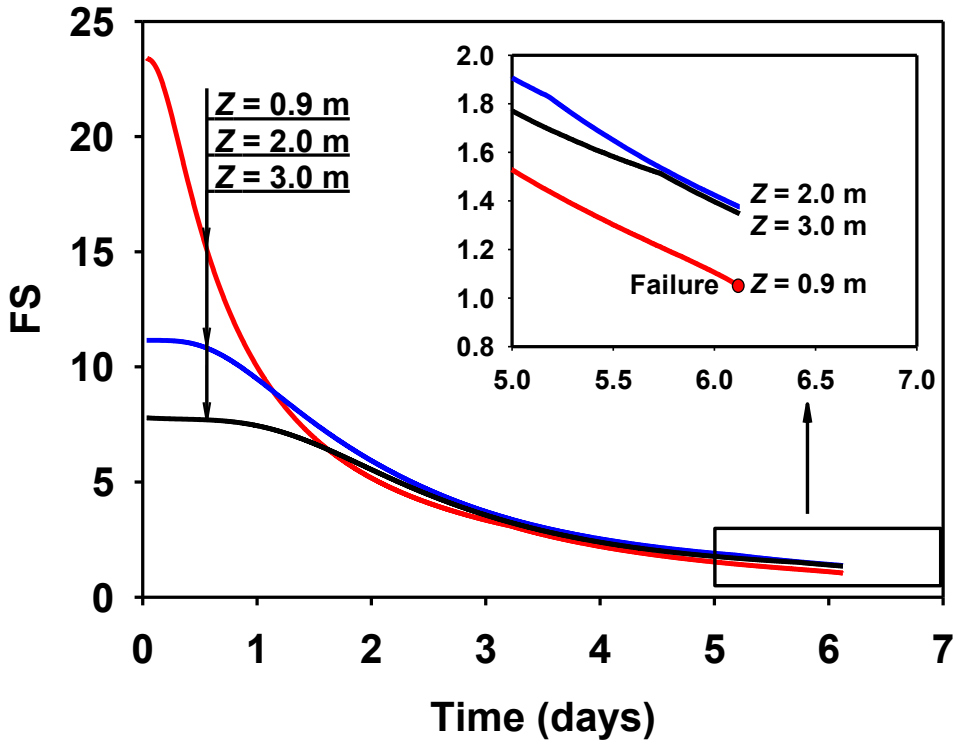

Fig. 4.14. The evolution of FS at the several depths with time.

Similar trends can be observed for the net stress evolution at the depth of 2.0 m and 3.0 m, but they reach their maximum values and the point of softening later than those at 0.9 m depth, which is mainly due to the slower suction decrease rate at deeper depth (see Fig. 4.11). When the slope failure occurs at the depth of 0.9 m, soils at 2.0 and 3.0 m depths are in the softening phase. However, the FSs at these two depths are approximately around 1.4 (see Fig. 4.14), indicating a fairly stable state at those depths.

When the stress paths followed at the three depths are plotted in the three dimensional (*p*-*q*-*s*) stress space in Fig. 4.15, three phases can be clearly observed: (i) purely elastic behaviour when stress state is below the yield surface; (ii) perfectly plastic behaviour when the stress state is

on the original yield surface; (iii) strain softening behaviour when the stress state falls back below original yield surface. It is worth mentioning that the stress state should also be on the yield surface during softening, Fig. 4.15 only shows the original yield surface without changing its positions according to reduced state parameters.

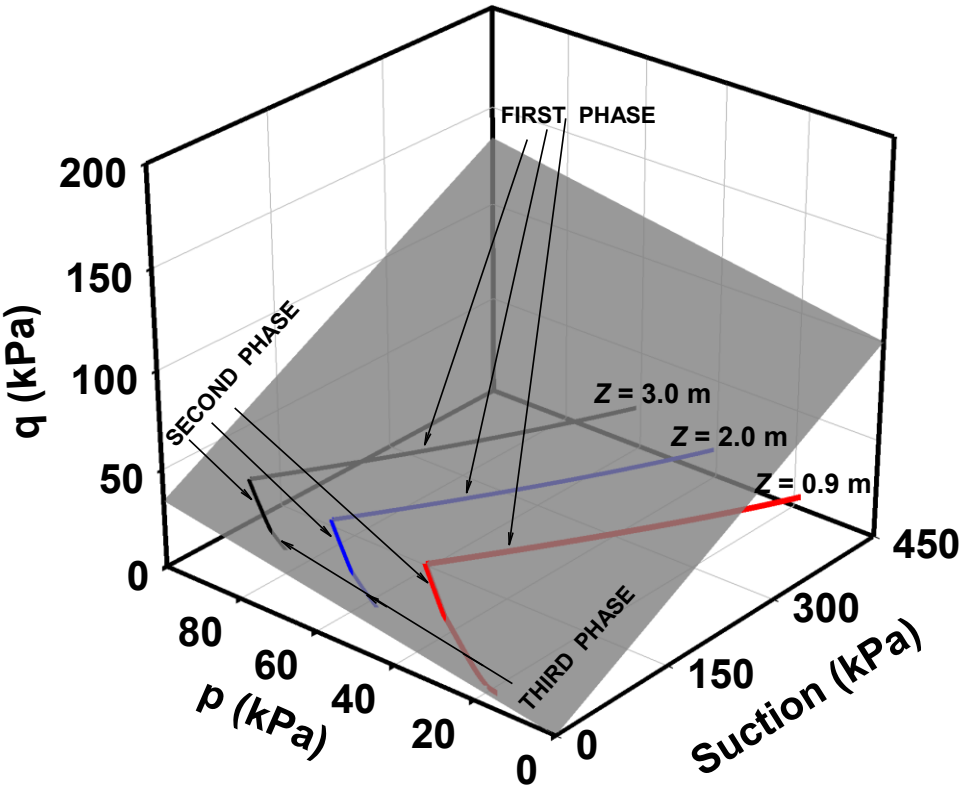

Fig. 4.15. The evolution of stress in three dimensional space at the several depths with time.

Fig. 4.16 depicts the stress state at the failure depth at several typical elapsed times in two dimensional space plots. The effect of suction on shear strength is included in the intercepts ($c_a = c' + s \tan\phi^b$) between extended Mohr-Coulomb yield envelope and shear stress axis. The Mohr-Circle always goes through the same point (σ_ξ, $\tau_{\xi\eta}$), because these two stress components are unchanged. Initially, the stress Mohr-circle is far below the yield envelope (see Fig. 4.16(a)). Once

the yielding occurs, the Mohr-circle is always tangential to the yield envelope during both the perfectly plastic (Fig. 4.16(b)) and strain softening (Fig. 4.16(c)) phases. During perfectly plastic phase, the failure envelopes are parallel to each other with changing intercepts (different suctions), as can be expected (Fig. 4.16(b)). The decrease in the inclination of failure envelope (ϕ) indicating a reduction of yield surface can be seen during the softening phase (Fig. 4.16(c)). Slope fails when tangential point between the Mohr-circle and the failure envelope evolves eventually to the point (σ_ξ, $\tau_{\xi\eta}$).

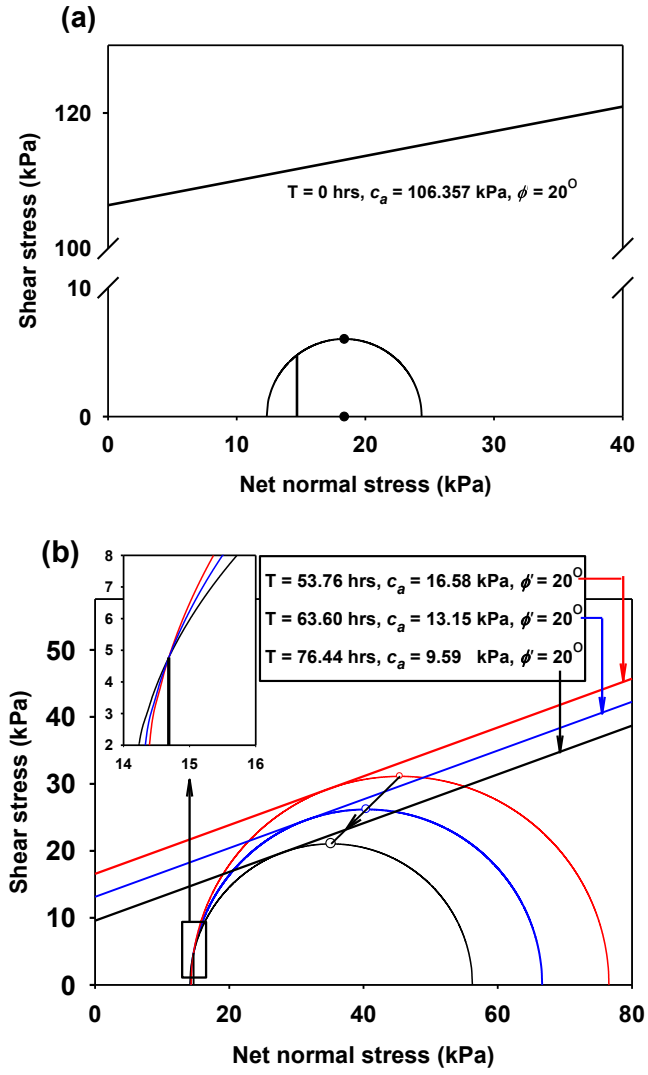

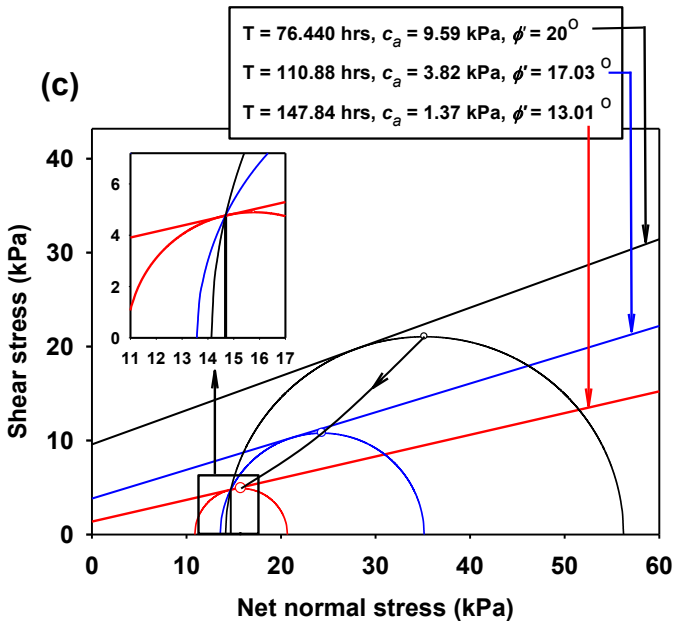

Fig. 4.16. The stress state at the failure depth at several typical elapsed times in two dimensional space plots: (a) elastic phase; (b) perfectly plastic phase; (c) softening phase.

4.5.3 Results of parametric analysis

The slope failure occurs at the depth of 0.9 m at 6.16 days (i.e. 147.84 hrs), from the "base case" analysis, it should be noted that the failure depths can be different for varying scenarios. The slip surface of infinite slope would be at the depth, at which the stress condition first evolves to such a condition: the failure envelope is tangential to the Mohr circle at point (σ_η, $\tau_{\xi\eta}$, s) in three dimensional space. This can be influenced by many factors including the initial net stress and suction state, suction decrease rate, softening rate, and the material properties, etc.

However, for a given slope, decrease in suction is the only factor that leads to changes in stress state and yield envelope position, and brings it to condition stated above. Thus, for a given initial suction profile within a given slope, the value of suction corresponding to failure condition for any depth stated above can be uniquely determined by conducting the elasto-plastic analysis.

The suctions corresponding to condition stated above at each depth are referred to as the "critical suction" profile for a given slope. The parametric analysis is conducted to investigate the effect of several factors (including the initial stress ratio, slope angle and softening rate) on the "critical suction" profile.

4.5.3.1 Effect of initial stress ratio

Fig. 4.17 shows the "critical suction" profiles obtained using different initial stress ratios. It can be seen that the initial stress ratio has a significant influence on the value of "critical suction" at deeper depth (below the depth of about 1.0 m). The smaller the initial stress ratio, the smaller will be the "critical suction". This can be interpreted as: the smaller initial stress ratio forms a smaller size of initial stress Mohr's circle. For this reason, more change in the suction is required to bring to soil element into yielding, softening and failure (note that the initial suction for the whole slope profile is 450 kPa). This can also be seen in relationship between the stress, σ_η, and suction, s, for three initial stress ratios (i.e. K_0 = 0.5, 1.5 and 2.5) shown in Fig. 4.18. At the depth of 2.5 m as a representative of value of greater depth, the initial value of stress, σ_η, for K_0 = 2.5 is significantly higher than the other two, which indicates a larger initial Mohr's circle, and results a failure at larger suction value.

However, at shallower depths near the ground surface (above 1.0m), the effect of initial stress ratio on the "critical suction" is negligible. The value of net stress, σ_ξ, (determined using Eq. (4.18)) at shallower depth due to overburden pressure is low. Therefore, changing the initial stress ratio will not lead to a big difference in the value of net stress, $\sigma_\eta = K_0\sigma_\xi$, as well as the size of initial stress Mohr's circle. As a result, the critical suction value is not substantially affected by the

initial stress ratio, as can be seen in the stress, σ_η, vs suction, s, relationship at the depth of 0.5 m in Fig. 4.18.

One of the basic applications of "critical suction" profile is to determine the failure time and depth for each case, combined with pore water pressure (suction) profile from seepage analysis under a particular infiltration condition. To be more specific, slope fails at that depth where the suction profile from seepage analysis first touches the "critical suction" profile. The results for different initial stress ratios under the infiltration used in the present study are graphically shown in Fig. 4.19. The suction profiles shown in Fig. 4.19 are extracted from pore water pressure profile in Fig. 4.7. It can be seen clearly seen that why the failure occur at a particular depth instead of others for each case. Generally, the larger initial stress ratio, the deeper and earlier will be the failure depth and time, for the scenarios illustrated in Fig. 4.19.

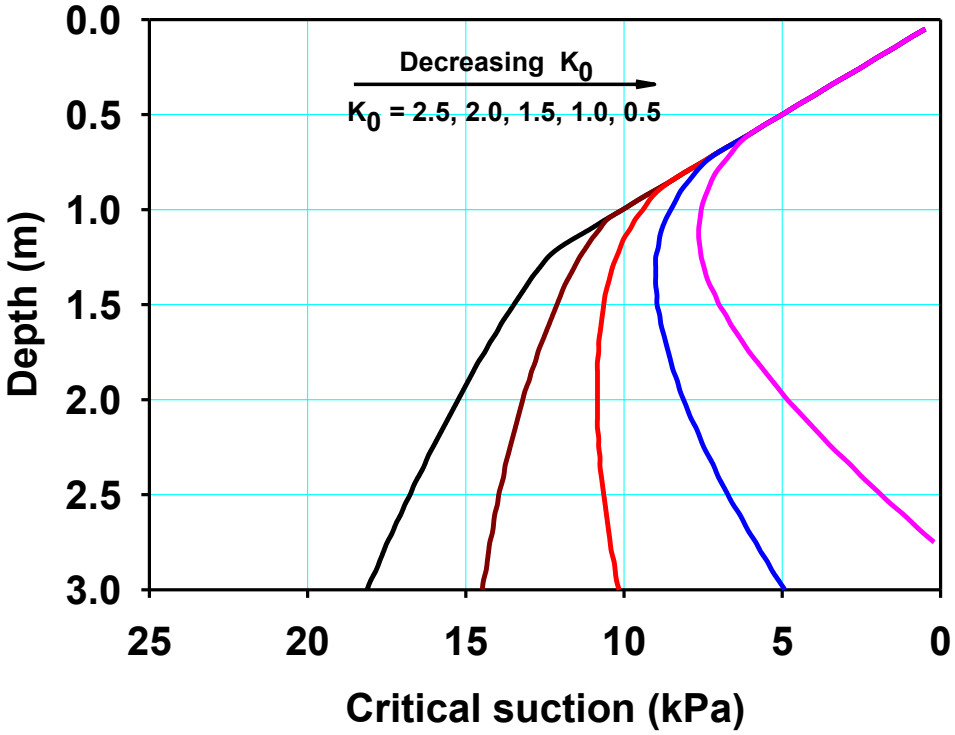

Fig. 4.17. Effect of initial stress ratio on the "critical suction" profile.

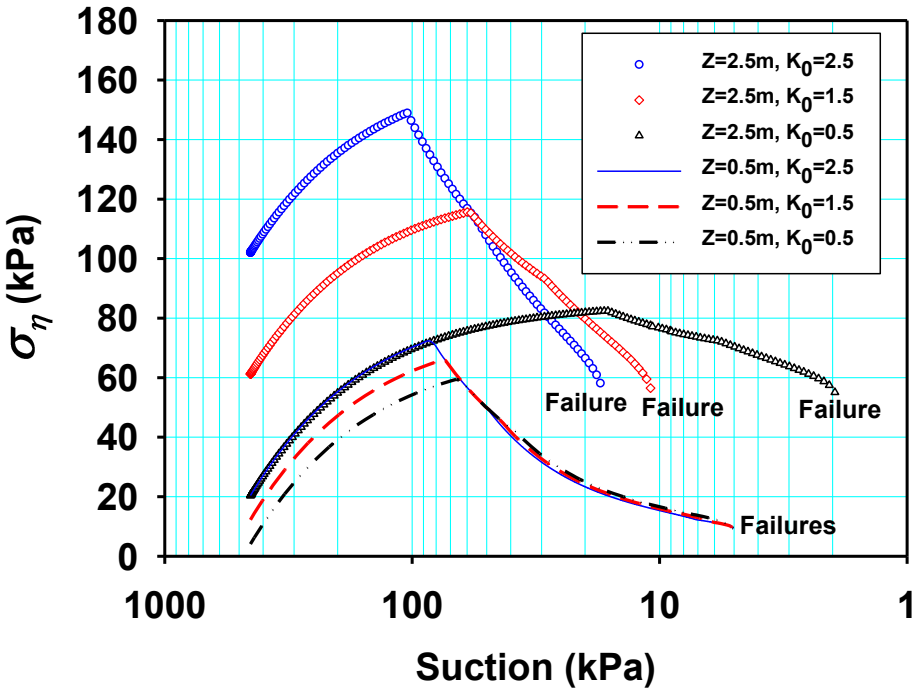

Fig. 4.18. The relationship between the stress, σ_η, and suction, s, for three initial stress ratios at shallower (0.5 m) and deeper (2.5 m) depths.

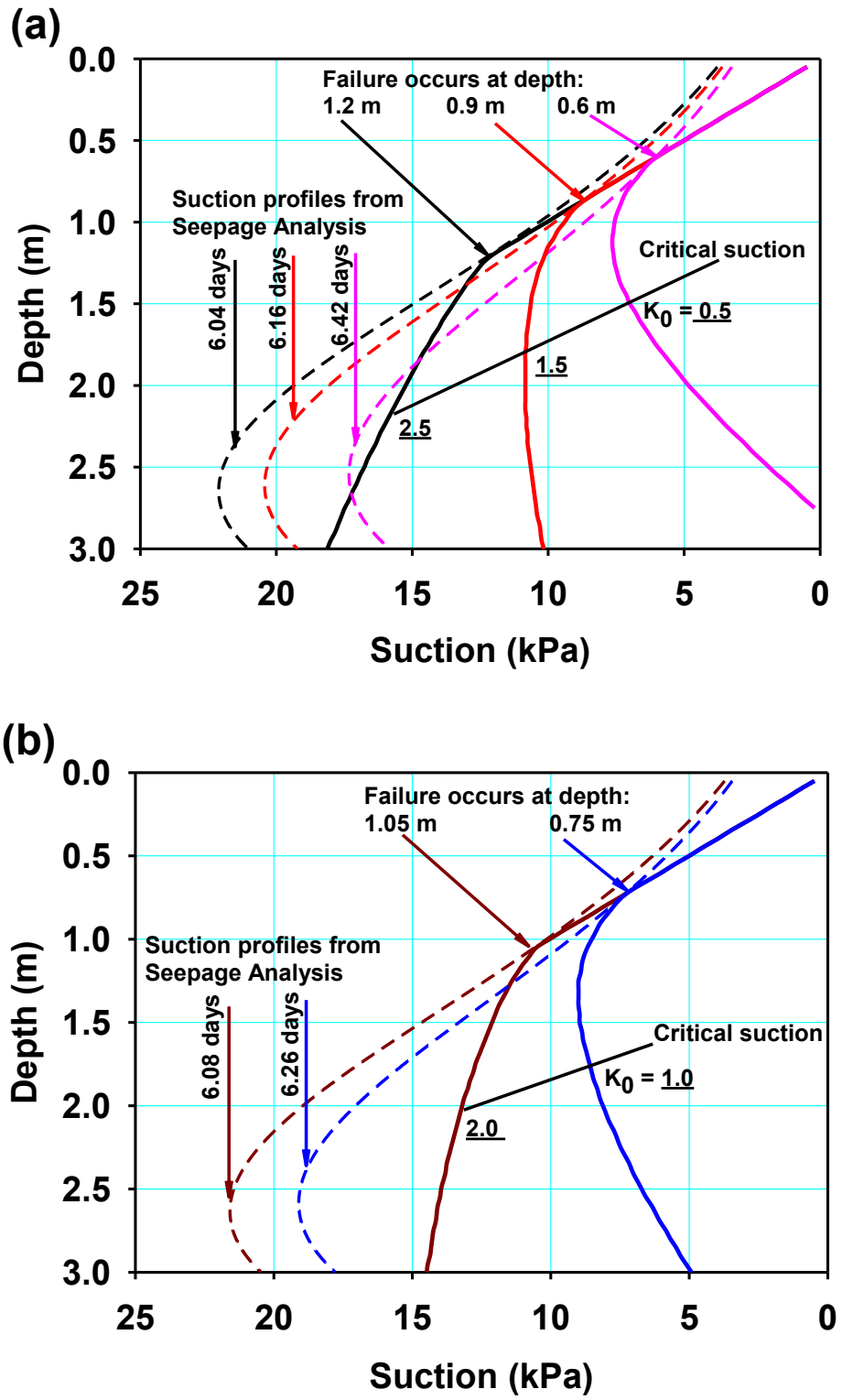

Fig. 4.19. Graphical determination of the failure time and depth for different initial stress ratios.

4.5.3.2 Effect of softening rate

Fig. 4.20 presents effect of softening rate on "critical suction" profiles. The softening rate here means the rate of decrease in state parameters with respect to plastic deviatoric strain. Different softening rates are considered by using different plastic deviatoric strains at residual state. Two smaller and three larger than the base value (0.12) are used in the parametric analysis to produce Fig. 4.20. Smaller plastic deviatoric strains at residual state indicate faster softening rates, and an unfavorable engineering material in terms of slope stability.

Generally, faster softening rates result in larger "critical suction" value, which means a smaller change in the suction (suction unloading) is needed to cause slope failure at that depth (Fig. 4.20). When softening rates are larger than that for base analysis, it has a substantial influence on the "critical suction" at deeper depths, and a negligible effect on the "critical suction" at shallower depths (e.g. above 1.0m). When softening rate are smaller than that for base analysis, the effect of the softening rate on "critical suction" suction value is evident for the entire slope profile.

This phenomenon can be better explained with the aid of Fig. 4.21. Fig. 4.21 illustrates the degradation of shear strength parameter, ϕ', with suction unloading for several softening rates, at 0.5 and 2.0 m depths as examples for shallow and deep depths, respectively. The other shear strength parameter, ϕ^b, exhibits the same change trend with suction, and is not included in Fig. 4.21 for simplicity. It can be seen that higher softening rates result in faster decrease in the value of ϕ', with respect to suction for two depths. The soil element at the depth of 0.5m starts to soften at a higher suction value than that at 2.5m depth. When the softening rate is equal to or higher than that for the "base analysis", the value of angle of internal friction, ϕ' decreases to residual value at the depth of 0.5m before reaching failure condition. The same shear strength parameters (i.e.

residual value) result in the same "critical suctions" at failure (see Eq. (4.30)) at this depth. While for other cases, the angle of internal friction, ϕ', is between peak and residual values at failure, and have different values due to different softening rates, and hence resulting in different "critical suctions" (see Eq. (4.30)) at failure.

Fig. 4.22 illustrates the failure time and depth determined using the "critical suction" profile and suction profile from seepage analysis for different softening rates considered in the present study. Since the "base case" is already shown in Fig. 4.19, it is not included in Fig. 4.22. When the softening rate is larger than that of the base case, the failure is deeper and earlier. However, no failure was observed in 7 days of infiltration when softening rate is lower than that of the base case, as the suctions from seepage analysis at the end of 7 days are still higher than the "critical suction" for the whole slope profile.

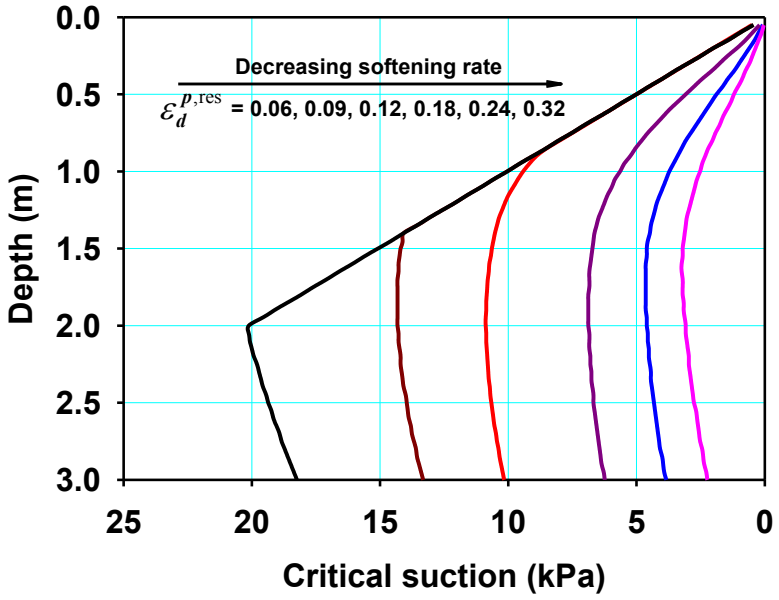

Fig. 4.20. Effect of softening rate on the "critical suction" profile.

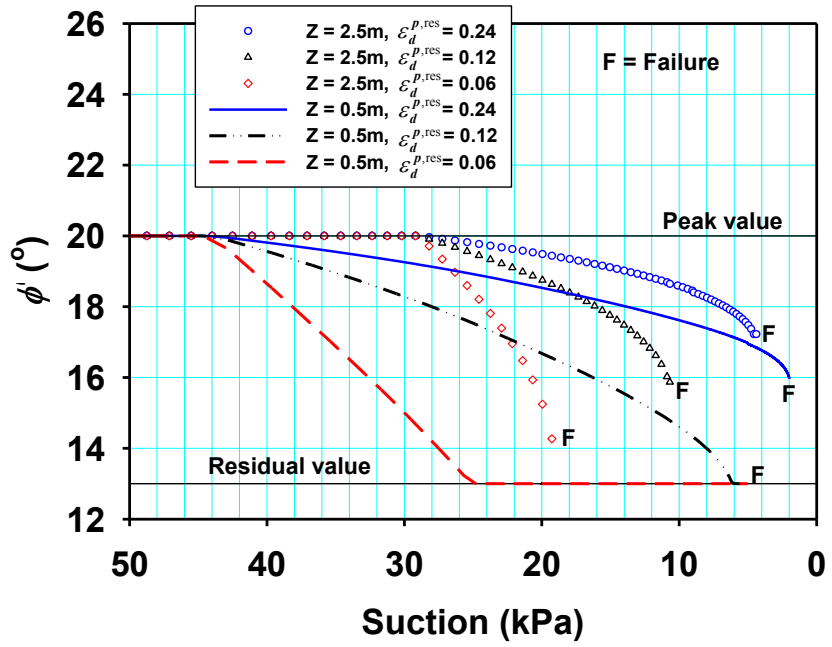

Fig. 4.21. Degradation of shear strength parameter, ϕ', with suction unloading for several softening rates, at shallower (0.5 m) and deeper (2.0 m) depths.

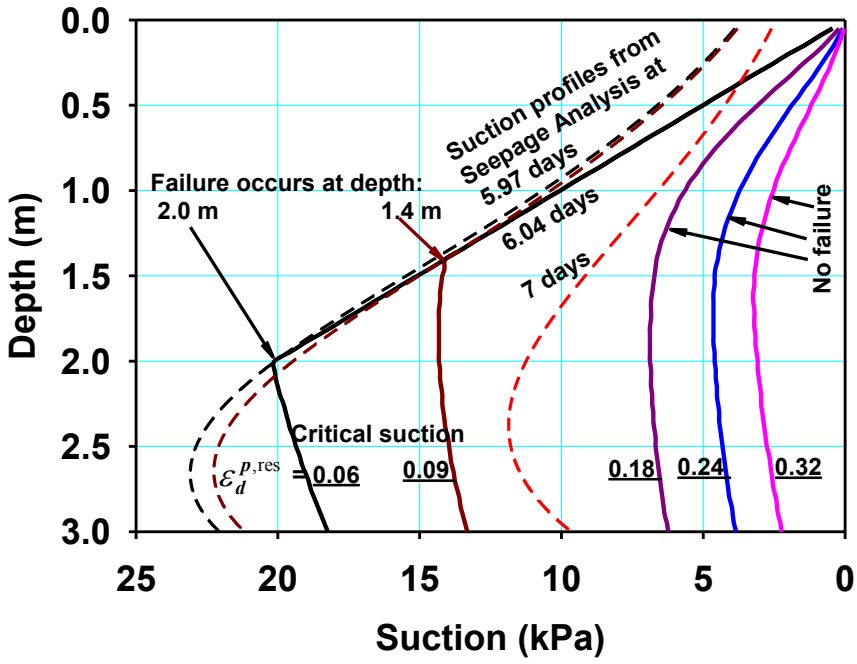

Fig. 4.22. Graphical determination of the failure time and depth for different softening rates.

4.5.3.3 Effect of slope angle

Fig. 4.23 illustrates effect of slope angle on the "critical suction" profile. Five different slope angles are adopted: a value of 22° which is larger than value of ϕ'^{peak}, another, a value of 20° which is equal to ϕ'^{peak}, and the remaining three (18°, 16°, 14°) are between ϕ'^{peak} and ϕ'^{res}.

Slope angle has influence on the "critical suctions" within the entire slope profile, as can be seen in Fig. 4.23. The influence of slope angle on the "critical suction" becomes gradually stronger with increasing depth. As can be expected, at a particular depth, the larger the slope angle, the larger the "critical suction" value is, since the suction change (suction unloading) required to cause slope failure is less.

Slopes with angles between ϕ'^{peak} and ϕ'^{res} (i.e. 18°, 16°, 14°), will never fail at unsaturated condition if softening is not considered, which can be interpreted using Eq. (4.30) as was suggested in the previous section. However, Fig. 4.23 shows that, for $\beta = 14°$, possible failure can still occur at certain depths (0m to 1.8m) at unsaturated condition when softening is included in the analysis. This means the ϕ' with this zone is already decreased below 14° from the peak value by strain softening when suction decreases to the "critical suction" value. While, at the zone (1.8m to 3.0m depth), the mobilized ϕ' is still larger than 14° when suction decreases to zero, slope failure does not occur within this zone at unsaturated condition. An appropriate engineering slope design should take the both the peak and residual shear strength parameters into consideration by conducting a strain softening analysis, if necessary. A slope angle lower than ϕ'^{peak} cannot ensure enduring stability, and expansive soils with high peak but very low residual strength could be unfavorable for fills and cuts.

Fig. 4.24 illustrates the failure time and depth determined using the "critical suction" profile and suction profile from seepage analysis for different slope angles considered in the present study. The "base case" is not included in Fig. 4.24. The failures occur at 0.8m after 5.09 days and 0.75m after 5.53 days, when the slope angle is 22° and 20°, respectively. A time period of 7 days of infiltration with intensity used in this study is not long enough to cause failures when slope angle is lower than that of the base case.

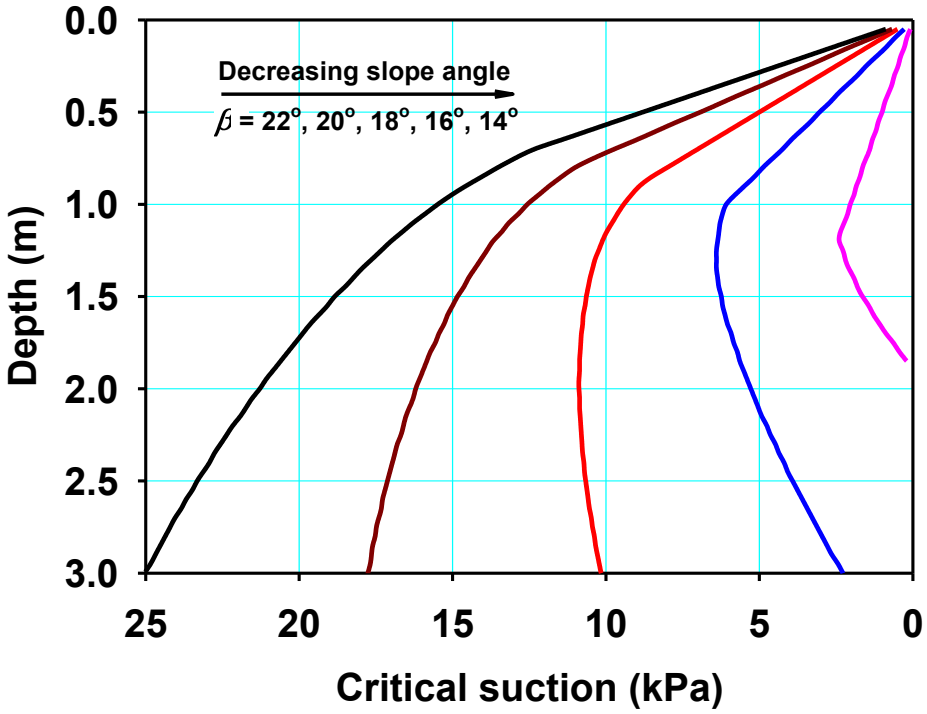

Fig. 4.23. Effect of slope angle on the "critical suction" profile.

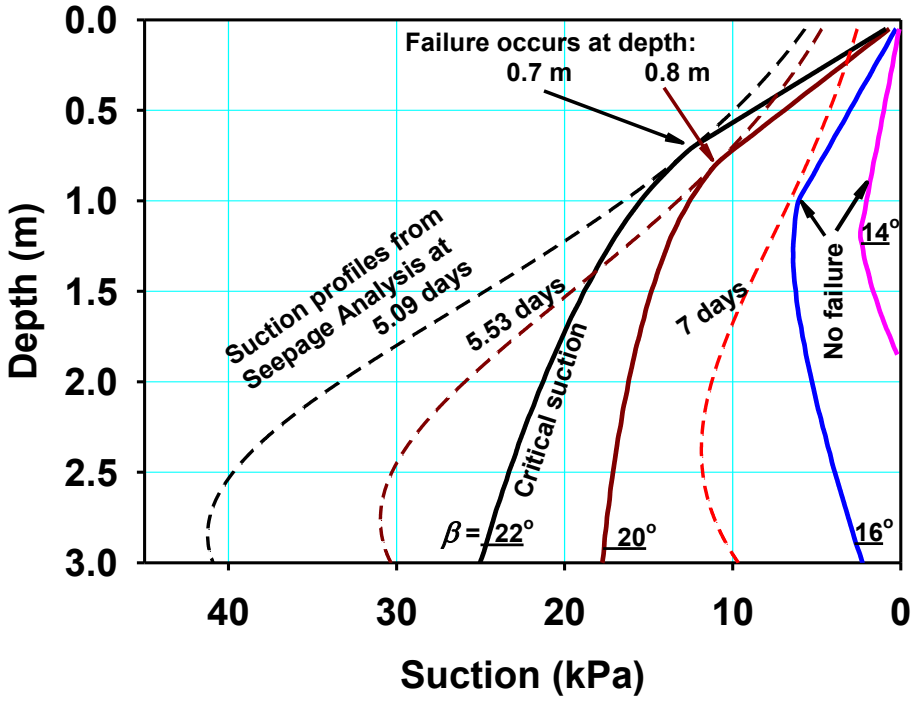

Fig. 4.24. Graphical determination of the failure time and depth for different slope angle.

4.6 Discussion

Two key characteristics associated with the expansive soil failure mechanism: (1) stress increase due to expansion upon wetting and (2) softening behaviour of the slope stability have been well captured in this study via the simple infinite slope formulation with an extended elasto-plastic strain softening constitutive model.

The constitutive model consists of three components: (*i*) suction-dependent yielding surface; (*ii*) nonlinear elastic behaviour; and (*iii*) a softening law. All the three components directly influence the computation results; specifically, the nonlinear elastic moduli affect the magnitude of stress increase during initial wetting, which, therefore, also affect the stress magnitude and time at onset of yielding. The mobilized shear strength parameters used to compute the FS are affected

by yielding and subsequent softening. The first two components have been well observed/deduced from the available experiments conducted on unsaturated soil samples. The third one includes an assumption that the residual shear strength of unsaturated soils can be described using extended Mohr-Coulomb strength criterion, and ϕ^b varies in the same linear manner with accumulated deviatoric plastic strain as those of c', ϕ'. This assumption can be regarded as a reasonable first approximation, in view of the evidence of recent experimental results (Hoyos et al. 2014; Gui and Wu 2014), as well as the similar artifice used in shear strength reduction technique for slope stability analysis of unsaturated soils (Griffiths and Lu 2005; Le et al. 2015). The measured constitutive properties for Regina clay that were used in the present study provide credence to the modeling results for the stability analysis of slopes in Regina clay and clays with similar properties and initial conditions.

Another assumption used in the present study is associated with the infinite slope framework (see Fig. 4.1), in which the strain in the η direction is zero (fully constrained). This constraint is also applied for strain in the direction perpendicular to ξ–η plain (i.e. the "direction perpendicular to the downslope"). Due to this reason, the model predicts the same magnitudes of stresses in η direction and the direction perpendicular to ξ–η plane. The field scenario however may be somewhat different, e.g. field measurements by Ng et al. (2003). The field condition is typically close to two-dimension problem considering the sloping ground with a long width, and is, more realistically, three-dimensional. Thus, the real stress state is impossible to be fully simulated using the one-dimensional infinite model. In spite of this limitation, the most important features (i.e. swelling stress increase, associated softening and failure) focused in this study, are reasonably well captured by stress analysis in ξ–η plane with the shear stress $\tau_{\xi\eta}$, using the framework of infinite slope.

4.7 Conclusions

In the present study, the infiltration-induced shallow failure of expansive soil slope has been critically discussed and addressed in the framework of plane strain infinite slope formulation, with emphases on the important roles of swelling-induced stress regime change and associated softening behaviour of unsaturated soils. The practical strain softening Mohr-Coulomb model in terms of two stress state variables, extended from that of saturated soil, is adopted. A computer program is developed to trace the highly nonlinear behaviour of unsaturated expansive soils and evaluate slope stability under infiltration, combined with the conventional FS definition in standard limit equilibrium method. A numerical exercise is conducted using the developed program on an infinite slope consisting of Regina clay, with carefully selected material parameters in the literature.

The following conclusions can be drawn from the analysis of the results presented in this study:

During wetting, the net stress in the sloping direction keeps increasing and reaches its maximum value at yielding, after which it decreases due to suction decrease and possible softening. The maximum value of net stress in the sloping direction can be several times the net stress perpendicular to the sloping direction. These phenomena are similar to those observed from the published experimental tests.

Using peak strength values and neglecting the softening behaviour may overestimate the conventional factor of safety under infiltration conditions, and will lead to an unsafe engineering design for expansive soil slopes.

Failures depths are not necessarily at the base of surface layer. It can be affected by many factors: such as softening rate, slope angle, initial stress ratio. The failure depth and time can be

well defined and recognized by combining the "critical suction" profile obtained from the developed program and suction profile from a seepage analysis.

The initial stress ratio, softening rate and slope angle have a more significant effect on the "critical suction" at greater depths than shallow depths. Due to softening-induced strength loss, a gentle slope with an angle lower than ϕ'^{peak} does not assure stability in unsaturated conditions as suggested in the traditional infinite slope formulations assuming no softening behaviour. An appropriate engineering slope design hence should consider both the peak and residual shear strength parameters. The results from parametric study have important implications for the design of slope in expansive soils.

Glossary

Symbols

$\{\sigma\}$	Stress state in stress space
$\{k\}$	State parameters
F	Yielding function
u_a	Pore air pressure
u_w	Pore water pressure
s	Suction
$\{g\}$	State parameters
G	Plastic potential
$\{d\varepsilon\}$	Total incremental strains
$\{d\varepsilon^e\}$	Elastic incremental strain due to change in net stress
$\{d\varepsilon^p\}$	Plastic incremental strain due to change in net stress
$\{d\varepsilon_s^e\}$	Incremental elastic strain due to change in suction
$\{d\varepsilon_s^p\}$	Incremental plastic strain due to change in suction
$[D]$	Elastic constitutive matrix
H	Elastic modulus (a scalar) for the soil structure with respect to suction change
Λ	Scalar plastic multiplier
η	Axis directed along the infinite slope
ξ	Axis orthogonally to the infinite slope
β	Slope angle of the infinite slope
x	Axis in Cartesian coordinate system
y	Axis in Cartesian coordinate system
σ_ξ	Total (net) normal stress acting on the plane of normal ξ
$\tau_{\xi\eta}$	Shear stress acting on the plane of normal ξ
Z	Depth under the ground surface measured along the y axis
σ_η	Total (net) normal stress in the η direction
K	The stress ratio of the total (net) normal stresses
γ	Unit weight of the soil
σ_1'	Major principal effective stress
σ_3'	Minor principal effective stress
c'	Effective cohesion
ϕ'	Effective angle of internal friction
ϕ^b	Friction angle relative to suction
φ	Dilatancy angle
c_a	Apparent cohesion
E	Young's modulus
μ	Poisson's ratio
$\varepsilon_{d,p}$	Deviatoric plastic strain

$\boldsymbol{k}^{peak}$	Peak values of state parameters
$\boldsymbol{k}^{res}$	Residual values of state parameters
$\boldsymbol{\varepsilon}_{d,p}^{\text{peak}}$	Deviatoric plastic strain at which softening starts
$\boldsymbol{\varepsilon}_{d,p}^{\text{res}}$	Deviatoric plastic strain when softening is completed
$[D^{p\varepsilon}]$	Elasto-plastic matrix associated with mechanical strain
$[D^{ps}]$	Elasto-plastic matrix associated with suction
K_0	Initial stress ratio between total (net) normal stresses
θ_s	Saturated volumetric water content
θ_r	Residual volumetric water content
θ_w	Volumetric water content
a	van Genuchten fitting parameters
n	van Genuchten fitting parameters
S_s	Saturated degree of saturation
S_r	Residual degree of saturation
k_s	Saturated permeability
e	Void ratio in Vu and Fredlund (2006) state surface model
e_0	Initial void ratio in Vu and Fredlund (2006) state surface model

Abbreviations

FS	Factor of Safety
MPM	Material Point Method

4.8 References

Ali, A., Huang, J., Lyamin, A. V., Sloan, S. W., & Cassidy, M. J. (2014). Boundary effects of rainfall-induced landslides. Computers and Geotechnics, 61, 341-354.

Ali, A., Huang, J., Lyamin, A. V., Sloan, S. W., Griffiths, D. V., Cassidy, M. J., & Li, J. H. (2014). Simplified quantitative risk assessment of rainfall-induced landslides modelled by infinite slopes. Engineering Geology, 179, 102-116.

Alonso, E. E., Gens, A., & Delahaye, C. H. (2003). Influence of rainfall on the deformation and stability of a slope in overconsolidated clays: a case study. Hydrogeology Journal, 11(1), 174-192.

Alonso, E. E., Vaunat, J., & Gens, A. (1999). Modelling the mechanical behaviour of expansive clays. Engineering geology, 54(1), 173-183.

Aubeny, C. P., & Lytton, R. L. (2004). Shallow slides in compacted high plasticity clay slopes. Journal of Geotechnical and Geoenvironmental Engineering, 130(7), 717-727.

Azañón, J. M., Azor, A., Yesares, J., Tsige, M., Mateos, R. M., Nieto, F., & Rodríguez-Fernández, J. (2010). Regional-scale high-plasticity clay-bearing formation as controlling factor on landslides in Southeast Spain. Geomorphology, 120(1), 26-37.

Bandara, S., & Soga, K. (2015). Coupling of soil deformation and pore fluid flow using material point method. Computers and Geotechnics, 63, 199-214.

Bani Hashem E. Volume change consideration in determining appropriate unsaturated soil properties for geotechnical applications. PhD thesis. USA:Arizona State University; 2013.

Bao, C. G., Ng, C. W. W., Rahardjo, H., Toll, D. G., & Leong, E. C. (2000). Some thoughts and studies on the prediction of slope stability in expansive soils. In Unsaturated soils for Asia. Proceedings of the Asian Conference on Unsaturated Soils, UNSAT-Asia 2000, Singapore, 18-19 May, 2000. (pp. 15-31). AA Balkema.

Bjerrum, L. (1967). Progressive failure in slopes of overconsolidated plastic clay and clay shales. Journal of the Soil Mechanics and Foundations Division, 93(5), 1-49.

Boyd, J. L., & Sivakumar, V. (2011). Experimental observations of the stress regime in unsaturated compacted clay when laterally confined. Géotechnique, 61(4), 345-363.

Brackley, I. J. A., & Sanders, P. J. (1992). In situ measurement of total natural horizontal stresses in an expansive clay, Géotechnique, 42(3), 443-451.

Chai, J., & Carter, J. P. (2009). Simulation of the progressive failure of an embankment on soft soil. Computers and Geotechnics, 36(6), 1024-1038.

Chao KC, Kang JB, Nelson JD. Challenges in water migration modeling for expansive soils. Soil behaviour and geomechanics, GSP236 ASCE; 2014. p. 204–13.

Chen, Z., Morgenstern, N. R., & Chan, D. H. (1992). Progressive failure of the Carsington Dam: a numerical study. Canadian Geotechnical Journal, 29(6), 971-988.

Cho, S. E. (2014). Probabilistic stability analysis of rainfall-induced landslides considering spatial variability of permeability. Engineering Geology, 171, 11-20.

Chowdhury, M. (2013). Shear Strength Properties of Compacted Expansive Soils (Master thesis, Faculty of Graduate Studies and Research, University of Regina).

Day, R. W. (1994). Surficial stability of compacted clay: case study. Journal of geotechnical engineering, 120(11), 1980-1990.

Di Prisco, C., & Pisanò, F. (2011). An exercise on slope stability and perfect elastoplasticity. Géotechnique, 61(11), 923-934.

Duncan, J. M., Wright, S. G., & Brandon, T. L. (2014). Soil strength and slope stability. John Wiley & Sons.

Escario, V., & Saez, J. (1986). The shear strength of partly saturated soils. Géotechnique, 36(3).

Fourie, A. B. (1989). Laboratory evaluation of lateral swelling pressure. Journal of Geotechnical Engineering, 115(10), 1481-1486.

Fredlund, D. G., & Rahardjo, H. (1993). Soil mechanics for unsaturated soils. John Wiley & Sons.

Fredlund, D. G., Morgenstern, N. R., & Widger, R. A. (1978). The shear strength of unsaturated soils. Canadian Geotechnical Journal, 15(3), 313-321.

Fredlund, D. G., Rahardjo, H., & Gan, J. K. M. (1987, December). Non-linearity of strength envelope for unsaturated soils. In Proc. 6th Int. Conf. Expansive Soils, New Delhi (Vol. 1, pp. 49-54).

GeoSlope International Ltd., 2012. Seep/W User's Guide for Finite Element Seepage Analysis. GEO-SLOPE International Ltd, Calgary, Alta.

Griffiths, D. V. (1981). Computation of strain softening behaviour. In proceedings of the Symposium on Implementation of Computer Procedures and Stress-Strain Laws in Geotechnical Engineering, Chicago, U.S.A., (editors: C. S. Desai and S. K. Saxena), Vol. II, pp. 591-604, Acorn Press.

Griffiths, D. V., & Lane, P. A. (1999). Slope stability analysis by finite elements. Geotechnique, 49(3), 387-403.

Griffiths, D. V., & Li, C. O. (1993). Analysis of delayed failure in sloping excavations. Journal of geotechnical engineering, 119(9), 1360-1378.

Griffiths, D. V., & Lu, N. (2005). Unsaturated slope stability analysis with steady infiltration or evaporation using elasto‐plastic finite elements. International journal for numerical and analytical methods in geomechanics,29(3), 249-267.

Griffiths, D. V., Fenton, G. A., & Ziemann, H. R. (2006). Seeking out failure: The random finite element method (RFEM) in probabilistic geotechnical analysis. In GeoCongress 2006: Geotechnical Engineering in the Information Technology Age (pp. 1-6).

Griffiths, D. V., Huang, J., & Dewolfe, G. F. (2011). Numerical and analytical observations on long and infinite slopes. International Journal for Numerical and Analytical Methods in Geomechanics, 35(5), 569-585.

Griffiths, D. V., Huang, J., & Fenton, G. A. (2011). Probabilistic infinite slope analysis. Computers and Geotechnics, 38(4), 577-584.

Gui, M. W., & Wu, Y. M. (2014). Failure of soil under water infiltration condition.Engineering Geology, 181, 124-141.

Hou, T. S., Xu, G. L., Shen, Y. J., Wu, Z. Z., Zhang, N. N., & Wang, R. (2013). Formation mechanism and stability analysis of the Houba expansive soil landslide. Engineering Geology, 161, 34-43.

Hoyos, L. R., Velosa, C. L., & Puppala, A. J. (2014). Residual shear strength of unsaturated soils via suction-controlled ring shear testing. Engineering Geology, 172, 1-11.

Ito, M., & Azam, S. (2010). Determination of swelling and shrinkage properties of undisturbed expansive soils. Geotechnical and Geological Engineering, 28(4), 413-422.

Iverson, R. M. (2000). Landslide triggering by rain infiltration. Water resources research, 36(7), 1897-1910.

Le, T. M. H., Gallipoli, D., Sanchez, M., & Wheeler, S. (2015). Stability and failure mass of unsaturated heterogeneous slopes. Canadian Geotechnical Journal, (ja).

Lechman, J. B., & Griffiths, D. V. (2000). Analysis of the progression of failure of earth slopes by finite elements. In Slope Stability 2000 (pp. 250-265)

Lytton, R.L. 1994. Prediction of movement in expansive clay. In Vertical and Horizontal Deformations of Foundations and Embankments: Proceedings of Settlement '94, College Station, Tex., 16–18 June 1994. Edited by A.T. Yeung and G.Y. Feaalio. American Society of Civil Engineers, Geotechnical Special Publication 40, pp. 1827–1845.

Miao, L., Liu, S., & Lai, Y. (2002). Research of soil–water characteristics and shear strength features of Nanyang expansive soil. Engineering Geology, 65(4), 261-267.

Milledge, D. G., Griffiths, D. V., Lane, S. N., & Warburton, J. (2012). Limits on the validity of infinite length assumptions for modelling shallow landslides.Earth Surface Processes and Landforms, 37(11), 1158-1166.

Ng, C. W. W., Zhan, L. T., Bao, C. G., Fredlund, D. G., & Gong, B. W. (2003). Performance of an unsaturated expansive soil slope subjected to artificial rainfall infiltration, Géotechnique, 53(2), 143-157.

Oh, W. T., Vanapalli, S. K., & Puppala, A. J. (2009). Semi-empirical model for the prediction of modulus of elasticity for unsaturated soils. Canadian Geotechnical Journal, 46(8), 903-914.

Potts, D. M., & Zdravkovic, L. (1999). Finite element analysis in geotechnical engineering: theory. London: Thomas Telford.

Potts, D. M., Dounias, G. T., & Vaughan, P. R. (1990). Finite element analysis of progressive failure of Carsington embankment. Géotechnique, 40(1), 79-101.

Potts, D. M., Kovacevic, N., & Vaughan, P. R. (1997). Delayed collapse of cut slopes in stiff clay. Géotechnique, 47(5), 953-982.

Qi, S., & Vanapalli, S. K. (2015). Hydro-mechanical coupling effect on surficial layer stability of unsaturated expansive soil slopes. Computers and Geotechnics, 70, 68-82.

Qi, S.C., & Vanapalli, S.K. (2015). Stability Analysis of an Expansive Clay Slope: A Case Study of Infiltration Induced Shallow Failure of an Embankment in Regina, Canada. International Journal of Geohazards and Environment, 1(1):7-19.

Rahardjo, H., Melinda, F., Leong, E. C., & Rezaur, R. B. (2011). Stiffness of a compacted residual soil. Engineering Geology, 120(1), 60-67.

Richards, B. G., & Kurzeme, M. (1973). Observations of Earth Pressures on a Retaining Wall at the Gouger Street Mail Exchange, Adelaide (No. Res Paper No. 220).

Rouainia, M., Davies, O., O'Brien, T., & Glendinning, S. (2009). Numerical modelling of climate effects on slope stability. Proceedings of the ICE-Engineering Sustainability, 162(2), 81-89.

Sánchez, M., Gens, A., Guimarães, L., & Olivella, S. (2008). Implementation algorithm of a generalised plasticity model for swelling clays. Computers and Geotechnics, 35(6), 860-871.

Sheng, D., Fredlund, D. G., & Gens, A. (2008). A new modelling approach for unsaturated soils using independent stress variables. Canadian Geotechnical Journal, 45(4), 511-534.

Sheng, D., Sloan, S. W., Gens, A., & Smith, D. W. (2003). Finite element formulation and algorithms for unsaturated soils. Part I: Theory. International Journal for Numerical and Analytical Methods in Geomechanics, 27(9), 745-765.

Shuai, F. (1996). Simulation of swelling pressure measurements on expansive soils. (Doctoral thesis, University of Saskatchewan)

Shuai, F., & Fredlund, D. G. (1998). Model for the simulation of swelling-pressure measurements on expansive soils. Canadian Geotechnical Journal,35(1), 96-114.

Šimůnek, J., Šeina, M., Saito, H., Sakai, M., and van Genuchten, M.Th. 2013. The Hydrus-1D Software Package for Simulating the Movement of Water, Heat, and Multiple Solutes in Variably Saturated Media, Version 4.17. Hydrus Software Series 3, Department of Environmental Sciences, University of California Riverside, Riverside, California, USA, 342 pages.

Skempton, A. W. (1964). Long-term stability of clay slopes. Géotechnique, (14), 77-102.

Sołowski, W. T., & Gallipoli, D. (2010). Explicit stress integration with error control for the Barcelona Basic Model: Part I: Algorithms formulations.Computers and Geotechnics, 37(1), 59-67.

Sołowski, W. T., Sloan, S. W., & Wang, D. (2014). Material point method simulation of triaxial shear tests. Hair Transplantation: The Art of Micrografting and Minigrafting, 169.

Srivastava, R., & Yeh, T. C. J. (1991). Analytical solutions for one‐dimensional, transient infiltration toward the water table in homogeneous and layered soils. Water Resources Research, 27(5), 753-762.

Sun, W., & Sun, D. A. (2012). Coupled modelling of hydro‐mechanical behaviour of unsaturated compacted expansive soils. International Journal for Numerical and Analytical Methods in Geomechanics, 36(8), 1002-1022.

Terzaghi, K., & Peck, R. B. (1948). Soil mechanics in engineering practice, 1st edn. Wiley, New York.

Teunissen, J. A. M., & Spierenburg, S. E. J. (1996). Stability of infinite slopes. In International Journal of Rock Mechanics and Mining Sciences and Geomechanics Abstracts (Vol. 3, No. 33, p. 137A).

Troncone, A. (2005). Numerical analysis of a landslide in soils with strain-softening behaviour. Géotechnique, 55(8), 585-596.

Urciuoli, G. (2002). Strains preceding failure in infinite slopes. The International Journal Geomechanics, 2(1), 93-112.

Urciuoli, G., Picarelli, L., & Leroueil, S. (2007). Local soil failure before general slope failure. Geotechnical and Geological Engineering, 25(1), 103-122.

van Genuchten, M. T. (1980). A closed-form equation for predicting the hydraulic conductivity of unsaturated soils. Soil science society of America journal, 44(5), 892-898.

Vanapalli, S. K., Fredlund, D. G., Pufahl, D. E., & Clifton, A. W. (1996). Model for the prediction of shear strength with respect to soil suction. Canadian Geotechnical Journal, 33(3), 379-392.

Vanapalli, S., & Lu, L. (2012). A state-of-the art review of 1-D heave prediction methods for expansive soils. International Journal of Geotechnical Engineering,6(1), 15-41.

Vu, H. Q., & Fredlund, D. G. (2006). Challenges to modelling heave in expansive soils. Canadian geotechnical journal, 43(12), 1249-1272.

Wang, G., & Wei, X. (2014). Modeling swelling–shrinkage behaviour of compacted expansive soils during wetting–drying cycles. Canadian Geotechnical Journal, 52(999), 1-12.

Widger, R. A., & Fredlund, D. G. (1979). Stability of swelling clay embankments. Canadian Geotechnical Journal, 16(1), 140-151.

Windal, T., & Shahrour, I. (2002). Study of the swelling behaviour of a compacted soil using flexible odometer. Mechanics Research Communications, 29(5), 375-382.

Wu, L. Z., & Zhang, L. M. (2009). Analytical solution to 1D coupled water infiltration and deformation in unsaturated soils. International Journal for Numerical and Analytical Methods in Geomechanics, 33(6), 773-790.

Wu, L. Z., Zhang, L. M., & Huang, R. Q. (2012). Analytical solution to 1D coupled water infiltration and deformation in two - layer unsaturated soils. International Journal for Numerical and Analytical Methods in Geomechanics, 36(6), 798-816.

Xu, L., Dai, F., Chen, J., Iqbal, J., & Qu, Y. (2014). Analysis of a progressive slope failure in the Xiangjiaba reservoir area, Southwest China. Landslides, 11(1), 55-66.

Zabala, F., & Alonso, E. E. (2011). Progressive failure of Aznalcóllar dam using the material point method. Géotechnique, 61(9), 795-808.

Zhan, T. L. T., Chen, R., & Ng, C. W. W. (2014). Wetting-induced softening behaviour of an unsaturated expansive clay. Landslides, 11(6), 1051-1061.

Zhan, T. L., & Ng, C. W. (2006). Shear strength characteristics of an unsaturated expansive clay. Canadian Geotechnical Journal, 43(7), 751-763.

Zhan, T. L., Jia, G. W., Chen, Y. M., Fredlund, D. G., & Li, H. (2013). An analytical solution for rainfall infiltration into an unsaturated infinite slope and its application to slope stability analysis. International Journal for Numerical and Analytical Methods in Geomechanics, 37(12), 1737-1760.

Zhang, L. L., Fredlund, D. G., Fredlund, M. D., & Wilson, G. W. (2014). Modeling the unsaturated soil zone in slope stability analysis 1. Canadian Geotechnical Journal, 51(12), 1384-1398.

Chapter 5 Simulating the hydraulic and mechanical responses of an unsaturated expansive soil slope to rainfall: a case history[3]

This chapter presents simulation results of the performance of an unsaturated expansive soil slope during artificial rainfall events from a field investigation, using a modified version of the numerical program developed in previous chapter. The field study was conducted on an intake canal of a major water transfer project in Zaoyang, Hubei, China. The hydraulic response of this slope is simulated with SEEP/W, followed by modelling of its mechanical response upon wetting using an expanded infinite slope formulation. The soils' mechanical behaviour is still described using a Mohr-Coulomb elasto-plastic model extended for unsaturated soils. A new elastic moduli equation, which can consider the influence of degree of saturation on nonlinear variations of elastic moduli (E and H) with suction, is proposed to describe the unsaturated soils' nonlinear deformation behaviour in the elastic stage. Incorporating this new model is advantageous for smoothly modeling the transition between saturated and unsaturated states. The simulation results using infinite slope formulation that incorporates these constitutive relationships are in reasonable agreement with the field observations, highlighting the capability of the expanded infinite slope formulation to interpret the complex response of this expansive soil slope to rainfall infiltration.

[3] A version of this chapter has been accepted for publication in ASCE International Journal of Geomechanics

5.1 Introduction

Unsaturated expansive soils are referred widely in the literature as problematic soils because they exhibit high swelling potential upon wetting due to the presence of active clay minerals, such as the montmorillonite or illite. Expansive soils can cause severe distress to the infrastructure constructed on or with them by inducing a substantial external swelling pressure, differential displacements, or a combination of both. Some examples include lightly loaded structures (Nelson et al. 2015; Houston et al. 2015; Vanapalli and Lu 2012), pile foundations (Xiao et al. 2011; Alonso et al. 2015) and retaining walls (Richards 1985; Thomas et al. 2009).

Shallow landslides are frequently reported in expansive soil regions all over the world (Widger and Fredlund 1979; Day 1994; Azañón et al. 2010; Hou et al. 2013). On a natural or formed sloping ground without influence of adjacent infrastructure, the swelling potential can be largely released through free swelling deformation in the direction normal to sloping surface. Conversely, the swelling potential will be converted to lateral stress by physical constraints in the direction along the sloping direction. The induced stress in excess of soil's resistance has to be digested by means of irrecoverable straining. The swelling-induced stress redistribution and associated displacements have been observed to play a vital role in initiating the sliding failure of slope shallow layer from both centrifuge model tests (Cheng et al. 2011) and field studies (Ng et al. 2003). Despite the expected significant impact, such interplay between the increasing stress accompanied by decreasing suction and increase in failure potential of slope has not yet been satisfactorily investigated and quantified.

Early classical works relied on the limit equilibrium concepts (Morgenstern and Price 1965, Duncan 1996; Widger and Fredlund 1979) or finite element techniques (Griffiths and Lane 1999; Stianson et al. 2011) for evaluation of slope stability. The studies assume a positive or zero water

pressure between the soil particles, which could lead to insufficient interpretation of soil behaviour in unsaturated zone that typically presents in an expansive soil slope. More recent numerical investigations on slope stability based on unsaturated soil mechanics have focused on simulating the hydrological variations within the sloping stratigraphy in response to rainfall events, using one (e.g Griffiths and Lu 2005; Ali et al. 2014; Chen and Zhang 2014) or two (e.g. Calabresi et al. 2013; Tommasi et al. 2013; Zhou et al. 2016) dimensional simplifications or a more realistic three dimensional models (e.g. Cai et al. 1998; Ng et al. 2001). These approaches appear to be able to provide reliable stability evaluation of slopes with non-expansive soils, such as residual soil slopes (Rahardjo et al. 2013). A number of coupled hydro-mechanical analyses have also been carried out on hypothetical slopes with simple geometry characteristics (e.g. Cho and Lee 2001; Qi and Vanapalli, 2015). Several case histories involving moderate to highly expansive soils have also been analyzed in detail in the recent literature (e.g. Alonso et al. 2003; Zhan 2003; Rouainia 2009; Hamdhan and Schweiger 2013) using coupled approaches by integrating the mechanical response into a whole framework. These documented case studies highlighted the high sensitivity of simulation results to specified hydraulic conductivity values and emphasized the importance of proper selection or calibration of the hydraulic conductivity (Alonso et al. 2003; Rouainia 2009).

Taking advantage of the fact that the failure surface is shallow, in the previous chapter the infinite slope formulation is used to address explicitly the role played by swelling-induced stress in expansive soil slope stability. One of the key goals of this chapter is to further assess the potential of this infinite slope formulation (Qi and Vanapalli 2016) to realistically quantify stresses and deformation in expansive soil slopes against a published field investigation (Ng et al. 2003).

The slope in field was well instrumented and monitored under two different artificially sprinkled rainfalls, with plentiful experimental and field data pertaining to both hydrologic and

mechanical responses (Ng et al. 2003). In addition to the behaviour accompanied by swelling, one important observation was that a perched water regime has formed twice (during two intensive artificial rainfalls) within the near-surface zone. The surficial soil was fully saturated during the rainfall period in spite of high initial suction in this zone. This implies that an essential physical phenomenon occurred in the surficial soil (i.e. the state transition between saturation and unsaturation), which needs to be smoothly modeled in numerical techniques. Most of the conventional unsaturated soil models are not capable of addressing the saturated soil behaviour when pore water pressure becomes positive, including the one adopted in Qi and Vanapalli (2016). In order to address this limitation, two key modifications are introduced to the algorithm described in Qi and Vanapalli (2016): (*i*) replacing the extended Mohr-Coulomb shear strength criterion (using the constant friction angle ϕ^b for shear strength associated with suction) with the Vanapalli et al. (1996) model as the yielding function, and (*ii*) implementing newly proposed models for elastic moduli which vary nonlinearly over suction similar to that of degree of saturation *vs.* suction. The modified algorithm can smoothly model the state transition regardless if the soil element is in elastic or plastic stages. This is a requisite for using elasto-plastic constitutive models to simulate state transition in unsaturated soils, as suggested in the formulation of the SFG model (Sheng et al. 2008).

This chapter presents the simulation results for hydraulic response using SEEP/W and for mechanical response using the infinite slope formulation with the modified algorithm, including variation of pore water pressure, evolution of swelling-induced stress regime, and recoverable and irrecoverable straining and displacements. Derivations of constitutive parameters (including those for hydraulic model and the newly proposed elastic moduli models) from available experiment data are discussed. Comparison between simulations and measurements are provided. These

results demonstrate that the most important observations in hydraulic and mechanical responses of unsaturated expansive soil slope under transient rainfall conditions can be reasonably well simulated using the proposed numerical procedure.

5.2 General information of the field test

An open channel that forms part of a huge infrastructure project for transferring the potable water from southern tropical regions to northern arid and semi-arid areas was constructed in Zaoyang, Hubei, China. Due to unfavorable engineering characteristics of unsaturated expansive soils in this area, it is challenging to design safe dimensions of the cuts or fills along this canal as well as to maintain their stability under extreme environmental conditions, e.g. high intensity rainfall and(or) fluctuations of water level (Bao et al. 2001). In order to better understand the failure mechanisms of expansive soil slopes upon wetting, comprehensive field tests were carried out at two selected sites (one was a bare slope and the other a grassed one) along this open channel and well documented in Ng et al. (2003) and Zhan et al. (2007), respectively. This chapter focuses on simulation of the bare slope, only information pertaining to the bare slope test are summarized here.

The borehole logs have suggested that the soil stratum typically consisted of mainly a yellow-brown clay, with active minerals (including illite and montmorillonite) of 47-57% in total. Two sprinkling tests were conducted during the experimental period in 2001: the first was from 18 to 25 August (7 days) and second was from 8 to 10 September (3 days), in between no-rain period lasted for two weeks. The rainfall intensity varied from day to day with an average value of 60 mm/day. The time history of a number of parameters was investigated during the monitoring period to characterize the spatial and temporal variability in near-surface hydrologic and

mechanical responses in the experimental areas, including pore water pressure (by tensiometers), soil suctions (by thermal conductivity sensors), volumetric water content (by Theta Probes), total horizontal stress changes (by earth pressure cells), horizontal displacement (by inclinometer) and vertical swelling (by movement point), in addition to other recordings (Ng et al. 2003). The devices pertaining to hydrologic measurements were concentrated at three locations along the sloping direction shown in Fig. 5.1, denoted as R1, R2 and R3 at the upper, middle and lower part of the slope, respectively.

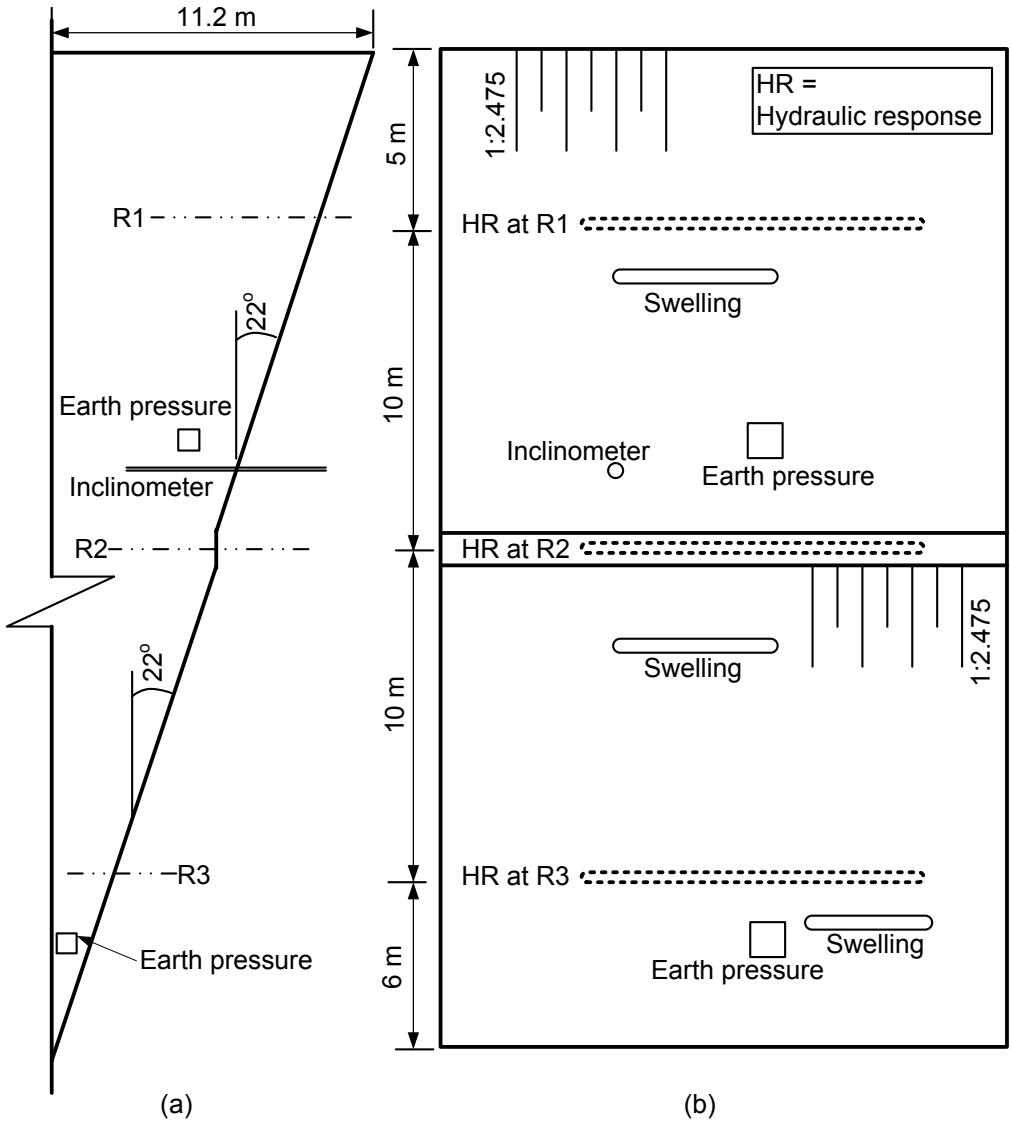

Fig. 5.1. The measurements simulated in the present study (modified after Ng et al. 2003): (a) cross-section (b) plan layout

The hydrologic data indicated that the water flow in response to the rainfall infiltration was predominantly vertical percolation in the near surface vadose zone. Perched water regimes have been inferred from the pore water pressure profiles during both rain periods at all three locations despite how dry the soils initially were. The formation of perched flow regime may be attributed

to an impermeable soil layer at around 1.5 depth, which was also derived from the soil borehole data. The flow regime was less affected by rainfalls below this depth. This constitutes an important consideration for establishing the virtual model stratigraphy in SEEP/W analysis and will be discussed in greater detail in a later section. The near surface vertical percolation exerted the most direct control on mechanical responses recorded near these three locations, including change of stress regime, vertical displacement indicating swelling and horizontal displacement implying potential sliding movement.

The near-surface measurements shown in Fig. 5.1 are simulated with a one-way hydro-mechanical coupling methodology described in the next section. The measurements at the middle slope (pertaining the hydraulic response at R2 and nearby mechanical response) are used to calibrate the established model, which is then validated by several measurements near the top and bottom of the slope. The constitutive models and parameters required in the simulation will also be discussed later.

5.3 Methodology

5.3.1 Hydraulic analysis

The water flow through a domain of interest can be modeled by solving the well-known Richards' equation (1931) with Darcy's Law

$$\frac{\partial \theta_w}{\partial t} = \nabla(k \nabla H_d) \tag{5.1}$$

where θ_w is volumetric water content, ∇ is the gradient operator, t is time, k is the hydraulic conductivity of soils. H_d is the total hydraulic head and equal to $u_w/\gamma_w + y$, where γ_w is the unit

weight of water, y is elevation and u_w is pore water pressure. u_w is positive in saturated zone and negative in unsaturated zone. Both the θ_w and k are designated as nonlinear functions of negative pore water pressure in unsaturated zone, namely soil water characteristic curve (SWCC) and hydraulic conductivity function (HCF).

A mechanical model for stress-strain analysis can utilize the pore water pressure from either analytical (Griffiths and Lu 2005) or numerical (e.g. SEEP/W (Geo-slope international Ltd. 2007)) solutions to Eq. (5.1). Most existing analytical solutions to Eq. (5.1) are limited to certain types of SWCC and HCF (e.g. van Genuchten 1980; Gardner 1958), to simple boundary conditions, and to one-dimensional problem. It is worth mentioning that, to model the infiltration flow through an infinite slope, Zhan et al. (2013) derived an analytical solution based on a modified form of Eq. (5.1) (where $H = u_w/\gamma_w + y\cos\beta$, and β is slope angle) using the Gardner (1958) hydraulic model. Some comparative studies (Zhan et al. 2013; Li et al. 2013) confirmed that the actual infiltration through surficial sloping layer can be adequately simulated using *one-dimensional* model with appropriate calibrations, using these analytical solutions. This is particularly true for scenarios where the water predominately flows in the direction normal to ground surface, such as the case investigated in this chapter. However, there are difficulties in applying these analytical solutions to practical problems with multiple soil stratum and irregular initial and boundary conditions. To accommodate these complexities, the numerical solution under one-dimensional condition was used to simulate the hydraulic response with the commercial software SEEP/W (Geo-slope International Ltd. 2012). One of the obvious numerical advantages of one-dimensional model is that it alleviates excessive computational expenses, which can be substantial for addressing highly nonlinear problems associated with two functional hydraulic properties.

The closed-form van Genuchten (1980) and van Genuchten and Nielsen (1985) models are used to generate the two functional hydraulic properties (i.e. SWCC and HCF), which are summarized thru Eqs (5.2) to (5.5):

$$\theta_e = \frac{\theta_w - \theta_r}{\theta_s - \theta_r} = \left[\frac{1}{1+(as)^n}\right]^m \tag{5.2}$$

$$S_e = \frac{S - S_r}{1 - S_r} = \left[\frac{1}{1+(as)^n}\right]^m \tag{5.3}$$

$$k_r = S_e^{1/2}\left[1-(1-S_e^{1/m})^m\right]^2 \tag{5.4}$$

$$k = k_s k_r \tag{5.5}$$

in which, both the effective volumetric water content θ_e and effective degree of saturation S_e (calculated as function of respective current values (θ_w, S), saturated values (θ_s, 1) and residual values (θ_r, S_r)) are related to suction s using the same types of function with three fitting parameters a, n, m. The parameter m is usually related to n with $m = (n\text{-}1)/n$. It should be noted that slight differences in three fitting parameters between Eqs. (5.2) and (5.3) may arise from errors in measurement of dataset, volumetric change of soil sample as suction varies, or a combination of both. Eq. (5.2) is required to make Richard's equation determinant. Eq. (5.3) is used to derive the relative hydraulic conductivity (see Eq. (5.4)) and to predict the unsaturated shear strength and stiffness properties in mechanical analysis as discussed in a later section. The unsaturated hydraulic conductivity k is calculated from relative conductivity using saturated value k_s as a reference (see Eq. (5.5)).

5.3.2 Mechanical analysis

In the framework of the infinite slope formulation described in Qi and Vanapalli (2016), elasto-plasticity was adopted to model the mechanical behaviour of soil in unsaturated zone. The stress-strain constitutive matrices for elastic (under yielding surface) and elasto-plastic (on yielding surface) phases are written, respectively, as:

$$d\boldsymbol{\sigma} = \mathbf{D}d\boldsymbol{\varepsilon} - \mathbf{h}ds \tag{5.6}$$

$$d\boldsymbol{\sigma} = \mathbf{D}^{p\varepsilon}d\boldsymbol{\varepsilon} - \mathbf{D}^{ps}ds \tag{5.7}$$

where, $d\boldsymbol{\sigma}$, $d\boldsymbol{\varepsilon}$ and ds are the incremental net stress, strain and suction, respectively. The net stress is total stress in excess of pore air pressure, (σ - u_a), and suction is pore air pressure in excess of pore water pressure, $s = (u_a - u_w)$. The pore air pressure is assumed to be atmospheric in the present study. **D** is the elastic constitutive matrix associated with change in net stress, which has the same form as for saturated soils and can be determined using Young's modulus, E, and Poisson's ratio, μ. **h** is a vector for volume change of soil structure associated with incremental suction and can be determined using elasticity modulus H. $\mathbf{D}^{p\varepsilon}$ and $\mathbf{D}^{ps}$ are the elasto-plastic constitutive matrices associated with strain and suction increments, respectively, which are derived from elastic parameters, yield function and plastic potential using theory of plasticity. $\mathbf{D}^{p\varepsilon}$ is equivalent to the commonly used notation, $\mathbf{D}^{ep}$, for saturated condition. The components of **D**, **h**, $\mathbf{D}^{p\varepsilon}$ and $\mathbf{D}^{ps}$ and their derivations are given in the Appendix.

The constitutive model adopted in Qi and Vanapalli (2016) is a practical elasto-plastic model that combines the extended Mohr-Coulomb shear strength criteria (Fredlund and Morgenstern 1978) as yield function with nonlinear elastic behaviour (elastic parameters, E and

H, derived from state surface approach suggested in Vu and Fredlund (2006) for expansive soil) under yielding surface. The nonlinearities associated with both elastic and elasto-plastic behaviours in Eqs (5.6) and (5.7) were solved using a numerical integration algorithm, which was based on modified Euler's scheme with automatic error control by treating suction as a "strain" variable, following the procedure formulated in Sheng et al. (2003) and Sołowski and Gallipoli (2010).

The extended Mohr-Coulomb criteria (Fredlund and Morgenstern 1978) assumes a linear increase of shear strength relative to suction with a parameter ϕ^b quantifying the increase rate. It has also been used as a yield function in elasto-plastic numerical modeling of unsaturated soils by several investigators (e.g. Le et al. 2015; Sołowski et al. 2014). However, it is not effective once soil approaches saturated states, neither is the elastic matrix described using *E* and *H* derived from state surface approach. This discontinuity at the transition between saturated and unsaturated states is the limitation of most existing unsaturated soil models formulated using two stress state variables approach (i.e. net stress and suction). A transformation of this group of models to effective stress space was recommended by Sheng (2011) in numerical implementation for modelling unsaturated soil problems involving state transition, for example, using the concept of constitutive stress (Sheng et al. 2003, 2004; Griffiths and Lu 2005).

In the shallow layer that is of primary concern in the case study herein, the perched water regime formation has been observed during the two artificial rainfall events from an initially drying condition, as suggested before. This suggests at least four switches of soil states: unsaturated (initial) → saturated (first rainfall) → unsaturated (no rain period) → saturated (second rainfall) → unsaturated (no rainfall). In order to model them smoothly, two modifications are made into the practical model implemented in the algorithm introduced in Qi and Vanapalli (2016). The first

one is related to the yielding surface and the second to the elastic component. These two aspects have to been integratedly considered in realizing both pure elastic and elasto-plastic state transitions, as suggested in formulation of the SFG model (Sheng et al. 2008).

First, the extended Mohr-Coulomb strength criterion is replaced with the nonlinear shear strength model proposed by Vanapalli et al. (1996) as the yield function:

$$\tau_f = c' + \sigma \tan\phi' + sS_e \tan\phi' \tag{5.8}$$

in which, σ is the net normal stress, s is the suction, c' and ϕ' are effective cohesion and effective angle of internal friction at saturated condition. In Eq. (5.8), the contribution to shear strength from suction is scaled by effective degree of saturation S_e at current suction value s, which is usually calculated from a continuous SWCC, such as the van Genuchten (1980) model (i.e. Eq. (5.3)). Eq. (5.3) was established for unsaturated zone where the value of suction s is non-negative or pore water pressure is non-positive. However, it is not physically meaningless when the soil is in saturated condition with a positive pore water pressure or negative suction s, and numerically gives a complex number since parameter n is rarely an integer from a regression analysis. To avoid the numerical issue, Eq. (5.3) is coded in the algorithm as

$$S_e = \frac{S - S_r}{1 - S_r} = \left[\frac{1}{1 + [a \cdot \max(0, -u_w)]^n} \right]^m \tag{5.9}$$

in which, $-u_w$ is numerically equal to s since pore air pressure is assumed to be atmospheric. The effective degree of saturation, S_e, from Eq. (5.9) gradually approaches unity as the soil undergoes a transition from unsaturated to saturated state, and remains unity thereafter. Correspondingly, Eq.

(5.8) reverts to that for saturated soil based on Terzaghi effective stress principle with a smooth transition.

$$\tau_f = c' + (\sigma + s)\tan\phi' \tag{5.10}$$

The second modification is associated with quantification of nonlinearities of two elastic moduli in both unsaturated (E_{unsat} and H_{unsat}) and saturated (E_{sat} and H_{sat}) conditions. In the context of saturated soil mechanics, the saturated elastic modulus, E_{sat}, is usually derived by differentiating the void ratio *vs.* effective stress curve for numerical implementation of some basic and advanced constitutive models (Potts and Zdravkovic 1999; Sheng et al. 2000). This approach was followed by Vu and Fredlund (2006) and Qi and Vanapalli (2016) where a differentiation was carried out on a three-dimensional void ratio constitutive surface. This differentiation did provide nonlinear variations of elastic parameters (E_{unsat} and H_{unsat}) in the space of net stress and suction as long as soils are in an unsaturated state. However, the resulted stress-strain relationship appears to be invalid for saturated state where pore water pressure and total stress should have equivalent effect on the volume change behaviour. Alternatively, saturated elastic modulus can be expressed as a power equation of effective stress with fitting parameters determined from experimental data. This approach is also in frequent use in numerical analysis (e.g. Locat et al. 2015). Rahardjo et al. (2011) extended the power law for unsaturated soils' modulus by including a suction-related component. However**,** the net contribution of suction towards the volume change behaviour has been shown to be directly influenced by water content (Wheeler et al. 2003, Lu and Kaya 2014), This is because the effect of suction on the soil skeleton is transmitted through water filled in the voids between particles. To account for the influence of water content, Oh et al. (2009) proposed the following equation for elasticity modulus of unsaturated soils

$$E_{unsat} = E_{sat}\left[1+\alpha\frac{s}{P_a/101.3}S^{\beta}\right] \tag{5.11}$$

in which, E_{unsat} is soils' elastic modulus under unsaturated condition, E_{sat} is soils' elastic modulus at saturated condition, α and β are two model parameters, and P_a the atmospheric pressure (i.e. 101.3 kPa) for maintaining consistency of units. The similarity shared by Eqs. (5.11) and (5.8) is that the contribution of suction on both mechanical properties is quantified using (effective) degree of saturation (an indicator of amount of water) to a power of β (β = 1 in Eq. (5.8)), thus, the advantage of Eq. (5.8) that assures continuity between the saturated and unsaturated states is inherited by Eq. (5.11). One shortcoming of Eq. (5.11) is that it is not flexible for a wide range of net stress level since it was originally established from data at a low stress condition (Oh et al. 2009). Some experimental data (e.g. Rahardjo et al. 2011) showed that there was a distinct coupling effect between suction and mechanical stress. In other words, the value of α in Eq. (5.11) varies with the mechanical stress with a different trend than that of E_{sat} over the mechanical stress. Based on these considerations, the elastic moduli in this study are proposed by combining the power law and concept of Eq. (5.11), and expressed as

$$E_{unsat} = E_{sat} + \left[\alpha_E P_a\left(\frac{\sigma}{P_a}\right)^{\kappa_E}\right] sS^{\beta_E} \tag{5.12}$$

$$H_{unsat} = H_{sat} + \left[\alpha_H P_a\left(\frac{\sigma}{P_a}\right)^{\kappa_H}\right] sS^{\beta_H} \tag{5.13}$$

in which

$$E_{sat} = K_E P_a\left(\frac{\sigma}{P_a}\right)^{M_E} \tag{5.14}$$

$$H_{sat} = \frac{E_{sat}}{1-2\mu} = K_E P_a (\frac{\sigma}{P_a})^{M_E} /(1-2\mu) \quad (5.15)$$

where, α_E, β_E, κ_E and α_H, β_H, κ_H are model parameters for elastic moduli E_{unsat} and H_{unsat}, respectively. Eqs. (5.12) and (5.13) account for the influence of net stress on variation of moduli with suction by replacing constant α with a power function, which greatly increases the flexibility of the models fitted to experimental data, with only one additional model parameter compared to Eq. (5.11). Eq. (5.14) is the simplest power law for saturated soils, where K_E and M_E are experimental constants. It is important to note that there is no physical definition of suction modulus H_{sat} at saturated condition, but the numerical value of H_{sat} should indicate the same effects of positive pore water pressure and total stress on volume change behaviour, which can be accounted for by the mathematical relation of Eq. (5.15), where v is the Poisson's ratio. Eqs. (5.12) through (5.15) along with Eqs. (5.8) through (5.9) will assure a smooth state transition regardless if it occurs in elastic or elasto-plastic stages. In other words, both the elastic and elasto-plastic matrices (see Eqs. (5.6) and (7)) derived from these equations are continuous when the soil switches from unsaturated state to saturated state, or vice versa. Detailed derivations can be found in the Appendix.

5.4 Simulating hydraulic response

5.4.1 Model description

Since SEEP/W (Geo-slope International Ltd. 2012) is coded for two-dimensional problems, the one-dimensional solution is achieved by performing seepage analysis on a thin and long soil column. Similar treatment in simulating one-dimensional condition has also been used by other researchers (e.g. Thomas and He 1998). The model established for simulating hydraulic response at R2 has a height of 8 m and a width of 0.2 m (Fig. 5.2). A simple two-layer system (a low-

permeability stratum underlying a more conductive layer of 1.5 m thickness) is used to model the hydraulic heterogeneity of the stratigraphy along the vertical direction. The transient seepage simulation is carried out from 18 August to 12 September 2001. The initial condition is constructed using the spline function in SEEP/W based on the several measured data of pore water pressure on 18 August 2001. The real-time rainfall data is applied on the top as time-dependent flux boundary (Neumann boundary condition). A zero water pressure head is specified as the bottom boundary (Dirichlet boundary condition), based on the observation that the ground water table in the deep flow regime was located around this depth of 8 m. Zero flux is assigned to the two side boundaries (Neumann boundary condition) to form a quasi-one-dimensional flow similar to Thomas and He (1998). A number of trial simulations showed that the calculated results, with sufficient accuracy from the numerical point of view, can be achieved when computational domain is discretized using only 320 quadrilateral elements (2 in horizontal direction × 160 in vertical direction) with a total of 483 nodes. It can be expected that the required computational time can be substantially reduced by using such a one-dimensional model, which is of significance when the computation has to be repeated many times; for example, for back analysis or sensitivity analysis (whether in terms of mesh size or material properties).

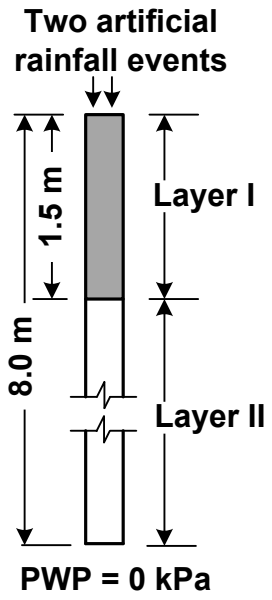

Fig. 5.2. Seepage model established for hydraulic analysis.

5.4.2 Soil hydraulic properties

Two sets of data for SWCC were reported by Zhan and Ng (2006) and Zhan et al. (2007) for Zaoyang clay in the field slope, one measured on natural and the other on compacted sample. (see Fig. 5.3). The difference in the water storage characteristics exhibited by natural sample from that of compacted sample can be attributed to the interactions with atmosphere, which continuously alters the soil's micro-structure, and also contributes to the development of cracks in expansive soil. Use of these two sets of data to represent the water storage characteristics of soils in layer I and II, respectively is justifiable. Fig. 5.3 illustrates SWCCs obtained from regression analysis using van Genuchten (1980) model performed on the measured data. The respective fitting parameters for both volumetric and degree of saturation are summarized in Table 5.1.

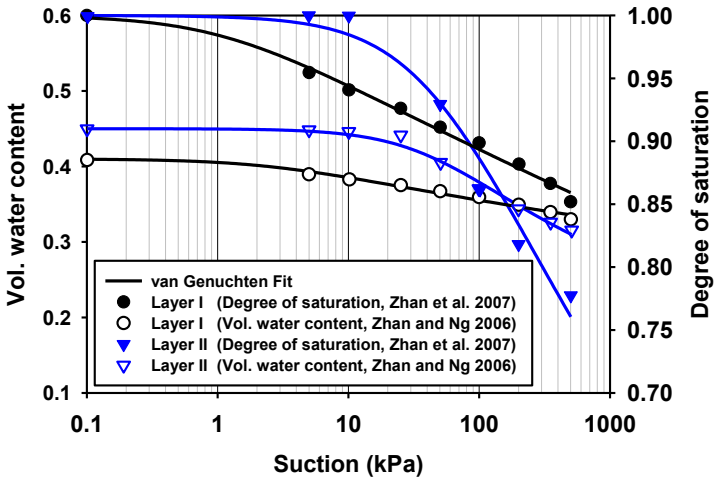

Fig. 5.3. SWCCs for Zaoyang Clay in terms of volumetric water content and degree of saturation.

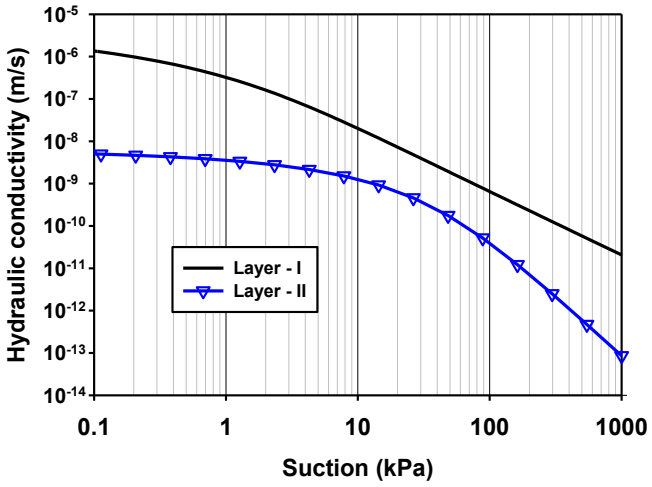

Fig. 5.4. Hydraulic conductivity functions for Zaoyang Clay used in seepage analysis.

Table 5.1. Hydraulic parameters used in the present study

Parameters	Symbol	Units	Layer I	Layer II
Saturated volumetric water content	θ_s	%	41.0	45.0
Residual volumetric water content	θ_r	%	20.0	18.0
* Fitting parameter	a	kPa^{-1}	0.368	0.022
* Fitting parameter	n		1.083	1.301
Saturated degree of saturation	S_s	%	100	100
Residual degree of saturation	S_r	%	20	20
† Fitting parameter	a	kPa^{-1}	0.901	0.020
† Fitting parameter	n		1.032	1.150
Saturated permeability	k_s	m/s	1.00×10^{-5}	5.79×10^{-9}†
Parameter	m		0.115†	0.13

Note: * van Genuchten (1980) fitting parameters for SWCC in terms of volumetric water content; † in terms of degree of saturation, † from back calculation.

It is quite difficult to reproduce the pore water pressures recorded by in-situ instrumentation using the hydraulic conductivity model (defined by Eq. (5.4)) with a single measured saturated value for the entire domain. The reason for this varies: (*i*) the established numerical stratigraphy cannot completely cover the complicated soil stratigraphy at every spatial point in the field, the soil's hydraulic conductivity may differ spatially and temporally. (*ii*) most hydraulic conductivity models in the literature (including Eq. (5.4)) are proposed based on the data for sandy type of soils which may not adequately represent the flow behaviour of clayey soils (Bani Hashem and Houston 2015); (*iii*) the presence of opening crack induced by soil shrinkage, particularly in expansive soils, might make the soil more conductive. (i*v*) there may be time lag in the response of certain instrumentation readings (e.g. suction measurements) in the field tests. Therefore, for simulation of the field conditions, a numerical parametric study is often conducted to obtain the most representative HCF by changing the saturated hydraulic conductivity (Alonso et al. 2003; Qi and Vanapalli, 2015) or the function shape (Tommasi et al. 2012). The representative HCFs in the

present study are obtained by adjusting a minimum number of model parameters on the basis of van Genuchten and Nielsen (1985) hydraulic conductivity model and available in situ measurements. It was reported by Zhan et al. (2007) that hydraulic conductivity of natural Zaoyang clay varied by three orders of magnitude from 10^{-7} to 10^{-4} m/s, depending on the cracks variability from the double-ring infiltration measurements. Based on this observation, a saturated hydraulic conductivity of 10^{-5} m/s is assigned to layer I, this value is also close to a typical value of 2×10^{-5} m/s for cracked soil estimated by Tommasi et al. (2013) using the equation $k = -\gamma_w a_h^3/(12\mu_w d)$, where γ_w and μ_w are the bulk unit weight and dynamic viscosity of water, respectively. a_h is the average hydraulic aperture of the fractures (calculated as a function of the observed aperture, a, and joint roughness coefficient, i.e. $a_h = a^2/\mathrm{JRC}^{2.5}$), and d is the average fracture spacing. The presence of cracks might also alter the shape defining the variation of hydraulic conductivity over suction, which is mostly reflected by parameter m in Eq. (5.4) (van Genuchten and Nielsen 1985). The value of m in Eq. (5.4) is usually set to be identical to that in Eq. (5.3) (van Genuchten 1980) from regression analysis, but is allowed to vary to account for the influence of cracks in layer I. In contrast to layer I, the model parameter m is fixed as that in original model for intact soil in layer II. The impermeable effect of layer II is modeled by gradually decreasing the saturated hydraulic conductivity to simulate lesser effect of rainfall on the layer below 1.5 m depth. In this way, only one parameter in the HCF needs to be back-calculated for each layer. This approach is not completely blind, but is based on a well-known model and some field observations. It is found that, when the '*m*' for layer-I is increased to 0.115 and k_s for layer-II is decreased to 5.79×10^{-9} m/s (see Table 5.1), the predicted and measured pore water pressures are in good agreement with each other, as presented in the following section. Fig. 5.4 shows the HCFs adopted in the numerical simulation.

The decreased '*m*' indicates a more conductive soil at high suction level, reflecting the effect of presence of cracks, which provides preferential flow path for the rain water.

5.4.3 Pore water pressure

Fig. 5.5 provides comparisons between the predicted pore water pressure with the measured values from Ng et al. (2003) at several depths at R2, namely, 0.6 m, 1.2 m, 1.4 m and 1.6 m. The observed changing trend of pore water pressures over time is well reproduced using the established numerical model and half-blind back-calculated hydraulic conductivities, including: (*i*) about 2-day delay in the response of pore water pressure to the first rainfall; (*ii*) rapid suction loss (from unsaturated to saturated states) during the first rainfall; (*iii*) suction rebound (decrease of positive pore water pressure) during the no-rain period between two rain events. The predicted magnitudes of rebounds are slightly lower than those observed in the field, which is probably due to the evaporation effect during no-rain period not accounted for in the numerical model. The actual evaporation rate from bare soil surface is highly coupled with near-surface unsaturated flow, affected by many climatic factors with much uncertainty (Wilson et al. 1994), and difficult to be predicted accurately (Zhang and Briaud 2015). Ongoing research on modeling evaporation is promising for proposing better models or approaches in the near future (Tran et al. 2016).

The predicted suction rebounds are a consequence of redistribution of pore water pressure under the unbalanced hydraulic gradients at the end of the first rainfall. This can also be seen in Fig. 5.6, which provides the comparison between the predicted pore water pressure profiles with the measured values in the field at several elapsed times (Ng et al. 2003). At the end of the first rainfall, a perched water zone has developed above the elevation of 1.5 m below ground surface

and Layer I has been fully saturated, in which the pore water pressures are essentially higher than those in layer II.

The resulting hydraulic gradient is generally downwards and brings the water from layer I to layer II during the two-week no-rain period. Consequently, the pore water pressure increases further below 1.5 m depth and decreases from the hydrostatic line above 1.5 m depth with a part of layer I becoming unsaturated. During the second rainfall period, the pore water pressure increases to hydrostatic state again within layer I and the pore water pressure increases further in layer-II. The zone that has been affected by these two rainfalls is limited to around the depth of 4 m. The good agreements between predictions and measurements indicate the reliability of the established one-dimensional simplified model along with the back-calculated hydraulic properties to reproduce the hydraulic response of this expansive soils cuts to rainfall. This can be further confirmed by reasonable agreements between the predictions using the model with the measurements at R1 (near the slope top) in Fig. 5.7.

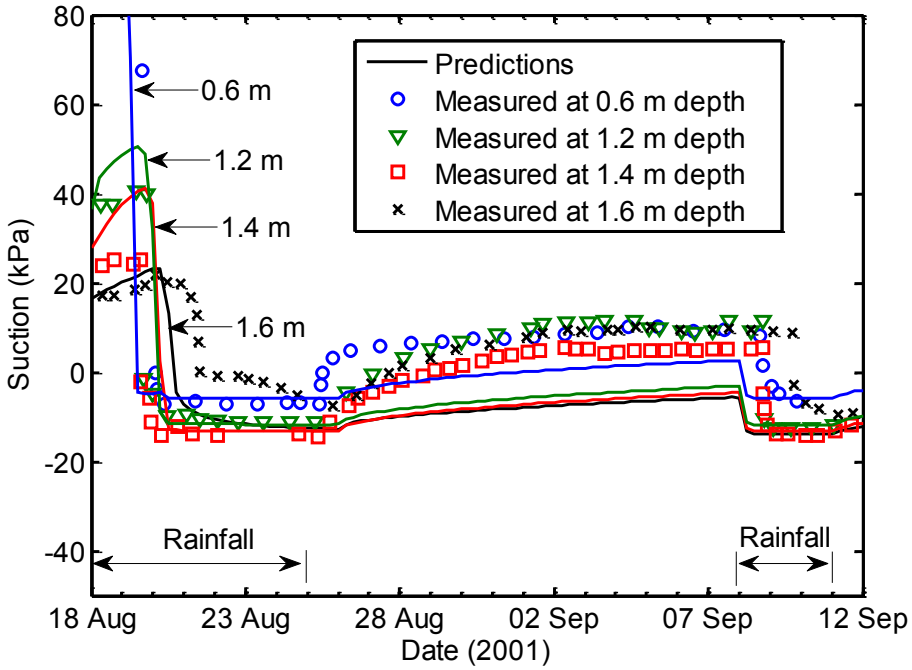

Fig. 5.5. Comparison of pore water pressure between prediction and measurement at several depths at middle slope.

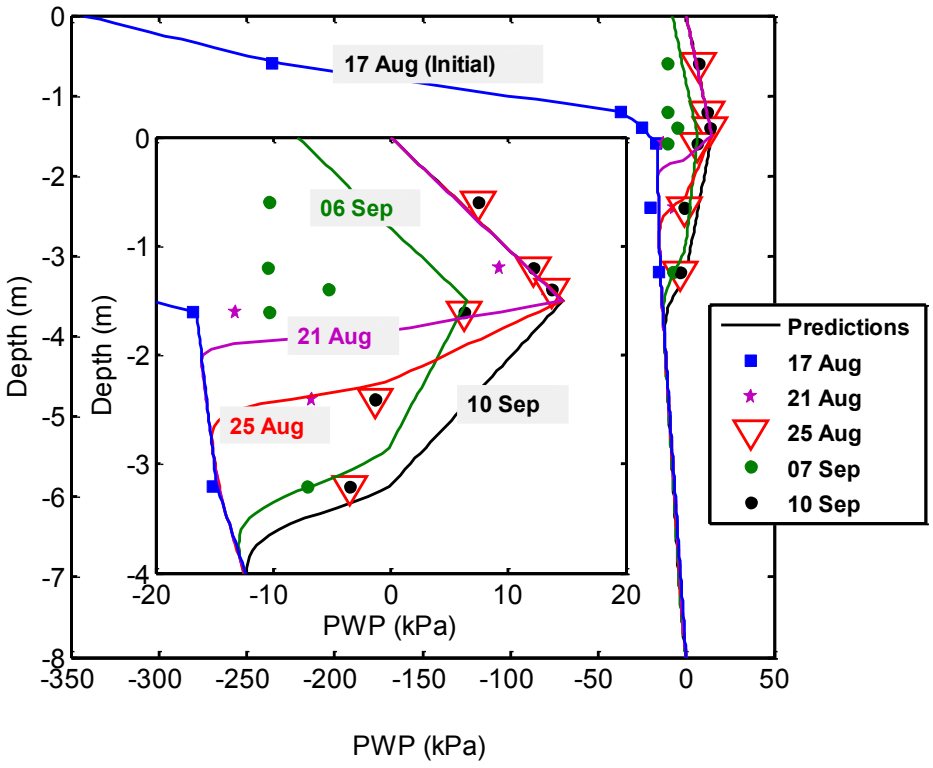

Fig. 5.6. Comparison of pore water pressure profile between prediction and measurement at several dates at middle slope.

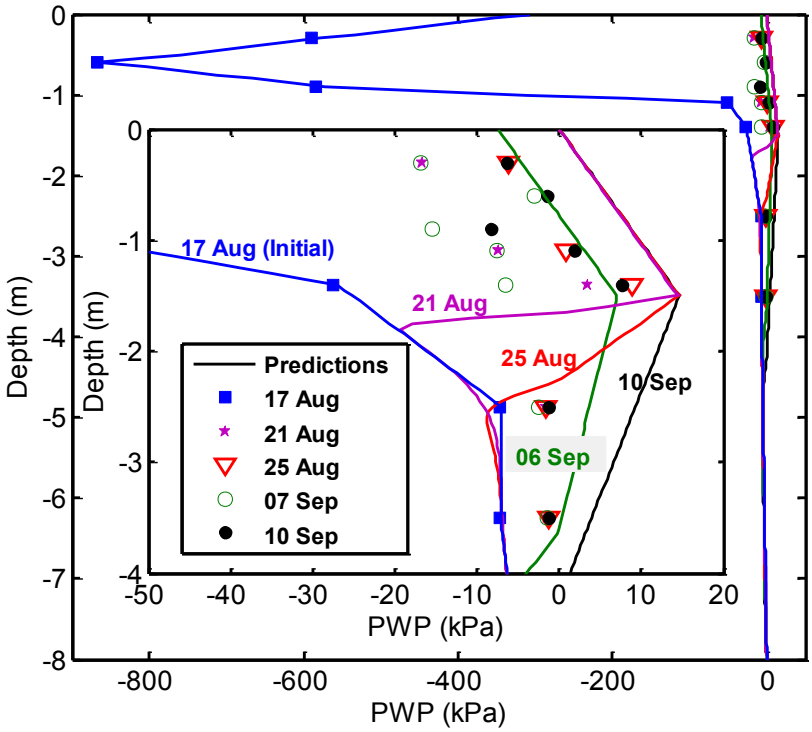

Fig. 5.7. Comparison of pore water pressure profile between prediction and measurement at several dates at R1 near the slope top.

5.5 Simulating mechanical response

5.5.1 Model description

Fig. 5.8 shows the stress field within an infinite slope under unsaturated condition, where η and ξ are the axes rotated by a slope angle, β, from the x (horizontal) and y (vertical) axes in Cartesian coordinate system, respectively. The net normal stress, σ_ξ, and shear stress, $\tau_{\xi\eta}$, at a certain depth can be determined by applying the static force equilibrium condition in the vertical direction for a unit width soil slice:

$$\sigma_{\xi} = \gamma Z \cos^2 \beta \tag{5.16}$$

$$\tau_{\xi\eta} = \gamma Z \cos \beta \sin \beta \tag{5.17}$$

where γ stands for the unit weight of the soil, Z for the element depth under the ground surface measured along the y axis. The initial net normal stress, σ_{η}, in the η direction is related to net normal stress, σ_{ξ}, by

$$\sigma_{\eta} = \mathrm{K}\sigma_{\xi} = \mathrm{K}\gamma Z \cos^2 \beta \tag{5.18}$$

where K is the stress ratio of the net normal stresses σ_{η} to σ_{ξ}. The stress ratio, K, is similar to the coefficient of earth pressure at rest. The initial stress components acting on any soil element can be determined using Eqs. (5.16) through (5.18). Upon wetting, the soil element exhibits swelling trends in all directions with decreasing suction. In the ξ direction, a certain magnitude of normal strain can be induced by swelling. The normal stress, σ_{ξ}, and shear stress, $\tau_{\xi\eta}$ will remain constant, since the entire infinite slope layer above the depth of Z is always under a static force equilibrium condition even though soil swelling occurs within it. In the η direction, the swelling-induced strain is restrained such that the net normal stress σ_{η} will be increased during a wetting process until yielding. Activation of yielding is promoted by two processes: increasing σ_{η} and decreasing s. The change of stress and elastic straining are calculated with Eq. (5.6) before onset of yielding. After yielding, the net stress σ_{η} decreases to maintain the stress state on the yielding surface that will shrink with decreasing suction. The change of stress and plastic straining are then calculated with Eq. (5.7). The development of stress and strain driven by varying suction (obtained from hydraulic analysis described in the previous section) is calculated using the improved version of algorithm in Qi and Vanapalli (2016).

To enable comparisons of global displacements between predictions and measurements, both the horizontal and vertical displacements are accumulated from bottom to top based on the strain obtained at a local level. First, the strain components in the *x*-*y* coordinates (see Fig. 5.8) are obtained through projections from those calculated in ε-η coordinates, as

$$\varepsilon_y = \gamma_{\xi\eta} \sin\alpha \cos\alpha + \varepsilon_\eta \cos^2\alpha \tag{5.19}$$

$$\gamma_{xy} = \gamma_{\xi\eta} \cos^2\alpha - \varepsilon_\eta \sin\alpha \cos\alpha \tag{5.20}$$

Then, the displacements in vertical and horizontal directions are calculated as summations of $\delta \cdot \varepsilon_y$ and $\delta \cdot \gamma_{xy}$, respectively, from the bottom, where δ is the spacing between two consecutive nodes along the vertical profile.

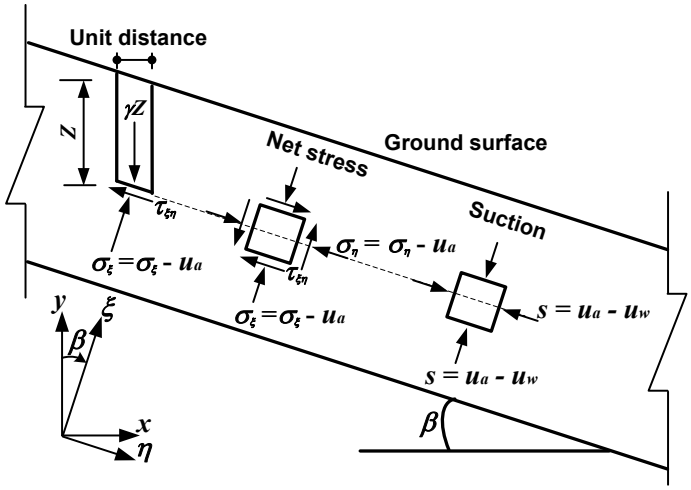

Fig. 5.8. Stress field within an infinite slope (modified after Qi and Vanapalli (2016)).

5.5.2 Soil mechanical properties

The modulus of elasticity, E, can be quantified by first fitting Eq. (5.14) to the data measured at saturated state using conventional equipment (i.e. obtaining K_E and M_E) followed by determining the remaining model parameters relevant to unsaturated states. Similar procedure can be applied to H. The suction-controlled triaxial tests (Zhan 2003) and wetting-drying tests (Zhan et al. 2013) on compacted samples of Zaoyang clay are used to derive the data for E and H, respectively. To maintain consistency, the secant slope of each stress-strain curve at 1% strain is adopted as the representing value of E. The slope of each volumetric strain-suction curve is adopted as the representing value of H following method in Meilani et al. (2005). The model parameters in Eqs. (5.12) and (5.13) are determined by regression analysis on these two sets of data. The obtained model parameters are summarized in Table 5.2, and variation of two elastic moduli with respect to two stress state variables are shown in Fig. 5.9 and Fig. 5.10, respectively. It can be seen that both moduli increase with increasing suction and net stress but with different trends. The increase of E with suction is concave downward (β_E positive) at each net stress level, while increase of H with suction is concave upward (β_H negative). The negative value of β_H implies the soils become increasingly inert in terms of the volumetric change under suction loading condition with decreasing saturation degree. This is consistent with observations in previous experiments; for example, no volume change will be observed with increasing suction once the soil state is beyond the shrinkage limit (Jennings and Burland 1962; Fredlund and Rahardjo 1993). Tsiampousi et al. (2013) used a similar but simpler power function of saturation degree for describing soil's compressibility with suction, $\kappa_s = \chi (S)^{\omega}$, where S is degree of saturation, χ and ω are fitting parameters. A positive value of ω is obtained by Tsiampousi et al. (2013), which is consistent to a

negative value of β_H in current study since H_{unsat} bears an inverse relationship to the compressibility index, i.e. $H_{unsat} = (1+e)s/\kappa_s$, where e is the void ratio.

Table 5.2. Mechanical properties used in the present study

Parameters	**Symbol**	**Units**	**Layer I**	**Layer II**
Effective cohesion	c'	kPa	9	16.2
Effective frictional angle	ϕ'	deg.	17	28.7
Dilatancy angle	φ	deg.	0	0
Model parameters for E	K_E	1/kPa	51.91	51.91
	M_E		0.691	0.691
	α_E		2.109	2.109
	κ_E		-0.214	-0.214
	β_E		4.447	4.447
Model parameters for H	α_H	1/kPa	1.618	1.618
	κ_H		0.481	0.481
	β_H		-5.934	-5.934
Poisson ratio	μ		0.40	0.40

Note that both the experimental data (Zhan 2003, Zhan et al. 2013) used above were from compacted samples to characterize the stress-deformation behaviour of soils in layer II. Correspondingly, the degree of saturation from SWCC for layer II (i.e. the one with solid down-pointing triangles illustrated in Fig. 5.3) is substituted in Eqs. (5.12) and (5.13) to obtain these model parameters (see Table 5.2) through fitting exercise. A similar regression procedure performed on experimental data from natural or undisturbed samples can provide model parameters to more appropriately reflect the soil behaviour in layer I. However, test results for this layer are limited. It is assumed that the elastic moduli (Eqs. (5.12) and (5.13)) for layer I have been approximated using the same model parameters for layer II, but with the degree of saturation being replaced with that in SWCC for layer I (i.e. the one corresponding to solid circles illustrated in Fig. 5.3). This approximation seems to be somehow rough, calibration will be used as a complement

to obtain a better simulation of field observation by adjusting a minimum number of model parameters for layer I, if necessary.

The saturated shear strength parameters reported in Zhan et al. (2007) are selected to define the yield function and plastic potential for layer II. For layer I, Ng et al. (2003) suggested that, from a simple calculation of passive stress ratio based on theoretical limiting conditions, the effective cohesion c' falls in the range of 5-15 kPa and effective internal frictional angle ϕ' is 17°. The simulated results of stress ratio using the current infinite slope formulation confirms the reasonableness of these sets of shear strength parameters. Use of c' = 9 kPa (close to the average value of the range given in Ng et al. (2003)) results in a better agreement with the measurements, and is adopted in all the simulations presented in the following sections. Dilatancy angle φ is assumed to be zero in the plastic potential for both layers to consider non-associativeness.

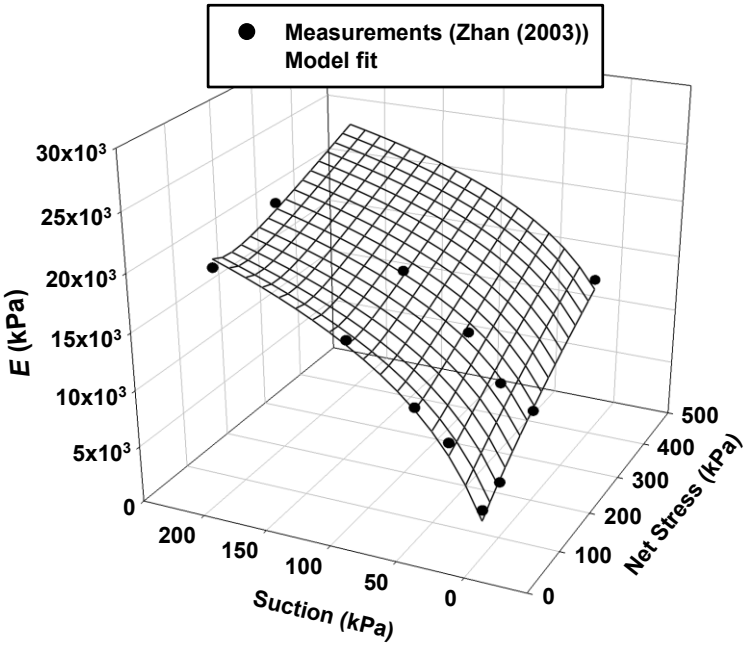

Fig. 5.9. Nonlinear variation of *E* with respect to two stress state variables

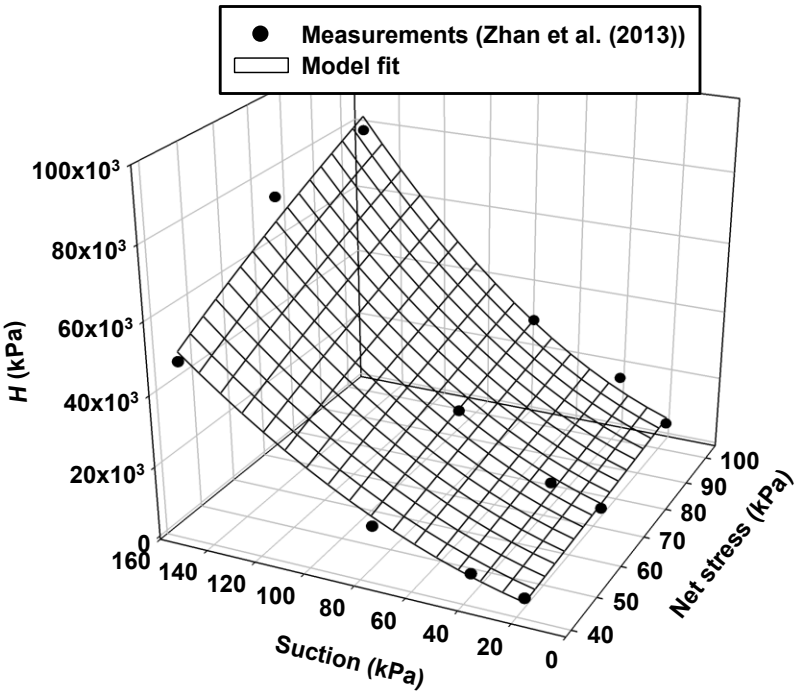

Fig. 5.10. Nonlinear variation of *H* with respect to two stress state variables

5.5.3 Horizontal/vertical stress ratio

Fig. 5.11 provides comparisons between the predicted horizontal *vs.* vertical net stress ratios, σ_η / σ_ξ , at several depths at L2, with the measurements available at 1.2 m depth. The variations of stress ratio are generally consistent with that of pore water pressures. The delayed initial increase in stress ratio has been predicted as that of pore water pressures in response to the first rainfall.

During the first rainfall, the changes in the stress ratio at three shallower depths (i.e. 0.6, 0.8 and 1.0 m) are different from those at three greater depths (i.e. 1.1, 1.2 and 1.6 m). At shallower depths the stress ratio initially increases substantially and subsequently reduces rapidly after reaching a maximum value. These maximum values indicate onset of yielding of soil elements with decreasing suctions at respective depths. Before yielding, soil swells elastically upon wetting, and induces an increase in the horizontal stress due to constraints in this direction. Once yielding initiates, the stress state should follow a trajectory along the yield surface. The size of the yield surface depicted in the net stress space will shrink with further suction decrease. Thus, the stress ratio (or the horizontal stress) is forced to decrease after yielding. It can also be seen that the maximum stress ratio varies with depth: the shallower the depth, the greater will be the stress ratio corresponding to yielding. This phenomenon is primarily attributed to the different initial pore water pressure (suction) values at different depths (see Fig. 5.6). A higher initial suction at shallow depth (i.e. close to natural ground level) indicates a wider range of suction decrease upon infiltration. Larger swelling potential can be expected in the soil element in this zone. At three greater depths (i.e. 1.1, 1.2 and 1.6 m), the initial suctions (see Fig. 5.6) or possible ranges of

suction changes are not significant enough to bring the soil element to yield. Only increases in the stress ratio due to elastic swelling of soil element are predicted (see Fig. 5.11).

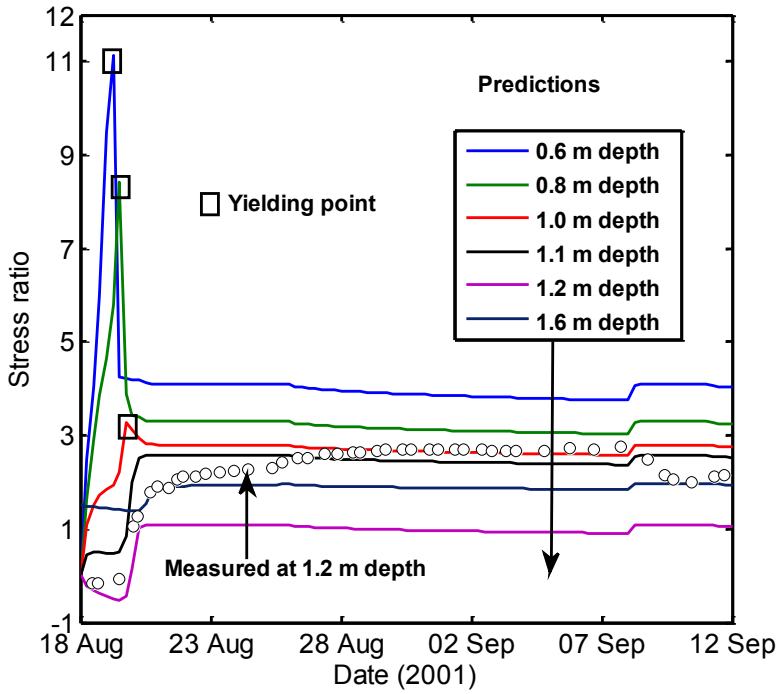

Fig. 5.11. Predicted horizontal vs. vertical stress ratios at several depths at L2 and comparison with available measurements

After the first rainfall, the stress ratios slightly decrease at all depths before rising up again during the second rainfall. This trend is somewhat different from the field observations (Ng et al. 2003), but is consistent with the pore water pressure input (i.e. Fig. 5.5) into the infinite slope model. The measured continuous increasing stress ratio after first rainfall may be associated to the ongoing 'soaking' of the soil element near the earth pressure sensor, and the measured decreasing stress ratio has been attributed to softening of the soil associated with swelling. The discrepancy

between the measurements and predictions can be explained as follows: (*i*) the input pore water pressure is obtained from simulation using SEEP/W at R2, which is close to but not exactly at location of earth pressure cell; (*ii*) it is nearly impossible to achieve perfect simulation of measured pore water pressure at all depths, particularly for this ongoing 'soaking' at a 'point' scale, even by using a more sophisticated model, in terms of the geometry, that is close to the real stratigraphy to the greatest extent possible. Nevertheless, the maximum magnitudes of stress ratio predicted at depths of 1.1 m or 1.0 m are comparable to that measured at 1.2 m depth. Furthermore, the magnitude of stress ratio corresponding to yielding at 1.0 m depth is also close to that measured at 1.2 m depth. This confirms the reasonableness of the mechanical properties (including the elastic moduli without calibration and strength parameters) adopted in the infinite slope model for the Zaoyang clay.

Fig. 5.11 shows that yielding of soil elements only occurs at shallower depths with high initial suction values near the ground surface. Plastic straining after yielding is of particular interest in slope stability due to two key reasons: *(i)* it may reduce the shear strength parameters (Qi and Vanapalli 2016); *(ii)* it can induce accumulative displacements under drying and wetting conditions for long period (Tommasi et al. 2012). Fig. 5.12 illustrates the variation of deviatoric plastic strain profile with a time interval of 0.25 day. Plastic straining occurs initially near the surface and gradually advances to greater depth, but is limited to 1.15 m depth. The majority of plastic straining is developed during the first two days of rainfall. This is because the predicted pore water pressure already decreased to the limiting profile (hydrostatic profile) on 21 August (see Fig. 5.6). After that, the soils' stress states within the entire profile go back under the yielding surface, and soil elements behave purely elastically in spite of the fluctuations of pore water pressure during drying (two-week no-rain period) and rewetting (the second rainfall) periods.

This type of stress path followed can be more clearly seen in Fig. 5.13, which illustrates the changes of stress ratio acting on soil element at several depths near the ground surface with reducing suction. The stress path at depth of 1.0 m is replotted in Fig. 5.14 for clarity purposes. For soil elements at the depths of 0.6 m, 0.8 m and 1.0 m, the stress paths are divided into three phases (see Fig. 5.14): (*i*) elastic increase of stress ratio before yielding with decreasing suction; (*ii*) plastic decrease of stress ratio after yielding with further decreasing suction or increasing positive pore water pressure; (*iii*) elastically cyclic change of stress ratio with cyclic changes of pore water pressure. During phase (*iii*), the stress ratio decreases or increases along the same trajectory when the pore water pressure decreases or increases, reflecting a pure elastic behaviour in this phase. In contrast to the stress paths at shallower depths, stress ratio increase at depth of 1.1 m with increasing suction implies no occurrence of yielding, which is consistent with observations in Fig. 5.11 and Fig. 5.12. Fig. 5.13 and Fig. 5.14 also illustrate that, when transition of soil states occurs (from unsaturation to saturation or vice versa), the soil elements at shallower depths (i.e. 0.6 m, 0.8 m and 1.0 m) are already in plastic stages while at depth of 1.1 m the soil element is still in an elastic state. This indicates the correctness of the program for dealing with the smooth state (i.e. saturated and unsaturated states) transition for both stages. The accumulated plastic strains at these depths are shown in Fig. 5.15, which are in correspondence with the evolution of stress paths in terms of three phases identified in Fig. 5.13.

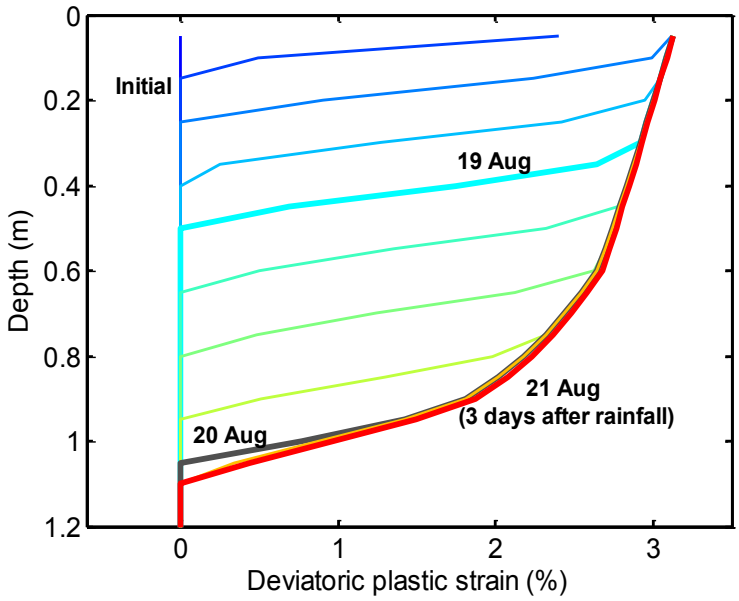

Fig. 5.12. Predicted development of plastic straining profile near the ground surface at L2

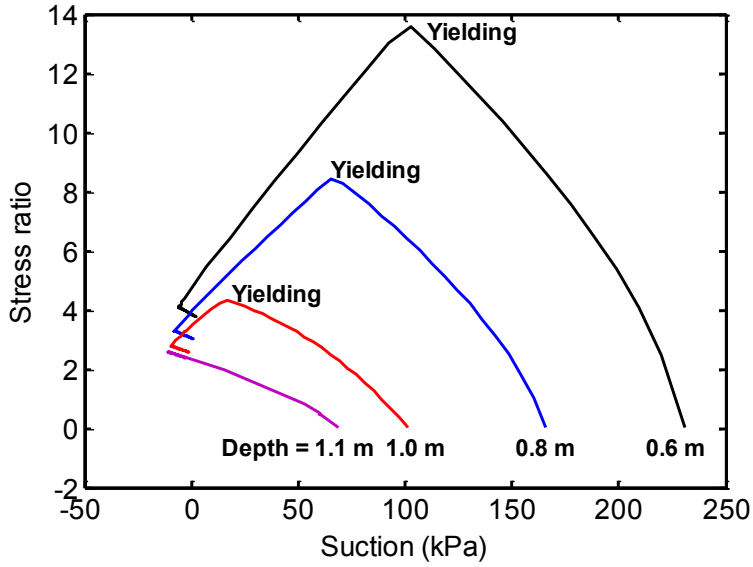

Fig. 5.13. Predicted stress paths followed at several depths near the ground surface at L2

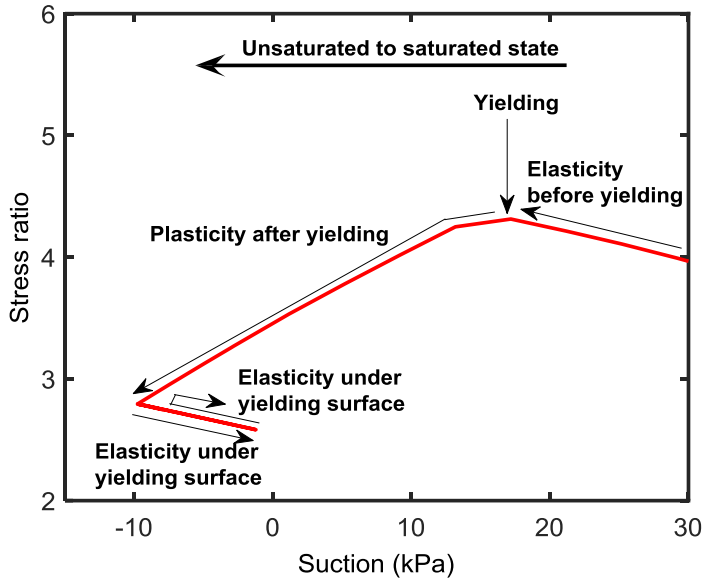

Fig. 5.14. Predicted stress paths followed at depth of 1.0 m near the ground surface at R2

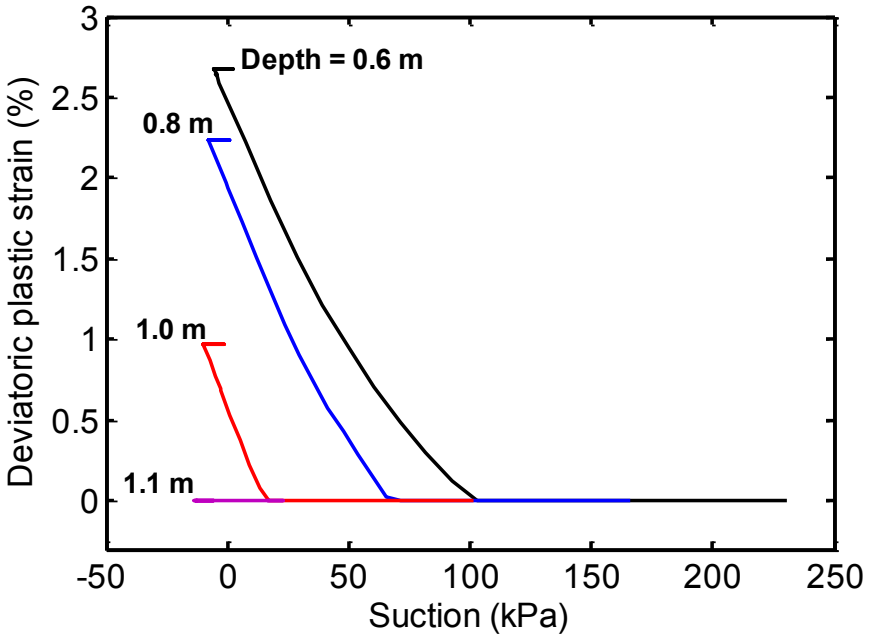

Fig. 5.15. Variation of plastic straining over suction at several depths near the ground surface

5.5.4 Swelling and displacement

Fig. 5.16 compares the vertical swelling predicted using infinite slope model to those measured using surface settlement markers at three depths. by Ng et al. (2003). The delayed soil swelling in response to the first rainfall are observed in both the predictions and measurements. It appears that the field study registered a longer duration of delayed response than predictions, particularly at the depth of 1.0 m. This may be attributed to instrumentation response delays to a certain extent and more to the effect of cracks and fissures into which the rain water is first stored and then slowly infiltrates into the surrounding soil. This progressive process is likely to take longer time for equilibration and is not yet accounted for in the current simulation. However, the general trends that deeper embedded movement point registered a longer delayed swelling (Ng et al. 2003) are reflected in the simulation. The accumulated swelling increases rapidly from Day 2 to Day 3 after the soil starts to swell at all three depths, and remains at a relative stable value during the no-rainfall period at all depths. The predicted stable values are in good agreement with the measurements for all three depths. It should also be noted that the recorded value of accumulative swelling is quite small, for example, in the order of a few millimeters at depth of 1.0 m. The predicted accumulative swelling at L1 and L2 are also compared to the respective measurements in Fig. 5.17 and Fig. 5.18, respectively. Similar findings can also be observed as those in Fig. 5.16. Comparing the three locations, one can find that the higher the initial suction, the larger the predicted accumulative swelling at a given depth will be, as concluded in the field study (Ng et al. 2003). Fig. 5.19 shows the comparison of down-slope displacement between prediction and measurement with this shallow layer near R2 at several dates. The recorded down-slope displacements were relatively small (several millimeters), indicating no significant collapse failure.

Both measurements and predictions show that most of displacements occurred in the near surface zone affected substantially by rainfall.

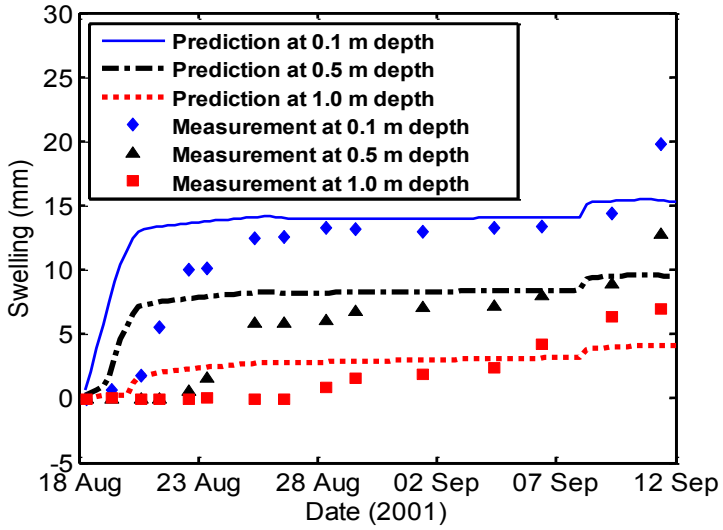

Fig. 5.16. Comparison of predicted and measured vertical swelling at R2

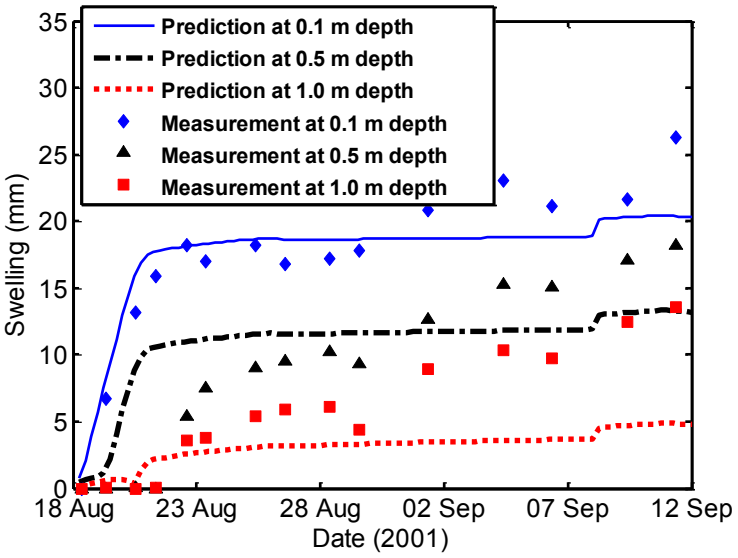

Fig. 5.17. Comparison of predicted and measured vertical swelling at R1

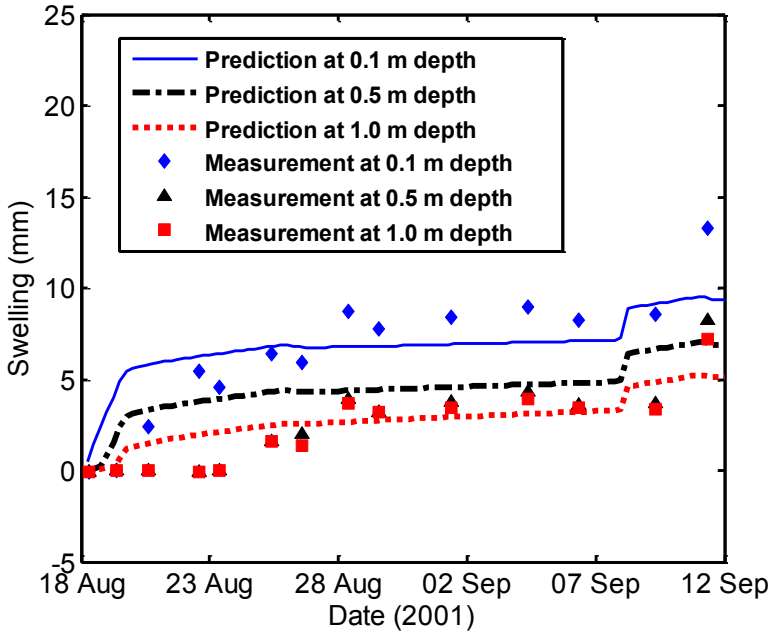

Fig. 5.18. Comparison of predicted and measured vertical swelling at R3

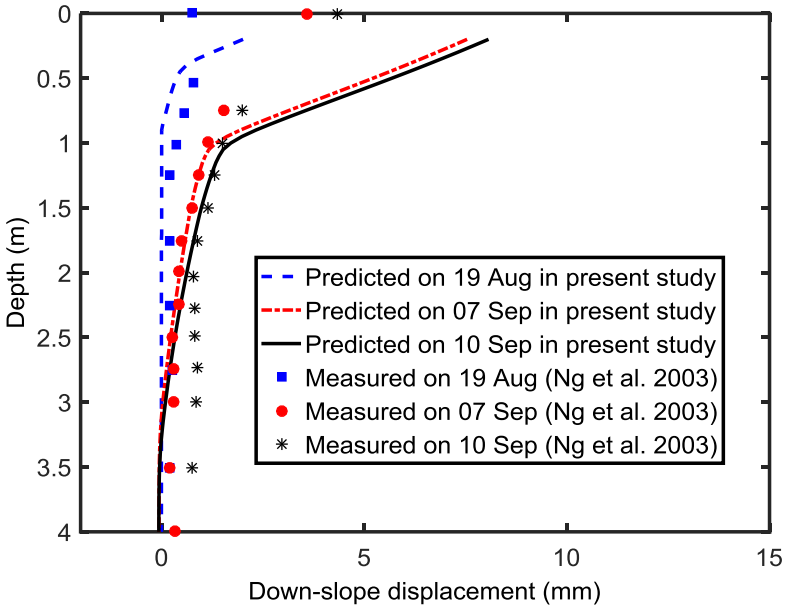

Fig. 5.19. Comparison of predicted and measured down-slope displacement near R2 at several dates

5.6 Discussion on applicability of infinite slope formulation to analysis of wetting-induced expansive soil slope failure

The early simplistic applications of infinite slope formulation is to calculate the factor of safety through use of overall force equilibrium condition for a thin and dry shallow layer in the vertical direction (Duncan and Wright 2014). The basic assumption of infinite slope formulation implies that it is only applicable to cases for which the potential failure mass has a large length/depth ratio (Milledge et al. 2012). The infinite slope formulation has later been applied to cases including saturated (Urciuoli 2002; Lade 2010) or unsaturated (Rahardjo 1995; Huang et al. 2016) water flow regimes, and has also been used to analyze stress and displacement developments (e.g. Teunissen and Spierenburg 1996) and mechanism of shear failure (e.g. Di Prisco and Pisanò 2011). For such applications involving hydraulic and mechanical processes, the rationale behind infinite slope formulation should be extended to include: (*i*) the changing pore water pressure (positive or negative) contours are parallel to the ground surface in hydraulic analysis; (*ii*) the changing stress and strain contours are parallel to the ground surface in mechanical analysis; (*iii*) the resulting safety factor contours are also parallel to the ground surface in stability analysis. Such idealized scenarios can never be strictly satisfied in any field condition, use of infinite slope formulation is still favored in practice problems (e.g. Conte and Troncone 2012), and can be regarded effective for the following weaker conditions: (1) Water flows predominantly in the direction normal to the slope, in other words, the water flows much more rapidly in the direction normal to the slope than parallel to the slope; (2) Significant non-uniform internal stress and strain levels are not caused along lateral extents of the slope by external factors, like rainfall infiltration. The field case studied herein can be characterized as such conditions, in view of the reasonable agreements between measurements and simulations, despite some minor discrepancies observed

at certain depths. The discrepancies are expectable when adopting a simple two-layer system to simulate the complicated field case with much heterogeneities in soil properties and variations in initial and boundary conditions. However, the employed two layer-system infinite slope formulation significantly simplifies the numerical procedure, in terms of model establishment and computational efforts.

The analysis presented herein highlights the substantial changes of stress field in expansive soil slope due to self-swelling, and evidences the need of a better understanding of its effect on shear failure of slopes. The infinite slope formulation for expansive soil in this study provides a basis which can be further expanded to include additional features. For example, it can be combined with the methods in Locat et al. (2013) or Bernander et al. (2016) to explain the progressive (upward) or retrogressive (downward) failure mechanisms, which are assumed to be triggered by lateral stress change induced by excavation at the toe or loading near the top of slope, respectively. While the stress change in the present study is caused by self-swelling of expansive soil. This approach also has the potential to be combined with probabilistic analysis (e.g. Griffiths et al. 2011; Zhou et al. 2016) to consider more reasonably the hydraulic and/or mechanical heterogeneities in the field, for which the simplicity of infinite slope formulation is an attractive advantage since stochastic risk analysis involves hundreds of thousands of computer runs if Monte Carlo simulated is performed.

5.7 Concluding remarks

Several key observations summarized by Ng et al. 2003 in a field study on an expansive slope in response to rainfall infiltrations are numerically simulated in the framework of the infinite slope formulation. In this analysis, the hydraulic response is simulated with SEEP/W. Using the pore

water pressure variation from the hydraulic analysis, the mechanical response is simulated with a modified version of the numerical program in Qi and Vanapalli (2016). It should be noted that the analysis presented herein involves some important simplifications (e.g. two-layer system for field heterogeneity). In spite of this assumption, the results are encouraging when considering that this simplified model is computationally inexpensive compared with those more complex models. The following conclusions regarding this field case study can be summarized:

(1) One of the most important observations regarding the hydraulic response, i.e. the relatively fast formulation of the perched flow regime in the near surface layer from a quite dry initial condition (with high initial suction), is well captured by a simple two-layer model using the hydraulic conductivity function predicted from laboratory SWCC with minimal calibration.

(2) Reasonable agreements in mechanical responses (including the swelling-induced stress increase and deformations) between prediction and measurement are achieved using the infinite slope framework. This also confirms the practical applicability of the newly proposed stress (suction and net stress)-dependent model for soil moduli (E and H) presented in Eqs. (5.12) through (5.15)). The model is extended from the conventionally used power law and includes the effect of effective saturation degree using SWCC.

(3) Combination of this model for elastic moduli and the shear strength model relative to SWCC (e.g. Vanapalli et al. 1996) lead to a smooth mathematical description of transition between saturation and unsaturation state for both elastic and elasto-plastic behaviours. This feature is necessary in the present study as well as other practical applications.

(4) The amount of swelling-induced stress along the down sloping direction seems to be significant enough to initiate progressive failure mechanism observed in expansive soil

slope. The ability of the present formulation to simulate swelling-induced stress and plastic straining is promising to explain this failure mechanism.

Glossary

Symbols

t	Time
k	Permeability of soil
H_d	Total hydraulic head
θ_w	Volumetric water content
ϕ^b	Friction angle relative to suction
γ_w	Unit weight of water
y	Elevation
u_w	Pore water pressure
u_a	Pore air pressure
β	Slope angle of the infinite slope
θ_e	Effective volumetric water content
S_e	Effective degree of saturation
θ_r	Residual volumetric water content
S_r	Effective degree of saturation
a, n, m	van Genuchten fitting parameters
k_s	Saturated permeability of soil
$\boldsymbol{\sigma}$	Net stress tensor
$\boldsymbol{\varepsilon}$	Strain tensor
s	Suction
$\mathbf{D}$	Elastic constitutive matrix associated with change in net stress
E	Young's modulus
μ	Poisson's ratio
$\mathbf{h}$	vector for volume change of soil structure associated with incremental suction
H	Elastic modulus (a scalar) for the soil structure with respect to suction change
$\mathbf{D}^{p\varepsilon}$	Elasto-plastic constitutive matrix associated with strain increment
$\mathbf{D}^{ps}$	Elasto-plastic constitutive matrix associated with suction increment
c'	Effective cohesion
ϕ'	Effective angle of internal friction
τ_f	Shear strength
E_{sat}	Value of E under saturated condition
E_{unsat}	Value of E under unsaturated condition
H_{sat}	Value of H under saturated condition
H_{unsat}	Value of H under unsaturated condition
α, β	Parameters of Oh et al. (2009) model
P_a	Atmospheric pressure
μ_w	Dynamic viscosity of water
a_h	Average hydraulic aperture of the fractures

d	Average fracture spacing
η	Axis directed along the infinite slope
ξ	Axis orthogonally to the infinite slope
β	Slope angle of the infinite slope
x	Axis in Cartesian coordinate system
y	Axis in Cartesian coordinate system
σ_ξ	Normal stress acting on the plane of normal ξ
$\tau_{\xi\eta}$	Shear stress acting on the plane of normal ξ
Z	Depth under the ground surface measured along the y axis
σ_η	The net normal stress in the η direction
K	The stress ratio of the net normal stresses
γ	Unit weight of the soil
ε_y	Normal strain in the y direction
γ_{xy}	Shear strain in the x-y plane
δ	Spacing between two consecutive nodes
ε_η	Normal strain in the η direction
$\gamma_{\xi\eta}$	Shear strain in the ε-η plane
M_E	Model parameters for E_{sat}
K_E	Model parameters for E_{sat}
α_E	Model parameters for E
κ_E	Model parameters for E
β_E	Model parameters for E
α_H	Model parameters for H
κ_H	Model parameters for H
β_H	Model parameters for H
μ	Poisson's ratio
φ	Dilatancy angle
κ_s	Soil's compressibility with suction
χ, ω	Fitting parameters in Tsiampousi et al. (2013)
e	Void ratio
$\{k\}$	Vector formed of state/material parameters
G	Plastic potential
F	Yielding function

Abbreviations

SWCC	Soil Water Characteristic Curve
HCF	Hydraulic Conductivity Function
JRC	Joint Roughness Coefficient

5.8 References

Ali, A., Huang, J., Lyamin, A. V., Sloan, S. W., & Cassidy, M. J. (2014). Boundary effects of rainfall-induced landslides. Computers and Geotechnics, 61, 341-354.

Alonso, E. E., Gens, A., & Delahaye, C. H. (2003). Influence of rainfall on the deformation and stability of a slope in overconsolidated clays: a case study. Hydrogeology journal, 11(1), 174-192.

Alonso, E. E., Sauter, S., & Ramon, A. (2015). Pile groups under deep expansion: a case history. Canadian Geotechnical Journal, 52(8), 1111-1121.

Aubeny, C. P., & Lytton, R. L. (2004). Shallow slides in compacted high plasticity clay slopes. Journal of Geotechnical and Geoenvironmental Engineering, 130(7), 717-727.

Azañón, J. M., Azor, A., Yesares, J., Tsige, M., Mateos, R. M., Nieto, Delgado, J., López-Chicano, M., Martín, W. & Rodríguez-Fernández, J. (2010). Regional-scale high-plasticity clay-bearing formation as controlling factor on landslides in Southeast Spain. Geomorphology, 120(1), 26-37.

Bani Hashem, E., & Houston, S. L. (2015). Volume change consideration in determining unsaturated soil properties for geotechnical applications. International Journal of Geomechanics, D4015003.

Bao, C. G., Ng, C. W. W., Rahardjo, H., Toll, D. G., & Leong, E. C. (2000). Some thoughts and studies on the prediction of slope stability in expansive soils. In Unsaturated soils for Asia. Proceedings of the Asian Conference on Unsaturated Soils, UNSAT-Asia 2000, Singapore, 18-19 May, 2000. (pp. 15-31). AA Balkema.

Bernander, S., Kullingsjö, A. A., Gylland, A., Bengtsson, P. E., Knutsson, S., Pusch, R., Olofsson, J. & Elfgren, L. (2016). Downhill Progressive Landslides in Long Natural Slopes. Triggering Agents and Landslide Phases modeled with a Finite Difference Method. Canadian Geotechnical Journal, (ja).

Cai, F., Ugai, K., Wakai, A., & Li, Q. (1998). Effects of horizontal drains on slope stability under rainfall by three-dimensional finite element analysis. Computers and Geotechnics, 23(4), 255-275.

Calabresi, G., Colleselli, F., Danese, D., Giani, G., Mancuso, C., Montrasio, L., Nocilla, A., Pagano, L., Reali, E. and Sciotti A. (2013). Research study of the hydraulic behaviour of the Po River embankments. Canadian Geotechnical Journal, 50(9), 947-960.

Chen, H. X., & Zhang, L. M. (2014). A physically-based distributed cell model for predicting regional rainfall-induced shallow slope failures.Engineering geology, 176, 79-92.

Cheng, Y. H., Cheng, Z.L., & Zhang, Y. B. (2011) Centrifugal model tests on expansive soil slope under rainfall. Chinese journal of geotechnical engineering, 33 (S1), 409-414. (in Chinese)

Cho, S. E., & Lee, S. R. (2001). Instability of unsaturated soil slopes due to infiltration. Computers and Geotechnics, 28(3), 185-208.

Conte, E., & Troncone, A. (2012). Stability analysis of infinite clayey slopes subjected to pore pressure changes. Géotechnique, 62(1), 87-91.

Day, R. W. (1994). Surficial stability of compacted clay: case study. Journal of Geotechnical Engineering, 120(11), 1980-1990.

Di Prisco, C., & Pisanò, F. (2011). An exercise on slope stability and perfect elastoplasticity. Géotechnique, 61(11), 923.

Duncan, J. M., Wright, S. G., & Brandon, T. L. (2014). Soil strength and slope stability. John Wiley & Sons.

Fredlund, D. G., & Rahardjo, H. (1993). Soil mechanics for unsaturated soils. John Wiley & Sons.

Fredlund, D. G., Morgenstern, N. R., & Widger, R. A. (1978). The shear strength of unsaturated soils. Canadian geotechnical journal, 15(3), 313-321.

Fredlund, D. G., Sheng, D., & Zhao, J. (2011). Estimation of soil suction from the soil-water characteristic curve. Canadian Geotechnical Journal, 48(2), 186-198.

Gardner, W. R. (1958). Some steady-state solutions of the unsaturated moisture flow equation with application to evaporation from a water table. Soil science, 85(4), 228-232.

GeoSlope International Ltd.. Seep/W user's guide for finite element seepage analysis. Calgary (Alta): GEO-SLOPE International Ltd; 2012.

Griffiths, D. V., & Lane, P. A. (1999). Slope stability analysis by finite elements. Geotechnique, 49(3), 387-403.

Griffiths, D. V., & Lu, N. (2005). Unsaturated slope stability analysis with steady infiltration or evaporation using elasto-plastic finite elements. International journal for numerical and analytical methods in geomechanics, 29(3), 249-267.

Griffiths, D. V., Huang, J., & Fenton, G. A. (2011). Probabilistic infinite slope analysis. Computers and Geotechnics, 38(4), 577-584.

Hamdhan, I. N., & Schweiger, H. F. (2012). Finite element method–based analysis of an unsaturated soil slope subjected to rainfall infiltration. International Journal of Geomechanics, 13(5), 653-658.

Hou, T. S., Xu, G. L., Shen, Y. J., Wu, Z. Z., Zhang, N. N., & Wang, R. (2013). Formation mechanism and stability analysis of the Houba expansive soil landslide. Engineering Geology, 161, 34-43.

Houston, S. L., Bharadwaj, A., Welfert, B., Houston, W. N., & Walsh, K. D. (2015). Unsaturated Soil Mechanics Principles to Remove and Replace Mitigation for Expansive Clays. Journal of Geotechnical and Geoenvironmental Engineering, 142(4), 04015102.

Huang, W., Leong, E.C., & Rahardjo, H. 2016. Translational slip failures on slope incorporating unsaturated soil mechanics. In Proceedings of the 6th Asia-pacific Conference on unsaturated soils, Guilin, China. 23 – 26 Octerber 2015. pp. 771-775.

Jennings, J. E. B., & Burland, J. B. (1962). Limitations to the use of effective stresses in partly saturated soils. Géotechnique, 12(2), 125-144.

Lade, P. V. (2010). The mechanics of surficial failure in soil slopes.Engineering Geology, 114(1), 57-64.

Le, T. M. H., Gallipoli, D., Sánchez, M., & Wheeler, S. (2015). Stability and failure mass of unsaturated heterogeneous slopes. Canadian Geotechnical Journal, 52(11), 1747-1761.

Li, W. C., Lee, L. M., Cai, H., Li, H. J., Dai, F. C., & Wang, M. L. (2013). Combined roles of saturated permeability and rainfall characteristics on surficial failure of homogeneous soil slope. Engineering Geology, 153, 105-113.

Locat, A., Leroueil, S., Fortin, A., Demers, D., & Jostad, H.P. (2015). The 1994 landslide at Sainte-Monique, Quebec: geotechnical investigation and application of progressive failure analysis. Canadian Geotechnical Journal, 52: 490-504.

Lu, N., & Kaya, M. (2013). Power law for elastic moduli of unsaturated soil.Journal of Geotechnical and Geoenvironmental Engineering, 140(1), 46-56.

Meilani, I., Rahardjo, H., & Leong, E. C. (2005). Pore-water pressure and water volume change of an unsaturated soil under infiltration conditions.Canadian geotechnical journal, 42(6), 1509-1531.

Milledge, D. G., Griffiths, D. V., Lane, S. N., & Warburton, J. (2012). Limits on the validity of infinite length assumptions for modelling shallow landslides.Earth Surface Processes and Landforms, 37(11), 1158-1166.

Morgenstern, N. R., & Price, V. E. (1965). The analysis of the stability of general slip surfaces. Geotechnique, 15(1), 79-93.

Nelson, J. D., Chao, K. C., Overton, D. D., & Nelson, E. J. (2015). Foundation Engineering for Expansive Soils. John Wiley & Sons.

Ng, C. W. W., Zhan, L. T., Bao, C. G., Fredlund, D. G., & Gong, B. W. (2003). Performance of an unsaturated expansive soil slope subjected to artificial rainfall infiltration. Geotechnique, 53(2), 143-157.

Ng, C. W. W., Wang, B., & Tung, Y. K. (2001). Three-dimensional numerical investigations of groundwater responses in an unsaturated slope subjected to various rainfall patterns. Canadian Geotechnical Journal, 38(5), 1049-1062.

Nixon, M. F., & Grozic, J. L. (2007). Submarine slope failure due to gas hydrate dissociation: a preliminary quantification. Canadian Geotechnical Journal, 44(3), 314-325.

Oh, W. T., Vanapalli, S. K., & Puppala, A. J. (2009). Semi-empirical model for the prediction of modulus of elasticity for unsaturated soils. Canadian Geotechnical Journal, 46(8), 903-914.

Potts, D. M., Zdravkovic, L., & Zdravković, L. (1999). Finite element analysis in geotechnical engineering: theory (Vol. 1). Thomas Telford.

Qi, S., & Vanapalli, S. K. (2015). Hydro-mechanical coupling effect on surficial layer stability of unsaturated expansive soil slopes. Computers and Geotechnics, 70, 68-82.

Qi, S., & Vanapalli, S. K. (2016). Influence of swelling behaviour on the stability of an infinite unsaturated expansive soil slope. Computers and Geotechnics, 76, 154-169.

Rahardjo, H., & Fredlund, D. G. (1995). Procedures for slope stability analyses involving unsaturated soils. Developments in deep foundations and ground improvement schemes. Balkema, Rotterdam, 33-56.

Rahardjo, H., Melinda, F., Leong, E. C., & Rezaur, R. B. (2011). Stiffness of a compacted residual soil. Engineering Geology, 120(1), 60-67.

Rahardjo, H., Santoso, V. A., Leong, E. C., Ng, Y. S., Tam, C. P. H., & Satyanaga, A. (2013). Use of recycled crushed concrete and Secudrain in capillary barriers for slope stabilization. Canadian Geotechnical Journal, 50(6), 662-673.

Richards, B. G. (1985). Pressures on a retaining wall by an expansive clay. Golden Jubilee of the International Society for Soil Mechanics and Foundation Engineering: Commemorative Volume, 241.

Richards, L. A. (1931). Capillary conduction of liquids through porous mediums. Journal of Applied Physics, 1(5), 318-333.

Rouainia, M., Davies, O., O'Brien, T., & Glendinning, S. (2009, June). Numerical modelling of climate effects on slope stability. In Proceedings of the Institution of Civil Engineers-Engineering Sustainability (Vol. 162, No. 2, pp. 81-89). Thomas Telford Ltd.

Sheng, D. (2011). Review of fundamental principles in modelling unsaturated soil behaviour. Computers and Geotechnics, 38(6), 757-776.

Sheng, D., Fredlund, D. G., & Gens, A. (2008). A new modelling approach for unsaturated soils using independent stress variables. Canadian Geotechnical Journal, 45(4), 511-534.

Sheng, D., Sloan, S. W., & Gens, A. (2004). A constitutive model for unsaturated soils: thermomechanical and computational aspects. Computational Mechanics, 33(6), 453-465.

Sheng, D., Sloan, S. W., & Yu, H. S. (2000). Aspects of finite element implementation of critical state models. Computational mechanics, 26(2), 185-196.

Sheng, D., Sloan, S. W., Gens, A., & Smith, D. W. (2003). Finite element formulation and algorithms for unsaturated soils. Part I: Theory. International Journal for Numerical and Analytical Methods in Geomechanics, 27(9), 745-765.

Sołowski, W. T., & Gallipoli, D. (2010). Explicit stress integration with error control for the Barcelona basic model: part I: algorithms formulations.Computers and Geotechnics, 37(1), 59-67.

Sołowski, W. T., Sloan, S. W., & Wang, D. (2014). Material point method simulation of triaxial shear tests. Computer Methods and Recent Advances in Geomechanics, 169.

Stianson, J. R., Fredlund, D. G., & Chan, D. (2011). Three-dimensional slope stability based on stresses from a stress-deformation analysis. Canadian Geotechnical Journal, 48(6), 891-904.

Teunissen, J. A. M., & Spierenburg, S. E. J. (1996). Stability of infinite slopes. In International Journal of Rock Mechanics and Mining Sciences and Geomechanics Abstracts (Vol. 3, No. 33, p. 137A).

Thomas, H. R., & He, Y. (1998). Modelling the behaviour of unsaturated soil using an elastoplastic constitutive model. Géotechnique, 48(5), 589-603.

Thomas, M. G., Puppala, A. J., & Hoyos, L. R. (2009). Influence of swell pressure from expansive fill on retaining wall stability. Contemporary Topics in Ground Modification, Problem Soils, and Geo-support, pp. 590-597.

Tommasi, P., Boldini, D., Caldarini, G., & Coli, N. (2012). Influence of infiltration on the periodic re-activation of slow movements in an overconsolidated clay slope. Canadian Geotechnical Journal, 50(1), 54-67.

Tran, D. T., Fredlund, D. G., & Chan, D. H. (2016). Improvements to the calculation of actual evaporation from bare soil surfaces. Canadian Geotechnical Journal, 53(1), 118-133.

Tschuchnigg, F., Schweiger, H. F., & Sloan, S. W. (2015). Slope stability analysis by means of finite element limit analysis and finite element strength reduction techniques. Part II: Back analyses of a case history. Computers and Geotechnics, 70, 178-189.

Tsiampousi, A., Zdravkovic, L., & Potts, D. M. (2013). A three-dimensional hysteretic soil-water retention curve. Geotechnique, 63(2), 155.

Urciuoli, G. (2002). Strains preceding failure in infinite slopes. International Journal of Geomechanics, 2(1), 93-112.

Van Genuchten, M. T. (1980). A closed-form equation for predicting the hydraulic conductivity of unsaturated soils. Soil science society of America journal, 44(5), 892-898.

van Genuchten, M. T., & Nielsen, D. R. (1985). On describing and predicting the hydraulic properties of unsaturated soils. Ann. Geophys, 3(5), 615-628.

Vanapalli, S. K., Fredlund, D. G., Pufahl, D. E., & Clifton, A. W. (1996). Model for the prediction of shear strength with respect to soil suction.Canadian Geotechnical Journal, 33(3), 379-392.

Vanapalli, S., & Lu, L. (2012). A state-of-the art review of 1-D heave prediction methods for expansive soils. International Journal of Geotechnical Engineering, 6(1), 15-41.

Vu, H. Q., & Fredlund, D. G. (2006). Challenges to modelling heave in expansive soils. Canadian Geotechnical Journal, 43(12), 1249-1272.

Wheeler, S. J., Sharma, R. S., & Buisson, M. S. R. (2003). Coupling of hydraulic hysteresis and stress–strain behaviour in unsaturated soils.Géotechnique, 53(1), 41-54.

Widger, R.A., & Fredlund, D.G. (1979). Stability of swelling clay embankments. Canadian Geotechnical Journal, 16(1), 140-151.

Wilson, G. W., Fredlund, D. G., & Barbour, S. L. (1994). Coupled soil-atmosphere modelling for soil evaporation. Canadian Geotechnical Journal,31(2), 151-161.

Xiao, H. B., Zhang, C. S., Wang, Y. H., & Fan, Z. H. (2011). Pile-soil interaction in expansive soil foundation: Analytical solution and numerical simulation. International Journal of Geomechanics, 11(3), 159-166.

Zhan, L. (2003). Field and laboratory study of an unsaturated expansive soil associated with rain-induced slope instability.

Zhan, L. T., Chen, P., & Ng, C. W. W. (2007). Effect of suction change on water content and total volume of an expansive clay. Journal of Zhejiang University SCIENCE A, 8(5), 699-706.

Zhan, T. L., & Ng, C. W. (2006). Shear strength characteristics of an unsaturated expansive clay. Canadian Geotechnical Journal, 43(7), 751-763.

Zhan, T. L., Jia, G. W., Chen, Y. M., Fredlund, D. G., & Li, H. (2013). An analytical solution for rainfall infiltration into an unsaturated infinite slope and its application to slope stability analysis. International Journal for Numerical and Analytical Methods in Geomechanics, 37(12), 1737-1760.

Zhan, T. L., Ng, C. W., & Fredlund, D. G. (2007). Field study of rainfall infiltration into a grassed unsaturated expansive soil slope. Canadian Geotechnical Journal, 44(4), 392-408.

Zhang, L. L., Fredlund, D. G., Fredlund, M. D., & Wilson, G. W. (2014). Modeling the unsaturated soil zone in slope stability analysis 1. Canadian Geotechnical Journal, 51(12), 1384-1398.

Zhang, X., & Briaud, J. L. (2015). Three dimensional numerical simulation of residential building on shrink–swell soils in response to climatic conditions.International Journal for Numerical and Analytical Methods in Geomechanics, 39(13), 1369-1409.

Zhou, A., Li, C. Q., & Huang, J. (2016). Failure analysis of an infinite unsaturated soil slope. Proceedings of the Institution of Civil Engineers-Geotechnical Engineering, 1-11.

Zhou, J. W., Xu, F. G., Yang, X. G., Yang, Y. C., & Lu, P. Y. (2016). Comprehensive analyses of the initiation and landslide-generated wave processes of the 24 June 2015 Hongyanzi landslide at the Three Gorges Reservoir, China. Landslides, 13(3), 589-601.

Appendix 5.1

Elastic stage

During the elastic stage, the net stress increment can be calculated from the corresponding strain increment, i.e. the component subtracted from total strain increment by that induced by suction increment.

$$d\boldsymbol{\sigma} = \mathbf{D}(d\boldsymbol{\varepsilon} - H^{-1}\mathbf{m}ds) \tag{A5.1}$$

where **m** is the vector $\{1, 1, 1, 0, 0, 0\}^{T}$, The elastic constitutive matrix associated with change in net stress, **D**, is symmetric as follows

$$[\mathbf{D}] = \begin{bmatrix} D_{11} & D_{12} & D_{13} & 0 & 0 & 0 \\ & D_{22} & D_{23} & 0 & 0 & 0 \\ & & D_{33} & 0 & 0 & 0 \\ & & & D_{44} & 0 & 0 \\ sym. & & & & D_{55} & 0 \\ & & & & & D_{66} \end{bmatrix} \tag{A5.2}$$

Its components are evaluated as

$$D_{11} = D_{22} = D_{33} = E(1\text{-}\mu)/[(1+\mu)(1\text{-}2\mu)] \tag{A5.3}$$

$$D_{12} = D_{13} = D_{23} = E\mu/[(1+\mu)(1\text{-}2\mu)] \tag{A5.4}$$

$$D_{44} = D_{55} = D_{66} = E/[2(1+\mu)] \tag{A5.5}$$

in which, $E = E_{unsat}$ and E_{sat} for unsaturated and saturated zones, respectively. Comparison of Eq. (A5.1) and Eq. (5.6) yields the expression for vector **h**

$$\mathbf{h} = \mathbf{D}H^{-1}\mathbf{m} \tag{A5.6}$$

Substituting the components of **D** (i.e. Eqs. (A5.3-A5.5)) into Eq. (A5.6), yields

$$\mathbf{h}=\mathbf{D}H^{-1}\mathbf{m}=\frac{E}{H(1-2\mu)}\{1 \quad 1 \quad 1 \quad 0 \quad 0 \quad 0\}^T \tag{A5.7}$$

in which, $H = H_{unsat}$ and H_{sat} for unsaturated and saturated zones, respectively. By using the relationship given in Eq. (5.15) for saturated zone, Eq. (A5.7) becomes

$$\mathbf{h}=\mathbf{m}=\{1 \quad 1 \quad 1 \quad 0 \quad 0 \quad 0\}^T \tag{A5.8}$$

Using Eq. (A5.8), Eq. (5.6) can be rearranged as

$$d(\boldsymbol{\sigma}+\mathbf{m}s)=\mathbf{D}d\boldsymbol{\varepsilon} \tag{A5.9}$$

In saturated zone, s is numerically equal to $-u_w$, thus the Eq. (A5.9) (i.e. the version of Eq. (5.6) for saturated state) is mathematically equivalent to that for saturated soils in terms of effective stress principle.

Plastic stage

During plastic stage, with given yielding function, F, and plastic potential, G (which has the same form as F (i.e. Eq. (5.10)), but with internal friction angle replaced by dilatancy angle), the matrices in Eq. (5.7) can be derived as follows

$$\mathbf{D}^{p\varepsilon}=\mathbf{D}-\frac{\mathbf{D}\mathbf{a}_g\mathbf{a}_f{}^{\mathrm{T}}\mathbf{D}}{\mathbf{a}_f{}^{\mathrm{T}}\mathbf{D}\mathbf{a}_g+A} \tag{A5.10}$$

$$\mathbf{D}^{ps}=-\mathbf{D}^{p\varepsilon}H^{-1}\mathbf{m}-\mathbf{W}^{ps} \tag{A5.11}$$

in which,

$$\mathbf{a}_g=\partial G/\partial\boldsymbol{\sigma}$$

$$\mathbf{a}_f=\partial F/\partial\boldsymbol{\sigma}$$

$$A = -(\partial F / \partial \mathbf{k})^{\mathrm{T}} d\mathbf{k} / \Lambda \quad \Lambda = \frac{\mathbf{a}_f{}^{\mathrm{T}} \mathbf{D} d\boldsymbol{\varepsilon} + C ds}{\mathbf{a}_f{}^{\mathrm{T}} \mathbf{D} \mathbf{a}_g + A}$$

$$C = \partial F / \partial s - \mathbf{a}_f{}^{\mathrm{T}} \mathbf{h}$$

$$\mathbf{W}^{ps} = \frac{\mathbf{D}\mathbf{a}_g (\partial F / \partial s)}{\mathbf{a}_f{}^{\mathrm{T}} \mathbf{D} \mathbf{a}_g + A}$$

where Λ is the plastic multiplier, used to calculate the plastic strain $\{d\varepsilon^p\} = \Lambda\{\partial G / \partial \sigma\}$. Note **k** is a column vector that is formed of state or material parameters. The $\mathbf{D}^{ps}$ (i.e. Eq. (A5.11)) can also be rearranged as

$$\begin{aligned} \mathbf{D}^{ps} &= -\mathbf{D} H^{-1} \mathbf{m} + \frac{\mathbf{D}\mathbf{a}_g \mathbf{a}_f{}^{\mathrm{T}} \mathbf{D}}{\mathbf{a}_f{}^{\mathrm{T}} \mathbf{D} \mathbf{a}_g + A} H^{-1} \mathbf{m} - \frac{\mathbf{D}\mathbf{a}_g (\partial F / \partial s)}{\mathbf{a}_f{}^{\mathrm{T}} \mathbf{D} \mathbf{a}_g + A} \\ &= -\mathbf{h} - C \frac{\mathbf{D}\mathbf{a}_g}{\mathbf{a}_f{}^{\mathrm{T}} \mathbf{D} \mathbf{a}_g + A} \end{aligned} \tag{A5.12}$$

where,

$$\begin{aligned} C &= \partial F / \partial s - \mathbf{a}_f{}^{\mathrm{T}} \mathbf{h} \\ &= \partial F / \partial s - \{\partial F / \partial \sigma\}^{\mathrm{T}} \{1 \quad 1 \quad 1 \quad 0 \quad 0 \quad 0\}^{T} \\ &= \partial F / \partial s - (\partial F / \partial \sigma_x + \partial F / \partial \sigma_y + \partial F / \partial \sigma_z) \end{aligned} \tag{A5.13}$$

Considering that the matric suction is numerically negative pore water pressure in saturated zone, the yield function can be written in the following form

$$F(\sigma_x + s, \sigma_y + s, \sigma_z + s, \cdots) = 0 \tag{A5.14}$$

Using the Chain rule, the derivative of F over suction is

$$\frac{\partial F}{\partial s} = \frac{\partial F}{\partial (\sigma_i + s)} \frac{\partial (\sigma_i + s)}{\partial s} \qquad i = x, y, z \tag{A5.15}$$

Since $\partial(\sigma_i + s) / \partial s = 1$, thus

$$\frac{\partial F}{\partial s} = \frac{\partial F}{\partial(\sigma_x + s)} + \frac{\partial F}{\partial(\sigma_y + s)} + \frac{\partial F}{\partial(\sigma_z + s)} \tag{A5.16}$$

Regarding the derivative of F over each normal stress component, the following identity holds

$$\frac{\partial F}{\partial \sigma_i} = \frac{\partial F}{\partial(\sigma_i + s)} \qquad i = x, y, z \tag{A5.17}$$

Substituting Eqs. (A5.16) and (A5.17) into Eq. (A5.13), we obtain that $C = 0$ in saturated zone. Recalling Eq. (A5.8), the $\mathbf{D}^{ps}$ is found to be identical to $\mathbf{m}$ in saturated zone using Eq. (A5.12), then the Eq. (5.7) can be rearranged as

$$d(\boldsymbol{\sigma} + \mathbf{m}s) = \mathbf{D}^{p\varepsilon} d\boldsymbol{\varepsilon} \tag{A5.18}$$

$\mathbf{D}^{p\varepsilon}$ for saturated zone, evaluated using Eq. (A5.10), is numerical equal to that for saturated soils based on Terzaghi effective stress principle. Thus, Eq. (A5.18) indicates that Eq. (5.7) can also revert to stress-strain constitutive relation for saturated soils in elastoplastic stage.

Chapter 6 Piecewise-Linear Formulation of Coupled Large Strain Consolidation and Unsaturated Flow. I: Model Development and Implementation [4]

The chapter introduces the development of the program for analysis of large strain consolidation coupled with unsaturated flow in soft soils. The theoretical and numerical development of the program (UNSAT-CON) for modeling single layer deposits is described in this chapter, including the constitutive models (based on state surface modelling approach) adopted to describe the hydraulic and mechanical behaviours of unsaturated soils, the numerical techniques used to deal with the associated nonlinearities, the novel algorithm developed to smoothly model transition between the saturated and unsaturated zones, and four types of top boundary conditions formulated to account for complex soil-atmosphere hydraulic interactions. Functionality for quasi-unsaturated analysis is also made available in UNSAT-CON. Verifications of the program implementation using a numerical example of saturated large strain consolidation and an analytical solution to unsaturated flow is presented to close this chapter. Validation of the quasi-unsaturated and unsaturated formulations is presented in the following chapter (Chapter 7), using comparisons with numerical cases as well as laboratory and field data.

[4] A version of this chapter has been published as Qi et al. 2017(a) in ASCE Journal Geotechnical and Geoenvironmental engineering

6.1 Introduction

The coupling of unsaturated flow with large strain consolidation is important in several engineering applications that involve the use of evaporation to aid dewatering of slurries, whether for land reclamation purposes or for management of mining residuals (tailings) (Simms et al. 2010; Daliri et al. 2014; Fujiyasu and Fahey 2000; Wells et al. 2011; Matthews et al. 2011; Soleimani et al. 2014). Several large strain consolidation formulations currently exist that incorporate some consideration of unsaturated flow or desiccation. Two of the most widely used models are CONDES (Yao et al. 2002) and MinTaCo (Seneviratne et al. 1996). Both these models solve a large strain Lagrangian equation for consolidation, using power-law constitutive relationships between void ratio and effective stress, and hydraulic conductivity and void ratio. CONDES models desiccation by considering 3D volume change in elements that are reduced below a critical void ratio due to drying. Deformation in these cracking elements is linked to evaporation, which is assumed to proceed at the potential rate from the surface, or at an empirically corrected reduced rate from crack surfaces. Crack depth increases as the soil shrinks below the critical void ratio, which is defined as the void ratio at the crack tip where the crack initiates and quantified using a four parameter empirical function of vertical effective stress. Deformation terminates in any element near the surface when the shrinkage limit is reached, and full soil saturation is assumed. The MinTaCo model handles evaporation by specifying a maximum value of suction at the soil surface, usually corresponding to the shrinkage limit of the soil, such that the top boundary condition switches from a constant flux boundary to a constant head boundary, after which point evaporation reduces below the potential rate. The MinTaCo model does not explicitly consider cracks nor does it model desaturation.

There are many practical reasons for advancing such models to include desaturation:

1. True soil-atmosphere coupling can only be predicted if unsaturated flow is modelled. Evaporation reduces below the potential rate due to the development of very high (> 1 MPa) total suctions at the surface (De Vries 1987; Wilson et al. 1997);

2. The compressibility and hydraulic conductivity relationships are different for unsaturated soils for suction values less than the air entry value;

3. Gas transport is important in many residual management applications, for instance, the transport of oxygen into acid generating tailings which is strongly affected by the degree of saturation;

4. The ability to model placement of slurry over previously desiccated soil, requires the model to capture the acceleration of the consolidation of the new soil through the resaturation of the previously desiccated soil (Daliri et al. 2015; Fisseha et al. 2010).

Various solutions are suggested in the literature using different dependent variables for modelling large strain consolidation problems in saturated soils (Gibson et al. 1967; Lee and Sills 1979; Yong et al. 1983; McVay et al. 1986; Townsend and McVay 1990). Among those, the CS2 model developed by Fox and Berles (1997) using a piece-wise linear formulation, appears to be versatile and accurate. This model has been extended or modified for other applications, such as coupled solute transport (Fox 2007), contaminant transport (Meric et al. 2013), layered soils consolidation (Fox et al. 2014), and more recently, electro-osmotic consolidation (Deng and Zhou 2015). Using the same framework of piece-wise linear model for CS2 (Fox and Berles 1997), the authors have developed a truly coupled unsaturated flow – large strain consolidation formulation. Two types of constitutive relations, two dimensional (2D) curves and three dimensional (3D) surfaces, are used to describe the hydro-mechanical behaviour of soil in the saturated and unsaturated zones, respectively. The formulation incorporates an algorithm to smoothly model the

transition between saturated and unsaturated zones. The formulation is mass conservative. Four boundary conditions are implemented to account for various possible hydraulic interactions at the soil-atmosphere interface. One implanted boundary condition is identical to the evaporation algorithm employed in the MinTaCo model, which allows for comparison with previously published numerical predictions using that particular formulation.

This chapter describes the model development and algorithm implementation. Verifications of the algorithm implementation using a numerical example for saturated soils large strain consolidation and an analytical solution to evaporation from porous media are also described in this chapter. Further model validation and performance are presented in a next chapter using both laboratory and field test results.

6.2 The model

6.2.1 Constitutive relationships

In the previous work on large strain consolidation in saturated soils, the compressibility and hydraulic conductivity functions have been defined using various forms of log-linear or power equations (Seneviratne 1996; Fox and Berles 1997; Fox et al. 2014). The simplest forms of the power equations that have been extensively used in practical applications are:

$$e = C_1(\sigma')^{C_2} \tag{6.1}$$

$$k = H_1 e^{H_2} \tag{6.2}$$

where, e is void ratio, k is the hydraulic conductivity, σ' is the vertical effective stress, defined as the difference between total stress and pore water pressure, $(\sigma - u_w)$. C_1, C_2 and H_1, H_2 are empirical material parameters for compressibility and hydraulic conductivity constitutive relationships,

respectively. Other forms of constitutive equation can also be adopted in certain applications, such as a variant of power law selected in CONDES which adds a constant to the effective stress term in the brackets of Eq. (6.1). This puts a limit on the maximum void ratio corresponding to zero effective stress condition.

The classical effective stress principle is difficult to extend to unsaturated soils (Bishop and Blight 1963; Fredlund and Morgenstern 1976, 1977). The effect of negative pore water pressure on the volume change can be very different from that of total mechanical stress, especially when soils are substantially desaturated. Many researchers have proposed constitutive relationships of unsaturated soils based on two independent stress state variables (Fredlund and Rahardjo 1993), namely, net stress ($\sigma - u_a$), and matric suction ($u_a - u_w$), where u_a is the pore-air pressure (usually assumed to be zero in nature) and u_w is the pore-water pressure.

If the two independent stress state variables approach is adopted, three 3D state surfaces are necessary to define the constitutive relationships for an unsaturated soil, namely, void ratio, degree of saturation (or water content), and hydraulic conductivity (Fredlund and Rahardjo 1993). The degree of saturation (or water content) surface is an extension of the soil-water characteristic curve (SWCC) to different states of net normal stress. The SWCC is usually measured under low net normal stress in pressure plates; however, it is well established that the SWCC changes with net normal stress. Fundamentally, this arises from changes in the pore-size distribution (Simms and Yanful 2002). The hydraulic conductivity of soil in unsaturated condition is dependent on the effective degree of saturation or water content, and therefore is usually modeled as a function of suction, and is often predicted from a measured SWCC using one of the so-called statistical methods (Leong and Rahardjo 1997). Incorporating suction dependency into Eq. (6.2) leads to the

third 3D constitutive surface describing the variation of hydraulic conductivity with respect to both suction and void ratio.

The 3D void ratio and water content surfaces can be generated or derived from various types of constitutive models that exist in the literature. These models have been established either based on phenomenological observation during conventional experimental tests at macroscopic scale (e.g. Fredlund and Morgenstern 1976; Alonso et al. 1990; Sheng et al. 2008), or obtained through pore-network modelling on a pore-by-pore basis at microscopic scale (e.g. Simms and Yanful 2005). The complex behaviour of unsaturated soils can be covered to varying degrees, depending on the level of sophistication of the adopted constitutive models. For example, some models (Alonso et al. 1990, 1999) are dedicated to interpret the irreversible deformation of unsaturated soils under both mechanical loading and suction changes within the framework of elastoplastic theory. Some are focused primarily on describing water retention characteristics of unsaturated soils (Fredlund and Xing 1994; van Genuchten 1980), or by incorporating an additional mechanical parameter to consider its effect on the hydraulic behaviour (Gallipoli et al. 2003; Tarantino 2009). There are some other models which can describe both hydraulic and mechanical components in a coupling manner by considering the effect of degree of saturation on the stress-strain relationship and (or) that of porosity on the saturation degree-suction relationship. (e.g. Vaunat et al. 2000; Wheeler et al. 2003; Sun and Sun 2012).

In the present study, the large strain consolidation of soft soils or tailings with evaporation involves, essentially, monotonic deformation and water content change only. Neither separation of plastic deformation from total deformation nor irrecoverable change from total change in water content is required. For this reason, the mathematical functions, proposed by Vu and Fredlund

(2006) based on state surfaces concepts for modeling swelling clays, are sufficient constitutive relationships for the present study. The three functions are expressed as

$$e = a + b\log\left[\frac{1+c(\sigma-u_a)+d(u_a-u_w)}{1+f(\sigma-u_a)+g(u_a-u_w)}\right] \tag{6.3}$$

$$w = A + B\log\left[\frac{1+C(\sigma-u_a)+D(u_a-u_w)}{1+F(\sigma-u_a)+G(u_a-u_w)}\right] \tag{6.4}$$

$$k = \frac{H_1 e^{H_2}}{1+m[(u_a-u_w)/(\rho_w g)]^n} \tag{6.5}$$

where, w is the gravimetric water content, ρ_w is the density of water, g is the gravitational acceleration, m and n are two material parameters accounting for the effect of suction on the hydraulic conductivity, a, b, c, d, f, g and A, B, C, D, F, G are empirical material parameters for void ratio and water content constitutive relationships, respectively. A total of six parameters allow for a wide range of flexibility in the shape of each surface, which is essential since the void ratio and water content may be quite high at low stress and suction level, but decrease dramatically with a slightly increasing stress or suction. Though the number of parameters is large, they are well-constrained by data measured in the extreme planes in the void ratio (or water content) - net stress - suction space (i.e. the $(\sigma - u_a) = 0$ kPa plane and $(u_a - u_w) = 0$ kPa plane, thus, the measured data can be obtained from the conventional void ratio - effective stress relationship, a measured SWCC, and a measured shrinkage curve).

Any other advanced unsaturated soil constitutive model could be adopted if knowledge of plastic and elastic deformations is required when the deformation and/or water content does not change monotonically. Such scenarios are similar to the case of saturated layers under unloading/reloading conditions modeled by Fox and Pu (2012). For unsaturated condition, the

irrecoverable changes can also be induced by drying/wetting, which are likely to occur, for instance, in multilayer deposition of tailings.

6.2.2 Configuration and initialization

The consolidation of soft soil or tailings under the action of self-weight and evaporation, which are usually deposited with a considerable lateral width, can be treated as an idealized one-dimensional problem, as illustrated in Fig. 6.1(b). In the piece-wise formulation, the deposit is discretized using R_j elements that are labeled from the top to bottom of the layer using "j". Each element has unit cross-sectional area (plan view) according to the 1D idealization. The initial heights of all the elements are generally set to be identical and computed as $L_j^{(0)} = H^{(0)}/R_j$, where $H^{(0)}$ is the initial total thickness of the deposit, the superscripts with brackets designate the time step during calculation in the piece-wise formulation, superscript (0) indicates the initial condition prior to the consolidation process or immediately after deposition. The nodes storing the information for calculation by the finite difference method are set initially to be and remain at the center of their respective elements throughout the consolidation process, the element elevation coordinates z_j that are measured positive upward from fixed base of the deposit to their respective nodes are updated after each time step in the piece-wise computation model.

Very often slurries are deposited at a fully saturated condition with a high initial void ratio, which can be considered uniform in most cases. In the numerical formulation, the initial effective stress profile is allowed to correspond with the initial void ratio in the constitutive relationship by assuming a small vertical load q_0 on the top of the deposit. In this case, the initial total pore water pressures (i.e. the total stresses in excess of the effective stresses) are higher than steady-state pore water pressures. In other words, there exist initial excess pore water pressures within the profile,

which gradually dissipate during the consolidation process. No separate sedimentation process is incorporated in this model.

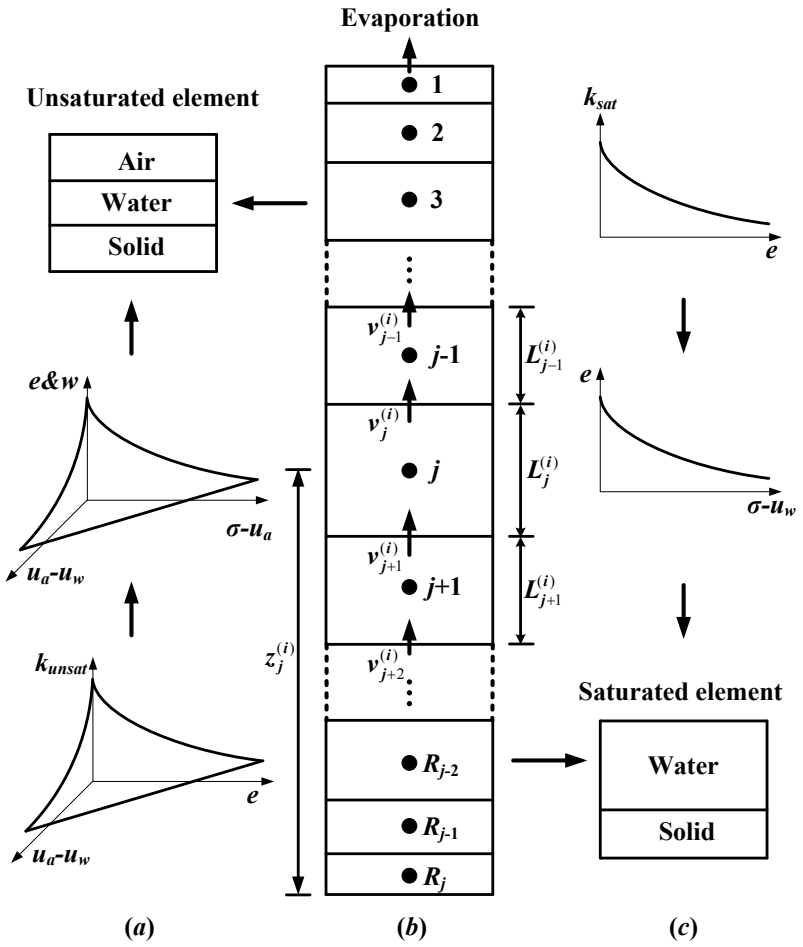

Fig. 6.1 Conceptual sketch of model formulation, using 3D consitutive surfaces for unsaturated zone and 2D constutive relationships for saturated zone

6.2.3 Flow in saturated and unsaturated zones and top boundary condition

The water flow modelled in this formulation is assumed in liquid form within the capillary regime using a given evaporative surface boundary without considering vapor flow. Although the volume change behaviour of soils in the near surface unsaturated zone and saturated zone

underneath should be characterized using two different types of constitutive relationships, i.e., 3D surfaces (Fig. 6.1(a)) for unsaturated and 2D curves (Fig. 6.1(c)) for saturated zones, respectively, the Darcy-Gersevanov law can be used to govern water flow relative to the movement of soil particles in both the zones. The key difference is that the unsaturated hydraulic conductivity for deformable soils varies not only with void ratio but also with matric suction. Thus, the hydraulic conductivity $k_j^{(i)}$ for each element within the entire profile at each time step is calculated according to (*i*) the current void ratio and suction from 3D hydraulic conductivity surface (see Fig. 6.1(a)) if the element is unsaturated or (*ii*) the current void ratio only from 2D hydraulic conductivity constitutive curve (see Fig. 6.1(c)), if the element is fully saturated. The hydraulic conductivity between two neighboring nodes *j* - 1 and *j*, which are used to calculate the water flowing across the interface between these two elements, is

$$k_{s,j}^{(i)} = \frac{k_{j-1}^{(i)} k_j^{(i)} (L_{j-1}^{(i)} + L_j^{(i)})}{L_{j-1}^{(i)} k_j^{(i)} + L_j^{(i)} k_{j-1}^{(i)}}, j = 2, 3, \ldots, R_j \tag{6.6}$$

where, $L_j^{(i)}$ is the height of element *j* at time step *i*. The subscript "*s*" represents that $k_{s,j}^{(i)}$ is equivalent series or harmonic average hydraulic conductivity between two neighboring nodes, calculated as that for layered soil system (i.e. Eq. (6.6)). The hydraulic head at node *j* is

$$h_j^{(i)} = z_j^{(i)} + \frac{u_j^{(i)}}{\gamma_w} \tag{6.7}$$

where, $z_j^{(i)}$ is the elevation of node *j* at time step *i* and $u_j^{(i)}$ the corresponding pore water pressure. γ_w is the unit weight of water. Eq. (6.7) is applicable for both positive (i.e. saturated zone) and negative (i.e. unsaturated zone) pore water pressures. Then, the hydraulic gradient between two nodes *j* - 1 and *j*, even when these two neighboring elements are in different states (i.e. one is saturated, the other is unsaturated), can be calculated as

$$i_j^{(i)} = \frac{h_{j-1}^{(i)} - h_j^{(i)}}{z_{j-1}^{(i)} - z_j^{(i)}}, j = 2, 3, \ldots, R_j \tag{6.8}$$

the relative discharge velocity between nodes j - 1 and j is calculated as

$$v_j^{(i)} = k_{s,j}^{(i)} i_j^{(i)}, j = 2, 3, \ldots, R_j \tag{6.9}$$

It should be noted that Eqs. (6.6), (6.8) and (6.9) are only applicable for j = 2, 3, …, R_j and calculation of the internal water flow within the profile. Boundary conditions are to be applied to obtain a solution. A zero hydraulic gradient $i_{R_j+1}^{(i)} = 0$ at the lower boundary is used to simulate a no flux condition (i.e. $v_{R_j+1}^{(i)} = 0$) at the stratum bottom in the present study. Other bottom boundary conditions can also be applied for any possible situations (including a known hydraulic head or none-zero flux) in reality.

Four possible scenarios of the top boundary conditions that may occur are considered in the present formulation:

Case (i): *No decantation and no evaporation*

If it assumed that water accumulating at the surface from consolidation is not removed, the top boundary is specified by determining the hydraulic gradient at the top surface using the expression provided by Fox and Berles (1997) for saturated case

$$i_1^{(i)} = \frac{H_w^{(0)} - h_1^{(i)}}{H^{(i)} - z_1^{(i)}} \tag{6.10}$$

in which, $H_w^{(0)}$ is the elevation of initial ground water table, which is equal to or higher than the initial total thickness of the deposit, and will keep constant with time if there is no decantation.

Case (ii): *Decantation and no evaporation*

In many practical cases, the water above the deposit is all or partially decanted (removed) or runs off. For full decantation, the boundary condition can be specified, by slightly modifying Eq. (6.10), as

$$i_1^{(i)} = \frac{H_w^{(i)} - h_1^{(i)}}{H^{(i)} - z_1^{(i)}} \tag{6.11}$$

in which, $H_w^{(i)} = H^{(i)}$ since the water table has the same elevation as the deposit surface at any time steps due to decantation.

Case (iii): *No decantation along with evaporation*

When evaporation is high such that cumulative evaporation at some point exceeds the volume of accumulated water on the surface, the hydraulic gradient at the surface is adjusted using

$$i_1^{(i)} = -\frac{E^{(i)} - (H_w^{(i)} - H^{(i)}) / \Delta t^{(i)}}{k_1^{(i)}} \tag{6.12}$$

in which, $\Delta t^{(i)}$ is the time increment and $E^{(i)}$ the evaporation rate that varies with time, but is assumed constant within each time step. The water mass conservation at the interface between deposits and evaporative environment is ensured by using Eq. (6.12). The negative pore water pressure at the surface induced by evaporation is calculated as

$$u_{top}^{(i)} = \frac{(H^{(i)} - z_1^{(i)}) i_1^{(i)} + h_j^{(i)} - H^{(i)}}{\gamma_w} \tag{6.13}$$

When the sum of the accumulated water on the surface and water flowing to the surface under self-weight consolidation gradients is sufficient to provide the amount of water for evaporation, the top boundary can still be approximately characterized using Eq. (6.10), but with the $H_w^{(0)}$ replaced by $H_w^{(i)}$. In this case, the water table elevation is affected by evaporation rather than decantation.

Case (iv): *Decantation with evaporation*

In the case of decantation (all accumulated water is removed) with high evaporation rates that exceed the rate of water flowing to the surface due to self-weight consolidation, the top boundary is characterized by simply modifying Eq. (6.12), as

$$i_1^{(i)} = -\frac{E^{(i)}}{k_1^{(i)}} \tag{6.14}$$

and the negative pore water pressure at the surface induced is calculated using Eq. (6.13) as with the previous case. When water flowing to the surface under self-weight consolidation gradients is sufficient to provide the amount of water for evaporation, the top boundary condition can be specified using Eq. (6.11) with $H_w^{(i)} = H^{(i)}$.

The top boundary relative discharge velocity is computed as

$$v_1^{(i)} = k_1^{(i)} i_1^{(i)} \tag{6.15}$$

in which, $i_1^{(i)}$ is determined by one of the Eqs. (6.10), (6.11), (6.12) or (6.14) depending on four different cases for top boundary conditions discussed above.

6.2.4 Deformation in unsaturated zone

The saturated formulation for deformation is extended to the unsaturated state by incorporating the volumetric water content in the governing equation for numerical analysis (Sheng et al. 2003, Georgiadis et al. 2005), since the volumetric strain of three-phase media is no longer equal to net fluid flow over an infinitesimal time increment, even though both the fluid and solid are assumed to be incompressible. Using the volumetric water content, the flow continuity equation can be temporally discretized by explicit finite difference technique, as

$$L_j^{(i)} \theta_{w,j}^{(i)} = L_j^{(i-1)} \theta_{w,j}^{(i-1)} - (v_j^{(i-1)} - v_{j+1}^{(i-1)}) \times \Delta t^{(i-1)} \tag{6.16}$$

in which, $\theta_{w,j}^{(i-1)}$ and $\theta_{w,j}^{(i)}$ are the volumetric water contents of element j before and after the time increment, $\Delta t^{(i-1)}$. $L_j^{(i-1)}$ and $L_j^{(i)}$ are the heights of element j before and after this time increment. The product of height L and volumetric water content θ_w is the elemental water volume, considering that each element has a unit cross-sectional area. Based on the basic volume-mass relationship (Fredlund and Rahardjo 1993), the volumetric water content can be calculated from degree of saturation or gravimetric water content, as

$$\theta_{w,j}^{(i)} = \frac{S_j^{(i)} e_j^{(i)}}{1+e_j^{(i)}} = \frac{w_j^{(i)} G_s}{1+e_j^{(i)}} \tag{6.17}$$

in which, $S_j^{(i)}$ and $w_j^{(i)}$ are degree of saturation or gravimetric water content for element j at time step i. $e_j^{(i)}$ *is* the void ratio for element j at time step i. G_s is the specific gravity. Multiplying element height on both sides of Eq. (6.17), the water volume of each element can be expressed as

$$L_j^{(i)} \theta_{w,j}^{(i)} = \frac{L_j^{(i)} G_s}{1+e_j^{(i)}} w_j^{(i)} \tag{6.18}$$

The mass of solids within each element is calculated as

$$M_{s,j}^{(i)} = \frac{L_j^{(i)} G_s}{1+e_j^{(i)}} \rho_w \tag{6.19}$$

There are no exchanges of soil particles between two adjacent elements in the present unsaturated formulation, as with the original saturated formulation in Fox and Berles (1997). Due to this reason, the solid mass for each element is invariant throughout and equal to its initial value

$$M_{s,j}^{(i)} = M_{s,j}^{(0)} = \frac{L_j^{(0)} G_s}{1+e_j^{(0)}} \rho_w \tag{6.20}$$

Combining Eqs. (6.18), (6.19), (6.20) and (6.16), gives

$$w_j^{(i)} M_{s,j}^{(0)} = w_j^{(i-1)} M_{s,j}^{(0)} - [(v_j^{(i-1)} - v_{j+1}^{(i-1)}) \Delta t^{(i-1)}] \rho_w \tag{6.21}$$

The product of $w_j^{(i)}$ and $M_{s,j}^{(0)}$ is the water mass for element j at time step i. Eq. (6.21) is alternative form of forward difference in terms of time, which is equivalent to Eq. (6.16), and explicitly indicates that the mass conversation of water is guaranteed between any two consecutive time steps. The weight for each soil element at the end of time step i can be obtained by summing the water and solid weight within the element as (noting that the element has a unit cross-sectional area)

$$W_j^{(i)} = (w_j^{(i)} M_{s,j}^{(0)} + M_{s,j}^{(0)})g \tag{6.22}$$

The vertical total stress at each node is computed from the self-weight of the deposits above, surface water weight and the assumed surface vertical load q_0 for forming the initial effective stress profile as

$$\sigma_j^{(i)} = (H_w^{(i)} - H^{(i)})\rho_w g + q_0 + \frac{W_j^{(i)}}{2} + \sum_{k=1}^{j-1} W_k^{(i)} \tag{6.23}$$

in which, $H_w^{(i)} = H^{(i)}$ for decantation and the first term vanishes. When there is no decantation the current value of $H_w^{(i)}$ depends on the evaporation rate or other possible environmental factors.

The gravimetric water content and total stress for each element at time step i can be directly obtained using the above derivations. Therefore, gravimetric water content surface (Eq. (6.4)) is selected herein and used to find the the suction at time step i for each unsaturated element as

$$(u_{a,j}^{(i)} - u_{w,j}^{(i)}) = \frac{1 + C(\sigma_j^{(i)} - u_{a,j}^{(i)}) - F[10^{(w_j^{(i)} - A)/B}](\sigma_j^{(i)} - u_{a,j}^{(i)}) - [10^{(w_j^{(i)} - A)/B}]}{G[10^{(w_j^{(i)} - A)/B}] - D} \tag{6.24}$$

With known suction, the void ratio for unsaturated element at time step i can be obtained from the 3D void ratio surface (Eq. (6.3)), as

$$e_j^{(i)} = a + b\log\left[\frac{1 + c(\sigma_j^{(i)} - u_{a,j}^{(i)}) + d(u_{a,j}^{(i)} - u_{w,j}^{(i)})}{1 + f(\sigma_j^{(i)} - u_{a,j}^{(i)}) + g(u_{a,j}^{(i)} - u_{w,j}^{(i)})}\right] \tag{6.25}$$

The height of the element can be obtained using

$$L_j^{(i)} = \frac{L_j^{(0)}}{1+e_j^{(0)}}[1+e_j^{(i)}] \tag{6.26}$$

in which, $e_j^{(0)}$ and $e_j^{(i)}$ are the initial void ratio for element j and void ratio for element j at time step i, respectively. $L_j^{(i)}$ is the height for element j at time step i. The degree of saturation for each element can be readily computed using the basic volume mass relationship

$$S_j^{(i)} = \frac{w_j^{(i)} G_s}{e_j^{(i)}} \tag{6.27}$$

It is found from the above derivation that all the state parameters related to unsaturated element can be expressed in explicit forms by using gravimetric water content surface as constitutive relationship. If the volumetric water content or degree of saturation surfaces are used, these unknown state parameters cannot be reached explicitly from the continuity equation of flow, since the volumetric water content and degree of saturation is related to current void ratio that is unknown and to be determined. Therefore, an iterative procedure on the constitutive surfaces would be required to obtain the solution, which may likely contribute to numerical non-convergence and instability.

6.2.5 Deformation in saturated zone and quasi-unsaturated formulation

Within the saturated zone, combining Eq. (6.17) with the degree of saturation $S = 1$ and Eq. (6.16), gives

$$L_j^{(i)} \frac{e_j^{(i)}}{1+e_j^{(i)}} = L_j^{(i-1)} \frac{e_j^{(i-1)}}{1+e_j^{(i-1)}} - (v_j^{(i-1)} - v_{j+1}^{(i-1)}) \times \Delta t^{(i-1)} \tag{6.28}$$

Substituting both sides of the equality $L_j^{(i)}/(1+ e_j^{(i)}) = L_j^{(i-1)}/(1+ e_j^{(i-1)})$ on the corresponding sides of Eq. (6.28), yields

$$L_j^{(i)} = L_j^{(i-1)} - (v_j^{(i-1)} - v_{j+1}^{(i-1)}) \times \Delta t^{(i-1)} \tag{6.29}$$

Eq. (6.29) states that the deformation of each element is equal to the net fluid outflow over a time increment for saturated elements, which was originally suggested by Fox and Berles (1997), and the void ratio for each element is calculated as

$$e_j^{(i)} = \frac{L_j^{(i)}}{L_j^{(0)}}(1 + e_j^{(0)}) - 1 \tag{6.30}$$

Once the void ratio is known in the saturated zone, the effective stress can be obtained using the 2D constitutive curve, and then pore water pressure is calculated as the total stress in excess of effective stress. The value of degree of saturation remains unity in saturated zone, and other parameters, such gravimetric water content, can also be determined using basic volume-mass relationship.

In the quasi-unsaturated formulation, calculations of deformation and pore water pressure in the whole computational domain are the same as that for saturated zone (i.e. using Eq. (6.29) and Eq. (6.30) based on the saturation assumptions mentioned above). Specifically, under evaporation, formation of negative pore water pressure within the soil near surface is allowed, but the voids between the solid particles are still considered to be fully saturated by fluids. In other words, the deformation behaviour and hydraulic conductivity of soil elements are still characterized by 2D constitutive relationships for saturated soils (i.e. Eqs (6.1) and (6.2)), the suction has the same effect on the volume change as the mechanical stress. In previous models, the saturation assumption has been regarded applicable as long as the surface soil under evaporation does not reach the shrinkage limit, as in CONDES (Yao et al. 2002), or the surface suction is lower than the air entry value, as in MinTaCo (Seneviratne et al. 1996). The latter approach is adopted in this study by prescribing a maximum value for the surface suction, i.e.

when the surface suction determined by Eq. (6.13) is larger than the prescribed value, the top boundary condition switches to a constant suction boundary and the actual evaporation reduces below the potential evaporation. Thus, the quasi-unsaturated formulation is similar to MinTaCo model except that numerical discretization is conducted by different strategies.

After every time step, the total thickness of the deposits can be simply obtained by summing up the new heights of all elements at both saturated and unsaturated zones, as

$$H^{(i)} = \sum L_j^{(i)} \tag{6.31}$$

6.2.6 Time increment

The time increment that can ensure a numerically stable explicit finite-difference solution to the saturated Terzaghi consolidation equation can be found elsewhere, which has been adapted by Fox and Berles (1997) to consider the large deformation problem. This time increment for each saturated element is written as

$$\Delta t_j^{(i)} = \frac{\alpha a_{v,j}^{(i)} (L_j^{(i)})^2}{k_j^{(i)} (1 + e_j^{(i)})} \tag{6.32}$$

where α is a constant smaller than 0.5, $\alpha = 0.4$ is employed herein as suggested in Fox and Berles (1997) and Deng and Zhou (2015). $a_{v,j}^{(i)}$ is the coefficient of compressibility, which can be obtained by differentiating compressibility curve (Eq. (6.1)) at respective stress state. In this study, Eq. (6.32) is modified by replacing $a_{v,j}^{(i)}$ in compressibility curve (Eq. (6.1)) with the coefficient of compressibility $a_{vs,j}^{(i)}$ with respect to suction in void ratio constitutive surface (Eq. (6.3)), in order to determine the time increment for elements in unsaturated zone. In this way, the smallest time increment can be obtained along all possible stress paths, since the coefficient of compressibility with respect to suction is usually smaller than that with total stress in void ratio constitutive surface.

In order to avoid the calculation of derivative functions, the coefficients of compressibility $a_{v,j}^{(i)}$ for saturated zone and $a_{vs,j}^{(i)}$ for unsaturated zone can be computed using Eqs. (6.33) and (6.34), respectively

$$a_{v,j}^{(i)} = -\left.\frac{\Delta e}{\Delta(\sigma - u_w)}\right|_{\sigma - u_w = \sigma_j^{(i)} - u_{w,j}^{(i)}} \tag{6.33}$$

$$a_{vs,j}^{(i)} = -\left.\frac{\Delta e}{\Delta(u_a - u_w)}\right|_{\substack{\sigma - u_a = \sigma_j^{(i)} - u_{a,j}^{(i)} \\ u_a - u_w = u_{a,j}^{(i)} - u_{w,j}^{(i)}}} \tag{6.34}$$

where, Δe is the increment in the void ratio with respect to an infinitesimal effective stress or suction increment, which can be calculated using the associated constitutive surfaces. Numerical studies discussed in detail later show that $\Delta(\sigma - u_w) = \Delta(u_a - u_w) = 10^{-3}$ kPa can provide results that are both stable and reliable. The time step that is smallest among those for all elements in both saturated and unsaturated zones is used to forward the calculation, i.e. $\Delta t^{(i)} = \min\{\Delta t_1^{(i)}, \Delta t_2^{(i)}, \ldots, \Delta t_{R_j}^{(i)}\}$.

6.3 Code development

The computer program for both unsaturated and quasi-unsaturated formulations, which will be called UNSAT-CON, is developed in this study. The flow chart illustrating the basic computational procedure is shown in Fig. 6.2. The input parameters required in this program include: (i) the initial height of the deposits $H^{(0)}$; (ii) the initial elevation of the water table $H_w^{(0)}$; (iii) the number of elements R_j; (iv) the specific gravity of solid G_s; (v) the initial void ratio profile $e_j^{(0)}$; (vi) the parameters in constitutive relationships for both saturated and unsaturated zones; (vii) top and bottom boundary conditions; (viii) the running time. The other initial parameters can be determined from these inputs, such as, the initial solid content profile using SC = $G_s/(G_s+e)$, the

initial gravimetric content profile by $w = Se/G_s$ since the initial degree of saturated are known to be 100% in the entire soil profile, and the value of q_0 for forming the initial effective stress profile determined from the initial void ratio and constitutive relationship.

After initialization of the problem to be analysed, UNSAT-CON calculates the elevation of each node, series hydraulic conductivities between two contiguous nodes, which are used to determine the time increment for current time step. The hydraulic gradients between two contiguous elements are calculated from the total hydraulic head at each node, and then the flow through element interfaces can be calculated during a time increment. The calculations until now are almost the same for both quasi-unsaturated and unsaturated analyses, except that the unsaturated analysis involves calculating hydraulic conductivities of unsaturated element according to both void ratio and suction.

The calculations for obtaining the new void ratio, element height, pore water pressure (or suction), stress state and water content for each element are dealt with differently in unsaturated and quasi-unsaturated analyses in UNSAT-CON. The detailed procedures are described as follows:

- *Unsaturated analysis.* As detailed earlier, the deposits are initially in a state of fully saturated condition, the possible evaporation will first lead to dewatering of deposits near the ground surface, and the unsaturated zone within the deposits will extend to a greater depth if there is a continuous evaporation acting on the surface. This means that the saturated and unsaturated zones are existing simultaneously within the deposit at a particular time, with a transition point moving downward. These two zones should be analysed using different constitutive relationships: 3D constitutive surface for unsaturated zone and 2D constitutive curve for saturated zone. The associated challenge in numerical implementation is to ensure a smooth transition between saturation and unsaturation states (i.e. track the movement of the transition point). In this study,

two checks, for all elements at every time step, are incorporated into the program to deal with two different zones and facilitate the state transition (see Fig. 6.2). The first check is made on the state of each element. If the element is already unsaturated at the beginning of the time step, UNSAT-CON computes the gravimetric water content and total stress using Eqs. (6.21) and (6.23), and then uses the 3D constitutive surfaces to obtain the negative pore water pressure (Fig. 6.3(a)), void ratio (Fig. 6.3(b)), element height and degree of saturation by Eqs. (6.24), (6.25), (6.26) and (6.27), respectively. If the element is saturated at the beginning of the time step, UNSAT-CON first calculates the new element height and void ratio using Eqs. (6.29) and (6.30) and total stress, and the second check is made on the calculated void ratio(see Fig. 6.3(c)). If the calculated void ratio is smaller than reference void ratio $e_{j,r}^{(i)}$ corresponding to calculated total stress in the 2D constitutive curve (i.e. the black circular point in Fig. 6.3(c)), this element has become unsaturated state at the end of the time step since the effective stress required for the calculated void ratio is higher than the actual total stress. The calculated void ratio and height from Eqs. (6.29) and (6.30) are abandoned for this element and the program reanalyzes this element using 3D constitutive surface (i.e. Fig. 6.3(a) and Fig. 6.3(b) or Eqs. (6.21), (6.23), (6.24), (6.25), (6.26) and (6.27)). If the calculated void ratio is larger than reference void ratio $e_{j,r}^{(i)}$, i.e. the black square point in Fig. 6.3(c), which means this element is still saturated at the end of this time step, effective stress and pore water pressure are calculated on the basis of 2D saturated constitutive curve.

- *Quasi-unsaturated analysis.* Two checks described above are not required, all the elements are dealt with using 2D saturated constitutive curves throughout the analysis (see Fig. 6.2), even though the effective stress is higher than the available total stress (i.e. the black circular point in Fig. 6.3(c)).

After performing the *unsaturated analysis* or *quasi-unsaturated analysis* over all elements for the current time increment, UNSAT-CON calculates the total thickness of deposit at the updated elapsed time t using Eq. (6.31). The *unsaturated analysis* or *quasi-unsaturated analysis* are defined in sections 6.2.4 and 6.2.5, respectively. The program terminates if $t \geq t_f$ or repeats the calculation sequence for the next time increment if $t < t_f$, where t_f is a user-specified elapsed time.

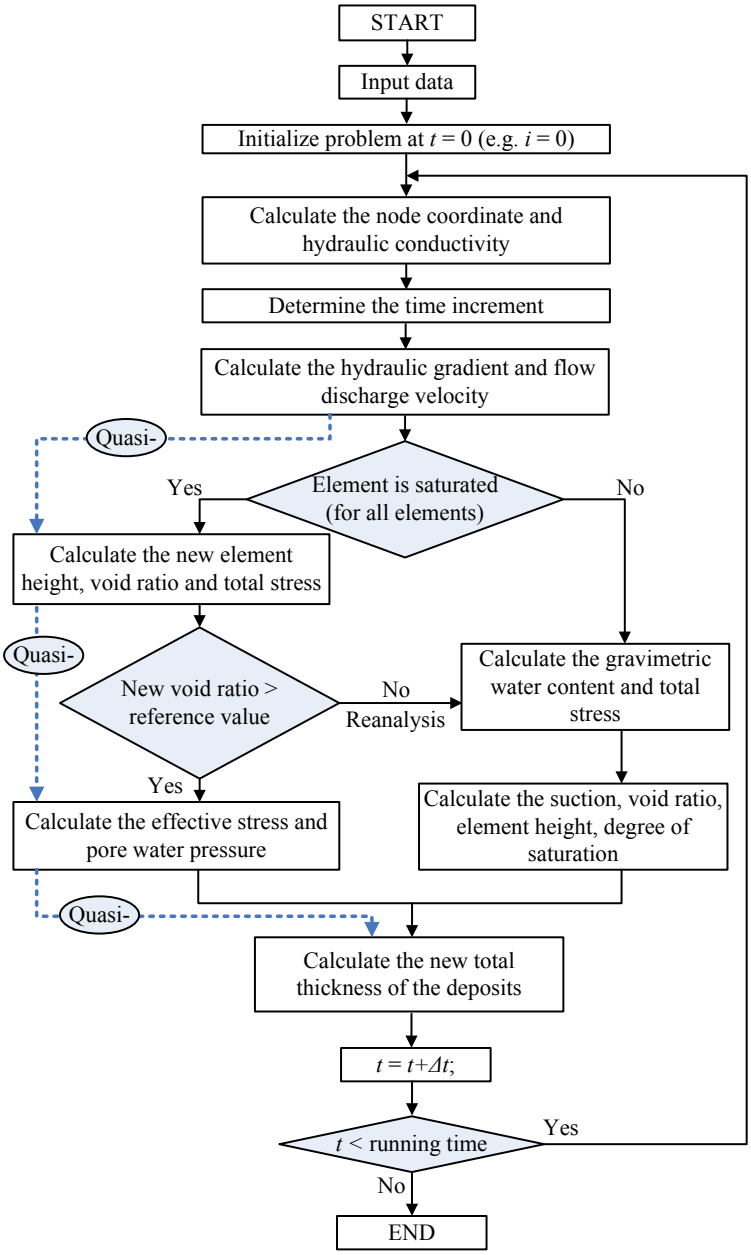

Fig. 6.2 Flow chart of computational procedure

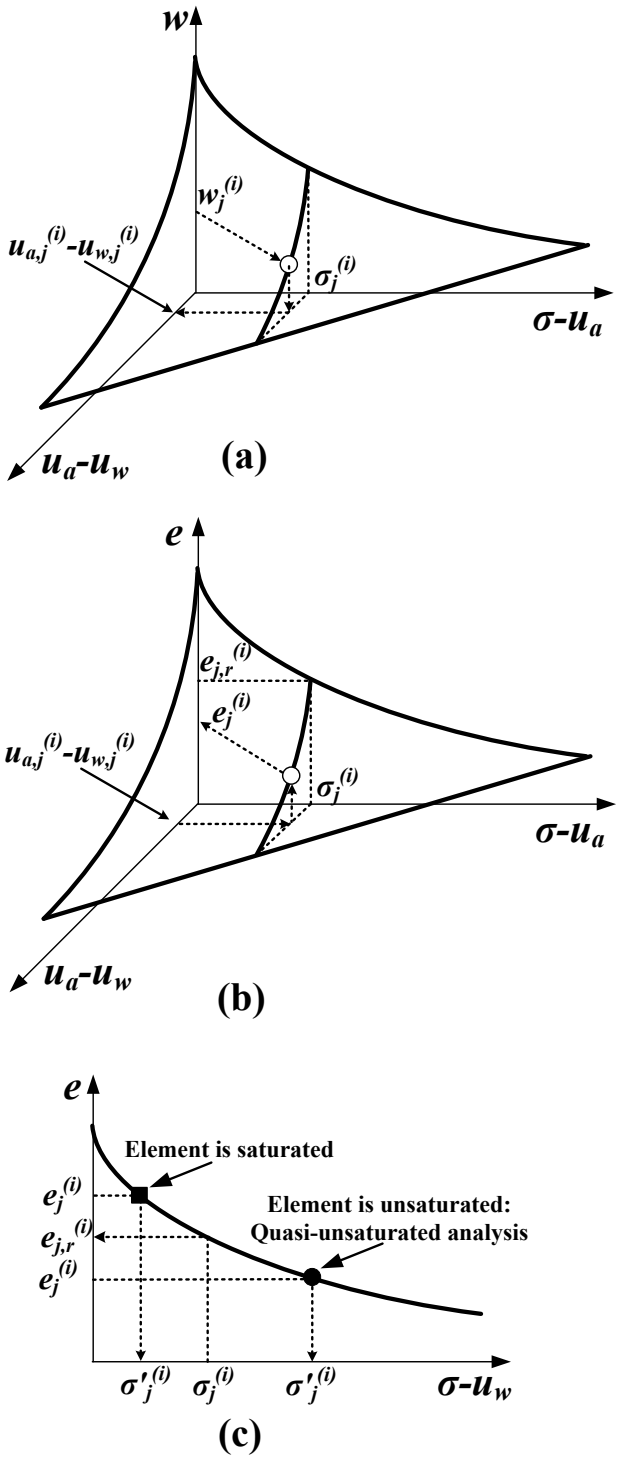

Fig. 6.3 Transition between saturation and unsaturation: (a) determination of suction for unsaturated elements; (b) determination of void ratio for unsaturated elements; (c) determination of the state of elements, and finding the effective stress for saturated elements as well as quasi-unsaturated analysis

6.4 Verification against Saturated Large Strain Consolidation

The numerical algorithm implementation is verified using an illustrative example of large strain consolidation of fully saturated soils from McVay et al. (1986), where reference solutions are available from different numerical techniques for solving various forms of mathematical expressions. A solution to this problem has also been provided by Fox and Berles (1997) using CS2. This example involves consolidation of a single-drained column of clay with an initial high uniform void ratio profile under its self-weight force only. The basic properties are provided in Table 6.1, and 2D saturated constitutive curves (Eqs. (6.1) and (6.2)) for this clay are

$$e = 12.19(\sigma'(\text{kPa}))^{-0.29} \tag{6.35}$$

$$k(\text{m/s}) = 1.41\times10^{-11} e^{4.11} \tag{6.36}$$

The bottom boundary has a zero flux for this example. Without evaporation, the top boundary is specified as Case (*i*) or Case (*ii*) to consider decantation and no decantation scenarios, respectively. UNSAT-CON reverts to CS2 and operates in fully saturated regime everywhere within the computational domain in the absence of evaporation on the surface. The difference is that the dimensionless approach in CS2 is not followed in UNSAT-CON. Three different resolutions (i.e. number of elements to discretize the column = 50, 100 and 200) are considered to perform simulations using UNSAT-CON.

Table 1. Basic properties for the example from McVay et al. (1986)

Parameters	Initial height	Initial void ratio profile	Initial effective stress profile	Specific gravity
Symbols (units)	$H^{(0)}$ (m)	$e_j^{(0)}$	$\sigma_j'^{(0)}$ (kPa)	G_s
Values	6.33	18.8	0. 224	2.71

Fig. 6.4(a) compares the value of soil column height as a function of logarithmic time from existing results reported by Fox and Berles (1997) and by McVay et al. (1986) during the first 400 days after deposition for decantation. All three curves obtained using different resolutions overlap each other, coincide with that from CS2 analysis, and are also in a good agreement with McVay et al. (1986). The column heights after 400 days of self-weight consolidation are 3.5757 m, 3.5759 m and 3.5760 m for number of elements = 50, 100, 200, respectively. The resolution in this range does not have a significant influence on the simulation accuracy, but the running time substantially increases from 17.24s to 43.51s and then 229.72s with increasing resolution for this case. Fig. 6.4(b) illustrates the comparison in the void ratio profile on the 400th day for decantation, and the same conclusion can be drawn as column height *vs*. time curve. The excellent agreements suggest that the algorithm is correctly implemented and reliable for modeling the large strain consolidation of saturated soils.

The no decantation condition is also simulated using UNSAT-CON. The obtained two curves are almost identical to those shown in Fig. 6.4(a) and (b), indicating that decantation has no effect on the computed results in this example. This is because whether decantation or not does not result in any difference in the outflow of water at the top for saturated case. The amount of water outflow is the product of hydraulic conductivity of the top element and the hydraulic gradient at the surface. The hydraulic gradients, for decantation and no decantation, are calculated using Eqs (6.10) and (6.11), respectively, in which, the pore water pressure that constitutes a component in hydraulic head, is the total stress in excess of effective stress, $u_1^{(i)} = \sigma_1^{(i)} - \sigma'^{(i)}_1$. The total stress is determined by Eq. (6.24) without the last term of summation, the effective stress is obtained from current void ratio, $e_1^{(i)}$, through the constitutive relationship. Then, the hydraulic gradient at the surface is derived as

$$i_1^{(i)} = \frac{H_w^{(i)} - [z_1^{(i)} + H_w^{(i)} - H^{(i)} + (q_0 + W_1^{(i)}/2 - \sqrt[C_2]{e_1^{(i)}/C_1})/\gamma_w]}{H^{(i)} - z_1^{(i)}} \qquad (6.37)$$

in which, the $H_w^{(i)} = H_{(i)}$ for decantation and $H_w^{(i)} = H_0^{(i)}$ for no decantation, but cancels in above equation for both cases. In other words, the hydraulic gradient near the surface is independent of $H_w^{(i)}$. If the void ratios are the same for both cases, the outflow will also be identical, since the hydraulic conductivity is also related to the void ratio through the constitutive relationship. Both cases, indeed, have equal void ratios since they are the derived from identical initial values one time step after another.

6.5 Verification against an analytical solution to unsaturated flow

An analytical solution to steady state evaporation provided by Sadeghi et al. (2012) is used to verify the capability of UNSAT-CON in modelling unsaturated flow. This exact solution was obtained by integrating the Darcy's law from a fixed shallow water table under a constant rate of evaporation, making use of hydraulic conductivity function of Brooks and Corey (1964):

$$k = \begin{cases} k_{sat} & (h \le h_b) \\ k_{sat}(h/h_b)^{-P} & (h > h_b) \end{cases} \qquad (6.38)$$

where k_{sat} is the saturated hydraulic conductivity, h and h_b are the pressure head and bobbing pressure head, and P is a material constant. The solution is presented in the form of z as a function of h and E, i.e. $z = (h, E)$, where z vertical distance from water table and E is the constant evaporation rate at steady state condition. This solution is able to predict the location of drying front where hydraulic conductivity approaches zero and hydraulic gradient approaches infinity, above which the Darcy's law is not applicable since water phase is not continuous.

Different from UNSAT-CON, this analytical solution does not involve any' deformation and is not time-dependent. In order to obtain comparable results, a minimal modification is made on UNSAT-CON by omitting codes for calculation of new element heights and therefore node elevations. UNSAT-CON is executed from a given initial condition until the pore water pressure profile does not change with time, i.e. reaching a steady state condition under a prescribed evaporation boundary condition.

A test case of evaporation in clay is reanalysed using UNSAT-CON in this way, adopting the same hydraulic conductivity function of Brooks and Corey (1964). The associated parameters are h_b = 90 cm, k_{sat} = 2.94 cm/day and P = 3.30, which are the only set of material parameters required for the analytical solution. The other constitutive parameters required in UNSAT-CON for this case are the same as those for a column test presented in the next chapter. A uniform of void ratio of 2.5 is used to initialise this example. These parameters for void ratio and water contents surfaces along with the initial condition will affect only the results before reaching the steady state condition. The steady state pore water pressure only depends on the hydraulic conductivity function as well as boundary conditions. The top boundary condition is specified as Case (*iv*) with evaporation rate of $0.05k_{sat}$, same as that used in the analytical solution. A zone flux is applied for the bottom boundary condition as long as the bottom element remains saturated, which switches to a constant head with pore water pressure of 0 kPa to simulate the ground water table.

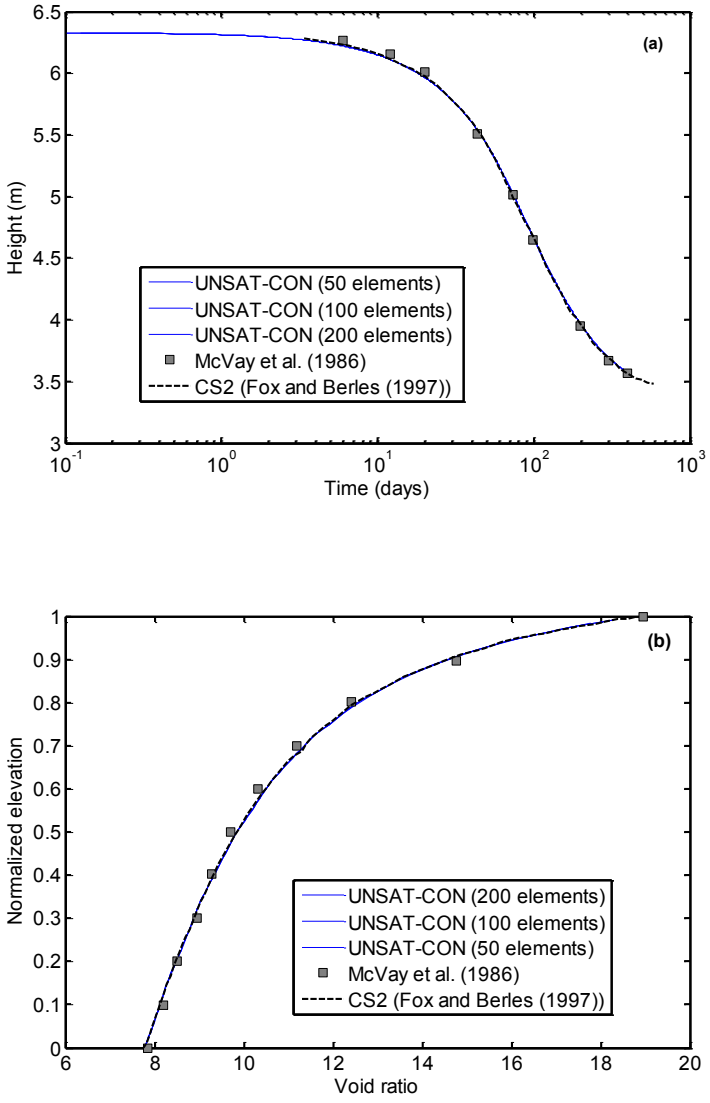

Fig. 6.4 Analysis results with decantation: (a) Height *vs.* Time curve; (b) void ratio profile after 400 days

Fig. 6.5 shows the pore water pressure profiles at some elapsed time predicted by UNSAT-CON for this case. The pore water pressure gradually decreases from the initial saturated condition, since the 700th day no variation in the profile can be observed, indicating the steady state condition has been reached. Fig. 6.6 compares the steady state pressure head profile predicted using UNSAT-

CON to the analytical solution given in Sadeghi et al. (2012) in the dimensionless scale. It should be noted that height of profile used UNSAT-CON is 2.55 m above the ground water table, a little lower than the location of drying front of around 2.57 m given by analytical solution. The ability of UNSAT-CON based on Darcy's law to model unsaturated flow is limited to the capillary regime with a continuous water phase below the drying front, also the infinity hydraulic gradient near the drying front is difficult to be predicted by a numerical method even using a very fine mesh. Nevertheless, the 2.55 m used in UNSAT-CON with 100 elements for discretization is almost identical to the value given by an alternative approximate closed-form solution in Sadeghi (2012). The excellent agreement shown in Fig. 6.6 illustrates the capability of UNSAT-CON in modeling unsaturated liquid water flow.

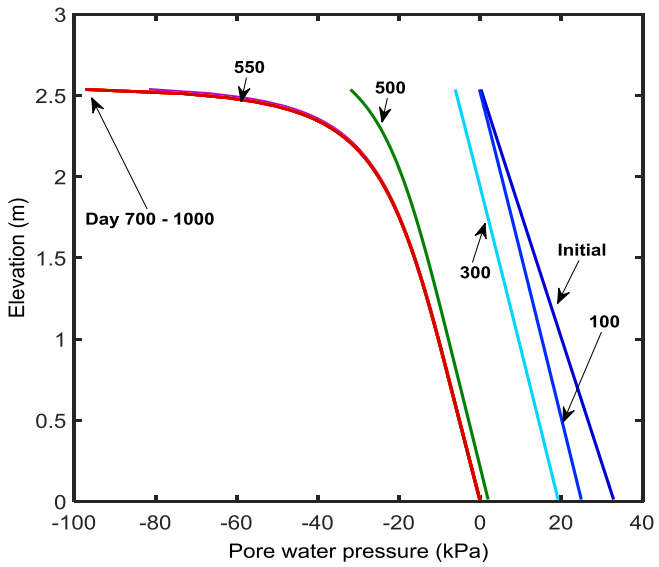

Fig. 6.5 Pore water pressure profiles predicted by UNSAT-CON

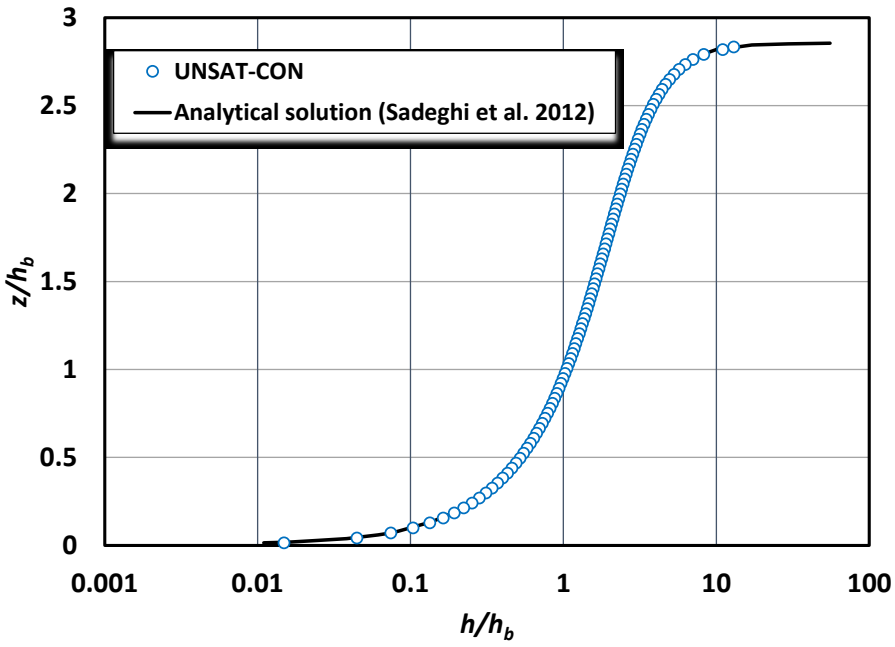

Fig. 6.6 Comparison of state steady pressure head profiles above the water table predicted by UNSAT-CON and analytical solution by Sadeghi et al. (2012)

6.6 Conclusion

The one dimensional numerical formulation for coupled large strain consolidation and saturated and unsaturated flow is developed using a piece-wise linear framework. Two types of constitutive relationships, either formulated using two independent stress variables, or the classical effective stress principle, are employed to describe the hydro-mechanical behaviour of soils in the unsaturated and saturated zones, respectively. In the unsaturated zone, both the void ratio and water content vary with net stress as well as matric suction, while hydraulic conductivity is dependent on void ratio as well as matric suction. In the saturated zone, void ratio varies only with effective stress and hydraulic conductivity depends on only void ratio.

This formulation is implemented in a novel algorithm, called UNSAT-CON, using the finite difference scheme, which can transit the soil element from saturated to unsaturated states in a smooth manner and does not require an iterative procedure. The developed formulation is strictly mass conservative not only within the computational domain but on the top surface where soil interacts hydraulically with the atmosphere. Decantation and evaporation are accounted for using boundary conditions of head or flow types, but formulated using a unified form, i.e. hydraulic gradient at the top. By omitting some computational procedures, UNSAT-CON can revert to a simplified formulation to perform quasi-unsaturation analysis, in which the hydro-mechanical behaviour in the unsaturated zone is also characterized using the effective stress principle.

The numerical implementation is verified in this chapter for large strain consolidation by self-weight only using the numerical solution, and for evaporation from fixed water table using an analytical solution. Testing of the unsaturated formulation of UNSAT-CON using comparable numerical solutions and laboratory and field studies of dewatering of a fine grained soil are presented in the next chapter.

Glossary

Symbols

e	Void ratio
k	Hydraulic conductivity
σ'	Effective stress
σ	Total stress
u_w	Pore water pressure
C_1, C_2	Material parameters for compressibility relationship
H_1, H_2	Material parameters for hydraulic conductivity relationship
u_a	Pore air pressure
w	Gravimetric water content
ρ_w	Density of water
g	Gravitational acceleration
m, n	Material parameters accounting for the effect of suction on the hydraulic conductivity
a, b, c, d, f, g	Material parameters for void ratio constitutive relationship
A, B, C, D, F, G	Material parameters for water content constitutive relationship
R_j	Number of the elements
j	Labeling of the element
i	Time step
$L_j^{(0)}$	Initial height of element
$H^{(0)}$	Initial total thickness of the deposit
z	Element elevation coordinates
q_0	Assuming a small vertical load on the top of the deposit
$k_j^{(i)}$	Hydraulic conductivity for each element
$k_{s,j}^{(i)}$	Equivalent series hydraulic conductivity
$u_j^{(i)}$	Pore water pressure of node j at time step i
γ_w	Unit weight of water
$v_j^{(i)}$	Relative discharge velocity between nodes
$H_w^{(0)}$	Elevation of initial ground water table
$H^{(i)}$	Elevation of deposit surface
$H_w^{(i)}$	Elevation of water table
E	Evaporation rate at time i
θ_w	Volumetric water contents
$\theta_{w,j}^{(i-1)}$	Volumetric water contents of element j before the time increment, $\delta t^{(i-1)}$
$\theta_{w,j}^{(i)}$	Volumetric water contents of element j after the time increment, $\delta t^{(i-1)}$
$e_j^{(i)}$	Void ratio for element j at time step i
G_s	Specific gravity

$M_{s,j}^{(i)}$	Mass of solids within each element
$W_{s,j}^{(i)}$	Weight of each soil element
α	Constant smaller than 0.5
$a_{v,j}^{(i)}$	Coefficient of compressibility for saturated zone
$a_{vs,j}^{(i)}$	Coefficient of compressibility with respect to suction
SC	Solid content
$e_{j,r}^{(i)}$	Reference void ratio
t_f	User-specified elapsed time
k_{sat}	Saturated hydraulic conductivity
h	Pressure head
h_b	Bobbing pressure head
P	Material constant in brooks and corey (1964)

Abbreviations

SWCC	Soil water characteristic curve
1D	One-dimensional
2D	Two-dimensional
3D	Three-dimensional

6.7 References

Alonso, E.E., Gens, A., & Josa, A. (1990). A constitutive model for partially saturated soils. Géotechnique, 40(3), 405-430.

Alonso, E. E., Vaunat, J., & Gens, A. (1999). Modelling the mechanical behaviour of expansive clays. Engineering Geology, 54(1), 173-183.

Bishop, A. W., & Blight, G. E. (1963). Some aspects of effective stress in saturated and partly saturated soils. Géotechnique, 13(3), 177-197.

Brooks, R. H., & Corey, A. T. (1964). Hydraulic properties of porous media and their relation to drainage design. Transactions of the ASAE, 7(1), 26-0028.

Daliri, F., Kim, H., Simms, P., & Sivathayalan, S. (2014). Impact of desiccation on monotonic and cyclic shear strength of thickened gold tailings. Journal of Geotechnical and Geoenvironmental Engineering, 140(9), 04014048.

Daliri, F., Simms, P., & Sivathayalan, S. (2015). Shear and dewatering behaviour of high density gold tailings in a laboratory simulation of multi-layer deposition. Canadian Geotechnical Journal, Manuscript ID: cgj-2014-0411.R2. Accepted with minor comments, December 2015.

Deng, A., & Zhou, Y. (2015). Modeling electroosmosis and surcharge preloading consolidation. I: Model formulation. Journal of Geotechnical and Geoenvironmental Engineering, 10.1061/(ASCE) GT.1943-5606.0001417 04015093.

De Vries, D. A. (1987). The theory of heat and moisture transfer in porous media revisited. International Journal of Heat and Mass Transfer, 30(7), 1343-1350.

Fisseha, B., Bryan, R., & Simms, P. (2010). Evaporation, unsaturated flow, and salt accumulation in multilayer deposits of "paste" gold tailings. Journal of Geotechnical and Geoenvironmental Engineering, 136(12), 1703-1712.

Fox, P. J., & Berles, J. D. (1997). CS2: A piecewise-linear model for large strain consolidation. International Journal for Numerical and Analytical Methods in Geomechanics, 21(7), 453-475.

Fox, P. J. (2007). Coupled large strain consolidation and solute transport. I: Model development. Journal of Geotechnical and Geoenvironmental Engineering. 10.1061/(ASCE)1090-0241(2007)133:1(3), 3–15.

Fox, P. J. and Pu, H. (2012). Enhanced CS2 Model for Large Strain Consolidation. International Journal of Geomechanics, 10.1061/(ASCE)GM.1943-5622.0000171, 574-583.

Fox, P. J., Pu, H., and Berles, J. (2014). CS3: Large strain consolidation model for layered soils. Journal of Geotechnical and Geoenvironmental Engineering. 10.1061/(ASCE)GT.1943-5606.0001128, 04014041.

Fredlund, D. G., & Morgenstern, N. R. (1976). Constitutive relations for volume change in unsaturated soils. Canadian Geotechnical Journal, 13(3), 261-276.

Fredlund, D. G., & Morgenstern, N. R. (1977). Stress state variables for unsaturated soils. Journal of Geotechnical and Geoenvironmental Engineering, 103(ASCE 12919).

Fredlund, D. G., & Rahardjo, H. (1993). Soil mechanics for unsaturated soils. John Wiley & Sons.

Fredlund, D. G., & Xing, A. (1994). Equations for the soil-water characteristic curve. Canadian Geotechnical Journal, 31(4), 521-532.

Fujiyasu, Y., & Fahey, M. (2000). Experimental study of evaporation from saline tailings. Journal of Geotechnical and Geoenvironmental Engineering, 126(1), 18-27.

Gallipoli, D., Wheeler, S. J., & Karstunen, M. (2003). Modelling the variation of degree of saturation in a deformable unsaturated soil. Géotechnique, 53(1), 105-112.

Georgiadis, K., Potts, D. M., & Zdravkovic, L. (2005). Three-dimensional constitutive model for partially and fully saturated soils. International Journal of Geomechanics, 5(3), 244-255.

Gibson, R. E., England, G. L., & Hussey, M. J. L. (1967). The theory of one-dimensional consolidation of saturated clays. Géotechnique, 17(3), 261-273.

Lee, K., & Sills, G. C. (1979). A moving boundary approach to large strain consolidation of a thin soil layer. In Proceedings, 3rd International Conference on Numerical Methods in Geomechanics (pp. 163-173).

Leong, E. C., & Rahardjo, H. (1997). Permeability functions for unsaturated soils. Journal of Geotechnical and Geoenvironmental Engineering, 123(12), 1118-1126.

McVay, M., Townsend, F., & Bloomquist, D. (1986). Quiescent consolidation of phosphatic waste clays. Journal of Geotechnical Engineering, 112(11), 1033-1049.

Matthews, J. G., Dhadli, N., House, P., & P. Simms. (2011). Field trials of thin-lift deposition of amended mature fine tailings at the Muskeg River Mine in Northern Alberta. Proceedings of the 14th International Seminar on Paste and Thickened Tailings, R. Jewell and A. Fourie, eds., Australian Centre for Geomechanics, Crawley, Australia, 271–280.

Meric, D., Hellweger, F., Barbuto, S., Rahbar, N., Alshawabkeh, A. N., and Sheahan, T. C. (2013). Model prediction of long-term reactive core mat efficacy for capping contaminated aquatic sediments. J. Environ. Eng., 10.1061/(ASCE)EE.1943-7870.0000635, 564-575.

Qi, S., Simms, P., & Vanapalli, S. (2017a). Piecewise-linear formulation of coupled large-strain consolidation and unsaturated flow. I: Model development and implementation. *Journal of Geotechnical and Geoenvironmental Engineering*, *143*(7), 04017018.

Sadeghi, M., Shokri, N., & Jones, S. B. (2012). A novel analytical solution to steady‐state evaporation from porous media. Water Resources Research,48(9).

Seneviratne, N. H., Fahey, M., Newson, T. A., & Fujiyasu, Y. (1996). Numerical modelling of consolidation and evaporation of slurried mine tailings. International Journal for Numerical and Analytical Methods in Geomechanics, 20(9), 647-671.

Sheng, D., Fredlund, D. G., & Gens, A. (2008). A new modelling approach for unsaturated soils using independent stress variables. Canadian Geotechnical Journal, 45(4), 511-534.

Sheng, D., Sloan, S. W., Gens, A., & Smith, D. W. (2003). Finite element formulation and algorithms for unsaturated soils. Part I: Theory. International Journal for Numerical and Analytical Methods in Geomechanics, 27(9), 745-765.

Simms, P. H., & Yanful, E. K. (2002). Predicting soil-water characteristic curves of compacted plastic soils from measured pore-size distributions. Géotechnique, 52(4), 269-278.

Simms, P. H., & Yanful, E. K. (2005). A pore-network model for hydromechanical coupling in unsaturated compacted clayey soils. Canadian Geotechnical Journal, 42(2), 499-514.

Simms, P., Dunmola, A., Fisseha, B., & Bryan, R. (2010). Generic modeling of desiccation for cyclic deposition of thickened tailings to maximize density and to minimize oxidation. Proceedings of the 13th International Seminar on Paste and Thickened Tailings, R. Jewell and A. Fourie. Australian Centre for Geomechanics, Crawley, Australia, 293-303.

Soleimani, S., Simms, P., Dunmola, A., Freeman, G., & Wilson, G. W. (2014) Desiccation and consolidation in thin-lift deposition of polymer-amended mature fine tailings. Proceedings of the 17th International Seminar on Paste and Thickened Tailings, R. Jewell, A. Fourie, P. S. Wells and D. van Zyl. eds., Australian Centre for Geomechanics, Crawley, Australia, 307-322.

Sun, W., & Sun, D. A. (2012). Coupled modelling of hydro‐mechanical behaviour of unsaturated compacted expansive soils. International Journal for Numerical and Analytical Methods in Geomechanics, 36(8), 1002-1022.

Tarantino, A. (2009). A water retention model for deformable soils. Géotechnique, 59(9), 751-762.

Townsend, F. C., & McVay, M. C. (1990). SOA: Large strain consolidation predictions. Journal of Geotechnical Engineering.

van Genuchten, M. T. (1980). A closed-form equation for predicting the hydraulic conductivity of unsaturated soils. Soil science society of America journal, 44(5), 892-898.

Vaunat, J., Romero, E., & Jommi, C. (2000). An elastoplastic hydromechanical model for unsaturated soils. Experimental evidence and theoretical approaches in unsaturated soils, 121-138.

Vu, H. Q., & Fredlund, D. G. (2006). Challenges to modelling heave in expansive soils. Canadian Geotechnical Journal, 43(12), 1249-1272.

Wells, P. S., Revington, A., & Omotoso, O. (2011). Mature fine tailings drying–technology update. Proceedings of the 14th International Seminar on Paste and Thickened Tailings, R. Jewell and A. Fourie, eds., Australian Centre for Geomechanics, Crawley, Australia, 155–166.

Wheeler, S. J., Sharma, R. S., & Buisson, M. S. R. (2003). Coupling of hydraulic hysteresis and stress–strain behaviour in unsaturated soils. Géotechnique, 53(1), 41-54.

Wilson, G. W., Fredlund, D. G., & Barbour, S. L. (1997). The effect of soil suction on evaporative fluxes from soil surfaces. Canadian Geotechnical Journal, 34(1), 145-155.

Yao, D. T., de Oliveira‐Filho, W. L., Cai, X. C., & Znidarcic, D. (2002). Numerical solution for consolidation and desiccation of soft soils. International Journal for Numerical and Analytical Methods in Geomechanics, 26(2), 139-161.

Yong, R. N., Siu, S. K., & Sheeran, D. E. (1983). On the stability and settling of suspended solids in settling ponds. Part I. Piece-wise linear consolidation analysis of sediment layer. Canadian Geotechnical Journal, 20(4), 817-826.

Chapter 7 Piecewise-Linear Formulation of Coupled Large Strain Consolidation and Unsaturated Flow. II: Testing and Performance [5]

The UNSAT-CON developed in previous chapter is tested in this chapter using numerical cases as well as laboratory and field data. First, UNSAT-CON is tested by comparing model predictions to published predictions from a finite element based model (i.e. the MinTaCo software) that uses a quasi-unsaturated formulation to model evaporation. The fully unsaturated formulation is tested on fine-grained tailings by calibration with a documented laboratory column test and verification with a 4.1 m deep field trial. This testing exercise showed (i) the three dimensional (3D) constitutive surfaces (i.e. the State Surface Model) are largely constrained when defined using conventional test data such as the saturated compressibility function and the soil water characteristic curve; (ii) good to excellent agreement between measurements and predictions are observed, including the developing suction, decreasing void ratio, increasing solid content, increasing settlement rate due to evaporation effect on the near surface zone; and (iii) modeling desaturation allows for a more realistic simulation of deformation in the unsaturated zone than using formulations that do not model desaturation.

[5] A version of this chapter was published as Qi et al. 2017(b) in ASCE Journal Geotechnical and Geoenvironmental engineering.

7.1 Introduction

The effect of evaporation on the large strain consolidation of slurries is important for various problems in engineering practice, for instance, in management of mining residuals. As described in previous chapter, current popular numerical models only partially couple evaporation and its influence on hydro-mechanical behaviour to large strain consolidation. None actually predict desaturation. A numerical approach that can quantitatively model desaturation with a sound theoretical basis is advantageous for several reasons, not only for more accurate predictions of dewatering and deformation near the surface, but because the degree of saturation control gas transport, and hence oxygen ingress and acid generation (Aachib et al. 2000), which is a problem encountered in many kinds of tailings.

A brief review is first made on the constitutive models adopted in the previous chapter: Three three-dimensional (3D) surfaces (variation of void ratio with total stress and matric suction; variation of water content with total stress and matric suction; and variation of hydraulic conductivity with void ratio and matric suction) and two two-dimensional (2D) curves (variation of void ratio with effective stress and void ratio dependent hydraulic conductivity) are used to describe the relationships between constitutive parameters in unsaturated and saturated zones, respectively. This chapter tests the proposed novel model using numerical examples and physical tests, which include a previously documented column test on fine-grained tailings in the laboratory (Soleimani et al. 2014), and a field test on the same kind of tailings (Dunmola et al. 2013). Modelling results, particularly for the field case, demonstrate the capability of UNSAT-CON to predict the development of the unsaturated zone in tandem with ongoing consolidation at depth.

7.2 Verification of Quasi-Unsaturated Analysis

The "quasi-unsaturated analysis" is defined as identical to the evaporation formulation originally implemented in the MinTaCo software (Seneviratne et al. 1996), whereby evaporation continues at the potential rate until a user-specified suction at the surface is reached, past which the suction at the surface is fixed at this value. The capability of UNSAT-CON to carry out quasi-unsaturated analysis is verified using an example problem presented by Seneviratne et al. (1996) with solutions from a finite element formulation. This example involves consolidation of clayey silt tailings under both self-weight and evaporation. The basic properties are summarized in Table 7.1. The compressibility curve has the form of basic power law, but hydraulic conductivity relationship is described using a variant of basic power law for this tailings, which are shown as

$$e = 2.65(\sigma'(\text{kPa}))^{-0.16} \tag{7.1}$$

$$k(\text{m/s}) = 2.55\times10^{-9}\left(\frac{e^{4.1}}{1+e}\right) \tag{7.2}$$

Zero flux is exerted at the bottom boundary for this example problem. Boundary condition Case (*iii*) or Case (*iv*) defined in previous chapter are specified on the top to simulate evaporation with or without decantation, respectively. Three potential evaporation rates (PERs) of 0.3, 1.5 and 3.0 m/yr with an air entry value of 1000 kPa from Seneviratne et al. (1996) are considered in this case.

Table 7.1. Basic properties for the example from Seneviratne et al. (1996)

Parameters	Initial height	Initial void ratio profile	Initial effective stress profile	Specific gravity
Symbols (units)	$H^{(0)}$ (m)	$e_j^{(0)}$	$\sigma_j'^{(0)}$ (kPa)	G_s
Values	20	4.6	0. 0416	2.8

The calculated tailings surface height versus time, for decantation during 20 years after instantaneous filling, are compared with the results provided by Seneviratne et al. (1996) in Fig. 7.1(a). Excellent agreement is observed between the two different numerical techniques. Discrepancy between cases with and without decantation only occurs for the evaporation rates of 0.3 and 1.5 m/yr, which are not sufficiently high to remove all the accumulated surplus water in the early part of the simulations when the rate of self-weight consolidation is relatively high(Fig. 7.1(b)).

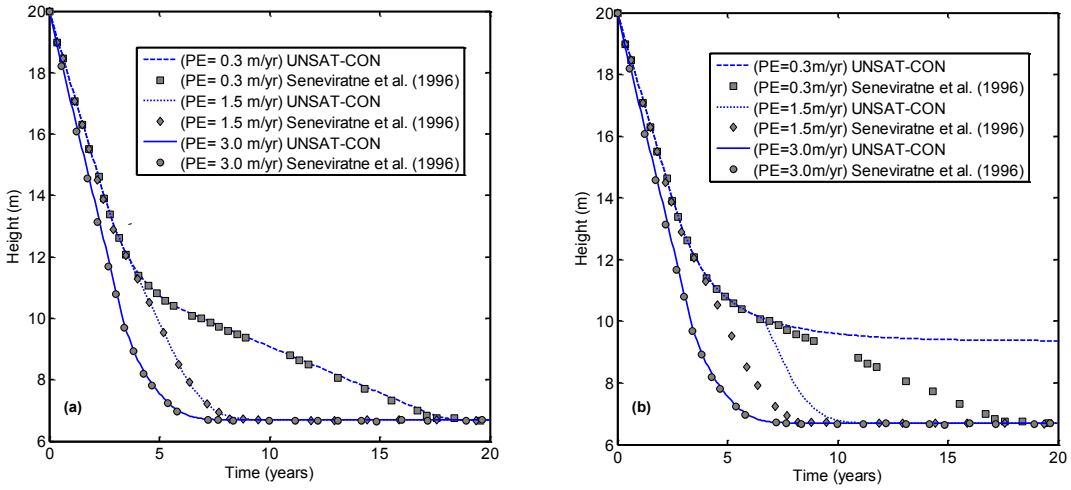

Fig. 7.1. Analysis results of example from Seneviratne et al. (1996) for (a) with decantation; (b) without decantation

Fig. 7.2 shows how UNSAT-CON moves between different surface boundary conditions in four of the above examples, low (0.3 m/yr) and high (3 m/yr) evaporation, with and without decantation. In Fig. 7.2(a), low evaporation with decantation, the surface flux is initially given by the flow from self-weight consolidation. When this drops below the potential evaporation rate, the boundary condition switches to constant flux. Subsequently, when the surface suction reaches the maximum value at the surface, the boundary condition switches to constant head, and the surface

flux thereafter decreases until the end of the simulation. For the case of low evaporation but no decantation, the rate of evaporation is insufficient to draw down the water to the tailings-water interface during the simulation (surface water accumulates, see Fig. 7.2(b)), and therefore the surface flux remains that given from self-weight consolidation. By contrast, the surface flux for the high evaporation case is identical for both the decantation (Fig. 7.2(c)) and non-decantation (Fig. 7.2(d)) cases, as evaporation consumes all water when it reaches the surface. The surface flux is then given by the potential evaporation rate until the maximum suction value is reached at the surface, whereupon the surface boundary condition switches to constant head, and the surface flux begins to decrease.

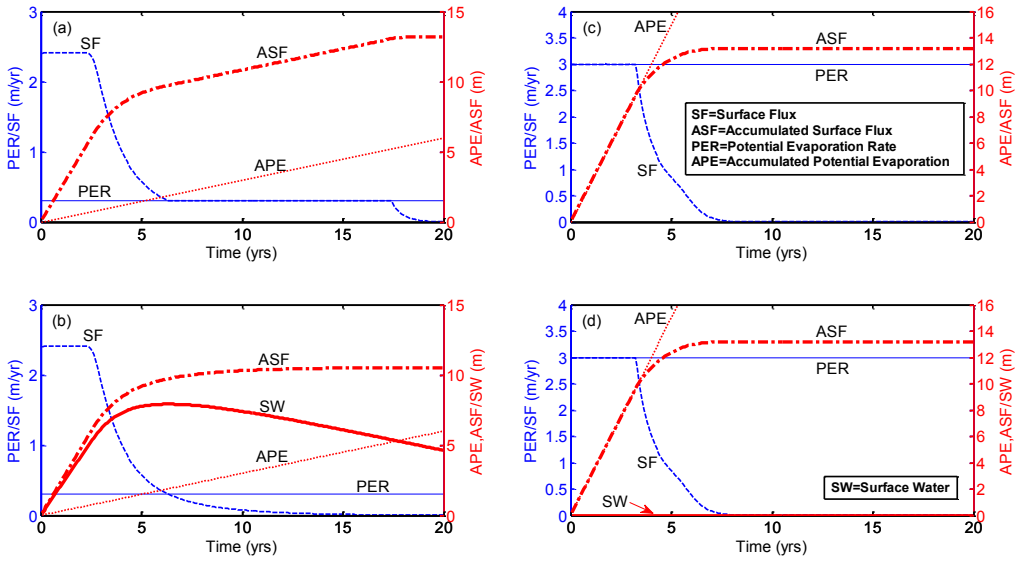

Fig. 7.2. The surface flux and the water mass balance at the top: (a) potential evaporation rate (PER) = 0.3 m/yr with decantation; (b) PER = 0.3 m/yr without decantation; (c) PER = 3.0 m/yr with decantation; (d) PER = 3.0 m/yr without decantation

The change from positive to negative PWP in the quasi-unsaturated analysis can be numerically problematic. Fig. 7.3 shows the profile of void ratio and pore water pressure one year

after the tailings filled for this example at an evaporation rate of 3.0 m/yr. When 50 elements are used to discretize this problem, a spurious oscillation is observed in computed void ratio near the transition point (i.e. PWP = 0 kPa) with some elements having void ratio even higher than its initial value. This phenomenon occurs if there is a significant difference in the hydraulic conductivities of two adjacent elements. The elements near the top are first affected by evaporation and may have low void ratios according to saturation assumption in quasi-unsaturated analysis. Near the transition point, if the computed void ratio of one element (already affected by evaporation) is substantially lower than that of the underlying element (not affected by evaporation yet), the hydraulic conductivity of the element below will be much higher than that of the element above according to the hydraulic conductivity constitutive curve. If the hydraulic conductivity difference is large enough to cause an inflow in excess of the outflow for an element, the computed void ratio will increase unrealistically. Then the hydraulic conductivity of this element can be much higher than that of the element underlying it, as a result, the outflow can exceed the inflow, causing unrealistically lower void ratio. This phenomenon propagates downward in this way, and eventually results in spurious oscillation of void ratio. This unrealistic phenomenon is also related to coarse spatial discretization, which can be alleviated by increasing the resolution as shown in Fig. 7.3(a). This “false swelling or shrinkage” problem can even be eliminated using 200 elements but at the expense of computational efficiency.

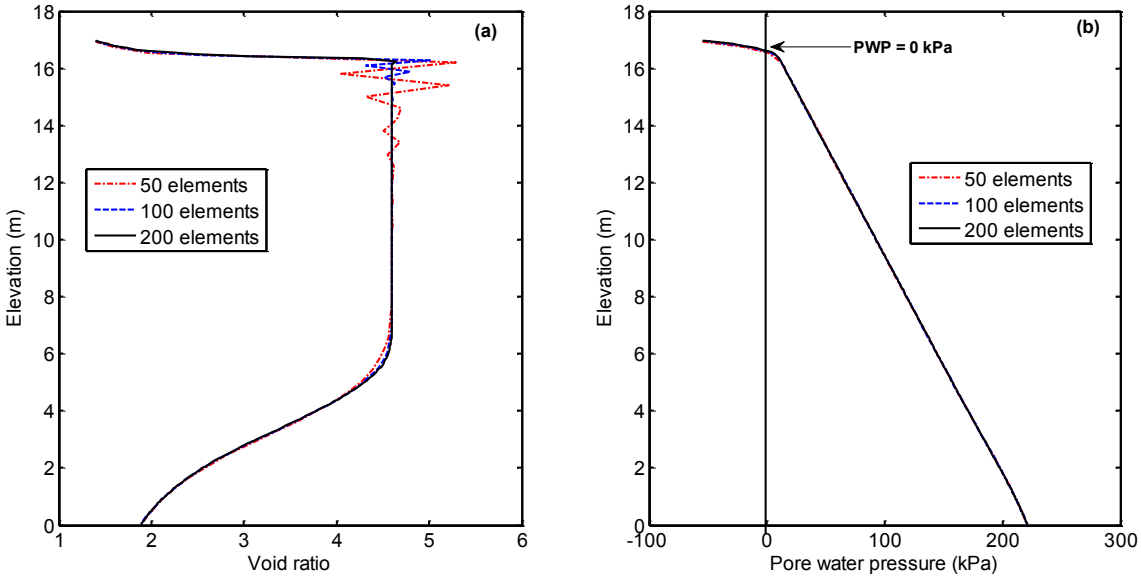

Fig. 7.3. Profiles one year after the tailings filled at 3.0 m/yr evaporation: (a) void ratio, (b) pore water pressure

7.3 Column Test

7.3.1 Column test and material properties

A laboratory column test is first used to test the fully unsaturated formulation of UNSAT-CON. The column test was undertaken by Soleimani et al. (2014) in a 0.15 m diameter plexiglass column to study the large strain consolidation behaviour of polymer-amended mature fine tailings (MFT) under both self-weight loading and evaporation. Basic geotechnical properties of the material include: PL and LL of 65% and 45% (by fall cone) SL of 55%, and solid particle density of 2.12 g /cm^3. The tailings was initially deposited to a height of 0.50 m with an initial void ratio, e = 4.0, which was instrumented to monitor positive and negative pore-water pressures (by T5 tensiometers), volumetric water content (by Model EC-5), height of water (by a ultrasonic sensor),

evaporation amount (by the scale upon which the column rested), and height of the tailings-water interface (by a webcam and reference marks on the column). The bottom boundary of the column test was sealed to allow no flow during the entire period of performing the experiment. During the first 9 days after initial deposition, neither evaporation nor decantation was applied on the top surface. The bleed water was removed at the end of 9th day, then evaporation with a rate of 1.5 mm/day was applied on the top surface for the following 18 days (i.e. from 10^{th} day to 27^{th} day) using two oscillating fans. After the 27^{th} day, the potential evaporation was increased to 5 mm/day by increasing the fan speed. The actual evaporation rate, as determined by total column mass change, remained equal to the potential rate during the respective time periods (Soleimani et al. 2014).

Basic constitutive properties of this polymer-amended MFT, including compressibility relationship under saturated condition, gravimetric water content and void ratio *vs.* suction under zero stress condition (i.e. soil water characteristic curve (SWCC) and shrinkage curve), hydraulic conductivity-void ratio relationship under saturated condition, were measured using various standard tests (Soleimani et al. 2014; Dunmola et al. 2013). The data for compressibility relationship and shrinkage curve, on two extreme planes of 3D void ratio constitutive surface, respectively, were used to obtain the fitting parameters of Eq. (6.3) in previous chapter. The data for SWCC, and gravimetric water content *vs*. stress under saturated condition (which can be derived using $w=e/G_s$ from compressibility relationship) on two extreme planes of 3D gravimetric water content constitutive surface were used to obtain the fitting parameters of Eq. (6.4) in previous chapter. The best-fitting parameters are listed in Table 7.3 and two 3D constitutive surfaces are illustrated in Fig. 7.4(a) and (b).

Table 7.2. Basic properties for column test

Parameters	Initial height	Initial void ratio profile	Initial effective stress profile	Specific gravity
Symbols (units)	$H^{(0)}$ (m)	$e_j^{(0)}$	$\sigma'^{(0)}_j$ (kPa)	G_s
Values	0.5	4.0	0.0021	2.12

Table 7.3. Constitutive surfaces

Surface	Void ratio	Gravimetric water content
*A/a	4.50E+00	2.12E+00
*B/b	7.80E-01	3.70E-01
*C/c	7.56E-03	7.56E-03
*D/d	1.36E-01	3.95E-02
*F/f	1.62E+03	1.62E+03
*G/g	2.17E+03	2.86E+03

Note:* indicate parameters for two 3D constitutive surfaces from Vu and Fredlund (2006) and defined in the chapter 6.

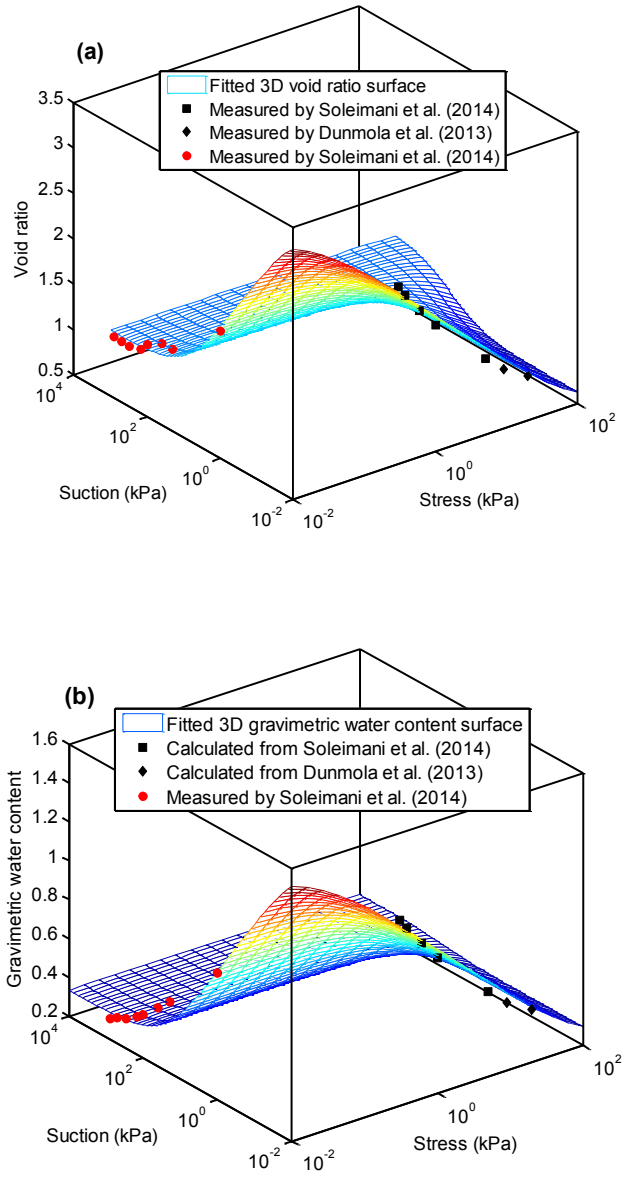

Fig. 7.4. Two 3D constitutive surfaces (a) void ratio surface; (b) gravimetric water content surface

7.3.2 Calibration of hydraulic properties

The measured data for hydraulic conductivity-void ratio relationships under saturated condition are shown in Fig. 7.5(a), along with the data for polymer amended MFT from other two sources from Dunmola et al. (2013) and Jeeravipoolvarn (2010) for polymer amended MFT. The data is best fitted using the basic power law (i.e. Set (i) in Fig. 7.5(a)). This, however, may not be an accurate representation of the actual value, since the hydraulic conductivity at high void ratio is difficult to measure. The measured data was obtained by calculating hydraulic conductivity from measured drainage and pore-water pressure measurements, which is problematic for the initial period of high self-weight consolidation where uniformity of gradient and void ratio between pore-water pressure sensors are likely inappropriate assumptions. Moreover, the data for variation of hydraulic conductivity with suction is not available. Therefore, a calibration exercise is first conducted on the fitting parameters of the hydraulic conductivity function, keeping the other constitutive parameters unchanged and consistent with the measurements (i.e. Table 7.3). The criterion of the calibration is to obtain a better prediction of the settlement curve (i.e. tailings-water interface height *vs*. time curve). The parameters of hydraulic conductivity function used in the calibration exercise are summarized in Table 7.4, and hydraulic conductive surface is illustrated in Fig. 7.5(b).

Table 7.4. The parameters of hydraulic conductivity function used for calibration

*Fitting parameters	Set (i)	Set (ii)	Set (iii)
H_1	3.5×10^{-11}	$5\times3.5\times10^{-11}$	$5\times3.5\times10^{-11}$
H_2	7	7	8
m	0.00289	0.00289	0.00289
n	0.85	0.85	0.85

Note: * fitting parameters are defined in chapter 6.

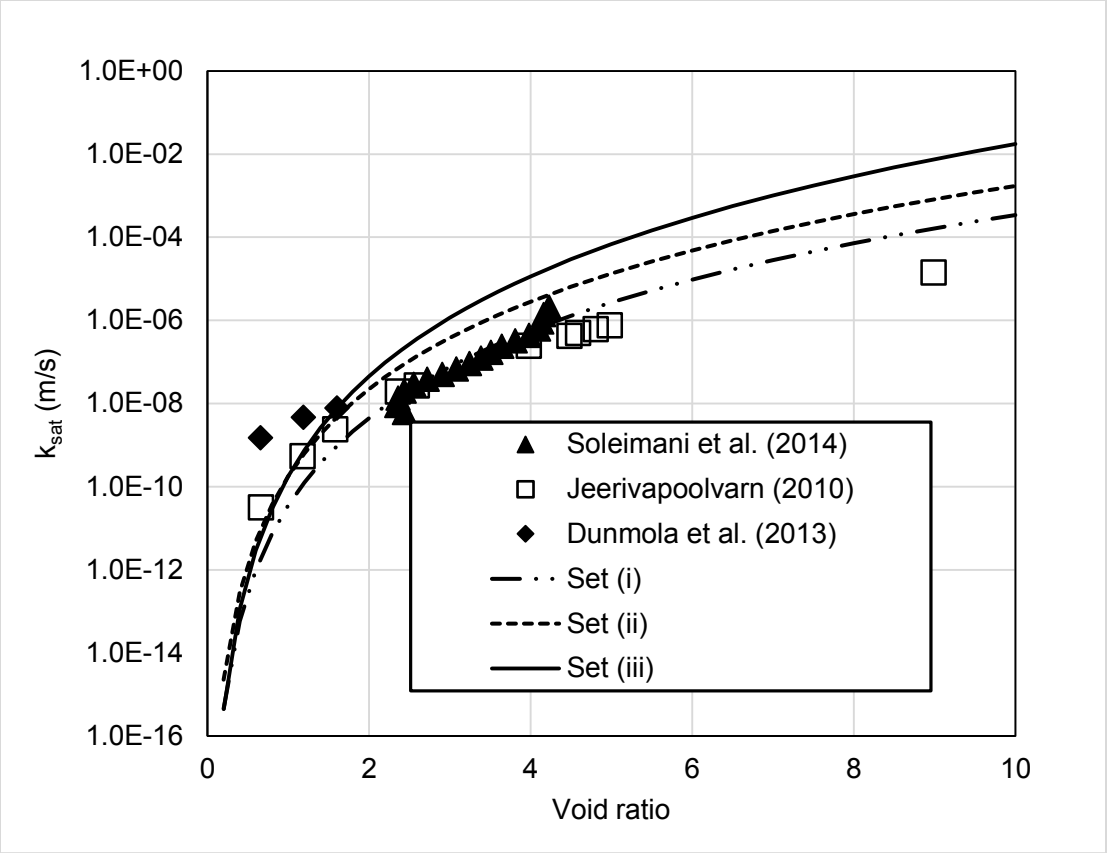

Fig. 7.5. Hydraulic conductivity of polymer-amended MFT

Fig. 7.6 compares the calculated height of the tailings-water interface over time using UNSAT-CON with measurements. When the best-fit hydraulic function from the measured data (Set (i)) is used, the calculated tailing heights are much higher than the measured results for all the three stages (i.e. (1) the self-weight consolidation; (2) self-weight consolidation with evaporation rate of 1.5 mm/day; and (3) self-weight consolidation with evaporation rate of 5.0 mm/day). During the last two stages with evaporation, the calculated height *vs*. time curve is essentially parallel to the measurement, which indicates the amount of deformation, relative to tailing height at the end of stage (1) calculated using UNSAT-CON, agrees well with the measurements. Therefore, the absolute difference between calculation and measurement can be mainly attributed

to the over-estimation of heights (i.e. under-estimation of deformation) during the first stage, where no evaporation is applied, and only Eq. (6.2) in Chapter 6 with parameters H_1 and H_2 is used to describe the hydraulic conductivity variation with void ratio in the program. The best-fit hydraulic conductivity function for saturated condition may be much lower than the actual value at initial condition with respect to high void ratio. It is, therefore, proposed to increase the H_1 by several times in the hydraulic conductivity function for calculation, and when it is increased to $5H_1$ (i.e. parameter Set (ii) in Table 7.4) a much closer match between prediction and measurement in the height *vs.* time curve is obtained (see Fig. 7.6). However, the calculated heights are still higher during the first stage compared to the measurements. More precisely, the calculated consolidation rate during the first 2 to 3 days is much lower but turns out to be slightly higher afterwards than the measured values for the first stage. This may be due to that hydraulic conductivity used (Set (ii)) is lower at high void ratio but higher at low void ratio than the actual value. Therefore, it is proposed, at this time, to increase the steepness of hydraulic conductivity *vs.* void ratio curve by increasing the parameter H_2. A good agreement between calculation and measurement in terms of the settlement curve is obtained for all the three stages for $H_2 = 8.0$ (i.e. parameter Set (iii) in Table 7.4) (see Fig. 7.6).

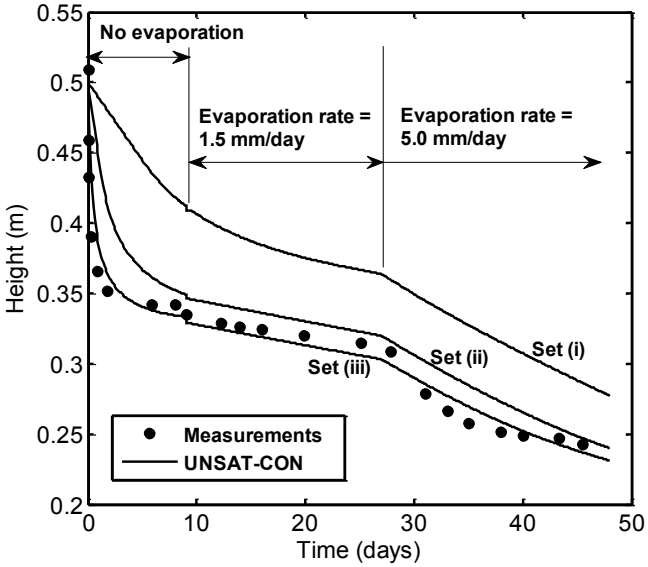

Fig. 7.6. Comparison in tailings heights over time between measurements and calculations using three sets of hydraulic conductivity

7.3.3 Comparison between predictions and measurements

More comparisons between the predictions and available measurements, including the pore-water pressure (or matric suction), volumetric water content (VWC), and void ratio are presented in this section. Fig. 7.7 (a) compares changes of PWPs (matric suctions) with time at the fixed elevations of 25 mm and 140 mm, respectively. Fig. 7.7 (b) compares changes of VWCs with time at the fixed elevations of 80 mm and 180 mm, respectively. The predictions in Fig. 7.7 are obtained using hydraulic conductivity of Set (iii). It can be seen from Fig. 7.7 that the predicted PWP (suction) and VWC values at these elevations are in reasonable agreement with the measurements. The suction increase and water content decrease trends are well captured by UNSAT-CON during the evaporation stage. The use of Set (iii) for hydraulic conductivity results in better predictions than those obtained from the Set (i) and (ii), which are not shown in Fig. 7.7 for lucidity.

Fig. 7.8 provides comparisons between the calculated void ratio profiles after 9 days and 32 days and measured data. It can be seen that the changes in trend of the void ratio profile, especially the faster decrease of void ratio at shallower depth than that of greater depth due to evaporation, are captured by UNSAT-CON, but with different degrees of accuracy using different set of parameters, compared with the measurements. Use of parameters of Set (iii) results in the better predictions than the other two.

Fig. 7.9 provides the simulation results of unsaturated large strain consolidation process for various profiles over time with a time interval of 3 days, using parameters of Set (iii). It can be clearly seen that self-weight consolidation process in the first stage (day 0 to day 9), and the coupled evaporation–consolidation processes in the second (day 9 to day 27) and third (day 27 to day 48) stages are well reproduced by UNSAT-CON. In the first stage, there is no suction developed near the surface (see Fig. 7.9(b)). Also, the decrease rate of void ratio at the greater depths is always faster than that at shallower depths, which is due to higher effective stress developed with dissipation of excess pore water pressure at greater depths. During the evaporation stage, suction gradually develops near the surface (see Fig. 7.9(b)) where the degree of saturation becomes less that 1 (see Fig. 7.9(d)). In the meantime, the void ratio near the surface decreases at a faster rate than that at greater depth under suction effect (see Fig. 7.9(a)). The acceleration of consolidation rate under higher evaporation during the third stage, which has been observed in Fig. 7.6 and Fig. 7.7, is also reflected in various varying profiles in Fig. 7.9. Moreover, the decantation at the end of stage (1) (sudden drop in both total stress and pore water pressure) is also successfully accounted for by UNSAT-CON, which can be seen in Fig. 7.9(b) and (c), and also in Fig 7(a). The transition point at every elapsed time from saturation to real unsaturation state is modeled in a smooth manner. Fig. 7.9(d) illustrates that the unsaturated zone gradually advances into greater

depths under evaporation condition. The rate of advance is speeded up by increasing the evaporation rate since the 27th day. The entire profile becomes unsaturated since around day 42. The four parameters shown in Fig. 7.9 in the upper unsaturated zone and lower saturated zone at every time step are found to be consistent with the 3D constitutive surfaces and 2D constitutive curves defined using the fitting parameters shown in Table 7.3, respectively.

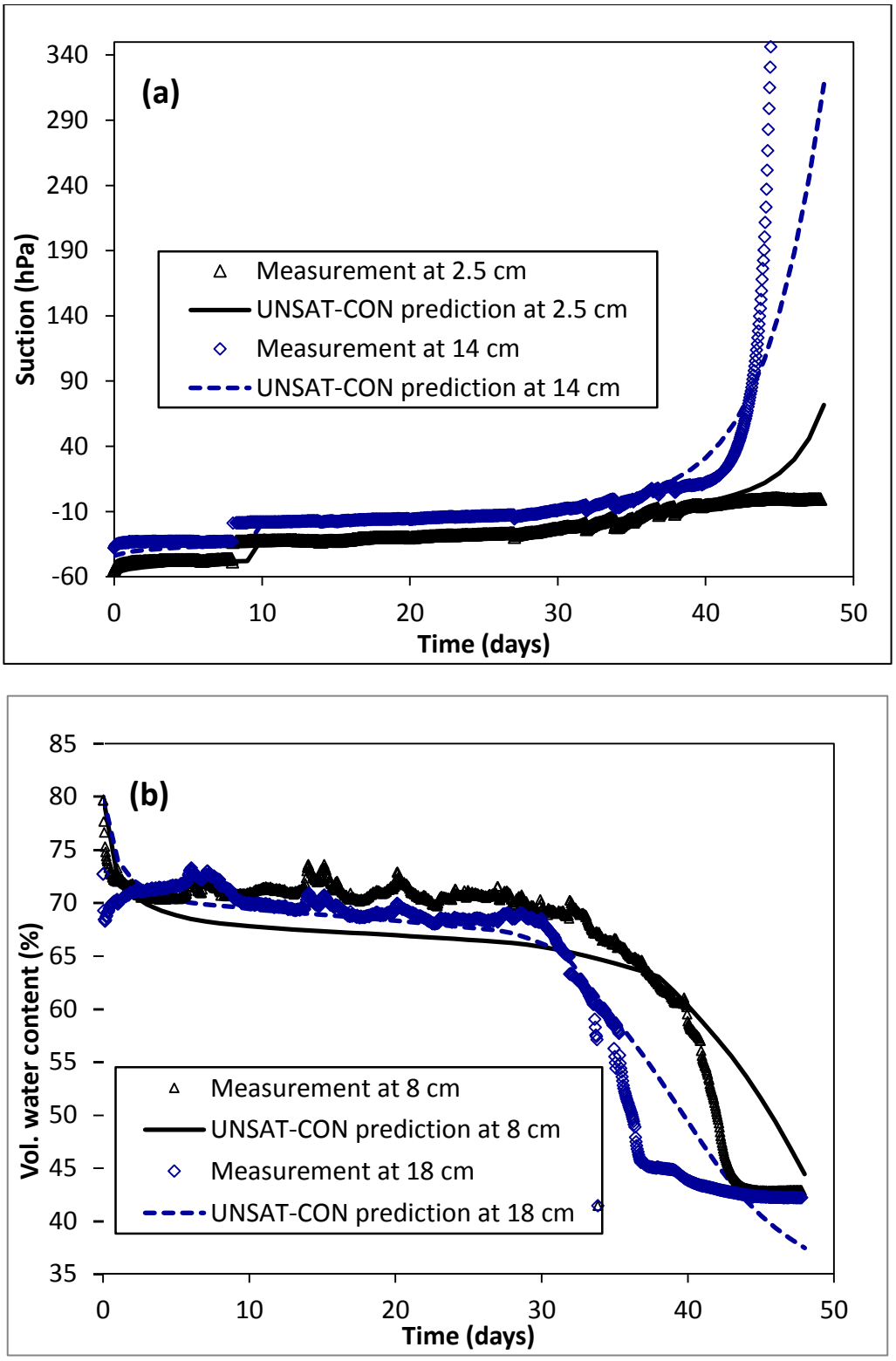

Fig. 7.7. Comparison in PWP (suction) and VWC over time between measurements and calculation using hydraulic conductivity of set (iii): (a) PWPs at fixed elevations of 2.5 and 14 cm; (b) VWCs at fixed elevations of 8 and 18 cm

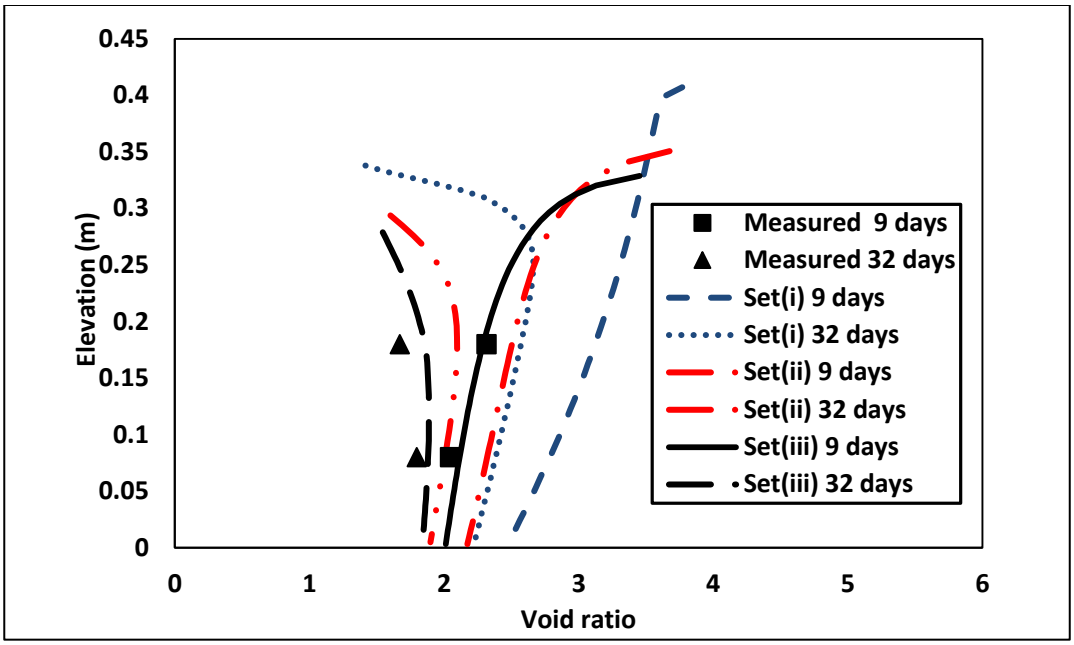

Fig. 7.8. Comparison of void ratio between predictions from three sets of parameters and measurements

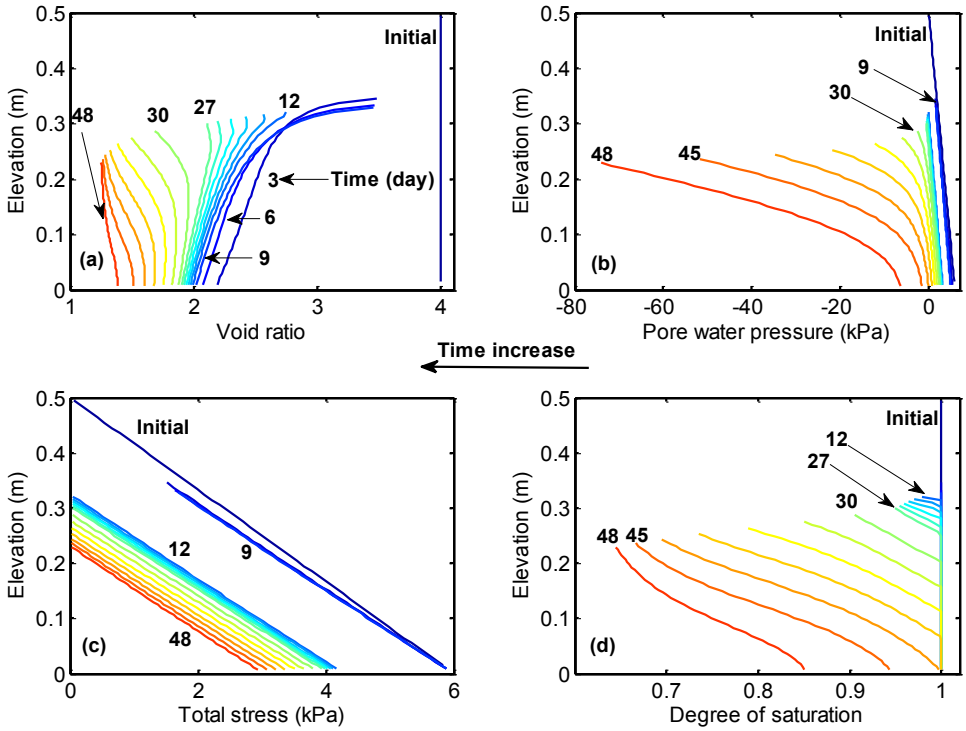

Fig. 7.9. Variation of profiles with time calculated using UNSAT-CON: (a) void ratio profile, (b) pore water pressure, (c) total stress, (d) degree of saturation

7.4 Case Study of Field Trial of Deposition of Polymer-amended MFT

7.4.1 General information on the field trial

Between 4 to 5 m of polymer amended MFT created by in-line flocculation was deposited during an industrial field trial in Northern Alberta in the Fall of 2012, and subsequently monitored for over a year. The initial height was somewhat uncertain due the rapid dewatering that occurred due to flocculation even as the material was being deposited. The field trial is documented in a number of sources, including Dunmola et al. (2013).

The initial condition for all numerical analyses was chosen to be 48 hours after deposition, when the average void ratio was 2.6 and the height was 4.1 m. A large degree of dewatering occurred during the initial 48 hours due to water release following flocculation, which occurred simultaneously with ongoing deposition into the test cell. The deposit had a surface area of about 2100 m^2. The specific gravity, G_s is 2.12. Table 7.5 lists the basic parameters.

Table 7.5. Basic properties of the field trial

Parameters	Initial height	Initial void ratio profile	Initial effective stress profile	Specific gravity
Symbols (units)	$H^{(0)}$ (m)	$e_j^{(0)}$	$\sigma'^{(0)}_j$ (kPa)	G_s
Values	4.1	2.6	0.1726	2.12

Two consolidation stages of the field trial, including (i) the self-weight consolidation from 15th October 2012 to 27th April 2013 (i.e. 194 days) during which evaporation is assumed to be effectively zero and (ii) consolidation under both self-weight and evaporation effect from 28th April to 15th October 2013 (i.e. 171 days), are simulated using UNSAT-CON. The saturated and quasi-unsaturated analyses are conducted as well as the fully coupled unsaturated – large strain consolidation analysis to compare and illustrate the utility of using the full formulation. Table 7.6

summarizes the three analyses. For the saturated analysis (SA), no evaporation is applied on the top surface during the entire period. A 2.0 mm/day evaporation rate, is applied for the quasi-unsaturated analysis (QUA) and unsaturated analysis (UA) during the last 171 days. The evaporation rate was estimated by calculating the change in mass over time using the measured solids content profile with depth, once evaporation exceeded surface water flux from consolidation, and assuming negligible loss of water out the bottom of the deposit. For the QUA, two cases with two different maximum surface suction values allowed are analyzed, i.e. 1,000 kPa and 10 kPa respectively designated as QUA-I and QUA-II. The calibrated material constitutive parameters from the column test are used in all three analyses.

Table 7.6. Three different analyses of the field trial

Parameters		Saturated analysis (SA)	Quasi-unsaturated analysis (QUA)		Unsaturated analysis (UA)
Analysis time		365 days	365 days		365 days
Top boundary condition	15^{th}/10-27^{th}/04	PER=0.0 mm/day	PER=0.0 mm/day		PER=0.0 mm/day
	28^{th}/04-15^{th}/10	PER=0.0 mm/day	PER=2.0 mm/day		PER=2.0 mm/day
Bottom boundary condition		Zero flux	Zero flux		Zero flux
Max. suction at the top (kPa)		Not required	10	1000	Not specified
Resolution		50	200	200	50

Note: all the analyses above are conducted with decantation during the entire period.

Several different spatial resolutions were employed for the three analyses. As shown in Fig. 7.3 in the previous section, the QUA requires a relatively high resolution (200 nodes) to avoid false numerical oscillation. For both the SA and UA, increasing the resolution above 50 did not affect the results significantly. A comparison of the SA, QUA and UA is first presented in the following section, followed by comparisons between the predictions from UA and field observations.

7.4.2 Comparison between the SA, the QUA, and the UA

Fig. 7.10 compares the profiles of void ratio, pore water pressure, solid content and degree of saturation on day 365 from the SA, the QUA, and the UA. Not surprisingly, neither the void ratio decrease nor the solid content increase observed in the field near the surface can be predicted using the SA, in which, the pore water pressure is always positive (Fig. 7.10(b)) under saturation condition (Fig. 7.10(d)). The QUA-I predicts the development of negative PWP near the surface, but the surface void ratio decreases to an unrealistically low (< 0.5) value, much lower than the void ratio at the shrinkage limit (measured 1.17 for this case), since the QUA follows the 2D saturated constitutive equations, 1000 kPa suction on the surface acts as effective stress compressing the surface soil element. From a numerical point of view, a low void ratio corresponds to a lower (several orders lower) hydraulic conductivity of the surface element, which limits the influence of evaporation to shallow depths. In the QUA-II, a maximum suction of 10 kPa is allowed at the surface, in order to ensure that the surface void ratio will not be lower than that at shrinkage limit, as recommended by Yao et al. (2002). The QUA-II predicted a comparable void ratio profile to the UA (Fig. 7.10(a)). However, for both QUAs desaturation (saturation degree less than 1) near the surface cannot be predicted (Fig. 7.10(d)), and the effects of evaporation on the shallow layer were reduced by limiting the suction on surface.

Fig. 7.10 shows that differences in these profiles between the three analyses can be observed only within the zone near the surface (i.e. the zone above 2 m elevation for the final deposits). The zone below this depth has not been affected by this evaporation. A detailed comparison illustrated in Fig. 7.11 is made between the three analyses in the time history of several parameters (including the pore water pressure, void ratio, degree of saturation, solid content and total stress) at three initial elevations selected within the shollow layer, i.e. 4.05 m, 3.75 m and 3.5

m. The deductions in the preceding paragraph can be better seen in Fig. 7.11 for the initial elevations. No suction is developed for three analyses for the first 174 days when no evaporation is applied. Once evaporation is applied, the suction at the initial elevation of 4.05 m gradually develops in QUA-II and UA until around Day 280. The suction in QUA-II at the initial elevation of 4.05 m has been constrained to a value of less than 10 kPa starting from the 280th day, while the UA predicts a further gradual suction increase at this elevation (see Fig. 7.11(a)). Although the void ratio at this elevation is constrained to the shrinkage limit in QUA-II (Fig. 7.11(b)), which is comparable with the final void ratio at the surface predicted by the UA, the QUA-II cannot predict a further increase in the solid content due to evaporation (Fig. 7.11(d)). In fact, the actual evaporation rate is lower than 2 mm/day after the 280th day in QUA-II, because the maximum permissible suction value has already been reached. At elevations of 3.5 m and 3.75 m, the QUA-II predicts a lower suction, higher void ratio and lower solid content (i.e. lower rate of consolidation induced by evaporation) than the UA after about 300th day. The QUA-I also predicts a lower consolidation rate evaporation at these two elevations, due to both limiting surface suction and hindering effect of low permeability. This can be seen in Fig. 7.10 although QUA-I is not included in Fig. 7.11 for clarity. The difference in the three analyses is more significant at the initial elevation of 3.75 m than that at 3.5 m, because the soil at greater depth is less affected by the evaporation. The degree of saturation values less than 100% can only be predicted by the UA (see Fig. 7.11(c)). It is interesting to note that at the initial elevation of 3.5 m the degree of saturation from UA is still 100% at the end as those in SA and QUA-II. However, there are differences in the PWP, void ratio, and solid content at this elevation, due to the differing treatments of evaporation between the analyses. For this case, the UA predicts an overall faster

evaporation-induced consolidation rate near the surface. In other words, a higher rate of solid content increase near the surface is predicted by the UA.

Fig. 7.12 shows that the paths of state variables (void ratio, water content, stress and matric suction) at the initial elevations of 4.05 m and 3.75 m predicted by UA in 3D spaces. These paths exactly follow the defined two constitutive surfaces. At these two elevations, the states switch from saturation to unsaturation at around Day 205 and 311, respectively.

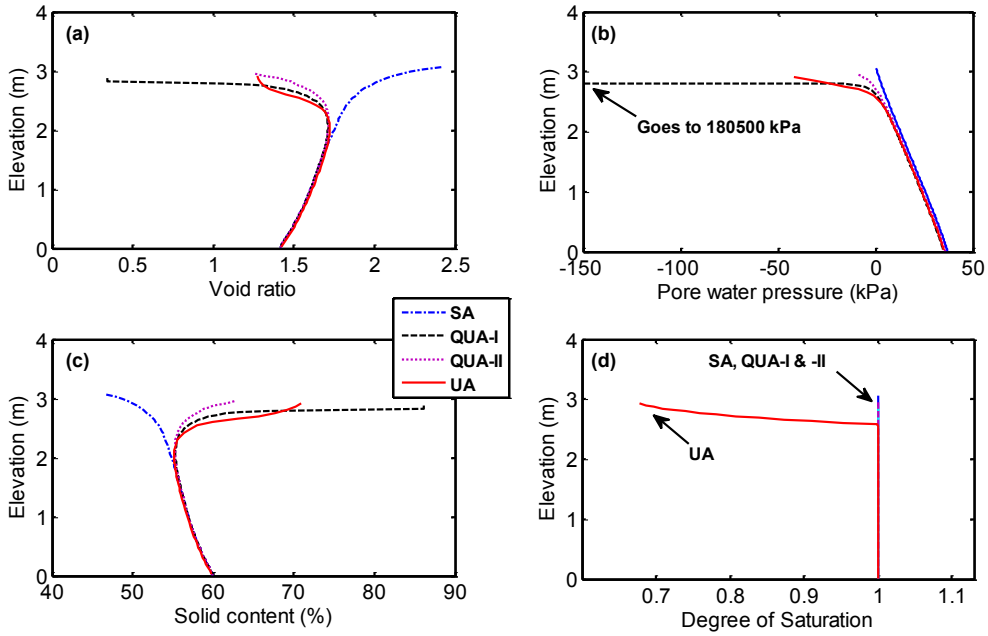

Fig. 7.10. Comparison in the final profiles between three analyses: (a) void ratio profile, (b) pore water pressure, (c) solid content, (d) degree of saturation

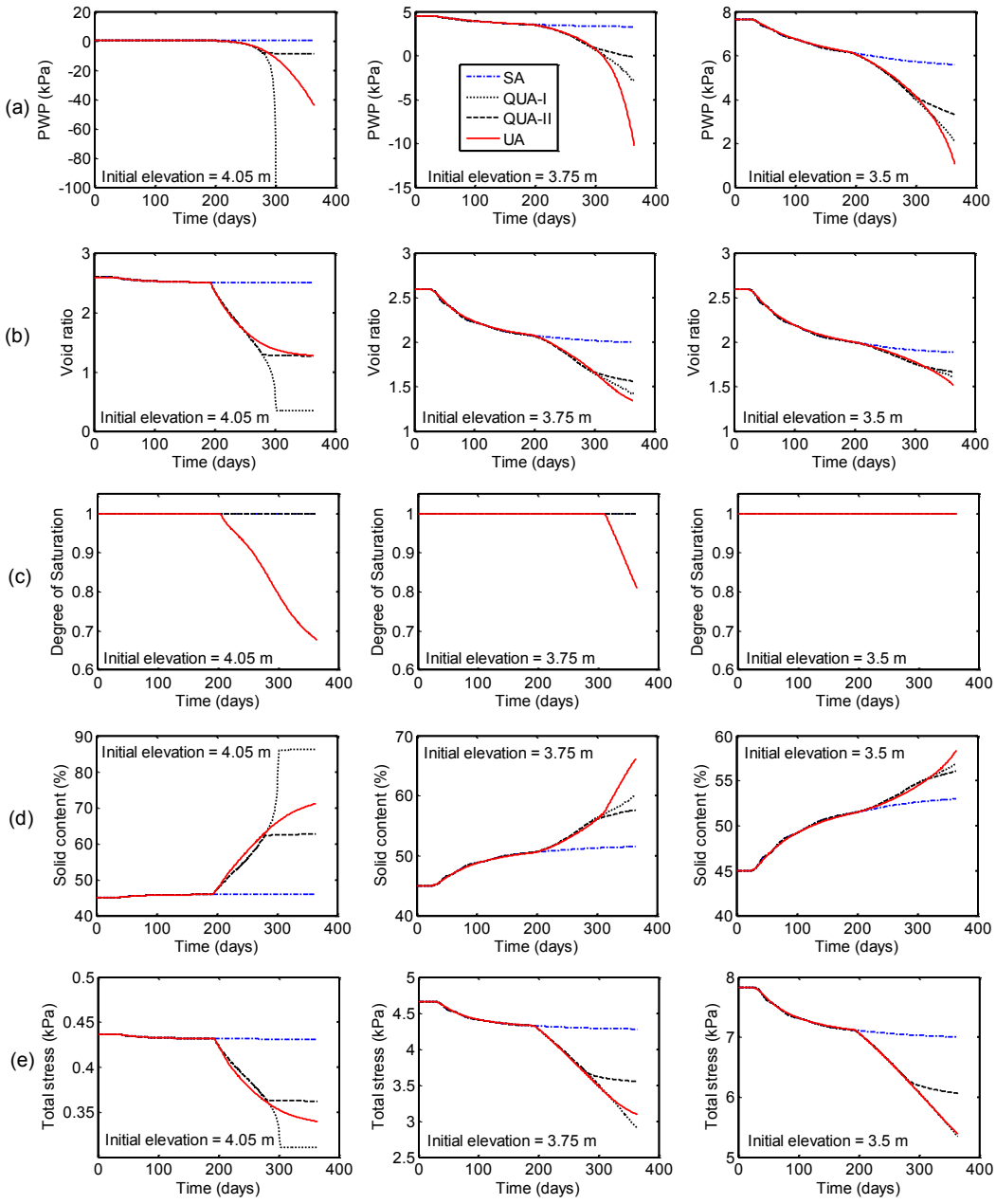

Fig. 7.11. Comparison in the time history at three initial elevations between three analyses: (a) pore water pressure, (b) void ratio, (c) degree of saturation, (d) solid content, (e) total stress

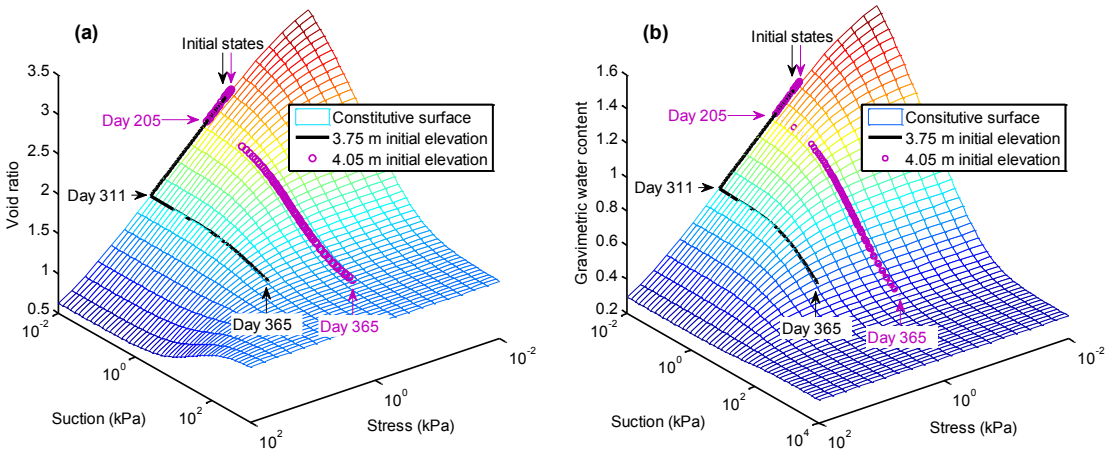

Fig. 7.12. The paths of state variables predicted by UA at the initial elevations of 3.75 m and 4.05 m: (a) along with void ratio surface, (b) along with gravimetric water content surface

7.4.3 Comparison between UA predictions and field measurements

The UA predictions use the calibrated constitutive relations from the column test, in which the saturated hydraulic conductivity parameters were the only parameters changed from the independently measured material properties. Comparison of the solid content profiles between the UA and field measurements at different times in the year 2013 are shown in Fig. 7.13. Also shown in Fig. 7.13 include: the predicted void ratio, PWP, and the degree of saturation profiles at corresponding dates. There is a good agreement in the solid content profile between prediction and measurement at the end of self-weight consolidation process (i.e. 27th April 2013). The solid contents near the surface are relatively lower than those at greater depth due to lower overburden stress. After that, solid contents near the surface gradually increase at a faster rate than those at greater depth due to evaporation. Due to this reason, the solid contents become higher at shallow zone after a certain period of evaporation. The predicted solid contents agree well with the measurements (the differences are less than ±1.5% within the unsaturated zone). It can also be seen

that depth affected by the evaporation (unsaturated zone) advances into greater depth zones. The results are consistent with the variations of predicted pore water pressure, void ratio and degree of saturation profiles (see Fig. 7.13(b), (c) and (d)). The measured solid contents near the base are slightly higher than the predictions. This may be attributed to the assumed boundary condition (zero flux) specified in the analysis, which may be different from that in the field, where the boundary condition is not well-defined.

Fig. 7.14 shows that the predicted heights of deposits at these dates are in good agreement with measurements. Comparisons in pore water pressure at three fixed elevations near the surface (i.e. 2.55 m, 3.05 m and 3.3 m) are illustrated in Fig. 7.15. The pore water pressures shown in Fig. 7.15 were measured using piezometers, which did not record the suction. However, trends of decrease in measured pore water pressures at three fixed elevations with time due to evaporation are also well captured by UNSAT-CON.

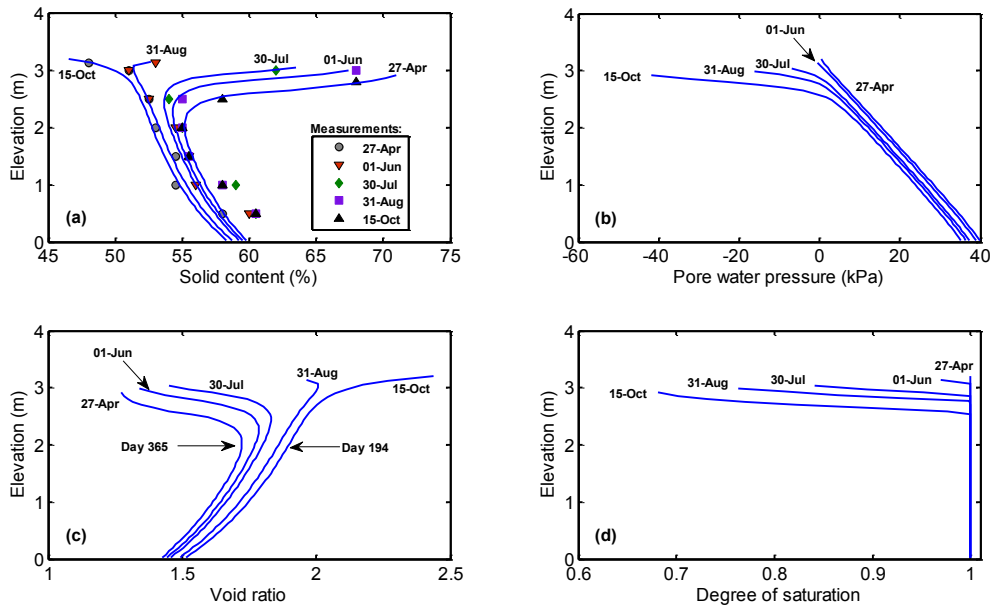

Fig. 7.13. Results of UA at different times in 2013: (a) solid content compared with field data, (b) pore water pressure, (c) void ratio profile, (d) degree of saturation profile

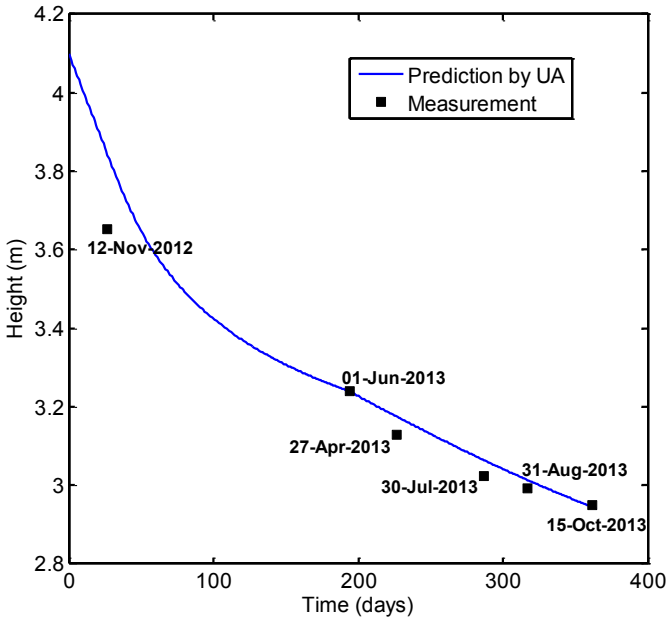

Fig. 7.14. Comparison of height *vs.* time between UA and measurement

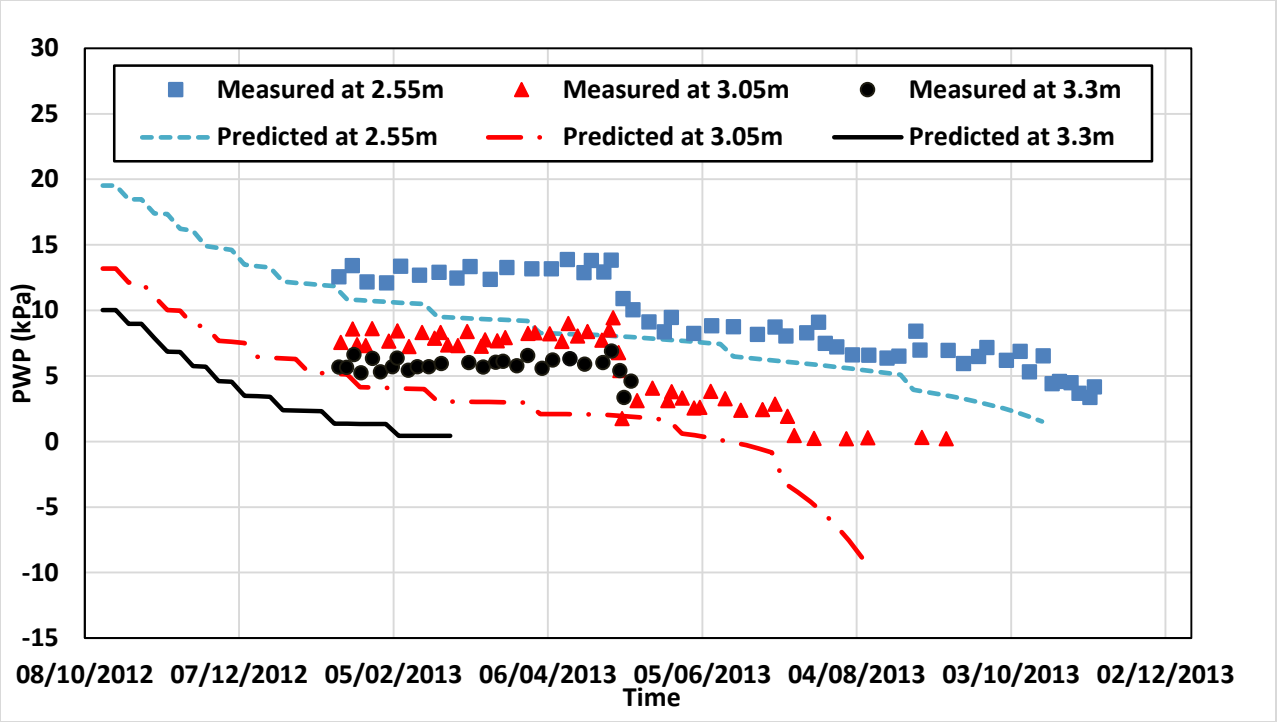

Fig. 7.15. Comparisons of pore water pressure between UA and measurement at three fixed elevations

7.5 Model Limitations

The current formulation is only valid for monotonically decreasing water contents, and does not consider hysteresis, either due to volume change or wetting and drying. This will have to be addressed for such models to analyze multilayer deposition in tailings deposits (Fisseha et al. 2010, Daliri et al. 2015).

In the cases analyzed, evaporation is a known boundary condition, and therefore the model does not consider the influence of cracks or osmotic suction on evaporation, and vapor flow under evaporation, all of which have been shown to be significant in affecting the evaporation rate of fine grained materials (Fujiyasu and Fahey 2000; Daliri et al. 2015; Rozina et al. 2015; Innocent-

Bernard et al. 2013). More sophisticated treatment of the top boundary condition is left for future work; however, the ability of the model to predict true desaturation will allow for the incorporation of more realistic treatment of this boundary.

The constitutive equations can likely be improved. For example, the present formulation does not predict zero water content at the theoretical suction limit (10^6 kPa). This may lower the value of predicted matric suction at the surface. This limitation applies to most formulations of the SWCC in the literature, excepting Fredlund and Xing (1994), which uses a correction factor to force the water content to zero at the theoretical suction limit.

7.6 Conclusion

The program UNSAT-CON developed for large strain consolidation analysis involving unsaturated flow is verified using an illustrative numerical example, a small scale laboratory test and field data from a fine-grained tailings site. The following conclusions were drawn from the analyses performed herein.

(i) An excellent agreement is observed in the settlement *vs*. time curve between quasi unsaturated analysis and published numerical solutions for a large strain consolidation example assuming saturation condition under evaporation and decantation conditions. Detailed analysis of hydraulic exchange at the soil-atmosphere interface shows that possible combinations of evaporation and decantation can be correctly handled by the boundary conditions formulated for the top surface. The settlement rate can be accelerated by increasing evaporation; however, the final settlement is only dependent on the cumulative surface water outflow under the saturation assumption, indicating that UNSAT-CON provides a strictly mass conservative solution.

(ii) The calibration-validation exercise for the unsaturated formulation, using a column test and field data on the same type of tailings, showed UNSAT-CON was able to make good to excellent predictions of a range of measured parameters (overall settlement, void ratio, PWP, and water content in the column test; settlement, water content and pore-water pressure in the field test), with only minimal calibration. Calibration was achieved by only altering the saturated hydraulic conductivity function. The 3D constitutive surfaces were defined only by measurements in their extreme planes (the SWCC and the saturated compressibility function for void ratio and water content); this seems to be adequate to make realistic predictions.

(iii) It is shown that modeling desaturation does substantially affect the prediction of deformation near the soil surface. Desaturation allows the evaporative boundary condition to be partially satisfied by water loss not associated with volume change. Models that do not handle desaturation will either over predict volume change, if the surface suction or surface void ratio is not limited, or conversely, if suction (and therefore volume change) is limited, such models will force an under-prediction of evaporation and therefore will also under-predict overall dewatering.

(iv) The ability to model desaturation is a promising feature for a number of possible applications, including using desaturation data to make evaporation predictions, to model gas transport in an acid generation context, or to model placement of fresh material over previously dried and unsaturated material.

Glossary

Symbols

w	Gravimetric water content
e	Void ratio
G_s	Specific gravity
a, b, c, d, f, g	Material parameters for void ratio constitutive relationship
A, B, C, D, F, G	Material parameters for water content constitutive relationship
m, n	Material parameters accounting for the effect of suction on the hydraulic conductivity
H_1, H_2	Material parameters for hydraulic conductivity relationship

Abbreviations

VWC	Volumetric water content
PWP	Pore water pressure
SA	Saturated analysis
QUA	Quasi-unsaturated analysis
UA	Unsaturated analysis
SWCC	Soil Water Characteristic Curve
PL	Plastic limit
LL	Liquid limit
MFT	Mature fine tailings

7.7 References

Daliri, F., Simms, P., & Sivathayalan, S. (2015). Shear and dewatering behaviour of high density gold tailings in a laboratory simulation of multi-layer deposition. Canadian Geotechnical Journal, Manuscript ID: cgj-2014-0411.R2. Accepted with minor comments, December 2015.

Dunmola, A., Cote, C., Freeman, G., Kolstad D., Song, J., and Masala S. 2013. Dewatering and shear strength performance of in-line flocculated mature fine tailings under different depositional schemes. Proceeding of Tailings and Mine Waste 2013 November 3rd-6th 2013, Banff, Alberta p5 -14.

Dunmola, A., Dhadli, N., Freeman, Kolstad, D., Fasking, T., Song, J., and Langseth, J. 2013. Geotechnical Benefits of Flocculation in Dewatering Oil Sands Mature Fine Tailings. In Proceedings of GeoMontreal 2013, Canadian Geotechnical Conference, Sept. 30th - Oct 3rd 2013, Electronic proceedings.

Fisseha, B., Bryan, R., & Simms, P. (2010). Evaporation, unsaturated flow, and salt accumulation in multilayer deposits of "paste" gold tailings. Journal of Geotechnical and Geoenvironmental Engineering, 136(12), 1703-1712.

Fox, P. J., & Berles, J. D. (1997). CS2: A piecewise-linear model for large strain consolidation. International Journal for Numerical and Analytical Methods in Geomechanics, 21(7), 453-475.

Fredlund, D. G., & Xing, A. (1994). Equations for the soil-water characteristic curve. Canadian geotechnical journal, 31(4), 521-532.

Fujiyasu, Y., & Fahey, M. (2000). Experimental study of evaporation from saline tailings. Journal of Geotechnical and Geoenvironmental Engineering, 126(1), 18-27.

Innocent-Bernard, T. (2013). Evaporation, Cracking, and Salinity in a Thickened Oil Sands Tailings (Doctoral dissertation, Carleton University Ottawa).

Jeeravipoolvarn, S. 2010. Geotechnical behaviour of in-line thickened oil sand tailings. Doctoral thesis, University of Alberta, 410 p.

Qi, S., Simms, P., Vanapalli, S., & Soleimani, S. (2017b). Piecewise-Linear Formulation of Coupled Large-Strain Consolidation and Unsaturated Flow. II: Testing and Performance. Journal of Geotechnical and Geoenvironmental Engineering, 143(7), 04017019.

Rozina, E., Mizani, S., Malek, M., Sanchez-Sardon, M., & Simms, P. (2015). Dewatering in a laboratory simulation of a multilayer deposit of inline flocculated mature fine tailings. Proceedings of the 18th International Seminar on Paste and Thickened Tailings, R. Jewell and A. Fourie. Australian Centre for Geomechanics, Crawley, Australia, 81-94.

Seneviratne, N. H., Fahey, M., Newson, T. A., & Fujiyasu, Y. (1996). Numerical modelling of consolidation and evaporation of slurried mine tailings. International Journal for Numerical and Analytical Methods in Geomechanics, 20(9), 647-671.

Simms, P., Dunmola, A., Fisseha, B., & Bryan, R. (2010). Generic modeling of desiccation for cyclic deposition of thickened tailings to maximize density and to minimize oxidation. Proceedings of the 13th International Seminar on Paste and Thickened Tailings, R. Jewell and A. Fourie. Australian Centre for Geomechanics, Crawley, Australia, 293-303.

Soleimani, S., Simms, P., Dunmola, A., Freeman, G., & Wilson, G. W. (2014) Desiccation and consolidation in thin-lift deposition of polymer-amended mature fine tailings. Proceedings of the 17th International Seminar on Paste and Thickened Tailings, R. Jewell, A. Fourie, P. S. Wells and D. van Zyl, eds., Australian Centre for Geomechanics, Crawley, Australia, 307-322.

Vu, H. Q., & Fredlund, D. G. (2006). Challenges to modelling heave in expansive soils. Canadian Geotechnical Journal, 43(12), 1249-1272.

Yao, D. T., de Oliveira‐Filho, W. L., Cai, X. C., & Znidarcic, D. (2002). Numerical solution for consolidation and desiccation of soft soils. International Journal for Numerical and Analytical Methods in Geomechanics, 26(2), 139-161.

Chapter 8 Piecewise-linear formulation of large strain consolidation with irrecoverable volume change and hydraulic hysteresis

In real practice, mine tailings are often deposited in layers that undergo variable stress histories in terms of desiccation and loading, as a given layer of tailings may undergo variable degrees of desiccation before burial by subsequent layers. Proper modelling of this scenario therefore requires not only an effective coupling of unsaturated flow with large strain consolidation, but also inclusion of stress history and hysteresis effects. This chapter presents the further development and testing of an existing coupled unsaturated flow-large strain consolidation model (UNSAT-CON), formulated for only monotonic dewatering in Chapter 6 and 7, to include such effects. The chapter proceeds by i) identifying the importance but lack of an appropriate model for multilayer deposition, ii) presentation of the adopted constitutive models (A modified/extended state surface model for elasto-plastic volume change and a void ratio dependent hysteretic model), iii) introduction of a novel numerical algorithm which ensures mass conservation and smooth state transition (inherited the merits of the algorithm developed in previous chapter 6) for numerical implementation of these models, and iv) testing the developed model, UNSATCON-ML, where ML denotes multilayer deposition, using a recently published study of multilayer deposition of thickened gold tailings (Daliri et al. 2016).

8.1 Introduction

Large strain consolidation models that incorporate some consideration of desiccation or unsaturated phenomena are frequently used, such as the MINTACO (Senerviratne et al. 1996) or CONDES models (Yao et al. 2000) (reviewed in Chapter 2). Such models incorporate some attributes of desiccation (limiting suction development to stop volume change, consideration of contribution of cracking to volume change), but do not truly incorporate unsaturated flow. In previous chapters, the coupled large strain consolidation – unsaturated flow model UNSAT-CON was developed, which employs three dimensional constitutive surfaces for unsaturated soils, uses a piece-wise linear method adopted from Fox and Berles (1997) to model large strains, and can smoothly transit from saturated to unsaturated regimes. It is showed that incorporating unsaturated flow leads to more realistic predictions of deformation, due to evaporative demand being satisfied partially by water from desaturation, not only volume change.

However, none of the preceding models is effective for predicting the evolution of tailings' behaviour in a multilayer deposition scheme, which may occur naturally, or by design. Multilayer deposition occurs for tailings that are deposited sub-aerially, and flow to different parts of a tailings impoundment. This results in tailings being desiccated to some degree before burial by other layers. Therefore, as shown by Daliri et al. (2014, 2016), Rozina et al. (2015), Soleimani et al. (2014), Fisseha et al. (2010), and Simms et al. (2007), the dewatering behaviour of such tailings exhibits both irrecoverable volume change and wet/dry hysteresis. Moreover, the consequences of desiccation stress history to the strength of subsequently buried tailings are non-trivial, as desiccation imparts increased dilatency to subsequently consolidated tailings (Daliri et al. 2014, 2016).

8.2 The model

8.2.1 Constitutive relationships

The following points are kept in mind in selecting the constitutive relationships in this chapter

(a) Adequately simulate both elastic and plastic volume change along stress paths encountered in sub-aerially deposited tailings.
(b) Account for recoverable and irrecoverable change in water content due to both hydraulic hysteresis and mechanical volume change
(c) While not sacrificing the necessary sophistication in a) and b), be sufficiently simple to enable implementation of numerical algorithm and determination of constitutive parameters from relatively conventional experiments in the laboratory.

Volume change behaviour. Apart from the Barcelona Basic Model (BBM). a number of elasto-plastic constitutive models have been proposed in the literature (e.g. Gens & Alonso 1992; Alonso et al. 1999; Cui and Delage 1996; Wheeler and Sivakumar 1995; Vaunat et al. 2000; Wheeler et al. 2003; Gallipoli et al. 2003; Sheng et al. 2004; Sheng et al. 2008; Cardoso et al. 2013), and reviewed by Wheeler and Karube (1996); Gens (2010); and Sheng (2011). These models separate the irrecoverable strain from total strain by defining the basic attributes of a general elasto-plastic model, including yielding surfaces, flow rules, hardening laws, in the space of generalised stress variables.

The integration of elasto-plastic models with the three-dimensional (3D) state surface approach for modelling unsaturated soil has been investigated by several researchers (Wheeler & Karube 1996; Delage & Graham 1996; Blatz & Graham 2003; Zhang & Lytton 2009). Thus, in

this chapter, a particular combination of plastic and elastic surfaces that expresses void ratio as two continuous functions of net stress and suction is selected: Eq. (8.1) being a plastic surface (this is the one used in UNSAT-CON), and Eq. (8.2) is the elastic surface from the BBM (this will be explained in details in the next chapter when implementing BBM into UNSAT-CON):

$$e = a + b\log\left[\frac{1 + c\bar{\sigma} + ds}{1 + f\bar{\sigma} + gs}\right] \tag{8.1}$$

$$e^e = C_e - \kappa \ln \bar{\sigma} - \kappa_s \ln(s+1) \tag{8.2}$$

where, e is void ratio, e^e is void ratio on the elastic surface, the net stress, $\bar{\sigma} = \sigma - u_a$, σ being the total stress, u_a being the pore-air pressure (usually assumed to be zero in nature, then $\bar{\sigma}$ is equivalent to σ), the suction, $s = u_a - u_w$, u_w being the pore-water pressure. a, b, c, d, f, g, κ and κ_s are model parameters. The "1 (kPa)" in Eq (8.2) is used to avoid a 0 value in the logarithmic function of suction. Eqs. (8.1) and (8.2) describe two 3D surfaces in the void ratio-net stress-suction space as shown in Fig. 8.1(a), namely, a plastic surface (representing the virgin consolidation behaviour of unsaturated soil under drying and/or loading conditions), and an elastic surface (tracking the recoverable volumetric deformation when soil states lies under the plastic surface). The location of the elastic surface varies depending on the value of the constant C_e calculated from soil current state, which is either on the stationary plastic surface or on an elastic surface. The intersection of these two surfaces on the net stress-suction plane constitutes the yield curve, which evolves as the location of the elastic surface varies (See Fig. 8.1(b)). Although 3D surfaces generated from other proper elasto-plastic models can also be selected, as introduced in the next chapter, Eqs. (1) and (2) give certain practical advantages for modeling tailings behaviour, such as a) the relatively simple conceptualization of the yield curve; b) the elastic surface at saturated state is theoretically consistent with saturated critical state models; c) the plastic surface

(Eq. (8.1) proposed by Vu and Fredlund (2006)) is sufficiently flexible to simulate the high compressibility at low stress/suction level and the shrinkage behaviour at high suction level (the void ratio approaches a minimum value at high values of suction) of initially slurry tailings, as shown in previous chapter; d) model parameters in Eq. (8.1) can be determined from conventional measurements of the soil water retention curve (SWRC) and the saturated compression curve, as several terms vanish when either suction or normal stress approach zero, and e) allowing for direct use of void ratio to represent the strain state, which, in numerical implementation, facilitates mass conservation and integration with the void ratio – dependent hysteretic SWRC and permeability models. The ability of plastic surface (Eq (1)) to model the virgin consolidation/drying behaviour of initially slurry tailing are identified by investigating its shape characteristic in e-log($\overline{\sigma}$ /s) plane. The limiting void ratio at low/high stress/suction levels (e.g. maximum void ratio, shrinkage limit), virgin (drying) compressibility at middle stress/suction levels, observed in shrinkage curve and the large strain consolidation data, are well defined in terms of parameters in Eq. (8.1), see Appendix 8.1.

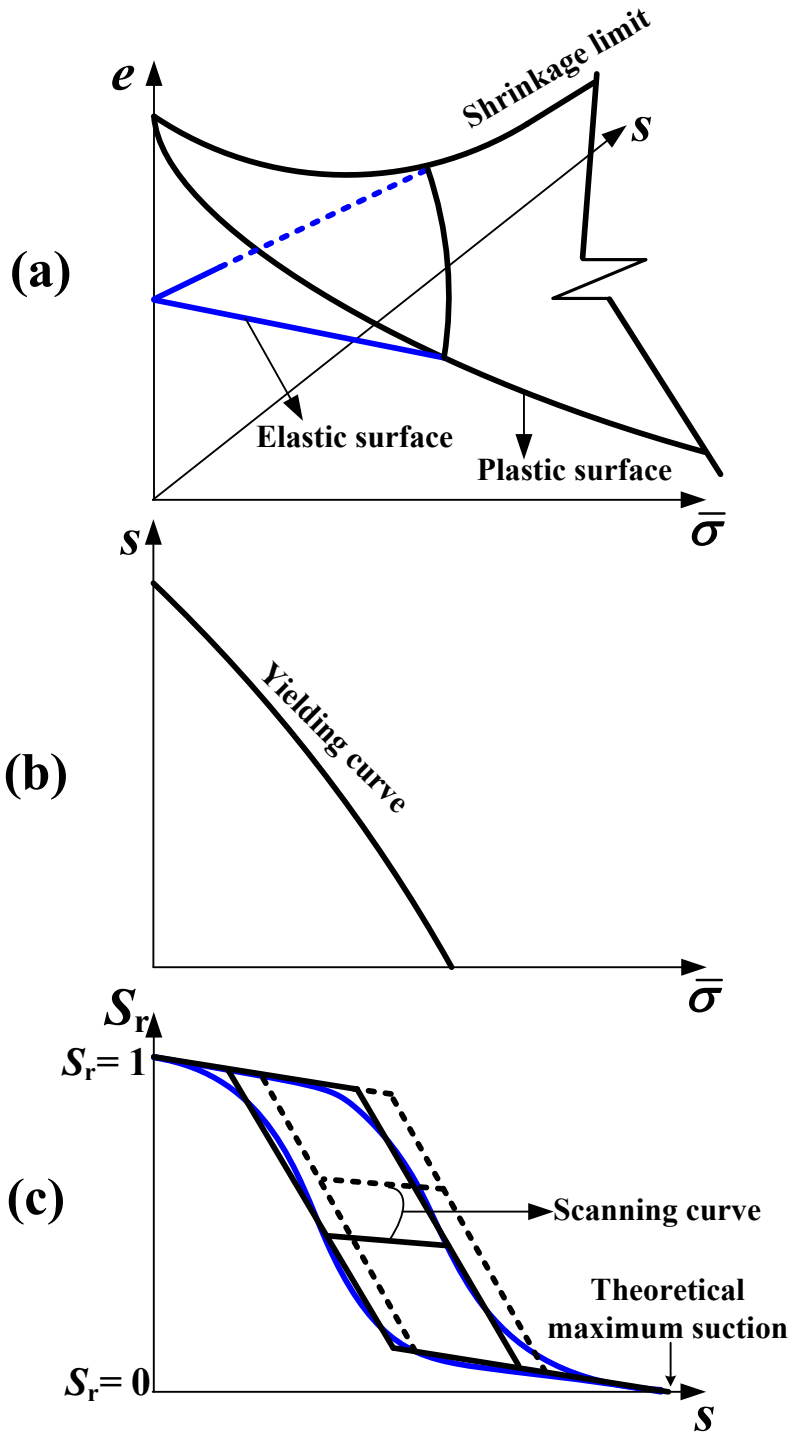

Fig. 8.1 Conceptual sketch of consitutive relationships

The *water retention behaviour* of unsaturated soil is conventionally described by the soil-water retention curve (SWRC). It is well established that the SWRC is not unique or water content is not in one-to-one correspondence with suction, as reviewed in Chapter 2. Taking water content as the other strain variable (Houlsby 1997), its irrecoverable behaviour has also been modeled by some researchers (Dangla 1997; Wheeler et al. 2003, Sheng et al. 2004) using a framework analogous to mechanical elasto-plasticity. The authors have adopted this framework, and use the following equations to define the SWRC expressed with a family of lines in log-linear space, similar to expressions proposed by Sun and Sun (2012):

$$S_{\mathrm{r}} = 1 - \kappa_{ss} \ln(s+1) \tag{8.3}$$

$$S_{\mathrm{r}} = \kappa_{ss} \ln(10^6+1) - \kappa_{ss} \ln(s+1) \tag{8.4}$$

$$S_{\mathrm{r}} = C_{drying} - \lambda_{se} e - \lambda_{sr} \ln(s+1) \tag{8.5}$$

$$S_{\mathrm{r}} = C_{wetting} - \lambda_{se} e - \lambda_{sr} \ln(s+1) \tag{8.6}$$

$$S_{\mathrm{r}} = C_{scanning} - \lambda_{se} e - \kappa_{ss} \ln(s+1) \tag{8.7}$$

where, S_{r} is the degree of saturation, C_{drying} , $C_{wetting}$, λ_{se}, λ_{sr} and κ_{ss} are five model parameters. Eqs. (3) and (4) describe the primary (drying and wetting) surfaces at lower and higher suction level, or the SWRC before the air entry or after the residual water content. Eq. (8.5) and (8.6) describe the primary surfaces at the medium suction level for drying and wetting paths, respectively, their locations are fixed by the experimental constants. Eq. (8.7) describes the scanning behaviour. Parameters κ_{ss}, λ_{se} and λ_{sr} quantify the increment of saturation degree, S_{r}, in response to a changes in void ratio and suction on the primary or scanning surfaces. Different from the mechanical behaviour, this formulation of elasto-plastic changes of degree of saturation requires two primary

surfaces (Eqs. (8.3-8.6)), see Fig. 8.1(c). Only the zone bounded by these two primary surfaces comprises attainable soils' state, within which change of S_r is recoverable (purely elastic) and described using a series of scanning surfaces. The value of $C_{scanning}$ calculated from current soils' state determines the location of the current scanning surface.

Due to the variance in both void ratio and the position of the elastic surface within some deposit of consolidating material, the gravimetric (used in previous chapters) and volumetric water contents at saturation will vary, even for the same total/net stress level. But degree of saturation, S_r, will of course be 100% at saturated condition (neglecting the air occlusion effect during wetting), no matter if the soil is on the plastic or the elastic void ratio surface. Therefore, using the degree of saturation to designate the water content in the adopted hysteretic hydraulic model is advantageous for smoothly modelling wetting/drying paths in conjunction with void ratio changes. Although the experimentally observed water-retention behaviour of soils is better described using surfaces extended from an *S*-shape curve (e.g. Fredlund and Xing, 1994; Tsiampousi et al. 2013; Gallipoli et al. 2015), the modelling results presented later shows that the chosen soil water retention model appears to be more adequate for the cases simulated later in this chapter, a comparison with *S*-shape model is made available in the next chapter.

A void ratio-dependent *permeability* function is employed that consists of two parts, one accounting for the effect of varying void ratio (power law) and the other (van Genuchten 1980) for effect of desaturation, expressed as:

$$k_{sat} = H_1 \times e^{H_2} \tag{8.8}$$

$$k_r = S_r^{1/2}[1-(1-S_r^{1/M})^M]^2 \tag{8.9}$$

The soil permeability for a given void ratio at a given degree of saturation is calculated as the product of saturated permeability k_{sat} and relative permeability k_r. H_1, H_2 and M are three constants

determined from experiments or using methods that estimate k_r from the SWRC (e.g. van Genuchten 1980, Leong and Rahardjo 1997). Relating permeability to degree of saturation rather than suction will tend to minimize, though probably not eliminate, hysteresis effects on the permeability function. In the following chapters, other models for volume change and hydraulic retention behaviours will be used but the permeability functions are kept the same as described here using Eqs. (8.8) and (8.9).

8.2.2. The piece-wise linear formulation

The piece-wise linear formulation is basically the same as that formulated in previous chapters. The flow continuity for water mass and vertical equilibrium for a soil element are described using

$$\frac{\partial}{\partial z}\left(k\frac{\partial h}{\partial z}\right)=\frac{1}{1+e}\frac{\partial(wG_s)}{\partial t} \tag{8.10}$$

$$\frac{\partial \sigma}{\partial z}=-\gamma=-\left(\frac{G_s+S_r e}{1+e}\right)\gamma_w \tag{8.11}$$

where, z is elevation convective coordinates measured positive upward from fixed base of the domain of interest, z is updated element by element after each time step for large strain problem (Fox and Berles 1997). The piece-wise linear formulation uses a Lagrangian approach that follows the motion of the solid phase during the consolidation process. k (=k_{sat} k_r) is the hydraulic permeability, h is the hydraulic head, w is the gravimetric water content, t is the time. σ is the vertical total stress and equivalent to net stress by assuming that air pressure remains atmospheric in nature, G_s the specific gravity. γ and γ_w are unit weights of soil and water, respectively. Applying finite difference discretization to Eq. (8.10)

$$w_j^{(i)} M_{s,j}^{(0)} = w_j^{(i-1)} M_{s,j}^{(0)} - \left[(v_j^{(i-1)} - v_{j-1}^{(i-1)}) \times \Delta t^{(i-1)} \right] \rho_w \tag{8.12}$$

which is the same as Eq. (6.21), where $w_j^{(i)}$ is the gravimetric water content of element j at time step i after a time increment $\Delta t^{(i-1)}$, ρ_w is the density of water, M_s is mass of solids within each element which is invariant (the superscript (0) in Eq. (8.12) indicates the value at initial condition) if assuming no exchanges of soil particles across elemental interface. $v_j^{(i)}$ is the relative discharge velocity across the elemental interface and calculated as $v_j^{(i)} = k_{e,j}^{(i)} (h_{j-1}^{(i)} - h_j^{(i)}) / (z_{j-1}^{(i)} - z_j^{(i)})$, where the $k_{e,j}^{(i)}$ is the equivalent hydraulic conductivity across elemental interface, and evaluated as that for layered soil system (detailed in chapter 6) since the soil permeability of two neighboring elements can be different due to different void ratios and/or degree of saturations. This treatment automatically ensures the flow continuity across the interface between old and newly deposited layers as discussed in Appendix 8.2, and therefore facilitates the programming for placing new layers. Eq. (8.12), indicating explicitly that the mass conservation of water has been strictly satisfied, can be alternatively expressed in terms of degree of saturation, which shows that these discretization forms are still applicable for saturated zone ($S_r = 1$), as derived in in previous chapter 6.

Under the one-dimensional condition, the vertical stress due to soil self-weight at a point can be obtained by integrating Eq. (8.11) over the appropriate depth, and is calculated in UNSATCON-ML in summation form:

$$\sigma_j^{(i)} = M_{s,j}^{(0)} (1 + w_j^{(i)}) g / 2 + \sum_{k=1}^{j-1} M_{s,k}^{(0)} (1 + w_k^{(i)}) g + \Delta h_w^{(i)} \rho_w g + q_0 \tag{8.13}$$

where, q_0 is the surface vertical load assumed for forming the initial effective stress profile and $\Delta h_w^{(i)}$ is the current thickness of surface water at the tailing surface if any, which is calculated according to different boundary conditions formulated in Chapter 6.

The gravimetric water content after each time increment for each element can be directly obtained from Eq. (8.12), the total/net stress for each node at time step *i* is then calculated using Eq. (8.13). Based on these two parameters, the remaining state variables that need to be obtained to complete the advancement of solution over a time increment, will be solved through an analysis at the constitutive level. The constitutive relationships for volume change and water retention behaviour described in the previous section are rewritten in the following generalised forms

$$e = f_e(\bar{\sigma}, s) \tag{8.14}$$

$$S_r = f_S(e, s) \tag{8.15}$$

The above two constitutive equations (Eqs. (8.14) and (8.15)) involve three unknowns, namely void ratio, degree of saturation, and matric suction, which can be made determinate with the addition of basic volume-mass relationship

$$S_r e = w G_s \tag{8.16}$$

The stress-path dependent volume change and hysteretic water retention behaviours substantially increases the nonlinearity of this set of equations (Eqs. (8.14), (8.15) and (8.16)), and it is not possible to achieve explicit expressions for the relevant unknowns. A novel numerical algorithm formulated to solve these equations is implemented in UNSATCON-ML and detailed in the following section.

8.3 Numerical implementation

The upgraded program, UNSATCON-ML, advances the coupled analysis of large strain consolidation and unsaturated flow in a similar procedure as its original version. After initialization the analysis during one time increment generally follows two main steps: (1) *global analysis* for calculating series hydraulic conductivities, the hydraulic gradients and then the water flow from

element to element based on the current elevation and hydraulic head of each node; (2) *local analysis* for calculating the new void ratio, pore water pressure (or suction) and degree of saturation based on the obtained total stress and gravimetric water content for all elements. After each time step, the node (element central) elevation coordinates z_j is updated element by element from the base upwards, according to the new element heights, $L_j^{(i)} = (1+ e_j^{(i)})L_j^{(0)}/(1+ e_j^{(0)})$.

The new algorithm for deformation analysis in UNSATCON-ML is capable of: (*i*) providing a robust solution to the constitutive analysis in unsaturated zone (i.e. solving the systems of equations (14), (15) and (16)); (*ii*) being simplified for constitutive analysis based on effective stress principle in saturated zone, and (*iii*) ensuring a smooth transition between these two states which may occurs when soil is experiencing elastic or elasto-plastic volume change behaviour. In UNSATCON-ML the volume change of saturated soil is described using Terzaghi's effective stress principle, using the saturated constitutive curves that are also the intersection curves between the three-dimensional constitutive surfaces and the s = 0 kPa plane, see Fig. 8.1. Fig. 8.2 replots these curves on the void ratio-effective stress plane. With the obtained gravimetric water content w and total stress σ at the end of current time step (superscript 'i' and subscript 'j' are omitted for clarity), a check is first made on the state of each element by comparing two void ratios. The first one corresponds to the current total stress on the two-dimensional constitutive curve (see Fig. 8.2), namely reference void ratio, e_r, and the other corresponds to current gravimetric water content assuming saturation, calculated as $e = wG_s$. If $e = wG_s >$ or = e_r, the element is in saturated state at the end of current time step, otherwise, the element is in unsaturated state.

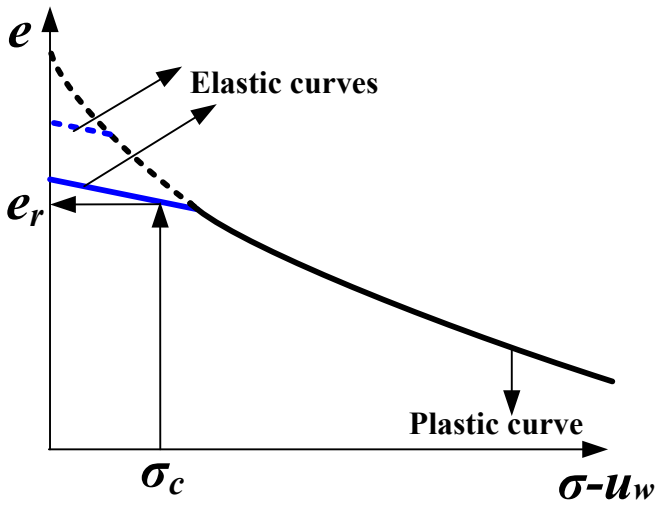

Fig. 8.2 Constitutive relationship for saturated zone

For unsaturated elements at the end of current time step, an iterative procedure must be adopted to obtain the solution (a set of S_r, e and s) to the system of nonlinear equations (8.14), (8.15) and (8.16). The bisection method appears to be robust and efficient for searching the root, which is found to lie within a bounded interval as sketched in Fig. 8.3. With the known gravimetric water content w at the end of current time step, the inverse relationship between S_r and e is defined by Eq. (8.16) with a minimum void ratio e_{min} corresponding to $S_r = 1$. With the known total stress σ, there is a maximum void ratio e_{max} defined by Eq. (8.14), which corresponds to zero suction (i.e. $S_r = 1$ as well). Substituting $e = e_{max}$ into Eq. (8.16) gives the minimum $S_{r,min}$ (see Fig. 8.3). The suction is likely to increase to a certain value according to Eq. (8.15) with degree of saturation decreasing from 1 to $S_{r,min}$, in the meantime, the void ratio determined by Eq. (8.14) continuously decreases to less than e_{max}. Thus, there exists an intersection point between two curves shown in Fig. 8.3, which is the true solution to the system of equations and can be approximated using the following iterative procedure:

Step 1. Start with the interval [1, $S_{r,min}$], calculate the midpoint $S_{r,try} = (1+S_{r,min})/2$, and then the $e_{try} = wG_s/S_{r,try}$ according to Eq. (8.16);

Step 2. Calculate the s_{try} according the Eq. (8.15) (water retention behaviour) by substituting $S_{r,try}$ and e_{try};

Step 3. Calculate a new void ratio e_{new} according the Eq. (8.14) (volume change behaviour) by substituting s_{try};

Step 4. Check the convergence criterion $|e_{new} - e_{try}| < 10^{-5}$: (*i*) if satisfied, stop iteration and return the trial values ($S_{r,try}$, e_{try} , s_{try}) as the solution; (*ii*) if not satisfied, go back to Step 1 with a halved interval in which the solution lies (see Fig. 8.3).

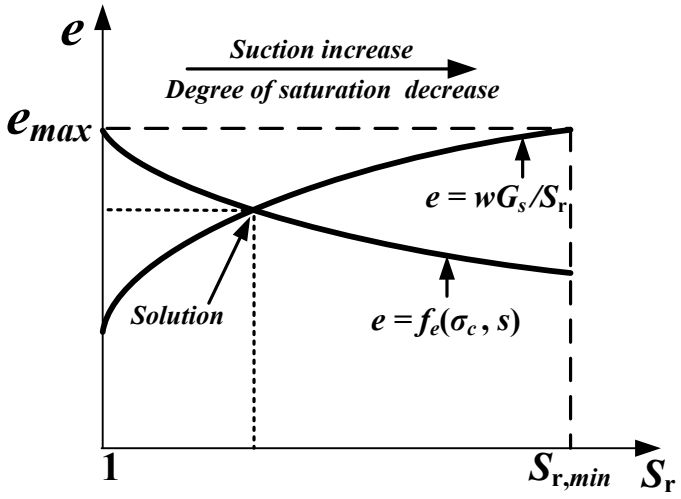

Fig. 8.3 Bisection method for unsaturated analysis

In the procedure, the program needs to select appropriate constitutive paths: primary drying/wetting or scanning path defined by water retention behaviour in Step 2; elastic unloading/reloading or virgin consolidation path defined by volume change behaviour in Step 3. For this to be feasible, the state variables as well as the locations of the current elastic surface and scanning curve at the beginning of the time step need be stored during the analysis, i.e. the values of C_e and $C_{scanning}$ defined in Eqs. (8.2) and (8.7), respectively. Fig. 8.4(a) sketches a hysteretic water retention surface in three dimensional space with an assumed scanning surface at the beginning of the current time step. The surfaces labeled with (a) through (e) in Fig. 8.4(a) are

plotted from Eqs. (8.3)-(8.7), respectively. Depending on the initial retention point at the beginning of the current time step, distinction is made in the employment of specific equation to determine the retention point at the end of the current time step.

Caution also needs to be exercised to select an appropriate equation (Eqs. (1) or (2)) in calculating the new void ratio in Step 4, which depends not only on the current location of elastic surface but on the value of suction s_{try} obtained in Step 2. The position of void ratio at the end of the current time step will be on the surface consisting of the current elastic surface (determined by value of C_e) and part of the plastic surface sketched in Fig. 8.4(b). To be more specific, the volume change point will end on the curve corresponding to current total/net stress at the end of time step, which is already known from Eq. (8.13) after the *flow analysis*, such as the dotted curves shown in Fig. 8.4(b). If the coordinate (σ_c, s_{try}) is located within the zone of projection of elastic surface in the horizontal plane, Eq. (8.2) is adopted to calculate the new void ratio in Step 3, otherwise, Eq. (8.1) should be used. It is worth repeating here that the constitutive curve for saturated condition in Fig. 8.2 is actually identical to intersection of the three dimensional constitutive surface and the zero suction plane in Fig. 8.4(b), which guarantees a smooth state transition for both elastic and elasto-plastic volume change conditions.

When the convergence criteria in Step 4 is satisfied, it is of central importance to update these variables, including C_e, $C_{scanning}$ and the location of the retention point on the water retention surface for each element after each time step, which will be stored as the initial retention point for analysis during the next time step.

In terms of hydraulic-mechanical coupling, the influence of mechanical on hydraulic behaviour is considered using *e*-dependent SWRC. While the influence of hydraulic on mechanical behaviour is not explicitly considered in Eq. (8.14), unlike some mechanical models that uses a S_r-

dependent stress variable (e.g. the GCM (Wheeler et al. 2003); some models in D'onza et al. (2011) among many others) or compressibility parameter (e.g. Tsiampousi et al. 2013), but has been implicitly accounted for in this algorithm. The calculated e, although expressed as a function of net stress and suction, will be influenced by the input retention behaviour, since suction used in Step 3 is obtained from the water retention model in Step 2. Thus the results obtained from this procedure depend on both mechanical and hydraulic retention models. The GCM will be implemented into UNSAT-CON in the next Chapter.

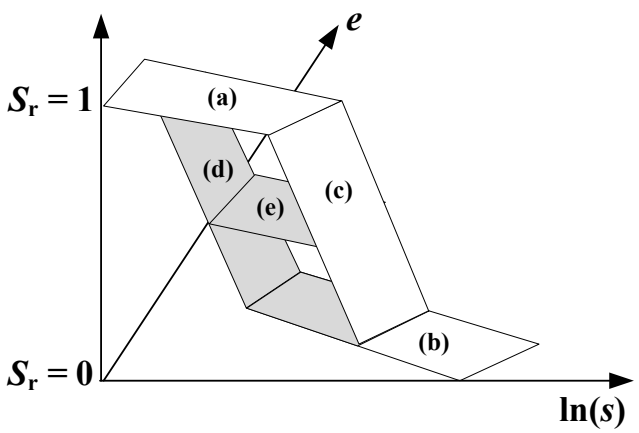

(a)

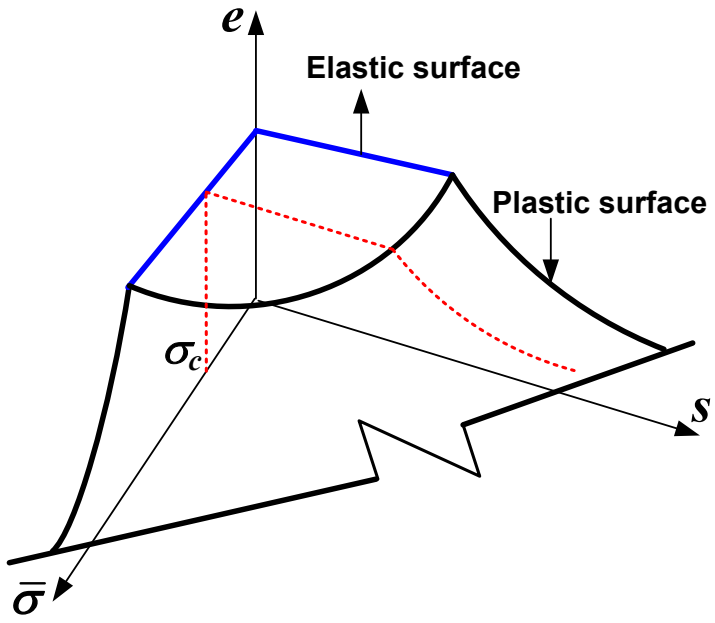

(b)

Fig. 8.4 Stress paths followed in constitutive analysis

8.4 Modelling of multi-layer deposition of gold tailings

8.4.1 Mesoscale Drying box test

Daliri et al (2016) and Daliri (2013) describe a detailed study on a physical simulation of multilayer deposition of thickened gold tailings (PL=20, LL=22.5; D_{90} =120, D_{50} =30, D_{10} = 1.5 microns) in a 0.7 m by 1 m in plan "drying box", which allows for direct measurement of evaporation, drainage, vertical volume change, and is instrumented with pore-water pressure (matric suction) and volumetric water content sensors. Gold tailings were prepared at a gravimetric water content of ~38% and deposited in layers of thickness of 14-18 cm. New layers were placed after no volume change was observed in the previous layer under evaporation. Between layers 4 and 5, the deposit was re-saturated twice by adding water. During the whole experimental period (lasting for 73 days), drainage was measured using a tipping bucket, actual evaporation was calculated by change in mass (experimental box mounted on load cells) less the drainage. The interlayer hydraulic interactions along with the consolidation behaviour were characterized using 3 or 4 point measurements of pore water pressure and volumetric water content within each layer. Initial and boundary conditions, material properties and analysis of results from simulating this test will be given in details in the following. The same drying box test will also be simulated in the following chapter using other implemented constitutive models, but just for model comparison there.

8.4.2 Initial and boundary conditions

The known saturated ($S_r \sim 1$) gravimetric water content (~38%) at deposition, with specific gravity G_s =2.89, is used to form a uniform initial condition for each layer, which, along with the condition of existing layers at each new deposition is used to proceed the calculation for a new

domain thereafter. The measured drainage is applied at the bottom as a flux boundary. Boundary condition Case (*iii*) described in Chapter 6 is applied at the top: actual evaporation (measured by Daliri et al. (2016)) is first used to remove un-decanted surface water generated by consolidation, until the accumulated water over the tailings surface vanishes, and then to desaturate the tailings from the top downwards. After each new deposition this boundary condition automatically moves to the top of updated computational domain in UNSATCON-ML.

8.4.3 Material properties

These gold tailings have been characterized extensively at three different universities (Carleton University, University of Alberta, and University of British Columbia). The volume change behaviour measured in elemental tests and large strain consolidation tests were available from Daliri (2013) and Salfate (2011). The soil water retention behaviour has been presented previously by Fisseha et al. (2010), and measured by Heidarian (2012). Saturated permeability data were deduced by Salfate (2011) from large strain consolidation tests. The material properties extracted from these sources are used in the model with constitutive constants summarized in Table 8.1.

Fig. 8.5(a) presents the plastic surface for volume change fitted from data during virgin compression by mechanical stress and suction, respectively. The mechanical unloading/ reloading compression index (κ = 0.015) is measured by Daliri (2013), comparatively, the hydraulic unloading/reloading compression index was found to be much smaller (κ_s = 0.0015). These two constants are used to define the elastic surface (Eq. (8.2)). Fig. 8.5(b) presents two primary retention surfaces, in which the primary drying surface corresponding to the medium suction level (i.e. Eq. (8.5)) is fitted from the data lying in respective zone. The value of κ_{ss} defining the primary

surface corresponding to the low suction level (i.e. Eq. (8.3)) is found to fall in a small range of 0.025-0.034, which, however, affects the prediction of suction development in the early desaturation state. Therefore, a calibration of κ_{ss} is performed targeting a good prediction of experimentally observed suction development during drying of the first layer by UNSATCON-ML (as subsequently demonstrated in Fig. 8.6(a)), which resulted in a κ_{ss} = 0.028, falling in the range of possible experimental values. The only remaining constant yet determined for retention behaviour: $C_{wetting}$ defines the location of the primary wetting surface and quantifies the degree of hysteresis. The degree of hysteresis is found to significantly influence prediction of the hydraulic interaction between desiccated and fresh layers, since the water retention behaviour of underlying desiccated layer during wetting is governed by a wetting path along a scanning and then the primary wetting surface. With this recognition, the value of $C_{wetting}$ is determined by another calibration targeting a good replication of interlayer hydraulic interaction (mostly the suction development since it is more reliable) after depositing the second layer (demonstrated in Fig. 8.6(a)), which gives $C_{wetting}$ = 2.65. The calibrated primary wetting surface (see Fig. 8.5(b)) matches well with the data, note that the wetting data is not necessarily on the primary wetting surface, as the maximum value of suction was not necessarily in excess of the residual state.

Fig. 8.5(c) shows the model for permeability with the measured saturated permeability. Due to the absence of data at unsaturated condition, another calibration is made in variation of the M parameter, which controls variation of permeability with degree of saturation. Values of M greater than 0.75 replicate the observed relatively uniform depth profiles of pore-water pressure, hence M=0.75 is used.

Table 8.1 Parameters for constitutive relationships

Volume change behaviour								
Parameters	a	b	c	d	f	G	κ	κ_s
Value	1.2	0.166	0.004	0.02	35.9	41	0.015	0.0015
Water retention behaviour								
Parameters	C_{drying}	$C_{wetting}$	λ_{se}	λ_{sr}	κ_{ss}			
Value	3.1	2.65	0.6	0.4	0.028			
Water hydraulic conductivity								
Parameters	H_1	H_2	M					
Value	3×10^{-7}	7.1057	0.75					

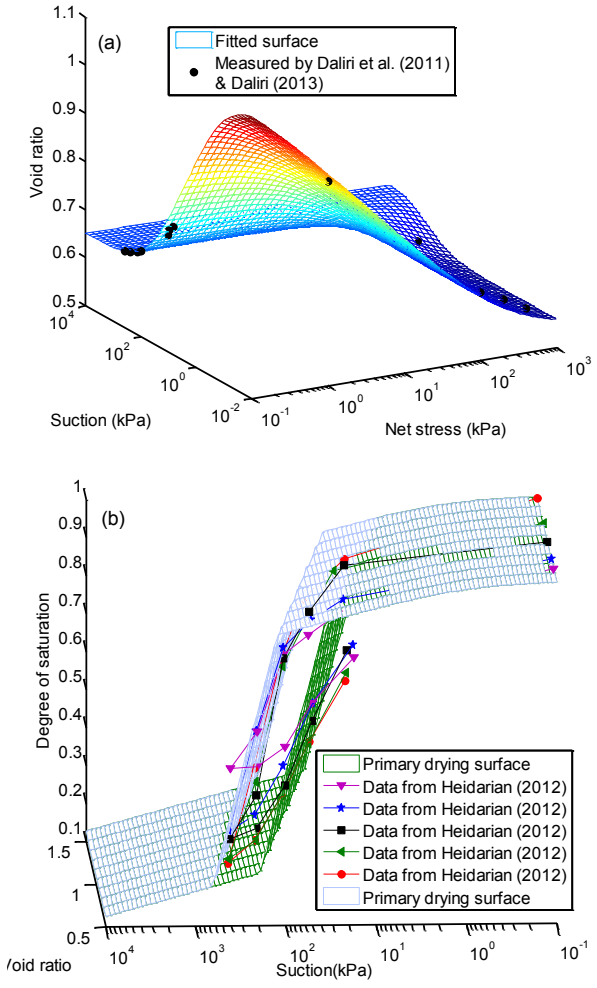

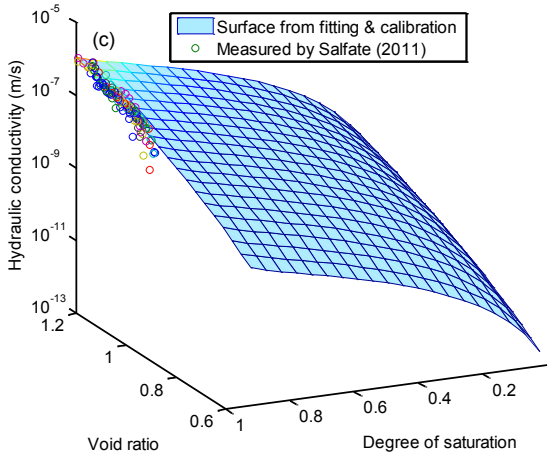

Fig. 8.5 Constitutive relationships: (a) volume change behaviour; (b) water retention behaviour; (c) hydraulic conductivity

8.4.4 Results

Fig. 8.6(a) compares modelled and measured pore water pressure from the first four layer of deposition that occurred before the rewetting events (Daliri et al. 2016). Two point measurements and predictions near the surface and bottom of each layer are included in Fig. 8.6(a) during the period from each deposition (Day 1, 9, 18, 29 for Layer 1, 2, 3, 4 respectively) to Day 38. Upon each deposition, the suction developed during previous drying in the underlying layers (e.g. layer 1 and 2 upon deposition of layer 3) disappears very shortly due to rewetting by the water from fresh layer. Then suction re-develops at almost the same rate as that in fresh layer. Suction decrease in some measurements at around 100 kPa was due to cavitation of sensors (Daliri 2013). As can be seen, adopting the calibrated parameters (based on suction development for 1st and 2nd layers discussed previously), a very good agreement in the pore water pressure has been obtained during deposition of 3rd and 4th layers. Fig. 8.6(b) illustrates that the observed interlayer water exchange (variations of w in each layer) is also adequately reproduced, which shows the averaged

w in each layer during the respective period as that in Fig. 8.6(a). The *w* data during deposition of 1st layer is known directly as the mass of the layer is measured by load cells on which the apparatus sits; for subsequent deposition, the *w* data is estimated based on average values from three volumetric water content sensors in each layer (Daliri et al. 2016), hence the accuracy is somewhat less than for the 1st layer. Further, the two phases of dewatering for each newly deposited layer, characterised by settling and post-settling drying (Daliri et al. 2016), are well captured by UNSATCON-ML, as is the influence of underlying desiccated layers on these two phases.

The rate of dewatering during the first day (Fig. 6(b) for *w* and Fig. 6(c) for void ratio) in the first layer was driven by (1) self-weight of tailings and (2) some bottom drainage where the pore water pressure was initially positive and exerted a downward hydraulic gradient. The rate of dewatering of the tailings themselves (discounting the bleed water) in the first layer decreased throughout the first day and effectively came to a stop, then increased again once the bleed water at the surface was consumed by evaporation and drainage (indicated as point "*E*" in Fig. 8.6(b)). For subsequent layers, dewatering occurs in two periods, delineated by increase or decrease in *w* in the underlying tailings (e.g. layers 1, 2, 3 upon deposition of layer 4). Dewatering in the first period is accelerated by adsorption of water by the previously desiccated tailings (See Fig. 8.6(b)). But eventually the capacity of the underlying tailings to absorb water is exhausted, in part due to the irreversible volume change induced by previous desiccation ($w = 0.2$ in the underlying layer corresponds to an almost saturated condition at current void ratio at shrinkage limit shown in Fig. 8.6(c)), and also due to reversal of the hydraulic gradient: the matric suction in the older tailings dissipates while it increases in the fresh tailings. This behaviour is evident in the modelled pore-water pressure and degree of saturation depth profiles (Fig. 8.7), where both parameters reverse directions (s(S_r) first decrease(increase) and then increase(decrease)) in the previously desiccated

tailings. Fig. 8.7 also shows that the S_r–s relationship is slightly different for each layer, which is due the void ratio dependency of the hydraulic behaviour. The void ratio varies from layer to layer, due to a) increasing total stress and also b) the slightly different position of the elastic surface, as the maximum suction that each layer experienced progressively increases with depth (Fig8.7).

To show the capacity of the model to track irrecoverable volume change and void ratio dependent hysteretic water retention behaviour, the stress paths for void ratio and degree of saturation for tailings at the top of the first layer in the respective 3D spaces are plotted in Fig. 8.8(a) and (b). Fig 8.8 (a) shows that after initial desiccation to ~ 240 kPa suction, all further volume change remains on the elastic surface for the duration of the experiment, as suctions do not exceed the original value, nor does total stress increase much due to the finite thickness of the experiment (< 1m). The selected elasto-plastic formulation implies that drying (suction increase) history dominates the subsequent volume change behaviour of the previously desiccated tailings, which appears to correctly simulate the behaviour observed in this experiment.

Fig. 8.9 shows two kinds of figures, one with w–s plane, the other with S_r–s plane, showing state paths for the top of the first deposited layer in terms of water retention. These state paths shows how the lower void ratio for older layers influences the hysteretic water retention behaviour, in terms of slightly shifting the air-entry value (from ~ 100 to 120 kPa), and of course reducing the w at which saturation is 100%, thereby capping the capacity of the older tailings to absorb water from the fresh layer. The degree of saturation is reduced the most during initial drying, and is reduced less and less with each new layer, as the evaporative boundary condition draws water from the full deposit, and so its influence on the bottom layer reduces with the addition of each new layer.

For completeness, the *w* and pore water pressure in the two rewetting events and the desiccation of the fifth layer are also shown in Fig. 8.10 and illustrates that model results using the calibrated parameters remain in good agreement with the measurements, though the physical and modelled behaviours in these last results are the same as for the first four layers, excepting the simulation of rewetting, which is given by constant fluxes over sets periods of time, corresponding to the experimental protocols for the addition of water (Daliri et al. 2016).

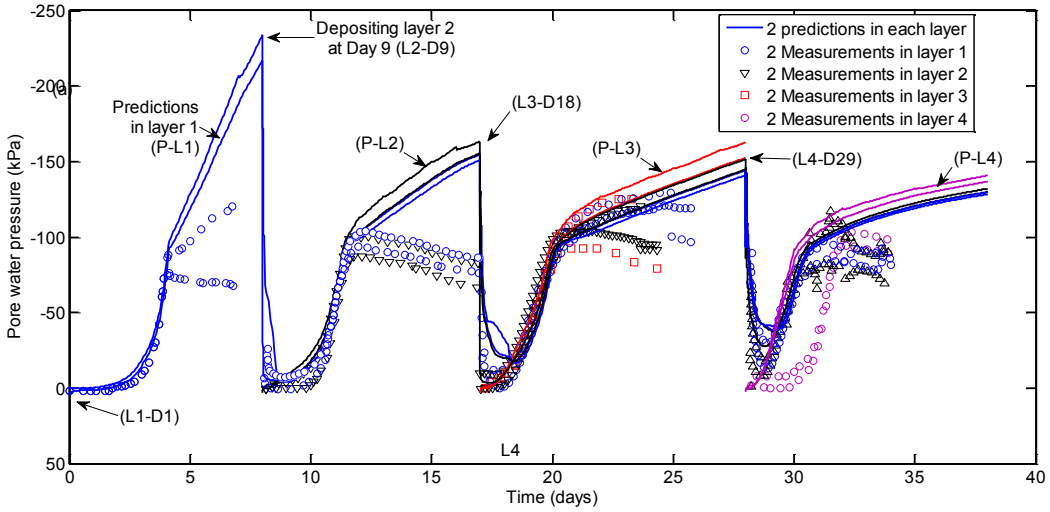
Depositing layer 2
at Day 9 (L2-D9)
Predictions
in layer 1
(P-L1)
(L3-D18)
(P-L2)
(P-L3)
(L4-D29)
(P-L4)
(L1-D1)
2 predictions in each layer
2 Measurements in layer 1
2 Measurements in layer 2
2 Measurements in layer 3
2 Measurements in layer 4
Pore water pressure (kPa)
Time (days)
L4

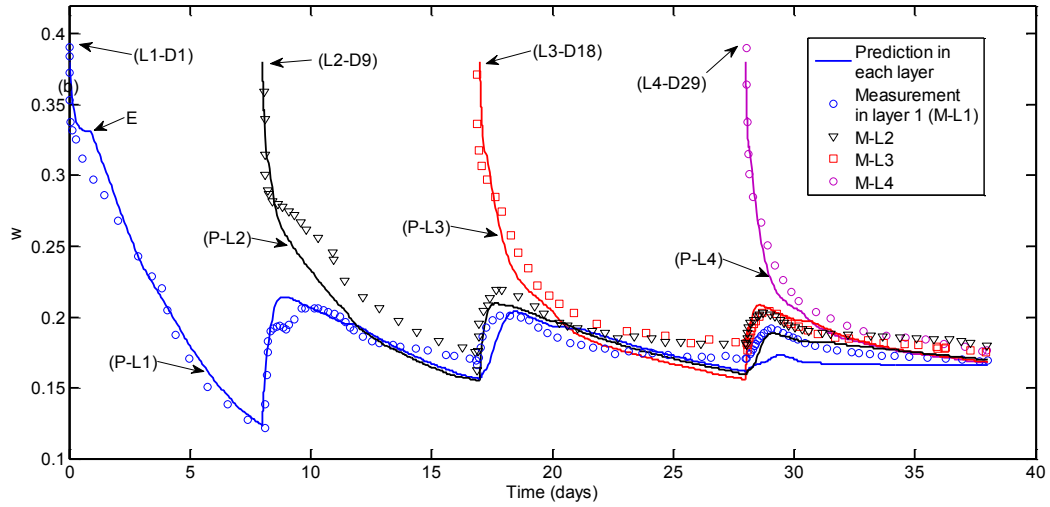
(L1-D1)
(L2-D9)
(L3-D18)
(L4-D29)
(P)
E
(P-L2)
(P-L3)
(P-L4)
(P-L1)
Prediction in
each layer
Measurement
in layer 1 (M-L1)
M-L2
M-L3
M-L4
w
Time (days)

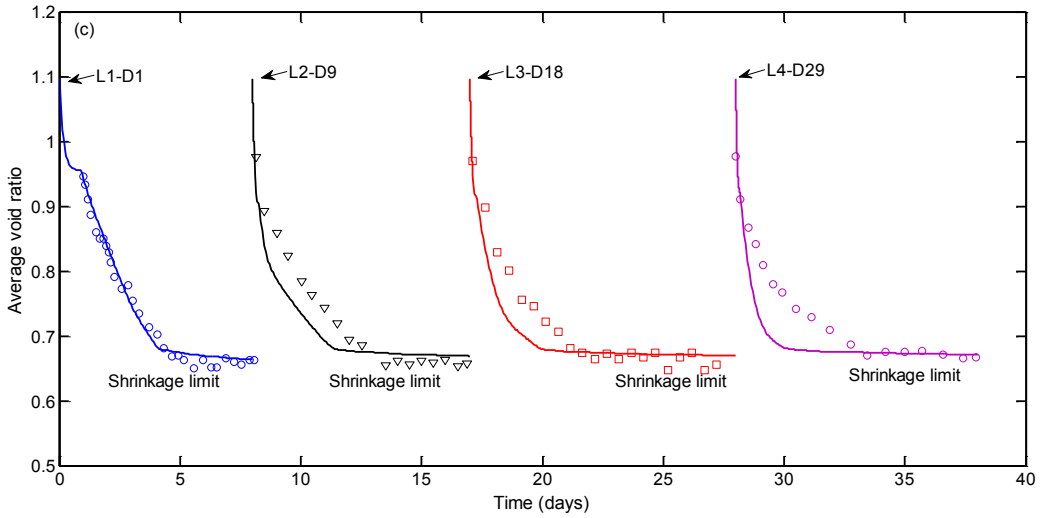

Fig. 8.6 Comparison between modelled and measured results: (a) pore water pressure or suction; (b) gravimetric water content; (c) void ratio

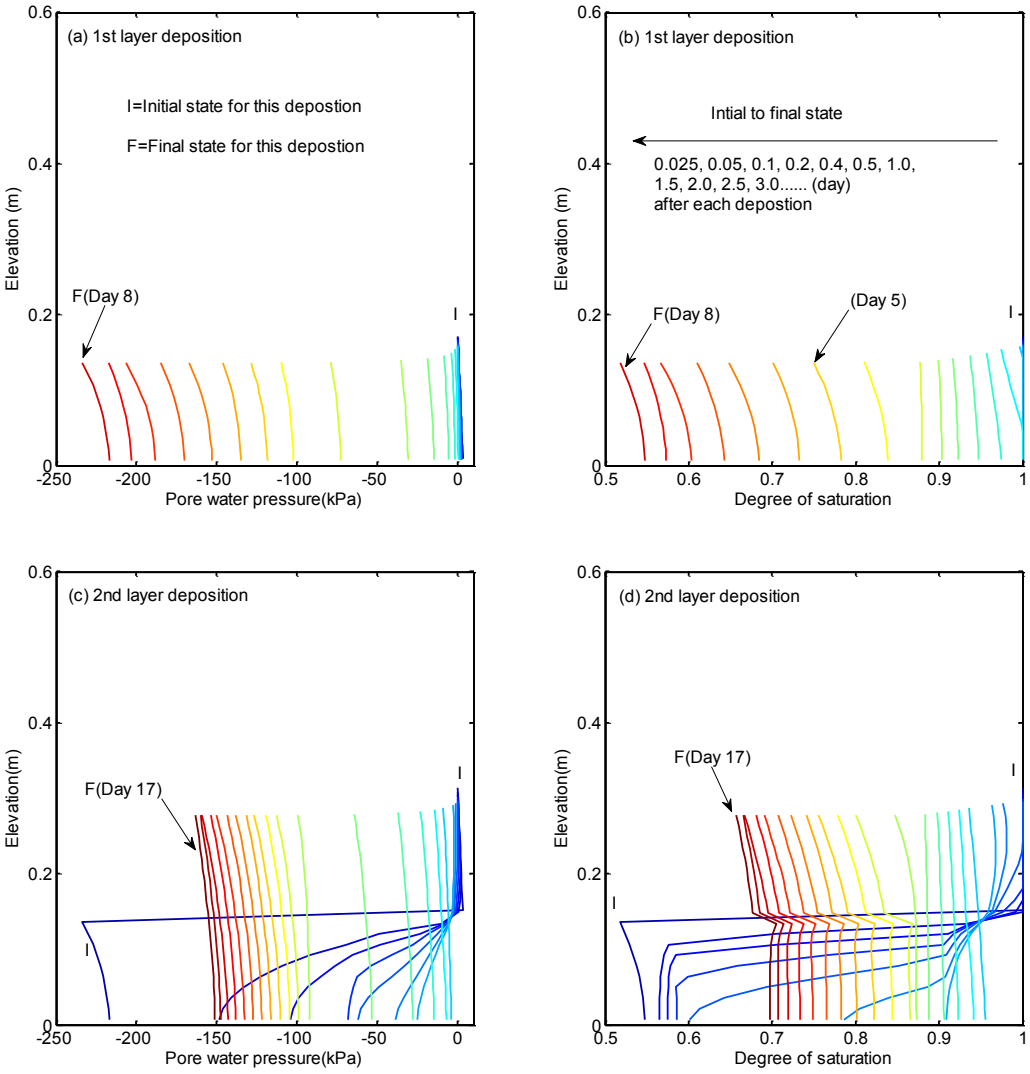
(a) 1st layer deposition
I=Initial state for this depostion
F=Final state for this depostion
F(Day 8)
I
Elevation (m)
Pore water pressure(kPa)
(b) 1st layer deposition
Intial to final state
0.025, 0.05, 0.1, 0.2, 0.4, 0.5, 1.0,
1.5, 2.0, 2.5, 3.0..... (day)
after each depostion
F(Day 8)
(Day 5)
I
Elevation (m)
Degree of saturation
(c) 2nd layer deposition
F(Day 17)
I
I
Elevation(m)
Pore water pressure(kPa)
(d) 2nd layer deposition
F(Day 17)
I
I
Elevation(m)
Degree of saturation

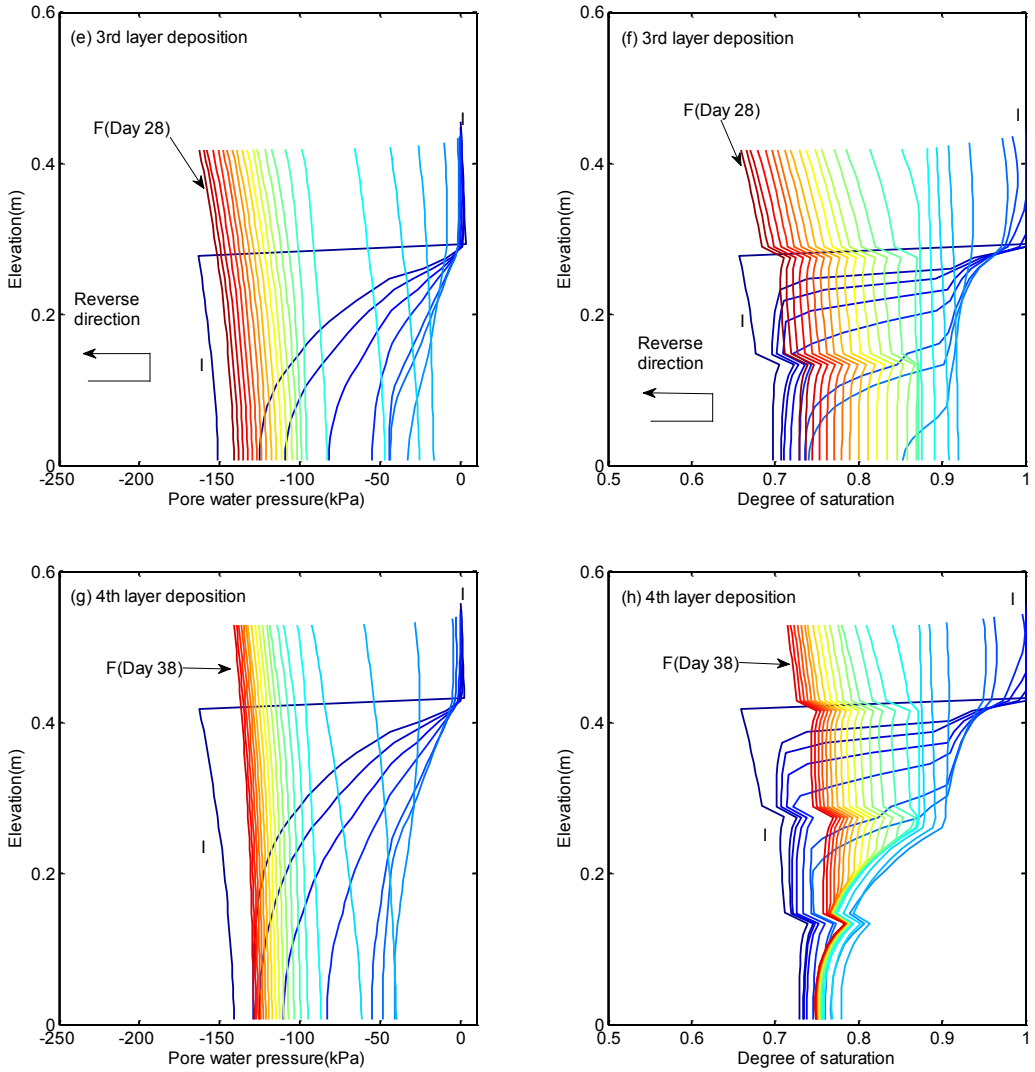

Fig. 8.7 Profiles of pore water pressure and degree of saturation after depositing each of the first four layers

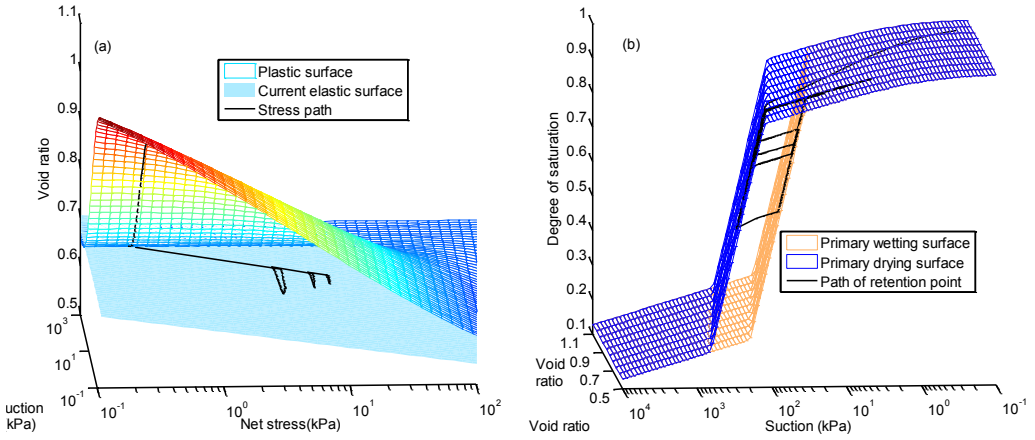

Fig. 8.8 State variable path fallowed by soil element at the top of layer one along the water retention and volume change constitutive relationship in three dimensional space

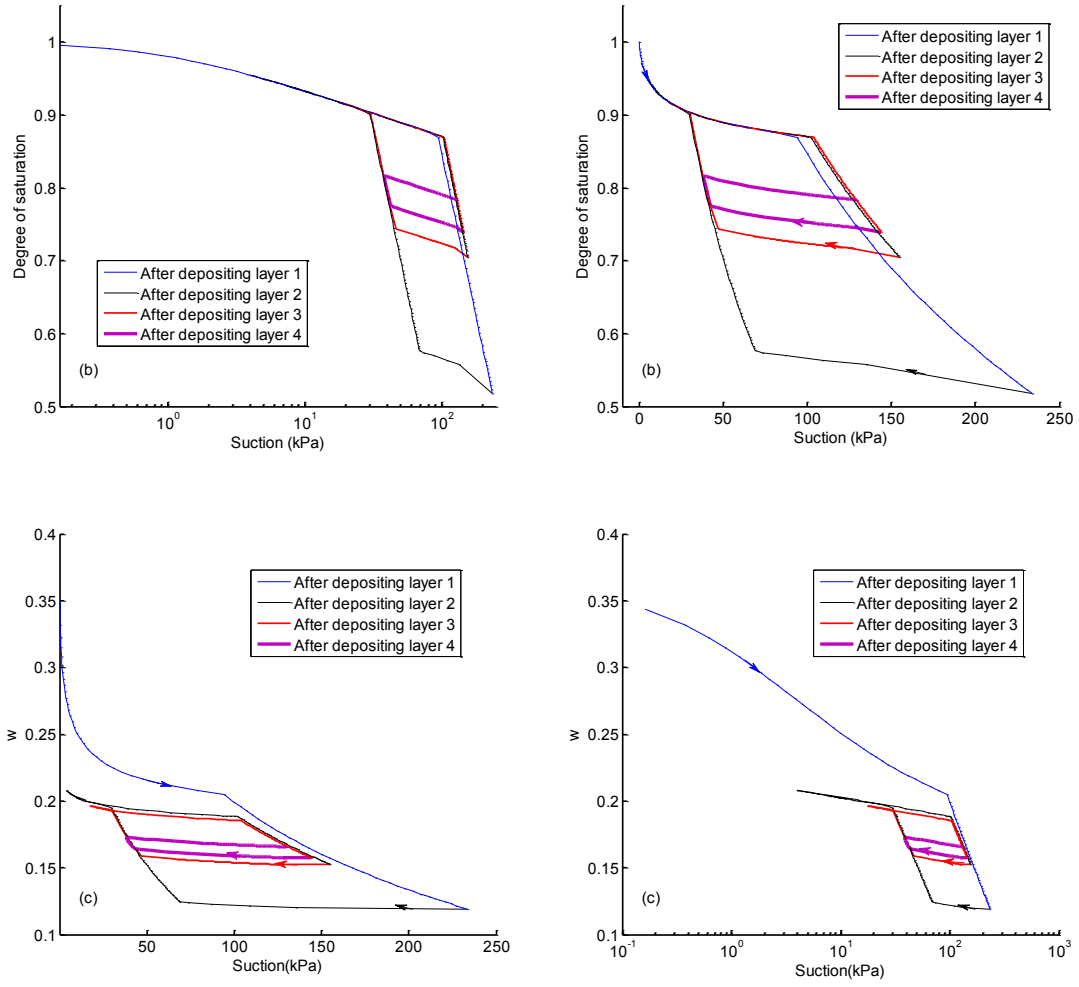

Fig. 8.9 Stress path at top of first layer along the void ratio dependent water retention constitutive relationship

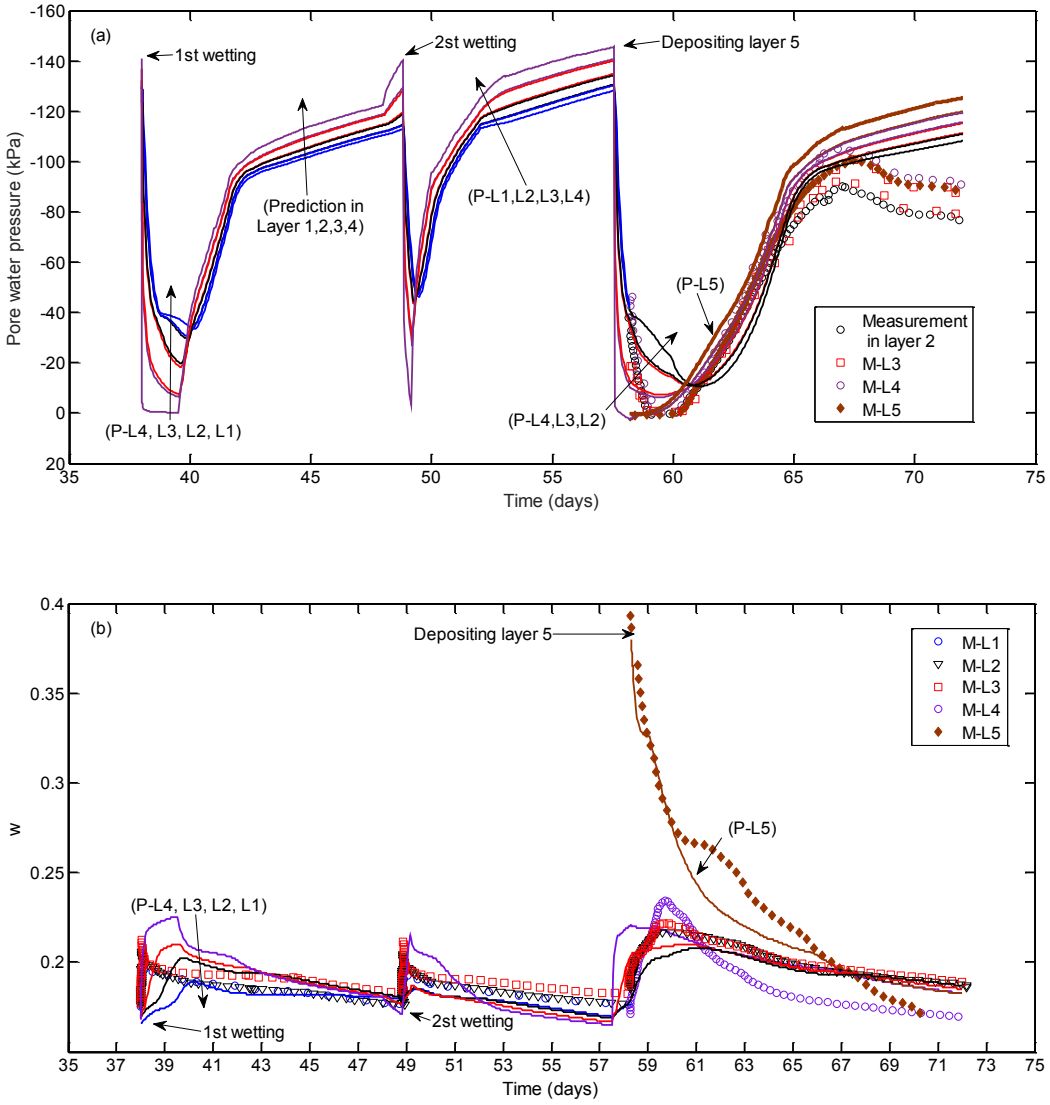

Fig. 8.10 Modelled and measured results during the two wetting events and after depositing the 5th layer: (a) pore water pressure or suction; (b) gravimetric water content

8.5 Discussion and limitations

The uniqueness of this model over its predecessor and other models is its capacity to simulate irrecoverable volume change in an elasto-plastic formulation, and to simulate void ratio dependent hydraulic hysteresis behaviour. The choice for the sub-model for elasto-plastic volume

change is essentially the simplest possible that is compatible with a log-linear elastic compression line in the saturated condition. Though this choice of elasto-plastic formulation with parameters from conventional tests appears satisfactory for modelling the test case, the author can make no claims as to the applicability of these two specific state surfaces for volumetric behaviour in other conditions. For example, at higher normal stress conditions at depth in the tailings impoundment, the swelling index associated with net stress change may depend on the unsaturated state, this nonlinear volumetric behaviour can not be simulated using the simple plane in e-ln$\overline{\sigma}$ -ln$s$ space. The evolution of yield curves with the material constants calibrated at lower stress level may not be able to accurate describe the wetting induced collapse – an important behaviour of unsaturated soils under high mechanical loading conditions. This is also not addressed in the numerical algorithm in UNSATCON-ML, which will be dealt with in the subsequent chapter. While the hysteretic water retention model appears to be sufficient for the gold tailings simulated in our case, which simplifies the more commonly *S*-shaped SWRC, and neglects both changes in the shape of isochoric SWRC (as indicated in some models, e.g Mašín 2010; Salager et al. 2013; D'Onza et al. 2010; Pasha et al. 2016) and in degree of hysteresis with deformation, may not be sufficient for other materials or problems. Implementing more comprehensive retention models will expand the applicability of UNSATCON-ML. These deficiencies will also be dealt with in the next chapter.

8.6 Conclusions

Accurate simulation of multilayer deposition of sub-aerially deposited tailings requires consideration of irrecoverable volume change following desiccation, and the consequences of stress history on both volume change and drying/wetting behaviour. Sub-models for unsaturated soils are selected to represent these tailings' behaviour at the elemental (constitutive) level: (*a*) a

stationery plastic surface in combination with a movable elastic surface, defined in void ratio – net stress – suction space is used to quantify elastic/plastic volume change; (*b*) a *e*-dependent hysteretic water retention model is adopted in conjunction with this mechanical model; and (*c*) water permeability is described using a traditional *e*-dependent power function at the saturated state combined simply with the van Genuchten model at the unsaturated state, expressed in terms of degree of saturation to minimize hysteresis effects.

These sub-models are then implemented into a piece-wise linear finite difference framework using a novel algorithm for performing the constitutive analysis at point level. This algorithm solves nonlinear constitutive equations in unsaturated zones using a bisection method, with ability to model state transition smoothly and ensure mass conservation. Void ratio is directly updated, facilitating coupling the mechanical behaviour to the void ratio-dependent hydraulic model.

The observed behaviours in the mesoscale drying box test, including suction development and volume change accompanying evaporation-induced desiccation, and interlayer hydraulic exchange/interaction capped by the irrecoverable volume change of previously desiccated layers, has been successfully reproduced by UNSATCON-ML. The necessary material parameters can be derived from fairly conventional tests, such as a conventional SWRC test, large strain consolidation tests, and consolidation tests on tailings previously desiccated and subsequently rewetted. The parameter for the variation of permeability with degree of saturation (M) required calibration to a subset of the test case data, as no independent data on unsaturated hydraulic data is available.

The abundant outcomes from UNSATCON-ML allows for a detailed analysis of the coupled large strain consolidation and unsaturated flow behaviour. Specific to tailings, the model results confirm previously suspected behaviour in terms of water flow direction during multilayer

deposition: The presence of desiccated underlying tailings will initially accelerate the consolidation of a fresh layer by absorbing water, but then subsequently delay further dewatering in the fresh layer due to a reversal of hydraulic gradient in the overall profile affected by continuous evaporation.

In the next chapter, it will be shown that other advanced model can also be implemented in UNSATCON-ML using a similar numerical procedure, and modeling this drying box test is also performed using other constitutive models.

Glossary

Symbols

e	Void ratio
a, b, c, d, f, g	Material parameters for void ratio constitutive relationship
e^e	Void ratio on the elastic surface
$\overline{\sigma}$	Net stress
σ	Total stress
u_a	Pore-air pressure
s	Suction
u_w	Pore-water pressure
κ	Elastic stiffness parameter for changes in net mean stress
κ_s	Elastic stiffness parameter for changes in suction
C_e	Constant related to location of the elastic surface
S_r	Degree of saturation
C_{drying} , $C_{wetting}$	Constants related to the location of primary drying and wetting surfaces
κ_{ss}	Parameter for elastic change of degree of saturation with change of suction
λ_{se}	Parameter for change of degree of saturation with change of void ratio
λ_{sr}	Parameter for plastic change of degree of saturation with change of suction
$C_{scanning}$	Constants related to the locations of scanning surfaces
k_{sat}	Saturated permeability
k_r	Relative permeability
H_1, H_2	Material parameters for hydraulic conductivity vs. Void ratio relationship
M	Constant in van genuchten (1980) model
z	Elevation convective coordinates
k	Hydraulic permeability
h	Hydraulic head
w	Gravimetric water content
t	Time
σ	Total stress
G_s	Specific gravity
γ	Unit weight of soil
γ_w	Unit weight of water
j	Label of element
i	Time step
$\Delta t^{(i-1)}$	Time increment
ρ_w	Density of water
M_s	Mass of solids within each element
$v_j^{(i)}$	Relative discharge velocity
$k_{e,j}^{(i)}$	Equivalent hydraulic conductivity

q_0	Assumed surface vertical load
$\Delta h_w^{(i)}$	Current thickness of surface water at the tailing surface
L	Element height
e_r	Reference void ratio
$S_{r,try}$	Trial degree of saturation in bisection method
$S_{r,min}$	Minimum degree of saturation in bisection method
e_{try}	Trial void ratio in bisection method
s_{try}	Trial suction in bisection method
e_{new}	New void ratio in bisection method
e_{max}	Maximum void ratio in bisection method
e_{min}	Minimum void ratio in bisection method
σ_c	Current total stress for bisection method
$\tilde{b}$	$= b/\ln 10$
$\lambda(0)$	The slope of virgin consolidation line at saturated condition
v_{if}	The flow across the inter-layer face
h_{if}	Hydraulic head at the inter-layer face
$k_{e,n}$	Equivalent hydraulic conductivity across the inter-layer face
$n+1$	Number of top elements in the old layer
n	Number of bottom element in the fresh layer

Abbreviations

BBM	Barcelona basic model
GCM	Glasgow coupled model
PL	Plastic limit
LL	Liquid limit
SWRC	Soil water retention curve

8.7 References

Alonso, E.E., Gens, A., & Josa, A. (1990). A constitutive model for partially saturated soils. Géotechnique, 40(3), 405-430.

Alonso, E. E., Vaunat, J., & Gens, A. (1999). Modelling the mechanical behaviour of expansive clays. Engineering Geology, 54(1), 173-183.

Blatz, J. A., & Graham, J. (2003). Elastic-plastic modelling of unsaturated soil using results from a new triaxial test with controlled suction. Géotechnique, 53(1), 113-122.

Cardoso, R., Alonso, E. E., & Neves, E. M. D. (2013). A constitutive model for compacted expansive and bonded marls. Géotechnique, 63(13), 1116.

Cui, Y. J., & Delage, P. (1996). Yielding and plastic behaviour of an unsaturated compacted silt. Géotechnique, 46(2), 291-311.

Daliri, F. (2013). The influence of desiccation and stress history on monotonic and cyclic shear response of thickened gold tailings (Doctoral dissertation, Carleton University Ottawa).

Daliri, F., Kim, H., Simms, P., & Sivathayalan, S. (2014). Impact of desiccation on monotonic and cyclic shear strength of thickened gold tailings. Journal of Geotechnical and Geoenvironmental Engineering, 140(9), 04014048.

Daliri, F., Simms, P., & Sivathayalan, S. (2016). Shear and dewatering behaviour of high density gold tailings in a laboratory simulation of multi-layer deposition. Canadian Geotechnical Journal, 2016, 53(8): 1246-1257.

Dangla, P., Malinsky, L., & Coussy, O. (1997, July). Plasticity and imbibition-drainage curves for unsaturated soils: a unified approach. In Proc. 6th Int. Symp. Numer. Models Geomech.(NUMOG VI) (pp. 141-146).

Delage, P., & Graham, J. (1996). Mechanical behaviour of unsaturated soils: understanding the behaviour of unsaturated soils requires reliable conceptual models. In PROCEEDINGS OF THE FIRST INTERNATIONAL CONFERENCE ON UNSATURATED SOILS/UNSAT'95/PARIS/FRANCE/6-8 SEPTEMBER 1995. VOLUME 3.

Dunmola, A., Cote, C., Freeman, G., Kolstad D., Song, J., and Masala S. 2013. Dewatering and shear strength performance of in-line flocculated mature fine tailings under different depositional schemes. Proceeding of Tailings and Mine Waste 2013 November 3rd-6th 2013, Banff, Alberta p5 -14.

Dunmola, A., Dhadli, N., Freeman, Kolstad, D., Fasking, T., Song, J., and Langseth, J. 2013. Geotechnical Benefits of Flocculation in Dewatering Oil Sands Mature Fine Tailings. In Proceedings of GeoMontreal 2013, Canadian Geotechnical Conference, Sept. 30th - Oct 3rd 2013, Electronic proceedings.

Fisseha, B., Bryan, R., & Simms, P. (2010). Evaporation, unsaturated flow, and salt accumulation in multilayer deposits of "paste" gold tailings. Journal of Geotechnical and Geoenvironmental Engineering, 136(12), 1703-1712.

Fox, P. J., & Berles, J. D. (1997). CS2: A piecewise-linear model for large strain consolidation. International Journal for Numerical and Analytical Methods in Geomechanics, 21(7), 453-475.

Fredlund, D. G., & Xing, A. (1994). Equations for the soil-water characteristic curve. Canadian geotechnical journal, 31(4), 521-532.Fujiyasu, Y., & Fahey, M. (2000). Experimental study of evaporation from saline tailings. Journal of Geotechnical and Geoenvironmental Engineering, 126(1), 18-27.

Gallipoli, D., Bruno, A. W., D'Onza, F., & Mancuso, C. (2015). A bounding surface hysteretic water retention model for deformable soils. Géotechnique, 65(10), 793-804.

Gallipoli, D., Gens, A., Sharma, R., & Vaunat, J. (2003). An elasto-plastic model for unsaturated soil incorporating the effects of suction and degree of saturation on mechanical behaviour. Géotechnique., 53(1), 123-136.

Gallipoli, D., Wheeler, S. J., & Karstunen, M. (2003). Modelling the variation of degree of saturation in a deformable unsaturated soil. Géotechnique, 53(1), 105-112.

Gens, A. (2010). Soil–environment interactions in geotechnical engineering. Géotechnique, 60(1), 3-74.

Gens, A., & Alonso, E. E. (1992). A framework for the behaviour of unsaturated expansive clays. Canadian Geotechnical Journal, 29(6), 1013-1032.

Heidarian, P. (2012). Effect of Initial Water Content and Stress History on Water-Retention Behaviour of Mine Tailings (Doctoral dissertation, Carleton University Ottawa).

Houlsby, G. T. (1997). The work input to an unsaturated granular material. Géotechnique, 47(1), 193-196.

Hu, R., Chen, Y. F., Liu, H. H., & Zhou, C. B. (2013). A water retention curve and unsaturated hydraulic conductivity model for deformable soils: consideration of the change in pore-size distribution. Géotechnique, 63(16), 1389.

Huang, J., & Griffiths, D. V. (2010). One-dimensional consolidation theories for layered soil and coupled and uncoupled solutions by the finite-element method. Geotechnique, 60(9), 709-713.

Klausner, Y. (1991). Fundamentals of continuum mechanics of soils. Springer-Verlag, New York.

Leong, E. C., & Rahardjo, H. (1997). Permeability functions for unsaturated soils. Journal of Geotechnical and Geoenvironmental Engineering, 123(12), 1118-1126.

Li, X. S. (2005). Modelling of hysteresis response for arbitrary wetting/drying paths. Computers and Geotechnics, 32(2), 133-137.

Mašín, D. (2010). Predicting the dependency of a degree of saturation on void ratio and suction using effective stress principle for unsaturated soils. International Journal for Numerical and Analytical Methods in Geomechanics, 34(1), 73-90.

Nuth, M., & Laloui, L. (2008). Advances in modelling hysteretic water retention curve in deformable soils. Computers and Geotechnics, 35(6), 835-844.

Pham, H. Q., Fredlund, D. G., & Barbour, S. L. (2003). A practical hysteresis model for the soil-water characteristic curve for soils with negligible volume change. Géotechnique, 53(2), 293-298.

Qi S., Simms P., & Vanapalli S. K. (2016a). Piecewise-Linear Formulation of Coupled Large Strain Consolidation and Unsaturated Flow. I: Model Development and Implementation, Journal of Geotechnical and Geoenvironmental Engineering, (Reference Number: GTENG-5390R1, in production)

Qi S., Simms P., & Vanapalli S. K. (2016b) Piecewise-Linear Formulation of Coupled Large Strain Consolidation and Unsaturated Flow. II: Testing and Performance, Journal of Geotechnical and Geoenvironmental Engineering, (Reference Number: GTENG-5390R1, in production)

Rozina, E., Mizani, S., Malek, M., Sanchez-Sardon, M., & Simms, P. (2015). Dewatering in a laboratory simulation of a multilayer deposit of inline flocculated mature fine tailings. Proceedings of the 18th International Seminar on Paste and Thickened Tailings, R. Jewell and A. Fourie. Australian Centre for Geomechanics, Crawley, Australia, 81-94.

Salfate, E. R. (2011). Predicting void ratio for surface paste tailings deposited in thin layers (Doctoral dissertation, University of British Columbia).

Seneviratne, N. H., Fahey, M., Newson, T. A., & Fujiyasu, Y. (1996). Numerical modelling of consolidation and evaporation of slurried mine tailings. International Journal for Numerical and Analytical Methods in Geomechanics, 20(9), 647-671.

Sheng, D. (2011). Review of fundamental principles in modelling unsaturated soil behaviour. Computers and Geotechnics, 38(6), 757-776.

Sheng, D., Fredlund, D. G., & Gens, A. (2008). A new modelling approach for unsaturated soils using independent stress variables. Canadian Geotechnical Journal, 45(4), 511-534.

Sheng, D., Sloan, S. W., & Gens, A. (2004). A constitutive model for unsaturated soils: thermomechanical and computational aspects. Computational Mechanics, 33(6), 453-465.

Simms, P. H., & Yanful, E. K. (2002). Predicting soil-water characteristic curves of compacted plastic soils from measured pore-size distributions. Géotechnique, 52(4), 269-278.

Simms, P. H., & Yanful, E. K. (2005). A pore-network model for hydromechanical coupling in unsaturated compacted clayey soils. Canadian Geotechnical Journal, 42(2), 499-514.

Simms, P., Dunmola, A., Fisseha, B., & Bryan, R. (2010). Generic modeling of desiccation for cyclic deposition of thickened tailings to maximize density and to minimize oxidation. Proceedings of the 13th International Seminar on Paste and Thickened Tailings, R. Jewell and A. Fourie. Australian Centre for Geomechanics, Crawley, Australia, 293-303.

Simms, P., Grabinsky, M., & Zhan, G. (2007). Modelling evaporation of paste tailings from the Bulyanhulu mine. Canadian Geotechnical Journal, 44(12), 1417-1432.

Soleimani, S., Simms, P., Dunmola, A., Freeman, G., & Wilson, G. W. (2014) Desiccation and consolidation in thin-lift deposition of polymer-amended mature fine tailings. Proceedings of the 17th International Seminar on Paste and Thickened Tailings, R. Jewell, A. Fourie, P. S. Wells and D. van Zyl. eds., Australian Centre for Geomechanics, Crawley, Australia, 307-322.

Sun, W., & Sun, D. A. (2012). Coupled modelling of hydro‐mechanical behaviour of unsaturated compacted expansive soils. International Journal for Numerical and Analytical Methods in Geomechanics, 36(8), 1002-1022.

Tarantino, A. (2009). A water retention model for deformable soils. Géotechnique, 59(9), 751-762.

Townsend, F. C., & McVay, M. C. (1990). SOA: Large strain consolidation predictions. Journal of Geotechnical Engineering.

Tsiampousi, A., Zdravkovic, L., & Potts, D. M. (2013). A three-dimensional hysteretic soil-water retention curve. Geotechnique, 63(2), 155.

van Genuchten, M. T. (1980). A closed-form equation for predicting the hydraulic conductivity of unsaturated soils. Soil science society of America journal, 44(5), 892-898.

Vaunat, J., Romero, E., & Jommi, C. (2000). An elastoplastic hydromechanical model for unsaturated soils. Experimental evidence and theoretical approaches in unsaturated soils, 121-138.

Vu, H. Q., & Fredlund, D. G. (2006). Challenges to modelling heave in expansive soils. Canadian Geotechnical Journal, 43(12), 1249-1272.

Wheeler, S. J., & Karube, D. (1996). Constitutive modelling. In proceedings of the first international conference on unsaturated soils/unsat'95/paris/france/6-8 september 1995. volume 3.

Wheeler, S. J., & Sivakumar, V. (1995). An elasto-plastic critical state framework for unsaturated soil. Géotechnique, 45(1), 35-53.

Wheeler, S. J., Sharma, R. S., & Buisson, M. S. R. (2003). Coupling of hydraulic hysteresis and stress–strain behaviour in unsaturated soils. Géotechnique, 53(1), 41-54.

Wilson, G. W., Fredlund, D. G., & Barbour, S. L. (1997). The effect of soil suction on evaporative fluxes from soil surfaces. Canadian Geotechnical Journal, 34(1), 145-155.

Yao, D. T., de Oliveira‐Filho, W. L., Cai, X. C., & Znidarcic, D. (2002). Numerical solution for consolidation and desiccation of soft soils. International Journal for Numerical and Analytical Methods in Geomechanics, 26(2), 139-161.

Zhang, X., & Lytton, R. L. (2009). Modified state-surface approach to the study of unsaturated soil behavior. Part I: Basic concept. Canadian Geotechnical Journal, 46(5), 536-552.

D'Onza, Francesca, et al. "Benchmark of constitutive models for unsaturated soils." Géotechnique 61.4 (2011): 283-302.

Salager, S., Nuth, M., Ferrari, A., & Laloui, L. (2013). Investigation into water retention behaviour of deformable soils. Canadian Geotechnical Journal, 50(2), 200-208.

Hemmati, S., Gatmiri, B., Cui, Y. J., & Vincent, M. (2012). Thermo-hydro-mechanical modelling of soil settlements induced by soil-vegetation-atmosphere interactions. Engineering Geology, 139, 1-16.

Cui, Y. J., Ta, A. N., Hemmati, S., Tang, A. M., & Gatmiri, B. (2013). Experimental and numerical investigation of soil-atmosphere interaction. Engineering Geology, 165, 20-28.

Pasha, A. Y., Khoshghalb, A., & Khalili, N. (2016). A void ratio dependent water retention curve model including hydraulic hysteresis. In E3S Web of Conferences (Vol. 9, p. 11010). EDP Sciences.

Lloret‐Cabot, M., Sánchez, M., & Wheeler, S. J. (2013). Formulation of a three‐dimensional constitutive model for unsaturated soils incorporating mechanical–water retention couplings. International Journal for Numerical and Analytical Methods in Geomechanics, 37(17), 3008-3035.

Appendix 8.1

In this appendix, Some mathematical analysis of the shape defined by Eq. (8.1) is carried out for the ease of model calibration.

Eq. (8.1) defines a series of '*S*' shape curves in e-$\log\bar{\sigma}$ plane, and are rewritten here

$$e = a + b\log\left[\frac{1+c\bar{\sigma}+ds}{1+f\bar{\sigma}+gs}\right] \tag{A1-1}$$

where, s is suction: u_a - u_w, and $\bar{\sigma}$ is net stress: σ-u_a, when $u_w < 0$; $s = 0$ and $\bar{\sigma} = \sigma$-u_w, when $u_w \geq 0$. Let us first consider the normally consolidation curve at saturated condition, i.e. $s = 0$:

$$e = a + b\log\left[\frac{1+c\bar{\sigma}}{1+f\bar{\sigma}}\right] \tag{A1-2}$$

For the convenience of differentiation, the "base-10 log" in Eq. (A1-2) is converted to the "natural log" as follows:

$$e = a + \tilde{b}\ln\left[\frac{1+c\bar{\sigma}}{1+f\bar{\sigma}}\right] = a + \tilde{b}\ln(1+c\bar{\sigma}) - \tilde{b}\ln(1+f\bar{\sigma}) \tag{A1-3}$$

where, $\tilde{b} = b/\ln 10$. The shape of the curve defined by Eq. (A1-3) in e-$\ln\bar{\sigma}$ plane can be investigated via the first-order differential (with respect to $\ln\bar{\sigma}$)

$$\frac{de}{d\ln\bar{\sigma}} = \frac{de}{d\bar{\sigma}}\frac{d\bar{\sigma}}{d\ln\bar{\sigma}} = \frac{\tilde{b}(c-f)\bar{\sigma}}{(1+f\bar{\sigma})(1+c\bar{\sigma})} \tag{A1-4}$$

and the second-order differential (with respect to $\ln\bar{\sigma}$)

$$\begin{aligned}\frac{d^2e}{d(\ln\bar{\sigma})^2} &= d\frac{(de/d\ln\bar{\sigma})}{d\bar{\sigma}}\frac{d\bar{\sigma}}{d\ln\bar{\sigma}} = \left[\frac{\tilde{b}(c-f)\bar{\sigma}}{(1+f\bar{\sigma})(1+c\bar{\sigma})}\right]'\bar{\sigma} \\ &= \tilde{b}\left[\frac{(c-f)(1+f\bar{\sigma})(1+c\bar{\sigma}) - \left[(f+c)+2fc\bar{\sigma}\right](c-f)\bar{\sigma}}{\left[(1+f\bar{\sigma})(1+c\bar{\sigma})\right]^2}\right]\bar{\sigma} \\ &= \tilde{b}\frac{\bar{\sigma}(c-f)(1-fc\bar{\sigma}^2)}{(1+f\bar{\sigma})^2(1+c\bar{\sigma})^2}\end{aligned} \tag{A1-5}$$

Inspection of Eq. (A1-3) indicates that both c and f should take positive values for the net stress range of 0 to +∞. If b (or $\tilde{b}$) takes a positive value, the value of c should be lower than f, then Eq. (A1-4) (the first-order differential) gives negative value, indicating a decrease in void ratio with increasing net stress. At both lower and higher stress ranges, changes in void ratio with respect to changes in net stress are insignificant, since

$$\lim_{\substack{x\to 0\\(x\to\infty)}} \frac{de}{d\ln\bar{\sigma}} = \lim_{\substack{x\to 0\\(x\to\infty)}} \frac{\tilde{b}(c-f)\bar{\sigma}}{(1+f\bar{\sigma})(1+c\bar{\sigma})} = 0 \qquad \text{(A1-6)}$$

Equating the second-order differential Eq. (A1-5) to '0' gives

$$\bar{\sigma} = 1/\sqrt{fc} \qquad \text{(A1-7)}$$

when $\bar{\sigma} < 1/\sqrt{fc}$, Eq. (A1-5) < 0, indicating an increase in the rate of change of e in response to net stress increase (i.e. increase in the slope of e-ln$\bar{\sigma}$ curve), while $\bar{\sigma} > 1/\sqrt{fc}$, Eq. (A1-5) > 0, indicating an decrease in the rate of change of e in response to net stress increase (i.e. decrease in the slope of e-ln$\bar{\sigma}$ curve). In other words, Eq. (A1-2) defines the "*S*" shape curve in e-ln$\bar{\sigma}$ plane, of which the inflection point is defined by Eq. (A1-7). Substituting Eq. (A1-7) into Eq. (A1-4), yields:

$$\frac{de}{d\ln\bar{\sigma}} = \frac{\tilde{b}(c-f)/\sqrt{fc}}{(1+f/\sqrt{fc})(1+c/\sqrt{fc})} = \tilde{b}\frac{(\sqrt{c}-\sqrt{f})}{(\sqrt{c}+\sqrt{f})} \qquad \text{(A1-8)}$$

Eq. (A1-8) defines the slope of the e-ln$\bar{\sigma}$ curve at the inflection point, or the slope of the e-ln$\bar{\sigma}$ curve in the middle stress range, within which a linear relationship is likely to occur, as indicated in the classical linear e-ln(stress) relationship. Eq. (A1-8) also indicates that this slope is rotated from the slope defined by the constant $\tilde{b}$ (or b) by an angle defined by constants c and f. If these two slopes (defined by $\tilde{b}$ and Eq. (A1-8), respectively) are normalised by $\tilde{b}$, the angle, δ,

$$\tan\delta = \tan(45-\alpha) = \frac{\tan 45 - \tan\alpha}{1+\tan 45\tan\alpha} = \frac{1-\left|\frac{\sqrt{c}-\sqrt{f}}{\sqrt{c}+\sqrt{f}}\right|}{1+\left|\frac{\sqrt{c}-\sqrt{f}}{\sqrt{c}+\sqrt{f}}\right|} = \sqrt{c/f} \qquad \text{(A1-9)}$$

Then, $$\delta = \arctan\sqrt{c/f} \qquad \text{(A1-10)}$$

where, $\tan\alpha$ is the normalised slope defined by Eq. (A1-8).

Overall, Eq. (A1-2) defines a variation of *e* with $\ln\overline{\sigma}$, following an "*S*" shape, which has a highest/lowest limit on the void ratio at very low/high stress level, respectively. The highest limit is obviously *a*, the void ratio at zero stress condition. The lowest limit can be obtained

$$\lim_{x\to\infty}\left\{a+\tilde{b}\ln\left[\frac{1+c\overline{\sigma}}{1+f\overline{\sigma}}\right]\right\} = a-\tilde{b}\ln\frac{c}{f} \qquad \text{(A1-11)}$$

Although, the net stress cannot be positive infinite, Eq. (A1-11) defines a limiting void ratio at very high stress level.

The physical meanings of *a, b, c, f* have been indicated in Eq. (A1-7), (A1-8), (A1-10) and (A1-11). The higher limiting void ratio, *a*, can be choose subjectively by the user according to the considered problem. Then the other three parameters *b, c, f* are constrained by three equations (A1-7), (A1-8), and (A1-11), thus different fitting excises will always result in almost the same values. In most case, the value of *c* is far less than *f*. For example in our paper, the *c* value is even significantly lower than 1. Then

$$\frac{de}{d\ln\overline{\sigma}} = \tilde{b}\frac{(\sqrt{c}-\sqrt{f})}{(\sqrt{c}+\sqrt{f})} \approx -\tilde{b} \text{ or } \delta = \arctan\sqrt{c/f} \approx 0 \qquad \text{(A1-12)}$$

Thus the slope of *e*-$\ln\overline{\sigma}$ curve in the middle stress range is largely controlled by value of *b* (or $\tilde{b}$), which is similar to but not the same as the slope of virgin consolidation line ($\lambda(0)$) in the classical linear *e*-$\ln\overline{\sigma}$ relationship. If the *c* value is significantly lower than 1, the effect of variation

in $\bar{\sigma}$ in the term $(1+c\bar{\sigma})$ would become insignificant compared to the term $(1+f\bar{\sigma})$ in Eq. (A1-3) in the low and middle stress ranges, Eq. (A1-3) can be regarded as a variant of the traditional *e*-$\ln\bar{\sigma}$ linear relationship: $e=a-\tilde{b}\ln(1+f\bar{\sigma})$. The introduction of "1" can also avoid infinite value of "*e*" at low stress level, and numerical issues in numerical analysis.

At zero stress level, Eq. (A1-1) is simplified to

$$e=a+b\log\left[\frac{1+ds}{1+gs}\right] \tag{A1-13}$$

Eq. (A1-13) has the same form as Eq. (A1-2), thus the *d* and *g* have similar physical meanings as those of *c* and *f*. It is worth noting here that the data from soil during drying with a shrinkage limit can be well fitted using Eq. (A1-13), the shrinkage limit is $a+b\log(d/g)$.

For the compression curves defined by Eq. (A1-1) at different suction levels, let $m(s)=1+gs$ and $n(s)=1+ds$, Eq. (A1-1) turns to be

$$e=a+\tilde{b}\ln\left[\frac{c\bar{\sigma}+n(s)}{f\bar{\sigma}+m(s)}\right]=a+\tilde{b}\ln(c\bar{\sigma}+n(s))-\tilde{b}\ln(f\bar{\sigma}+m(s)) \tag{A1-14}$$

Using similar procedures, we obtain the first and seconder order differential with respect to $\ln\bar{\sigma}$, as

$$\frac{de}{d\ln\bar{\sigma}}=\frac{de}{d\bar{\sigma}}\frac{d\bar{\sigma}}{d\ln\bar{\sigma}}=\frac{\tilde{b}[cm(s)-fn(s)]\bar{\sigma}}{(m(s)+f\bar{\sigma})(n(s)+c\bar{\sigma})} \tag{A1-15}$$

and

$$\frac{d^2e}{d(\ln\bar{\sigma})^2}=\tilde{b}\frac{\bar{\sigma}[cm(s)-fn(s)][m(s)n(s)-fc\bar{\sigma}^2]}{[m(s)+f\bar{\sigma}]^2[n(s)+c\bar{\sigma}]^2} \tag{A1-16}$$

The inflection point is defined as:

$$\overline{\sigma} = \sqrt{mn / fc} \tag{A1-17}$$

The slope at middle stress level is:

$$\frac{de}{d\ln\overline{\sigma}} = \tilde{b}\frac{(\sqrt{cm(s)} - \sqrt{fn(s)})}{(\sqrt{cm(s)} + \sqrt{fn(s)})} \tag{A1-18}$$

It can be seen from Eq. (A1-18), as suction, *s*, increases, the slope defined in Eq. (A1-18) will change accordingly. The performance of Eq. (1) to fit the experimental data and relative physical meaning of parameters are illustrated in Fig. 8.11.

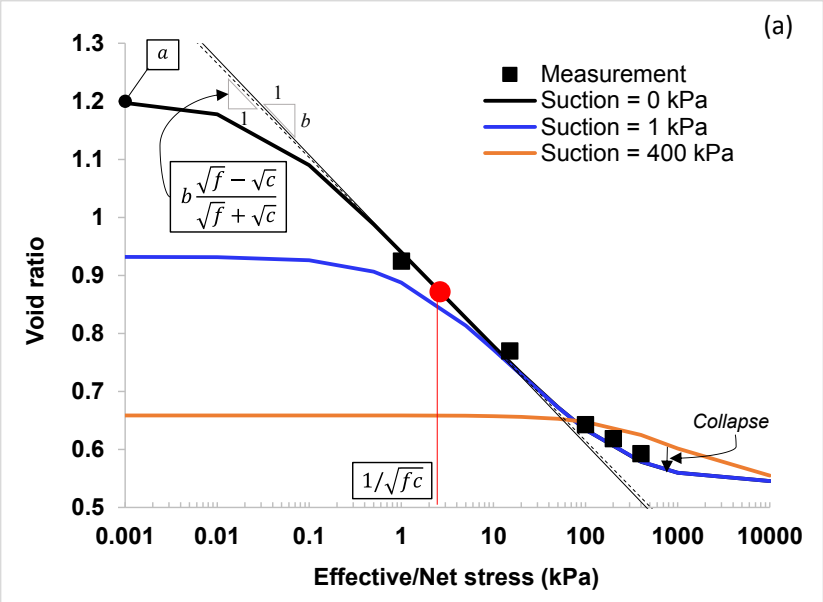

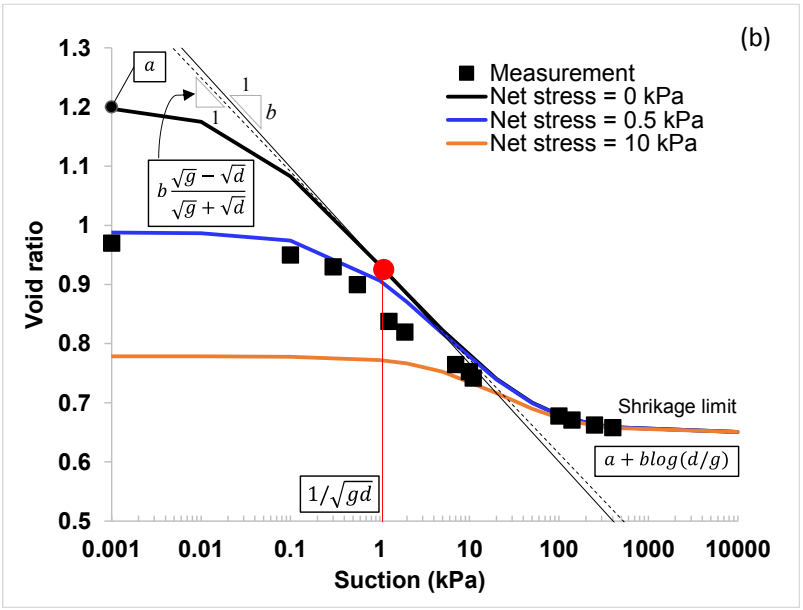

Fig. 8.11 “S” shape curve defined by Eq. (1): (a) on the e vs. net stress plane (b) on the e vs. suction plane.

Appendix 8.2

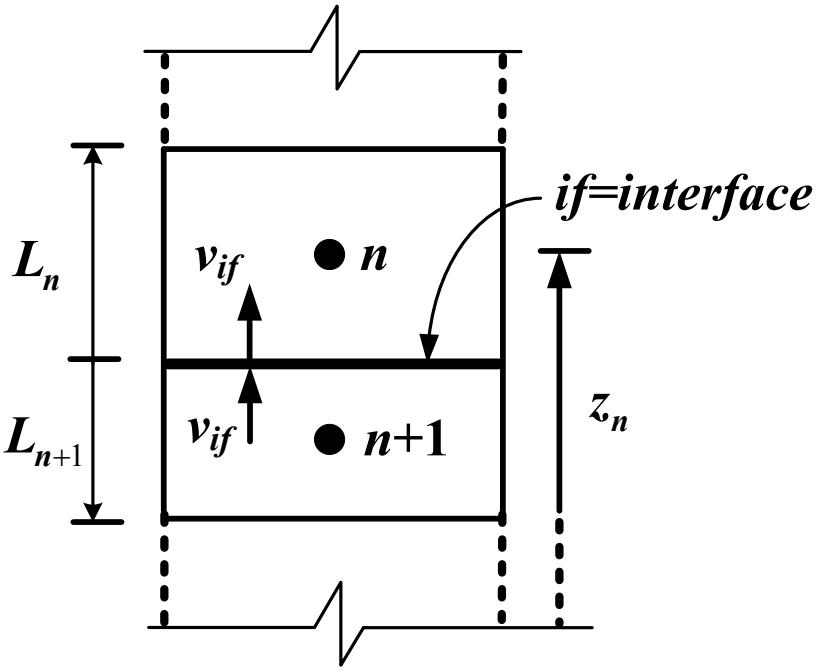

Fig. 8.12 Water flow across inter-layer face

In UNSATCON-ML, the numbers of bottom and top elements in the fresh and old layers, respectively, are updated to, say 'n' and 'n+1' after a new deposition, as shown in Fig. 8.12. The inter-layer face flow continuity condition requires that the flow into(out of) the element 'n' should be equal to flow out of (into) the element 'n+1' (Huang and Griffiths 2010) i.e., the flow across the inter-layer face is

$$v_{if} = k_n \frac{\partial h_n}{\partial z} = k_{n+1} \frac{\partial h_{n+1}}{\partial z} \tag{A2-1}$$

Eq. (A2-1) can be discretized as

$$v_{if} = k_n \frac{h_n - h_{if}}{0.5L_n} = k_{n+1} \frac{h_{if} - h_{n+1}}{0.5L_{n+1}} \tag{A2-2}$$

The hydraulic head at the inter-layer face is derived as

$$h_{if} = \frac{k_n L_{n+1} h_n + k_{n+1} L_n h_{n+1}}{k_{n+1} L_n + k_n L_{n+1}} \tag{A2-3}$$

Substituting h_{if} into Eq. (A2-2), yields

$$v_{if} = k_{e,n} \frac{(h_n - h_{n+1})}{0.5(L_n + L_{n+1})} = k_{e,n} \frac{h_n - h_{n+1}}{z_n - z_{n+1}} \tag{A2-4}$$

where

$$k_{e,n} = \frac{k_n k_{n+1} (L_n + L_{n+1})}{k_{n+1} L_n + k_n L_{n+1}} \tag{A2-5}$$

The $k_{e,n}$ calculated as Eq. (A2-5) is exactly identical to series hydraulic conductivity for layered system. The hydraulic conductivity across the elemental interface is evaluated in the same form. With this consistency, the codes for old layer can be directed applied to new computational domain with updated numbers of elements and other variables after placing the new deposit.

Chapter 9 Enhanced piece-wise linear formulation of large strain consolidation using other soils models

This chapter further develops the coupled unsaturated flow-large strain consolidation model (UNSATCON-ML), which can already (introduced in the previous chapter) model large amounts of plastic volumetric compression during initial drying and small amounts of elastic volumetric swelling during subsequent wetting, as well as hydraulic hysteresis. In order to enhance the capacity of UNSATCON-ML to simulate the other important behaviours of unsaturated soils, for instance, wetting-induced plastic collapse and irrecoverable volumetric compression during wetting and drying cycles, additional constitutive models will be implemented into UNSATCON-ML in this chapter.

9.1 Introduction

It is difficult to use SSM to simulate all the beahviours of unsaturated soils observed in the experiments. There are some other models in the literature established using different theoretical frameworks, which can simulate some additional unsaturated soils behaviour that might be important for modeling multiple layer deposition of tailings. Three models, including the Barcelona Basic Model (or BBM, Alonso et al. 1990) and the Glasgow Coupled Model (or GCM, Wheeler et al. 2003), the SWRM (Gallipoli et al. 2015) formulated with the framework of bounding surface plasticity, will be implemented in UNSATCON-ML. The BBM simulates the mechanical behaviour using net stress and suction as stress variables, and must be coupled with a

void ratio-dependent water retention model. The hysteretic SWRM (Gallipoli et al. 2015) is formulated using the bounding surface concept and must be coupled with a mechanical model, such as the BBM. The GCM itself is a highly coupled model which integrates the stress-strain behaviour and the soil water retention behaviour into a complete elasto-plastic framework. It will be shown in this chapter, and very importantly, that both the volumetric behaviour (whether plastic or elastic) and the water retention behaviour of all of these models can be actually described by a series of surface or planes in corresponding three-dimensional spaces, similar to the three dimensional constitutive surfaces defined in the modified state surface approach used in the previous chapter. Therefore, the solution used to converge between alternative surfaces used in the previous chapter, namely the bisection method, is still capable of performing the constitutive analysis in UNSATCON-ML. Constitutive analysis is still performed as follows: finding the remaining state variables (void ratio, degree of saturation and suction) from gravimetric water content and total/net stress, therefore, to fit to the global piece-wise linear solution and to keep strict mass-conservation. The mesoscale drying box test studied in the previous chapter is reanalysed using UNSATCON-ML with each of the newly implemented constitutive models for a comparison.

9.2 BBM implementation

9.2.1 Analytical form of BBM

A family of log-linear Normal Compression/Consolidation Lines (NCLs) whose slope depends on suction is defined in BBM for virgin consolidation behaviour at different suction level. This forms a surface described by a hyperbolic paraboloid in $v - \ln \bar{p} - \ln s$ space. Another surface

for virgin drying behaviour is also defined in BBM (Zhang and Lytton 2009). These two plastic surfaces are expressed as

$$v = 1 + e = N(0) - \lambda(s)\ln(\frac{\bar{p}}{p^c}) - \kappa_s \ln(\frac{s + p_a}{p_a}) \tag{9.1}$$

$$v = 1 + e = C - \kappa \ln \bar{p} - \lambda_s \ln(s + p_a) \tag{9.2}$$

where, $\lambda(s) = \lambda(0)[(1-r)\exp(-\beta s) + r]$. The constants and variables have been defined by Alonso et al. (1990). Note, the plastic surface of BBM is made up of the comparative lower parts of these two 3D surfaces (see Fig. 9.1 and Fig. 9.2.). The elastic volume change behaviour associated with changes in net stress and suction is described using two incremental relationship: $dv = -\kappa d\bar{p} / \bar{p}$ and $dv = -\kappa_s ds /(s + p_{at})$ in BBM, which can be integrated to give the expression for three dimensional elastic surface

$$v = 1 + e = N_\kappa - \kappa \ln \bar{p} - \lambda_s \ln(s + p_a) \tag{9.3}$$

The atmospherics pressure 'P_a' that has a value of 101.3 kPa, can been replaced by "1kPa" or other small numeric value for modeling problems at low stress level, such as the work presented in this thesis. N_κ is a integration constant instead of a material parameter, it controls the position of the elastic surface and plays a similar role as the hardening parameter in classical elasto-plastic model. As most of the classical elasto-plastic models, the elastic volumetric behaviour is assumed to be path-independent (any combinations of suction and net stress changes) in BBM, so a simple expression (Eq. (9.3)) for elastic surface can be easily obtained. For some other models, these two elastic constants (κ and κ_s) are assumed to depend on the stress and/or suction levels, a simple expression for the elastic surface can not be obtained. Five parameters are required to define Eq.

(9.1). One more parameter, λ_s, is needed for defining Eq. (9.2). As can be seen (see red surface in Fig. 9.1), the virgin drying surface is assumed to have a constant slope, λ_s, with respect to the suction axis. With this simplification, the shrinkage behaviour observed in experiments during initial drying cannot be simulated by BBM, which always predicts a decrease in void ratio as suction increases.

The yielding curves of BBM and their evolution can be more intuitively visualised now: the load-collapse (LC) curve is the projection of the intersection of the elastic surface (Eq. (9.3)) and one of the plastic (Normal Consolidation) surfaces (Eq. (9.1)) (Wheeler and Karube 1996; Delage and Graham 1996; Zhang and Lytton 2009) in the $\bar{p}-s$ plane, see Fig. 9.3 (a) and (b). The projection of suction-increase (SI) curve in the $\bar{p}-s$ plane is the intersection of the elastic surface (Eq. (9.3)) and plastic virgin drying surface (Eq. (9.2)) (Zhang and Lytton, 2009), see Fig. 9.3 (a) and (b). Fig. 9.3 (a) shows the positions of two yield curves when a soil sample is ever dried/loaded to the situation where any wetting path could only induce elastic volume swelling. Fig. 9.3 (b) shows the positions of two yield curves when a soil sample is ever dried/loaded to the situation where a wetting path could probably induce plastic volume collapse. Wetting-induced volume collapse can only occur at net stress higher than a certain value. Obviously, the soil sample indicated by Fig. 9.3 (b) has experienced a higher degree of hardening (by hydraulic drying and/or mechanical loading) than that indicated by Fig. 9.3 (a). The projection of intersection of two plastic surfaces in the $\bar{p}-s$ plane is the path of the corner of SI and LC with yielding (hardening) (Fig. 9.3 (c)), the postulation of coupled movement of LC and SI is also intuitively visualised in this way.

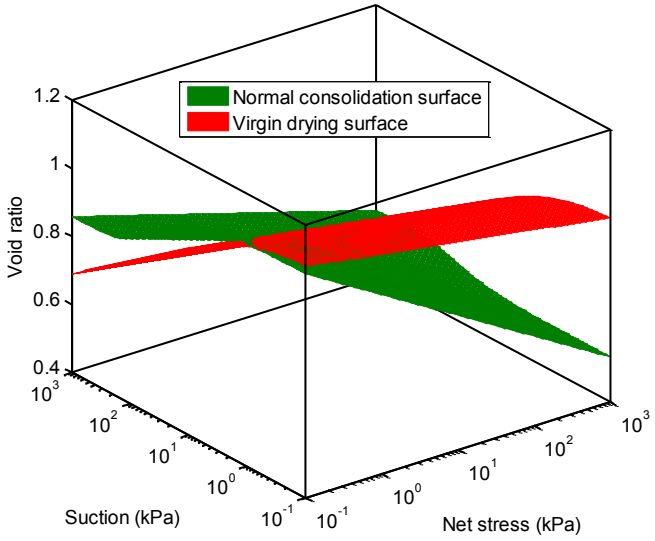

Fig. 9.1. An example of virgin drying surface and normal consolidation surface from BBM

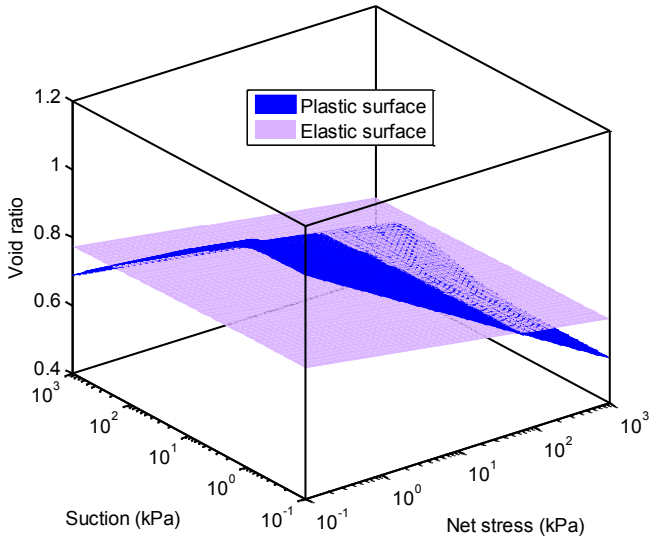

Fig. 9.2 An example of plastic and elastic surfaces from BBM

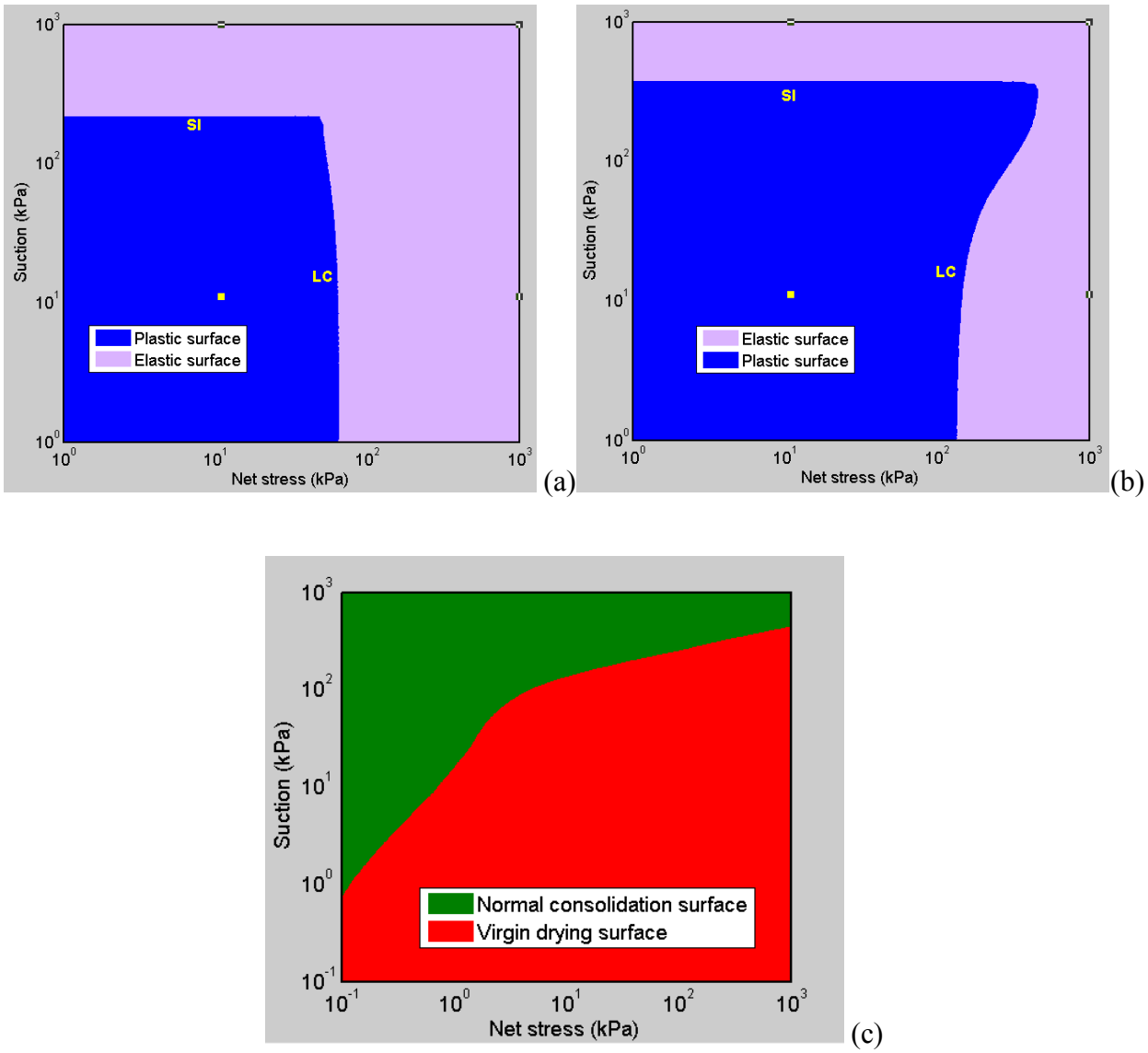

Fig. 9.3 Another visualization of the yielding curves LC and SI in BBM and evolution of their intersection during plastic compression (a) the positions of two yield curves when a soil sample is ever dried/loaded to the situation where any wetting path could only induce elastic volume swelling, (b) the positions of two yield curves when a soil sample is ever dried/loaded to the situation where a wetting path could probably induce plastic volume collapse, (c) the path of corner of SI and LC with yielding (hardening)

9.2.2 Implementing BBM into UNSATCON-ML

Implementing the BBM into UNSATCON-ML can be done by replacing the Vu and Fredlund (2006) equation (Eq 8.1) used in the previous chapter with Eq. (9.2) and Eq. (9.1). However the Bisection Method needs to be used with caution to find the solution along certain stress paths, distinction has to be made between volumetric elastic swelling and plastic collapse when the soil element is subjected to wetting. The algorithm introduced in the previous chapter is modified here to deal with this issue.

Recall that the total/net stress and gravimetric water content have been obtained from the global analysis. If the calculated total stress $\sigma^{(i)}$ at the end of the time step is higher than σ_0^* (the hardening parameters at saturated conditions), the *e-s* relationship of BBM for this stress level comprises two segments: (*i*) *e* decreases as *s* decreases (indicating plastic collapse upon wetting from an initial state, e.g. **b** or **c** in Fig. 9.4, and (*ii*) *e* increases as *s* decreases (indicating elastic volumetric behaviour or virgin plastic compression). Two useful characteristic void ratios can be easily identified from this void ratio *vs.* suction relationship as shown by blue curves in Fig. 9.4: (*i*) the maximum void ratio occurring at the demarcation point between these two segments, denoted as e_m; (*ii*) the void ratio corresponding to zero suction, donated as e_s.

Further, another void ratio *vs.* suction relationship can be constructed using the calculated gravimetric water content $w^{(i)}$ at the end of time step and the defined soil water retention behaviour. First, substitution of *s* and associated *e* from the mechanical model (i.e. the blue line discussed above) into the water retention model, the S_r can be calculated following the appropriate drying/wetting path from the initial state, which results in a $S_r - s$ relation as plotted in Fig. 9.4. Then the void ratio corresponding to each *s* can be calculated using $e = w^{(i)}G_s/S_r$, as illustrated by

black lines in Fig. 9.4. The e bears an inverse relationship to S_r and therefore increases monotonically with increasing s.

Note here a curved shaped SWRC is used for illustration, but the formulated algorithm is still applicable for other simpler and practical SWRC, such as the one used in the previous chapter. And this illustration of SWRC here is for introduction of bounding surface water retention model implemented in the next section and will not be repeated there

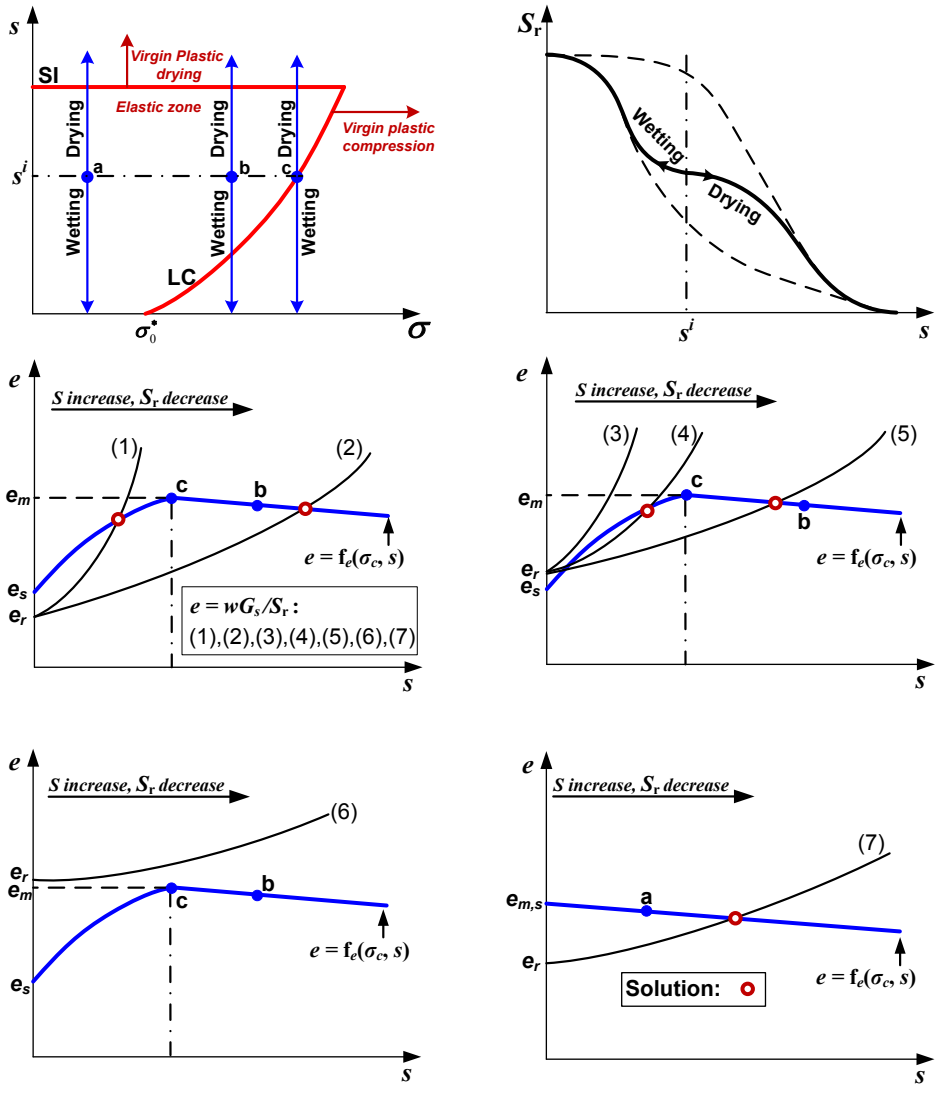

Fig. 9.4 Algorithm for implementation of BBM in conjunction with a SWRC

The intersection point between the obtained two *e-s* curves is the mathematical solution wanted. This should be considered for three different scenarios by comparing the void ratio $e(=w^{(i)}G_s)$ to the values of e_s and e_m:

(a) $e(= wG_s) < e_s$: there must be an intersection point between these two curves (since the e $(=wG_s/S_r)$ will theoretically increase to infinity when S_r approaches 0), which can be in either collapse or the elastic range, depending on the trend of the curve $e=w^{(i)}G_s/S_r$ or the magnitude of $w^{(i)}$, as labeled by (1) and (2) in Fig. 9.4.

(b) $e(= wG_s) > e_s$ and $e(= wG_s) < e_m$: there might (as labeled by (4) and (5)) or might not (indicated by (3)) be intersection points. For cases (4) and (5), there are likely to be two intersection points, in which the one closer to the initial point is assumed to be the solution wanted. Case (3) implies that the soil has already been wetted to a fully saturated state since no solution can be found in the unsaturated range.

(c) $e(= wG_s) > e_m$: similar to case (3), the soil element is saturated, as labeled by (6) in Fig. Fig. 9.4.

If the calculated total stress $\sigma^{(i)}$ at the end of each time step is lower than σ_0^* (Fig. 9.4), a wetting process from the initial point **a** would correspond to an elastic swelling, while a drying process will induce an elastic/plastic compression. For both processes, the void ratio at this stress level decreases monotonically with increasing suction with the maximum void ratio at zero suction, $e_{m,s}$, see Fig. 9.4. This is a much simpler scenario with only two cases:

(d) $e(= wG_s) >= e_{m,s}$: the soil element is in saturated state at the end of current time step.

(e) $e(=wG_s) < e_{m,s}$: there will be an intersection point between these two curves, this is the solution wanted.

For cases (1), (2) and (7), an interval within which the intersection points are located can be readily determined using characteristic points on these two curves, then the true solution can be found employing the bisection method. For (4) and (5), many basic or advanced numerical techniques applicable for finding multiple roots can be employed. The basic incremental search technique is selected to locate the interval bounding the solution closest to the initial state for application of the bisection method subsequently. For the soil element in the saturated state the constitutive analysis in UNSATCON-ML is performed using Terzaghi's effective stress principle as in the previous chapter.

An implied assumption in that the local analysis accounting for elasto-plastic mechanical behaviour in conjunction with the hysteretic hydraulic behaviour is that the net stress de/increment is first applied followed by change of gravimetric water content. This is different from many traditional constitutive integration algorithms, where the strains (mostly strain-driven) are assumed to vary 'proportionally' over an increment (i.e. the ratio between the strain components is the same as that for the incremental strains). The assumption in this thesis is considered to be suitable for our problem where change of net stress only occurs for two cases: (1) evaporation induced weight loss which is very small (negligible) and only brings the soil back to the elastic range, (2) weight from the deposition of a new layer which usually occurs immediately compared to the time-dependent water flow process. Considering the latter case, this assumption seems to be necessary based on the findings of Potts and Ganendra (1994), which indicated that the strain increments in any numerical solution should vary in the same manner (in terms of the ratio between strain components) as in a specific physical problem to obtain accurate results.

9.2.3 Reanalysing the mesoscale drying box test

Calibration of BBM to the drying box problem follows procedures developed by Zhang and Xiao (2013). There exists some other calibration procedures for BBM in the literature (Gallipoli et al. 2010; D'Onza et al. 2011; Zhang and Xiao 2013; D'Onza et al. 2015). According to Wheeler et al. (2002) and D'Onza et al. (2015), the value of reference pressure p^c in Eq. (9.1) should be much lower (with a value of $r < 1$) or higher (with a value of $r > 1$) than the range of p over which the BBM is applied, in order to model collapse behaviour. For both cases, void ratio (or specific volume) defined by Eq. (9.1) increases with increasing suction in the considered range of p.

In the test case we have used to develop UNSATCON-ML (Daliri et al. 2016), the net stress range considered is from near 0 kPa to about 10 kPa, the deposited tailings is initially saturated without any suction or desiccation history. At this low stress range, void ratio decreases (involving a significant amount of plastic deformation) with self-weight consolidation following by drying (suction increase) according to the observation in our test. The stress path would first follow the surface defined by Eq. (9.2), and activate the SI curve. According to the postulation (Alonso et al. 1990) of coupled movement of LC and SI curves, both curves are controlled by the total plastic volumetric deformation (induced by suction and/or net stress changes). Thus, during the initial drying of the tailings, both SI and LC expand in the *s-p* plane. As the LC moves to a higher stress range, the LC curve develops a positive slope with respect to suction, which allows for collapse behaviour. At low stresses, this slope of LC curve with respect to suction is negative, and therefore BBM predicts a swelling behaviour upon wetting. Usually, soils only swell at low stress level, and possibly collapse at a certain high stress level. Based on this analysis, it is more

important to determine the constants controlling virgin drying behavior for the problem studied herein.

The model parameters are presented in Table 9.1 (note that BBM is used in conjunction with the practical SWRM with associated parameters presented in the previous chapter). BBM uses a single parameter λ_s to describe the virgin drying behaviour, and predicts a linear compression line in $e(v)$-ln$s$ plane (void ratio decreases with increasing suction), which is not the case observed in most existing measurements (e.g. Tsiampousi et al. 2013)), including our experimental data. The data shows shrinkage behaviour at large suction level. Fig. 9.5(a),(c),(e) and (b),(d),(f) shows the results for λ_s = 0.057 and λ_s = 0.1, respectively. As can be seen, a satisfactory prediction in terms of void ratio is difficult to be obtained using a constant λ_s. This indicates that the original version of BBM may not be a good candidate for the purpose of our study. BBM was originally formulated for compacted soils under substantial total/net stress, unlike near surface mine tailings.

Table 9.1 Parameters of BBM

Plastic Normal consolidation behavior	N_0	λ	r	β	p_c
	0.68	0.057	0.5	0.02	75
Plastic Normal consolidation behavior	C	λ_s			
	1.05	0.057, 0.1			
Elastic behavior	κ	κ_s			
	0.015	0.0015			

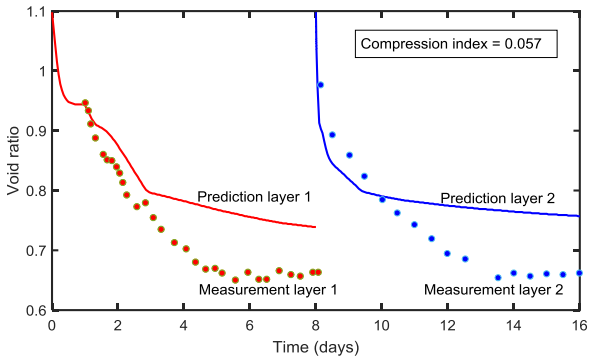
Compression index = 0.057
Void ratio
Time (days)
Prediction layer 1
Prediction layer 2
Measurement layer 1
Measurement layer 2

(a)

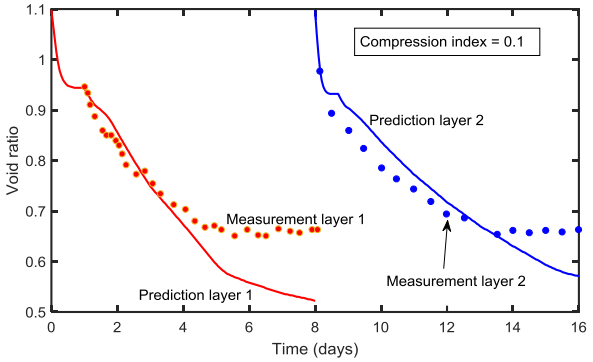
Compression index = 0.1
Void ratio
Time (days)
Prediction layer 2
Measurement layer 1
Measurement layer 2
Prediction layer 1

(b)

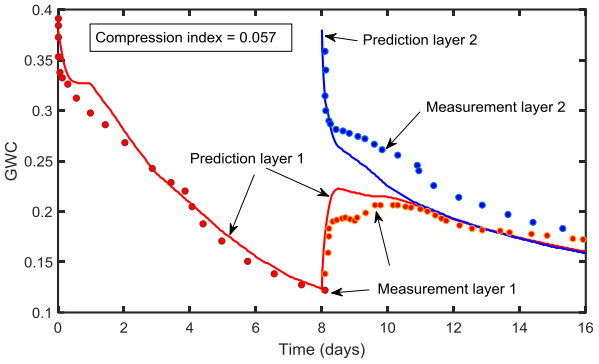
Compression index = 0.057
GWC
Time (days)
Prediction layer 2
Measurement layer 2
Prediction layer 1
Measurement layer 1

(c)

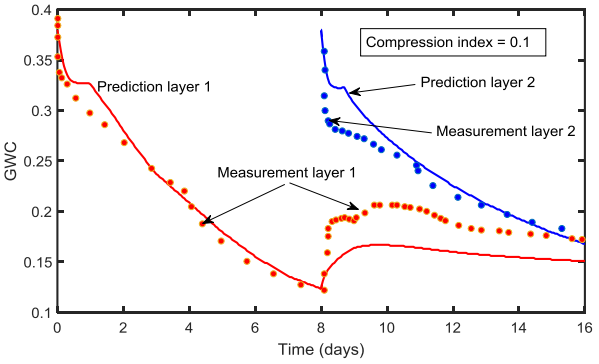
Compression index = 0.1
GWC
Time (days)
Prediction layer 1
Prediction layer 2
Measurement layer 2
Measurement layer 1

(d)

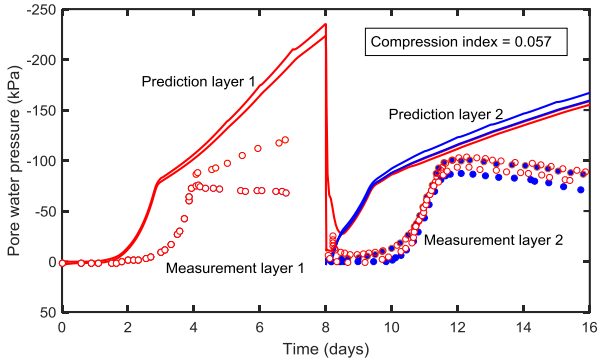

(e)

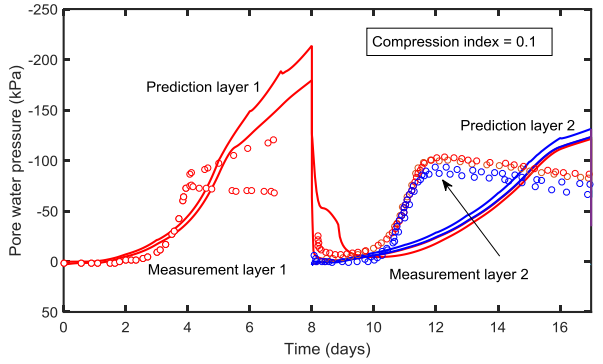

(f)

Fig. 9.5. Predicted results for depositions of layer 1 and 2 in drying box test (Daliri et al. 2016) using BBM: (a) void ratio (b) gravimetric water content and (c) pore water pressure for λ_s = 0.057; (b) void ratio (d) gravimetric water content and (f) pore water pressure for λ_s = 0.1.

Possible modifications to BBM to better replicate shrinkage behaviour have been suggested by some researchers. For example, Tsiampousi et al. (2013) assumed that this constant (κ_s or λ_s) is a function of S_r, to account for the shrinkage behaviour (SI yielding curve becomes unnecessary). This technique also results in a type of coupled (explicitly including S_r in κ_s or λ_s in mechanical model) hydro-mechanical constitutive model if combined with a void ratio (or stress, or (plastic) strain) -dependent SWRC, and perhaps approaches a model similar to GCM. The author thinks that similar or other modifications can also be introduced into original BBM, making λ_s a variable instead of a constant. Then the shrinkage behaviour can be modeled while keeping the basic concepts of coupling SI and LC in BBM. But this is beyond the scope of this thesis.

In the literature, activation of SI in BBM has seldom been calibrated from experimental data. The calibrations has often been conducted on compacted samples with a high initial suction (Gallipoli et al. 2010; Zhang and Xiao 2013; D'Onza et al. 2015). Coupling SI and LC (if involved) would make the calibration more complicated, since their relative locations in *net stress-suction* plane will also be affected by two elastic parameters, κ, κ_s, which should be calibrated together with the other five parameters defining the plastic surface. Solowiski (2008) suggests that SI can be removed from BBM, which then predicts only elastic behaviour as suction increases. D'Onza et al. (2015) highlighted that "Extrapolating predictions far from the experimentally explored stress range in boundary value problems is risky" from their extensive benchmarking exercise on compacted samples.

9.3 Bounding surface SWRM implementation

9.3.1 Expressions of the SWRM by Gallipoli (2015)

The void ratio-dependent SWRC implemented in UNSATCON-ML so far assumes a linear relationship between S_r and e and between S_r and ln$s$, which though worked well for modeling the case in the previous chapter. However, there are so many other experiments indicating that a continuous curve (usually '*S*' shaped curve) will give a better fit to the data. This section will implement such a soil water retention model into UNSATCON-ML.

It is found that the soil water retention model proposed by Gallipoli et al. (2015) appears to be very suitable for implementation using a similar algorithm. This model, accounting for void ratio-dependency based on the work of Gallipoli et al. (2003), is capable of modeling the hydraulic hysteresis based on definition of two bounding surfaces, in which, the scanning paths tend asymptotically towards the main paths as a result of an assumption of relationship between

function derivative (Zhou et al. 2012). What makes this model easy to be implemented using the bisection method is that all the retention paths are expressed by two closed form equations:

$$(S_{\mathrm{r}})_d = \left[1+\left(\frac{(se^{1/\lambda_s})^{\beta_d}+C_d}{\omega_d{}^{\beta_d}}\right)^{\lambda_s/\beta_d m_d}\right]^{-m_d} \tag{9.4}$$

$$(S_{\mathrm{r}})_w = \left[1+\left(\frac{(se^{1/\lambda_s})^{\beta_w}}{\omega_w{}^{\beta_w}\left(1+C_w(se^{1/\lambda_s})^{\beta_w}\right)}\right)^{\lambda_s/\beta_w m_w}\right]^{-m_w} \tag{9.5}$$

Equations (9.4) and (9.5) represent (primary and scanning) drying surfaces and (primary and scanning) wetting surfaces in $S_{\mathrm{r}}-s-e$ space. C_d and C_w are two integration constants. When $C_d = C_w = 0$, Equations (9.4) and (9.5) represent primary surfaces. Non-zero values of C_d and C_w represents scanning behaviours and can be calculated from soil's initial retention point, which are analogous to the integration constant that controls the position of the elastic surface in BBM. The other parameters are model parameters determined from the experiments. The two equations (Eqs. (9.4) and (9.5)) are derived from the work of Gallipoli et al. (2003), which modified the van Genuchten (1980) model without considering the hysteresis. The Gallipoli et al. (2003) equation is also available in UNSATCON-ML and is presented here

$$S_{\mathrm{r}} = \left\{\frac{1}{1+[\phi e^{\varphi} s]^n}\right\}^m \tag{9.5}$$

As can be imagined, implementing the Gallipoli et al. (2015) model using a similar algorithm is even simpler with less lines of codes than that for semi-log linear relationship used in

the previous chapter, thanks to its closed-form and asymptotical characteristics (These will also bring advantages for developing a more sophisticated stress integration algorithm for 2D/3D numerical analysis where the function derivatives will be used). Thus, repetition of implementation details is not necessary here.

An important assumption in Gallipoli et al. (2015) model regarding the reversal of retention point from drying to wetting or vice versa, involves the introduction of scaled suction: The increase of scaled suction producing a decrease of S_r indicates a drying path. Although physically whether increase of GWC or S_r should correspond to a wetting path remains unanswered for deforming soils, numerically it is usually assumed that suction increase or S_r decrease corresponding to drying path (as in the algorithm developed in this thesis). Here it will be shown that S_r decrease also corresponds to suction (not just scaled suction) increase in Gallipoli et al. (2015), indicating the rigorousness of the numerical algorithm presented in the previous section for stress paths involving whether volume decrease or increase.

The BBM for volume change behaviour is used for example. For a stress path where the wetting- induced collapse occurs, the void ratio decreases with decreasing suction (from BBM), resulting in a monotonically decreasing scaled suction and increasing degree of saturation (from SWRC), this is obviously consistent with the calculatioin procedure in the algorithm developed in the thesis. While for stress path where elastic swelling occurs upon wetting, the e can be calculated using

$$e = v - 1 = N_\kappa - \kappa \ln(p) - \kappa_s \ln(s + p_{at}) - 1 \tag{9.7}$$

Then the scaled suction is calculated as

$$\bar{s} = s\left[N_\kappa - \kappa \ln(p) - \kappa_s \ln(s + p_{at}) - 1\right]^{1/\lambda_s} \tag{9.8}$$

The change rate of scaled suction with changing suction is

$$\begin{aligned} \frac{d\bar{s}}{ds} &= s\left[N_\kappa - 1 - \kappa \ln(p) - \kappa_s \ln(s + p_{at})\right]^{\frac{1}{\lambda_s}} \\ &\left[N_\kappa - 1 - \kappa \ln(p) - \kappa_s \ln(s + p_{at})\right]^{\frac{1}{\lambda_s}} - s\frac{\kappa_s}{s + p_{at}}\left\{\frac{\left[N_\kappa - 1 - \kappa \ln(p) - \kappa_s \ln(s + p_{at})\right]^{\frac{1}{\lambda_s}-1}}{\lambda_s}\right\} \\ &= e^{\frac{1}{\lambda_s}}\left(1 - \frac{s\kappa_s}{(s + p_{at})\lambda_s e}\right) \end{aligned} \tag{9.5}$$

The value of κ_s is typically one order of magnitude smaller than the value of λ_s, and the s is less than $(s + p_{at})$. Overall, the value of $d\bar{s}/ds$ is positive, indicating that scaled suction increases with increasing suction, i.e. the degree of saturation increases with suction as in the wetting-induced collapse path.

9.3.2 Testing the correctness of implementation

As in the previous chapter, implementation is carried out directly on the analytical forms of Gallipoli et al. (2015) as well as the BBM. The algorithm should be able to give an accurate result (the error can be controlled within any specified tolerance). However, it is still worth testing the algorithm as it is now used to solve two constitutive relationships together from a given pair of gravimetric water content and net stress. Fig. 9.6 shows the comparison between the calculation using the developed algorithm and the analytical solution for a K_o loading test (EDO-200) calibrated in D'Onza et al. (2011). After equalisation under net stress of 20 kPa and suction of 200 kPa, the sample was subjected to the following stress path: wetting to a suction of 10 kPa, drying

to 200 kPa, loading to a vertical net stress of 800 kPa, unloading to 100 kPa, reloading to 800 kPa, wetting to a suction of 55 kPa and drying to 200 kPa.

Table 9.2 Parameters of BBM and Gallipoli et al. (2003) retention model used by D'Onza et al. (2011)

Plastic Normal consolidation behavior	N_0	$\lambda(0)$	r	β	p_c
	-0.4928	0.1385	1.19597	0. 00397	826 699 057
Plastic Normal consolidation behavior	C_1	λ_s			
	--	--			
Elastic behavior	κ	κ_s			
	0.004	0.006			
Soil water retention curve	ϕ	φ	m	n	
	1.318	6. 036	0. 146	1. 341	

Fig. 9.6, Fig. 9.7 and Fig. 9.8 show that the algorithm developed for UNSATCON-ML gives the same results as analytical solutions (note analytical solutions are only given at several key points (triangles) along the stress path as in Table 9.3), using the same parameters presented in D'Onza et al. (2011), see Table 9.2. In fact, UNSATCON-ML algorithm also solves the constitutive equations analytically but in a different manner: finding the degree of saturation, suction and void ratio from gravimetric water content and total stress. While inputs in the analytical solution are net stress and suction as detailed in Table 9.3 and Table 9.4. The accuracy of UNSATCON-ML algorithm can be seen from the calculation results during the constant suction (200 kPa) path (highlighted using Yellow background in Table 9.4), the little discrepancy in the predicted suction (not exactly 200 kPa) is due to that the input GWC is not exactly representing the real value, they are interpolated linearly along this stress path. However, the predicted suctions are exactly 200 kPa at two key points (highlighted using Red in Table 9.4), indicating the high accuracy of the program.

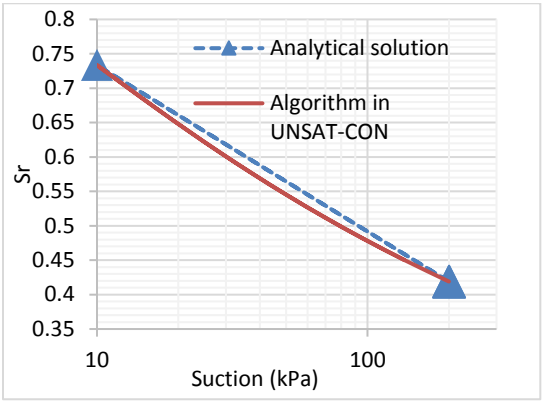

Fig. 9.6. UNSATCON-ML algorithm and analytical solution using BBM and Gallipoli et al. (2003) retention model during first wetting–drying cycle of test EDO-200 in D'Onza et al. (2011): variation of degree of saturation plotted against suction

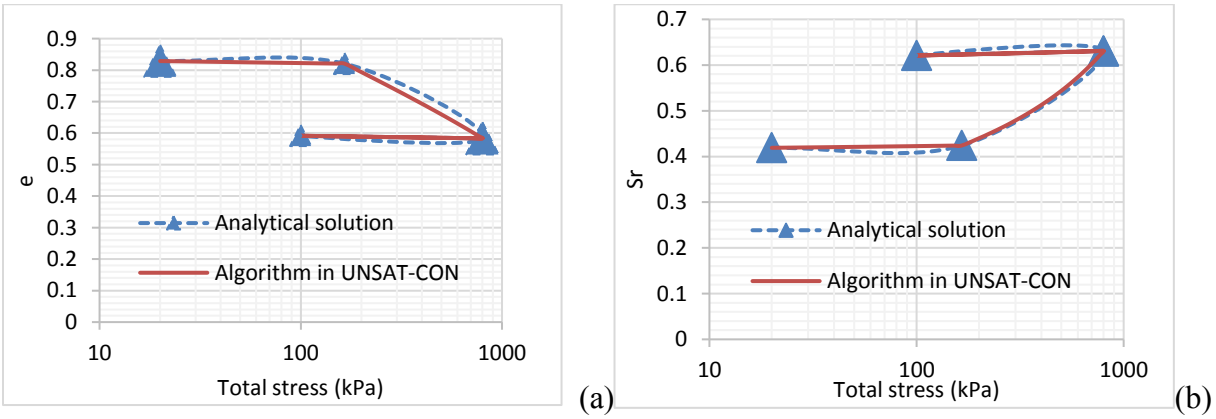

Fig. 9.7. UNSATCON-ML algorithm and analytical solution using BBM and Gallipoli et al. (2003) retention model during loading– unloading–reloading cycle of test EDO-200 in D'Onza et al. (2011): (a) variation of void ratio and (b) degree of saturation plotted against vertical total/net stress

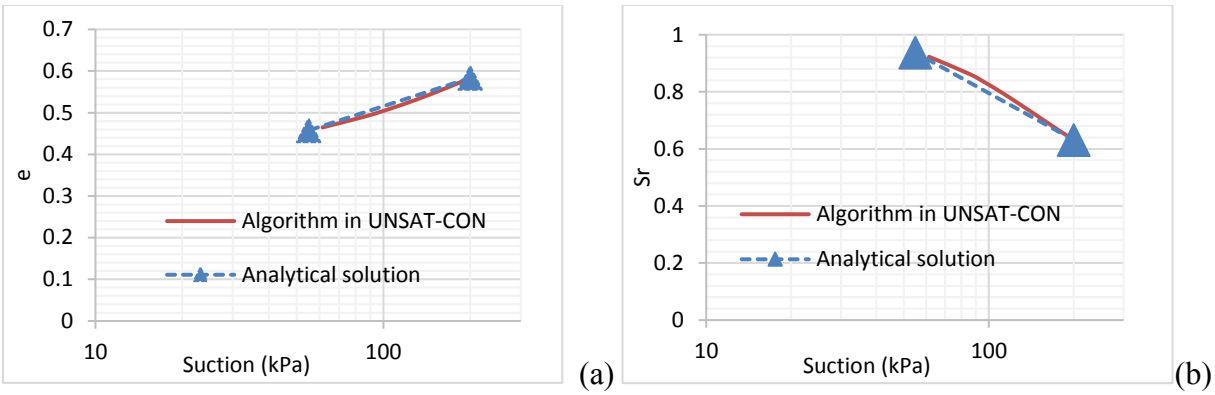

Fig. 9.8. UNSATCON-ML algorithm and analytical solution using BBM and Gallipoli et al. (2003) retention model during second wetting path of test EDO-200 in D'Onza et al. (2011): variation of (a) void ratio and (b) degree of saturation plotted against suction

Table 9.3 Analytical solution to BBM and Gallipoli et al. (2003) retention model for stress path of test EDO-200 in D'Onza et al. (2011)

Stress path	Net stress (kPa)	Suction (kPa)	Void ratio (BBM)	Degree of saturation (Gallipoli 2003)	GWC
	Inputs	**Inputs**	**Outputs**	**Outputs**	**Outputs**
Initial condition	20	200	0.829	0.419	0.129
Wetting	20	10	0.835	0.733	0.228
Drying	20	200	0.829	0.419	0.129
Loading to yielding	165.321	200	0.820	0.424	0.129
Loading after yielding	800	200	0.583	0.631	0.137
unloading	100	200	0.592	0.621	0.137
Reloading	800	200	0.583	0.631	0.137
Wetting	800	55	0.457	0.937	0.159
Drying	800	200	0.454	0.819	0.138

Table 9.4 UNSATCON-ML algorithm solution to BBM and Gallipoli et al. (2003) retention model for stress path of test EDO-200 in D'Onza et al. (2011) (the results corresponding to the constant suction (200 kPa) path are highlighted using Yellow background, the start and end of this path are highlighted using Red)

Calculation step	Net stress (kPa)	GWC	Suction (kPa)	e	Sr
	Inputs		**Outputs**		
Initial state	20.000	0.129	200	0.829	0.41902
1	20.000	0.139	136.999	0.830	0.450
2	20.000	0.149	96.260	0.831	0.481
3	20.000	0.159	69.128	0.832	0.513
4	20.000	0.169	50.584	0.833	0.544
5	20.000	0.178	37.612	0.833	0.576
6	20.000	0.188	28.350	0.834	0.607
7	20.000	0.198	21.610	0.834	0.639
8	20.000	0.208	16.620	0.834	0.670
9	20.000	0.218	12.867	0.835	0.702
10	20.000	0.228	10.000	0.835	0.733
11	20.000	0.218	12.867	0.835	0.702
12	20.000	0.208	16.620	0.834	0.670
13	20.000	0.198	21.610	0.834	0.639
14	20.000	0.188	28.350	0.834	0.607
15	20.000	0.178	37.612	0.833	0.576
16	20.000	0.169	50.584	0.833	0.544
17	20.000	0.159	69.128	0.832	0.513
18	20.000	0.149	96.260	0.831	0.481
19	20.000	0.139	136.999	0.830	0.450
20	20.000	0.129	200.000	0.829	0.419
21	34.532	0.129	200.297	0.827	0.420
22	49.064	0.129	200.421	0.825	0.421
23	63.596	0.129	200.464	0.824	0.422
24	78.128	0.129	200.460	0.823	0.422
25	92.661	0.129	200.424	0.823	0.423
26	107.193	0.129	200.365	0.822	0.423
27	121.725	0.129	200.291	0.822	0.423
28	136.257	0.129	200.203	0.821	0.424
29	150.789	0.129	200.106	0.821	0.424

30	165.321	0.129	200.000	0.820	0.424
31	197.055	0.130	202.614	0.796	0.438
32	228.789	0.130	204.589	0.775	0.452
33	260.523	0.130	206.072	0.756	0.464
34	292.257	0.131	207.164	0.740	0.476
35	323.991	0.131	207.935	0.724	0.487
36	355.725	0.132	208.438	0.711	0.498
37	387.459	0.132	208.713	0.698	0.508
38	419.193	0.132	208.790	0.686	0.519
39	450.927	0.133	208.696	0.675	0.529
40	482.661	0.133	208.448	0.665	0.538
41	514.395	0.133	208.064	0.655	0.548
42	546.128	0.134	207.557	0.646	0.558
43	577.862	0.134	206.936	0.637	0.567
44	609.596	0.135	206.212	0.628	0.576
45	641.330	0.135	205.391	0.620	0.585
46	673.064	0.135	204.479	0.612	0.595
47	704.798	0.136	203.481	0.605	0.604
48	736.532	0.136	202.400	0.597	0.613
49	768.266	0.136	201.239	0.590	0.622
50	800.000	0.137	**200.000**	0.583	0.631
51	730.000	0.137	**200.115**	0.584	0.630
52	660.000	0.137	**200.221**	0.584	0.630
53	590.000	0.137	**200.315**	0.584	0.629
54	520.000	0.137	**200.396**	0.585	0.629
55	450.000	0.137	**200.459**	0.586	0.628
56	380.000	0.137	**200.498**	0.586	0.627
57	310.000	0.137	**200.502**	0.587	0.626
58	240.000	0.137	**200.455**	0.588	0.625
59	170.000	0.137	**200.320**	0.589	0.623
60	100.000	0.137	**200.000**	0.592	0.621
61	170.000	0.137	**200.320**	0.589	0.623
62	240.000	0.137	**200.455**	0.588	0.625
63	310.000	0.137	**200.502**	0.587	0.626
64	380.000	0.137	**200.498**	0.586	0.627
65	450.000	0.137	**200.459**	0.586	0.628
66	520.000	0.137	**200.396**	0.585	0.629
67	590.000	0.137	**200.315**	0.584	0.629
68	660.000	0.137	**200.221**	0.584	0.630
69	730.000	0.137	**200.115**	0.584	0.630
70	800.000	0.137	**200.000**	0.583	0.631

71	800.000	0.139	185.229	0.573	0.652
72	800.000	0.141	171.410	0.564	0.674
73	800.000	0.144	158.388	0.554	0.697
74	800.000	0.146	146.011	0.545	0.720
75	800.000	0.148	134.112	0.535	0.745
76	800.000	0.150	122.497	0.525	0.771
77	800.000	0.153	110.895	0.515	0.798
78	800.000	0.155	98.851	0.503	0.828
79	800.000	0.157	85.275	0.490	0.863
80	800.000	0.159	61.461	0.465	0.923

9.3.3 Reanalysing the mesoscale drying box test

In this section, UNSATCON-ML will be used to reanalyse the mesoscale drying box test employing the bounding surface hysteretic water retention model in conjunction with the state surface model (Vu and Fredlund 2006) for volume change behaviour. The model parameters for volume change behaviour and hydraulic conductivity are the same as used in the previous chapter. The parameters of the bounding surface hysteretic water retention model have been determined using the second calibration strategy (i.e. least-square regression to experimental data) suggested in Gallipoli et al. (2015), and are presented in Table 9.5. Since the initial condition of this case is in fully saturated condition, so initially C_d=C_w=0, which will vary throughout the analysis.

Table 9.5. Parameter values for Gallipoli et al. (2015) model

Drying surfaces	λ_s	ω_d	β_d	m_d	C_d
	0.6654	55.47	16.4	0.3731	0
Wetting surfaces	λ_s	ω_w	β_w	m_w	C_w
	0.6654	30	0.8	0.8	0

Fig. 9.9 compares modelled and measured pore water pressure, GWC and void ratio from the first four layers of deposition that occurred before the rewetting events (Daliri et al. 2016). Figure legends (not included here for clarity) are the same as those in Fig. 8.6. By using the

retention model proposed by Gallipoli et al. (2015), UNSATCON-ML can also give a reasonable prediction of overall change of PWP, void ratio and gravimetric water content over time. Comparatively, the PWP is predicted to increase at a slower rate in the range of 30-90 kPa than the measurements during the first and second layer depositions. This is due to the shape of retention surface used in this range of suction. The curved retention surface here indicate that a smaller increase of suction is required to decrease the same amount of degree of saturation than that for the simpler log-linear retention models used in the previous chapter (see Fig. 9.10). Interestingly, this set of experimental retention data (S_r vs s relationship) showed a more shaper transition during this range of suction, which can be better captured using a simpler log-linear retention model. Obviously, this conclusion drawn from this particular case can never be universally true, considering that the calculated retention point (Fig. 9.11) goes from primary drying to wetting surface (or vice-versa) along a scanning path smoothly and asymptotically in S_r - s - e space, such as indicated in many other experimental data.

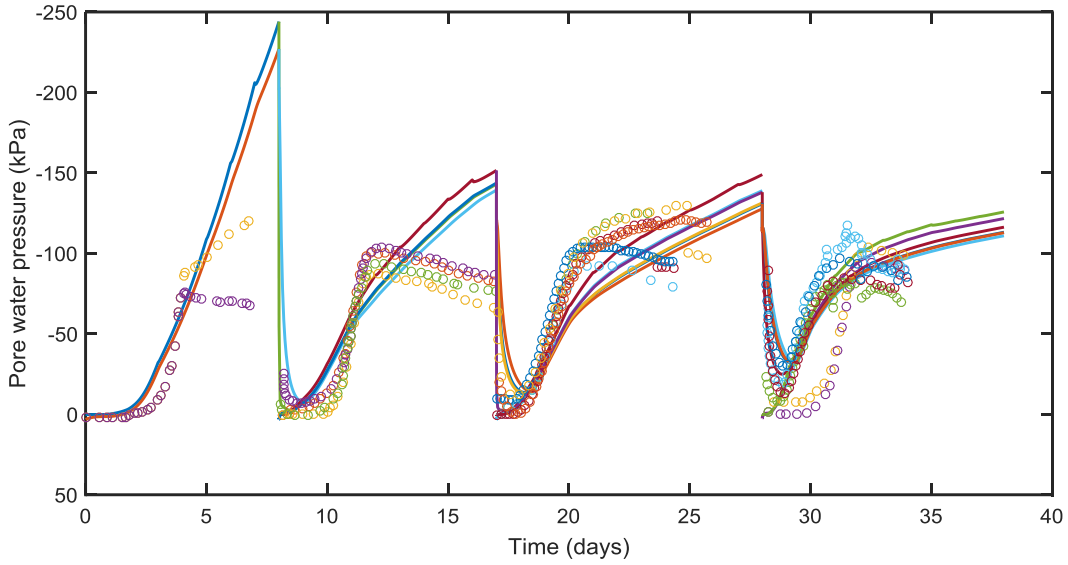
Pore water pressure (kPa)
-250
-200
-150
-100
-50
0
50
0
5
10
15
20
25
30
35
40
Time (days)

(a)

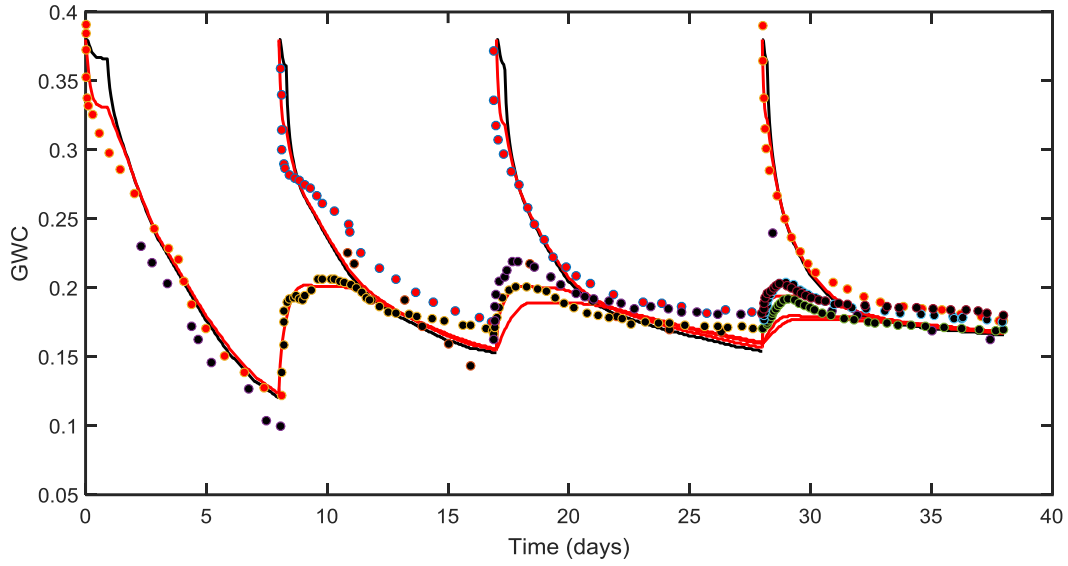
GWC
0.4
0.35
0.3
0.25
0.2
0.15
0.1
0.05
0
5
10
15
20
25
30
35
40
Time (days)

(b)

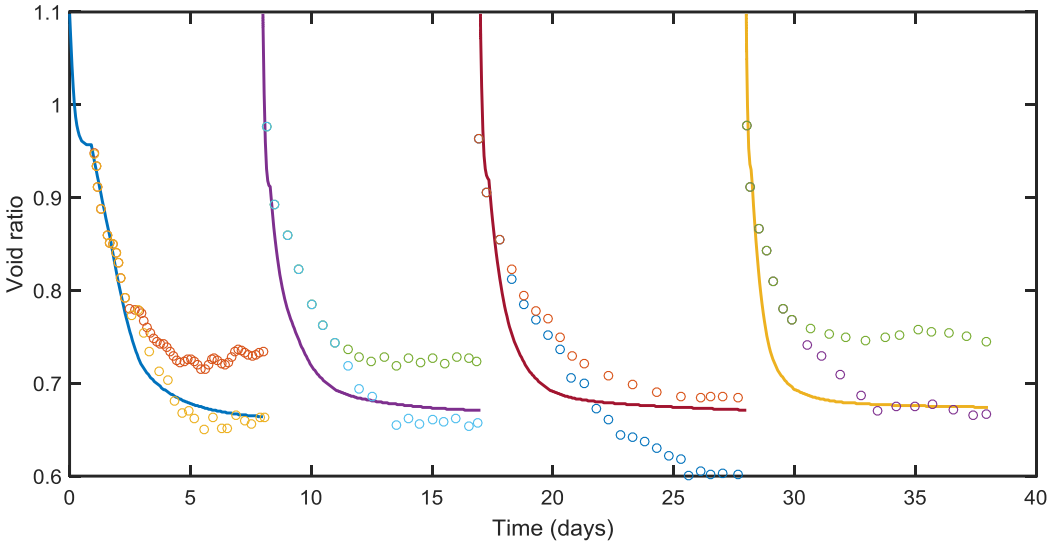

(c)

Fig. 9.9 Results from reanalysis of Daliri et al. (2016)'s case using Gallipoli et al. (2015) model

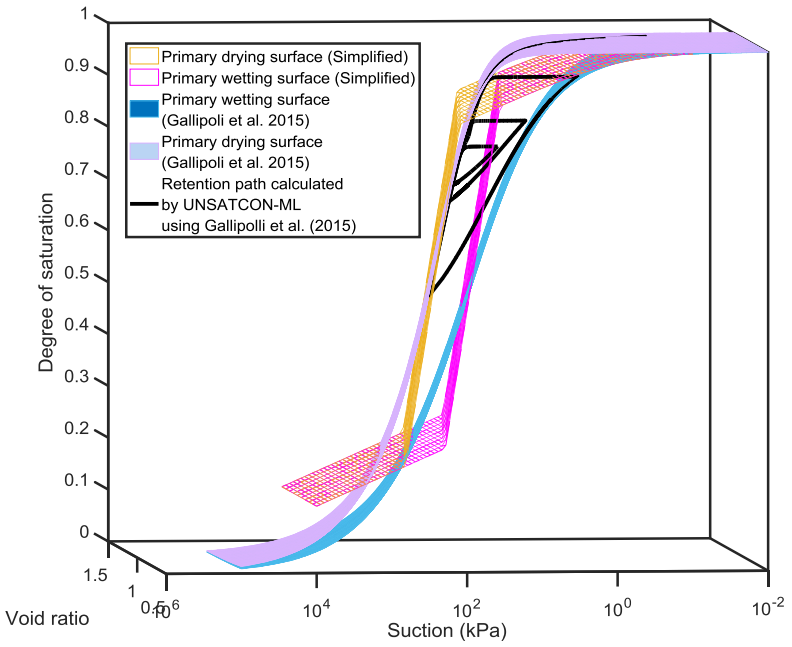

Fig. 9.10 Curved SWRC used here and simpler SWRC used in previous chapter

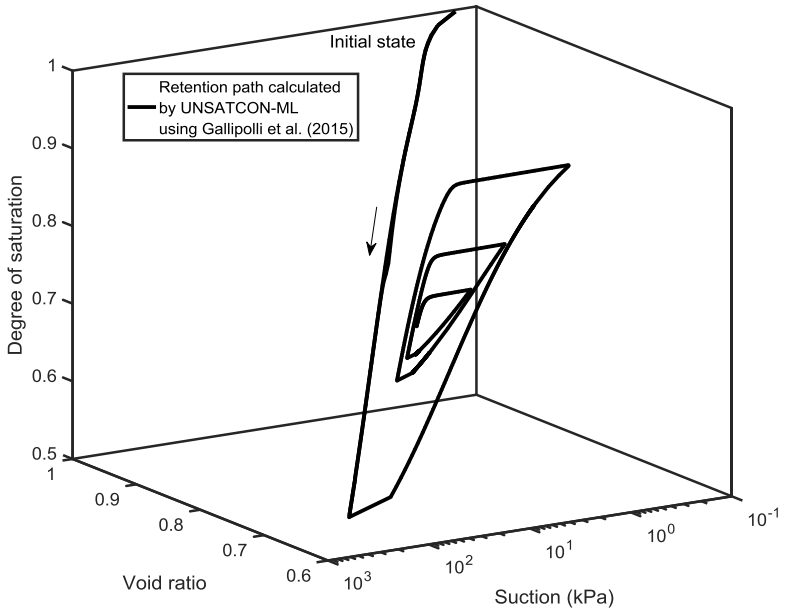

Fig. 9.11 Path of water retention point followed by the top element of first layer using the curved SWRC

9.4 GCM implementation

9.4.1 Analytical form of GCM

The Glasgow Coupled model (GCM) proposed by Wheeler et al. (2003) is quite appealing as its ability to model both the mechanical and water retention behaviour of unsaturated soil in a highly coupled fashion. A set of work-conjugate stresses and strain rates suggested by Houlsby (1997) were used to establish the incremental relationships using elasto-plastic theory, namely, the Bishop's stress (defined as $p^* = \bar{p} + S_r s$) and modified suction (defined as $s^* = ns$, $n=e/(1+e)=(v-1)/v$), and the work-conjugate strain increments ($d\varepsilon_v$ and dS_r). The physical meaning of these two

macroscopic stress variables has been interpreted by Wheeler et al. (2003), as (*i*) the Bishop's stress reflects combined contributions of total stress, pore air pressure, and pore-water pressure, with two pore pressures being weighted by S_r, on the overall mechanical behaviour and (*ii*) modified suction represents the effect of meniscus water and acts to change S_r along a water retention model that has unique spacing in terms of $\ln(s^*)$ between primary drying and wetting curves in S_r- $\ln s^*$ plane.

The soil water retention behaviour is described using a relationship between modified suction and degree of saturation and modeled using a framework similar to mechanical elasto-plasticity. Thus, two yielding curves (**SD** for wetting and **SI** for drying) are introduced for ***hydraulic*** elasto-plastic modelling. Recall the terminology "**SI"** in GCM is for hydraulic behaviour and in BBM is for mechanical behaviour. The mechanical behaviour is still modeled as that for saturated soils but using Bishop's stress as the constitutive stress variable. The incremental relationships, for isotropic stress state, between strain and Bishop's stress, and between degree of saturation and modified suction are expressed as those in conventional elasto-plastic soils' models (Wheeler et al. 2003):

$$d\varepsilon_v^e = \frac{dv^e}{v} = \frac{\kappa dp^*}{vp^*} \text{ (For mechanical unloading/reloading)} \quad (9.10)$$

$$d\varepsilon_v = \frac{dv}{v} = \frac{\lambda}{vp^*} dp^* \text{ (For mechanical yielding only)} \quad (9.11)$$

$$-dS_r^e = \frac{\kappa_s ds^*}{s^*} \text{ (For hydraulic scanning)} \quad (9.12)$$

$$-dS_r = \frac{\lambda_s}{s^*} ds^* \text{ (For hydraulic yielding only)} \quad (9.13)$$

Then, yielding in this coupled model is described using three straight lines in the plane of Bishop's stress and modified suction. A coupled movement mechanism of these yielding curves is introduced to reflect the influence of hydraulic behaviour on mechanical behaviour, and vice versa. The effect of meniscus water on the mechanical behaviour is accounted for by a coupled movement of LC when SI(SD) is activated during a stress path. The effect of plastic volumetric strain on the water retention behaviour is accounted for by a coupled movement of SI(SD) when LC is activated during a stress path. These are mathematically expressed as:

$$\frac{dp_0^*}{p_0^*} = k_1 \frac{ds_{\mathrm{I}}^*}{s_{\mathrm{I}}^*} = k_1 \frac{ds_{\mathrm{D}}^*}{s_{\mathrm{D}}^*} \quad \text{and} \quad \frac{ds_{\mathrm{I}}^*}{s_{\mathrm{I}}^*} = \frac{ds_{\mathrm{D}}^*}{s_{\mathrm{D}}^*} = k_2 \frac{dp_0^*}{p_0^*} \tag{9.14}$$

where, p_0^*, s_{I}^* and s_{D}^* represent **LC** (mechanical), **SI** (hydraulic) and **SD** (hydraulic) yield curves in the Bishop's stress and modified suction plane. As a result of the coupled movements of yield curves, when hydraulic and mechanical yielding simultaneously occur, the plastic volumetric strain and plastic change of degree of saturation should be calculated as:

$$d\varepsilon_v^{\mathrm{p}} = \frac{\lambda - \kappa}{v(1 - k_1 k_2)} \left(\frac{dp_0^*}{p_0^*} - k_1 \frac{ds_{\mathrm{D}}^*}{s_{\mathrm{D}}^*} \right) \quad \text{and} \quad dS_{\mathrm{r}}^{\mathrm{p}} = \frac{-(\lambda_s - \kappa_s)}{(1 - k_1 k_2)} \left(\frac{ds_{\mathrm{D}}^*}{s_{\mathrm{D}}^*} - k_2 \frac{dp_0^*}{p_0^*} \right) \tag{9.15}$$

Introduction of the coupled movement mechanism and adoption of more complex stress variable have, somehow, complicated the use or calculation procedure of this coupled model. But it is found that this model is fully integrable, the analytical form of this coupled model may help to facilitate its utilisation and parameter calibration. Integration of Eqs. (9.10), (9.11), (9.12),(9.13) gives:

$$v = N_\kappa - \kappa \ln p^* \tag{9.16}$$

$$v = N - \lambda \ln p^* \tag{9.17}$$

$$S_r = \Omega_\kappa - \kappa_s \ln s^* \tag{9.18}$$

$$S_r = \Omega_{w,d} - \lambda_s \ln s^* \tag{9.19}$$

where, N_κ, Ω_κ, N and $\Omega_{w,d}$ (d for drying and w for wetting) are four integration constants, N_κ and Ω_κ determine the locations of current elastic swelling and scanning line in respective semi-log plane, their values can be calculated from the current soil's state, as in conventional model. Eqs. (9.17) and (9.19) represents the normal compression line and primary drying/wetting lines in respective semi-log plane. Wheeler et al. (2003) explicitly suggested that the position of SWRC will shift with the accumulation of plastic volumetric strain. It is also found in this thesis the position of the normal compression line (which is unique for saturated soil) will move with the accumulation of plastic change of degree of saturation in GCM. The mutual influences between hydraulic and mechanical components are actually mathematically reflected by or consistent with the coupled movement mechanism of yield (SI, SD and LC) curves. Therefore, using mathematical description of the coupled movement of yield curves in the incremental formulation, it is possible to derive the specific expressions of N and $\Omega_{w,d}$ (as functions of plastic change of degree of saturation and plastic volume compression, respectively), resulting in the analytical forms of the normal consolidation line (NCL) and primary retention lines (PRL). The derivation by the author of this thesis is presented in the following.

Yielding on SI or SD alone causes coupled movements of LC to the right or left in GCM. This can also be represented or interpreted as the upward/downward movements of NCL in the v-lnp^* plane, as shown in Fig. 9.12. Let the soil state be initially at point A in the v-lnp^* plane, no

mechanical yielding indicates that the soil state is always on the current and fixed unloading/reloading line. It crosses the current NCL (indicated as N_1) at the current yielding point ($p^*_{0,1}$, v_1) in v-lnp^* plane, this yielding (preconsolidation) Bishop's stress, $p^*_{0,1}$, corresponds to the current location of LC in p^*-s^* plane. If the respective soil state is on the SI yield curve in p^*-s^* plane (see A1 in Fig. 9.12), further drying the soil will induce in plastic decrease of S_r, making the soil skeleton harder to be mechanically yielded, which is represented by coupled outward movement of LC, for example, to the line indicated by $p^*_{0,2}$. This mathematical treatment is equivalent to an upward movement of NCL, for example, to the line indicated by N_2. This updated NCL crosses the fixed (no mechanical yielding) unloading/reloading curve at the new yielding point ($p^*_{0,2}$, v_2) in v-lnp^* plane. The two mechanical yielding points: ($p^*_{0,1}$, v_1) -- before hydraulic yielding, and ($p^*_{0,2}$, v_2) -- after hydraulic yielding are on the same unloading/reloading curve, but different NCLs in v-lnp^* plane, which are, respectively, expressed as

$$v_1 - v_2 = \kappa(\ln p^*_{0,2} - \ln p^*_{0,1}) \tag{9.20}$$

$$v_1 = N_1 - \lambda \ln p^*_{0,1} \text{ and } v_2 = N_2 - \lambda \ln p^*_{0,2} \tag{9.21}$$

Combining Eqs. (9.20) and (9.21) and eliminating the specific volume, gives

$$N_2 - N_1 = (\lambda - \kappa)(\ln p^*_{0,2} - \ln p^*_{0,1}) \tag{9.22}$$

The coupled movement of LC curve (or increase of the yielding Bishop's stress) is quantified as

$$\frac{dp^*_0}{p^*_0} = k_1 \frac{ds^*_I}{s^*_I} = k_1 \frac{ds^*_D}{s^*_D} = -\frac{k_1}{\lambda_s - \kappa_s} dS^p_r \tag{9.23}$$

Integrating Equation (9.23) gives

$$\ln p^*_{0,2} - \ln p^*_{0,1} = -\frac{k_1}{\lambda_s - \kappa_s}(S^{\mathrm{p}}_{\mathrm{r},2} - S^{\mathrm{p}}_{\mathrm{r},1}) \tag{9.24}$$

Substituting Eq. (9.24) into Eq. (9.22), gives

$$N_2 - N_1 = -\frac{k_1(\lambda - \kappa)}{\lambda_s - \kappa_s}(S^{\mathrm{p}}_{\mathrm{r},2} - S^{\mathrm{p}}_{\mathrm{r},1}) \tag{9.25}$$

where, $k_1, \lambda, \kappa, \lambda_s, \kappa_s$ are five material constants. The above derivation is unequivocally valid when hydraulic yielding is occurring on SD curve and NCL moves downward, as long as the soil state is below the updated NCL in v-lnp^* plane. Equation (9.25) indicates N bears a linear relationship with the accumulated plastic degree of saturation.

Similarly, the relationship between the position of PRL (indicated by $\Omega_{w,d}$) in the S_{r}-lns^* plane and accumulated plastic volume change, v^{p} , can also be derived from the condition of yielding on the LC surface alone, as shown in Fig. 9.12. The corresponding key procedures are presented as follows using the primary wetting line as an example. The two hydraulic yielding points: ($s^*_{D,1}, S_{\mathrm{r},1}$) -- before mechanical yielding, and ($s^*_{D,2}, S_{\mathrm{r},2}$) -- after mechanical yielding are on the same scanning curve, but different PRLs in S_{r}-lns^* plane, which are, respectively, expressed as

$$S_{\mathrm{r},1} - S_{\mathrm{r},2} = \kappa_s(\ln s^*_{\mathrm{D},2} - \ln s^*_{\mathrm{D},1}) \tag{9.26}$$

$$S_{\mathrm{r},1} = \Omega_{w,1} - \lambda_s \ln s^*_{\mathrm{D},1} \text{ and } S_{\mathrm{r},2} = \Omega_{w,2} - \lambda_s \ln s^*_{\mathrm{D},2} \tag{9.27}$$

Combining Eqs. (9.26) and (9.27) and eliminating the degree of saturation, gives

$$\Omega_{w,2} - \Omega_{w,1} = (\lambda_s - \kappa_s)(\ln s^*_{\mathrm{D},2} - \ln s^*_{\mathrm{D},1}) \tag{9.28}$$

The coupled movement of SD curve (or increase of the yielding modified suction) is quantified as

$$\frac{ds^*_{\mathrm{D}}}{s^*_{\mathrm{D}}} = k_2 \frac{dp^*_0}{p^*_0} = \frac{k_2}{\lambda - \kappa} dv^{\mathrm{p}} \tag{9.29}$$

Integrating Equation (9.29) gives

$$\ln s^*_{\mathrm{D},2} - \ln s^*_{\mathrm{D},1} = \frac{k_2}{\lambda - \kappa}(v^{\mathrm{p}}_2 - v^{\mathrm{p}}_1) \tag{9.30}$$

Substituting Eq. (9.30) into (9.28), gives

$$\Omega_{w,2} - \Omega_{w,1} = \frac{k_2(\lambda_s - \kappa_s)}{\lambda - \kappa}(v^{\mathrm{p}}_2 - v^{\mathrm{p}}_1) \tag{9.31}$$

The coupled movement of primary drying line induced by mechanical yielding is the same as that of primary wetting line. Thus,

$$\Omega_{w,2} - \Omega_{w,1} = \Omega_{d,4} - \Omega_{d,3} = \frac{k_2(\lambda_s - \kappa_s)}{\lambda - \kappa}(v^{\mathrm{p}}_2 - v^{\mathrm{p}}_1) \tag{9.32}$$

Equation (9.32) indicates $\Omega_{w,d}$ also bears a linear relationship with the accumulated plastic volume change.

Several important points regarding the above derivation include:

a) *Differences between mechanical and hydraulic behaviour.* The NCL in v-lnp^* plane can move upwards or downwards while the PRL in the S_{r}-lns^* plane can only move to the right, since there can be increase or decrease of plastic S_{r}, but there is only plastic volumetric

compression during any stress path. Plastic volumetric swelling is not considered in GCM. There is only one set of NCLs for mechanical behaviour but two sets of PRLs for hysteretic hydraulic behaviour.

b) *These resulted relationships are also valid for simultaneous yielding on both* (LC and SD (SI)) *curves*. This can be illustrated considering a stress path causing simultaneous yielding on LC and SD: For instance, the soil state moves from M to N in v-lnp^* and S_r-lns^* planes, as shown in Fig. 9.12. Following this stress path, the positions of NCL and PRL move downward and rightward, respectively. The plastic changes of v and S_r cannot be simply calculated from the changes of yielding Bishop's stress and modified suction. But they can still be calculated from the total changes of v and S_r subtracted by the elastic changes of v and S_r, where the elastic changes of v and S_r can be evaluated by the changes of corresponding stress variables in any elasto-plastic models, therefore,

$$v_n^p - v_m^p = -(v_n - v_m) - \kappa(\ln p_{0,n}^* - \ln p_{0,m}^*) \tag{9.33}$$

$$S_{r,n}^p - S_{r,m}^p = (S_{r,n} - S_{r,m}) + \kappa_s(\ln s_{D,n}^* - s_{D,m}^*) \tag{9.34}$$

The specific volume and degree of saturation are calculated using the old and new NCLs and PRLs, as

$$v_m = N_m - \lambda \ln p_{0,m}^* \text{ and } v_n = N_n - \lambda \ln p_{0,n}^* \tag{9.35}$$

$$S_{r,m} = \Omega_{w,m} - \lambda_s \ln s_{D,m}^* \text{ and } S_{r,n} = \Omega_{w,n} - \lambda_s \ln s_{D,n}^* \tag{9.36}$$

Substituting Eq. (9.35) and (9.36) into (9.33) and (9.34), yields,

$$v_n^p - v_m^p = (N_m - N_n) + (\lambda - \kappa)(\ln p_{0,n}^* - \ln p_{0,m}^*) \tag{9.37}$$

$$S_{\mathrm{r},n}^{\mathrm{p}} - S_{\mathrm{r},m}^{\mathrm{p}} = (\boldsymbol{\Omega}_{w,n} - \boldsymbol{\Omega}_{w,m}) - (\lambda_s - \kappa_s)(\ln s_{\mathrm{D},n}^{*} - s_{\mathrm{D},m}^{*}) \tag{9.38}$$

Substituting Eqs. (9.25) and (9.32) (derived from mechanical yielding only and hydraulic yielding only, respectively) into the above equations, and rearranging for plastic changes of v and S_{r}, gives,

$$(v_n^{\mathrm{p}} - v_m^{\mathrm{p}}) = \frac{(\lambda - \kappa)\left[(\ln p_{0,n}^{*} - \ln p_{0,m}^{*}) - k_1(\ln s_{\mathrm{D},n}^{*} - s_{\mathrm{D},m}^{*})\right]}{1 - k_1 k_2} \tag{9.39}$$

$$(S_{\mathrm{r},n}^{\mathrm{p}} - S_{\mathrm{r},m}^{\mathrm{p}}) = \frac{(\lambda_s - \kappa_s)\left[k_2(\ln p_{0,n}^{*} - \ln p_{0,m}^{*}) - (\ln s_{\mathrm{D},n}^{*} - s_{\mathrm{D},m}^{*})\right]}{1 - k_1 k_2} \tag{9.40}$$

These two equations are, in fact, the integrated forms of Eqs. (19) and (20) in Wheeler et al. (2003) for calculating the plastic change of volumetric strain and degree of saturation for simultaneous yielding condition. Thus, it can be concluded that N and $\Omega_{w,d}$ bear the same linear relationship with the accumulated plastic changes of S_{r} and v for any yielding scenarios.

c) *Uniqueness of NCLs and PRLs*. Equations (9.25) and (9.32) can be further simplified, particularly considering the fact that the same linear relationships hold for any stress path, to

$$N = N_0 - \frac{k_1(\lambda - \kappa)}{\lambda_s - \kappa_s} S_{\mathrm{r}}^{\mathrm{p}} \tag{9.41}$$

$$\Omega_{w,d} = \Omega_{w0,d0} + \frac{k_2(\lambda_s - \kappa_s)}{\lambda - \kappa} v^{\mathrm{p}} \tag{9.42}$$

where, N_0, Ω_{w0} and Ω_{d0} are three material constants. Correspondingly, the NCL and PRL can now be completely represented by

$$v = N_0 - \frac{k_1(\lambda - \kappa)}{\lambda_s - \kappa_s} S_{\mathrm{r}}^{\mathrm{p}} - \lambda \ln p^* \tag{9.43}$$

$$S_{\mathrm{r}} = \Omega_{w0,d0} + \frac{k_2(\lambda_s - \kappa_s)}{\lambda - \kappa} v^{\mathrm{p}} - \lambda_s \ln s^* \tag{9.44}$$

Equation (9.43) indicates that the soil's normal compression behaviour are represented by a unique (fixed) planer in the $v - S_{\mathrm{r}}^{\mathrm{p}} - \ln p^*$ space, which forms a bounding surface for the soil state in this space. Any stress paths corresponding to a soil's state under this planer produce elastic volume change. Equation (9.44) indicates that the primary soil water retention behaviour is represented by two unique (fixed) planers in the $S_{\mathrm{r}} - v^{\mathrm{p}} - \ln s^*$ space, which also form two bounding surfaces for the soil's state in this space. Any stress paths corresponding to a soil's state within these two planers produce elastic change of degree of saturation. The coupled movements of yielding curves (LC and SD (SI)) are equivalent to interventions of $S_{\mathrm{r}}^{\mathrm{p}}$ and v^{p} in the expressions of NLC and PRL. In the conventional space of $v - \ln p^* - \ln s^*$, the volume change behaviour in GCM is fully described by two movable planes: one plastic plane affected by $S_{\mathrm{r}}^{\mathrm{p}}$, and one elastic plane affected by v^{p}. In the conventional space of $S_{\mathrm{r}} - \ln p^* - \ln s^*$, the water retention behaviour in GCM is fully described by three movable planes: two (for wetting and drying) plastic planes affected by v^{p}, and one elastic plane affected by $S_{\mathrm{r}}^{\mathrm{p}}$. The new physical meaning of coupling parametes k_1 and k_2 emerges from Equation (9.43) and Equation (9.44), controlling the spacing between NCLs and PRLs.

d) *Transition modeling.* When GCM is applied to problems involving transition between saturated and unsaturated states, the parameter $\kappa_s = 0$ is suggested by Lloret et al. (2017).

With this treatment, any change of S_r should be plastic, and the normal consolidation behaviour in GCM is actually described by NCL at different level of S_r.

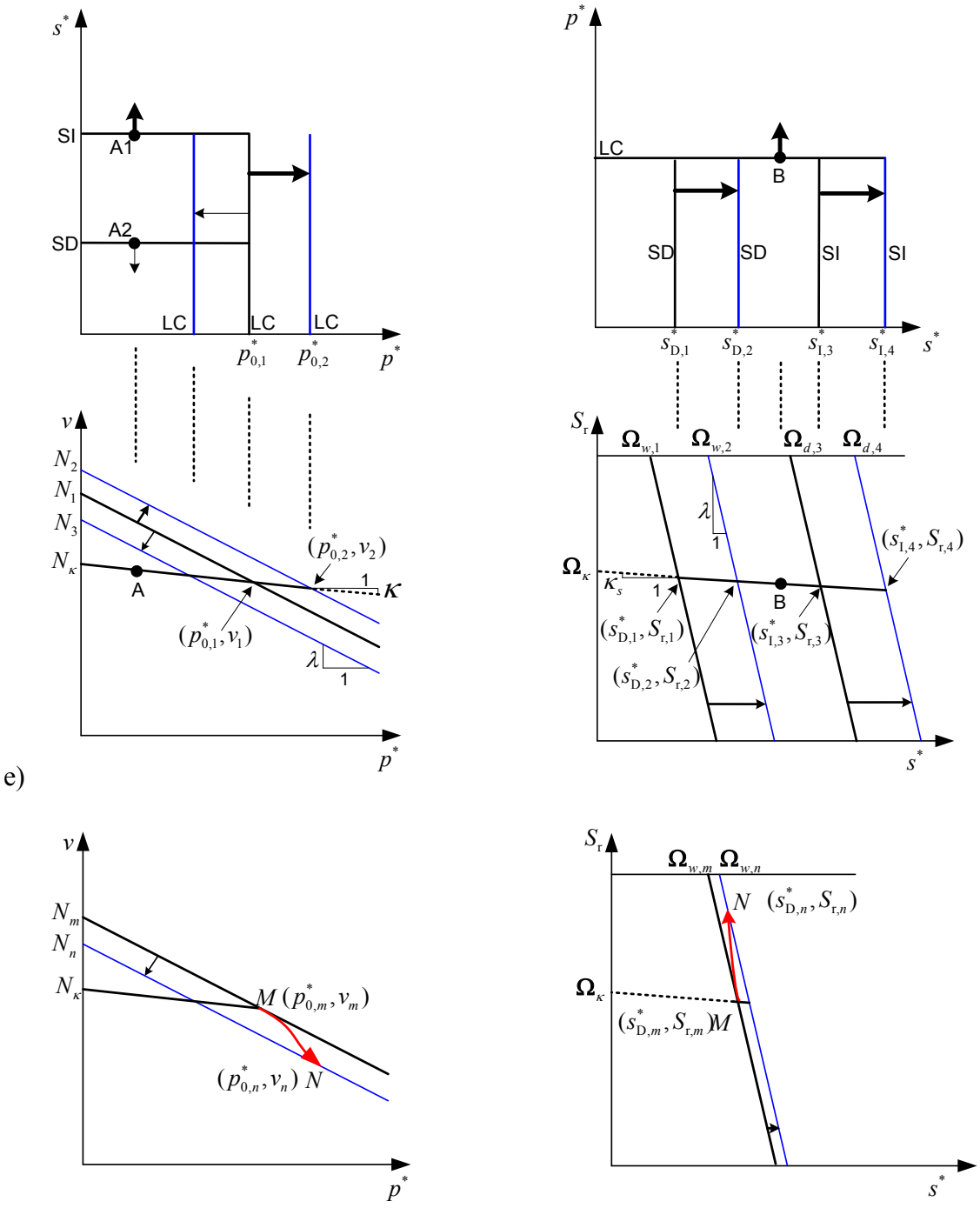

Fig. 9.12 Derivation of NCLs and PRLs of GCM

9.4.2 Implementing GCM into UNSATCON-ML

With this obtained analytical (integrated) formulation in this thesis, GCM can be readily implemented into UNSATCON-ML using a similar numerical technique with a tiny adaptation.

In UNSATCON-ML, the gravimetric water content and total/net stress at each node/element are obtained from the global analysis, which are used to find the other constitutive variables obeying the adopted constitutive law. In commonly-used constitutive integration algorithms, the information pertaining to the stress-path dependency, such as the hardening parameter defining the size of yield surface, has also to be stored and updated throughout the analysis. For implementation of the analytical form of GCM, variables of this type include, N_κ (position of mechanical elastic swelling line), S_r^p (position of NCL), v^p (position of PRL). Noting if κ_s is set to 0 for state transition, $S_r^p = S_r$, which also marks the position of hydraulic scanning line. Now, the task of the algorithm is to find a set of variables $[s^{(i)}, p^{*(i)}, s^{*(i)}, v^{(i)}, S_r^{(i)}, N_\kappa^{(i)}, S_r^{p,(i)}, v^{p,(i)}]$ from the obtained $w^{(i)}$ and $\bar{p}^{(i)}$ at the end of current time step.

Similarly, it is found that starting with an assumed pair of S_r and v (satisfying the basic/ intrinsic volume-mass relationship $(v\text{-}1)S_r=wG_s$) will led to a simpler calculation procedure, due to (*a*) the constitutive law in GCM relates the S_r and v to p^* and s^*, which are defined as functions of S_r and v, and (b) the real solution of S_r are physically bounded within the interval [0,1]. Activations of different yielding curve are now distinguished by comparing the assumed S_r and v to yielding $S_{r,y}$ and v_y (corresponding to intersection of current PRL and scanning line, and intersection of current NCL and swelling line), for selecting the respective constitutive equations for calculation. The assumption of κ_s=0 implies that any increase/decrease of S_r is plastic (i.e.

yielding S_r equals current S_r). Adoption of $S_{r,y}$ and v_y to distinguish the elastic and plastic zones (similar to role of yield surface defined using stress variables) is not strange considering that thare are another group of elasto-plastic model developed in the strain-space. While no change of S_r indicates a scanning path is followed by the retention point, and s^* cannot now be determined according to only the retention constitutive relationship. Thus, treatment of this case (no hydraulic yielding) should be slightly different from that with hydraulic yielding, and is first considered in the algorithm. The whole calculation procedure is as follows

(1) Assuming $S_{r,try} = S_r^{(i-1)}$, and $v_{try} = \dfrac{w^{(i)} G_s}{S_{r,try}} + 1$. Set $S_{r,try}^p = S_{r,try}$ (the trial accumulated plastic change of S_r always equals to the trial degree of saturation for any cases). if $v_{try} > v_y$, goes to (2); if $v_{try} <= v_y$, goes to (3).

(2) There is no plastic volume change, set $N_{\kappa,try} = N_\kappa^{(i-1)}$ and $v_{try}^p = v^{p,(i-1)}$. Calculate the trial Bishop's stress $p_{try}^* = \exp(\dfrac{N_{\kappa,try} - v_{try}}{\kappa})$, the trial suction $s_{try} = (p_{try}^* - \bar{p}^{(i)}) / S_{r,try}$, and trial modified suction $s_{try}^* = s_{try}(v_{try} - 1)/v_{try}$. Goes to (4).

(3) Calculate the trial Bishop's stress $p_{try}^* = \exp(\dfrac{N_0 - k_1 m S_{r,try}^p - v_{try}}{\lambda})$, the trial suction $s_{try} = (p_{try}^* - \bar{p}^{(i)}) / S_{r,try}$, trial modified suction, $s_{try}^* = s_{try}(v_{try} - 1)/v_{try}$. The position of swelling line $N_{\kappa,try} = v_{try} + \kappa \ln p_{try}^*$, and the accumulated plastic volume change is $v_{try}^p = v^{p,(i-1)} + (v^{(i-1)} - v_{try}) - \kappa \ln \dfrac{p_{try}^*}{p^{*(i-1)}}$. Goes to (4).

(4) Check the location of the trail retention point, if $S_{\mathrm{r,try}} \le \Omega_{d0} + k_2 m^{-1} v_{\mathrm{try}}^{\mathrm{p}} - \lambda_s \ln s_{\mathrm{try}}^*$ and $S_{\mathrm{r,try}} \ge \Omega_{w0} + k_2 m^{-1} v_{\mathrm{try}}^{\mathrm{p}} - \lambda_s \ln s_{\mathrm{try}}^*$, this trial $S_{\mathrm{r,try}}$ and other obtained trail variables are the solution wanted, goes to the end. Otherwise, goes to (5): starting the binary search procedure assuming that an interval [$S_{\mathrm{r,min}}$, $S_{\mathrm{r,max}}$] in which the root of S_r must lie is known. Determination of the initial interval will be explained later.

(5) Calculate $S_{\mathrm{r,try}} = 0.5(S_{\mathrm{r,max}} + S_{\mathrm{r,min}})$, and $v_{\mathrm{try}} = \frac{w^{(i)} G_s}{S_{\mathrm{r,try}}} + 1$. Set $S_{\mathrm{r,try}}^{\mathrm{p}} = S_{\mathrm{r,try}}$. if $v_{\mathrm{try}} > v_{\mathrm{y}}$, goes to (6); if $v_{\mathrm{try}} <= v_{\mathrm{y}}$, goes to (8).

(6) Set $N_{\kappa,\mathrm{try}} = N_{\kappa}^{(i-1)}$ and $v_{\mathrm{try}}^{\mathrm{p}} = v^{\mathrm{p},(i-1)}$. Calculate the trial Bishop's stress $p_{\mathrm{try}}^* = \exp(\frac{N_{\kappa,\mathrm{try}} - v_{\mathrm{try}}}{\kappa})$, the trial modified suction $s_{\mathrm{try}}^* = \exp(\frac{\Omega_{w0,d0} + k_2 m^{-1} v_{\mathrm{try}}^{\mathrm{p}} - S_{\mathrm{r,try}}}{\lambda_s})$, Goes to (7).

(7) Check the location of soil state in $v - S_{\mathrm{r}}^{\mathrm{p}} - \ln p^*$ space, if $v_{\mathrm{try}} < N_0 - k_1 m S_{\mathrm{r,try}}^{\mathrm{p}} - \lambda \ln p_{\mathrm{try}}^*$, the trial $S_{\mathrm{r,try}}$ and other obtained trail variables are potential solutions, goes to (9). Otherwise, goes to (8).

(8) Calculate the trial Bishop's stress $p_{\mathrm{try}}^* = \exp(\frac{N_0 - k_1 m S_{\mathrm{r,try}}^{\mathrm{p}} - v_{\mathrm{try}}}{\lambda})$, update the potential position of elastic swelling line $N_{\kappa,\mathrm{try}} = v_{\mathrm{try}} + \kappa \ln p_{\mathrm{try}}^*$, the accumulated plastic volume change, $v_{\mathrm{try}}^{\mathrm{p}} = v^{\mathrm{p},(i-1)} + (v^{(i-1)} - v_{\mathrm{try}}) - \kappa \ln \frac{p_{\mathrm{try}}^*}{p^{*(i-1)}}$. Now it is possible to calculate the trial modified suction $s_{\mathrm{try}}^* = \exp(\frac{\Omega_{w0,d0} + k_2 m^{-1} v_{\mathrm{try}}^{\mathrm{p}} - S_{\mathrm{r,try}}}{\lambda_s})$, Goes to (9).

(9) A pair of trial stress variables, (p^*_{try} , s^*_{try}), have been obtained from the procedure outlined from step (5) to (8). Now calculate the trial suction $s_{\text{try}} = s^*_{\text{try}} v_{\text{try}} / (v_{\text{try}} - 1)$ and then trial net stress $\bar{p}_{\text{try}} = p^*_{\text{try}} - S_{\text{r,try}} s_{\text{try}}$. Goes to (10).

(10) Check the difference between net stresses from global analysis and local constitutive analysis, if $\left|\bar{p}^{(i)} - \bar{p}_{\text{try}}\right|$<$10^{-7}$: return the trial $S_{\text{r,try}}$ and the other obtained variables as the solution; otherwise, goes back to Step 5 with a halved interval in which the solution lies.

For problems where the modelling state transition is not necessary, a similar algorithm with some modifications (particularly regarding the simultaneous yielding condition, where $S^{\text{p}}_{\text{r,try}}$ should be evaluated as that of $v^{\text{p}}_{\text{try}}$) can be used.

Although the solution of S_{r} lies absolutely within the interval [0, 1], it is not wise to use [0, 1] as the initial interval in step 5. It is suggested to incorporate an incremental search before performing the bisection method. It consists of starting at $S^{(i-1)}_{\text{r}}$ and then making evaluations of $\bar{p}^{(i)} - \bar{p}_{\text{try}}$ at small increments across the region of [0, 1]. When the $\bar{p}^{(i)} - \bar{p}_{\text{try}}$ changes sign, a root should fall within the current increment, of which the S_{r} values at the beginning and the end can then serve as boundaries of the initial interval in step 5. This incremental search should be performed towards both directions (decreasing S_{r} for drying path and increasing S_{r} for wetting, here a distinction in the use of primary drying and wetting lines should also be made correspondingly) alternatively. The root closest to $S^{(i-1)}_{\text{r}}$ is deemed to be the solution wanted if multiple roots exist (although this is not common). It is found that real root is usually very close

to $S_r^{(i-1)}$ as illustrated by an example (Fig. 9.13), thus, with only one to a few times of incremental search the initial interval bounding the root can be identified.

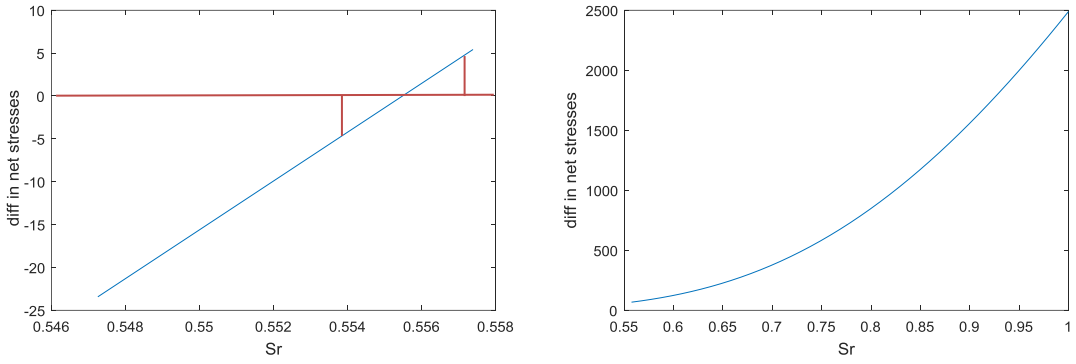

(a) (b)

Fig. 9.13 Example of determining the interval bounding the root

9.4.3 Reanalysing the mesoscale drying box test

The mesoscale drying box test is now reanalysed using UNSATCON-ML with the implemented GCM. Excepting for the constitutive model, all the other inputs, for example, the initial and boundary conditions are set to be same as those in the previous chapter. The adopted model parameters of GCM are presented in **Table 9.6**.

Table 9.6 Parameters of GCM

Parameters	λ	κ	λ_s	κ_s	k_1	k_2
Value	0.074	0.015	0.4	0	0.55	0.70
Parameters	R	N_0	Ω_{d0}			
Value	1.14	1.988	Calculated in the program			

The tailings is initially deposited with a high water content at fully saturation condition in the drying box. A significant amount of plastic volume change occurred before the tailings desaturated (S_r becomes less than 1). This will move the two PRLs (or initial SI and SD) to the right from an initial position. This initial PRLs are positioned by one of the constants, Ω_{d0} and Ω_{w0}, and the fixed distance, R, between them. The value of R measures the degree of hysteresis. Trial analyses suggest that parameters (Ω_{d0} or Ω_{w0}) have small values, but movement of PRLs in the log-scale indicates that the absolute rate of movement will increases at higher (modified)suction levels. A successful analysis depend highly on the value of Ω_{d0} or Ω_{w0}, which, however, seems to be difficult to determine from large-strain experiment data from initially slurry samples (where the PWP is positive), unlike the compacted soil where the GCM is usually applied. It is, fortunately, found by the author that their values can be analytically calculated from the air entry value and other determined model parameters (if determined *a priori*).

If the air entry value s_{AEV} and initial effective stress $p'_{initial}$ are known a priori, by the time suction reaches s_{AEV} the accumulated plastic change of volume can be computed as

$$v^p = (\lambda - \kappa)\ln\frac{p^*_{desaturation}}{p'_{initial}} = (\lambda - \kappa)\ln\frac{\bar{p} + s_{AEV}}{p'_{initial}} \tag{9.45}$$

The specific volume now is calculated as

$$v = v^0 - \lambda \ln\frac{\bar{p} + s_{AEV}}{p'_{initial}} \tag{9.46}$$

then, the current modified suction is

$$s^* = \frac{(v-1)s_{AEV}}{v} \tag{9.47}$$

The retention point ($s^* = s_{AEV}(v-1)/v$, $S_r = 1$) should be on the current drying PRL, i.e.

$$\boldsymbol{\Omega}_{d0} + k_2 m^{-1} v^p = \lambda_s \ln s^* + S_r = \lambda_s \ln \frac{(v-1)s_{AEV}}{v} + 1 \tag{9.48}$$

Rearranging Eq. (9.48) gives

$$\boldsymbol{\Omega}_{d0} = \lambda_s \ln \frac{(v-1)s_{AEV}}{v} + 1 - k_2 m^{-1} v^p \tag{9.49}$$

and the corresponding initial positions of wetting PRL, SI and SD can be also be calculated, for example,

$$s_D^{*,i} = \exp\left[\frac{\boldsymbol{\Omega}_{d0} - 1}{\lambda_s} - R\right] \tag{9.50}$$

It is found that this procedure has proved effective every time in determining the initial position of PRL for numerical analysis.

Fig. 9.14 compares modelled and measured pore water pressure from the first four layers of depositions (Daliri et al. 2016) using the GCM. Figure legends (not included here for clarity) are the same as those in Fig. 8.6.

By using GCM, the predicted pore water pressure are in a very good agreement with the measurements, as obtained using simpler log-linear retention model in previous chapter. So is the prediction of gravimetric water content. Note that, this results are obtained using the model parameters calibrated based on the measured PWP during first layer deposition. Fig. 9.14(c) shows that use of GCM underpredicts the void ratio as it decreases towards shrinkage limit. This is

attributed to assumption of $\kappa_s = 0$ for smooth state transition. Fig. 9.15 shows that paths of state parameters (plotted in corresponding planes) followed by the top element of bottom layer before depositing the 3rd layer. The measurements and predicted path using the model in previous chapter is also included in this figure. From the retention path, one can see that before the air entry value (around 80 kPa, corresponding to a modified suction of 35 kPa) the degree of saturation predicted using GCM is always equal to 1 with the assumption of $\kappa_s = 0$, unlike the log-linear model used in last chapter where a gentle slope is allowed. The predicted GWCs are the same regardless of the constitutive models adopted. For the given GWC, the void ratio bears an inverse relationship with degree of saturation according to $eS_r = wG_s$. Thus, use of GCM predicts a lower void ratio (overpredict the platic shrinkage) at the same suction level during initial drying of each deposition.

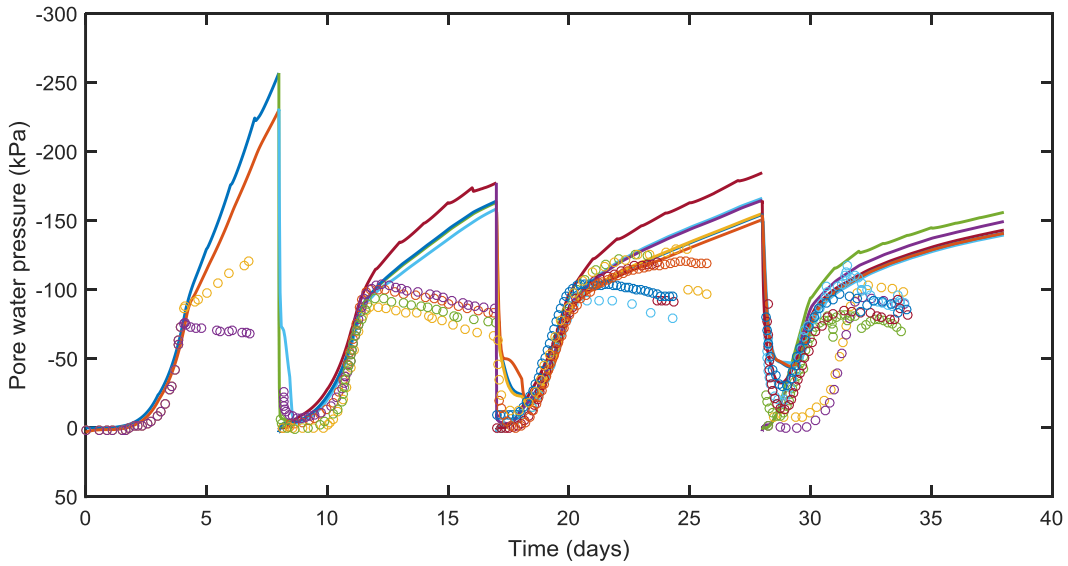

(a)

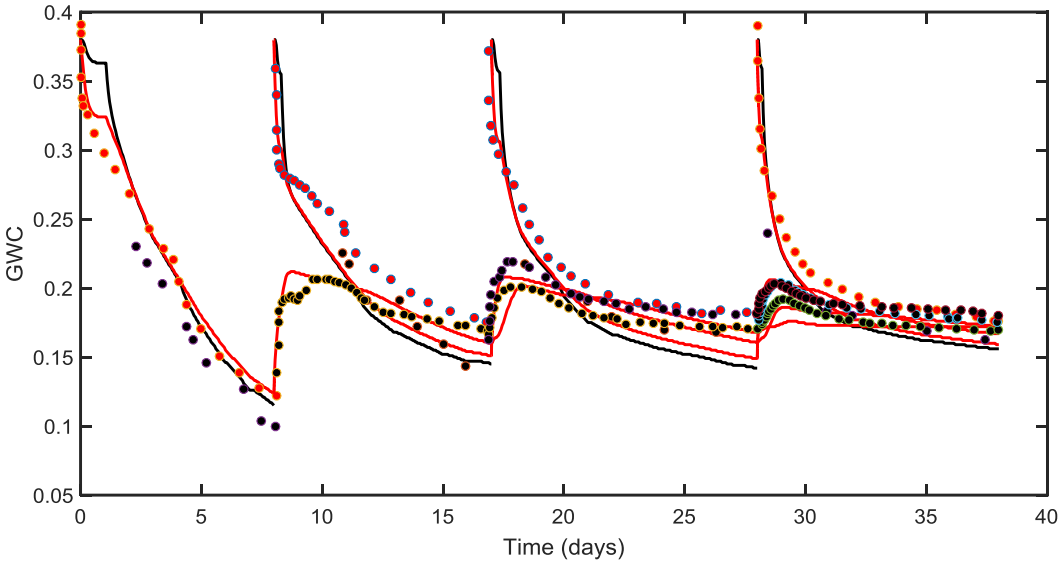

(b)

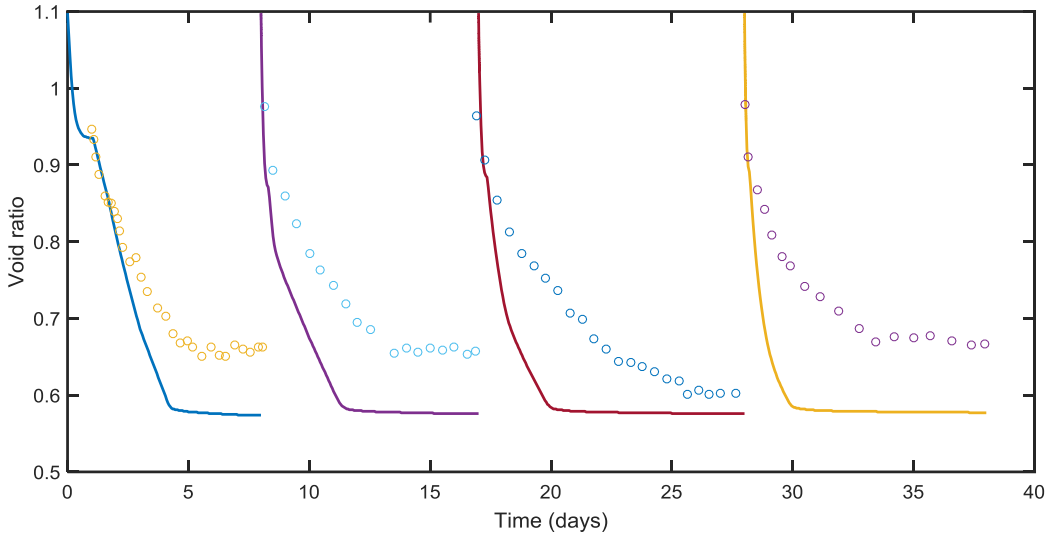

(c)

Fig. 9.14 Results from reanalysis of Daliri et al. (2016)'s case using GCM

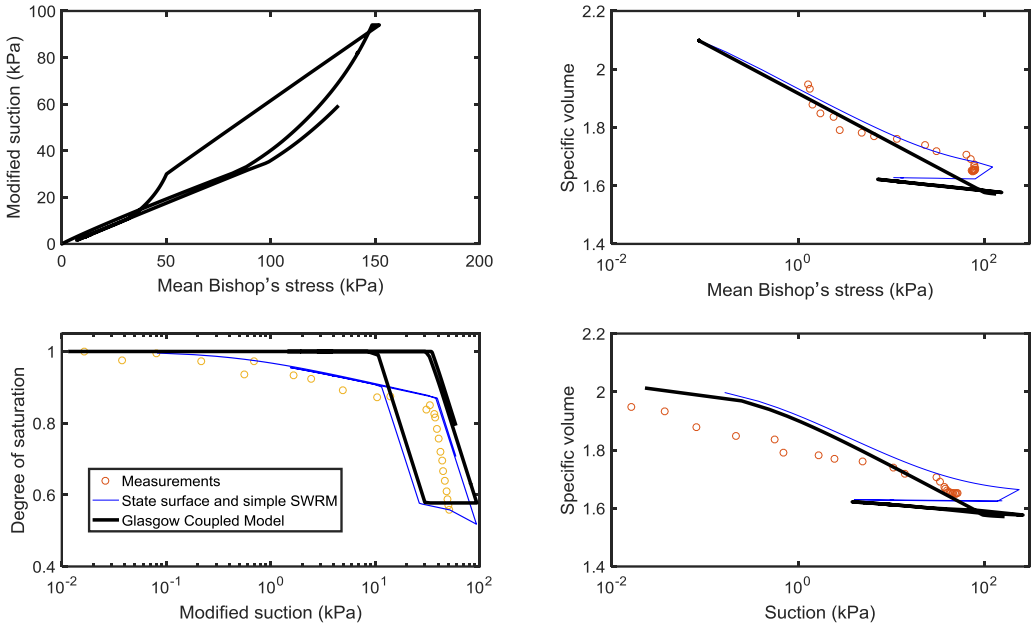

Fig. 9.15 Stress path followed by the top element of 1st layer using GCM, during first wetting and drying cycle (measurments are closer to the bottom of 1st layer).

Interestingly, it is found from the calculated virgin drying behavior (specific volume plotted against the suction) that GCM also predicts a shrinkage behaviour. Success of modeling the shrinkage behaviour here does not rely on the insignificant change of Bishop's stress as a result of decreasing S_r associated s increases (i.e. the resulting $S_r s$ product does not increase significantly). The shrinkage behaviour is modeled as an elastic compression for this case by GCM. This can be seen from the calculated stress path followed by the bottom element of first layer (another point here as an example illustration) and changes of position of SI, SD, LC, NCL and PRL (plotted in respective plane) over time before depositing 2nd layer (Fig. 9.16). First, the plastic consolidation at fully saturation condition causes the movement of PRL to the right (in the S_r-s*plane) and SI (SD) upward (in p*-s* plane), during this stage, only mechanical yielding occurs. At the point, the modified suction reaches the SI and there will be plastic decrease of S_r, causing the movements of LC to the right and NCL upwards, during this stage, yielding occurs both mechanically and hydraulically. Continuous drying induces a significant decrease of S_r, and upward movement of

the NCL, making the mechanical yielding more and more difficult to occur. Correspondingly, stress path moves always from the LC yielding curve in p^*-s^* plane, during this stage, only hydraulic yielding occurs, thus, the shrinkage behaviour is here modeled as an elastic compression with suction increase. The shrinkage behaviour has also been treated as a predominantly elastic compression in some other models that uses effective stress variable, e.g. the bounding surface model by Khalili et al. (2008), and elasto-plastic model by Zhou et al. (2012) which is also due to that preconsolidation (yielding) stress increases faster than the effective stress. But there are also some other models that treat the soil's volume shrinkage (very small amount of volume change) as an elasto-plastic processes, such as SFG (Sheng et al. 2008).

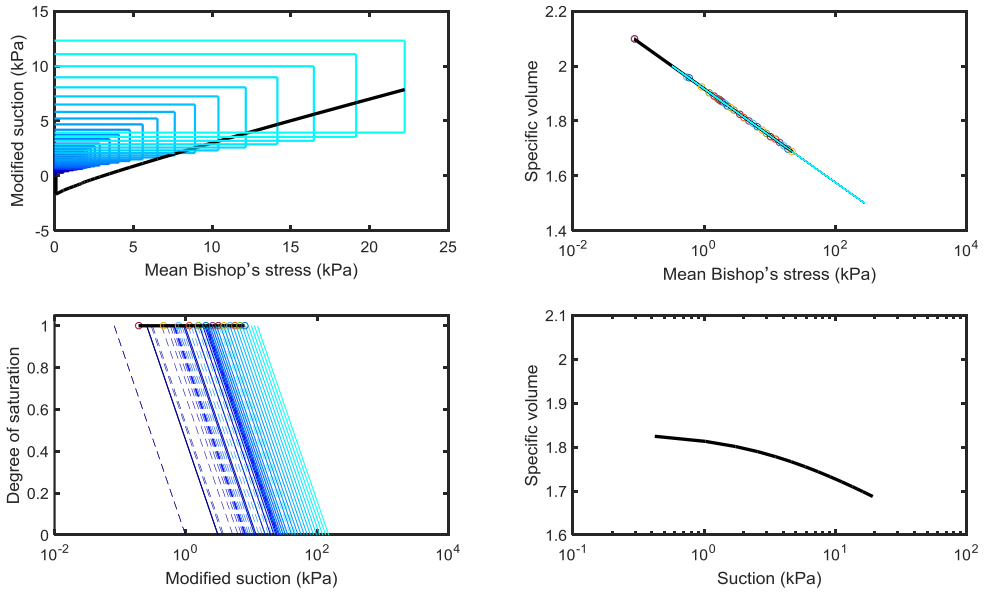

(a)

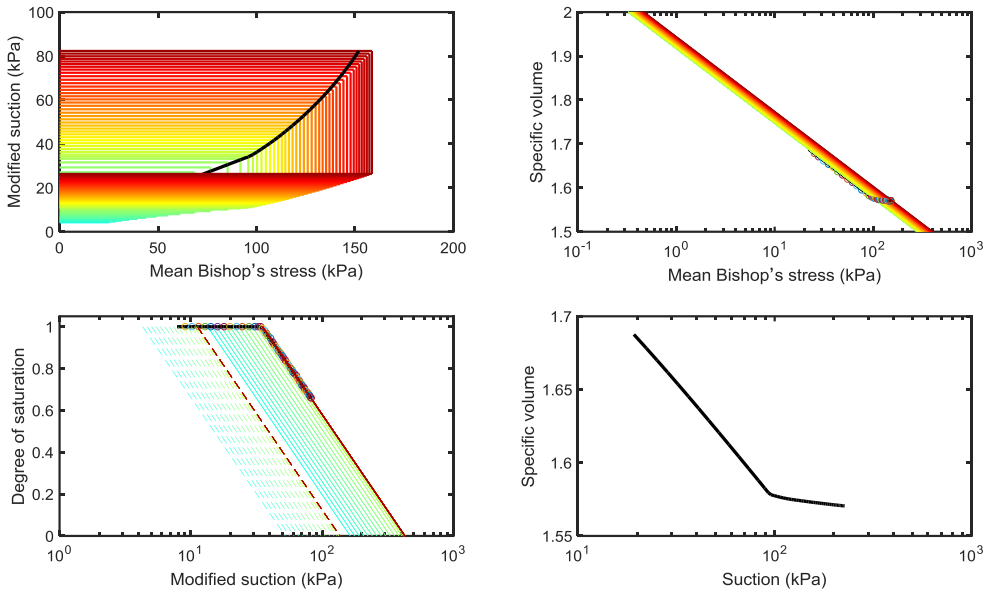

(b)

Fig. 9.16 Stress path followed by the bottom element of 1st layer using GCM and corresponding coupled movement of SI, SD, LC, NCL and PRL, during first drying.

The ability of GCM to predict some soil behaviour that is difficult to be simulated using traditional models are also reflected in this analysis, for example, the plastic compression has been accumulated during the drying-wetting cycles, even though the suction is not increased beyond the highest value to which the soil element has been subjected (see Fig. 9.17 and Fig. 9.18). This is modelled by the coupled movement of LC (i.e. the coupled movement of NCL) induced by hydraulic yielding, since the mechanical strain is only calculated according to the change of Bishop's stress (combined stress variable), unlike some other models using independent stress variables, the strain, particularly elastic strain, is explicitly separated into two parts associated with suction and net stress changes.

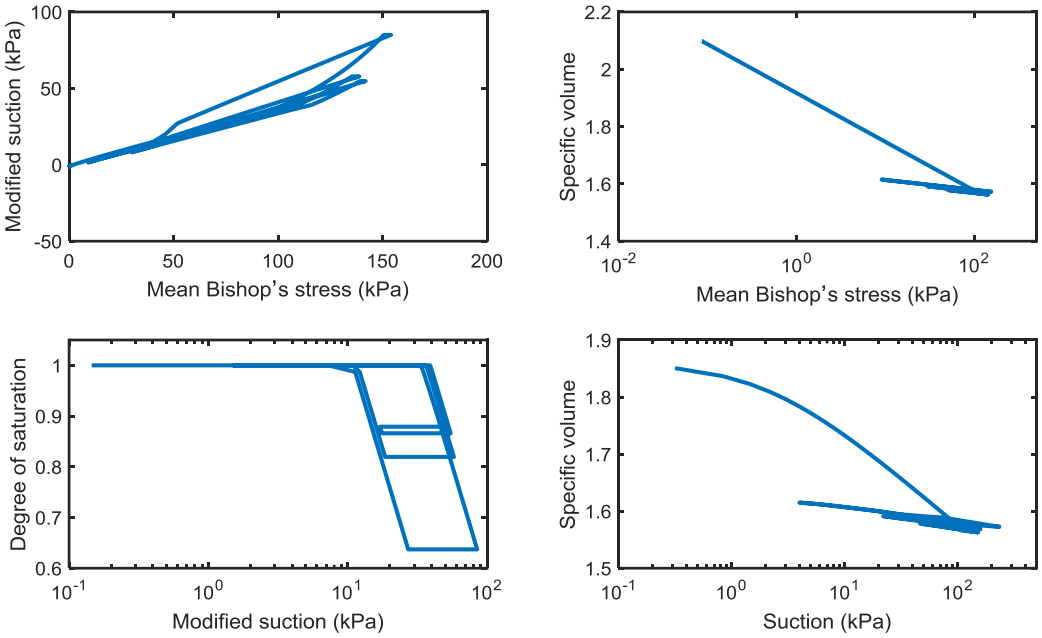

Fig. 9.17. The paths of state followed by soil element in the middle of bottom layer during first four layers deposition

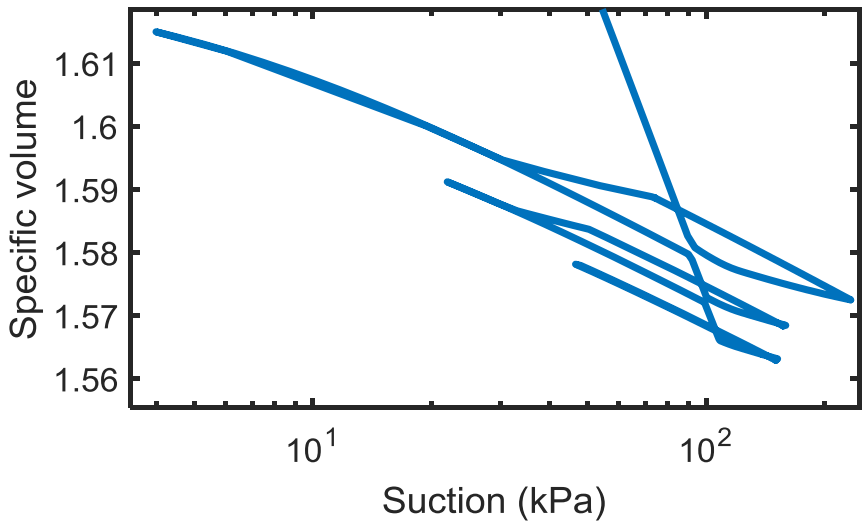

Fig. 9.18. Variation of specific volume plotted against the suction for the soil element in the middle of bottom layer

Since the GCM is formulated using Bishop's stress and modified suction (combination of several state variables), it would be intuitive to compare the predictions of degree of saturation and void ratio plotted against the (experimental) suction and net stress in respective plane or space (see Fig. 9.19) for interested readers who are more familiar with the use of net stress and suction. The variation of predicted profiles of S_r and s over time after each deposition are shown in Fig. 9.20.

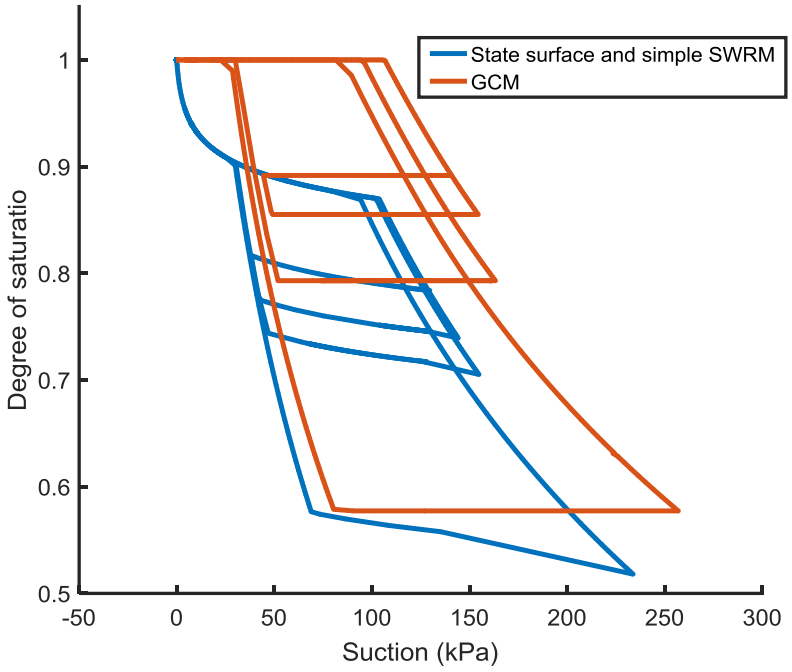
State surface and simple SWRM
GCM
Degree of saturatio
Suction (kPa)
1
0.9
0.8
0.7
0.6
0.5
-50
0
50
100
150
200
250
300

(a)

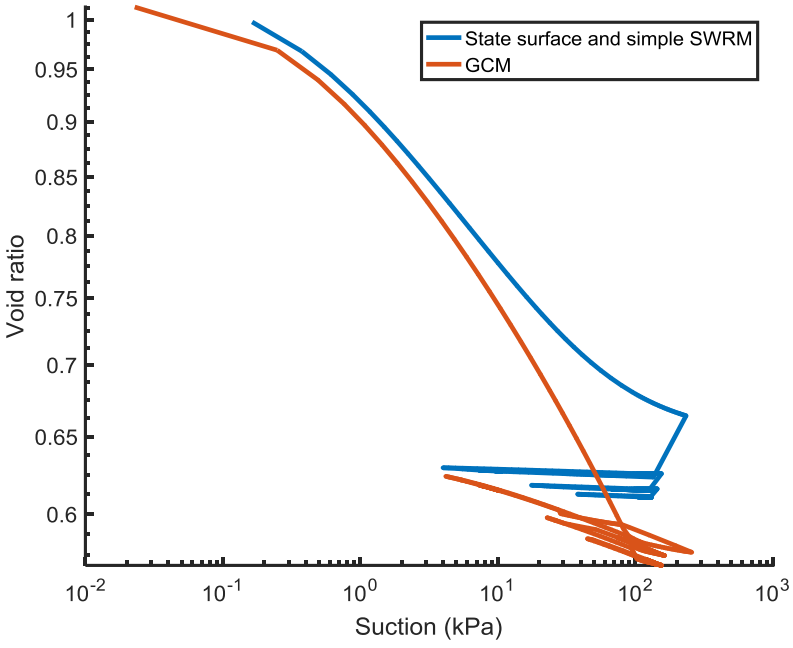
State surface and simple SWRM
GCM
Void ratio
Suction (kPa)
1
0.95
0.9
0.85
0.8
0.75
0.7
0.65
0.6
10-2
10-1
100
101
102
103

(b)

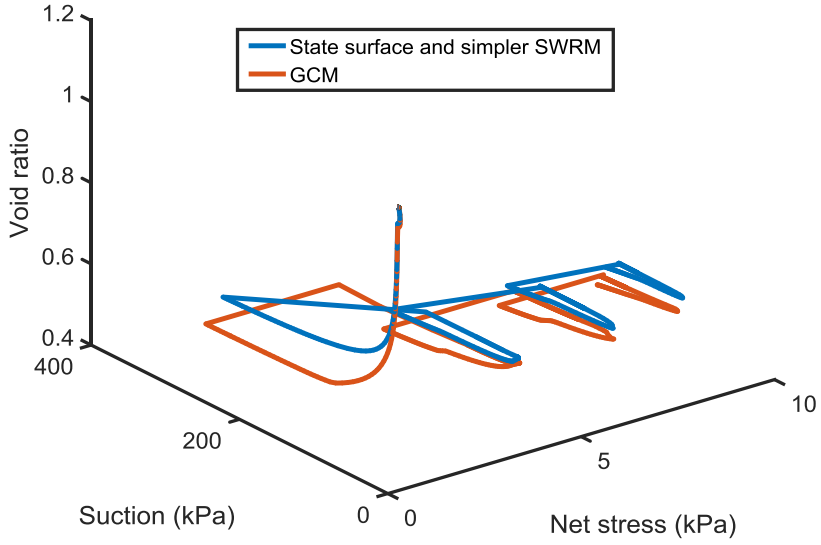

(d)

Fig. 9.19. The paths of state followed by one soil element in the middle of bottom layer during first four layer deposition

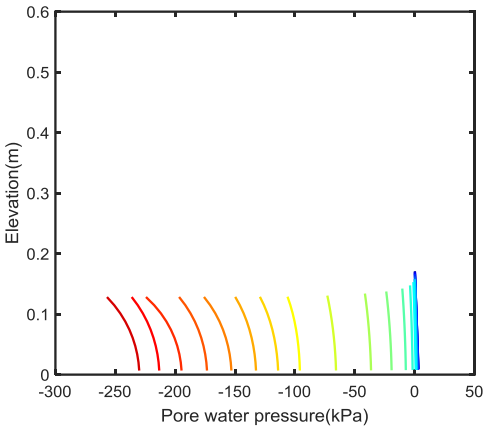
Elevation(m)
Pore water pressure(kPa)

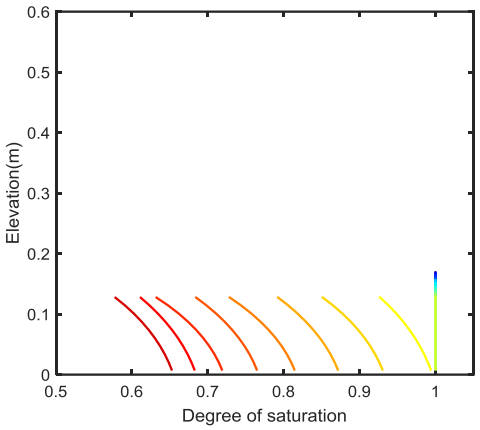
Elevation(m)
Degree of saturation

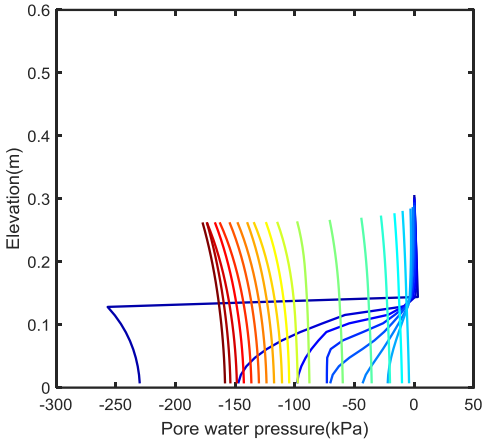
Elevation(m)
Pore water pressure(kPa)

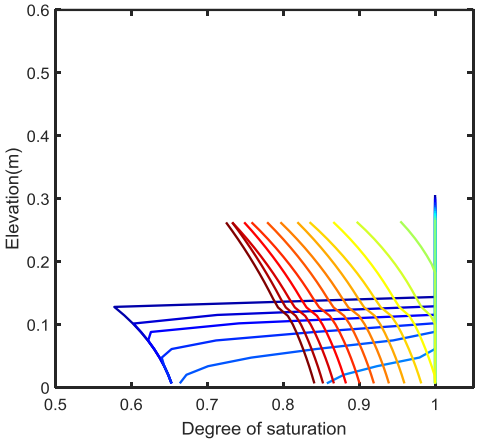
Elevation(m)
Degree of saturation

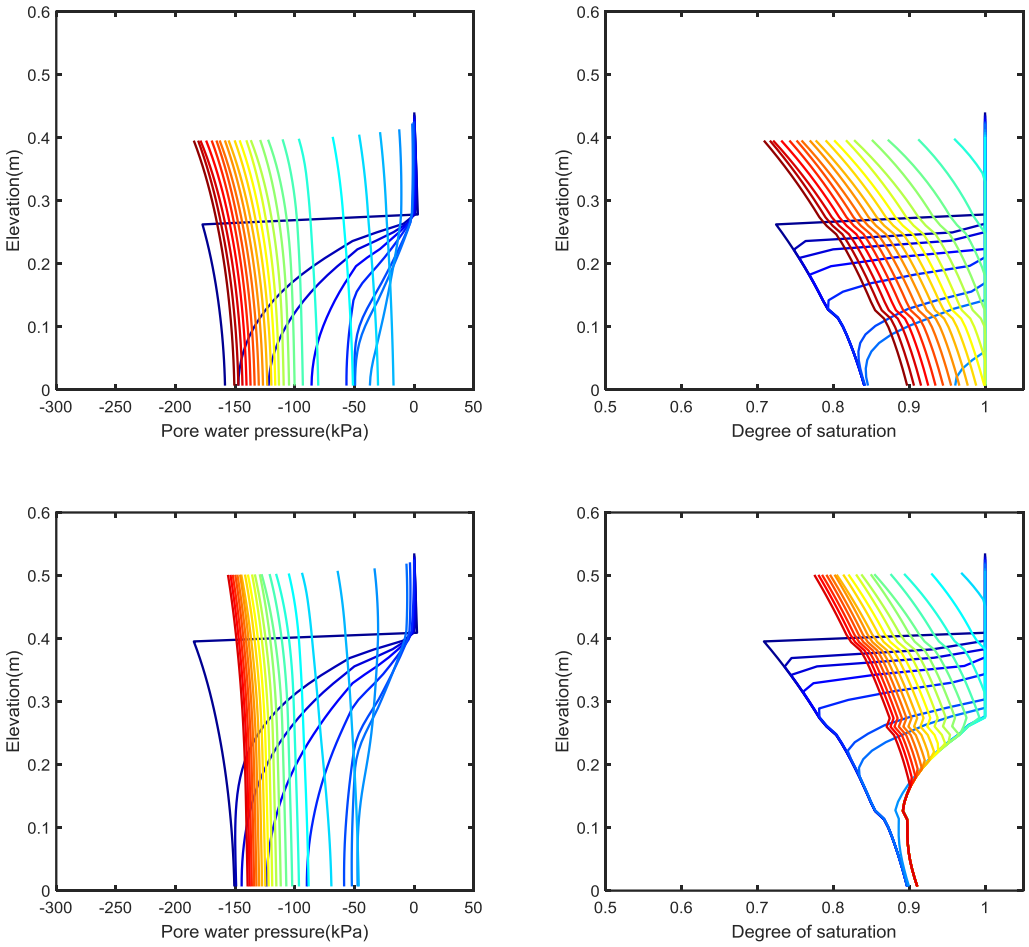

Fig. 9.20. The variation of predicted profiles of S_r and s over time after each deposition

9.5 Conclusion

The capacity of UNSATCON-ML has been enhanced through implementation of several constitutive model with sound theoretical basis, including a mechanical model-BBM (Alonso et al. 1990), a hydraulic model-bounding surface SWRM (Gallipoli et al. 2015), and a highly coupled model-GCM (Wheeler et al. 2003). An analytical form of GCM is derived in this chapter. The analytical nature of these models has been utilized for implementation into the numerical method.

The formulated algorithms performing local constitutive analyses for different models share common features as in Chapter 8: (1) finding other constitutive variables from the gravimetric water content and total/net stress, (2) high accuracy due to analytical nature, (3) strictly mass conservation, (4) bisection method dealing with non-smooth functions in some models and avoiding possible numerical instability. The drying box test (Daliri et al. 2016) on gold mining tailings is reanalysed using UNSATCON-ML with these newly implemented models. The ability and inability of different models to simulate some aspects of the unsaturated tailings behaviour are shown.

From these simulations, it can be seen that the BBM is not able to simulate the shrinkage behaviour of tailings subjected to virgin drying, which needs necessary modification in this plastic component. Compared to other model implemented into UNSATCON-ML, the GCM can simulate more unsaturated soils behaviours, including the shrinkage behaviour, wetting-induced collapse, and accumulation of plastic compression under cyclic suction changes. All these behaviours can be observed in the tailings in the multi-layer deposition. Thus use of GCM can provide a more complete quantification of the effects/benefits of multi-layer deposition, e.g. the densification of tailings subjected to cyclic suction changes. Further, the GCM requires lesser constitutive constants, which simulates most of the unsaturated soils' behaviour with its coupling mechanism. However, the GCM faces difficulties in simulating a gradual desaturation near the AEV, i.e. a gradual decrease in S_r with increasing s, and in simulating the retention behaviour when tailings tends to extremely dry conditions. These are attributed to the simple retention formulation adopted in GCM and puts a limit on the capacity of GCM in fully evaluating the performance of multilayer deposition of tailings. The SSM can simulate the tailings behaviour under a wider range of degree of saturation by using more soil constants. However, the SSM cannot simulate some behaviours

of unsaturated soils, e.g. accumulation of plastic compression under cyclic suction changes, due to its simple mechanical component. However, the advantages of different models can be combined to formulate improved version of these models for use in practice, e.g. (1) incorporating the influence of Sr on the mechanical model in SSM, (2) using a more flexible formulation for describing the retention behavior in GCM.

Glossary

Symbols

v	Specific volume
e	Void ratio
$\overline{p}$	Net mean stress
s	Suction
$\lambda(s)$	Stiffness parameter for changes in net mean stress for virgin states of the soil in BBM
$\lambda(0)$	Stiffness parameter for changes in net mean stress for virgin states of saturated soil in BBM
r	Parameter defining the maximum soil stiffness in BBM
β	Parameter controlling the rate of increase of soil stiffness with suction in BBM
p_{at}	Atmospheric pressure
p^c	Reference stress in BBM
$N(s)$	Specific volume at $p=p^c$ in BBM
κ_s	Elastic stiffness parameter for changes in suction
C	Constant related to location of the plastic surface in BBM
κ	Elastic stiffness parameter for changes in net mean stress in BBM
λ_s	Stiffness parameter for changes in suction for virgin states of the soil in BBM
N_κ	Constant related to location of the elastic surface in BBM
σ	Total stress
i	Time step
σ_0^*	Hardening parameters at saturated conditions in bisection method
e_s	Saturated void ratio in bisection method
e_m	Maximum void ratio in bisection method
w	Gravimetric water content
S_r	Degree of saturation
G_s	Specific gravity
$e_{m,s}$	Maximum void ratio at zero suction
b_d	Parameter governing drying between main surfaces in Gallipoli et al. (2015) model
b_w	Parameter governing wetting between main surfaces in Gallipoli et al. (2015) model
C_d	Constant of integration during drying paths in Gallipoli et al. (2015) model
C_w	Constant of integration during wetting paths in Gallipoli et al. (2015) model
m_d, λ_s, ω_d	Parameters of main drying surface in Gallipoli et al. (2015) model
m_w, λ_s, ω_w	Parameters of main wetting surface in Gallipoli et al. (2015) model
m, n, α	Parameters of water retention curve in van Genuchten (1980) model
$\bar{s}$	Scaled suction in Gallipoli et al. (2015) model

m, n, ϕ, ψ	Parameters of water retention surface in Gallipoli et al. (2003) model
p^*	Mean Bishop's stress
s^*	Modified suction
ε	Volumetric strain
$\varepsilon_v^{\mathrm{e}}$	Elastic volumetric strain
$\varepsilon_v^{\mathrm{p}}$	Plastic volumetric strain
$S_{\mathrm{r}}^{\mathrm{e}}$	Elastic change of degree of saturation
$S_{\mathrm{r}}^{\mathrm{p}}$	Plastic change of degree of saturation
n	Porosity
k_1	Coupling parameter for movement of LC yield curve in GCM
k_2	Coupling parameter for movements of SI and sd yield in GCM
s_{D}^*	Hardening parameter defining location of SD curve in GCM
s_{I}^*	Hardening parameter defining location of SI curve in GCM
p_0^*	Hardening parameter defining location of LC curve in GCM
κ	Parameter for elastic volumetric strains in GCM
κ_s	Parameter for elastic changes of degree of saturation in GCM
λ	Parameter for volumetric strains on LC curve in GCM
λ_s	Parameter for change of degree of saturation on SI or SD curves in GCM
N_κ	Integration constant for elastic volumetric strain in GCM in GCM
Ω_κ	Integration constant for elastic change of degree of saturation in GCM
N	Integration constant for plastic volumetric strain in GCM
$\Omega_{w.d}$	Integration constants for primary retention behaviour in GCM
v^{p}	Accumulated plastic volume change
N_0 , Ω_{w0} , Ω_{d0}	Three material constants determining the location of NCL and PRL in analytical GCM
i	Time step
$S_{\mathrm{r,y}}$	Yielding degree of saturation
v_{y}	Yielding specific volume
$[\bullet]_{try}$	Trial values of parameters in Bisection method
$[\bullet]_{\max,\min}$	Maximum or minimum Values of parameters in Bisection method
R	Measures the degree of hysteresis
v_0	Initial specific volume

Abbreviations

SWRM	Soil Water Retention Model
BBM	Barcelona Basic Model
GCM	Glasgow Coupled Model
LC	Load Collapse mechanical yield curve in BBM
SI	Suction Increase mechanical yield curve in BBM
AEV	Air Entry Value

PRL	Primary Retention Line in the analytical form of GCM
NCL	Normal Consolidation Line
GWC	Gravimetric Water Content
SSM	State Surface Model
SD	Hydraulic yielding curve for wetting in GCM
SI	Hydraulic yielding curve for drying in GCM

9.7 References

Alonso, E. E., Gens, A., & Josa, A. (1990). A constitutive model for partially saturated soils. Géotechnique, 40(3), 405-430.

D'Onza, F., Gallipoli, D., Wheeler, S., Casini, F., Vaunat, J., Khalili, N., ... & Pereira, J. M. (2011). Benchmark of constitutive models for unsaturated soils. Géotechnique, 61(4), 283-302.

Daliri, F., Simms, P., & Sivathayalan, S. (2016). Shear and dewatering behaviour of densified gold tailings in a laboratory simulation of multi-layer deposition. Canadian Geotechnical Journal, 53(8), 1246-1257

Delage, P., & Graham, J. (1996). Mechanical behaviour of unsaturated soils: understanding the behaviour of unsaturated soils requires reliable conceptual models. In PROCEEDINGS OF THE FIRST INTERNATIONAL CONFERENCE ON UNSATURATED SOILS/UNSAT'95/PARIS/FRANCE/6-8 SEPTEMBER 1995. VOLUME 3.

D'Onza, Francesca, S. J. Wheeler, Domenico Gallipoli, M. Barrera Bucio, M. Hofmann, M. Lloret-Cabot, A. Lloret Morancho et al. "Benchmarking selection of parameter values for the Barcelona basic model." Engineering Geology 196 (2015): 99-118.

Gallipoli, D., Bruno, A. W., D'Onza, F., & Mancuso, C. (2015). A bounding surface hysteretic water retention model for deformable soils. Géotechnique, 65(10), 793-804.

Gallipoli, D., D'Onza, F., & Wheeler, S. J. (2010). A sequential method for selecting parameter values in the Barcelona basic model. Canadian Geotechnical Journal, 47(11), 1175-1186.

Gallipoli, D., Wheeler, S. J., & Karstunen, M. (2003). Modelling the variation of degree of saturation in a deformable unsaturated soil. Géotechnique., 53(1), 105-112.

Khalili, N., Habte, M. A., & Zargarbashi, S. (2008). A fully coupled flow deformation model for cyclic analysis of unsaturated soils including hydraulic and mechanical hystereses. Computers and Geotechnics, 35(6), 872-889.

Lloret-Cabot, M., Wheeler, S. J., & Sánchez, M. (2017). A unified mechanical and retention model for saturated and unsaturated soil behaviour. Acta Geotechnica, 12(1), 1-21.

Potts, D. M., & Ganendra, D. (1994). An evaluation of substepping and implicit stress point algorithms. Computer methods in applied mechanics and engineering, 119(3-4), 341-354.

Sheng, D., Fredlund, D. G., & Gens, A. (2008). A new modelling approach for unsaturated soils using independent stress variables. Canadian Geotechnical Journal, 45(4), 511-534.

Tsiampousi, A., Zdravkovic, L., & Potts, D. M. (2013). A three-dimensional hysteretic soil-water retention curve. Geotechnique, 63(2), 155.

Van Genuchten, M. T. (1980). A closed-form equation for predicting the hydraulic conductivity of unsaturated soils. Soil science society of America journal, 44(5), 892-898.

Vu, H. Q., & Fredlund, D. G. (2006). Challenges to modelling heave in expansive soils. Canadian Geotechnical Journal, 43(12), 1249-1272.

Wheeler, S. J., & Karube, D. (1996). Constitutive modelling. In PROCEEDINGS OF THE FIRST INTERNATIONAL CONFERENCE ON UNSATURATED SOILS/UNSAT'95/PARIS/FRANCE/6-8 SEPTEMBER 1995. VOLUME 3.

Wheeler, S. J., Gallipoli, D., & Karstunen, M. (2002). Comments on use of the Barcelona Basic Model for unsaturated soils. International journal for numerical and analytical methods in Geomechanics, 26(15), 1561-1571.

Wheeler, S. J., Sharma, R. S., & Buisson, M. S. R. (2003). Coupling of hydraulic hysteresis and stress–strain behaviour in unsaturated soils. Géotechnique, 53(1), 41-54.

Zhang, X., & Lytton, R. L. (2009). Modified state-surface approach to the study of unsaturated soil behavior. Part I: Basic concept. Canadian Geotechnical Journal, 46(5), 536-552.

Zhang, X., & Lytton, R. L. (2009). Modified state-surface approach to the study of unsaturated soil behavior. Part II: General formulation. Canadian Geotechnical Journal, 46(5), 553-570.

Zhang, X., & Xiao, M. (2013). Using modified state surface approach to select parameter values in the Barcelona basic model. International Journal for Numerical and Analytical Methods in Geomechanics, 37(12), 1847-1866.

Zhou, A. N., Sheng, D., Sloan, S. W., & Gens, A. (2012). Interpretation of unsaturated soil behaviour in the stress–Saturation space, I: Volume change and water retention behaviour. Computers and Geotechnics, 43, 178-187.

Chapter 10 Hypothetical field case analysis of tailings deposition

The development of UNSATCON-ML are described in the previous chapters, including the formulation of fundamental numerical techniques and implementation of several unsaturated soils models. Testing of UNSATCON-ML against laboratory data from the column and drying box tests shows its promising feature for application in the field. In this chapter, UNSATCON-ML is used to carry out a number of hypothetical field case analyses, selected results are presented with several important implications to the optimization of deposition scheme in the tailings management industry.

10.1 Introduction

Development of UNSATCON-ML initiated with a piece-wise linear formulation for large strain consolidation of fully saturated soils in chapter 6, where the practical three-dimensional state surface models (SSM) for unsaturated soils are implemented . Subsequent testing of the program in chapter 7 illustrated the successful improvements adequate and necessary for analysis of large strain consolidation coupled with unsaturated flow in single layer deposits. Extension based on SSMs to simulate irrecoverable volume change and hydraulic hysteresis of unsaturated soils are presented in chapter 8, where the entire structure of program is also upgraded including attributes to simulate multilayer depositions. Chapter 9 presented the enhancements of the UNSATCON-ML with several advanced unsaturated constitutive models. Now, in this chapter, a number of

hypothetical field case analyses are carried out using UNSATCON-ML. Two types of tailings, including the oil sands and hard rock tailings, are considered to fabricate these hypothetical deposition schemes. The outcomes from UNSATCON-ML are abundant and fruitful, this chapter presents selected results that illustrates the ability of this program and that are of concern to the industry practice. Results are also compared and discussed regarding several important considerations in optimizing the deposition schemes, for example, the influence of deposition time (season), benefits of multi-layer deposition, particularly, from the drying/desiccation history.

10.2 Hypothetical case analyses of oil sands tailings deposits

10.2.1 Material properties and boundary condition

The oils sands tailings' constitutive parameters are selected based on the study presented in Chapter 7, where both column test and field trial has been analyzed (but only for single layer deposition). The predicted variation of solid content profiles at several elapsed time within the field trial deposit (which was an initially 4.1 m thickness deposit) showed a very good agreement with the field data, which are replotted here (Fig. 7.13 in chapter 7), see Fig. 10.1. After the evaporation exerted effectively on the deposits, the predicted near-surface solid content increased gradually due to dewatering by evaporation, and an unsaturated zone formed and advanced to an elevation of around 2.5 m.

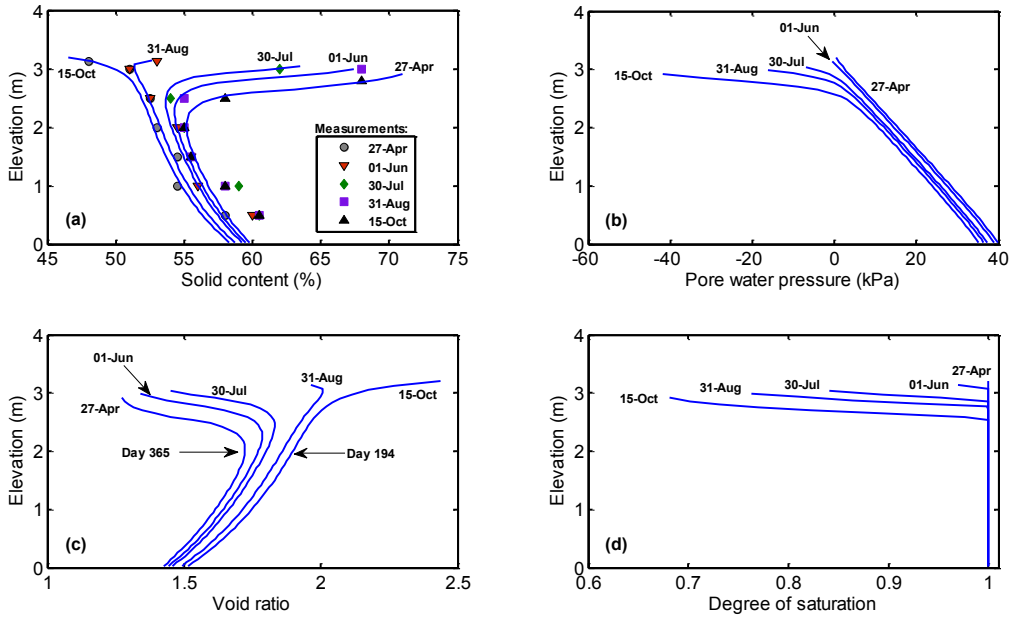

Fig. 10.1. Replotting Fig. 7.13 in chapter 7: Results of UA at different times in 2013: (a) solid content compared with field data, (b) pore water pressure, (c) void ratio profile, (d) degree of saturation profile

The constitutive model adopted in Chapter 7 was the state surface model proposed by Vu and Fredlund (2006), which is found to be very flexible to fit the consolidation data with high compressibility at very low stress level, as the case of oil sands tailing with high initial void ratio. The constitutive parameters are presented in Table 10.1. In this chapter this surface is used to describe the virgin drying/compression (elasto-plastic) volume change behaviour. An elastic surface as defined in Chapter 8 (same as the one in BBM) is added to describe the elastic volumetric behaviour, the assumed two slopes of the elastic surface with respect to suction and net stress are also given in Table 10.1. And water retention behaviour is described using the simple practical void ratio-dependent degree of saturation vs. suction relationship including the hydraulic hysteresis (as defined in Chapter 8). The hydraulic conductivity is described using van Genuchten

model combined with the power law considering the void ratio-dependency (as defined in Chapter 8). Constitutive parameters used for hydraulic conductivity and retention model are also summarized in Table 10.1.

A simple boundary condition is assumed to be consistent with that back-calculated from the field trial in chapter 7, that is, 2mm/day evaporation is applied during every summer (from 5th May to 1st October), and zero flux is applied during the remaining time with each year on the top surface of the fresh layer tailings. Note during the summer the desaturation can occur only when the evaporation rate is higher than rate of water flowing to the top due to self-weight. When the rate of water flowing to the top due to self-weight is higher than the evaporation rate, the remaining water after consumption by evaporation is automatically removed. Zero flux is applied at the bottom of the bottom-layer tailings. The initial condition is also the same as the column test studied in section 7.3 in chapter 7, that is, saturated tailings are deposited at a very loose state with high void ratio of 4.0. The specific gravity of these tailings is 2.12.

Table 10.1. Oil sands tailing parameters based on study in chapter 7

Volume change behaviour								
Parameters	a	b	c	d	f	g	κ	κ_s
Value	4.50	7.80E-01	7.56E-03	1.36E-01	1.62E+03	2.17E+03	0.015	0.0015
Water retention behaviour								
Parameters	C_{drying}	$C_{wetting}$	λ_{se}	λ_{sr}	κ_{ss}			
Value	2.65	2.5	0.4	0.5	0.04			
Hydraulic conductivity								
Parameters	H_1	H_2	M					
Value	17.5E-11	8	0.75					

10.2.2 The influence of deposition season

This first group of hypothetical field deposition analyses are conducted to study the effect of deposition season: is deposition starting from winter (referred to as winter deposition) more

effective in terms of using evaporation to dewater the tailings, compared to summer deposition (standing for deposition starting from summer). For each case (winter deposition and summer deposition), eight subcases are considered: seven multilayer depositions and one single layer deposition over one year. Table 10.2 summaries all 8 subcases for summer deposition. Winter deposition means that tailings are deposited starting from 1st October with all the same subcases. The total deposited tailings (the mixture of tailings solid and water, with void ratio of 4.0) are 2.4 m in thickness for all subcases, which is distributed equally over one year. For example, the subcase 1 in Table 10.2 means that 10 cm thickness of tailings is deposited every half month, with a total of 24 depositions. In total, 16 subcases of deposition scheme are analysed.

Fig. 10.2 compares the variation of overall GWC (within the tailings) over one year from winter deposition to those from summer deposition for each subcase. For the most frequent deposition schemes (24 (number of deposition) × 10 cm (Deposition thickness per time), summer deposition results in a significantly lower GWC during the first half of the year, which is obviously due to atmospheric drying force. The winter deposition can just use the self-weight to dewater the tailings during the first half of the year. During the last half of the year, the overall GWC decreases for the winter deposition (due to evaporation) and increases for summer deposition (dewatering relies on self-weight only), at the end of this year the overall GWC is comparable between winter and summer scheme for this subcase.

Difference in the final overall GWC can be seen for less frequent deposition schemes. For example, for single-layer deposition scheme, the initial dewatering rate is essentially the same, until the rate of water flowing to top (due to self-weight) cannot satisfy the evaporation (evaporation is not used to dewater the tailings for summer deposition, recall the top boundary condition described in the previous section). At the last half of year, the evaporation exerts a

continuous influence on the tailings for winter deposition, which results in a much lower GWC at the end. The single-layer winter deposition produces the lowest overall GWC at the end of this year compared to all other cases since both forces (self-weight and evaporation) have been fully used to dewater the tailings for this case. For this case, most of the water is first removed by self-weight (the thickest case) consolidation during winter season, during the subsequent summer, self-weight consolidation is almost finished (rate of water flowing to the top is close to zero), and evaporation can exert a influence until the end of this year.

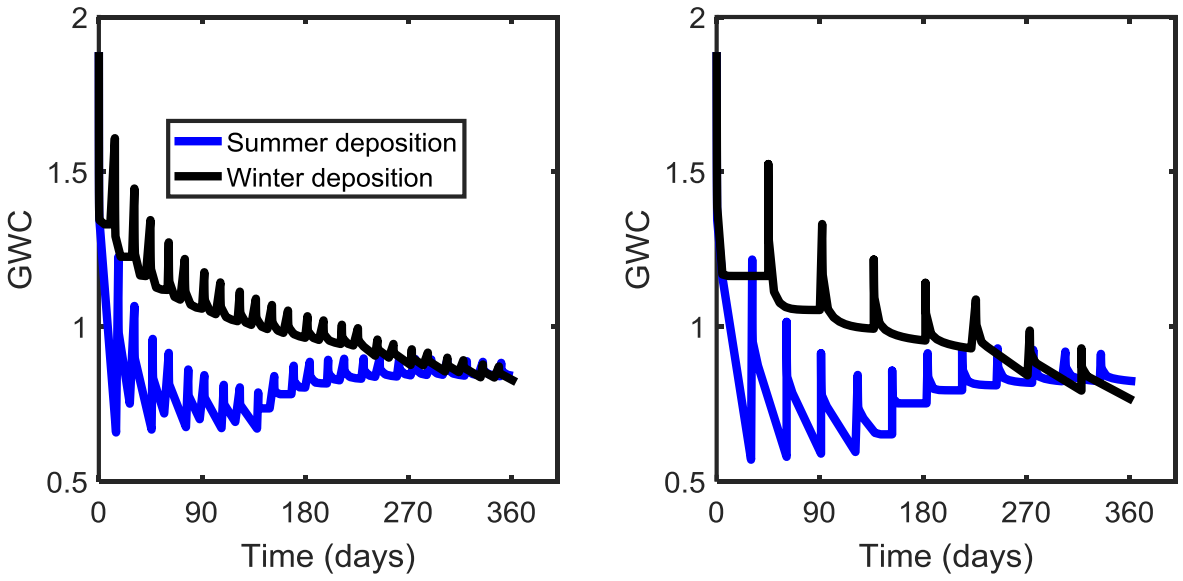

(a) (b)

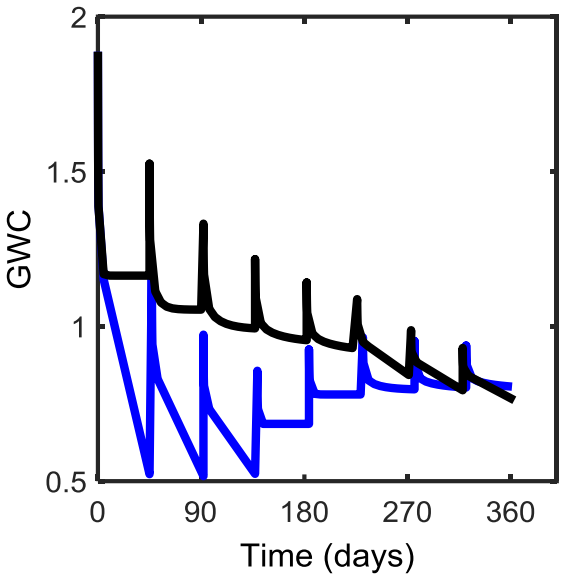
GWC
Time (days)
0
90
180
270
360
0.5
1
1.5
2

(c)

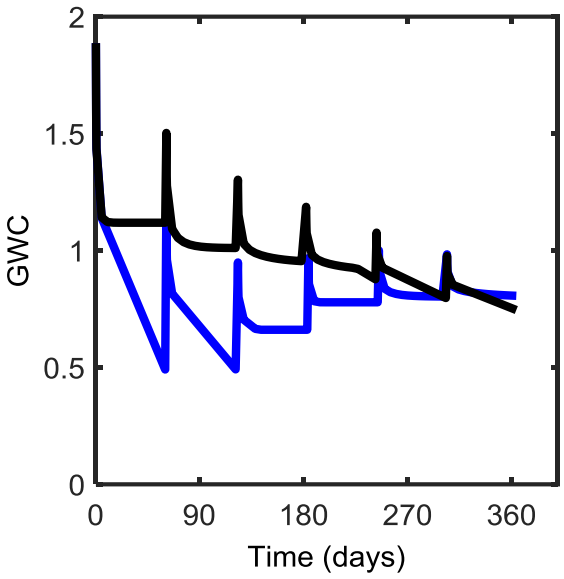
GWC
Time (days)
0
90
180
270
360
0
0.5
1
1.5
2

(d)

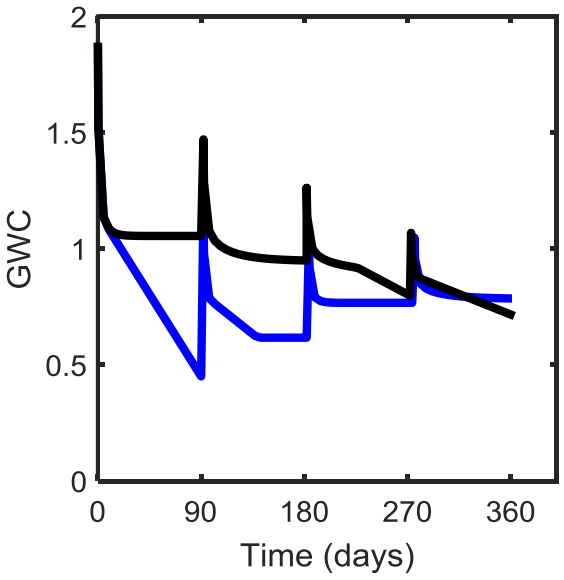
GWC
Time (days)
0
90
180
270
360
0
0.5
1
1.5
2

(e)

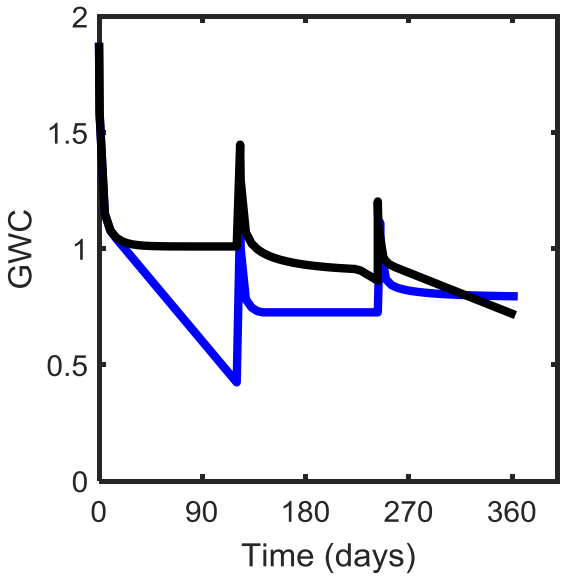
GWC
Time (days)
0
90
180
270
360
0
0.5
1
1.5
2

(f)

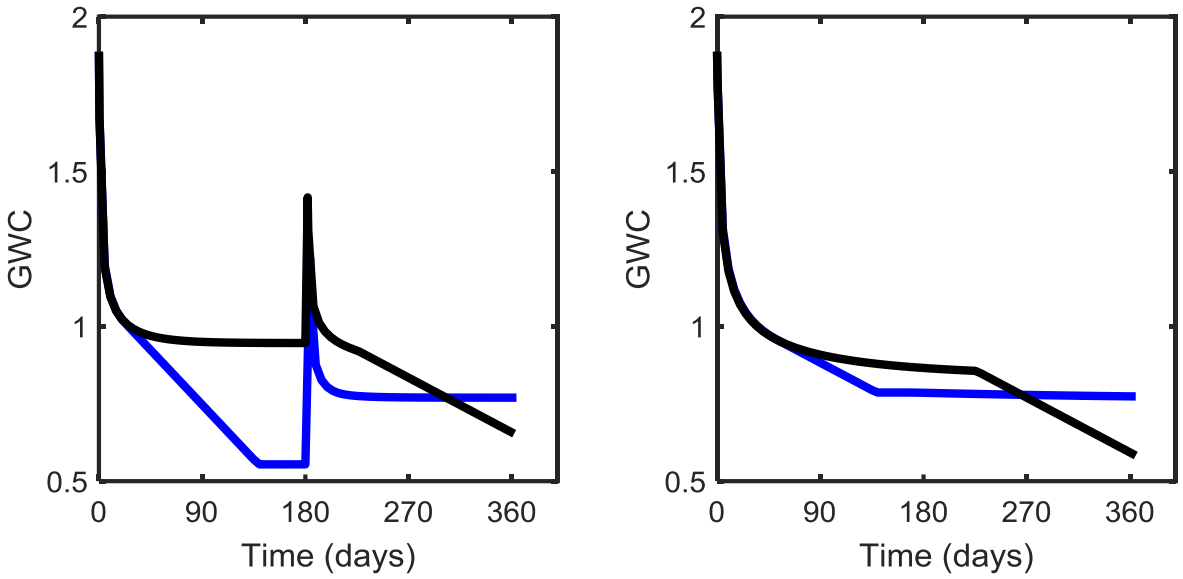

(g) (h)

Fig. 10.2 the variation of overall GWC over one year from winter deposition to summer deposition for each subcase

Table 10.2. Short-term (1 years) deposition scheme (starting from summer)

	Deposition date			Deposit thickness (cm)							
Evaporation (mm/day)	Y	M	D	Deposit scheme							
				1	2	3	4	5	6	7	8
2	2016	5	15	10	20	30	40	60	80	120	240
	2016	6	1	10							
	2016	6	15	10	20						
	2016	7	1	10		30					
	2016	7	15	10	20		40				
	2016	8	1	10							
	2016	8	15	10	20	30		60			
	2016	9	1	10							
	2016	9	15	10	20		40		80		
0	2016	10	1	10		30					
	2016	10	15	10	20						
	2016	11	1	10							
	2016	11	15	10	20	30	40	60		120	
	2016	12	1	10							
	2016	12	15	10	20						
	2017	1	1	10		30					
	2017	1	15	10	20		40		80		
	2017	2	1	10							
	2017	2	15	10	20	30		60			
	2017	3	1	10							
	2017	3	15	10	20		40				
	2017	4	1	10		30					
	2017	4	15	10	20						
	2017	5	1	10							
Total thickness (cm)				**240**	**240**	**240**	**240**	**240**	**240**	**240**	**240**

10.2.3 The influence of multi-layer deposition

This group of hypothetical field case analyses are conducted to evaluate the influence of multi-layer deposition on the performance of tailings over a longer period of time (10 years). Since winter deposition is comparatively more effective in dewatering tailings from previous section, winter deposition is used for the majority of subcases in this group. That is only one deposition at the start of each winter per year over 10 years. Table 10.3 summarises the analysed subcases in this group. Seven different deposition thickness (varying from 0.6 m to 2.4 m) per year are considered, the deposited tailings are 6 m to 24 m in thickness in total over 10 years. For comparison, single layer depositions (one deposition at the beginning of 1st year) for each thickness are also analysed. In total, 14 subcases of deposition scheme are analyzed.

The ultimate goal of tailings management is to get a sufficient strength/stiffness for reclamation of tailings impoundments, thus a denser tailings profile would be always preferable, which is expected to be obtained by optimizing the deposition scheme. Fig. 10.3 and Fig. 10.4 shows the final (at the end of 10 years) void ratio profiles calculated by UNSATCON-ML for multiple and single layer deposition, respectively. The comparative effectiveness between multi and single layer depositions differs for different deposition thicknesses, so does the shape of the final void ratio profiles.

For cases with thicker layer deposit (greater than 1.5 m) per year, it can be seen that denser (stronger) and looser (weaker) layers alternatively formed along the depth during multiple layer deposition case, this type of non-uniform profile is attributed to the drying/desiccation effect exerted on the upper part of tailings layer every year. For the corresponding single layer deposition (greater than 15 m thickness), only a continuous portion of tailings near the surface has been

affected by evaporations during the 10 years, see Fig. 10.5(a)(b)(c). A significant portion below has a higher void ratio (consolidation mainly relies on self-weight).

Table 10.3. Long-term (10 years) deposition scheme

Deposition scheme		**Total thickness (m) = Deposition thickness per time (m)×Depositing time**						
Single layer deposition	Only 1 deposition during 10 year	6.0×1	8.0×1	10.0×1	12.0×1	15.0×1	20.0×1	24.0×1
Multiple layer deposition	**1 deposition per year over 10 years**	0.6×10	0.8×10	1.0×10	1.2×10	1.5×10	2.0×10	2.4×10
	Multiple layer deposition within each year, 0.3 m per deposition				0.3×40			0.3×80
	Multiple layer deposition within each year, 0.6 m per deposition				0.6×20			0.6×40
Total thickness (m)		**6**	**8**	**10**	**12**	**15**	**20**	**24**

For two cases with relatively medium thickness (1.0 m and 1.2 m) per year, a more uniform denser profile has been produced, since the evaporation is able to have more or less influence on the entire layer deposited each year. For the corresponding single layer depositions with 10 m and 12 m thicknesses, only the portion of tailings near the surface has been affected by evaporation during the 10 years, see Fig. 10.5(c) and (d). A significant amount of portion below has a higher void ratio (consolidation mainly relies on self-weight), which are similar to those with thickener single layer deposition. For the deposits with thickness greater than 1.0 m, single layer deposition is less effective than multilayer deposition in terms of overall dewatering, as can seen from the comparison in see Fig. 10.5 (a),(b)(c) and (d). This is because (1) evaporation is limited to a certain depth, and (2) the effect of self-weight is also restricted by the long drainage path.

As the thickness of deposit decreases further, it seems that multilayer-deposition gradually turns out to be less effective than single layer deposition (see Fig. 10.5(f) for 0.6m per year), this is because that the self-weight during multilayer deposition is applied for a shorter time and cannot be effectively used for consolidation, which primarily depends on the evaporation. For single layer deposit of 6 m thickness, self-weight is applied for a longer period and can be effectively used with a relatively short drainage path, evaporation can also have an influence on the overall profile.

Comparatively, the subcases with 1.0 m and 1.2 m thick of tailings deposited per year is more effective than the other cases, in terms of obtaining a denser profile. This is not only due to that both self-weight and evaporation for these two cases can be more efficiently used for dewatering, but also a different hydraulic interlayer interaction:

(a) After each deposition, the unsaturated zone near the surface of the underlying layer provides some room for dissipation of newly generated PWP in the tailings below, where void ratio decreases further.

(b) More importantly, the new layer will dewater faster due to the existence of underlying desiccated layer, and then the new unsaturated zone induced by evaporation can be more easily connected to the old unsaturated zone within underlying tailings. This connection can further help to dewater the saturated tailings below. The can be seen from Fig. 10.6 and Fig. 10.7 present the variation of profile over time during the deposition process. In Fig. 10.6 and 10.7, each line represents the depth profile of the state parameter, e.g. *e*, in respective subplot at a specific elapsed time. From initial to final states during each deposition, each line is designated with different color from Blue to Red. During the first half day after each deposition, a higher temporal resolution is used to plotting these profiles, including 10 profiles evenly distributed over time. After that, a lower temporal resolution is used to plotting these profiles, with a time interval of 5 days after Day 5.

As a supplementary, several subcases of multiple depositions within each year are analyzed, which are summarized correspondingly in Table 10.3. Fig. 10.8 compares the void ratio profiles after 10 years from these multiple layer deposition (also including one deposition per year) and single layer deposition. It seems that one deposition per year remains the most effective scheme; this is because that the evaporation is offset by the upward flow of water due to self-weight consolidation for cases with more than one deposition within year, such as those deposited in the summer.

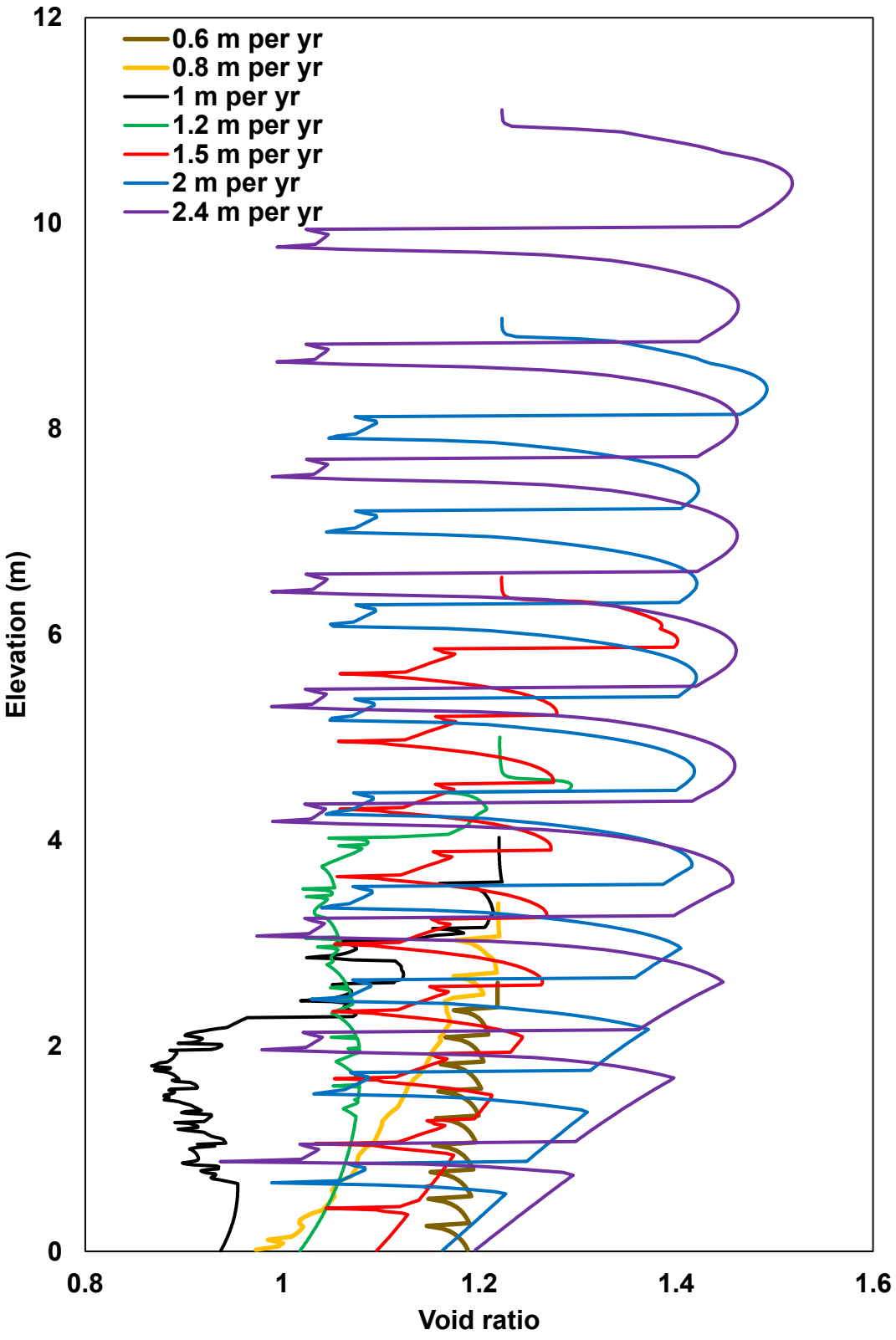

Fig. 10.3 The void ratio profiles calculated by UNSATCON-ML for multiple layer deposition

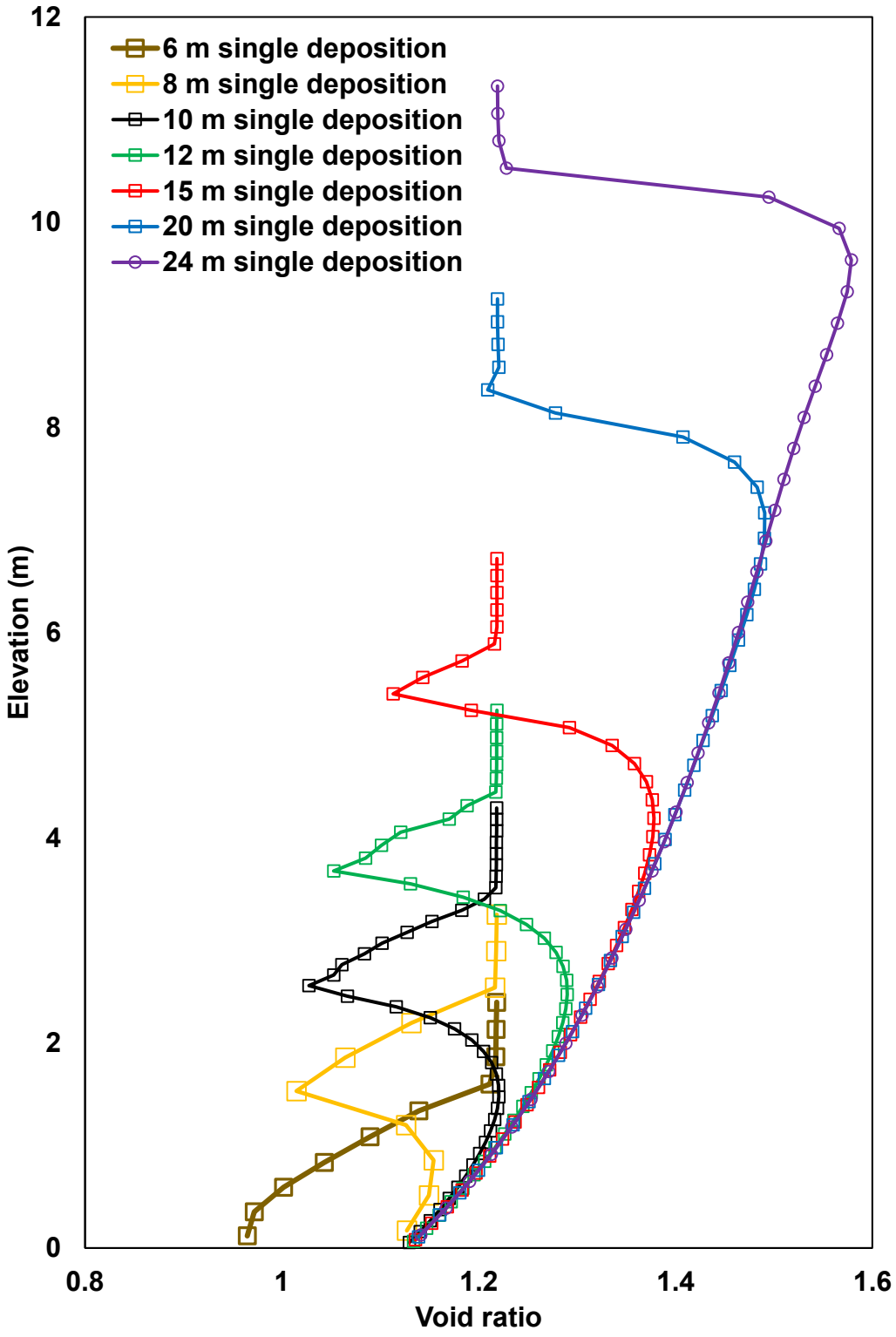

Fig. 10.4 The void ratio profiles calculated by UNSATCON-ML for single layer deposition

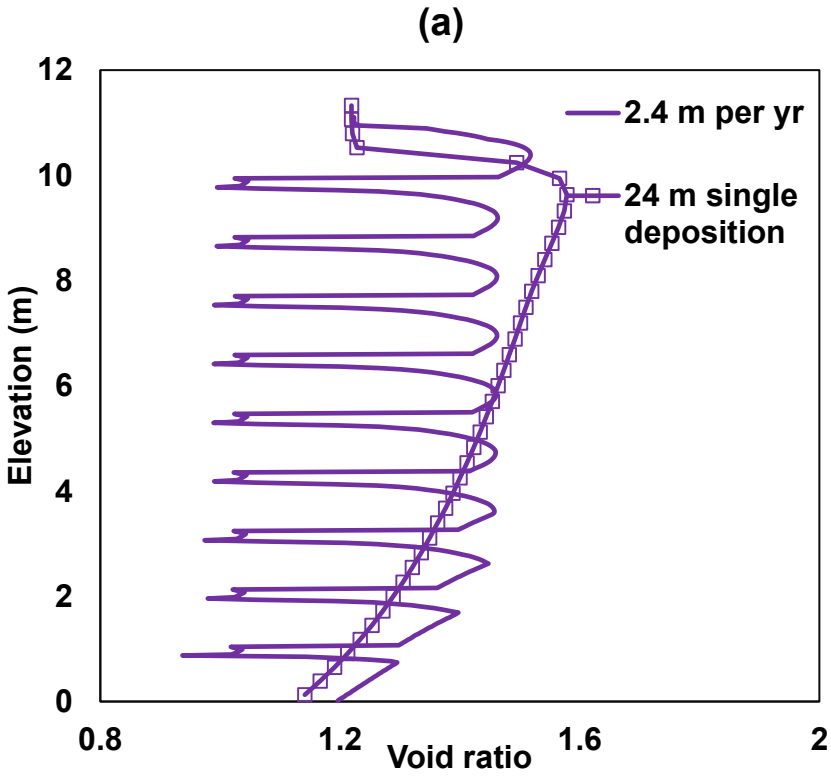
(a)
12
10
8
6
4
2
0
Elevation (m)
0.8
1.2
1.6
2
Void ratio
2.4 m per yr
24 m single deposition

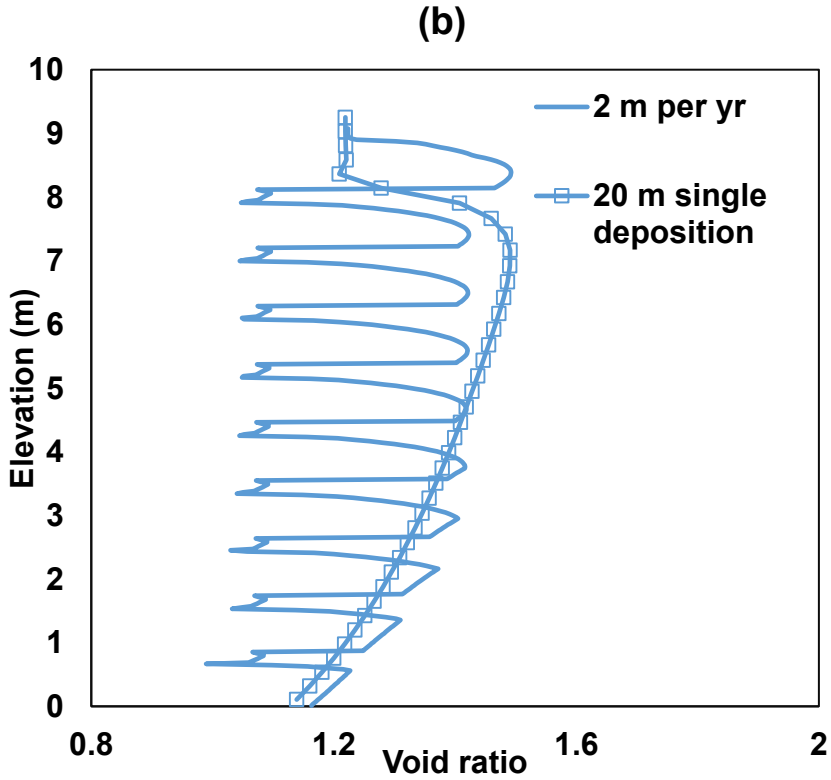
(b)
10
9
8
7
6
5
4
3
2
1
0
Elevation (m)
0.8
1.2
1.6
2
Void ratio
2 m per yr
20 m single deposition

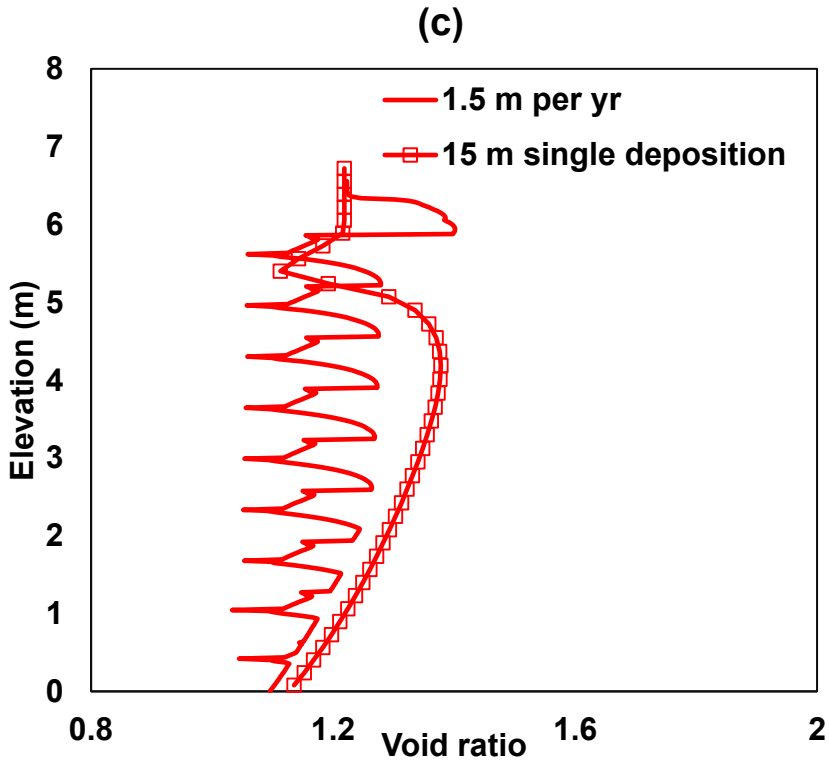
(c)
1.5 m per yr
15 m single deposition
Elevation (m)
Void ratio
0
1
2
3
4
5
6
7
8
0.8
1.2
1.6
2

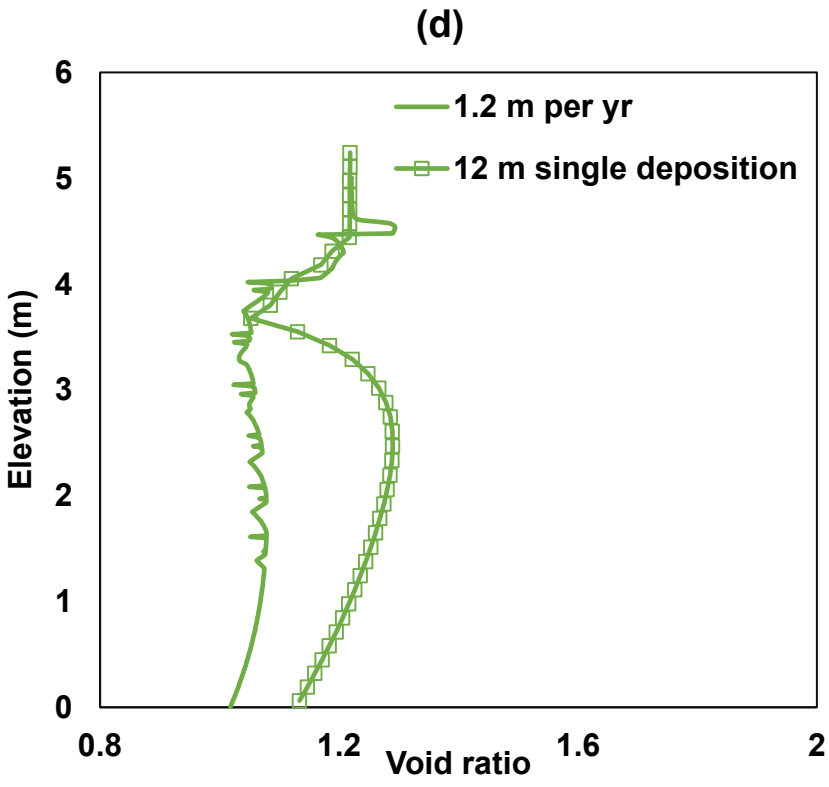
(d)
1.2 m per yr
12 m single deposition
Elevation (m)
Void ratio
0
1
2
3
4
5
6
0.8
1.2
1.6
2

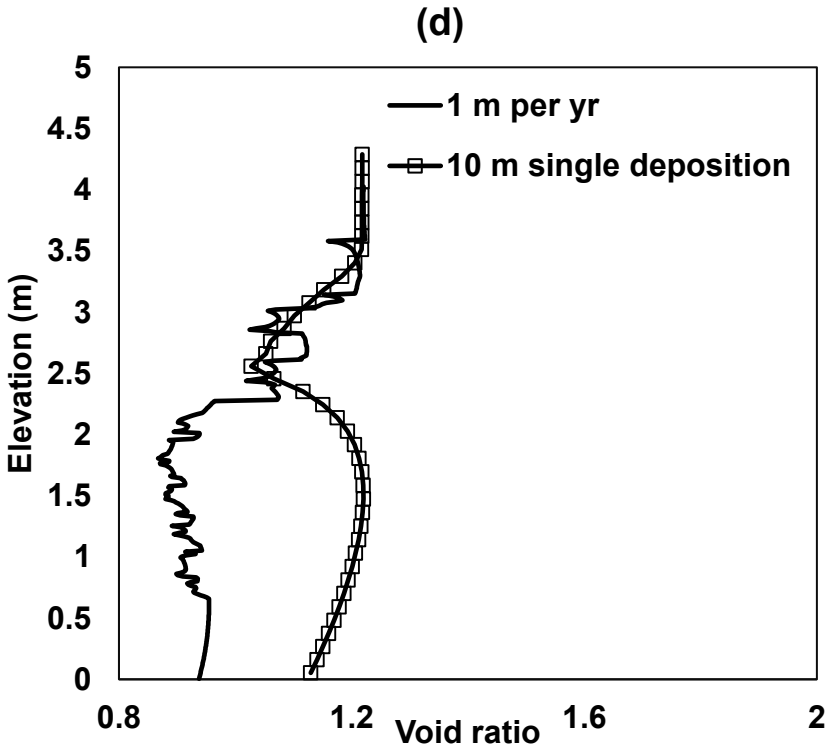
(d)
1 m per yr
10 m single deposition
Elevation (m)
Void ratio
0
0.5
1
1.5
2
2.5
3
3.5
4
4.5
5
0.8
1.2
1.6
2

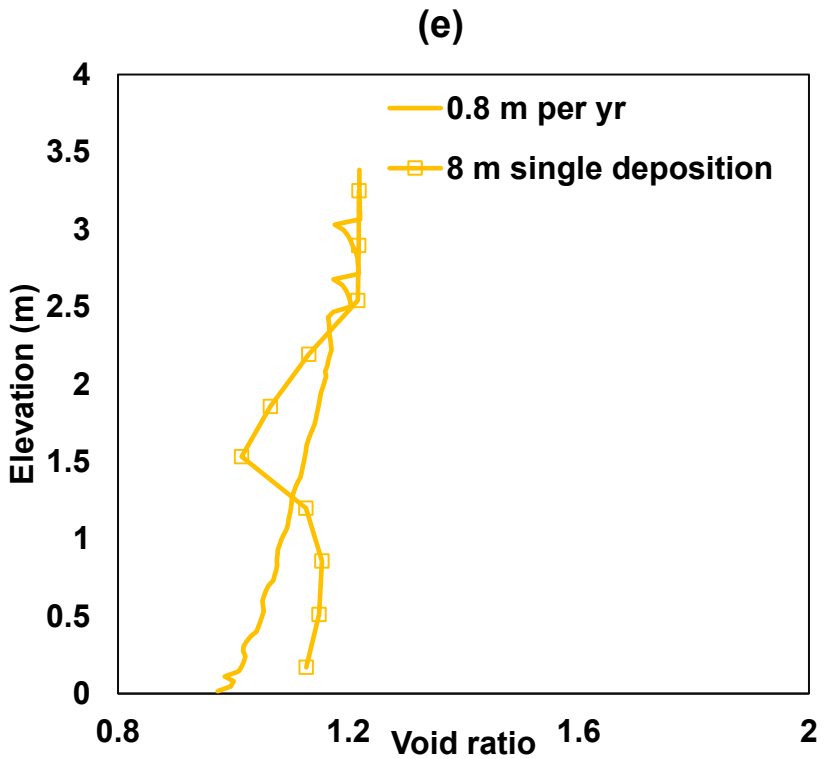
(e)
0.8 m per yr
8 m single deposition
Elevation (m)
Void ratio
0
0.5
1
1.5
2
2.5
3
3.5
4
0.8
1.2
1.6
2

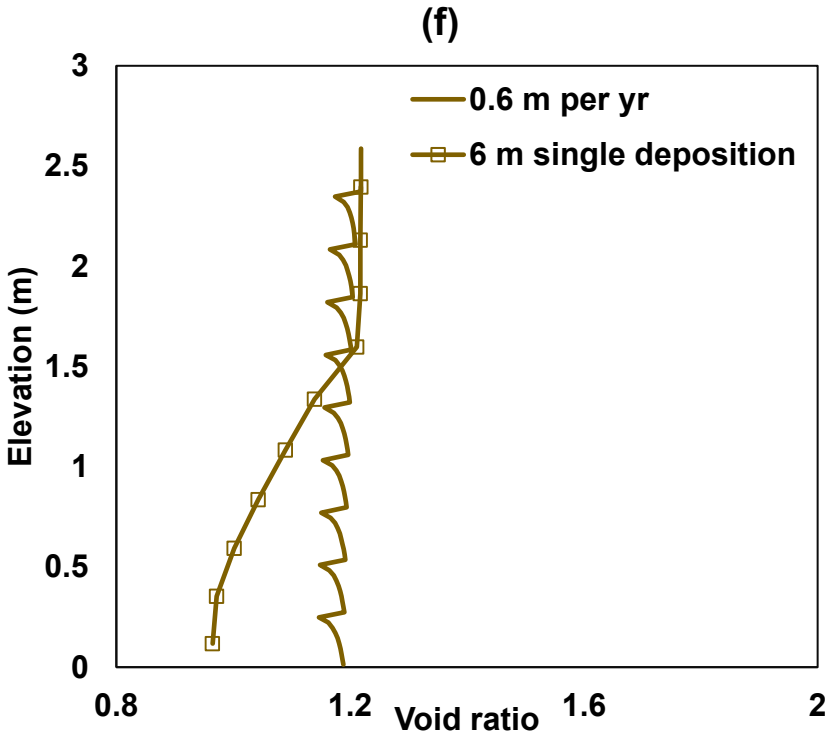

Fig. 10.5 Comparison in void ratio between multilayer and single deposition for each thickness

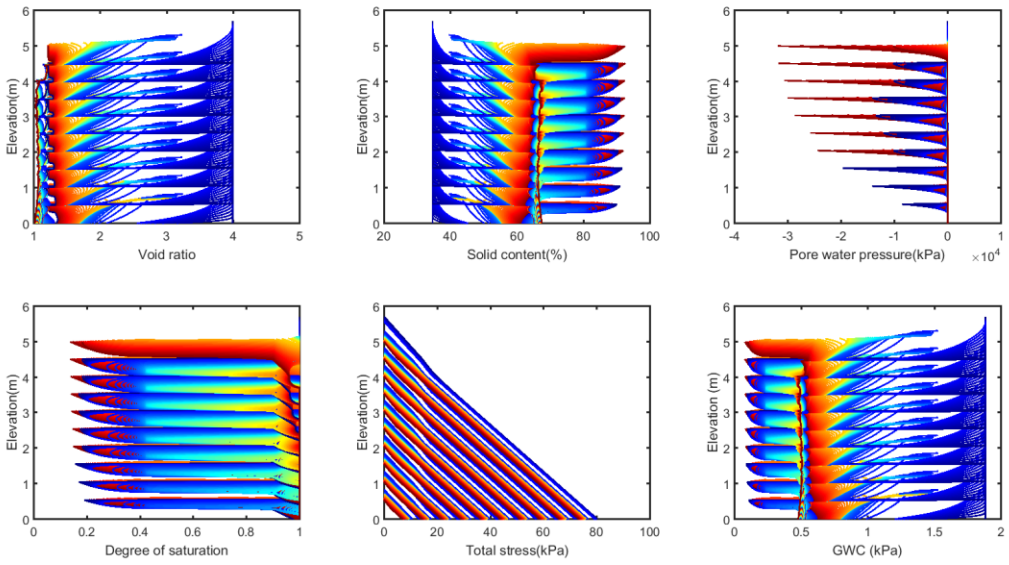

Fig. 10.6 Variation of profile over time during the deposition process for the case of 1.2 m per year over 10 years

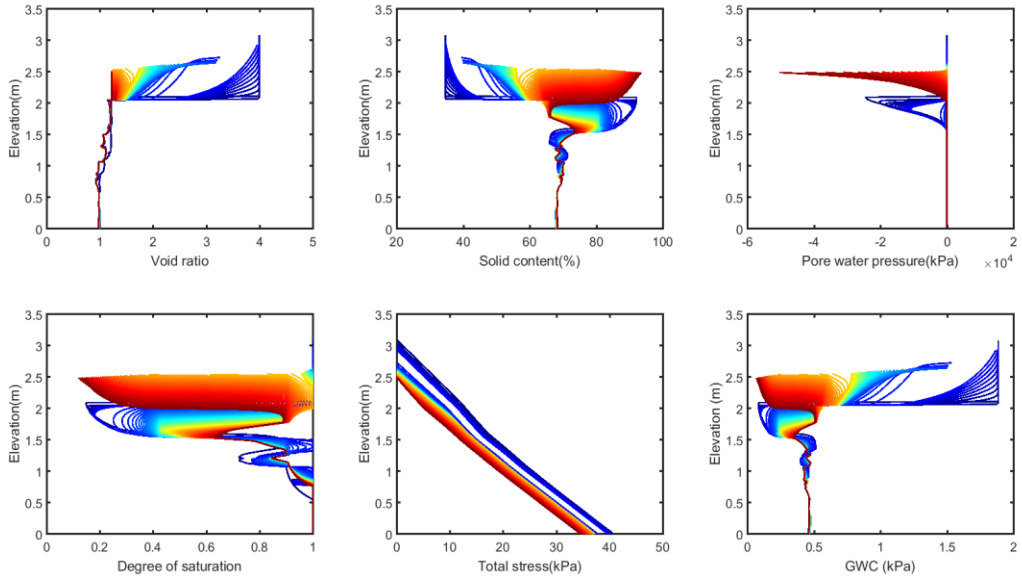

Fig. 10.7 Variation of profile over time during the deposition process for the case of 1.0 m per year during the 10th year

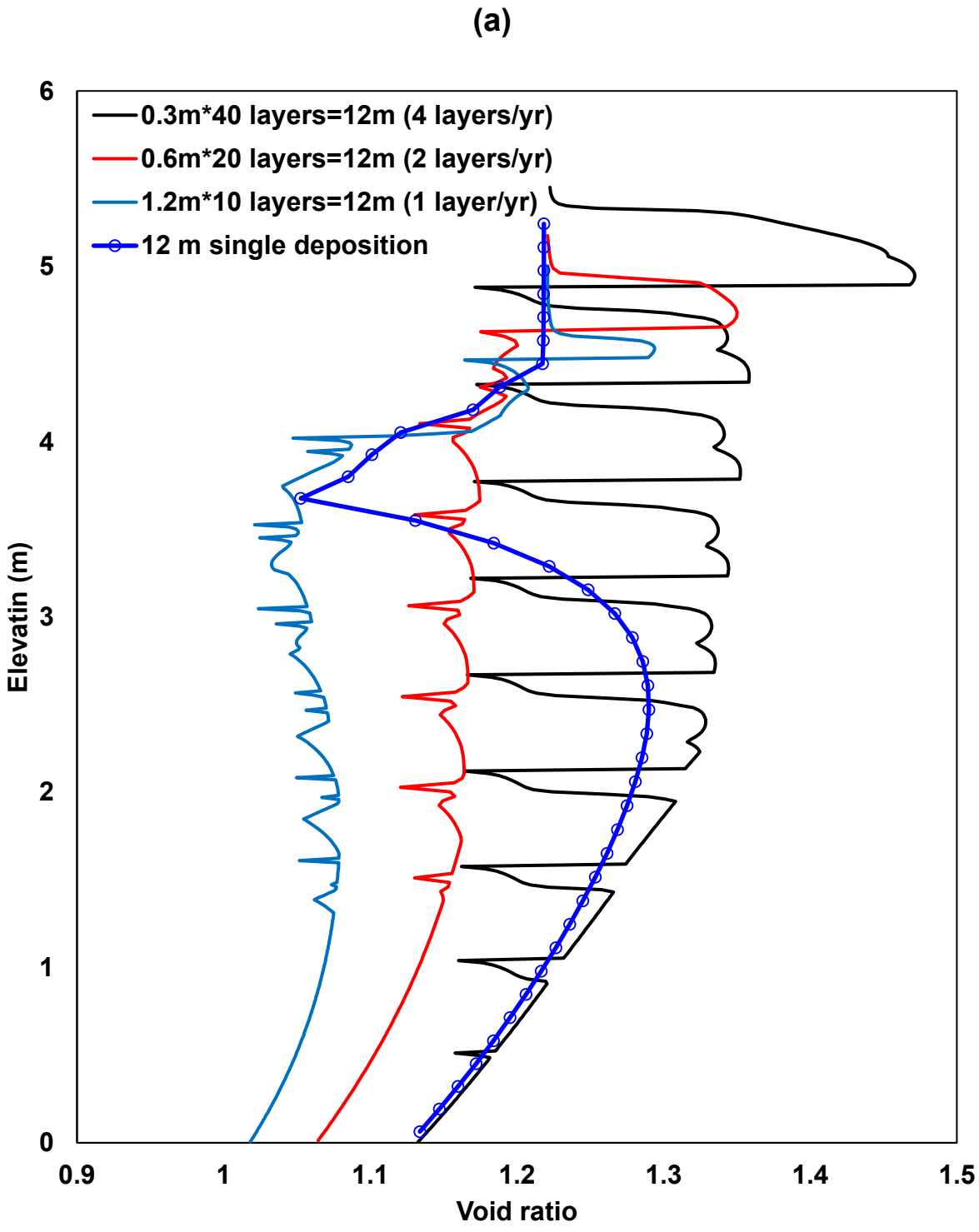
(a)
0.3m*40 layers=12m (4 layers/yr)
0.6m*20 layers=12m (2 layers/yr)
1.2m*10 layers=12m (1 layer/yr)
12 m single deposition
Elevatin (m)
Void ratio
0
1
2
3
4
5
6
0.9
1
1.1
1.2
1.3
1.4
1.5

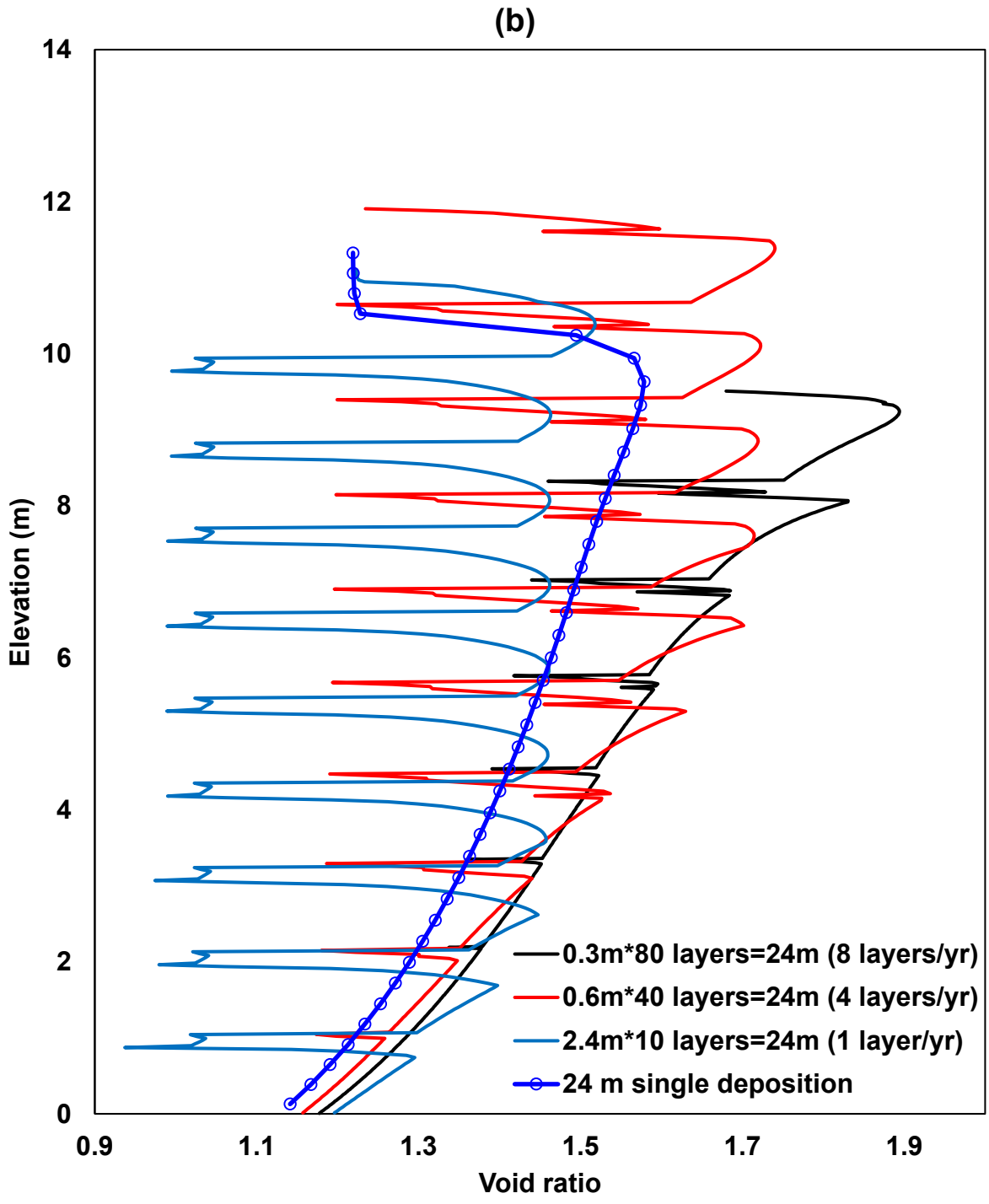

Fig. 10.8 Comparisons in void ratio profiles after 10 years from multiple layer deposition (including one deposition per year and more than one deposition within each year) and single layer deposition.

10.2.4 Analyses with different soil models (SSM and GCM)

The results presented until now in this chapter are obtained by using the practical state surface model for volume change behaviour in conjunction with the practical water retention model. Several other constitutive models for unsaturated soils are made available to increase the diversity of UNSATCON-ML in chapter 9. It would be of great interest, both theoretically and practically, to compare the results using the same program (UNSATCON-ML) with different soil models. In this section, a number of multi-layer depositions have been analysed using two soil models, namely SSM (i.e. the practical models used in previous sections) and GCM (Glasgow Coupled Model), in parallel. In order to enrich the diversity of the results as well, the water retention capacity of the tailings is changed, but the other soil constants of SSM are kept the same as previous section. The model parameters of GCM are selected such that the described volume change and water retention behaviours are as close to those described by SSM as possible, if they were transformed into the same space (void ratio-net stress-suction or void ratio-Bishop's stress, and degree of saturation-void ratio-suction or degree of saturation-modified suction). This will be shown following the results presentation. Table 10.4 and Table 10.5 present the parameters of two models used here. All the other parameters (including the permeability and evaporation rate) and conditions (initial, top and bottom boundary) are kept the same as those in the previous section for both models.

Table 10.4. Parameters of SSM

Volume change behaviour								
Parameters	a	b	c	d	f	g	κ	κ_s
Value	4.50	7.80E-01	7.56E-03	1.36E-01	1.62E+03	2.17E+03	0.015	0.0015
Water retention behaviour								
Parameters	C_{drying}	$C_{wetting}$	λ_{se}	λ_{sr}	κ_{ss}			
Value	1.5	1.35	0.15	0.16	0.04			
Water permeability								
Parameters	H_1	H_2	M					
Value	17.5E-11	8	0.75					

Table 10.5. Parameters of GCM

Coupled hydro-mechanical behaviour						
Parameters	λ	κ	λ_s	κ_s	k_1	k_2
Value	0.32	0.015	0.16	0	0.70	0.70
Parameters	R	N_0	Ω_{d0}			
Value	0.273	4.4418	Calculated in the program			
Permeability						
Parameters	H_1	H_2	M			
Value	17.5E-11	8	0.75			

Table 10.6. Long-term (10 years) deposition scheme

Deposition scheme		**Total thickness (m) = Deposition thickness per time (m)×Depositing time**		
Multiple layer deposition	1 deposition per year over 10 years	0.8×10	1.2×10	1.5×10
Total thickness (m)		8	12	15

The hypothetical deposition schemes considered here are basically the same as those in the previous section, only three subcases (deposition thickness = 0.8, 1.2 and 1.5 m per year) from Table 10.3 are reanalysed using GCM and SSM, see Table 10.6.

Fig. 10.9 presents a summary of the final (at the end of 10 years) void ratio profiles calculated by UNSATCON-ML for the three deposition schemes with SSM and GCM. Comparisons between different thicknesses (per year) using same constitutive model are presented in Fig. 10.10 (a) and (b). Comparisons between two constitutive models for the same deposition thickness are presented in Fig. 10.10 (c) (d) and (e).

Generally, the findings that can be drawn regarding the influence of deposition thickness (per year) from this group of results are similar to those from previous section:

(1) For cases with thicker layer deposit (i.e. 1.5 m) per year, denser (stronger) and looser (weaker) layers alternatively formed along the depth, due to the drying/desiccation effect exerted on the upper part of tailings layer every year. This is true for results from both models (SSM and GCM). Note, the SWRM used here is different from that used in SSM in previous section.

(2) For cases with relatively medium and thin thicknesses (i.e. 1.2 m and 0.8 m) per year, a more uniform denser profile has been produced using SSM, since the evaporation is able to have more or less influence on the entire layer deposited each year. With GCM, the calculated void ratio using UNSATCON-ML still exhibits a non-uniform (denser and looser layers alternatively formed), but trends of uniformization can be observed.

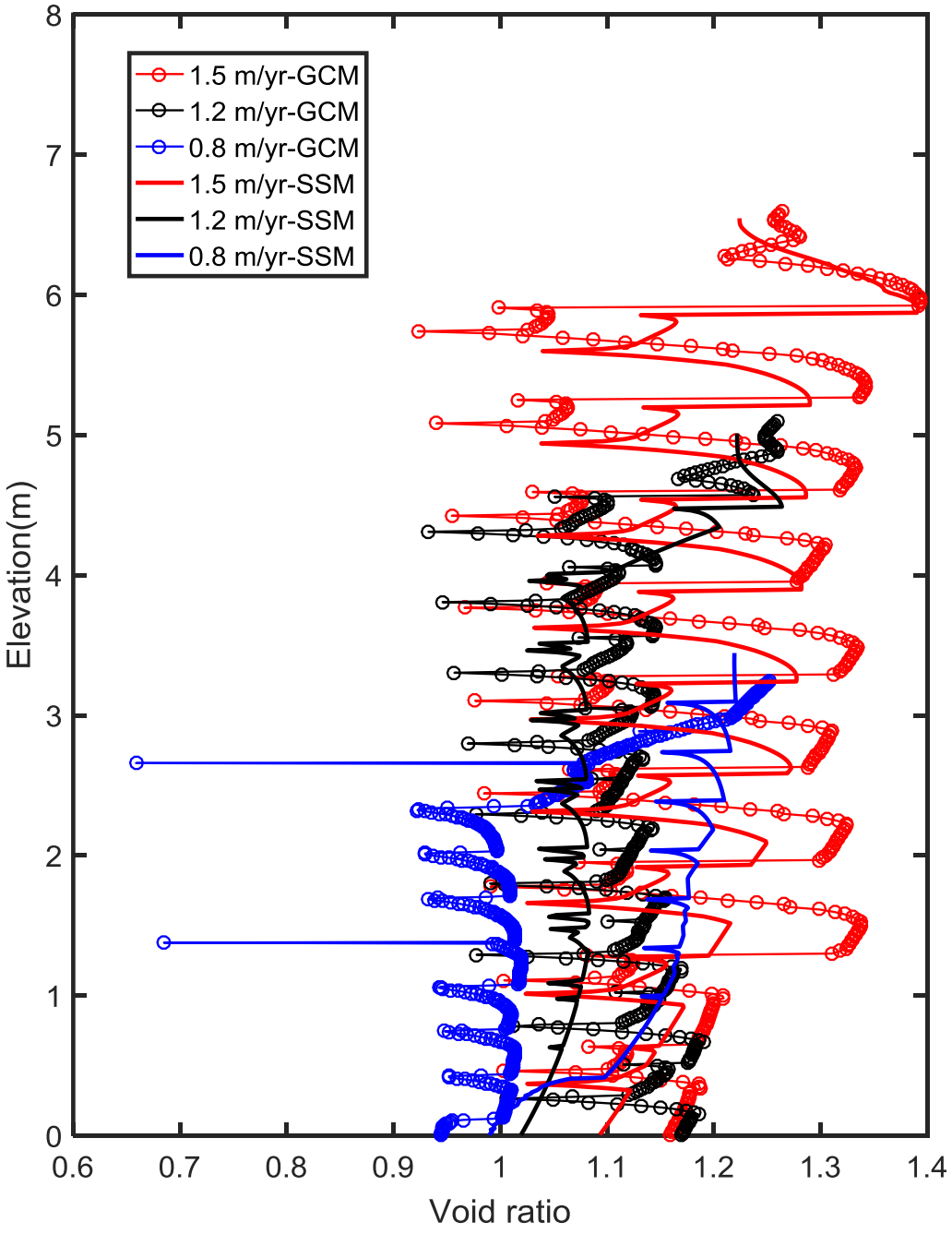

Fig. 10.9 A summary of void ratio profiles calculated by UNSATCON-ML with GCM and SSM

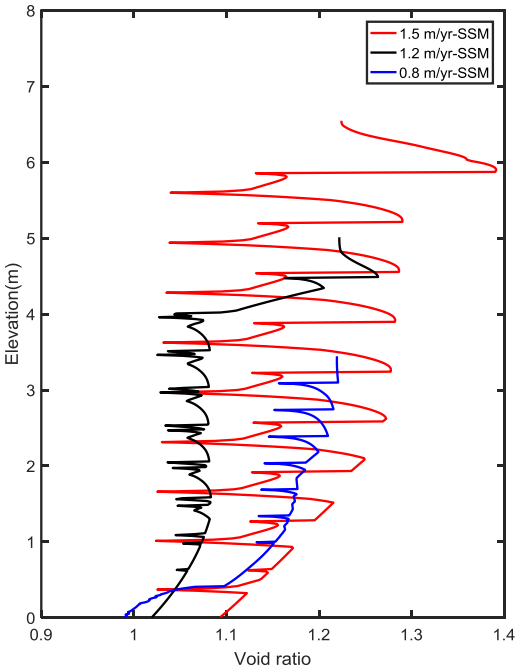
1.5 m/yr-SSM
1.2 m/yr-SSM
0.8 m/yr-SSM
Elevation(m)
Void ratio

(a)

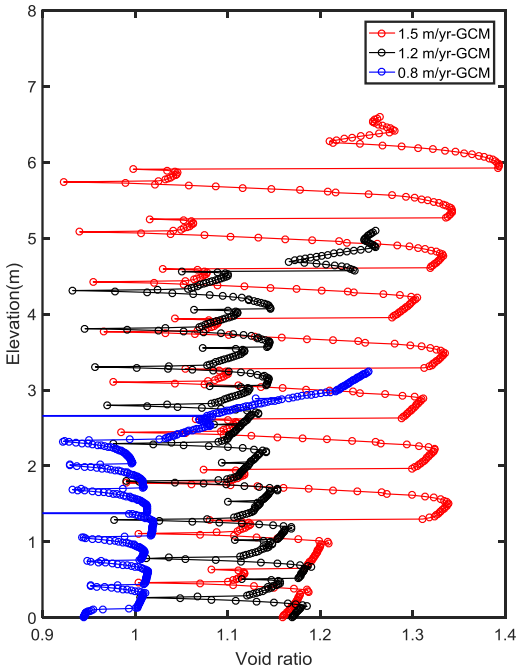
1.5 m/yr-GCM
1.2 m/yr-GCM
0.8 m/yr-GCM
Elevation(m)
Void ratio

(b)

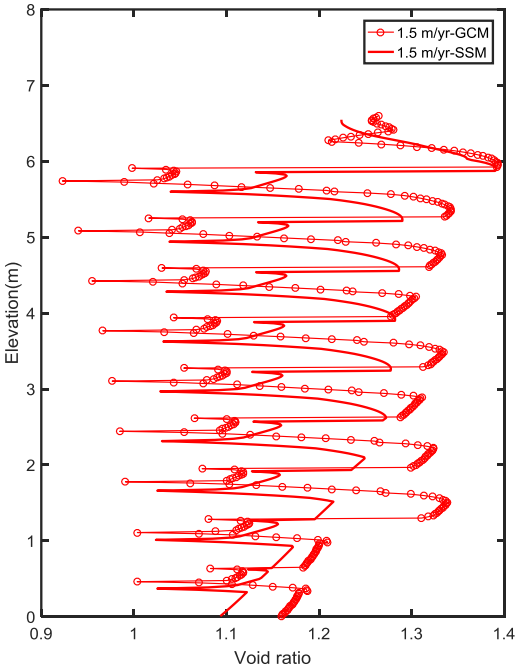
1.5 m/yr-GCM
1.5 m/yr-SSM
Elevation(m)
Void ratio

(c)

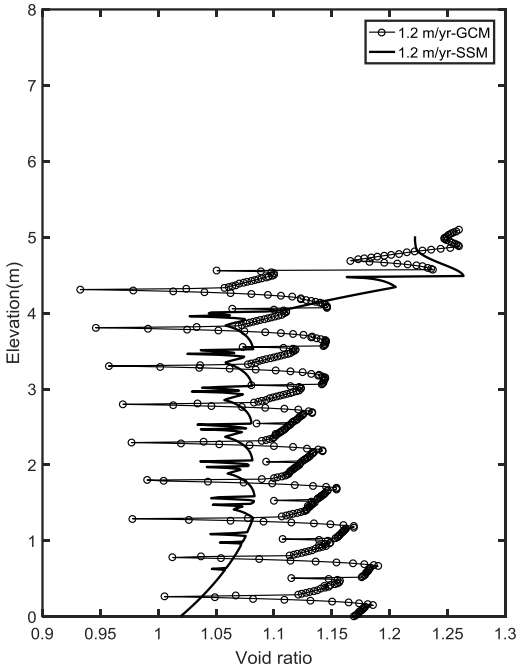
1.2 m/yr-GCM
1.2 m/yr-SSM
Elevation(m)
Void ratio

(d)

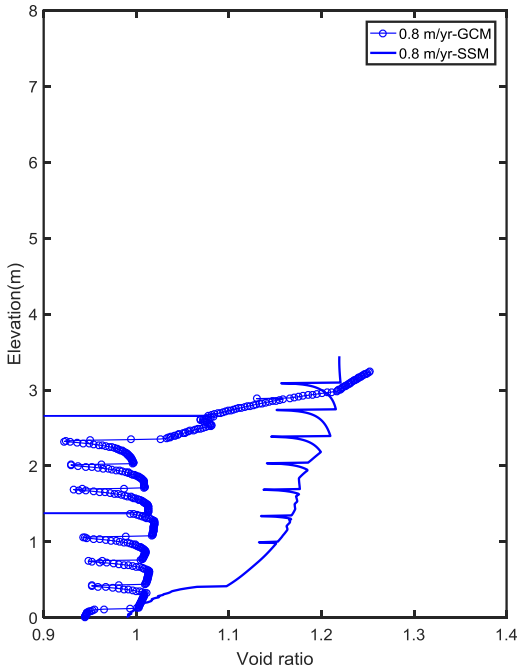

(e)

Fig. 10.10 Comparison of void ratio profiles calculated by UNSATCON-ML: (a) different deposition thicknesses with SSM; (b) different deposition thicknesses with GCM; (c) 1.5 m thick deposit per year with SSM and GCM; (d) 1.2 m thick deposit per year with SSM and GCM; (e) (d) 0.8 m thick deposit per year with SSM and GCM

Fig. 10.10 shows that use of different constitutive models produces different results. The difference can be expected, given the fact that the specific constitutive paths described by these two models are not exactly the same in terms of the numerical value. This can be seen in Fig. 10.11. Fig. 10.11 presents a comparison of calculated constitutive paths (followed by the top element of the 1st layer for the case of 1.2 m per year during the first 2 years) between SSM and GCM. These two models employ different assumptions and are established using different constitutive stress variables. For example, the SSM uses net stress and suction as independent stress variables, while

the GCM uses Bishop's stress and modified suction as the stress variables. A simple transformation is made for plotting the constitutive paths in Fig. 10.11 for comparison.

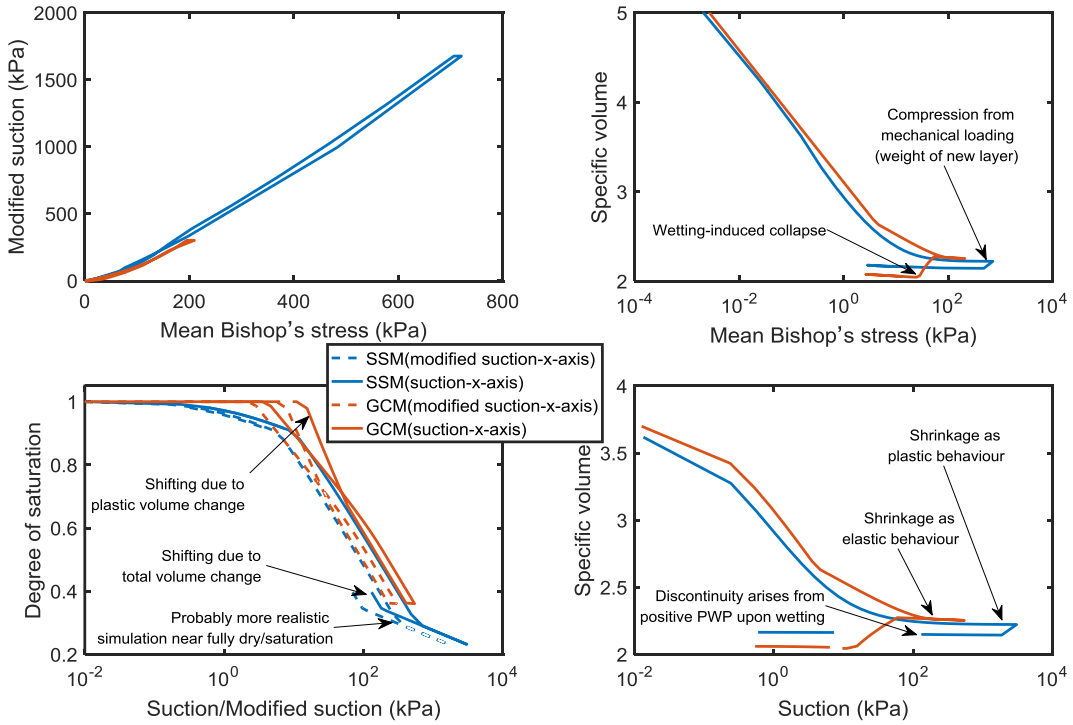

Fig. 10.11 Calculated constitutive paths followed by the top element of the 1st layer for the case of 1.2 per year during the first 2 years using SSM and GCM.

In addition to the numerical values along specific constitutive paths modelled by these two models, there are some other fundamental differences in simulations produced by these two models. Different aspects of the tailings behaviour are modelled in different ways. In the following, several specific unsaturated soil behavioural features at the constitutive level (using Fig. 10.12 through Fig. 10.17) simulated by SSM and GCM are explained separately. This will manifest the differences performed by these two models in the particular simulation (multilayer deposition of oil sands tailings, or soft soils in a more general sense). Fig. 10.12 through Fig. 10.15 present the paths of state parameters followed by the top and bottom elements of the first layer (for the case

of 1.2 per year) over 10 years after initial deposition calculated by UNSATCON-ML employing SSM and GCM. Fig. 10.16 and Fig. 10.17 present the variations of profiles of several parameters (pore water pressure, void ratio, total stress and degree of saturation) over time calculated using UNSATCON-ML with SSM and GCM, respectively.

- *Use of SSM*

Fig. 10.12 shows the calculated deformation paths followed by the top and bottom elements of the 1st layer during 10 years using SSM in the space of void ratio - net stress - suction. Fig. 10.13 shows the time history of several state parameters (pore water pressure, void ratio, total stress and degree of saturation) over 10 years at top and bottom elements of the 1st layer using SSM. Fig. 10.16 presents the variations of profiles of several parameters (pore water pressure, void ratio, total stress and degree of saturation) over first 3 years calculated using UNSATCON-ML with SSM.

The deformation paths (see Fig. 10.12) during the first year (1st layer deposition) are very similar to that of the field case shown in Chapter 7. During the second year, the top element is first subjected to a elastic mechanical (overburden of layer 2) compression see Fig. 10.12 (c) , followed by elastic swelling upon wetting by downward flow of water from fresh layer, see Fig. 10.12(d). The top element is wetted to a fully saturated condition before being re-dried (not as much as in the 1st layer) by 2nd evaporation in the last half of 2nd year, see Fig. 10.12(b). During the 3rd year, the top element of 1st layer is compressed mainly mechanically, by the overburden of 2nd and 3rd layers, to a fully saturated condition, see Fig. 10.12(b,c,d). After which the top elements of 1st layer remains at fully saturated condition, the volume change is mostly elastic swelling (unloading due to loss of water weight by evaporation) and compression (loading due to new deposition).

The deformation path of the bottom element of the 1st layer is similar to that of the top element during the first year, see Fig. 10.12(e,f,g) which is then mechanically compressed to saturated condition after adding the 2nd layer, see Fig. 10.12(e,f), like that of top element after adding the 3rd layer in the 3rd year. The bottom element is desaturated a little bit during the middle of the 2nd year, see Fig. 10.12(e,g), which is not by evaporation that is applied much latter. This can also be seen in Fig. 10.13 and Fig. 10.16**.** This can be interpreted as: when the element is mechanically saturated by the adding the 2nd layer, the PWP becomes from negative (a little bit for this case) to positive instantaneously (see Fig. 10.13), while the significant negative PWP (high suction) in the upper part of the 1st layer (for example, the top element of 1st layer) can only gradually decreases during rewetting by the water from the 2nd fresh layer (see Fig. 10.13 and Fig. 10.16). Then a hydraulic gradient is established to drive the water flowing from the bottom to the top in the 1st layer. Since there is no water source at the bottom, the bottom element is temporally desaturated by this phenomenon. However, when the upper part of the 1st layer is fully saturated, the bottom element of the 1st layer is again saturated and remains saturated afterwards (see Fig. 10.13). The deformation thereafter is mostly elastic swelling (unloading due to loss of water weight by evaporation) and compression (loading due to new deposition).

The hydro-mechanical significance implied by deformation paths shown in Fig. 10.12 can be better understood by looking at the Fig. 10.13 and Fig. 10.16, particularly the temporary upward hydraulic gradient within the 1st layer in the middle of the 2nd layer. It can also be seen that the hydraulic mechanical behaviours of the 1st layer are less and less being affected by the new deposition since the deposition of the 4th layer (see Fig. 10.13 and also refer to all the profiles in the appendix 10.1).

- *Use of GCM*

Fig. 10.14 shows the calculated stress, compression and retention paths followed by the top, middle and bottom elements of the 1st layer during 10 years using GCM in four planes: Bishop's stress - modified suction, specific volume - Bishop stress, Degree of saturation - modified suction and specific volume – suction. Fig. 10.15 shows the time history of several state parameters (pore water pressure, void ratio, total stress and degree of saturation) over 10 years at top and bottom elements of the 1st layer using GCM. Fig. 10.17 presents the variations of profiles of several parameters (pore water pressure, void ratio, total stress and degree of saturation) over first 3 years calculated using UNSATCON-ML with GCM.

The compression path (in the specific volume – Bishop's stress plane, see Fig. 10.14) of the top element during the first year (the 1st layer deposition) are very similar to that of the drying box test simulated in Chapter 8. During the second year, the top element is subjected to a large amount of wetting-induced plastic compression/collapse (downward flow of water from fresh layer), followed by elastic swelling upon further wetting along the saturated line. It can be seen that, the state of the top element has collapsed to the saturated NCL (which can be said "fully collapsed"), the elastic compression from the overburden (weight of the 2nd layer) is comparatively much smaller than the plastic compression/collapse. The top element is re-dried by the 2nd evaporation in the last half of the 2nd year, this can be seen in the development of suction (less than air entry value, see Fig. 10.15), and the top element stays at fully saturated ($S_r = 1$) state and remains saturated thereafter. The volume change of this element is mostly elastic swelling (unloading due to loss of water weight by evaporation) and compression (loading due to new deposition) along the current saturated swelling line.

The compression path (in the specific volume – Bishop's stress plane in Fig. 10.14) of the middle element of 1st layer is similar to that of top element. Both of this element and top element

has collapsed to the same saturated NCL (fully collapsed) during the 2nd year. The middle element has lower void ratio after collapse, due to higher overburden stress. Similarly, this element remain fully saturated thereafter. The volume change of this middle element is also mostly elastic swelling (unloading due to loss of water weight by evaporation) and compression (loading due to new deposition) along the current saturated swelling line. The compression path (in the specific volume – Bishop's stress plane) of the bottom element of 1st layer remains on fully saturated NCL in the first years. The bottom element is also indeed affected by evaporation in the first year, as can be seen from the development of suction in the last half of 1st year, but the suction is less than the air entry value and this element remains fully saturated over 10 years (see Fig. 10.15). The volume change of this element is therefore mostly elastic swelling (like the other elements) after a plastic compression (due to Bishop's stress increase that arises from the self-weight consolidation and drying) in the first year.

Using GCM, The bottom element is also desaturated a little bit during the early of the 2nd year, which is not by evaporation (applied much latter). This is similar to that from use of SSM, and the reason behind is the same as interpreted before for the results from use of SSM (see Fig. 10.15 and Fig. 10.17).

The differences performed by SSM and GCM from these discussions include:

GCM predicts shrinkage behaviour as elastic process, this treatment is similar to some models using Bishop's stress as the fundamental stress variable (in the frameworks of elasto-plasticity or bounding surface plasticity). SSM predicts shrinkage behaviour as plastic process (although this total deformation becomes gradually negligible with continuous drying) by the shape of the constitutive function. Treating shrinkage behaviour as a plastic process is also

employed in SFG model (reviewed in Chapter 2), where change of suction can directly/independently induce volume change, unlike the models using the Bishop's stress as the stress variable.

Wetting-induced collapse (after adding a new layer) is simulated using GCM using the coupled movement mechanism of two types of yielding curves. The volume decrease in the old layer (after adding a new layer) is simulated as a elastic compression (due to loading of overburden) in SSM in this case. Wetting-induced collapse can also be simulated using SSM at higher net stress level, which uses a similar technique (shape of loading collapse (LC)) as BBM. But the evolution of LC in SSM at higher net stress level should be well controlled by carefully calibrating constitutive parameters if simulation of wetting collapse is important in some cases.

For simulation of water retention behaviour, the SSM allows more flexibilities in the shape of the retention path near the fully dry/saturation conditions. In the GCM, the constraint that the soil remains fully saturated conditions before the AEV is adopted, a consequent of this would be that the GCM under predicts the void ratio before the AEV, which is not really consistent with some experimental data. Moreover, the GCM predicts a lower suction due to the simplicity of water retention components near the drying conditions. However, it is worth mentioning that the GCM requires lesser constitutive constants, most of the behaviour is simulated by the coupling mechanism.

These differences between two models may be accumulated during cyclic stress paths that may occur when new deposits are continuously added, which therefore result in an overall different predictions (depending also on the other parameters) at the end. Selection/calibration of the models should be based on the real behaviour of the particular tailings before performing the simulation.

For example, if significant accumulation of plastic compression, including wetting-induced collapse, is observed in behaviour of tailings to be deposited, the GCM can be employed to capture this behaviour in the deposits deposited in layers. But the coupling parameters require to be calibrated carefully over data measured on samples subjected to the stress paths expected in multi-layer deposition. If retention behaviour over a wide range of suction, especially that close to fully saturated and drying condition, needs to be very well simulated, the practical SSM is more appropriate with more parameters defining the retention behaviour.

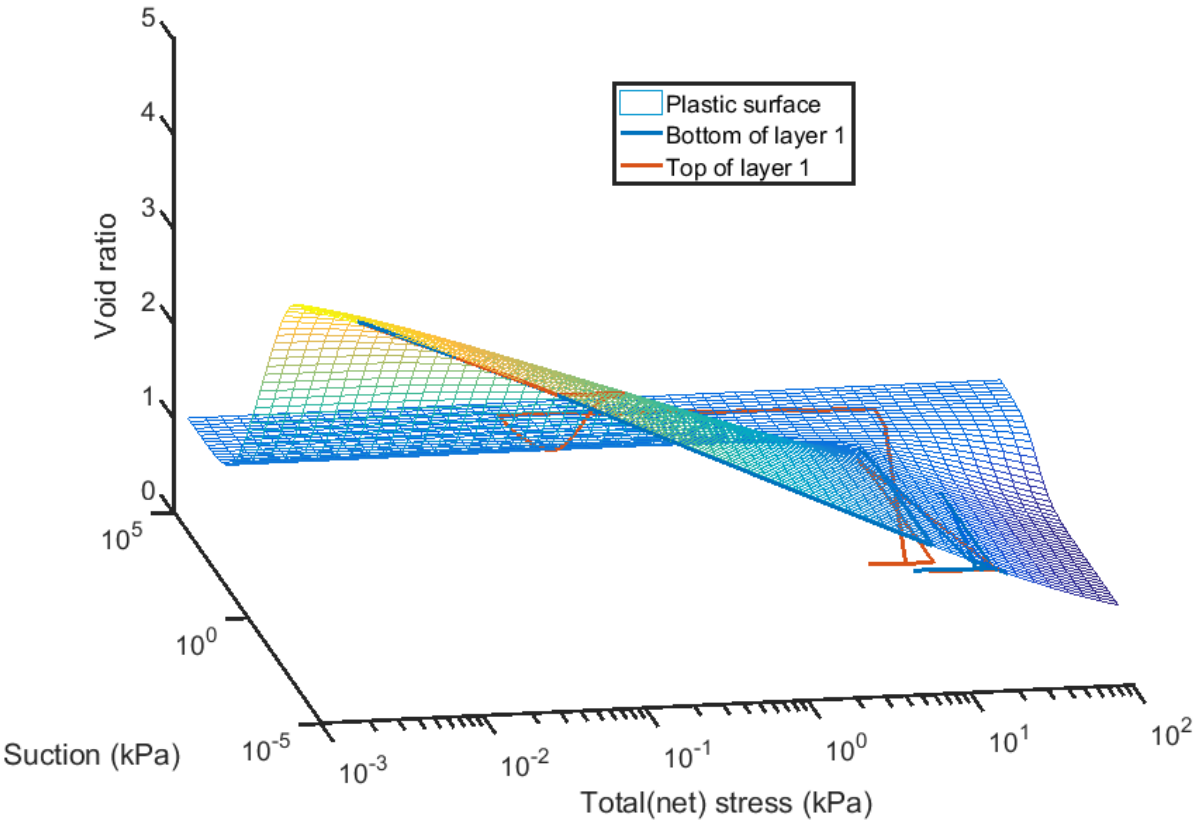

(a)

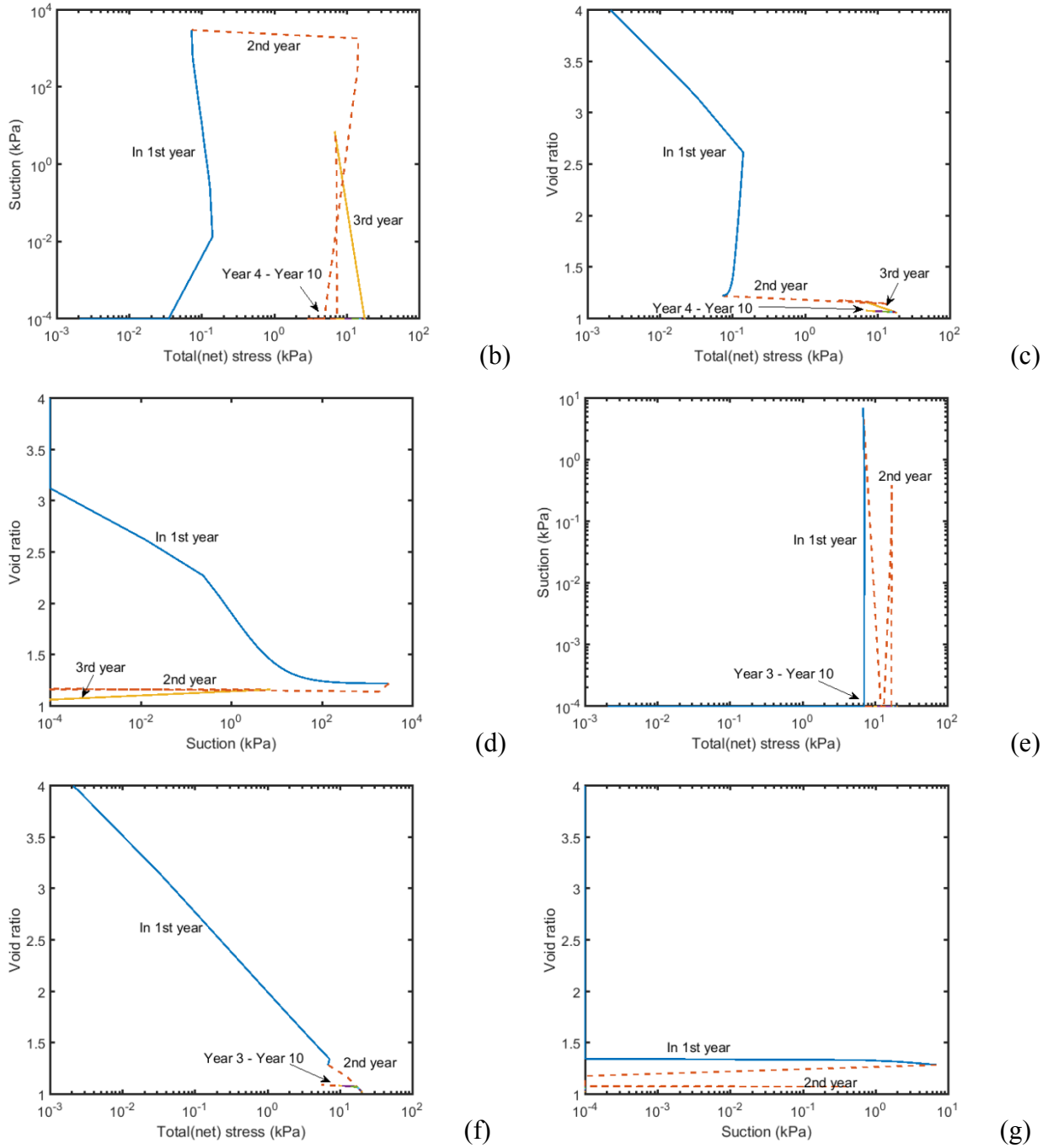

Fig. 10.12 Calculated constitutive paths followed by the top and bottom elements of the 1st layer for the case of 1.2 m per year during 10 years using SSM: (a) both elements in three dimensional space, (b) top element in net stress *vs.* suction plane, (c) top element in void ratio *vs.* net stress plane, (d) top element in void ratio *vs.* suction plane, (e) bottom element in net stress *vs.* suction plane, (f) bottom element in void ratio *vs.* net stress plane, (g) bottom element in void ratio *vs.* suction plane,

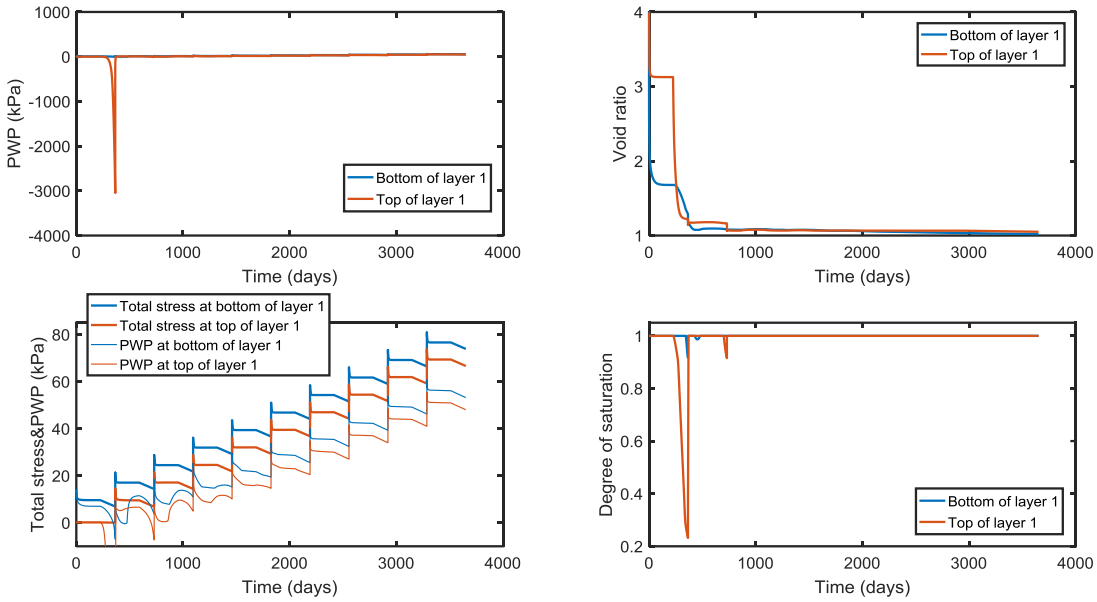

Fig. 10.13 Calculated change of several state parameters (pore water pressure, void ratio, total stress and degree of saturation) over 10 years at top and bottom elements of the 1st layer using SSM

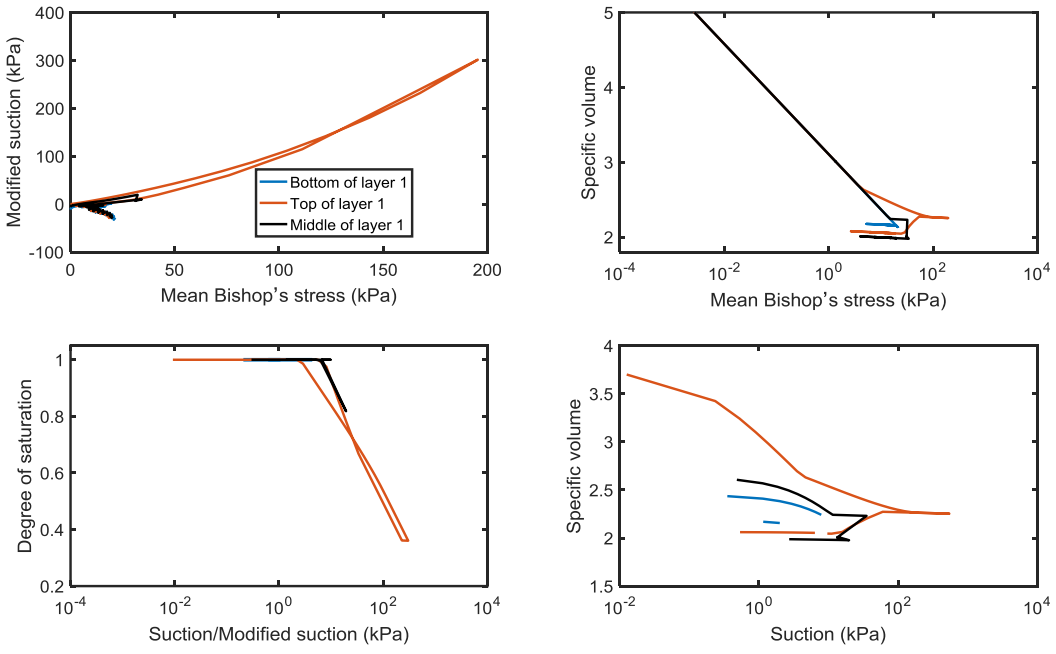

Fig. 10.14 The calculated stress, compression and retention paths followed by the top and bottom elements of the 1st layer during 10 years using GCM in four planes: Bishop's stress - modified suction, specific volume - Bishop stress, Degree of saturation - modified suction and specific volume – suction.

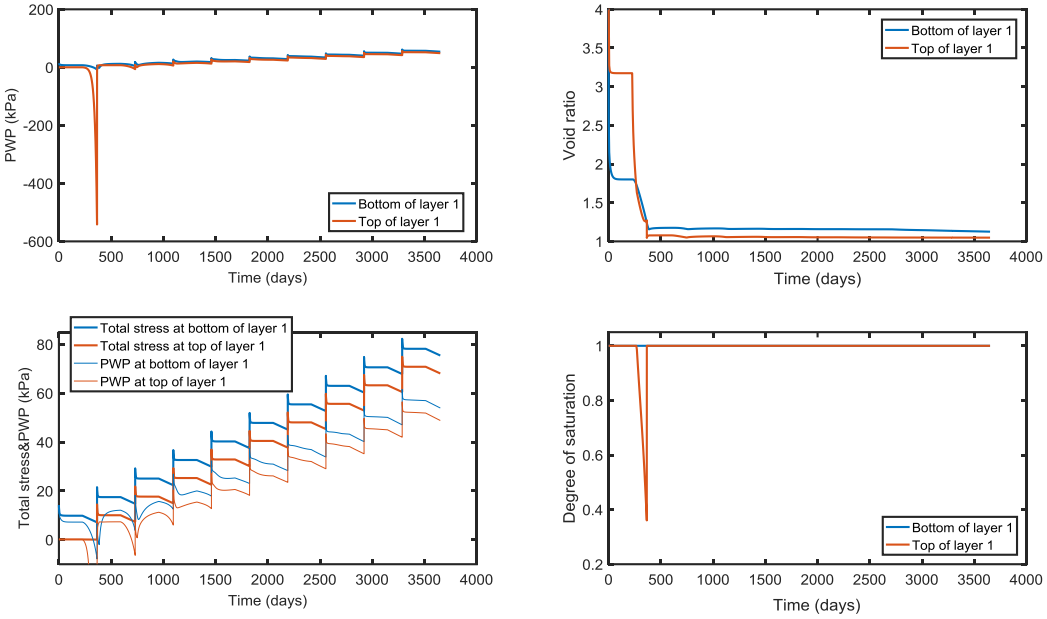

Fig. 10.15 Calculated change of several state parameters (pore water pressure, void ratio, total stress and degree of saturation) over 10 years at top and bottom elements of the 1st layer using GCM

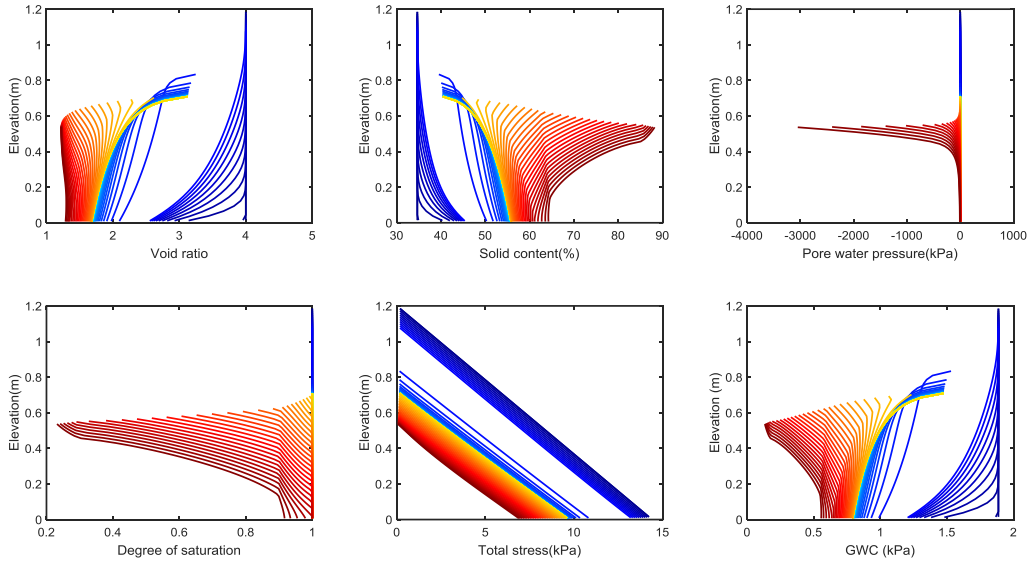

(a)

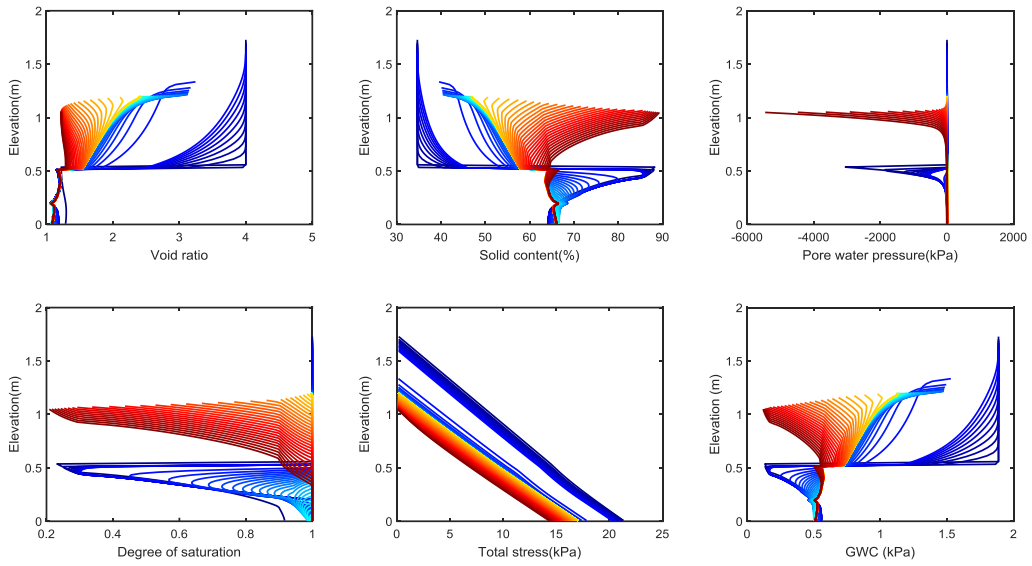

(b)

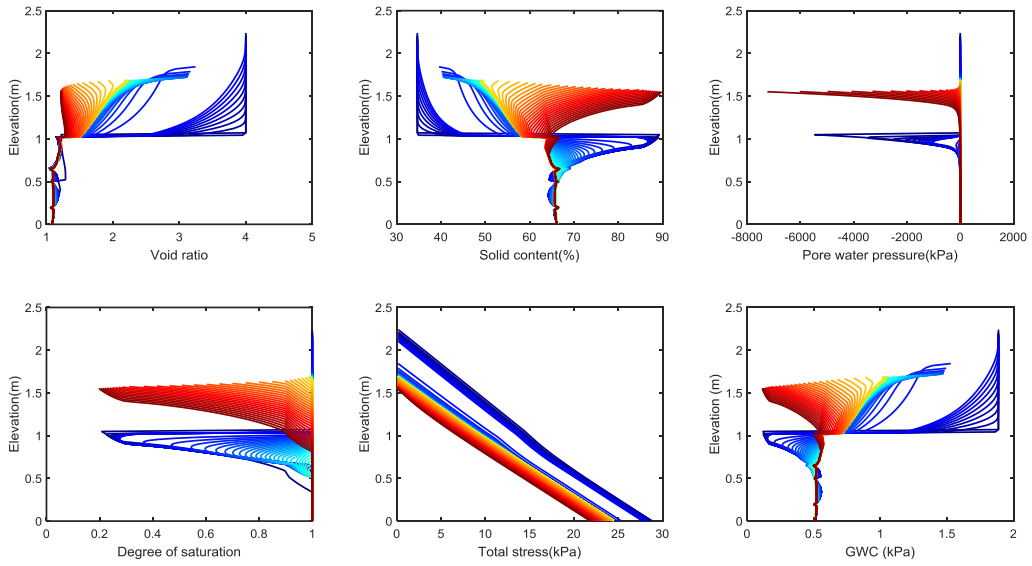

(c)

Fig. 10.16 Calculated variations of profiles of several parameters (pore water pressure, void ratio, total stress and degree of saturation) over time using SSM: (a) during the 1st year (1st layer deposition), (b) during the 2nd year (2nd layer deposition), and (c) during the 3rd year (3rd layer deposition).

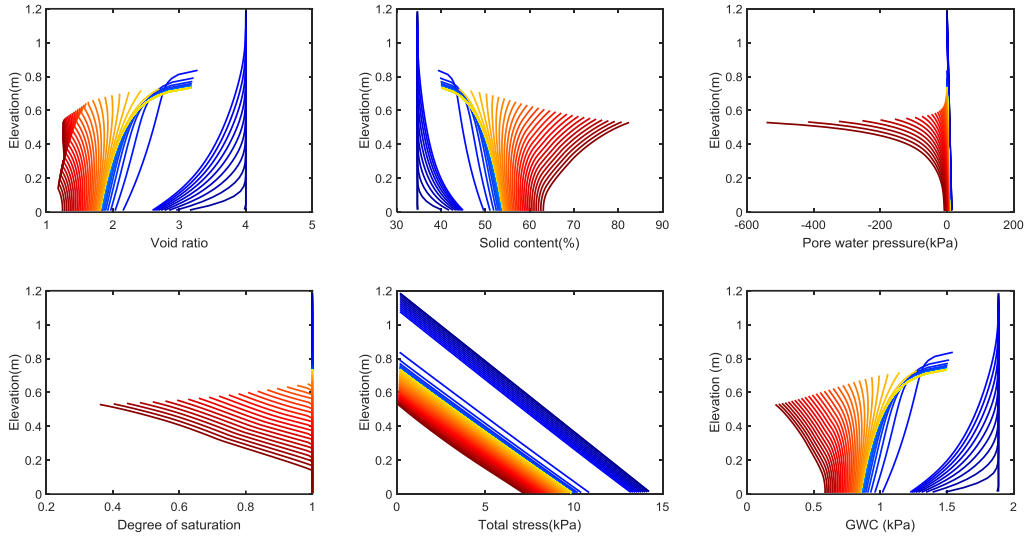
Elevation(m)
Void ratio
Solid content(%)
Pore water pressure(kPa)
Degree of saturation
Total stress(kPa)
GWC (kPa)

(a)

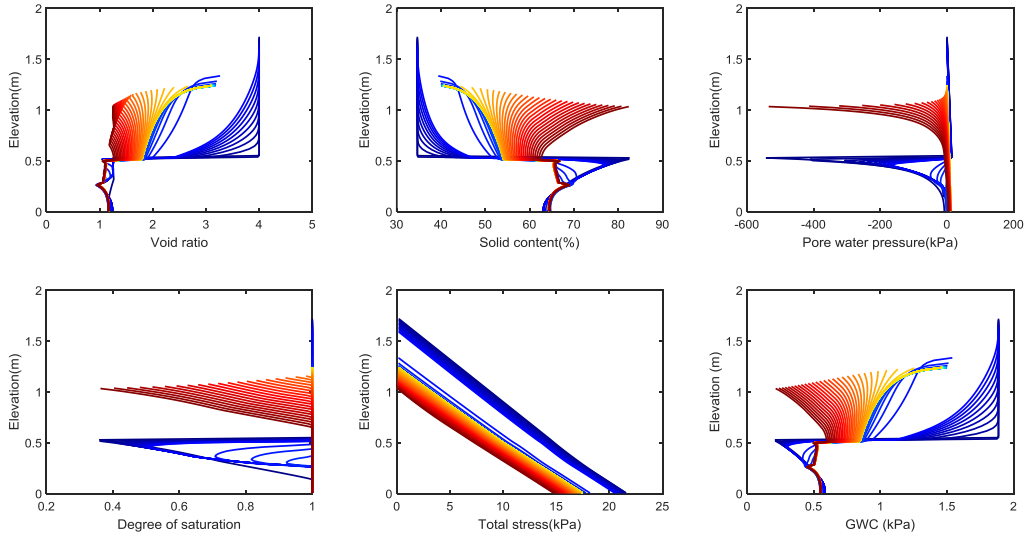
Elevation(m)
Void ratio
Solid content(%)
Pore water pressure(kPa)
Degree of saturation
Total stress(kPa)
GWC (kPa)

(b)

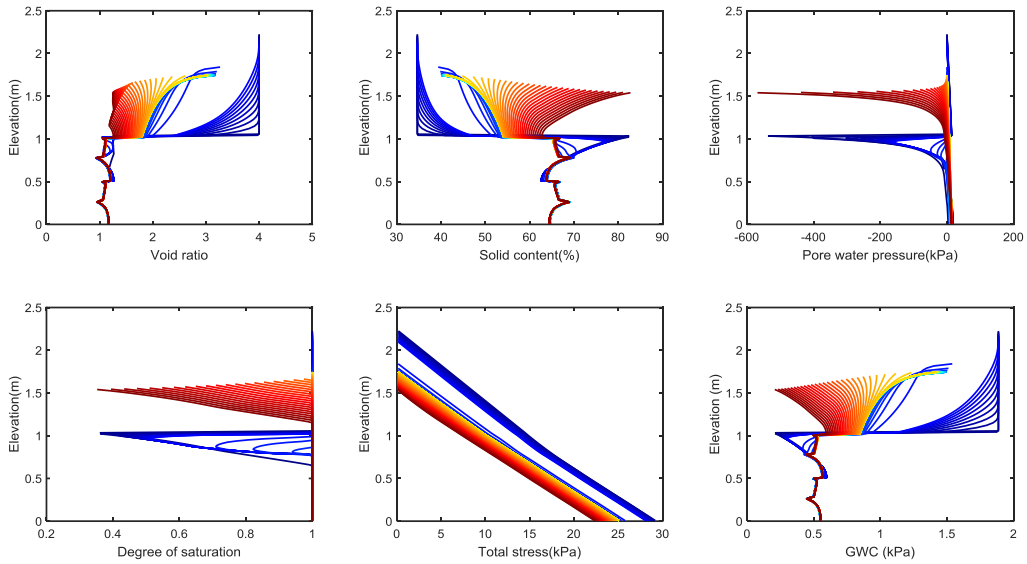

(c)

Fig. 10.17 Calculated variations of profiles of several parameters (pore water pressure, void ratio, total stress and degree of saturation) over time using GCM: (a) during the 1st year (1st layer deposition), (b) during the 2nd year (2nd layer deposition), and (c) during the 3rd year (3rd layer deposition)

10.3. Hypothetical case analyses of hard rock tailings deposits

10.3.1 Material properties

Analysis in this section is performed based on management of the hard rock tailings from Musselwhite Mine (LL=21.5% and PL=12 %), which is located in Opapamiskan Lake, Ontario, Canada. Elementary and column tests have been performed in Carleton University to study both the dewatering and consolidation behaviour of Musselwhite tailings. These test results shows that the Musselwhite tailings do not exhibit significant different behaviour of volume change and water retention from the Buly tailings studied in Chapter 8. Thus, the constitutive parameters for volume change and water retention behaviors are selected based on the analysis of a drying box test presented in Chapter 8 and 9. The initial void ratio at deposition is around 1.4-1.8, which is higher

than that (around 1.1) of Buly tailings at deposition (Daliri et al. 2016). The specific state surface for volume change behaviour in chapter 8 has a limit on the maximum void ratio (1.2) which is not applicable for this case now. Thus, the constitutive parameters for the volume change are slightly adjusted allowing a maximum void ratio of 1.8 as shown in Table 10.7. This set of parameters represent almost the same volume change behaviour as that in Chapter 8, as compared in Fig. 10.18. Difference only exists at extremely low stress level, but seems unimportant for this study. This also demonstrates the flexibility of the shape of the State Surface Model proposed by Vu and Fredlund (2006). The G_s=3.27 for this tailings. The results of the column test showed that the hydraulic conductivity of Musselwhite tailings is much higher than that of Buly tailings studied in Chapter 8, as also shown by the analysis exercise presented in the following section before analyses of field cases.

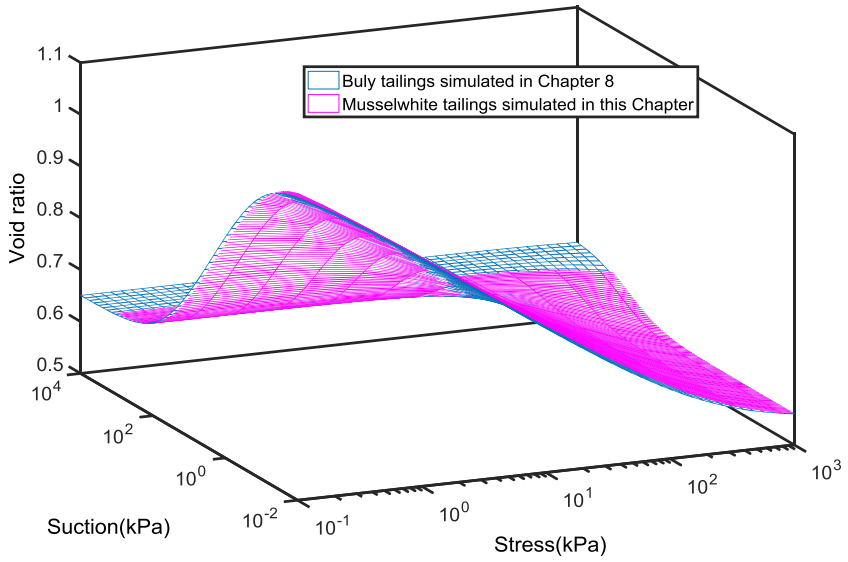

Fig. 10.18 Two comparable state surfaces with different maximum void ratios

Table 10.7. Parameters for constitutive relationships

Volume change behaviour								
Parameters	a	b	c	d	f	g	κ	κ_s
Value	1.8	0.1603	0.003084	0.02306	223257.4553	326718.8209	0.015	0.0015
Water retention behaviour								
Parameters	C_{drying}	$C_{wetting}$	λ_{se}	λ_{sr}	κ_{ss}			
Value	3.1	2.65	0.6	0.4	0.028			
Water hydraulic conductivity*								
Parameters	H_1	H_2	M					
Value	5×10^{-6}	4	0.75					

*Different from the tailings studied in Chapter 8.

10.3.2 Simulating the column test on hard rock tailings

The column tests have been performed in a similar way (see Fig. 10.19 for the instrument) as that introduced in Chapter 7. Four column tests for two different initial solid concentrations, two for 65% (void ratio is around 1.7608) and the other two for 70% (void ratio is around 1.4014), have completed. In each test, 50 cm thick tailings saturated with water have been deposited in the column, which is allowed to consolidate under self-weight. The boundary conditions are different from that of the column test in chapter 7: free draining through porous stone is allowed at the bottom, no water can escape from the top with a closed cap. Webcams were used to track the height of water and tailings. Three tensiometers fixed at different elevations of wall of the column are used to measure the positive pore-water pressure and matric suction (see Fig. 10.19). The total mass was recorded by a scale. Volumetric water content at the several elevations have been recorded by water content sensors. The average void ratio can be easily calculated from the measured heights.

Three numerical simulations have been performed using UNSATCON-ML with uniform initial void ratio of 1.7608, 1.4014, and 1.45, respectively. The void ratio of 1.45 is closer to the

average value of the field tailings from the thicker underflow in Musselwhite. A water pressure head of 0 kPa is set at the bottom to simulate the effect of porous stone until the pore water pressure at node above (the bottom node) becomes negative, after which, the boundary condition switches to zero flux. A no decantation/no evaporation boundary (boundary condition ***Case (i)*** formulated in Chapter 6)is applied at the top (water-tailings interface) (which is moving as the tailings consolidate). Material properties used are given in Table 10.7, as discussed in previous section. These tailings have a much higher permeability, equal to $4\times10^{-6}\times e^4$ m/s.

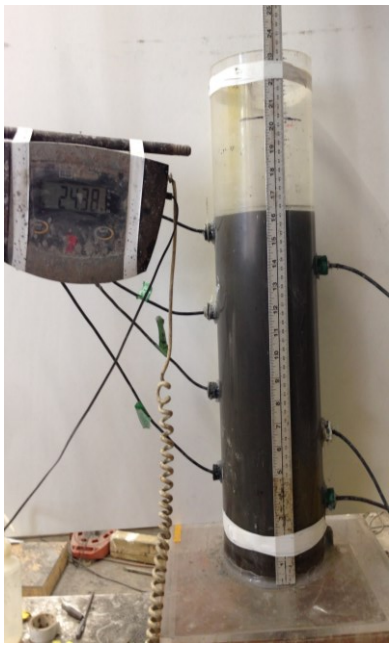

Fig. 10.19 The instrument for column test at Carleton University

Fig. 10.20 shows variation of various profiles along depth of the column calculated using UNSATCON-ML for two analyses. Fig. 10.20 is produced in the same way as that for Fig.10.6 and Fig.10.7. The only difference is that a lower temporal resolution is used to plotting the profiles, with a time interval of 0.5 days after 0.5 day.

No significant difference between this two analyses in the trends of these variations can be visualised. After deposition, consolidation initiates from the bottom of column, which is the same as previous cases (where zero flux is applied). But the consolidation rate here for this case is much higher due to a downward flux boundary condition. Less than half day after deposition, a steady state condition is approached, with a negative pore water pressure profile formed along the depth of the column. The predicted degree of saturation is slightly less than one (corresponding to the negative PWP according to the constitutive law), indicating a final partially saturated condition within the profile. This is controlled by this type of boundary condition, not by the other external environments (such as evaporation in previous cases).

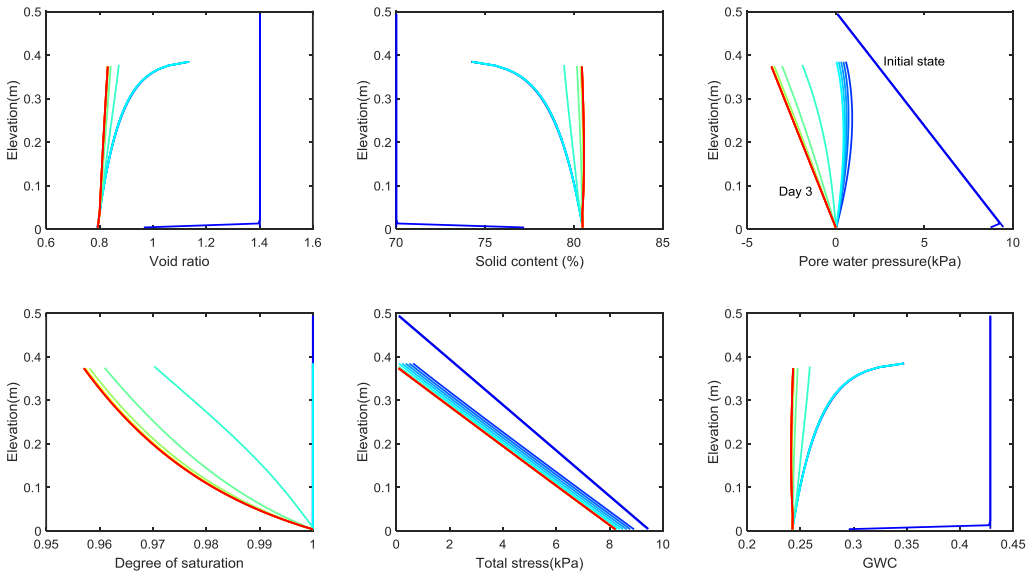

(a)

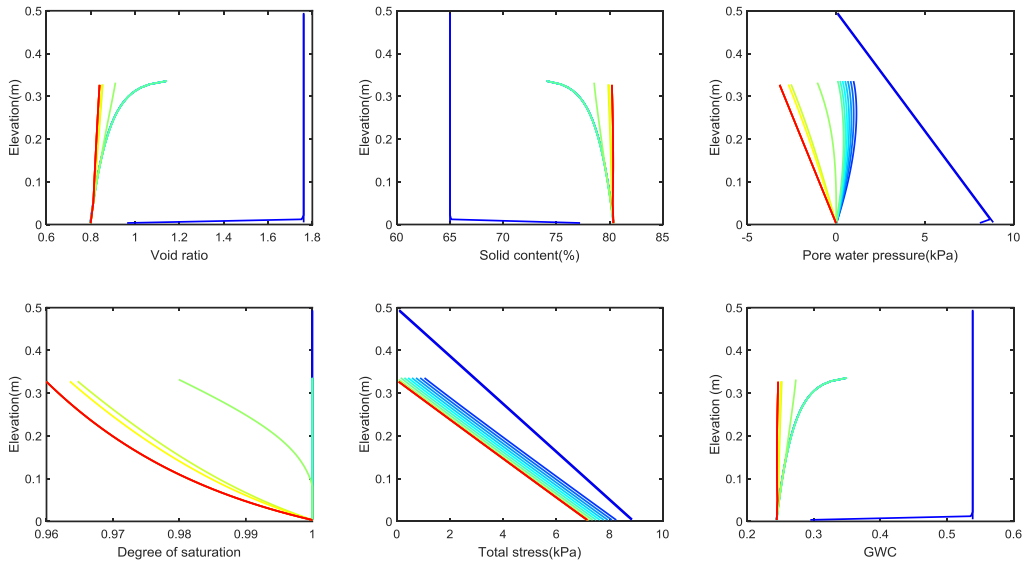

(b)

Fig. 10.20 Variation of profiles with time calculated using UNSAT-CON: (a) for initial void ratio of 1.4014 (b) for initial void ratio of 1.7608

Fig. 10.21 shows comparison between predicted and measured variations of heights (the heights of both tailings and water) over time for this column test. Again it can be seen that the initial consolidation rate is quite high, and has almost finished at 0.3 day after start of the experiment. This is also due to high permeability of this tailings as highlighted in Fig. 10.21, which also contribute to a fast decrease of water elevation (water flows out from the system through bottom drainage). The slight decrease in the predicted tailings' height after the disappearance of surplus water is because of additional compression induced by hydraulic loading (see the suction profile in Fig. 10.20). Similar observation is found in the experiment data. The predictions by UNSATCON-ML are in a good agreement with the measurements, taking into consideration that (1) the constitutive parameters for mechanical and hydraulic retention models in chapter 8 for another and similar hard rock tailings are adopted here for this tailings, only the permeability is

different and higher, (2) variability in the material properties. Fig. 10.22 shows that predicted average void ratios are in a good agreement with and measurements for both initial densities. Fig. 10.23 shows that the predicted pore water pressure using UNSATCON-ML is also in a good agreement with measurements at two elapsed times.

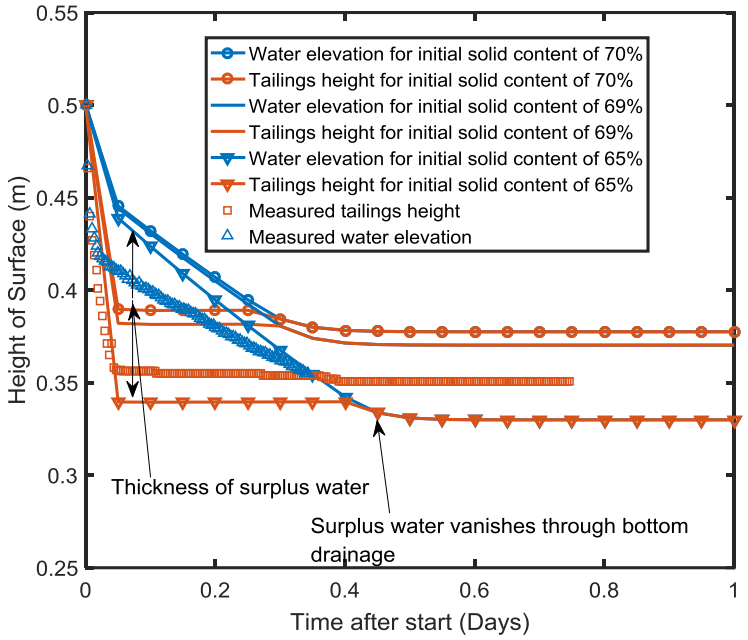

Fig. 10.21. Comparison between predicted and measured variations of heights (the heights of both tailings and water) over time for this column test

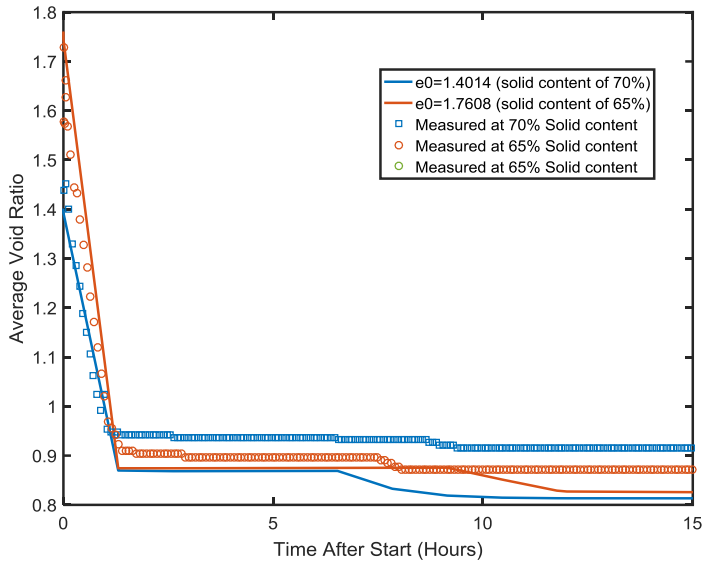

Fig. 10.22. Comparison between predicted and measured average void ratio over time for this column test

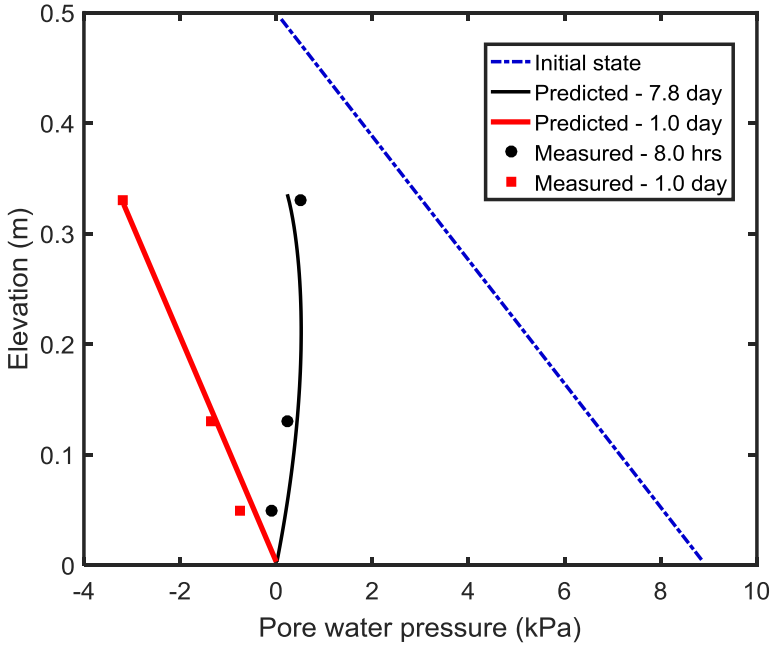

Fig. 10.23. Comparison between predicted pore water pressure profile with measurements at two elapsed times

10.3.3 Hard rock tailings field case analysis

The good agreements obtained for the column test provides credence to the constitutive parameters for analysis of large strain consolidation behaviour of this tailings from Musselwhite Mine. In this section, UNSATCON-ML will be applied to simulation of consolidation and dewatering behaviours of Musselwhite tailings deposited in layers in the field. Musselwhite Mine began gold extraction in 1997 and had produced a total of 21.7 Mt of tailings by the end of 2013. Since the spring of 2010 thickened tailings with about 70% solids have been disposed of from the perimeter area using the upstream stacking method (Kam et al. 2014). Based on the field practice reported in Kam et al. (2014), a number of multi-layer deposition schemes have been simulated over 3 years (from 2010 to 2013 during which thickened tailings disposal is adopted in Musselwhite). These simulated schemes are summarized in Table 10.8. Firstly, only one deposition per year is considered , with a different deposition thickness (varying from 2.0 m to 3.0 m in terms of initial slurry) per year. The deposited tailings are 6.0 m to 9.0 m in thickness in total over 3 years. Both winter and summer depositions (as defined previously) have been analysed. In total, 6 subcases of deposition scheme are analysed.

Table 10.8. Simulated deposition schemes for Musselwhite tailings (one layer deposition per year)

Deposition scheme		Total thickness (m) = Deposition thickness per time (m)×Depositing time		
Multiple layer deposition	1 deposition per year Summer deposition	2.0×3	2.5×3	3.0×3
	1 deposition per year Winter deposition	2.0×3	2.5×3	3.0×3
Total thickness (m)		6.0	7.5	9.0

For the field case, a zero water flux is assumed and applied at the bottom. An evaporation rate of 2.877 mm/day, corresponding to a total evaporation of 400 mm in each summer (from May 15th to Oct 1st), is applied at the top surface, zero flux across the top surface is specified in the remaining period (from Oct 1st to the coming May 15th) of each year. The average solid content of thickener underflow (slurry tailings) at the discharge varied from 60% to 72%, with an average of about 67% (the target value was set at 68%) in Musselwhite (Kam et al. 2014). In the numerical analysis, the corresponding initial void ratio of slurry tailings at deposition of each layer is set at 1.45 neglecting the temporal and spatialvariability.

Fig. 10.24 presents the predicted tailings height *vs.* time and normalised height (the absolute height divided by the total initial thickness of deposits) *vs*. time for different deposition schemes. A significant difference exhibited by the Musselwhite tailings from the oil sands tailings analysed before would be the much higher rate of self-weight consolidation, which is mainly due to its much higher permeability. The time to approaching the end of self-weight consolidation is generally less than 1 day for all deposition thicknesses (2.0 m – 3.0 m per year) considered here, indicating a negligible influcece of length of the drainage path. The consequence of this is the negligible difference in the tailings heights (and other states, e.g. GWC, presented later) between winter (labeled as 'W' in Figures) and summer (labeled as 'S' in Figures) depositions at end of each (1st, 2nd and 3rd) year, for all the deposition thicknesses. Once the self-weight consolidation is almost completed, the upward water flow is mainly driven by the evaporation. For winter deposition, the tailings remains the same height until the start of the summer, after which, tailings deposits shrink upon desiccation to a shrinkage limit. For summer deposition, these two behaviours of deposits occur in an opposite order, that is, the tailings height first decreases to the shrinkage limit and remains thereafter until a new deposition in the next year. It is also found that there is no

difference in the final profiles between winter and summer depositions at the end of each year, see Fig. 10.27 and Fig. 10.28, which illustrates the profiles (including void ratio, degree of saturation, gravimetric water content, total stress, solid content, and suction) for cases at the end of the 1st year and the 3rd year, respectively.

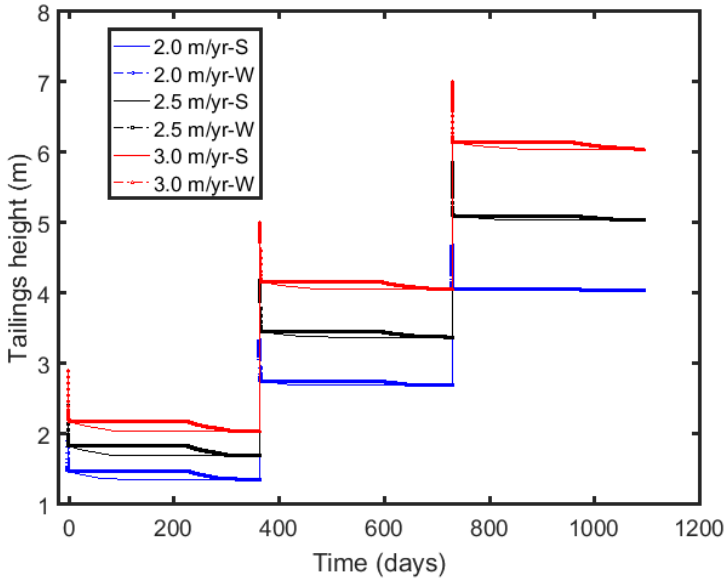

(a)

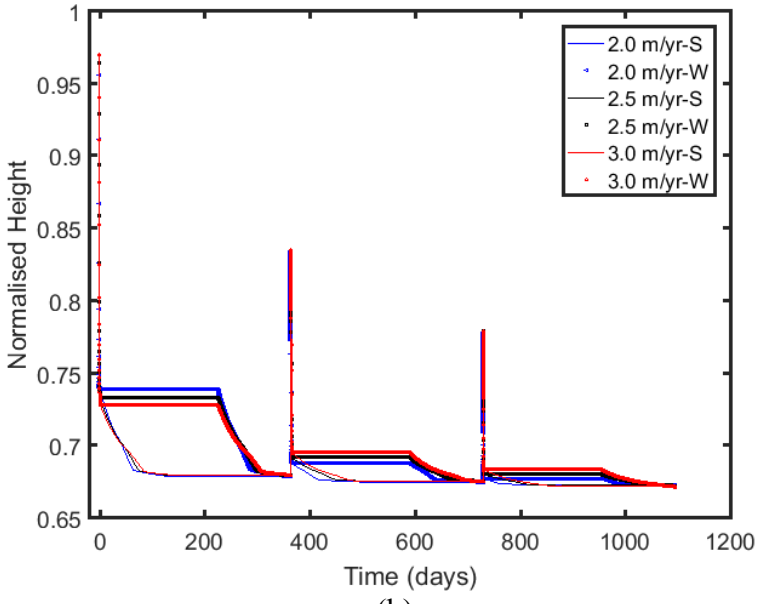

(b)

Fig. 10.24. Predicted tailings height *vs.* time for different deposition schemes: (a) absolute height and (b) normalised height.

The existance of underlying deccicated tailings do accelarate the consolidation of the new deposits. This is not very evident in thicker deposition shemes, but can be infered from thiner lifts in Fig. 10.24. Fig. 10.24 shows that for thinner lifts (2.0 m per year) the difference is not too much between the winter and summer depositions once the self-weight is completed. This is due to the water absorption capacity of underlying tailings which brings the average void ratio of the new deposition closer to the shrinkage limit. While for thicker deposition schemes (2.5 and 3.0 m per year), these effects become less and less significant, because of lesser degree of desiccation (higher degree of saturation) of the underlying tailings, see Fig. 10.27(e). This effect of can be more seen clearly (quantitatively by comparison) from Fig. 10.25. Fig. 10.25 (a) shows the predicted overall void ratio *vs.* time. The variations of average void ratio of each layer over time are separately shown in Fig. 10.25 (b) (c) and (d). Fig. 10.25 (b) shows that deposits of 1st layer after initial settling for 3.0 m per year are densest after the 1st deposition, due to the highest overburden stress. In contrast, Fig. 10.25 (c) and (d) shows that deposits of 2nd (3rd) layer after initial settling for 2.0 m per year are densest after the 2nd (3rd) deposition, and their void ratios are closer to the shrinkage limit.

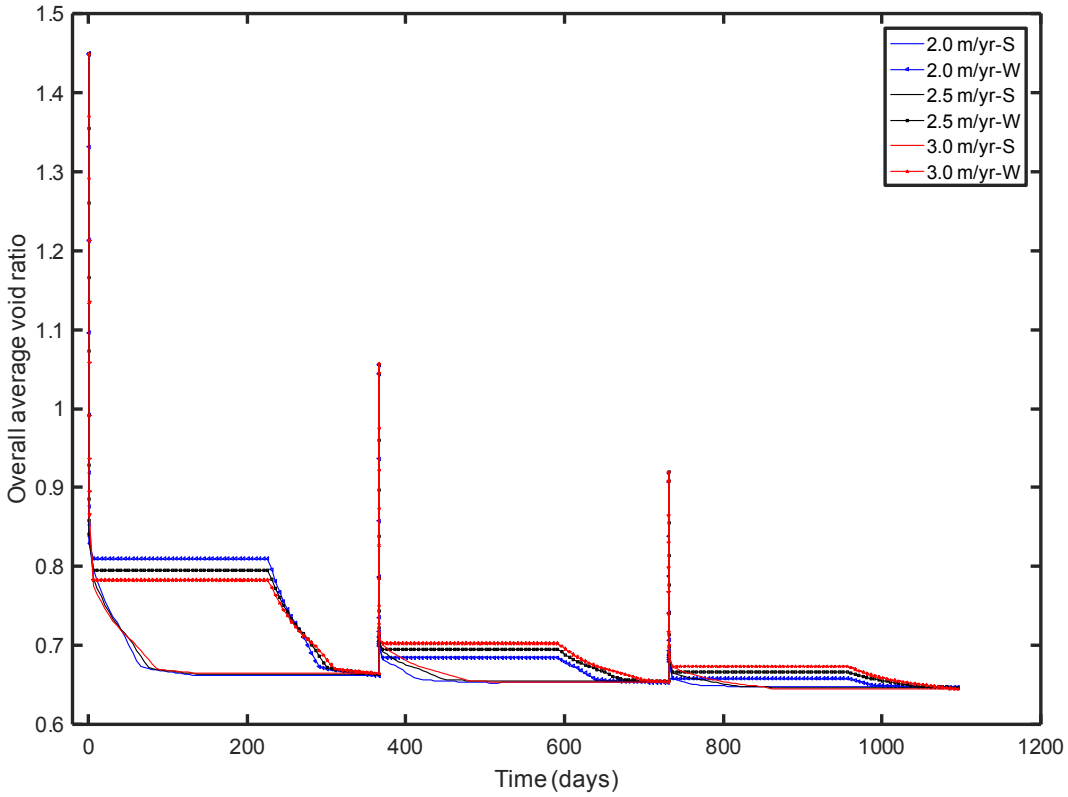
Overall average void ratio
Time (days)
2.0 m/yr-S
2.0 m/yr-W
2.5 m/yr-S
2.5 m/yr-W
3.0 m/yr-S
3.0 m/yr-W

(a)

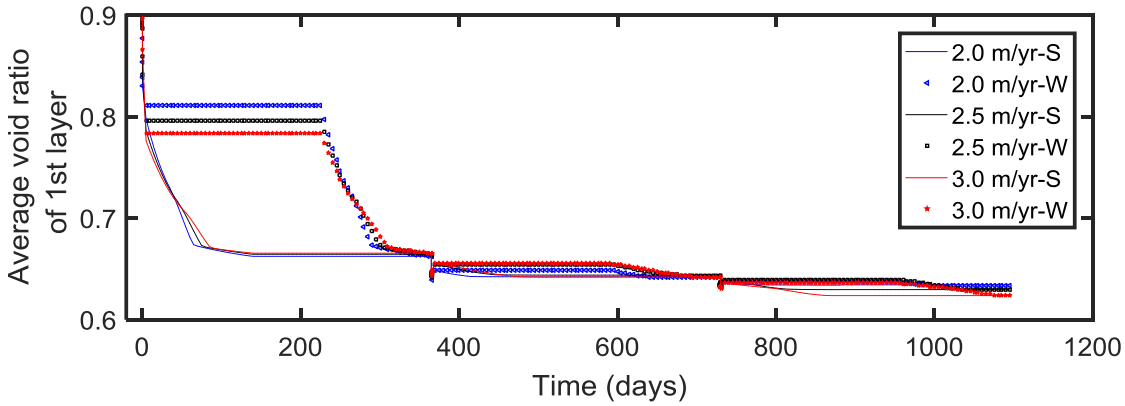
Average void ratio of 1st layer
Time (days)
2.0 m/yr-S
2.0 m/yr-W
2.5 m/yr-S
2.5 m/yr-W
3.0 m/yr-S
3.0 m/yr-W

(b)

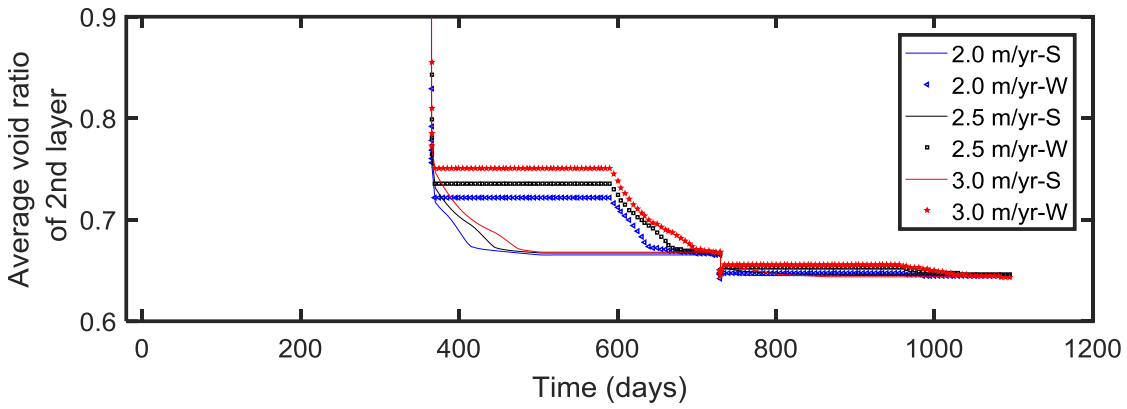

(c)

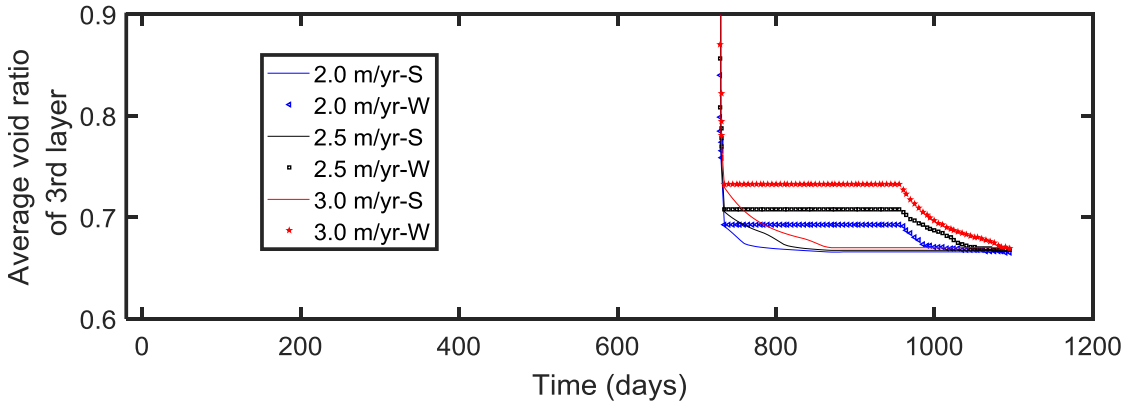

(d)

Fig. 10.25. Predicted void ratio *vs.* time for different deposition schemes: (a) overall average void ratio, (b) average void ratio of 1st layer (c) average void ratio of 2nd layer (d) average void ratio of 3rd layer

Overall, the predicted void ratios after initial settling are in a good agreement with the measurements of dry density (between 1.8 and 1.9 tonnes/m^3) in the field (Kam et al. 2014). Another important consideration would be the degree of dewatering of the deposits, since the gain in shear strength is strongly correlated to the reduction in moisture content in the field. Kam et al. (2014) reported that, the gain in shear strength (measured with a Geonor H-60 Hand-Held Vane

Tester) during the dry season is immediate and much faster than that in wet season after deposition. Fig. 10.26 (a) shows the predicted overall GWC *vs.* time. The variations of average GWC of each layer over time are separately shown in Fig. 10.26 (b) (c) and (d). the predicted variations of GWC with time are similar to those of void ratio for both winter and summer deposition. the difference is that GWC continuously decreases with drying in the summer seasons while the void ratio is limited to the shrinkage limit. The predicted average void ratios for both winter and summer depositions converge to almost the same values (shrinkage limit) for different thicknesses, while the predicted average GWC are different for different deposition thicknesses. The effects of underlying desiccated tailings on GWC are also similar to that on the void ratio. The predicted variation of GWCs are also in a good agreement with the measurements in the field: during the dry summer periods GWC dropped to about 15-17.5% 40 days after deposition (Kam et al. 2014).

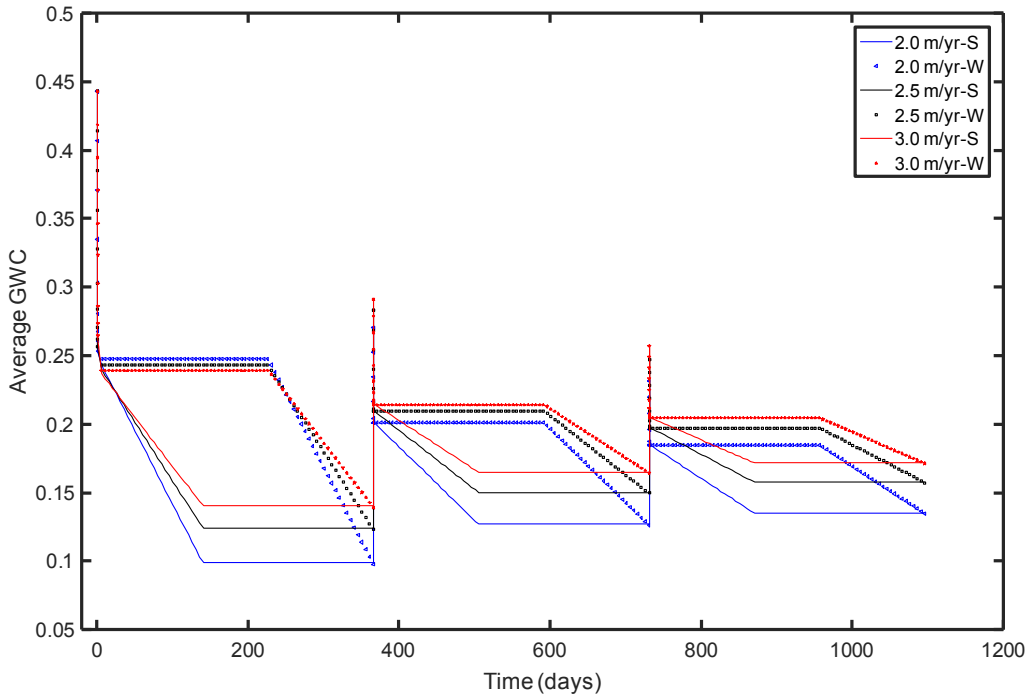

(a)

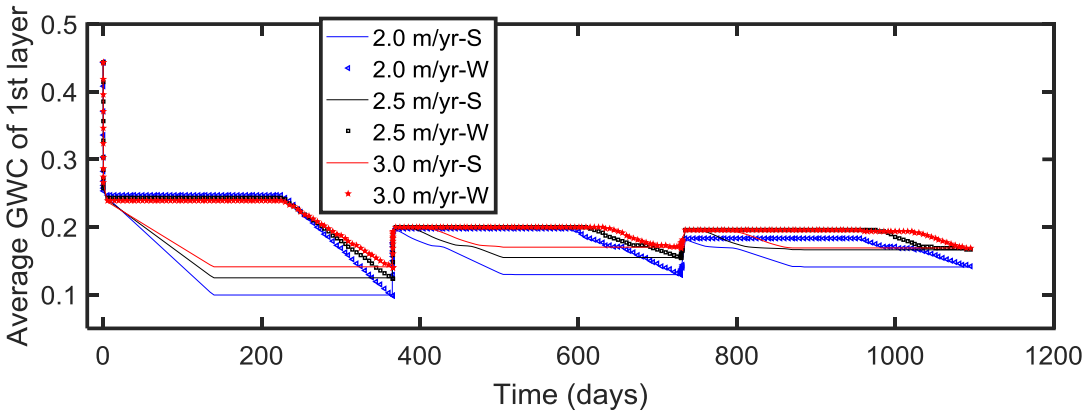

(b)

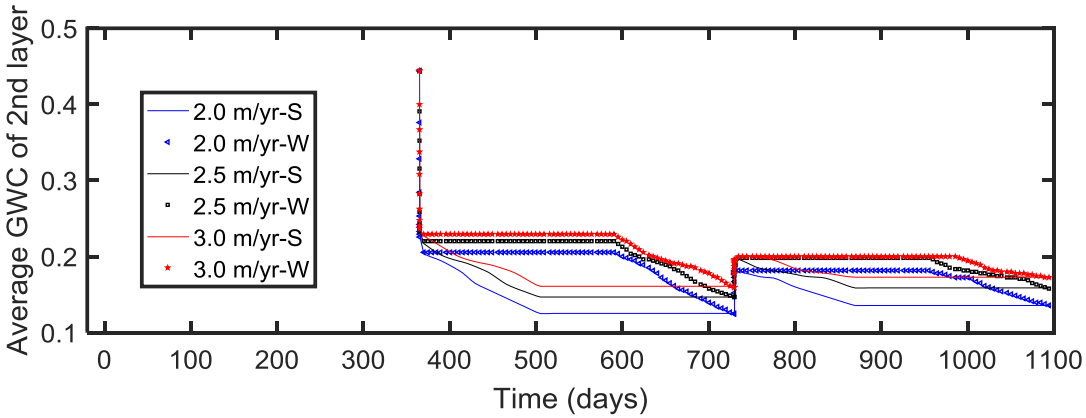

(c)

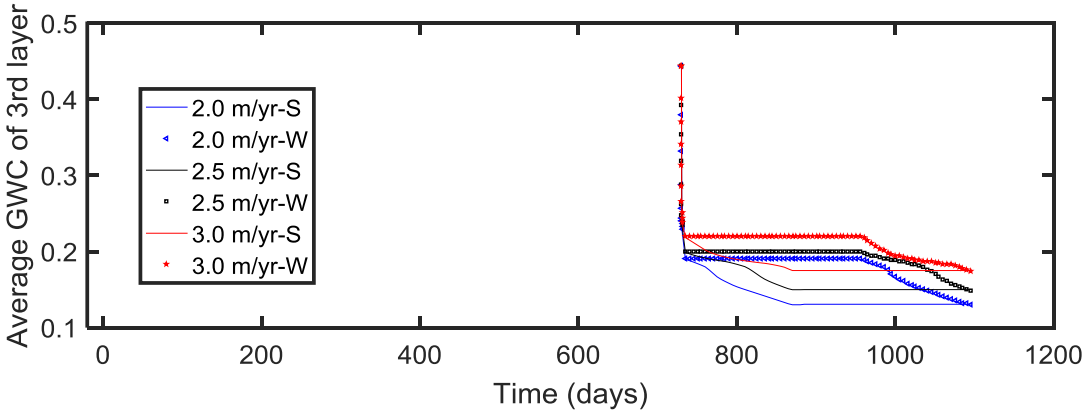

(d)

Fig. 10.26. Predicted GWC *vs.* time for different deposition schemes: (a) overall average GWC, (b) average GWC of 1st layer (c) average GWC of 2nd layer (d) average GWC of 3rd layer

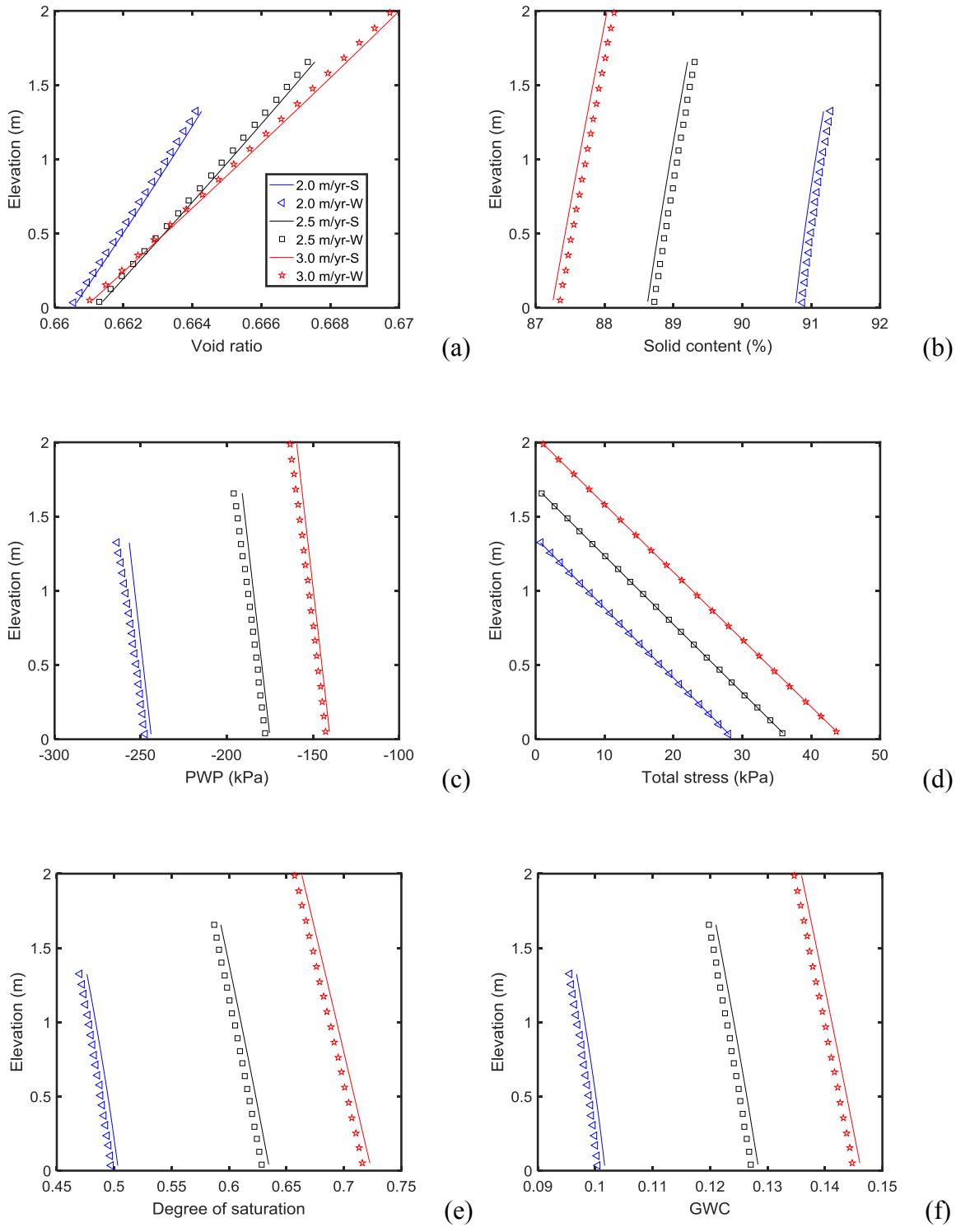

Fig. 10.27. Predicted profiles after 1 year for all deposition schemes for (a) void ratio, (b) solid content, (c) PWP, (d) total stress, (e) Degree of saturation and (f) GWC

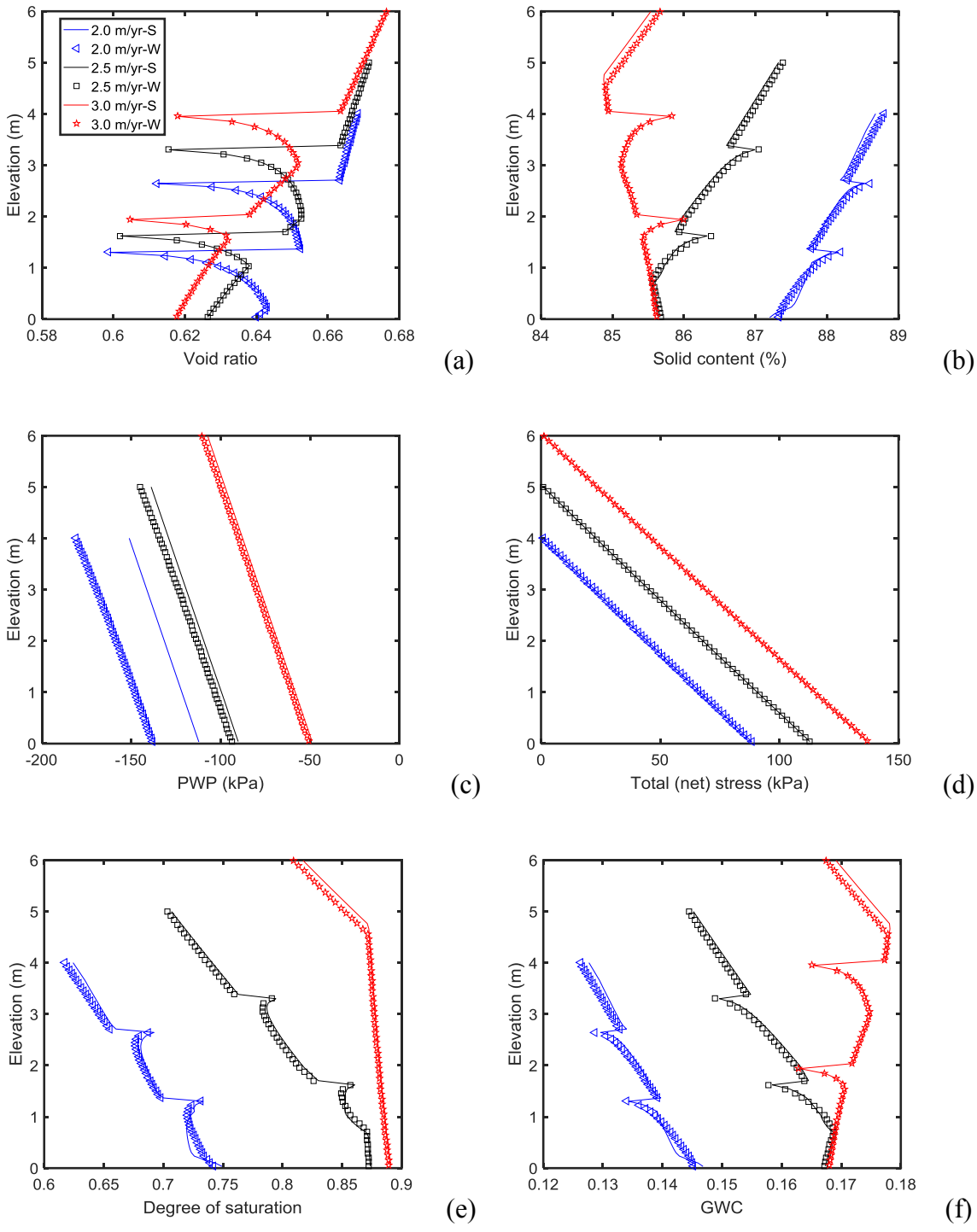

Fig. 10.28. Predicted profiles after 3 years for all deposition schemes for (a) void ratio, (b) solid content, (c) PWP, (d) total stress, (e) Degree of saturation and (f) GWC

In order to study the effect of multi-layer deposition within one single year, three other cases are simulated using UNSATCON-ML, as described in the following:

(1) two depositions per year (one at the beginning of the summer of this year (May 15th), the other half year later (Nov. 15th)), each with a thickness of 1.5 m. there are 6 layers (total thickness of 9 m) over 3 years.

(2) two depositions per year (one at the beginning of the winter of this year (Oct. 1st), the other half year later (April 1st)), each with a thickness of 1.5 m. there are 6 layers (total thickness of 9 m) over 3 years.

(3) two depositions per year (one at the beginning of the summer of this year (May 15th), the other two months later (July 15th)), each with a thickness of 1.0 m. there are 6 layers (total thickness of 6 m) over 3 years.

The first two cases are very similar to the winter and summer depositions (with a deposition thickness of 3.0 m per year), respectively. The simulated results for 2 layers per year are therefore compared with those two cases for 1 layer per year in Fig. 10.30. Fig. 10.30 (a) (b) and (c) show the variations of predicted tailings height, average GWC and void ratio over time, respectively. It is shown that with thinner deposition may result in a faster overall dewatering and consolidation rates induced by evaporation during the summer at initial stages, however, these two different deposition schemes (2 layers per year and one layer per year) converge to almost the same final values in terms of tailings height and overall void ratio. This is because the applied evaporation rate (or total amount) is able to bring the tailings to the shrinkage limit, no matter when they are deposited. If the deposited total solid contents are the same (this is the case here), finally, the height would be almost the same. The last case uses two depositions (1 m per layer) in the summer, the

results of which are compared with 1 layer per year (with a deposition thickness of 2.0 m per year) in Fig. 10.30. Similar findings can be observed as the first two cases: the final heights are almost the same corresponding to the shrinkage limit. In these cases with 2 layers deposition per year, the influence of underlying desiccated tailings can also be observed. For thinner deposition, the overall consolidation and dewatering rate in the summer is higher, this might be helpful for formation of a steeper beach slope (higher shear strength at unsaturated state) at the discharge point, which facilitates the flow of deposited slurry tailings further away from the discharge point. In contract to the oil sands tailings, summer deposition results in the same degree of dewatering and consolidation in the end as winter deposition, this is due to the much higher permeability of this tailings, and evaporation can also be fully used for the summer deposition case. In practice, summer deposition may be easier considering the risk of freezing of high-density of thickened tailings and clogging of spigot lines.

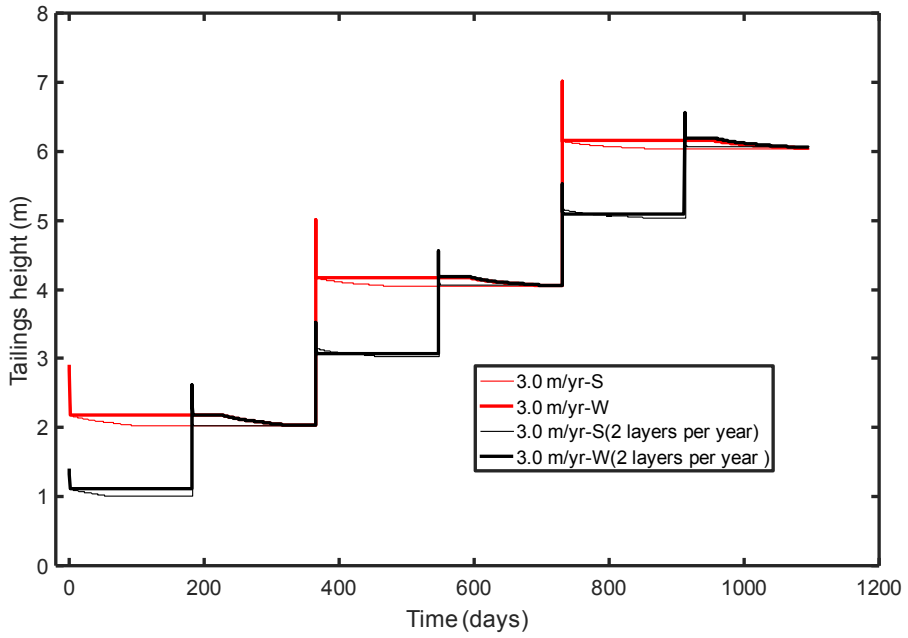

(a)

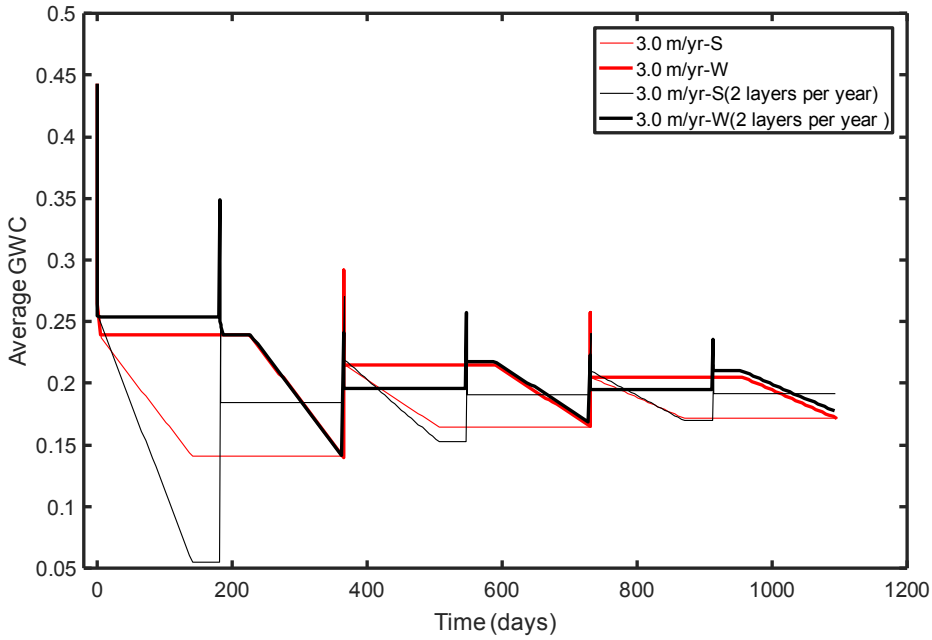

(b)

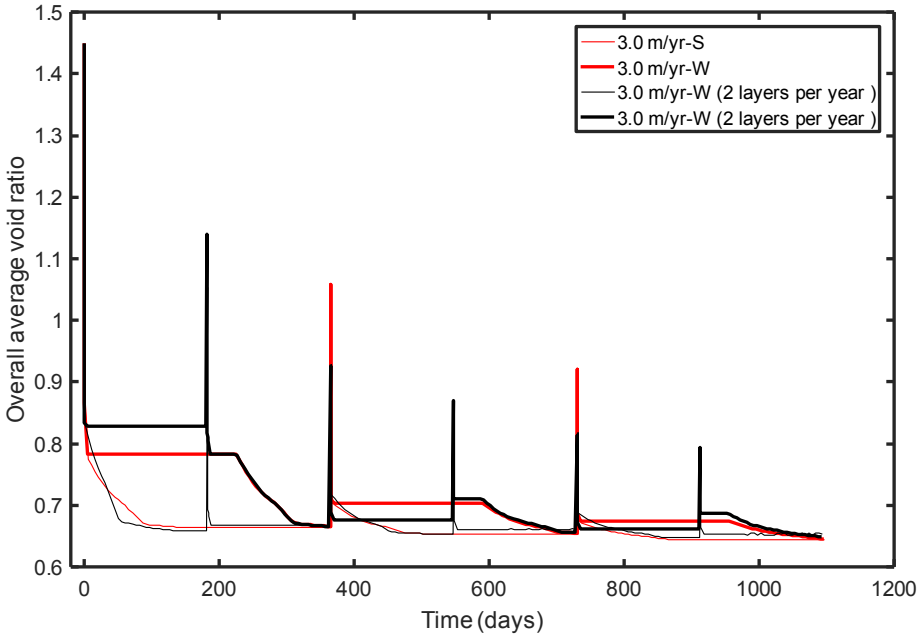

(c)

Fig. 10.29. Comparison between 1 layer deposition per year and 2 layers deposition per year (3m per year in total): (a) tailings height (b) GWC and (c) void ratio

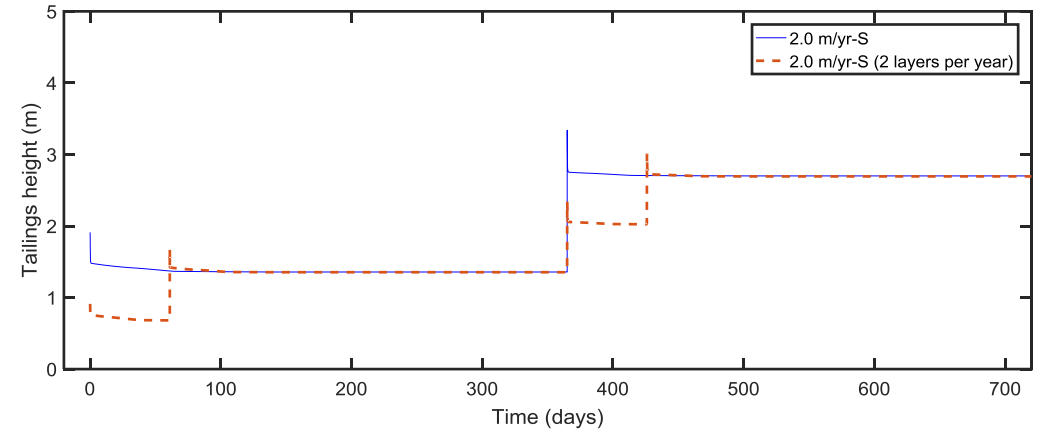

(a)

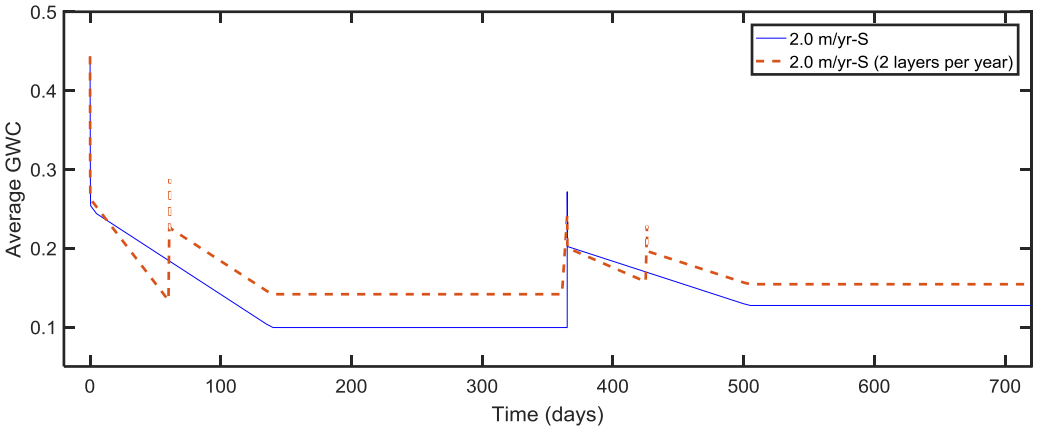

(b)

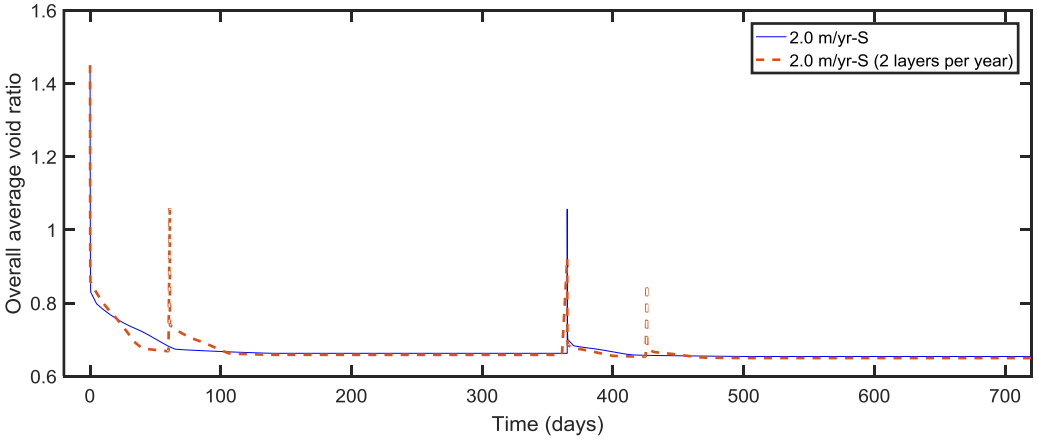

(c)

Fig. 10.30. comparison between 1 layer deposition per year and 2 layers deposition per year (2m per year in total): (a) Tailings height (b) GWC and (c) void ratio

10.4. Conclusion

In this chapter, the program UNSATCON-ML developed in this thesis has been used to carry out a couple of hypothetical cases of tailings deposition. Two types of tailings are considered: oil sands tailings and hard rock tailings. The adopted constitutive parameters in both tailings are mainly consistent with those in previous chapters (Chapter 6 to Chapter 9) for development and testing of UNSATCON-ML. The abundant results from UNSATCON-ML help to understand the hydro-mechanical process in tailings deposits in the field scenarios, which is important for optimization of deposition scheme. Specific results are selected and presented for each subcases with a particular focus. Several conclusions for these two tailings are obtained:

For oil sands tailings:

(1) Winter deposition is better in terms of the deposition time, as it can use both the self-weight and evaporation to consolidate/dewater tailings effectively/fully.

(2) For long term performance (10 years selected here), Multilayer deposition can generally result in a denser final profile than single layer deposition for thicker (above 1.5 m per year for oil sand tailings studied in this chapter) layer deposition, due to the effect of desiccation history on underlying tailings deposited each year. It seems that there exists a optimum deposition thickness in terms of resulting in a denser final profile, which is 1.0-1.2 m per year for oil sand tailings studied in this chapter. This is a consequence of the overall interlayer hydraulic interaction and associated mechanical behaviour within the whole accumulated tailings that is affected by desiccation history of each deposited layer. This optimum deposition thickness might be different for different scenarios, including both internal and external factors. In other words, the optimum deposition scenario recommended here only pertains to tailings with specific characteristics in a

specific average evavaporation conditions used in numerical anlaysis**.** UNSATCON-ML serves as a effective tool for helping the optimum deposition design.

For hard rock tailings:

(3) There is no significant difference in the final state of tailings deposition between winter and summer depositions. This is due to the much higher permeability of this tailings (from Musselwhite Mine): the self-weight consolidation can finish in less than one day after deposition, and evaporation can also be fully used in dewatering the tailings for the summer deposition case.

(4) The final overall void ratio (or height) of deposits are almost the same as long as the total deposited tailings contents are the same. Since the applied evaporation rate or total amount evaporation in the summer is able to desaturate the tailings to the shrinkage limit, no matter when they are deposited.

(5) The underlying desiccated tailings do have an effect of accelerating the dewatering and consolidation of new deposited tailings on the top, which is helpful for strength gain.

(6) With the effect of underlying tailings, multiple deposition of lifts within a year will increase the average degree of saturation that a fresh layer is exposed to and therefore reduce the risk of acid generation.

The results presented in the chapter also have implications on other activities involved in the tailings management, such as, design and construction of dykes.

Glossary

Symbols

a, b, c, d, f, g	Material parameters for void ratio constitutive relationship
κ	Elastic stiffness parameter for changes in net mean stress
κ_s	Elastic stiffness parameter for changes in suction
C_{drying} , $C_{wetting}$	Constants related to the location of primary drying and wetting surfaces
κ_{ss}	Parameter for elastic change of degree of saturation with change of suction
λ_{se}	Parameter for change of degree of saturation with change of void ratio
λ_{sr}	Parameter for plastic change of degree of saturation with change of suction
H_1, H_2	Material parameters for hydraulic conductivity vs. void ratio relationship
M	Constant in van Genuchten (1980) model
k_1	Coupling parameter for movement of LC yield curve in GCM
k_2	Coupling parameter for movements of SI and sd yield in GCM
κ	Parameter for elastic volumetric strains in GCM
κ_s	Parameter for elastic changes of degree of saturation in GCM
λ	Parameter for volumetric strains on LC curve in GCM
λ_s	Parameter for changes of degree of saturation on SI or SD curves in GCM
N_0 , Ω_{w0} , Ω_{d0}	Three material constants determining the location of NCL and PRL in analytical GCM
R	Measures the degree of hysteresis in GCM

Abbreviations

PWP	Pore Water Pressure
NCL	Normal Consolidation Line
PRL	Primary Retention Line
AEV	Air Entry Value
LL	Liquid Limit
PL	Plastic Limit
GWC	Gravimetric water content
SSM	State Surface Model
BBM	Barcelona basic model

10.5. References

S. Kam, N. Hmidi, Y. Mao. Field performance of thickened tailings disposal at Musselwhite Mine the Proceedings of the 17th International Seminar on Paste and Thickened Tailings, held in Vancouver, Canada, June 8-12, 2014. Published by InfoMine Inc., June 2014.

Appendix 10.1

Calculated variations of profiles using UNSATCON-ML with SSM and GCM.

Figs 10.31 and 10.32 in this appendix are produced in the same way as that for Fig.10.6 and Fig.10.7.

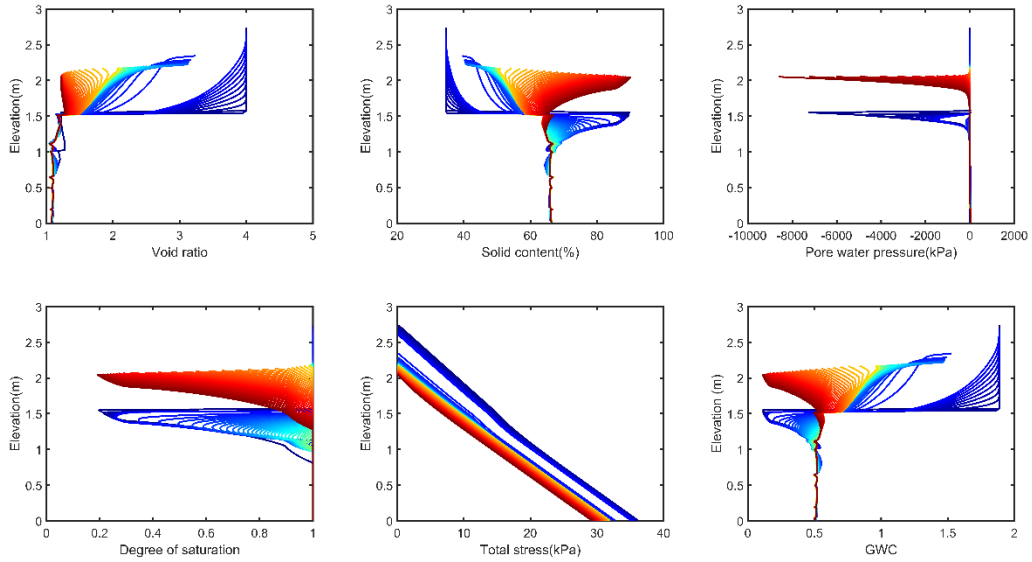

(a)

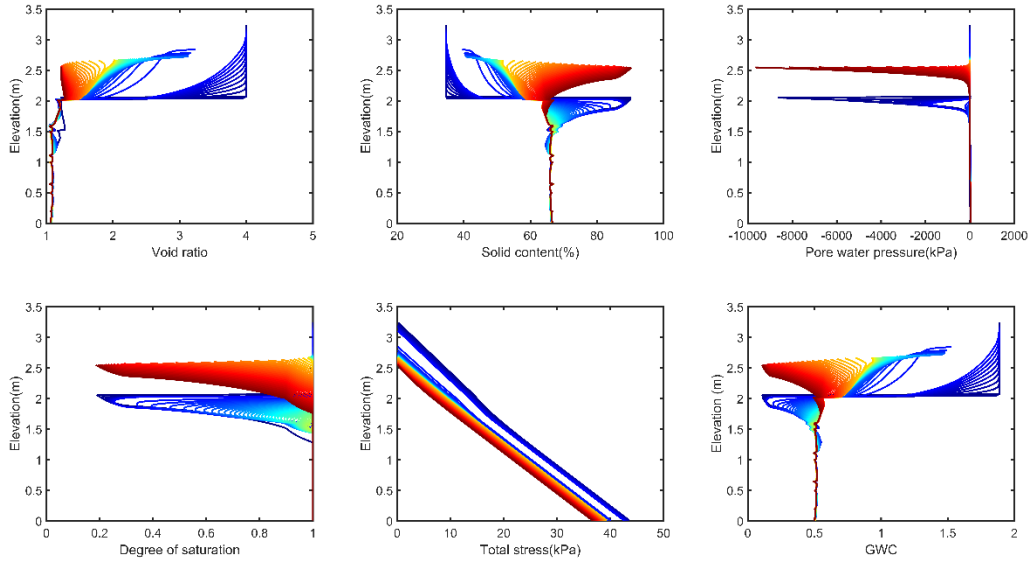

(b)

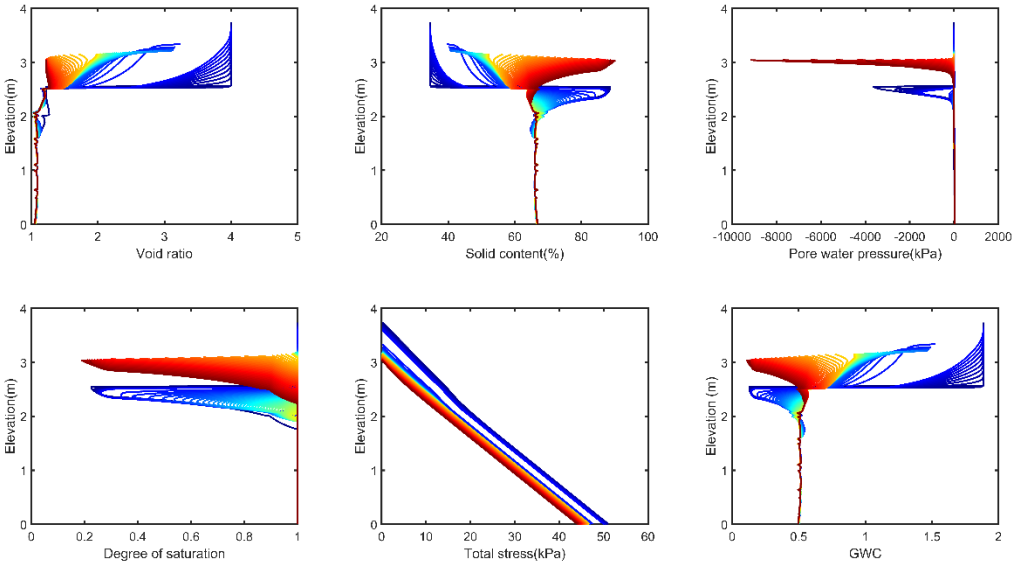
Elevation(m)
Void ratio
Solid content(%)
Pore water pressure(kPa)
Degree of saturation
Total stress(kPa)
GWC

(c)

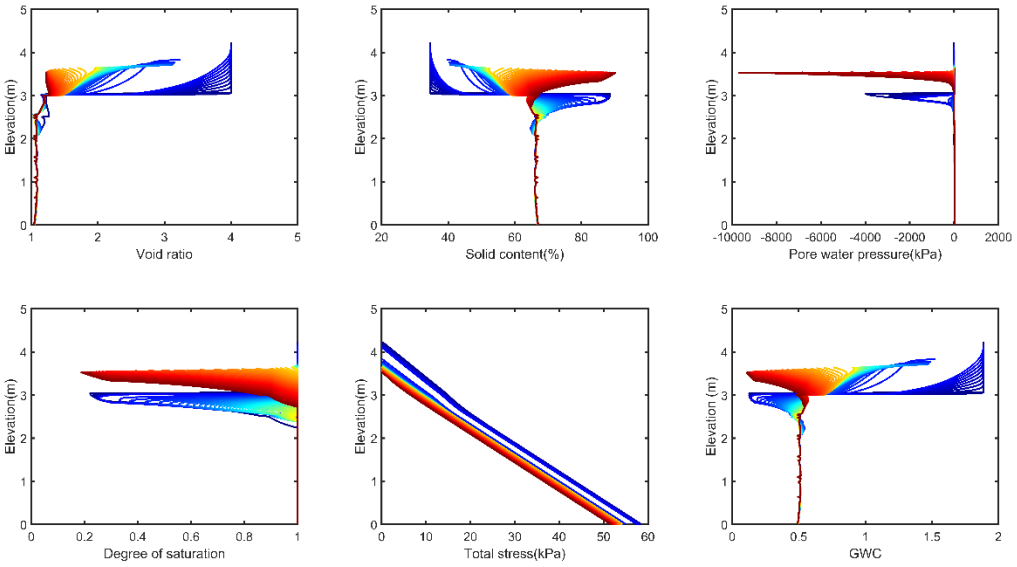
Elevation(m)
Void ratio
Solid content(%)
Pore water pressure(kPa)
Degree of saturation
Total stress(kPa)
GWC

(d)

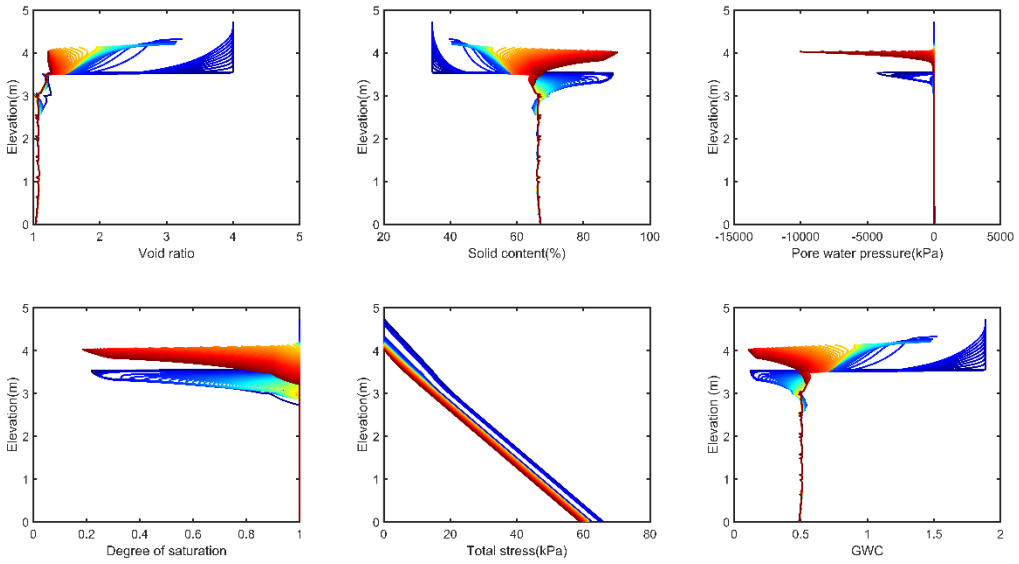
Elevation(m)
Void ratio
Solid content(%)
Pore water pressure(kPa)
Degree of saturation
Total stress(kPa)
GWC

(e)

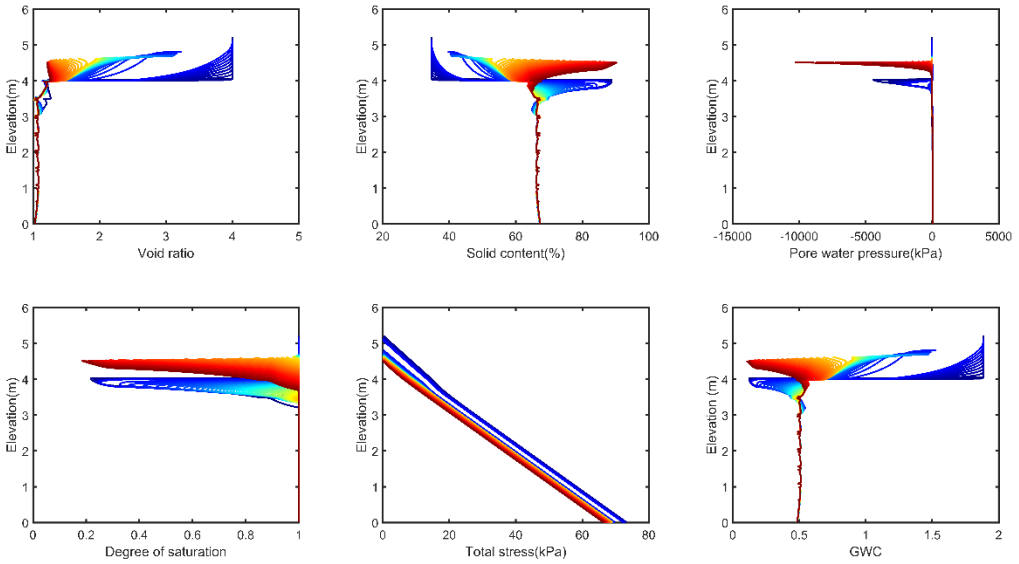
Elevation(m)
Void ratio
Solid content(%)
Pore water pressure(kPa)
Degree of saturation
Total stress(kPa)
GWC

(f)

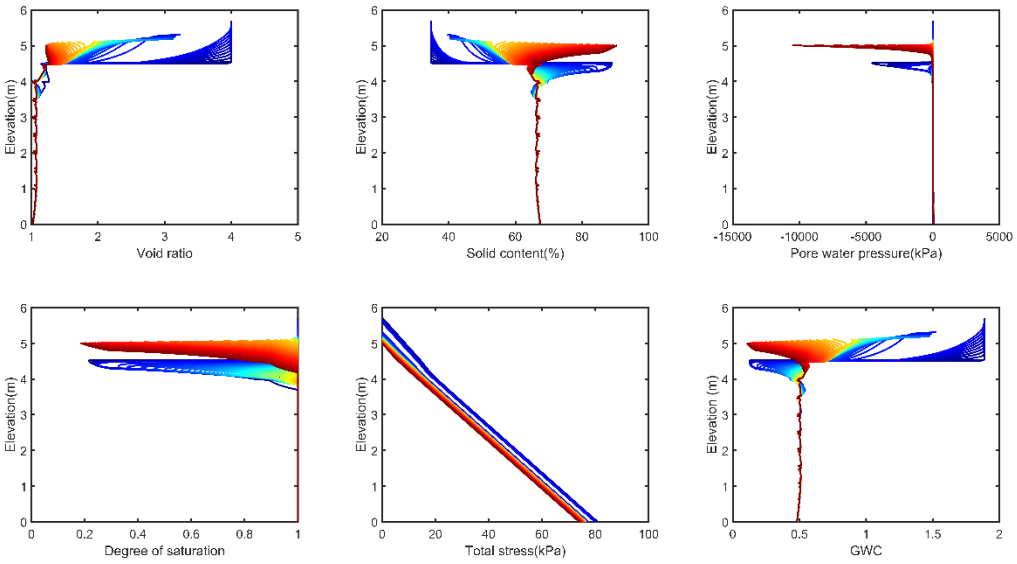

(g)

Fig. 10.31. Calculated variations of profiles of several parameters (pore water pressure, void ratio, total stress and degree of saturation) over time using SSM: (a) during the 4th year (4th layer deposition), (b) during the 5th year (5th layer deposition), (c) during the 6th year (6th layer deposition), (d) during the 7th year (7th layer deposition), (e) during the 8th year (8th layer deposition), (f) during the 9th year (9th layer deposition), and (g) during the 10th year (10th layer deposition).

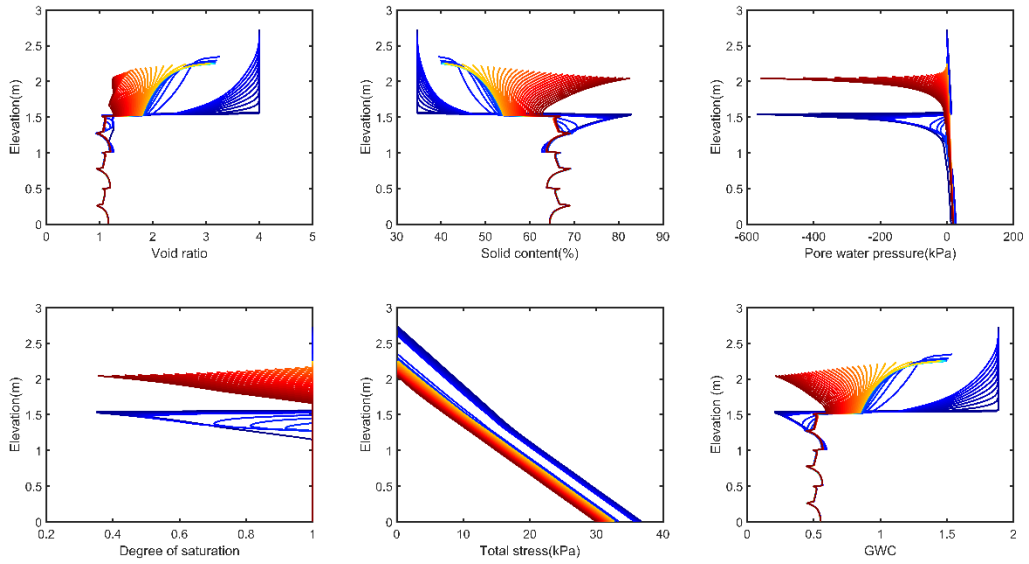
Elevation(m)
Void ratio
Solid content(%)
Pore water pressure(kPa)
Degree of saturation
Total stress(kPa)
GWC

(a)

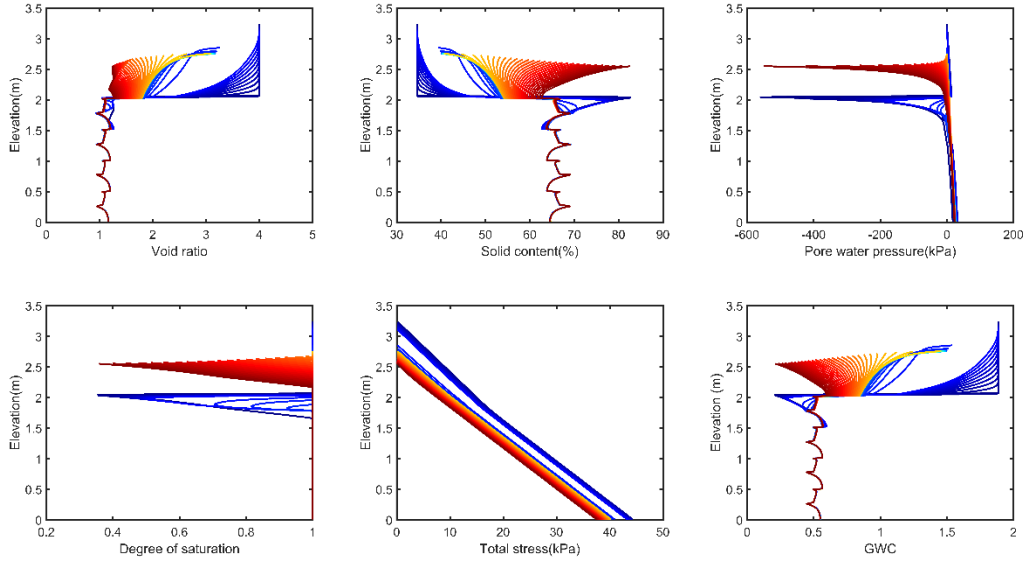
Elevation(m)
Void ratio
Solid content(%)
Pore water pressure(kPa)
Degree of saturation
Total stress(kPa)
GWC

(b)

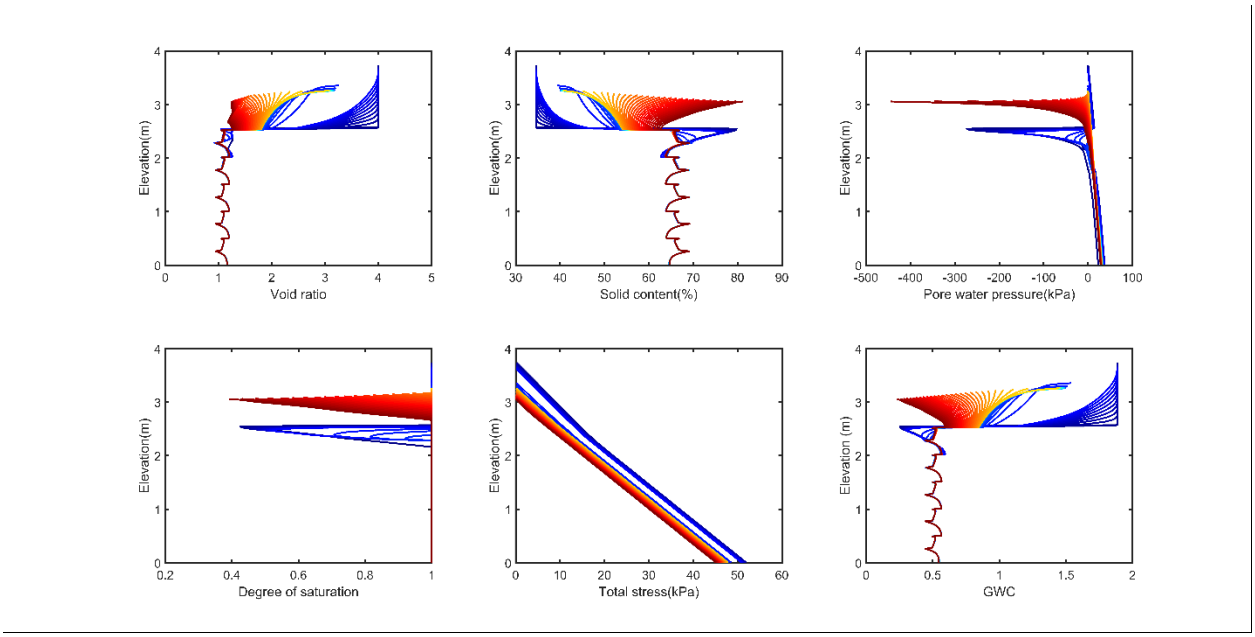
Elevation(m)
Void ratio
Solid content(%)
Pore water pressure(kPa)
Degree of saturation
Total stress(kPa)
GWC

(c)

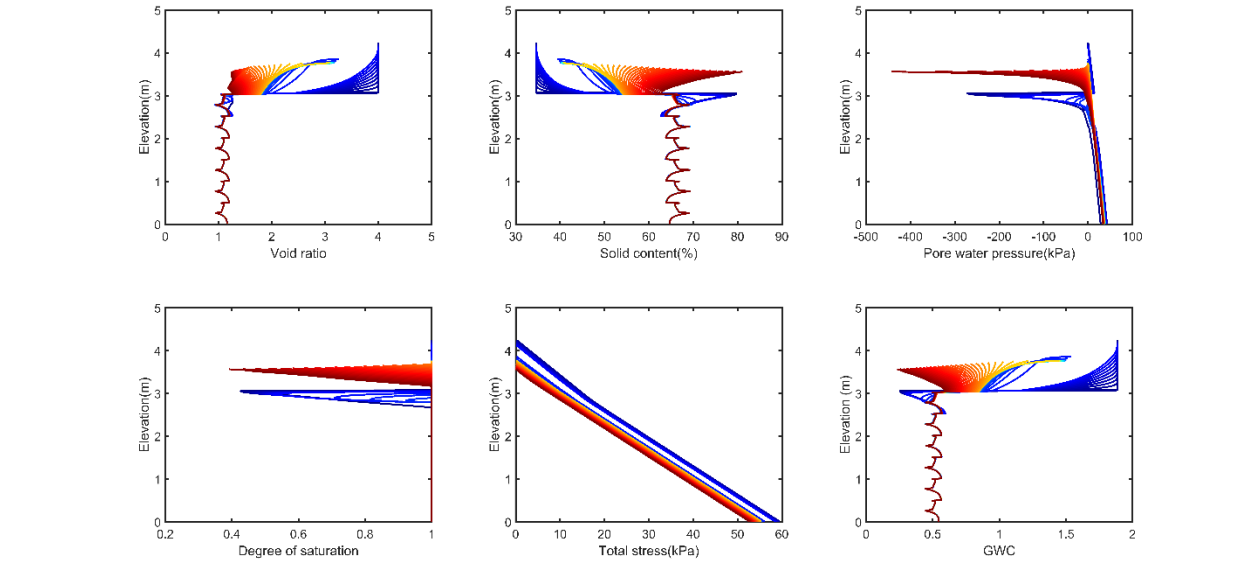
Elevation(m)
Void ratio
Solid content(%)
Pore water pressure(kPa)
Degree of saturation
Total stress(kPa)
GWC

(d)

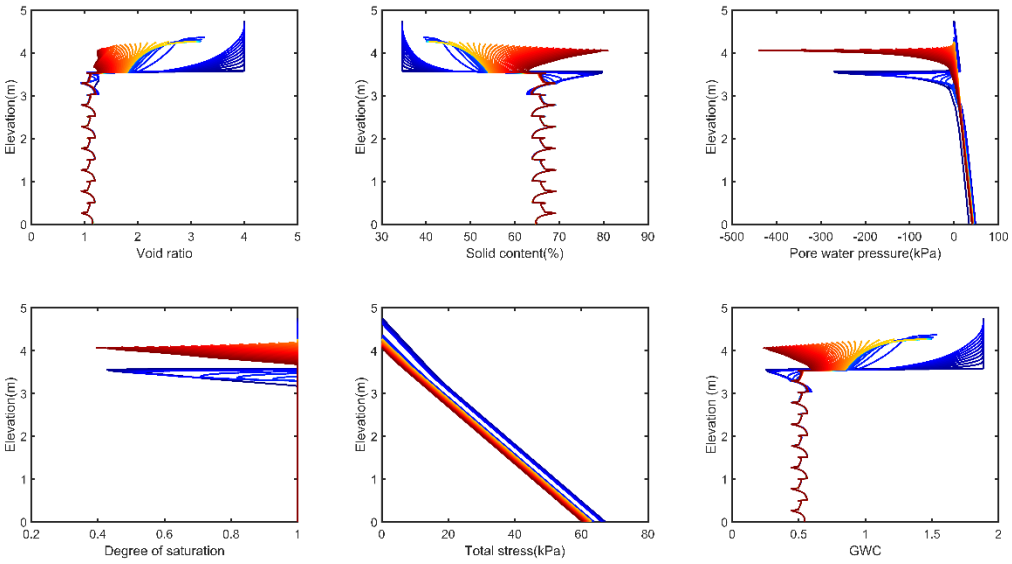
Elevation(m)
Void ratio
Solid content(%)
Pore water pressure(kPa)
Degree of saturation
Total stress(kPa)
Elevation (m)
GWC

(e)

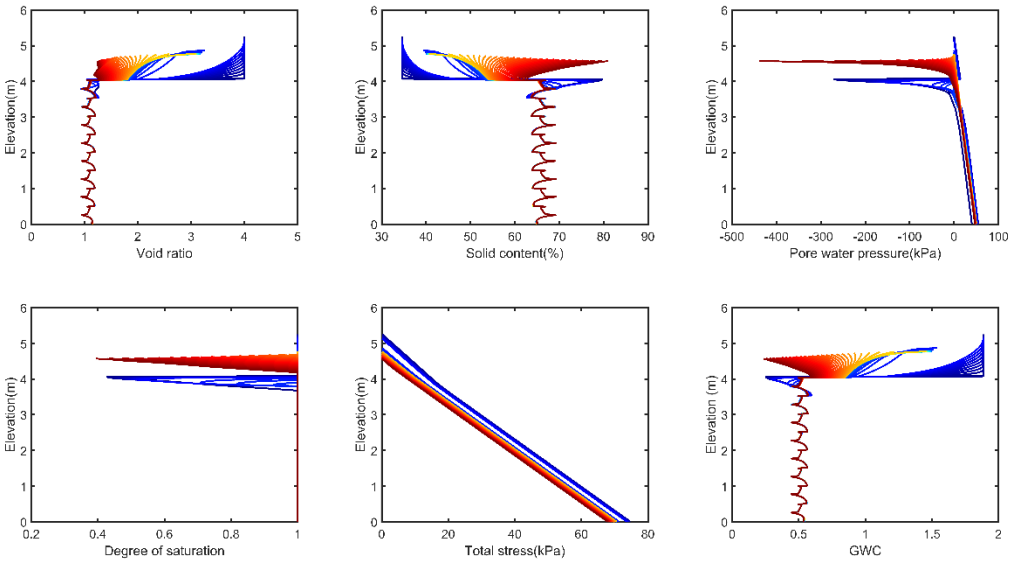
Elevation(m)
Void ratio
Solid content(%)
Pore water pressure(kPa)
Degree of saturation
Total stress(kPa)
Elevation (m)
GWC

(f)

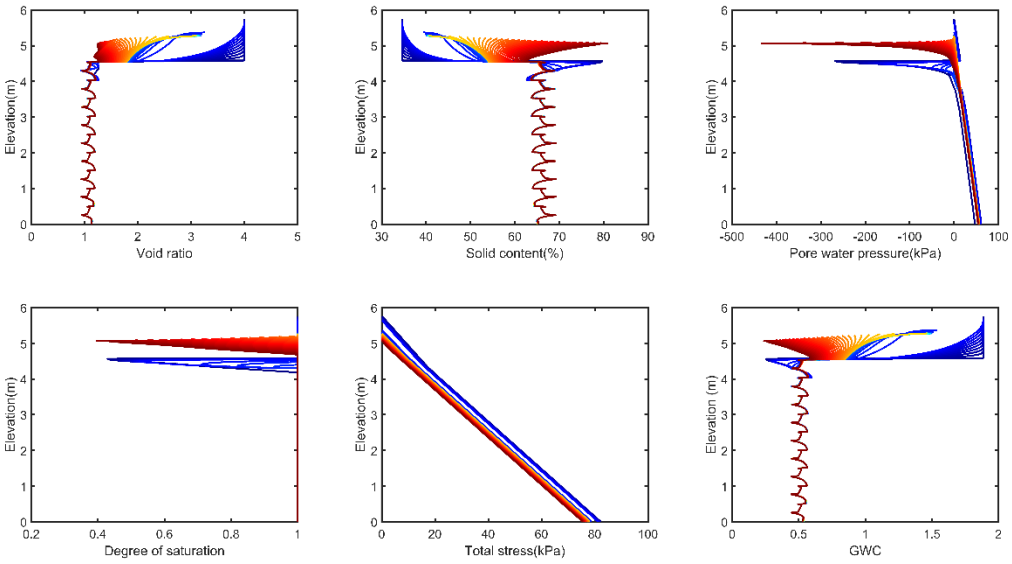

(g)

Fig. 10.32. Calculated variations of profiles of several parameters (pore water pressure, void ratio, total stress and degree of saturation) over time using GCM: (a) during the 4th year (4th layer deposition), (b) during the 5th year (5th layer deposition), (c) during the 6th year (6th layer deposition), (d) during the 7th year (7th layer deposition), (e) during the 8th year (8th layer deposition), (f) during the 9th year (9th layer deposition), and (g) during the 10th year (10th layer deposition).

Chapter 11 Conclusions and Recommendations for Future Work

11.1 Conslusions

Research on the fundamental behaviour of soil in partially saturated condition has been highly active in the past two or three decades, however, application of knowledge gained in academia in geotechnical and geo-environmental practice remains quite limited. The reasons for this are manifold, for instances, (*i*) Modeling the constitutive behaviour of unsaturated soils involves constructing mathematical formulations that are much more complicated compared to saturated soils. In spite of a high level of sophistication, some of these constitutive models still face difficulties in *accurately* describing all features of unsaturated soil observed in the laboratory. (*ii*) Calibration of the modelling parameters from data in laboratory tests, which are usually expensive and time-consuming to conduct, involves complicated procedures; (*iii*) Introducing these models for unsaturated soils into a numerical (e.g. finite element or finite difference) method requires a relatively high level of expertise. Software commercially available can only deal with a limited number of features of unsaturated soil. (*iv*) Unsaturated soil mechanics principle tend to lead to greater stiffness & strength due to suction that are not by practitioners.

The work reported in this thesis has dealt with the hydraulic and mechanical behaviours of unsaturated soils subjected to varying environmental factors through numerical investigation. Numerical analyses have been conducted on two typical practical problems where soils can be in

a state of unsaturated condition for the project lift span or their state switches between saturated and unsaturated condition constantly. The main conclusions of this thesis include:

11.1.1 Stability of expansive soil

The effects of two *characteristic* features of expansive soils on slope stability under rainfall, which are not easy to be quantitatively examined experimentally, are isolatedly studied using a number of numerical investigation:

- *Hydro-mechanical coupling effect*. The hydro-mechanical effect is examined by comparing the FSs calculated based on flow regime (suction and water content distribution) from hydro-mechanical (coupled) and hydraulic (uncoupled) analyses of the slope to a low intensity prolonged rainfall. Soils' properties of Regina clay (a typical expansive soil, Canada), is adopted. In the coupled analysis, a semi-empirical model is implemented to consider the nonlinear relationship between the elastic moduli and suction. It is found from this analysis that coupling behaviour of soils has a negative effect on the slope stability in expansive soils.

(1) The coupled analysis produces a reasonably well defined wetting front than uncoupled analysis. Wetting front advances faster in coupled analysis than uncoupled analysis, resulting in a faster suction loss near the slope surface.

(2) Calculation of FS profile with depth indicates that the smallest FS occurs at the depth of wetting front. Thus, the coupled analysis results in a lower critical FS at a greater depth than uncoupled analysis.

(3) The influence of geometry changes of expansive soils slopes is small in comparison to the difference in the wetting front depth between coupled and uncoupled analysesThe influence of geometry change induced by soil swelling is negligible on slope stability.

- *Effect of soils swelling upon wetting*: This effect is studied using an extended infinite slope formulation focusing on the mechanical behaviour (swelling-induced change of stress and strain regime), isolating the effect of coupling effect. The nonlinear elasto-plastic, strain- softening Mohr-Coulomb model for unsaturated soils is adopted to describe the constitutive behaviour of soils. Numerical parametric exercise conducted using a specifically developed program indicates:

(4) The net normal stress in the sloping direction keeps increasing due to constraints on the soils swelling potential upon wetting), until reaching a maximum value at yielding, after which, possible softening occurs with plastic straining and shear strength parameters decrease. Neglecting this softening behaviour may overestimate the conventional FS, leading to unsafe engineering designs.

(5) The failures depths are not necessarily at the base of surface layer. It is a consequence of the combined effects of changes in water flow regime and stress-deformation regime (induced by water flow regime here).

(6) Effect of the swelling-induced softening is influenced by other factors, e.g. initial stress ratio, softening rate and slope angle.

(7) Application of an improved version of this infinite slope formulation (with a newly proposed stress dependent model for soil moduli, incorporating the effect of degree of saturation using SWCC) to the case study confirms its practical applicability.

11.1.2 Large strain consolidation of soft soil

Simulation of large strain consolidation of soft soils (under self-weight and induced by evaporation) is performed using a numerical program developed in this thesis, UNSATCON-ML,

which implements several constitutive models being developed/advanced recently, and includes a number of new important features/capabilities.

(i) UNSATCON-ML adopts a piece-wise formulation to deal with the geometrical nonlinearity. The moving boundaries with continuously large deforming configuration is tracked numerically as it behaves in reality. An advantage of this technique would be that the top boundary condition (e.g. accumulation of water at top may be gradually removed by evaporation) can be realistically simulated.

(ii) UNSATCON-ML implements four boundary conditions for handing any possible combinations of decantation and evaporation (frequently encountered in lab and field conditions), infiltration can also be modeled in UNSATCON-ML. Accurately simulating the water accumulation on the top surface during the initial settling of soft soils is important for successfully obtaining a solution (without convergence issues), due to the existence of not only a changing hydraulic head boundary but also a force (weight of water) boundary on the top boundary. The top boundary is also moving due to geometric nonlinearity.

(iii) UNSATCON-ML ensures mass conservation, since (a) the time discretization is performed directly on the mixed formulation of governing equation, by which the void ratio for the saturated zone and the gravimetric water content for unsaturated zone are obtained during global analysis; (b) the constitutive analysis is performed without using a linear approximation of the nonlinear material (hydraulic and mechanical) properties.

(iv) UNSATCON-ML includes a module capable of performing a quasi-unsaturated analysis, in which suction induced by evaporation is allowed but is assumed to have the same effect on the volume change behaviour of unsaturated soils as total stress.

(v) UNSATCON-ML ensures a smooth state transition modeling (soil's state switches between saturated and unsaturated states) for both the elastic and elasto-plastic processes, even though the soils' hydro-mechanical behaviours in different states are modelled using different types of mathematical models, including those using independent stress variables, i.e. net stress and suction.

(vi) UNSATCON-ML implements a number of unsaturated soil constitutive models formulated using different stress state variables (pairs), including state surface model (Vu and Fredlund, 2006), BBM (Alonso et al. 1990) and GCM (Wheeler et al. 2003), and a bounding surface SWRC (Gallipoli et al. 2015). Variation of void ratio is used as the measure of straining in finite strain condition. Elasto-plastic (following virgin consolidation/drying paths) and elastic (following hydro/mechanical unloading /reloading paths) volumetric behaviours are described using two general functions (3D surface in different space depending on the specific model). An analytical form of GCM for the virgin consolidation/drying behaviour is developed in this thesis (Wheeler et al. 2003). Hydraulic retention models implemented in UNSATCON-ML include two types: (1) the first one relates gravimetric water content to net stress and suction; and (2) the second one relates degree of saturation to suction and void ratio, with or without hydraulic hysteresis.

(vii) UNSATCON-ML is of high efficiency and accurate. It uses an algorithm performing the constitutive analysis (solving mechanical model in conjunction with hydraulic

retention model at local point level) without iterations for single layer deposition modeling and with one iteration for multi-layer deposition modeling. These two types of models (hydraulic and mechanical model) are solved ***analytically*** in a coupled manner employing a bisection method. The highly coupled GCM is also solved in this way. bisection method is proved to be very suitable for this application considering that the constitutive functions of classic elasto-plastic are not smooth and continuous (function for elastic (scanning) behaviour is different from plastic (primary) behaviour). The interval bounding the root can be easily identified physically or numerically.

During the two main phases of development of program: (1) UNSATCON for single layer deposition modeling and (2) UNSATCON-ML for multi-layer deposition modeling, its ability/validity has been extensively tested:

(viii) Testing (1) the component for large strain consolidation again a well-established numerical example under saturated condition; (2) the component for unsaturated flow against an analytical solution; (3) the component of quasi-unsaturated formulation against other type of numerical results, illustrating the robustness and accuracy of the UNSATCON-ML.

(ix) Testing ability of UNSATCON-ML to couple large strain consolidation and unsaturated water flow against the data from both laboratory and field tests. Experimental observations, including the developing suction, decreasing void ratio but limited at shrinkage limit, increasing solid content, increasing settlement rate due to evaporation effect on the near surface zone; can be well reproduced by UNSATCON.

(x) Results also shows that modeling desaturation allows for a more realistic simulation of deformation in the unsaturated zone than using formulations that do not model desaturation.

(xi) Testing UNSATCON-ML against data from the multi-layer deposition of tailings in drying box test, illustrates the effectiveness of implementation of elasto-plastic and water retention models for unsaturated soils. Again good agreements are obtained with a little calibration of the model constants interfered from elemental tests. Inter-layer water exchange is an important phenomenon affecting the degrees of consolidation/dewatering of tailings, which is affected by many internal and external factors, e.g. degree of hydraulic hysteresis of water retention model. The performance of different constitutive models in these applications can be compared using UNSATCON-ML.

(xii) Several hypothetical field cases have been modelled using UNSATCON-ML. The results clearly illustrate how UNSATCON-ML can be used in optimizing tailings deposition scheme. The benefits of winter deposition (for oil sands tailings) and multi-layer depositions can be quantified using UNSATCON-ML. In multi-layer deposition, the inter-layer hydraulic exchange seems to be a very important process affecting the overall degree of large-strain consolidation/dewatering, which is, of course, case-dependent. UNSATCON-ML is able to provide results in an effective way.

In conclusion, UNSATCON-ML is capable of assisting in design of tailings deposition scheme in the tailings managements industry.

11.2 Recommendations for future work

(1) Long term behaviour of expansive soils slopes

Results in this thesis reflects the behaviour of expansive soils and its influence on slope stability during a single period rainfall condition. Some field observations indicate that the possibility of expansive soil slope failure increases with time after construction. In other words, seasonal weather conditions (cyclic hydraulic/suction loading) may progressively deteriorate the mechanical properties of expansive soils. Several unsaturated expansive soils' behavioural features are recommended to be included in the analysis: e.g. (a) hydraulic hysteresis; (b) plastic volumetric straining (both swelling and shrinkage) during cyclic suction and its influence on softening behaviour; (c) cracks induced by cyclic hydraulic condition and its influence on subsequent hydro-mechanical behaviour.

(2) Softening behaviour

The softening model used in this thesis is a semi-empirical model, which relates the ϕ^b (quantifying contribution of suction to shear strength) with plastic strain using a simple linear relation. This needs experimental verifications considering, particularly, volumetric plastic swelling strain. Incorporating this softening component into a whole framework is recommended for future work.

(3) Plasticity model

All the existing plasticity models for unsaturated soils are formulated traditionally in stress space. Formulating, innovatively, the plasticity models in strain-space may bring advantages for numerical investigation, which is also recommended in future work on unsaturated soils behaviour.

(4) Stochastic analysis of slope stability

Modeling unsaturated soils involves a great number of soils constants, which vary in space and time. Introducing probabilistic approach into slope stability analysis of unsaturated expansive soils can definitely provides more reasonable conclusions. Random numerical analysis, e.g. The Random Finite Element Method (Griffiths and Fenton 1993, Fenton and Griffiths 2008) is recommended to be extended to unsaturated soils studies.

(5) Time-dependent behaviour of tailings

The time-dependent behaviour has been observed a long time ago during consolidation of soft soils in small-strain condition, e.g. secondary consolidation settlement. This is a more significant phenomenon in large strain consolidation of loosely deposited tailings, not only during self-weight consolidation stages, but also post-settling stages (creep or thixotropic behaviours), which may be affected by desaturation or desiccation history. Examining the effectiveness of existing time-dependent constitutive models (mostly established from small strain consolidation tests) in this application, can be accomplished with UNSATCON-ML. New time-dependent models (for behaviour of tailings during large strain consolidation under both saturated and unsaturated condition, if necessary) should be proposed and incorporated into UNSATCON-ML, strengthening and enriching the program's capabilities.

(6) Stochastic analysis of large strain consolidation

The parameters of large strain consolidation exhibit great uncertainty and variability. In particular, the saturated permeability or compressibility relationships at very low effective stress level, result in variances in the predicted degree of consolidation, even for well-controlled lab tests. Heterogeneity is very likely to be induced during the deposition of

tailings due to its high initial void ratio (extremely loose state) in the field. Introducing probabilistic model into UNSATCON-ML is important to investigate the consolidation behaviour under self-weight condition. The final amount of settlement induced by self-weight and the time to reach this point are important measures in examining the effectiveness of various techniques used to accelerate the consolidation of deposited tailings. Introduction of probabilistic approach into UNSATCON-ML may provide a more comprehensive picture of long term behaviours of deposited tailings for tailings management if uncertainties in unsaturated soil properties are also taken into consideration.

UNSATCON-ML is a foundation on which many other promising features can be built for a number of possible applications involving coupling with large strain consolidation, including predicting evaporation rate, modeling gas transport in an acid generation context.

References

Adem HH, Vanapalli SK. A simple method for prediction of the modulus of elasticity of unsaturated expansive soils. In Proceedings of the 6th International Conference on Unsaturated Soils, Sydney, Australia, Unsaturated Soils: Research & Applications, Edited by N. Khalili, A. Russell, and A. Khoshghalb, CRC Press, 2014; 343-349.

Adem HH, Vanapalli SK. Constitutive modeling approach for estimating the 1-D heave with respect to time for expansive soils. International Journal of Geotechnical Engineering, 2013;7 (2): 199-204.

Adem HH, Vanapalli SK. Prediction of the modulus of elasticity of compacted unsaturated expansive soils. International Journal of Geotechnical Engineering, 2014;0(0): 1-13.

Adikari G S N, Cummins P J. An effective stress slope stability analysis method for dams[C]. In Proceedings of the Eleventh International Conference on Soil Mechanics and Foundation Engineering, San Francisco Calif, A A Balkema, Rotterdam, the Netherlands, 1985: 713-718.

Ali, A., Huang, J., Lyamin, A. V., Sloan, S. W., & Cassidy, M. J. (2014). Boundary effects of rainfall-induced landslides. Computers and Geotechnics, 61, 341-354.

Ali, A., Huang, J., Lyamin, A. V., Sloan, S. W., Griffiths, D. V., Cassidy, M. J., & Li, J. H. (2014). Simplified quantitative risk assessment of rainfall-induced landslides modelled by infinite slopes. Engineering Geology, 179, 102-116.

Alonso EE, Gens A, Delahaye CH. Influence of rainfall on the deformation and stability of a slope in overconsolidated clays: a case study. Hydrogeology Journal 2003;11(1): 174–192.

Alonso, E. E., Gens, A., & Delahaye, C. H. (2003). Influence of rainfall on the deformation and stability of a slope in overconsolidated clays: a case study. Hydrogeology journal, 11(1), 174-192.

Alonso, E. E., Gens, A., & Josa, A. (1990). A constitutive model for partially saturated soils. Géotechnique, 40(3), 405-430.

Alonso, E. E., Pinyol, N. M., & Gens, A. (2013). Compacted soil behaviour: initial state, structure and constitutive modelling. Géotechnique, 63(6), 463.

Alonso, E. E., Sauter, S., & Ramon, A. (2015). Pile groups under deep expansion: a case history. Canadian Geotechnical Journal, 52(8), 1111-1121.

Alonso, E. E., Vaunat, J., & Gens, A. (1999). Modelling the mechanical behaviour of expansive clays. Engineering Geology, 54(1), 173-183.

Aubeny, C. P., & Lytton, R. L. (2004). Shallow slides in compacted high plasticity clay slopes. Journal of Geotechnical and Geoenvironmental Engineering, 130(7), 717-727.

Azam S, Ito M. Unsaturated soil properties of a fissured expansive clay. Proceedings, 64th Canadian Geotechnical Conference, Toronto, Canada. 2011.313:1-5.

Azañón, J. M., Azor, A., Yesares, J., Tsige, M., Mateos, R. M., Nieto, Delgado, J., López-Chicano, M., Martín, W. & Rodríguez-Fernández, J. (2010). Regional-scale high-plasticity clay-bearing formation as controlling factor on landslides in Southeast Spain. Geomorphology, 120(1), 26-37.

Bandara, S., & Soga, K. (2015). Coupling of soil deformation and pore fluid flow using material point method. Computers and Geotechnics, 63, 199-214.

Bani Hashem E. Volume change consideration in determining appropriate unsaturated soil properties for geotechnical applications. PhD thesis. USA:Arizona State University; 2013.

Bao, C. G., Ng, C. W. W., Rahardjo, H., Toll, D. G., & Leong, E. C. (2000). Some thoughts and studies on the prediction of slope stability in expansive soils. In Unsaturated soils for Asia. Proceedings of the Asian Conference on Unsaturated Soils, UNSAT-Asia 2000, Singapore, 18-19 May, 2000. (pp. 15-31). AA Balkema.

Bao, C., Gong, B., and Zhan, L. 1998. Properties of unsaturated soils and slope stability of expansive soils. In Proceedings of the Second International Conference on Unsaturated Soils (UNSAT 98), Beijing. Vol. 1, pp. 71–98.

Bartholomeeusen, G., Sills, G. C., Znidarcic, D., Van Kesteren, W., Merckelbach, L. M., Pyke, R., ... & Masala, S. (2002). Sidere: numerical prediction of large-strain consolidation.

Bernander, S., Kullingsjö, A. A., Gylland, A., Bengtsson, P. E., Knutsson, S., Pusch, R., Olofsson, J. & Elfgren, L. (2016). Downhill Progressive Landslides in Long Natural Slopes. Triggering Agents and Landslide Phases modeled with a Finite Difference Method. Canadian Geotechnical Journal, (ja).

BGC Engineering Inc. (2010). Oil Sands Tailings Technology Review. Oil Sands Research and Information Network (Vol. OSRIN Repo, p. OSRIN Report No. TR–1. 136 pp.). Edmonton, Alberta.

Biot MA. General theory of three-dimensional consolidation. Journal of Applied Physics, 1941;12(2): 155–164.

Bishop, A. W. (1959). The principle of effective stress. Teknisk ukeblad, 39, 859-863.

Bishop, A. W. 1955. The use of the slip circle in the stability analysis of slopes. Géotechnique, (5): 7-17.

Bishop, A. W., & Blight, G. E. (1963). Some aspects of effective stress in saturated and partly saturated soils. Géotechnique, 13(3), 177-197.

Bjerrum, L. (1967). Progressive failure in slopes of overconsolidated plastic clay and clay shales. Journal of the Soil Mechanics and Foundations Division, 93(5), 1-49.

Blatz, J. A., & Graham, J. (2003). Elastic-plastic modelling of unsaturated soil using results from a new triaxial test with controlled suction. Géotechnique, 53(1), 113-122.

Borja RI, White JA, Liu XY, Wu W. Factor of safety in a partially saturated slope inferred from hydro-mechanical continuum modeling. International journal for numerical and analytical methods in geomechanics. 2012;36(10):23-248.

Bower, A. F. (2009). Applied mechanics of solids. CRC press.

Boyd, J. L., & Sivakumar, V. (2011). Experimental observations of the stress regime in unsaturated compacted clay when laterally confined. Géotechnique, 61(4), 345-363.

Brackley, I. J. A., & Sanders, P. J. (1992). In situ measurement of total natural horizontal stresses in an expansive clay, Géotechnique, 42(3), 443-451.

Brooks, R. H., & Corey, A. T. (1964). Hydraulic properties of porous media and their relation to drainage design. Transactions of the ASAE, 7(1), 26-0028.

Buscarnera, G., & Prisco, C. D. (2012). Discussing the definition of the second‐order work for unsaturated soils. International Journal for Numerical and Analytical Methods in Geomechanics, 36(1), 36-49.

Bussiere, B. (2007). Colloquium 2004: Hydrogeotechnical properties of hard rock tailings from metal mines and emerging geoenvironmental disposal approaches. Canadian Geotechnical Journal, 44(9), 1019-1052.

Cai F, Ugai K. (2004). Numerical analysis of rainfall effects on slope stability. International Journal of Geomechanics,;4(2): 69-78.

Cai, F., Ugai, K., Wakai, A., & Li, Q. (1998). Effects of horizontal drains on slope stability under rainfall by three-dimensional finite element analysis. Computers and Geotechnics, 23(4), 255-275.

Calabresi, G., Colleselli, F., Danese, D., Giani, G., Mancuso, C., Montrasio, L., Nocilla, A., Pagano, L., Reali, E. and Sciotti A. (2013). Research study of the hydraulic behaviour of the Po River embankments. Canadian Geotechnical Journal, 50(9), 947-960.

Cardoso, R., Alonso, E. E., & Neves, E. M. D. (2013). A constitutive model for compacted expansive and bonded marls. Géotechnique, 63(13), 1116.

Cargill, K. W. (1984). Prediction of consolidation of very soft soil. Journal of Geotechnical Engineering, 110(6), 775-795.

Chai, J., & Carter, J. P. (2009). Simulation of the progressive failure of an embankment on soft soil. Computers and Geotechnics, 36(6), 1024-1038.

Chao KC, Kang JB, Nelson JD. Challenges in water migration modeling for expansive soils. Soil behaviour and geomechanics, GSP236 ASCE; 2014. p. 204–13.

Chen RH, Chen HP, Chen KS, Zhung HB. Simulation of a slope failure induced by rainfall infiltration. Environmental Geology 2009;58(5): 943–952.

Chen, C. F., Liu, H. X., & Li, Y. P. (2007). Study on grassroots-reinforced soil by laboratory triaxial test. Yantu Lixue(Rock and Soil Mechanics), 28(10), 2041-2045.

Chen, F. H. (1975). Foundation on Expansive Soil, Development in Geotechnical Engineering 12.

Chen, H. X., & Zhang, L. M. (2014). A physically-based distributed cell model for predicting regional rainfall-induced shallow slope failures.Engineering geology, 176, 79-92.

Chen, Z., Morgenstern, N. R., & Chan, D. H. (1992). Progressive failure of the Carsington Dam: a numerical study. Canadian Geotechnical Journal, 29(6), 971-988.

Cheng YH, Cheng ZL, Zhang YB. Centrifugal model tests on expansive soil slope under rainfall. Chinese Journal of Geotechnical Engineering, (2011);33(1):409-414. (in Chinese)

Cheng, Z., Ding, J., Rao, X., Cheng, Y., & Xu, H. (2013). Physical model tests of expansive soil slope. In Geo-Congress 2013: Stability and Performance of Slopes and Embankments III (pp. 731-740).

Cho SE, Lee SR. Evaluation of surficial stability for homogeneous slopes considering rainfall characteristics. Journal of Geotechnical and Geoenvironmental Engineering 2002;128, 756–763.

Cho, S. E. (2014). Probabilistic stability analysis of rainfall-induced landslides considering spatial variability of permeability. Engineering Geology, 171, 11-20.

Cho, S. E., & Lee, S. R. (2001). Instability of unsaturated soil slopes due to infiltration. Computers and Geotechnics, 28(3), 185-208.

Chowdhury, M. (2013). Shear Strength Properties of Compacted Expansive Soils (Master thesis, Faculty of Graduate Studies and Research, University of Regina).

Christiansen, E. A., & Sauer, E. K. (2002). Stratigraphy and structure of Pleistocene collapse in the Regina Low, Saskatchewan, Canada. Canadian Journal of Earth Sciences, 39(9), 1411-1423.

Collins BD, Znidarcic D. Stability analyses of rainfall induced landslides. Journal of Geotechnical and Geoenvironmental Engineering, ASCE, 2004;130(4): 362–372.

Conte, E., & Troncone, A. (2012). Stability analysis of infinite clayey slopes subjected to pore pressure changes. Géotechnique, 62(1), 87-91.

Cui, Y. J., & Delage, P. (1996). Yielding and plastic behaviour of an unsaturated compacted silt. Géotechnique, 46(2), 291-311.

Cui, Y. J., Ta, A. N., Hemmati, S., Tang, A. M., & Gatmiri, B. (2013). Experimental and numerical investigation of soil-atmosphere interaction. Engineering Geology, 165, 20-28.

D'Onza, F., Gallipoli, D., Wheeler, S., Casini, F., Vaunat, J., Khalili, N., ... & Pereira, J. M. (2011). Benchmark of constitutive models for unsaturated soils. Géotechnique, 61(4), 283-302.

D'Onza, Francesca, et al. "Benchmark of constitutive models for unsaturated soils." Géotechnique 61.4 (2011): 283-302.

Daliri, F. (2013). The influence of desiccation and stress history on monotonic and cyclic shear response of thickened gold tailings (Doctoral dissertation, Carleton University Ottawa).

Daliri, F., Kim, H., Simms, P., & Sivathayalan, S. (2014). Impact of desiccation on monotonic and cyclic shear strength of thickened gold tailings. Journal of Geotechnical and Geoenvironmental Engineering, 140(9), 04014048.

Daliri, F., Simms, P., & Sivathayalan, S. (2016). Shear and dewatering behaviour of high density gold tailings in a laboratory simulation of multi-layer deposition. Canadian Geotechnical Journal, 2016, 53(8): 1246-1257.

Dangla, P., Malinsky, L., & Coussy, O. (1997, July). Plasticity and imbibition-drainage curves for unsaturated soils: a unified approach. In Proc. 6th Int. Symp. Numer. Models Geomech.(NUMOG VI) (pp. 141-146).

Day, R. W. (1994). Surficial stability of compacted clay: case study. Journal of Geotechnical Engineering, 120(11), 1980-1990.

De Vries, D. A. (1987). The theory of heat and moisture transfer in porous media revisited. International Journal of Heat and Mass Transfer, 30(7), 1343-1350.

Delage, P., & Graham, J. (1996). Mechanical behaviour of unsaturated soils: understanding the behaviour of unsaturated soils requires reliable conceptual models. In PROCEEDINGS OF THE FIRST INTERNATIONAL CONFERENCE ON UNSATURATED SOILS/UNSAT'95/PARIS/FRANCE/6-8 SEPTEMBER 1995. VOLUME 3.

Deng, A., & Zhou, Y. (2015). Modeling electroosmosis and surcharge preloading consolidation. I: Model formulation. Journal of Geotechnical and Geoenvironmental Engineering, 10.1061/(ASCE) GT.1943-5606.0001417 04015093.

Di Prisco, C., & Pisanò, F. (2011). An exercise on slope stability and perfect elastoplasticity. Géotechnique, 61(11), 923.

Donaldson, G. W. (1969). The Occurrence of Problems of Heave and the Factors Affeting its Nature. In Second International Research and Engineering Conference on Expansive Clay Soils (pp. 25-36). Texas A & M Press.

Daosheng, L. I. N. G., Shunchao, Q., Feng, C. H. E. N., & Nan, L. (2013). A limit equilibrium method based on Morgenstern-Price method for 3D slope stability analysis. Chinese Journal of Rock Mechanics and Engineering, 32(1), 107-116.

D'Onza, Francesca, S. J. Wheeler, Domenico Gallipoli, M. Barrera Bucio, M. Hofmann, M. Lloret-Cabot, A. Lloret Morancho et al. "Benchmarking selection of parameter values for the Barcelona basic model." Engineering Geology 196 (2015): 99-118.

Duncan JM, Wright SG. 1995. Soil Strength and Slope Stability. Wiley, Hoboken, N J, USA.

Duncan, J. M. (1996). Soil slope stability analysis. Landslides: Investigation and Mitigation, Transportation Research Board Special Report 247, 337-371.

Duncan, J. M., Wright, S. G., & Brandon, T. L. (2014). Soil strength and slope stability. John Wiley & Sons.

Dunmola (2012). Predicting Evaporative Fluxes in Saline Soil and Surface-deposited Thickened Mine Tailings. Ph.D. thesis.

Dunmola, A., Cote, C., Freeman, G., Kolstad D., Song, J., and Masala S. 2013. Dewatering and shear strength performance of in-line flocculated mature fine tailings under different depositional schemes. Proceeding of Tailings and Mine Waste 2013 November 3rd-6th 2013, Banff, Alberta p5 -14.

Dunmola, A., Dhadli, N., Freeman, Kolstad, D., Fasking, T., Song, J., and Langseth, J. 2013. Geotechnical Benefits of Flocculation in Dewatering Oil Sands Mature Fine Tailings. In Proceedings of GeoMontreal 2013, Canadian Geotechnical Conference, Sept. 30th - Oct 3rd 2013, Electronic proceedings.

Ehlers W, Graf T, Ammann M. Deformation and localization analysis of partially saturated soil. Computer methods in applied mechanics and engineering, 2004; 193(27): 2885-2910.

Elizaveta Rozina (2015) Bearing Capacity of Multilayer-deposited In-line Flocculated Oil Sands Tailings, Master thesis, Carleton University, Canada.

Escario, V., & Saez, J. (1986). The shear strength of partly saturated soils. Géotechnique, 36(3).

Fellenius, W. 1936. Calculation of the stability of earth dams. In Transactions of the 2nd congress on large dams, Washington, D.C. Vol. 4, pp. 445-463.

Fenton, G. A., & Griffiths, D. V. (2008). Risk assessment in geotechnical engineering (Vol. 461). Hoboken, NJ: John Wiley & Sons.

Fisseha, B., Bryan, R., & Simms, P. (2010). Evaporation, unsaturated flow, and salt accumulation in multilayer deposits of "paste" gold tailings. Journal of Geotechnical and Geoenvironmental Engineering, 136(12), 1703-1712.

Flanagan, Erin, and Jennifer Grant. "Losing Ground–Why the problem of oil sands tailings waste keeps growing." Pembina Institute (2013): 1-6.

Foundation-repair-guide, http://www.foundation-repair-guide.com/expansive-soil.html.

Fourie, A. B. (1989). Laboratory evaluation of lateral swelling pressure. Journal of Geotechnical Engineering, 115(10), 1481-1486.

Fox, P. J. (2007). Coupled large strain consolidation and solute transport. I: Model development. Journal of Geotechnical and Geoenvironmental Engineering. 10.1061/(ASCE)1090-0241(2007)133:1(3), 3–15.

Fox, P. J., & Berles, J. D. (1997). CS2: A piecewise-linear model for large strain consolidation. International Journal for Numerical and Analytical Methods in Geomechanics, 21(7), 453-475.

Fox, P. J., Pu, H., and Berles, J. (2014). CS3: Large strain consolidation model for layered soils. Journal of Geotechnical and Geoenvironmental Engineering. 10.1061/(ASCE)GT.1943-5606.0001128, 04014041.

Fox, P. J. and Pu, H. (2012). Enhanced CS2 Model for Large Strain Consolidation. International Journal of Geomechanics, 10.1061/(ASCE)GM.1943-5622.0000171, 574-583.

Fredlund DG, Houston SL. Interpretation of soil water characteristic curves when volume change occurs as soil suction is changed. Proceedings, 1st Pan-American Conference on Unsaturated Soils, Cartagena de Indias, Colombia, 2013; vol. 1, pp. 15–31.

Fredlund DG, Rahardjo H. 1993. Soil Mechanics for Unsaturated Soils. John Wiley & Sons, New York.

Fredlund MD, Fredlund DG, Wilson GW. An equation to represent grain-size distribution. Canadian Geotechnical Journal, 2000;37(4): 817-27.

Fredlund, D. G., & Krahn, J. (1977). Comparison of slope stability methods of analysis. Canadian Geotechnical Journal, 14(3), 429-439.

Fredlund, D. G., & Morgenstern, N. R. (1976). Constitutive relations for volume change in unsaturated soils. Canadian Geotechnical Journal, 13(3), 261-276.

Fredlund, D. G., & Morgenstern, N. R. (1977). Stress state variables for unsaturated soils. Journal of Geotechnical and Geoenvironmental Engineering, 103(ASCE 12919).

Fredlund, D. G., & Rahardjo, H. (1993). Soil mechanics for unsaturated soils. John Wiley & Sons.

Fredlund, D. G., & Xing, A. (1994). Equations for the soil-water characteristic curve. Canadian geotechnical journal, 31(4), 521-532.

Fujiyasu, Y., & Fahey, M. (2000). Experimental study of evaporation from saline tailings. Journal of Geotechnical and Geoenvironmental Engineering, 126(1), 18-27.

Fredlund, D. G., and Krahn, J. 1977. Comparison of slope stability methods of analysis. Canadian Geotechnical Journal, 14(3): 429-439.

Fredlund, D. G., Morgenstern, N. R., & Widger, R. A. (1978). The shear strength of unsaturated soils. Canadian geotechnical journal, 15(3), 313-321.

Fredlund, D. G., Rahardjo, H., & Fredlund, M. D. (2012). Unsaturated soil mechanics in engineering practice. John Wiley & Sons.

Fredlund, D. G., Rahardjo, H., & Gan, J. K. M. (1987, December). Non-linearity of strength envelope for unsaturated soils. In Proc. 6th Int. Conf. Expansive Soils, New Delhi (Vol. 1, pp. 49-54).

Fredlund, D. G., Sheng, D., & Zhao, J. (2011). Estimation of soil suction from the soil-water characteristic curve. Canadian Geotechnical Journal, 48(2), 186-198.

Fredlund, D. G., Xing, A., Fredlund, M. D., & Barbour, S. L. (1996). The relationship of the unsaturated soil shear to the soil-water characteristic curve. Canadian Geotechnical Journal, 33(3), 440-448.

Fredlund, M. D., Fredlund, D. G., & Wilson, G. W. (2000). An equation to represent grain-size distribution. Canadian Geotechnical Journal, 37(4), 817-827.

Fujiyasu, Y., & Fahey, M. (2000). Experimental study of evaporation from saline tailings. Journal of Geotechnical and Geoenvironmental Engineering, 126(1), 18-27.

Gallipoli, D., Bruno, A. W., D'Onza, F., & Mancuso, C. (2015). A bounding surface hysteretic water retention model for deformable soils. Géotechnique, 65(10), 793-804.

Gallipoli, D., D'Onza, F., & Wheeler, S. J. (2010). A sequential method for selecting parameter values in the Barcelona basic model. Canadian Geotechnical Journal, 47(11), 1175-1186.

Gallipoli, D., Gens, A., Sharma, R., & Vaunat, J. (2003). An elasto-plastic model for unsaturated soil incorporating the effects of suction and degree of saturation on mechanical behaviour. Géotechnique., 53(1), 123-136.

Gallipoli, D., Wheeler, S. J., & Karstunen, M. (2003). Modelling the variation of degree of saturation in a deformable unsaturated soil. Géotechnique., 53(1), 105-112.

Gardner, W. R. (1958). Some steady-state solutions of the unsaturated moisture flow equation with application to evaporation from a water table. Soil science, 85(4), 228-232.

Gens A, Alonso EE. A framework for the behaviour of unsaturated expansive clays. Canadian Geotechnical Journal, 1992; 29(6):1013-1032.

Gens, A. (1996). Constitutive modelling: Application to compacted soils. In proceedings of the first international conference on unsaturated soils/unsat'95/paris/france/6-8 september 1995. Volume 3.

Gens, A. (2010). Soil–environment interactions in geotechnical engineering. Géotechnique, 60(1), 3-74.

Gens, A., & Alonso, E. E. (1992). A framework for the behaviour of unsaturated expansive clays. Canadian Geotechnical Journal, 29(6), 1013-1032.

Georgiadis, K., Potts, D. M., & Zdravkovic, L. (2005). Three-dimensional constitutive model for partially and fully saturated soils. International Journal of Geomechanics, 5(3), 244-255.

GeoSlope International Ltd., 2007a. Seep/W User's Guide for Finite Element Seepage Analysis. GEO-SLOPE International Ltd, Calgary, Alta.

GeoSlope International Ltd., 2007b. Sigma/W User's Guide for Stress-Deformation Analysis. GEO-SLOPE International Ltd, Calgary, Alta.

GeoSlope International Ltd., 2012. Seep/W User's Guide for Finite Element Seepage Analysis. GEO-SLOPE International Ltd, Calgary, Alta.

Gibson, R. E., England, G. L., & Hussey, M. J. L. (1967). The Theory of One-Dimensional Consolidation of Saturated Clays: 1. Finite Non-Linear Consildation of Thin Homogeneous Layers. Geotechnique, 17(3), 261-273.

Gibson, R. E., Schiffman, R. L., & Cargill, K. W. (1981). The theory of one-dimensional consolidation of saturated clays. II. Finite nonlinear consolidation of thick homogeneous layers. Canadian geotechnical journal, 18(2), 280-293.

Government of Alberta, "Fact Sheet Tailings" (PDF), Government of Alberta, September 2013, archived from the original (PDF) on 25 March 2014, retrieved 12 April 2014.

Griffiths, D. V. (1980).Finite element analyses of walls, footings and slopes. PhD thesis, University of Manchester.

Griffiths, D. V. (1981). Computation of strain softening behaviour. In proceedings of the Symposium on Implementation of Computer Procedures and Stress-Strain Laws in Geotechnical Engineering, Chicago, U.S.A., (editors: C. S. Desai and S. K. Saxena), Vol. II, pp. 591-604, Acorn Press.

Griffiths, D. V., & Fenton, G. A. (1993). Seepage beneath water retaining structures founded on spatially random soil. Geotechnique, 43(4), 577-87.

Griffiths, D. V., & Fenton, G. A. (2000). Influence of soil strength spatial variability on the stability of an undrained clay slope by finite elements. In Slope stability 2000 (pp. 184-193).

Griffiths, D. V., & Fenton, G. A. (2004). Probabilistic slope stability analysis by finite elements. Journal of Geotechnical and Geoenvironmental Engineering, 130(5), 507-518.

Griffiths, D. V., & Lane, P. A. (1999). Slope stability analysis by finite elements. Geotechnique, 49(3), 387-403.

Griffiths, D. V., & Li, C. O. (1993). Analysis of delayed failure in sloping excavations. Journal of geotechnical engineering, 119(9), 1360-1378.

Griffiths, D. V., & Lu, N. (2005). Unsaturated slope stability analysis with steady infiltration or evaporation using elasto-plastic finite elements. International journal for numerical and analytical methods in geomechanics, 29(3), 249-267.

Griffiths, D. V., Fenton, G. A., & Ziemann, H. R. (2006). Seeking out failure: The random finite element method (RFEM) in probabilistic geotechnical analysis. In GeoCongress 2006: Geotechnical Engineering in the Information Technology Age (pp. 1-6).

Griffiths, D. V., Huang, J., & Dewolfe, G. F. (2011). Numerical and analytical observations on long and infinite slopes. International Journal for Numerical and Analytical Methods in Geomechanics, 35(5), 569-585.

Griffiths, D. V., Huang, J., & Fenton, G. A. (2011). Probabilistic infinite slope analysis. Computers and Geotechnics, 38(4), 577-584.

Gui, M. W., & Wu, Y. M. (2014). Failure of soil under water infiltration condition.Engineering Geology, 181, 124-141.

Hamdhan, I. N., & Schweiger, H. F. (2012). Finite element method–based analysis of an unsaturated soil slope subjected to rainfall infiltration. International Journal of Geomechanics, 13(5), 653-658.

Hawlader, B. C., Muhunthan, B., & Imai, G. (2008). State-dependent constitutive model and numerical solution of self-weight consolidation. Géotechnique, 58(2), 133-141.

Heidarian, P. (2012). Effect of Initial Water Content and Stress History on Water-Retention Behaviour of Mine Tailings (Doctoral dissertation, Carleton University Ottawa).

Hemmati, S., Gatmiri, B., Cui, Y. J., & Vincent, M. (2012). Thermo-hydro-mechanical modelling of soil settlements induced by soil-vegetation-atmosphere interactions. Engineering Geology, 139, 1-16.

Hornbaker, D. J., Albert, R., Albert, I., Barabási, A. L., & Schiffer, P. (1997). What keeps sandcastles standing?. Nature, 387(6635), 765.

Hou, T. S., Xu, G. L., Shen, Y. J., Wu, Z. Z., Zhang, N. N., & Wang, R. (2013). Formation mechanism and stability analysis of the Houba expansive soil landslide. Engineering Geology, 161, 34-43.

Houlsby, G. T. (1997). The work input to an unsaturated granular material. Géotechnique, 47(1), 193-196.

Houston, S. L., Bharadwaj, A., Welfert, B., Houston, W. N., & Walsh, K. D. (2015). Unsaturated Soil Mechanics Principles to Remove and Replace Mitigation for Expansive Clays. Journal of Geotechnical and Geoenvironmental Engineering, 142(4), 04015102.

Hoyos, L. R., Velosa, C. L., & Puppala, A. J. (2014). Residual shear strength of unsaturated soils via suction-controlled ring shear testing. Engineering Geology, 172, 1-11.

Hu, R., Chen, Y. F., Liu, H. H., & Zhou, C. B. (2013). A water retention curve and unsaturated hydraulic conductivity model for deformable soils: consideration of the change in pore-size distribution. Géotechnique, 63(16), 1389.

Huang, S., Fredlund, D. G., & Barbour, S. L. (1998). Measurement of the coefficient of permeability for a deformable unsaturated soil using a triaxial permeameter. Canadian Geotechnical Journal, 35(3), 426-432.

Huang, W., Leong, E.C., & Rahardjo, H. 2016. Translational slip failures on slope incorporating unsaturated soil mechanics. In Proceedings of the 6th Asia-pacific Conference on unsaturated soils, Guilin, China. 23 – 26 Octerber 2015. pp. 771-775.

Huang, J., & Griffiths, D. V. (2010). One-dimensional consolidation theories for layered soil and coupled and uncoupled solutions by the finite-element method. Geotechnique, 60(9), 709-713.

ICOLD (2001) Tailings Dams, Risk of dangerous occurrences, Bulletin 121. Paris, 45 pp.

Innocent-Bernard, T. (2013). Evaporation, Cracking, and Salinity in a Thickened Oil Sands Tailings (Doctoral dissertation, Carleton University Ottawa).

Innocent-Bernard, T., Simms, P., Xiaoli, Y., & Sedgwick, A. (2014, December). Multilayer deposition of two batches of thickened oil sands tailings: experiments and modeling. In *Proceedings of the International Oil Sands Tailings Conference, Lake Louise, Alta* (pp. 7-10).

Ito M, Azam S. Engineering characteristics of a glacio-lacustrine clay deposit in a semi-arid climate. Bulletin of Engineering Geology and the Environment, 2009;68:551-557.

Ito, M., & Azam, S. (2010). Determination of swelling and shrinkage properties of undisturbed expansive soils. Geotechnical and Geological Engineering, 28(4), 413-422.

Iverson RM. Landslide triggering by rain infiltration. Water Resources Research, 2000;36(7): 1897-1910.

Iverson, R. M. (2000). Landslide triggering by rain infiltration. Water resources research, 36(7), 1897-1910.

Janbu, N. 1954. Application of composite slip surfaces for stability analysis. InProc. European Conf. on Stability of Earth Slopes, Stockholm, 1954. Vol. 3, pp. 43-49.

Janbu, N. 1975, April. Slope stability computations: In Embankment-dam Engineering. Textbook. Eds. RC Hirschfeld and SJ Poulos. JOHN WILEY AND SONS INC., PUB., NY, 1973, 40P. In International Journal of Rock Mechanics and Mining Sciences and Geomechanics Abstracts Vol. 12, No. 4, p. 67. Pergamon.

Jeeravipoolvarn, S. 2010. Geotechnical behaviour of in-line thickened oil sand tailings. Doctoral thesis, University of Alberta, 410 p.

Jeldes IA, Drumm EC, Schwartz JS. Partial saturation and seismicity on steep reclaimed slopes. Geotechnical Geological Engineering, 2014;32:1065–1079.

Jennings, J. E. B., & Burland, J. B. (1962). Limitations to the use of effective stresses in partly saturated soils. Géotechnique, 12(2), 125-144.

Khalili, N., & Khabbaz, M. H. (1998). A unique relationship of chi for the determination of the shear strength of unsaturated soils. Geotechnique, 48(5).

Khalili, N., Habte, M. A., & Zargarbashi, S. (2008). A fully coupled flow deformation model for cyclic analysis of unsaturated soils including hydraulic and mechanical hystereses. Computers and Geotechnics, 35(6), 872-889.

Klausner, Y. (1991). Fundamentals of continuum mechanics of soils. Springer-Verlag, New York.

Kulhawy, F. H. (1969). Finite element analysis of the behavior of embankments (Doctoral dissertation, Library Photographic Service, University of California).

Lade, P. V. (2010). The mechanics of surficial failure in soil slopes.Engineering Geology, 114(1), 57-64.

Lai, W. M., Rubin, D. H., Rubin, D., & Krempl, E. (2009). Introduction to continuum mechanics. Butterworth-Heinemann.

Le, T. M. H., Gallipoli, D., Sanchez, M., & Wheeler, S. (2013). Rainfall-induced differential settlements of foundations on heterogeneous unsaturated soils. Géotechnique, 63(15), 1346.

Le, T. M. H., Gallipoli, D., Sánchez, M., & Wheeler, S. (2015). Stability and failure mass of unsaturated heterogeneous slopes. Canadian Geotechnical Journal, 52(11), 1747-1761.

Lechman, J. B., & Griffiths, D. V. (2000). Analysis of the progression of failure of earth slopes by finite elements. In Slope Stability 2000 (pp. 250-265)

Lee, K., & Sills, G. C. (1979). A moving boundary approach to large strain consolidation of a thin soil layer. In Proceedings, 3rd International Conference on Numerical Methods in Geomechanics (pp. 163-173).

Leong, E. C., & Rahardjo, H. (1997). Permeability functions for unsaturated soils. Journal of Geotechnical and Geoenvironmental Engineering, 123(12), 1118-1126.

Li JH, Zhang LM, Li X. Soil-water characteristic curve and hydraulic conductivity function for unsaturated cracked soil. Canadian Geotechnical Journal, 2011;48: 1010-1031.

Li WC, Lee LM, Cai H, Li HJ, Dai FC, Wang ML. Combined roles of saturated hydraulic conductivity and rainfall characteristics on surficial failure of homogeneous soil slope. Engineering Geology 2013;153: 105-113.

Li X, Li JH, Zhang LM. Predicting bimodal soil-water characteristic curves and hydraulic conductivity functions using physically based parameters. Computers and Geotechnics, 2014;57: 85-96.

Li X, Zhang LM. Characterization of dual-structure pore-size distribution of soil. Canadian Geotechnical Journal, 2009;46(2):129–41.

Li, W. C., Lee, L. M., Cai, H., Li, H. J., Dai, F. C., & Wang, M. L. (2013). Combined roles of saturated permeability and rainfall characteristics on surficial failure of homogeneous soil slope. Engineering Geology, 153, 105-113.

Li, X. S. (2005). Modelling of hysteresis response for arbitrary wetting/drying paths. Computers and Geotechnics, 32(2), 133-137.

Li, Y. C., Chen, Y. M., Zhan, T. L., Ling, D. S., & Cleall, P. J. (2010). An efficient approach for locating the critical slip surface in slope stability analyses using a real-coded genetic algorithm. Canadian Geotechnical Journal, 47(7), 806-820.

Lloret‐Cabot, M., Sánchez, M., & Wheeler, S. J. (2013). Formulation of a three‐dimensional constitutive model for unsaturated soils incorporating mechanical–water retention couplings. International Journal for Numerical and Analytical Methods in Geomechanics, 37(17), 3008-3035.

Lloret-Cabot, M., Wheeler, S. J., & Sánchez, M. (2017). A unified mechanical and retention model for saturated and unsaturated soil behaviour. Acta Geotechnica, 12(1), 1-21.

Locat, A., Leroueil, S., Fortin, A., Demers, D., & Jostad, H.P. (2015). The 1994 landslide at Sainte-Monique, Quebec: geotechnical investigation and application of progressive failure analysis. Canadian Geotechnical Journal, 52: 490-504.

Lu N, Godt J. Infinite slope stability under steady unsaturated seepage conditions. Water Resources Research, 2008;44 (11):1-13.

Lu, N., & Kaya, M. (2013). Power law for elastic moduli of unsaturated soil.Journal of Geotechnical and Geoenvironmental Engineering, 140(1), 46-56.

Lumb P. 1962. Effect of rain storms on slope stability. In Symposium on Hong Kong Soils, Hong Kong, May 1962. Edited by P. Lumb. pp. 73–87.

Lytton, R.L. 1994. Prediction of movement in expansive clay. In Vertical and Horizontal Deformations of Foundations and Embankments: Proceedings of Settlement '94, College Station, Tex., 16–18 June 1994. Edited by A.T. Yeung and G.Y. Feaalio. American Society of Civil Engineers, Geotechnical Special Publication 40, pp. 1827–1845.

Mašín, D. (2010). Predicting the dependency of a degree of saturation on void ratio and suction using effective stress principle for unsaturated soils. International Journal for Numerical and Analytical Methods in Geomechanics, 34(1), 73-90.

Matsui T, San K C. Finite element slope stability analysis by shear strength reduction technique[J]. Soils and foundations, 1992, 32(1): 59-70.

Matthews, J. G., Dhadli, N., House, P., & P. Simms. (2011). Field trials of thin-lift deposition of amended mature fine tailings at the Muskeg River Mine in Northern Alberta. Proceedings of the 14th International Seminar on Paste and Thickened Tailings, R. Jewell and A. Fourie, eds., Australian Centre for Geomechanics, Crawley, Australia, 271–280.

Matyas, E. L., & Radhakrishna, H. S. (1968). Volume change characteristics of partially saturated soils. Géotechnique, 18(4), 432-448.

McKeen R, Johnson L. Climate‐Controlled Soil Design Parameters for Mat Foundations. J. Geotech. Engrg., 1990; 116(7), 1073-1094.

McVay, M., Townsend, F., & Bloomquist, D. (1986). Quiescent consolidation of phosphatic waste clays. Journal of Geotechnical Engineering, 112(11), 1033-1049.

Meilani, I., Rahardjo, H., & Leong, E. C. (2005). Pore-water pressure and water volume change of an unsaturated soil under infiltration conditions.Canadian geotechnical journal, 42(6), 1509-1531.

Meric, D., Hellweger, F., Barbuto, S., Rahbar, N., Alshawabkeh, A. N., and Sheahan, T. C. (2013). Model prediction of long-term reactive core mat efficacy for capping contaminated aquatic sediments. J. Environ. Eng., 10.1061/(ASCE)EE.1943-7870.0000635, 564-575.

Miao, L., Liu, S., & Lai, Y. (2002). Research of soil–water characteristics and shear strength features of Nanyang expansive soil. Engineering Geology, 65(4), 261-267.

Michalowski, R. L. (2002). Stability charts for uniform slopes. Journal of Geotechnical and Geoenvironmental Engineering, 128(4), 351-355.

Miguel MG, Bonder BH. Soil-water characteristic curves obtained for a colluvial and lateritic soil profile considering the macro and micro porosity. Geotechnical Geological Engineering, 2012;30:1405-20.

Milledge, D. G., Griffiths, D. V., Lane, S. N., & Warburton, J. (2012). Limits on the validity of infinite length assumptions for modelling shallow landslides. Earth Surface Processes and Landforms, 37(11), 1158-1166.

Mizani, S., & Simms, P. (2016). Method-dependent variation of yield stress in a thickened gold tailings explained using a structure based viscosity model. *Minerals Engineering*, *98*, 40-48.

Mizani, S., Simms, P., & Wilson, W. (2017). Rheology for deposition control of polymer-amended oil sands tailings. *Rheologica Acta*, 1-12.

Monte, J. L., & Krizek, R. J. (1976). One-dimensional mathematical model for large-strain consolidation. Geotechnique, 26(3), 495-510.

Morgenstern, N. R., & Price, V. E. (1965). The analysis of the stability of general slip surfaces. Geotechnique, 15(1), 79-93.

Morris, P. H. (2002). Analytical solutions of linear finite-strain one-dimensional consolidation. Journal of geotechnical and geo-environmental engineering, 128(4), 319-326.

Morris, P. H. (2005). Analytical solutions of linear finite‐and small‐strain one‐dimensional consolidation. International journal for numerical and analytical methods in geomechanics, 29(2), 127-140.

Muntohar AS, Liao HJ. Analysis of rainfall-induced infinite slope failure during typhoon using a hydrological geotechnical model. Environmental Geology, 2009;56(6): 1145-1159.

Nelson, J. D., Chao, K. C., Overton, D. D., & Nelson, E. J. (2015). Foundation engineering for expansive soils. John Wiley & Sons.

Nelson, J. D., Chao, K. C., Overton, D. D., & Nelson, E. J. (2015). Foundation Engineering for Expansive Soils. John Wiley & Sons.

Ng CWW, Zhan LT, Bao CG, Fredlund DG, Gong BW. Performance of an unsaturated expansive soil slope subjected to artificial rainfall infiltration. Geotechnique, 2003;53(2): 143-157.

Ng, C. W. W., Wang, B., & Tung, Y. K. (2001). Three-dimensional numerical investigations of groundwater responses in an unsaturated slope subjected to various rainfall patterns. Canadian Geotechnical Journal, 38(5), 1049-1062.

Ng, C. W. W., Zhan, L. T., Bao, C. G., Fredlund, D. G., & Gong, B. W. (2003). Performance of an unsaturated expansive soil slope subjected to artificial rainfall infiltration. Geotechnique, 53(2), 143-157.

Nixon, M. F., & Grozic, J. L. (2007). Submarine slope failure due to gas hydrate dissociation: a preliminary quantification. Canadian Geotechnical Journal, 44(3), 314-325.

Nuth, M., & Laloui, L. (2008). Advances in modelling hysteretic water retention curve in deformable soils. Computers and Geotechnics, 35(6), 835-844.

Oh, W. T., Vanapalli, S. K., & Puppala, A. J. (2009). Semi-empirical model for the prediction of modulus of elasticity for unsaturated soils. Canadian Geotechnical Journal, 46(8), 903-914.

Oh, W. T. Vanapalli, S. K. Qi, S., and Han, Z. (2016). Stability of an unsaturated vertical trench. 2016 European Conference on Unsaturated Soils, Paris, France.

Olivella, S., Gens, A., Carrera, J., & Alonso, E. E. Numerical formulation for a simulator (CODE_BRIGHT) for the coupled analysis of saline media. Engineering computations, 1996;13(7): 87-112.

Pasha, A. Y., Khoshghalb, A., & Khalili, N. (2016). A void ratio dependent water retention curve model including hydraulic hysteresis. In E3S Web of Conferences (Vol. 9, p. 11010). EDP Sciences.

Pasha, A. Y., Khoshghalb, A., & Khalili, N. (2017). Hysteretic Model for the Evolution of Water Retention Curve with Void Ratio. Journal of Engineering Mechanics, 143(7), 04017030.

Pedroso, D. M., & Williams, D. J. (2010). A novel approach for modelling soil–water characteristic curves with hysteresis. Computers and Geotechnics, 37(3), 374-380.

Petterson, K. E. (1955). The early history of circular sliding surfaces. Geotechnique, 5(4), 275-296.

Pham H T V, Fredlund D G. The application of dynamic programming to slope stability analysis[J]. Canadian Geotechnical Journal, 2003, 40: 830-847.

Pham, H. Q., Fredlund, D. G., & Barbour, S. L. (2003). A practical hysteresis model for the soil-water characteristic curve for soils with negligible volume change. Géotechnique, 53(2), 293-298.

Potts, D. M., & Ganendra, D. (1994). An evaluation of substepping and implicit stress point algorithms. Computer methods in applied mechanics and engineering, 119(3-4), 341-354.

Potts, D. M., & Zdravkovic, L. (1999). Finite element analysis in geotechnical engineering: theory. London: Thomas Telford.

Potts, D. M., Dounias, G. T., & Vaughan, P. R. (1990). Finite element analysis of progressive failure of Carsington embankment. Géotechnique, 40(1), 79-101.

Potts, D. M., Kovacevic, N., & Vaughan, P. R. (1997). Delayed collapse of cut slopes in stiff clay. Géotechnique, 47(5), 953-982.

Qi, S., & Vanapalli, S. K. (2015). Hydro-mechanical coupling effect on surficial layer stability of unsaturated expansive soil slopes. Computers and Geotechnics, 70, 68-82.

Qi, S., & Vanapalli, S. K. (2016). Influence of swelling behaviour on the stability of an infinite unsaturated expansive soil slope. Computers and Geotechnics, 76, 154-169.

Qi, S., Simms, P., & Vanapalli, S. (2017a). Piecewise-linear formulation of coupled large-strain consolidation and unsaturated flow. I: Model development and implementation. *Journal of Geotechnical and Geoenvironmental Engineering*, *143*(7), 04017018.

Qi, S., Simms, P., Vanapalli, S., & Soleimani, S. (2017b). Piecewise-Linear Formulation of Coupled Large-Strain Consolidation and Unsaturated Flow. II: Testing and Performance. Journal of Geotechnical and Geoenvironmental Engineering, 143(7), 04017019.

Qi, S., & Vanapalli, S. K. (2015). Stability Analysis of an Expansive Clay Slope: A Case Study of Infiltration-Induced Shallow Failure of an Embankment in Regina, Canada. International Journal of Georesources and Environment-IJGE (formerly Int'l J of Geohazards and Environment), 1(1), 1-1.

Qi, S., & Vanapalli, S. K. (2017). Simulating the hydraulic and mechanical responses of an unsaturated expansive soil slope to rainfall: a case study. *International Journal of Geomechanics*, in press.

Qi, S. (2013). Slope Stability Analysis Based on Critical Stable State (Master's thesis, Zhejiang University).

Qi, S., Simms, P., Vanapalli, S. Daliri F. (2016). A coupled large strain consolidation-unsaturated flow model for tailings deposition analysis. In Proceedings of the 69th Canadian Geotechnical Conference, Vancouver City, Canada.

Qi, S., & Vanapalli, S. K. (2015) Numerical study on expansive soil slope stability considering the effect of swelling behaviour and cracks. In Proceedings of the 2015 Asia-Pacific Conference on Unsaturated Soils, Guilin, China.

Qi, S., & Vanapalli, S. K. (2015) Numerical analysis of slope stability in expansive soil: a case study of field test in Henan province, Canada. In Proceedings of the 68th Canadian Geotechnical Conference & 7th Canadian Permafrost Conference, Québec City, Canada

Rahardjo H, Lim TT, Chang MF, Fredlund DG. Shear strength characteristics of a residual soil. Canadian Geotechnical Journal, 1995;32(1): 60–77.

Rahardjo H, Ong TH, Rezaur RB, Leong EC. Factors controlling instability of homogeneous soil slopes under rainfall. Journal of Geotechnical and Geoenvironmental Engineering, 2007;133 (12), 1532–1543.

Rahardjo, H., & Fredlund, D. G. (1995). Procedures for slope stability analyses involving unsaturated soils. Developments in deep foundations and ground improvement schemes. Balkema, Rotterdam, 33-56.

Rahardjo, H., Melinda, F., Leong, E. C., & Rezaur, R. B. (2011). Stiffness of a compacted residual soil. Engineering Geology, 120(1), 60-67.

Rahardjo, H., Santoso, V. A., Leong, E. C., Ng, Y. S., Tam, C. P. H., & Satyanaga, A. (2013). Use of recycled crushed concrete and Secudrain in capillary barriers for slope stabilization. Canadian Geotechnical Journal, 50(6), 662-673.

Raveendiraraj A (2009) Coupling of mechanical behaviour and water retention behaviour in unsaturated soils. Ph.D. Thesis, University of Glasgow.

Ren, J., & Vanapalli, S. K. (2017) Prediction of the Resilient Modulus of Frozen Unbound Road Materials Using the Soil-Freezing Characteristic Curve. Canadian Geotechnical Journal. (ja).

Richards, B. G. (1985). Pressures on a retaining wall by an expansive clay. Golden Jubilee of the International Society for Soil Mechanics and Foundation Engineering: Commemorative Volume, 241.

Richards, B. G., & Kurzeme, M. (1973). Observations of Earth Pressures on a Retaining Wall at the Gouger Street Mail Exchange, Adelaide (No. Res Paper No. 220).

Richards, L. A. (1931). Capillary conduction of liquids through porous mediums. Journal of Applied Physics, 1(5), 318-333.

Rouainia, M., Davies, O., O'Brien, T., & Glendinning, S. (2009, June). Numerical modelling of climate effects on slope stability. In Proceedings of the Institution of Civil Engineers-Engineering Sustainability (Vol. 162, No. 2, pp. 81-89). Thomas Telford Ltd.

Rozina, E., Mizani, S., Malek, M., Sanchez-Sardon, M., & Simms, P. (2015). Dewatering in a laboratory simulation of a multilayer deposit of inline flocculated mature fine tailings. Proceedings of the 18th International Seminar on Paste and Thickened Tailings, R. Jewell and A. Fourie. Australian Centre for Geomechanics, Crawley, Australia, 81-94.

S. Kam, N. Hmidi, Y. Mao. Field performance of thickened tailings disposal at Musselwhite Mine the Proceedings of the 17th International Seminar on Paste and Thickened Tailings, held in Vancouver, Canada, June 8-12, 2014. Published by InfoMine Inc., June 2014.

Sadeghi, M., Shokri, N., & Jones, S. B. (2012). A novel analytical solution to steady‐state evaporation from porous media. Water Resources Research,48(9).

Salager, S., Nuth, M., Ferrari, A., & Laloui, L. (2013). Investigation into water retention behaviour of deformable soils. Canadian Geotechnical Journal, 50(2), 200-208.

Salfate, E. R. (2011). Predicting void ratio for surface paste tailings deposited in thin layers (Doctoral dissertation, University of British Columbia).

Sánchez, M., Gens, A., Guimarães, L., & Olivella, S. (2008). Implementation algorithm of a generalised plasticity model for swelling clays. Computers and Geotechnics, 35(6), 860-871.

Santoso AM, Phoon KK, Quek ST. Effect of 1D infiltration assumption on stability of spatially variable slope. GeoRisk ASCE, 2011;704-711.

Sarma, S. K. 1973. Stability analysis of embankments and slopes. Géotechnique, 23(3), 423-433.

Satyanaga A, Rahardjo H, Leong EC, Wang JY. Water characteristic curve of soil with bimodal grain-size distribution. Computers and Geotechnics, 2013;48:51-61.

Scoular, R. E. G. (1997). Limit equilibrium slope stability analysis using a stress analysis. M. Sc, University of Saskatchewan, Saskatoon, Canada.

Seneviratne, N. H., Fahey, M., Newson, T. A., & Fujiyasu, Y. (1996). Numerical modelling of consolidation and evaporation of slurried mine tailings. International Journal for Numerical and Analytical Methods in Geomechanics, 20(9), 647-671.

Sheng, D. (2011). Review of fundamental principles in modelling unsaturated soil behaviour. Computers and Geotechnics, 38(6), 757-776.

Sheng, D., Fredlund, D. G., & Gens, A. (2008). A new modelling approach for unsaturated soils using independent stress variables. Canadian Geotechnical Journal, 45(4), 511-534.

Sheng, D., Sloan, S. W., & Gens, A. (2004). A constitutive model for unsaturated soils: thermomechanical and computational aspects. Computational Mechanics, 33(6), 453-465.

Sheng, D., Sloan, S. W., & Yu, H. S. (2000). Aspects of finite element implementation of critical state models. Computational mechanics, 26(2), 185-196.

Sheng, D., Sloan, S. W., Gens, A., & Smith, D. W. (2003). Finite element formulation and algorithms for unsaturated soils. Part I: Theory. International Journal for Numerical and Analytical Methods in Geomechanics, 27(9), 745-765.

Sheng, D., Smith, D. W., W Sloan, S., & Gens, A. Finite element formulation and algorithms for unsaturated soils. Part II: Verification and application. International Journal for Numerical and Analytical Methods in Geomechanics, 2003;27(9): 767-790.

Shi, B., Jiang, H., Liu, Z., & Fang, H. Y. (2002). Engineering geological characteristics of expansive soils in China. Engineering Geology, 67(1), 63-71.

Shuai, F. (1996). Simulation of swelling pressure measurements on expansive soils. (Doctoral thesis, University of Saskatchewan)

Shuai, F., & Fredlund, D. G. (1998). Model for the simulation of swelling-pressure measurements on expansive soils. Canadian Geotechnical Journal,35(1), 96-114.

Simms, P. (2017). 2013 Colloquium of the Canadian Geotechnical Society: Geotechnical and geoenvironmental behaviour of high-density tailings. Canadian Geotechnical Journal, 54(4), 455-468.

Simms, P. H., & Yanful, E. K. (2002). Predicting soil-water characteristic curves of compacted plastic soils from measured pore-size distributions. Géotechnique, 52(4), 269-278.

Simms, P. H., & Yanful, E. K. (2005). A pore-network model for hydromechanical coupling in unsaturated compacted clayey soils. Canadian Geotechnical Journal, 42(2), 499-514.

Simms, P., Dunmola, A., Fisseha, B., & Bryan, R. (2010). Generic modeling of desiccation for cyclic deposition of thickened tailings to maximize density and to minimize oxidation. Proceedings of the 13th International Seminar on Paste and Thickened Tailings, R. Jewell and A. Fourie. Australian Centre for Geomechanics, Crawley, Australia, 293-303.

Simms, P., Grabinsky, M., & Zhan, G. (2007). Modelling evaporation of paste tailings from the Bulyanhulu mine. Canadian Geotechnical Journal, 44(12), 1417-1432.

Simms, P., Sivathayalan, S., & Daliri, F. (2013). Desiccation in dewatering and strength development of high-density hard rock tailings. In *Proc., 16th Int. Seminar on Paste and Thickened Tailings* (pp. 75-86). Australian Centre for Geomechanics, Crawley, Australia.

Simms, P., Soleimani, S., Mizani, S., Daliri, F., Dunmola, A., Rozina, E., & Innocent-Bernard, T. (2017). Cracking, salinity and evaporation in mesoscale experiments on three types of tailings. Environmental Geotechnics, 1-15.

Šimůnek, J., Šejna, M., Saito, H., Sakai, M., and van Genuchten, M.Th. (2013). The Hydrus-1D Software Package for Simulating the Movement of Water, Heat, and Multiple Solutes in Variably Saturated Media, Version 4.17. Hydrus Software Series 3, Department of Environmental Sciences, University of California Riverside, Riverside, California, USA, 342 pages.

Šimunek, J., Van Genuchten, M. T., & Šejna, M. (2012). HYDRUS: Model use, calibration, and validation. Transactions of the ASABE, 55(4), 1263-1274.

Skempton AW, Deloy FA. 1957. Stability of natural slopes in London Clay. Proceedings of the 4th International Conference on Soil Mechanics and Foundation Engineering, vol. 2, pp. 378–381.

Skempton, A. W. (1964). Long-term stability of clay slopes. Géotechnique, (14), 77-102.

Soleimani, S., Simms, P., Dunmola, A., Freeman, G., & Wilson. G. W. (2014) Desiccation and consolidation in thin-lift deposition of polymer-amended mature fine tailings. Proceedings of the 17th International Seminar on Paste and Thickened Tailings, R. Jewell, A. Fourie, P. S. Wells and D. van Zyl. eds., Australian Centre for Geomechanics, Crawley, Australia, 307-322.

Sołowski, W. T., & Gallipoli, D. (2010). Explicit stress integration with error control for the Barcelona Basic Model: Part I: Algorithms formulations.Computers and Geotechnics, 37(1), 59-67.

Sołowski, W. T., Sloan, S. W., & Wang, D. (2014). Material point method simulation of triaxial shear tests. Computer Methods and Recent Advances in Geomechanics, 169.

Spencer, E. 1967. A method of analysis of the stability of embankments assuming parallel inter-slice forces. Géotechnique, 17(1): 11-26.

Srivastava, R., & Yeh, T. C. J. (1991). Analytical solutions for one‐dimensional, transient infiltration toward the water table in homogeneous and layered soils. Water Resources Research, 27(5), 753-762.

Stianson, J. R., Fredlund, D. G., & Chan, D. (2011). Three-dimensional slope stability based on stresses from a stress-deformation analysis. Canadian Geotechnical Journal, 48(6), 891-904.

Sun, W., & Sun, D. A. (2012). Coupled modelling of hydro‐mechanical behaviour of unsaturated compacted expansive soils. International Journal for Numerical and Analytical Methods in Geomechanics, 36(8), 1002-1022.

Tarantino, A. (2009). A water retention model for deformable soils. Géotechnique, 59(9), 751-762.

Tavenas, F., Trak, B., & Leroueil, S. (1980). Remarks on the validity of stability analyses. Canadian Geotechnical Journal, 17(1), 61-73.

Taylor DW. 1948. Fundamentals of Soil Mechanics. John Wiley & Sons, Inc., New York, N. Y.

Terzaghi, K., & Peck, R. B. (1948). Soil mechanics in engineering practice, 1st edn. Wiley, New York.

Teunissen, J. A. M., & Spierenburg, S. E. J. (1996). Stability of infinite slopes. In International Journal of Rock Mechanics and Mining Sciences and Geomechanics Abstracts (Vol. 3, No. 33, p. 137A).

Thomas, H. R., & He, Y. (1998). Modelling the behaviour of unsaturated soil using an elastoplastic constitutive model. Géotechnique, 48(5), 589-603.

Thomas, M. G., Puppala, A. J., & Hoyos, L. R. (2009). Influence of swell pressure from expansive fill on retaining wall stability. Contemporary Topics in Ground Modification, Problem Soils, and Geo-support, pp. 590-597.

Tommasi, P., Boldini, D., Caldarini, G., & Coli, N. (2012). Influence of infiltration on the periodic re-activation of slow movements in an overconsolidated clay slope. Canadian Geotechnical Journal, 50(1), 54-67.

Townsend, F. C., & McVay, M. C. (1990). SOA: Large strain consolidation predictions. Journal of Geotechnical Engineering.

Tran, D. T., Fredlund, D. G., & Chan, D. H. (2016). Improvements to the calculation of actual evaporation from bare soil surfaces. Canadian Geotechnical Journal, 53(1), 118-133.

Troncone, A. (2005). Numerical analysis of a landslide in soils with strain-softening behaviour. Géotechnique, 55(8), 585-596.

Tschuchnigg, F., Schweiger, H. F., & Sloan, S. W. (2015). Slope stability analysis by means of finite element limit analysis and finite element strength reduction techniques. Part II: Back analyses of a case history. Computers and Geotechnics, 70, 178-189.

Tsiampousi, A., Zdravkovic, L., & Potts, D. M. (2013). A three-dimensional hysteretic soil-water retention curve. Geotechnique, 63(2), 155.

Urciuoli, G. (2002). Strains preceding failure in infinite slopes. International Journal of Geomechanics, 2(1), 93-112.

Urciuoli, G., Picarelli, L., & Leroueil, S. (2007). Local soil failure before general slope failure. Geotechnical and Geological Engineering, 25(1), 103-122.

van Genuchten, M. T. (1980). A closed-form equation for predicting the hydraulic conductivity of unsaturated soils. Soil science society of America journal, 44(5), 892-898.

van Genuchten, M. T., & Nielsen, D. R. (1985). On describing and predicting the hydraulic properties of unsaturated soils. Ann. Geophys, 3(5), 615-628.

Vanapalli SK, Oh WT. A model for predicting the modulus of elasticity of unsaturated soils using the soil-water characteristic curve. International Journal of Geotechnical Engineering, 2010;4: 425-433.

Vanapalli, S. K. (2009, November). Shear strength of unsaturated soils and its applications in geotechnical engineering practice. In Keynote Address. Proc. 4th Asia-Pacific Conf. on Unsaturated Soils. New Castle, Australia (pp. 579-598).

Vanapalli, S. K., Fredlund, D. G., & Pufahl, D. E. (1999). The influence of soil structure and stress history on the soil–water characteristics of a compacted till. Géotechnique, 49(2), 143-159.

Vanapalli, S. K., Fredlund, D. G., Pufahl, D. E., & Clifton, A. W. (1996). Model for the prediction of shear strength with respect to soil suction.Canadian Geotechnical Journal, 33(3), 379-392.

Vanapalli, S., & Lu, L. (2012). A state-of-the art review of 1-D heave prediction methods for expansive soils. International Journal of Geotechnical Engineering, 6(1), 15-41.

Vaunat, J., Romero, E., & Jommi, C. (2000). An elastoplastic hydromechanical model for unsaturated soils. Experimental evidence and theoretical approaches in unsaturated soils, 121-138.

Vilar, O. M. (2006). A simplified procedure to estimate the shear strength envelope of unsaturated soils. Canadian Geotechnical Journal, 43(10), 1088-1095.

Vu, H. Q., & Fredlund, D. G. (2006). Challenges to modelling heave in expansive soils. Canadian Geotechnical Journal, 43(12), 1249-1272.

Wang, G., & Wei, X. (2014). Modeling swelling–shrinkage behaviour of compacted expansive soils during wetting–drying cycles. Canadian Geotechnical Journal, 52(999), 1-12.

Wells, P. S. (2011). Long term in-situ behaviour of oil sands fine tailings in Suncor's Pond 1A. Proceeding of the Conference on Tailings and Mine Waste 2011. Vancouver, BC

Wells, P. S., Revington, A., & Omotoso, O. (2011). Mature fine tailings drying–technology update. Proceedings of the 14th International Seminar on Paste and Thickened Tailings, R. Jewell and A. Fourie, eds., Australian Centre for Geomechanics, Crawley, Australia, 155–166.

Wheeler, S. J., & Karube, D. (1996). Constitutive modelling. In proceedings of the first international conference on unsaturated soils/unsat'95/paris/france/6-8 september 1995. volume 3.

Wheeler, S. J., & Sivakumar, V. (1995). An elasto-plastic critical state framework for unsaturated soil. Géotechnique, 45(1), 35-53.

Wheeler, S. J., Gallipoli, D., & Karstunen, M. (2002). Comments on use of the Barcelona Basic Model for unsaturated soils. International journal for numerical and analytical methods in Geomechanics, 26(15), 1561-1571.

Wheeler, S. J., Sharma, R. S., & Buisson, M. S. R. (2003). Coupling of hydraulic hysteresis and stress–strain behaviour in unsaturated soils. Géotechnique, 53(1), 41-54.

Widger, R.A., & Fredlund, D.G. (1979). Stability of swelling clay embankments. Canadian Geotechnical Journal, 16(1), 140-151.

Wilson, G. W., Fredlund, D. G., & Barbour, S. L. (1994). Coupled soil-atmosphere modelling for soil evaporation. Canadian Geotechnical Journal,31(2), 151-161.

Wilson, G. W., Fredlund, D. G., & Barbour, S. L. (1997). The effect of soil suction on evaporative fluxes from soil surfaces. Canadian Geotechnical Journal, 34(1), 145-155.

Windal, T., & Shahrour, I. (2002). Study of the swelling behaviour of a compacted soil using flexible odometer. Mechanics Research Communications, 29(5), 375-382.

Wong TT, Fredlund DG, Krahn J (1998). A numerical study of coupled consolidation in unsaturated soils. Canadian Geotechnical Journal, 1998;35: 926–937.

Wright, S. G., Kulhawy, F. G., & Duncan, J. M. (1973). Accuracy of equilibrium slope stability analysis. Journal of Soil Mechanics & Foundations Div, 99(Proc Paper 10097).

Wu, L. Z., & Zhang, L. M. (2009). Analytical solution to 1D coupled water infiltration and deformation in unsaturated soils. International Journal for Numerical and Analytical Methods in Geomechanics, 33(6), 773-790.

Wu, L. Z., Zhang, L. M., & Huang, R. Q. (2012). Analytical solution to 1D coupled water infiltration and deformation in two‐layer unsaturated soils. International Journal for Numerical and Analytical Methods in Geomechanics, 36(6), 798-816.

Xiao, H. B., Zhang, C. S., Wang, Y. H., & Fan, Z. H. (2011). Pile-soil interaction in expansive soil foundation: Analytical solution and numerical simulation. International Journal of Geomechanics, 11(3), 159-166.

Xu, L., Dai, F., Chen, J., Iqbal, J., & Qu, Y. (2014). Analysis of a progressive slope failure in the Xiangjiaba reservoir area, Southwest China. Landslides, 11(1), 55-66.

Yao, D. T., de Oliveira‐Filho, W. L., Cai, X. C., & Znidarcic, D. (2002). Numerical solution for consolidation and desiccation of soft soils. International Journal for Numerical and Analytical Methods in Geomechanics, 26(2), 139-161.

Yong, R. N., Siu, S. K., & Sheeran, D. E. (1983). On the stability and settling of suspended solids in settling ponds. Part I. Piece-wise linear consolidation analysis of sediment layer. Canadian Geotechnical Journal, 20(4), 817-826.

Yoshida RT, Fredlund DG, Hamilton JJ. The prediction of total heave of a slab-on-grade floor on Regina clay. Canadian Geotechnical Journal, 1983; 20(1): 69-81.

Zabala, F., & Alonso, E. E. (2011). Progressive failure of Aznalcóllar dam using the material point method. Géotechnique, 61(9), 795-808.

Zhan TLT, Jia GW, Chen YM, Fredlund DG, Li H. An analytical solution for rainfall infiltration into an unsaturated infinite slope and its application to slope stability analysis, Int. J. Numer. Anal. Meth. Geomech. 2013;37:1737–1760.

Zhan, L. (2003). Field and laboratory study of an unsaturated expansive soil associated with rain-induced slope instability (Doctoral dissertation).

Zhan, L. T., Chen, P., & Ng, C. W. W. (2007). Effect of suction change on water content and total volume of an expansive clay. Journal of Zhejiang University SCIENCE A, 8(5), 699-706.

Zhan, T. L. T., Chen, R., & Ng, C. W. W. (2014). Wetting-induced softening behaviour of an unsaturated expansive clay. Landslides, 11(6), 1051-1061.

Zhan, T. L., & Ng, C. W. (2006). Shear strength characteristics of an unsaturated expansive clay. Canadian Geotechnical Journal, 43(7), 751-763.

Zhan, T. L., Jia, G. W., Chen, Y. M., Fredlund, D. G., & Li, H. (2013). An analytical solution for rainfall infiltration into an unsaturated infinite slope and its application to slope stability analysis. International Journal for Numerical and Analytical Methods in Geomechanics, 37(12), 1737-1760.

Zhan, T. L., Ng, C. W., & Fredlund, D. G. (2007). Field study of rainfall infiltration into a grassed unsaturated expansive soil slope. Canadian Geotechnical Journal, 44(4), 392-408.

Zhang L.L., Fredlund DG, Zhang LM, Tang WH. Numerical study of soil conditions under which matric suction can be maintained. Canadian Geotechnical Journal, 2004;41: 569–582.

Zhang L.L., Zhang J, Zhang LM, Tang WH. Stability analysis of rainfall-induced slope failure: a review. Geotechnical Engineering, 2010;164(GE5): 299–316.

Zhang L.L., Zhang LM, Tang WH. Rainfall-induced slope failure considering variability of soil properties. Geotechnique, 2005;55(2): 183–188.

Zhang L.M., Fredlund DG. Characteristics of water retention curves for an unsaturated fractured rock mass. In Proceedings of the Second Asian Conference on Unsaturated Soils, Osaka, Japan, 9–13 November 2003. Edited by D. Karrube, A. Iizuka, S. Kato, and K. Kawai. 2003;pp. 425–429.

Zhang, F. Z., & X.P., Chen. (2010). Influence of repeated drying and wetting cycles on mechanical behaviors of unsaturated soil. Chinese Journal of Geotechnical Engineering, 32(1), 41-46.

Zhang, L. L., Fredlund, D. G., Fredlund, M. D., & Wilson, G. W. (2014). Modeling the unsaturated soil zone in slope stability analysis 1. Canadian Geotechnical Journal, 51(12), 1384-1398.

Zhang, L. L., Fredlund, D. G., Zhang, L. M., & Tang, W. H. (2004). Numerical study of soil conditions under which matric suction can be maintained. Canadian Geotechnical Journal, 41(4), 569-582.

Zhang, L. L., Fredlund, M. D., Fredlund, D. G., Lu, H., & Wilson, G. W. (2015). The influence of the unsaturated soil zone on 2-D and 3-D slope stability analyses. Engineering Geology, 193, 374-383.

Zhang, X., & Briaud, J. L. (2015). Three dimensional numerical simulation of residential building on shrink–swell soils in response to climatic conditions. International Journal for Numerical and Analytical Methods in Geomechanics, 39(13), 1369-1409.

Zhang, X., & Lytton, R. L. (2009a). Modified state-surface approach to the study of unsaturated soil behavior. Part I: Basic concept. Canadian Geotechnical Journal, 46(5), 536-552.

Zhang, X., & Lytton, R. L. (2009b). Modified state-surface approach to the study of unsaturated soil behavior. Part II: General formulation. Canadian Geotechnical Journal, 46(5), 553-570.

Zhang, X., & Xiao, M. (2013). Using modified state surface approach to select parameter values in the Barcelona basic model. International Journal for Numerical and Analytical Methods in Geomechanics, 37(12), 1847-1866.

Zheng, Hong, L. G. Tham, and Defu Liu. "On two definitions of the factor of safety commonly used in the finite element slope stability analysis." Computers and Geotechnics 33.3 (2006): 188-195.

Zhou, A. N., Sheng, D., Sloan, S. W., & Gens, A. (2012). Interpretation of unsaturated soil behaviour in the stress–Saturation space, I: Volume change and water retention behaviour. Computers and Geotechnics, 43, 178-187.

Zhou, A., Li, C. Q., & Huang, J. (2016). Failure analysis of an infinite unsaturated soil slope. Proceedings of the Institution of Civil Engineers-Geotechnical Engineering, 1-11.

Zhou, J. W., Xu, F. G., Yang, X. G., Yang, Y. C., & Lu, P. Y. (2016). Comprehensive analyses of the initiation and landslide-generated wave processes of the 24 June 2015 Hongyanzi landslide at the Three Gorges Reservoir, China. Landslides, 13(3), 589-601.

Zienkiewicz O C, Humpheson C, Lewis R W. Associated and non-associated visco-plasticity and plasticity in soil mechanics. Geotechnique, 1975, 25(4): 671-689.

Znidarčić, D., Schiffman, R. L., Pane, V., Croce, P., Ko, H. Y., & Olsen, H. W. (1986). The theory of one-dimensional consolidation of saturated clays: part V, constant rate of deformation testing and analysis. Géotechnique, 36(2), 227-237.

Publications

Journal publications

1. **Shunchao QI,** Paul Simms. Daliri F. Heidarian, P. Vanapalli Sai. Coupled analysis of large strain consolidation and unsaturated flow accounting for stress history. *Submitted*.

2. **Shunchao QI,** Sai K. Vanapalli. Simulating the hydraulic and mechanical responses of an expansive soil slope to rainfall, a case history. *International Journal of Geomechanics*. Accepted for publication.

3. **Shunchao QI**, Paul Simms, Sai K. Vanapalli. Piecewise-Linear Formulation of Coupled Large Strain Consolidation and Unsaturated Flow. I: Model Development and Implementation, *Journal of Geotechnical and Geoenvironmental Engineering*, 2017. DOI: http://dx.doi.org/10.1061/(ASCE) GT.1943-5606.0001657.

4. **Shunchao QI**, Paul Simms, Sai K. Vanapalli. Piecewise-Linear Formulation of Coupled Large Strain Consolidation and Unsaturated Flow. II: Testing and Performance, Journal of Geotechnical and Geoenvironmental Engineering, 2017. DOI: http://dx.doi.org/10.1061/(ASCE)GT.1943-5606.0001658.

5. **Shunchao QI**, Sai K. Vanapalli. Influence of swelling behavior on the stability of an infinite unsaturated expansive soil slope, *Computers and Geotechnics***,** 2016. 76: 154-169. DOI: 10.1016/j.compgeo.2016.02.018

6. **Shunchao QI**, Sai K. Vanapalli. Hydro-mechanical coupling effect on surficial layer stability of unsaturated expansive soil slopes, *Computers and Geotechnics*, 2015, 70: 68-82. DOI: 10.1016/j.compgeo.2015.07.006.

7. **Shunchao QI**, Sai K. Vanapalli. Stability analysis of an expansive clay slope: a case study of infiltration-induced shallow failure of an embankment in Regina, Canada. *International Journal of Geohazards and Environment*, 2015, 1(1):7-19. DOI: 10.15273/ijge.2015.01.003.

8. LING Daosheng, **QI Shunchao**, CHEN Feng, LI Nan. A limit equilibrium model based on Morgenstern-Price method for 3D slope analysis, *Chinese Journal of Rock Mechanics and Engineering*. 2013, 32(1):107-116.

9. Zhong Shiying, Huang Genqing, **Qi Shunchao**, et al. Interface property between soft landing foot pad and simulant lunar soil[J]. *Rock and Soil Mechanics*, 2013, 34(4): 1058-1062**.**

10. **Shunchao Qi,** Penghai Yin, & Sai K. Vanapalli. Numerical analysis of slope stability in expansive soil: a case study of field test. *Indian Geotechnical Journal*. Submitted.

Selected conference publications

11. **Shunchao QI**, and Vanapalli, S. K. Numerical study on expansive soil slope stability considering the effect of swelling behaviour and cracks. In Proceedings of the 2015 Asia-Pacific Conference on Unsaturated Soils, Guilin, China.

12. **Shunchao QI**, and Vanapalli, S. K. Numerical analysis of slope stability in expansive soil: a case study of field test in Henan province, Canada. In Proceedings of the 68th Canadian Geotechnical Conference & 7th Canadian Permafrost Conference, Québec City, Canada.

13. Sai K. Vanapalli, **Shunchao QI.** The effect of swelling behavior on the surficial layer stability of an expansive soil slope. 2014 international conference on expansive soil engineering techniques, **Keynote lecture**, Wuhan, China. 2014.

14. Oh, W. T. Vanapalli, S. K. **Shunchao QI**, and Han, Z. (2016). Stability of an unsaturated vertical trench. 2016 European Conference on Unsaturated Soils, Paris, France.

15. **Shunchao QI**, Paul Simms, Sai K. Vanapalli, F. Daliri (2016). A coupled large strain consolidation-unsaturated flow model for tailings deposition analysis. In Proceedings of the 69th Canadian Geotechnical Conference, Vancouver City, Canada.

16. Penghai Yin, **Shunchao Qi** & Sai K. Vanapalli. A Framework for Predicting the Depth of Desiccation-induced Cracks in Clayey Soils. In Proceedings of the 69th Canadian Geotechnical Conference, Vancouver City, Canada.

17. **Shunchao QI**, Paul Simms, Sai K. Vanapalli, F. Daliri (2016). A coupled large strain consolidation-unsaturated flow model for tailings deposition analysis. In Proceedings of the 70th Canadian Geotechnical Conference, Ottawa, Canada.

18. **Shunchao QI**, Paul Simms (2017). Modelling thixotropy at short and long time scales in dewatering analyses for soft soil or tailings. In Proceedings of the 70th Canadian Geotechnical Conference, Ottawa, Canada.

19. **Shunchao QI**, Penghai Yin, Sai Vanapalli (2017). Modelling thixotropy at short and long time scales in dewatering analyses for soft soil or tailings. In Proceedings of the 70th Canadian Geotechnical Conference, Ottawa, Canada.

20. **Shunchao Qi**, Wiliam Thomas, Paul Simms, Nuri Hmidi. (2017) Hydro-geotechnical analysis of a thickened tailings deposit in Northern Canada. Tailings and Mine Waste Conference, Banff, Alberta**.**